The University Of Sheffield.

Application of Novel Flame Acceleration Enhancing Obstacles to Pulse Detonation Engines

by

Jonathan.N.Knapton

A thesis submitted in partial fulfillment for the degree of Doctor of Philosophy

in the
Faculty of Engineering
Department of Mechanical Engineering

July 2016

UNIVERSITY OF SHEFFIELD

ABSTRACT

FACULTY OF ENGINEERING
DEPARTMENT OF MECHANCIAL ENGINEERING

Doctor of Philosophy

by Jonathan.N.Knapton

This work aims to explore the effect of novel obstacle geometries on flame acceleration and transition to detonation in pulse detonation engines. To this end, a pulse detonation engine ground test demonstration rig has been developed and tested using stoichiometric propane-air mixtures. Much of this work has been invested into rig and instrumentation development as well as performing and analysing experiments. The rig has been tested using two different combustion chamber diameters, 88.9mm and 38.1mm, with lengths of 1m and 1.18m respectively. In addition, experiments were carried out with an orifice filled tubular insert which restricted the internal diameter to 31.75mm over a distance of 14 tube diameters.

A semi-empirical model has also been developed and validated for use in the prediction of flame acceleration (FA) through circular orifice plates. This was validated for a range of obstacle BRs and tube lengths. The model was found to perform well, within one order of magnitude in all cases. Where modelling predictions fell beyond one standard deviation of the experimental mean it is thought that the discrepancy is a result of insufficient purging.

Experimental shock speed, pressure and flame speed have been analysed using statistical density functions for a range of orifice fractal dimensions, orifice plate blockage ratios (BR) and obstacle lengths. Of particular interest are the novel experimental results produced by varying orifice fractal dimension or BR in separate tests along the length of the obstacle. It was found that decreasing the orifice plate BR along the obstacle length increased the exit flame speed by a mean value of 27% over a constant 0.57BR orifice. Experimental results for higher fractal dimension orifice plates produced greater shock speeds than circular orifices with 12D long obstacles. This effect diminished with increased obstacle length.

Contents

List of Figures

List of Tables

Nomenclature

Label	Description	Units
Latin		
A	Empirical Modelling Constant	
a_b	Speed of sound in combustion products	*(m/s)*
a_d	Cross sectional area of duct	*(m^2)*
A_f	Accelerating flame surface area	*(m^2)*
A_N	Nozzle hole surface area	*(m^2)*
a_v	Empirical Modelling Constant	
A_{wel}	Weller combusiton model empirical constant	*(m/s)*
b	Reaction regress variable	*(-)*
b_v	Empirical Modelling Constant	
c	Venting number	*(-)*
c_3	Speed of sound in the combustion products	*(m/s)*
c_p	Specific heat capacity	*(kJ/kg.K)*
D	PDE tube largest internal diameter	*(m)*
d	Orifice or other obstacle internal diameter	*(m)*
d_c	Critical (minimum) tube diameter	*(m)*
Da	Damkholer Number	*(-)*
D_L	Diffusion rate of the limiting reactant	(M/s)
Ea	Activation Energy	*(J)*
e	Enthalpy	*(kJ/Kg)*
f	Frequency	*(Hz)*
ff	Fill Factor	*(-)*
f_i	Species body force	*(N)*
g_0	Gravitational constant, 9.80665	(m/s^2)
h	Obstacle radial height from the tube wall	*(m)*
I_v	Impulse per unit volume	
I_{sp}	Specific Impulse	
k	Turbulent kinitic energy	*(J/kg)*
$Ka_{0.8}$	Karlovitz stretch factor	

l_0	Integral turbulence length scale	*(m)*
l_κ	Kolmogorov turbulence length scale	*(m)*
L	Critical DDT geometric length	*(m)*
L_1	Critical DDT geometry length variable	*(m)*
L_e	Lewis Number	*(-)*
L_M	Markstein Length	*(m)*
ℓ_k	Kolmogorov turbulence length scale	
ℓ_0	Integral turbulence length scale	
$\dot{m}$	Mass flow	*(Kg/s)*
M	Mach Number	*(-)*
Ma	Markstein Number	*(-)*
Ma_{sr}	Markstein Number for stretch rate	*(-)*
P	Pressure	*(bar)*
pf	Purge Factor	*(-)*
Pe	Peclet Number	*(-)*
$P_{cr}e$	Critical Peclet Number	*(-)*
Pr	Prandtl Number	*(-)*
P_CJ	Chapman Jouget Detonation Pressure	*(bar)*
r	Orifice plate pressure ratio	*(-)*
R_g	Gas constant	$(units)$
R	Radius of combustion chamber (widest)	*(m)*
Re	Reynolds Number	*(-)*
R_f	Flame characteristic radius of curvature	*(m)*
S	Orifice spacing	*(m or Dia.)*
S_f	Flame speed	(m/s)
S_g	Gas speed	(m/s)
S_{ij}	Strain rate tensor in the ij direction	$(units)$
S_L	Laminar flame speed	(m/s)
S_n	Normal stretched flame speed	(m/s)
T	Thrust	*(N)*
t	Time	*(s)*
T_b	Temperature of burnt reactants	*(K)*
T_u	Temperature of unburnt products	*(K)*
u	Gas velocity	*(m/s)*
u'	Turbulent rms gas velocity	*(m/s)*
u'_0	Integtal length scale turbulence rms gas velocity	*(m/s)*
u_tm	Turbulent flame speed	*(m/s)*
V	Volume N	(m^3)
V_f	Flame tip velocity	*(m/s)*
V_g	Gas velocity	*(m/s)*
V_{CJ}	Chapman Jouguet Detonation Velocity	*(m/s)*

V_i	Species diffusion rate	*(M/s)*
W	Empirical constant	*(-)*
w_i	Species mass reaction rate	*(kg/s)*
X/D	Non dimensional distance along the PDE axis	*(-)*
X_{DDT}	Distance from ignition to DDT location	*(Dia. or m)*
X_S	Distance from ignition to flame choking	*(Dia. or m)*
Y_i	Species mass fraction	*(-)*
Y_f	Fuel mass fraction	*(-)*
Y	Product mass fraction	*(-)*
Z_f	Flame tip location	*(m or X/D)*

Greek

α	Stretch rate	(s^{-1})
α_β	Ratio of internal to external dia.	$(-)$
α_B	Empirical Modelling constant	$(-)$
α_c	Curvature rate	(s^{-1})
α_D	Empirical Modelling constant	$(-)$
α_g	Modelling constant	$(-)$
α_o	Orifice plate flow coefficient	
α_s	Strain rate	(s^{-1})
α_1	Modeling constant	
β	Zeldovich number	*(-)*
β_B	Empirical Modeling constant	
β_o	orifice diameter ratio	*(-)*
β_1	Modeling constant	
β_2	Modeling constant	
β^*	Modeling constant	
β_G	Empirical modeling constant	
γ	Ratio of specific heats	*(-)*
δ_l	Laminar flame thickness	(m)
δ_{CH}	Flame reaction zone thickness	(m)
δ_{PR}	Flame preheat zone thickness	(m)
η	turbulent energy dissipation rate	
η_g	Empirical modelling constant	
η_t	Modelling constant	
η_o	Orifice plate flow expansion factor	
ϵ	Turbulent kinetic energy dissipation rate	$(units)$
ϵ_1	Empirical modelling constant	
θ_{By}	Scaled acceleration rate	(m/s^2)

λ	Detonation cell width	(mm)
λ_{th}	Thermal conductivity	*(units)*
μ	Dynamic viscosity	*(units)*
ν	Kinematic viscosity	*(units)*
ν_T	Eddy Kinematic viscosity	*(units)*
Ξ_k	Flame wrinkling coefficient	*(-)*
ξ_g	Empirical modelling constant	*(-)*
π	Numerical constant (3.14159)	*(-)*
ρ_u	Unburnt mixture density	(kg/m^{-1})
σ	Density ratio of unburnt to burnt gas	
σ_{k1}	Modelling constant	
σ_{k2}	Modelling constant	
$\sigma_{\omega 1}$	Modelling constant	
$\sigma_{\omega 2}$	Modelling constant	
τ	Shear stress	*(N/m^2)*
τ_0	Integral length scale turbulence period	*(s)*
τ_f	Flame time period	*(s)*
τ_k	Kolmogorov length scale eddy period	*(s)*
ϕ	Equivalence ratio	$(-)$
χ_k	Thermal diffusivity	(m^2/s)
ω	Specific k dissipation rate	

Accronyms

BR	Blockage Ratio
CDE	Continuous Detonation Engine
CFD	Computational Fluid Dynamics
CJ	Chapman Jouguet
DAQ	Data Aquisition System
DDT	Deflagration to Detonation Transition
DL	Darieus Landau instability
FA	Flame Acceleration
HPC	High Pressure Chamber
IPN	Iso propanol nitrate
JP	Jet Propellant fuel
$LCCC$	Low Carbon Combustion Center
LDA	Laser Doppler Anemometry
LES	Large Eddy Simulation
LV	LabView
LIF	Laser Induced Fluorescence
LPC	Low Pressure Chamber

LPG	Liquid Petroleum Gas
NI	National Instruments
$ODWE$	Ordinary Detonation Wave Engine (Scramjet engine)
PDE	Pulse Detonation Engine
PO	Propylene Oxide
pdf	Probability Density Function
$PDWE$	Pulse Detonation Rocket Engine
PIV	Particle Image Velocimetry
PVC	Poly Vinyl Chloride Plastic
$RDE, RDWE$	Rotating Detonation (Wave) Engine
$RANS$	Reynolds Averaged Navier Stokes
$TSFC$	Thrust Specific Fuel Consumption
TOF	Time of Flight Measurement
UOS	University of Sheffield
$UoSPDE$	University of Sheffeild PDE
$USAF$	United States Air Force
VSD	Variable Speed Drive
ZND	Zeldovich Neuman Doring Detonation theory
$2D$	Two Dimensional
$3D$	Three Dimensional

Acknowledgements

Thanks to my wife Rezleen for all of her support, her sense of humor and patience whilst I've been working on this Doctorate, also for keeping my life full of fun and interesting! Thanks to my parents and grandparents who from an early age have shown me how to steadfastly pursue goals even when things are difficult, not to mention inspiring my analytical engineering mind. They're passion for practical engineering design and build tasks ranging from sprayers to grain dryers and even composite light aircraft first sparked my interest in engineering and gave me an excellent environment to talk about gear boxes, the inner workings of combines and engines from a young age as well as plenty of practical experimental experience.

I would like to remember the late Professor Chris Wilson, whose enthusiasm and charisma for all things propulsion and combustion related not only prepared me as an undergraduate but also set my sights high as a post graduate student working under his supervision. His expert guidance and knack for problem solving any technical issue was enough to encourage many students to pursue a career in the field. Without Chris's vision and passion for engineering his legacy of the Low Carbon Combustion Center pilot plant experimental facility where this research was completed would not exist. Thanks to Dr Simon Blakey, who has taken up the tough task of filling in the late Chris Wilson's shoes and supervised me through the last years of my PhD. Simon's input has provided a fresh perspective to many of the problems involving this work and has maintained a lighthearted approach to my frustrations which resulted in me walking out of our meetings happier than when I went in! Simon's encouragement to dig deeper into the fundamental science behind the practical issues of problem solving the rigs latest fault and his comments on my writing have been invaluable.

I would also like to thank the technical staff from the Low Carbon Combustion Center, specifically Andrew Delorenzi, Markus Mohorco, Ben Kitchener, Ben Wadsworth, Andrew Hemstock, Dave Dunstan, Sam Chapman and Timothy Hackock for their assistance with welding, instrumentation design and so on.

Lastly, but not least I would like to thank Almighty God for providing problems as complicated as flame acceleration and detonation to grasp, which keep us guessing for centuries whilst we try to come up with a model which actually captures them! His creativity never ceases to amaze me.

To my wife, Rezleen.

In memory of the late Professor Chris Wilson.

This thesis contains a limited amount of media content which will appear as blank space when printed.

Chapter 1

Introduction

1.1 Pulse Detonation Propulsion History

The first pulse detonation engine (PDE) patent was granted to Bollay in 1960 after filling for patent in 1952 [1]. This simple engine was designed around a rotating detonation chamber with stationary inlet valves. To understand the history of detonation however it is necessary to look back further to the work of Malard and Le Chatelier (1883) and the work of Berthelot and Vielle (1883) [2], which was undertaken as a result of serious mining accidents in France and Belgium. The theory of detonation was initially developed Chapman and Jouguet then further advanced independently by Zeldovich in the 1940s [3, 4], von Neumann [5] and Doring [6] with ZND theory. Since 1960 there has been a vast amount of work carried out with a recent resurgence into the field from the late 1990's until the late 2000's when there appears to have been a slump in the research within this field. Work is beginning to grow across the world at the current time, with many new countries developing PDE technology in recent years. A thorough review of the current state of PDEs can be seen in the works of Roy [7], Frolov [8] and Wolanski [9] and Philipov [10].

1.2 Why investigate PDEs?

PDEs are being investigated as an alternative to the standard constant pressure combustion cycle, the Brayton cycle, which has been the state of the art since the late 1930s, when it was first developed for use in aviation with the advent of the Whittle turbojet [11]. Over time the theoretical maximum efficiency of the turbojet has been approached with ever increasing resources spent on fewer percentage points of increase in thermal efficiency. It is therefore prudent to investigate alternative thermodynamic cycles for use in the aerospace industry as disruptive technologies, particularly as the

current Brayton cycle engines are limited by the maximum material temperature of the hot end components such as the combustor and turbine. A disruptive technology such as the pulse detonation engine could be used to revolutionise aero engine design in low pressure engines which would be used to provide propulsive power for small aerial vehicles such as unmanned aerial vehicles, ships, or light aircraft [12, 13, 9]. Many potential applications for the PDE include combined Brayton PDE cycles such as those described in the work of Bhattrai et al. and Goldmeer et al. [14, 15, 16]. The US Department of Defence invested $33 million in developing constant volume combustion systems during 2010 which combine the use rotating detonation engine technology with gas turbine engines for naval power systems [17].

1.2.1 Pulsed Combustion History

Throughout WWII, during which there was considerable technological advancement in many different areas, both constant pressure engines such as the turbojet and constant volume engines such as the pulse jet were investigated. Once such example of the pulse jet is the V1 'buzz bomb' aptly named after the noise which it made whilst in operation, which can be seen in Figure 1.1. Several V1 flying bombs failed to explode during WWII and were delivered to Wright Patterson Airforce Base in the US for reverse engineering. The technology in this engine was used as the basis of early US guided cruise missiles known as the JB-1 and JB-2 Loon [18].

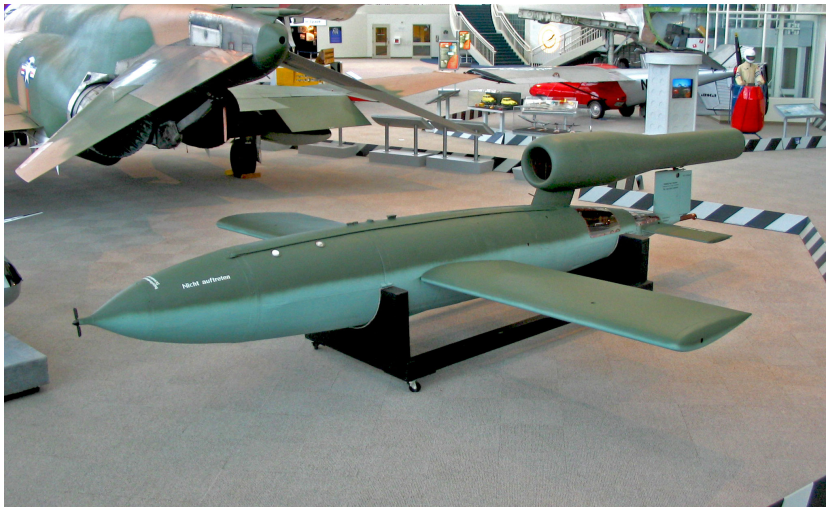

FIGURE 1.1: V1 'Buzz Bomb' on display at the Museum of Flight, Seattle, USA [19]

Propulsion for the V1 flying bomb was supplied by a pulse jet named the Argus As 014 [20]. The Argus As 014 engine flew using the constant volume combustion principles in a pulsed manner and with a cycle frequency of approximately 50Hz [21]. The Argus engine made use of inlet reed valves to control the direction of the explosion generated by the engine, producing a thrust wall at the inlet end of the engine. These valves were

open by oncoming inlet air when the combustor was not firing and closed due to the explosion when the combustor fired, generating a pressure tight seal which directed the flow aft of the valves, from the combustion chamber through the engine exhaust.

The main difference between pulse jet engines and PDE engines is that the PDE combusts fuel by generating a detonation, or supersonic combustion where as a pulse jet burns fuel using deflagration, or subsonic combustion. The pulse jet cycle can be seen in Figure 1.2, which includes the purging, filling, ignition, blow down and thrust stages.

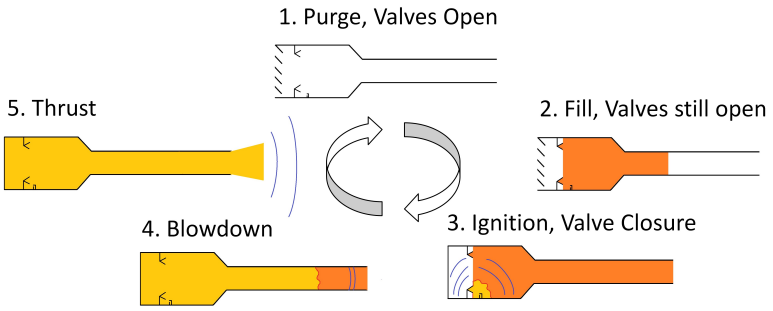

FIGURE 1.2: Pulse Jet Cycle

1.2.2 PDE flight demonstrators

Although PDE engines are not yet commercially available practical engine demonstrations have already been made in 2008 with the flight of a PDE powered Scaled Composites Long EZ, a composite aircraft flown with a pulsed detonation engine based on a four cylinder engine valve system as shown in Figure 1.3. The engine ran with four separate detonation chambers operating at a composite cycle frequency of 80 Hz.

FIGURE 1.3: Scaled Composites Long EZ PDE powered aircraft, image reproduced from Flight Global [22]

This flight lasted tens of seconds under PDE powered cruise conditions, and was flown at an altitude of less than 100 meters above the run way [22].

1.2.3 Potential future engines

Other engine designs which use detonation are called continuous detonation engines (CDEs). The main two varieties of such engine are the oblique detonation wave engine (ODWE) and rotating detonation engine (RDE or RDWE), both of which use continuous detonation waves to produce thrust. The scramjet (supersonic combustion ramjet) uses a supersonic diffuser to focus shock waves and compress inlet air approaching the combustor. After compressing the reactants the fuel-air mixture is detonated and expanded, propelling the vehicle along at hypersonic speeds. In contrast the rotating detonation wave engine generates continuous circumferentially travelling detonation waves in a parallel walled annulus which then expand through a nozzle to generate thrust in the axial direction [23]. The RDE engine is capable of operating at subsonic speeds although at the current stage of development is unable to run continually for more than a few seconds.

1.3 PDE Cycle overview

The PDE cycle is described in Figure 1.4. The PDE cycle has seven distinctive consecutive steps:

1. To begin the cycle the PDE combustion chamber must have already purged of all reactants from the previous combustion cycle in order to give the best opportunity for the fresh mixture to burn well.

2. During the second stage the PDE is filled with a mixture of fuel and an oxidiser, which is air in the case of a pulse detonation engine, or another oxidiser in the case of a pulse detonation rocket engine (PDRE). This air is usually filled through valves on the normally closed wall of the tube, called the thrust wall. Alternative valve configurations are currently under investigation and are the source of a number of patents for PDE propulsion systems [24, 25, 26, 27].

3. In the third stage, once the tube has been filled with fuel air mixture to the required amount, the valves are closed an the mixture is ignited in the closed end of the tube, usually close to the thrust wall. Sometimes a point further along the tube is used.

4. The fourth stage is the flame acceleration stage, at which point the flame is still subsonic relative to the speed of sound in the combustion products (around 900m/s). During the flame acceleration (FA) stage, the flame accelerates to approximately half of the theoretical detonation velocity, named the CJ velocity after Chapman and Jouguet, which is also approximately half the speed of sound in the combustion products.

5. In the fifth stage the key process of deflagration to detonation transition (DDT) or the phenomenon of the explosion within the explosion occurs during which the flame interacts with shock waves ahead of the flame in the venting reactants generating at least one hot spot which later forms a detonation and begins to traverse the tube in the longitudinal and lateral directions. If successful, the DDT event will give rise to a full blown detonation, which will continue to traverse along the tube unless disturbed by a change in mixture or boundary conditions. Such a detonation can either be:

    - Planar with a lead shock wave traversing along the tube at the same time as interacting with multiple transverse shocks which reflect from the walls of the PDE tube. The locations at which the lead shock and transverse shocks interact are known as triple points and are the points of highest pressure in the system. The trace left behind by the path of multiple triple points provides a fish scale shape which is a characteristic of planar detonation. The transverse dimension of the fish scale is known as the transverse detonation cell size and is a critical parameter in choosing PDE tube geometry.
    - Spinning with a single rotating head in which pressure contours 'spin' forming a detonation wave front which has a rotating peak pressure traversing at an angle of 45^o formed from a single transverse shock which rotates around the perimeter of the detonation chamber. A spinning detonation only ever exists in the limiting case at which the mixture is on the cusp of decaying into a subsonic deflagration reaction front and a shock wave.

6. By stage six the detonation wave has a stable velocity of around 2 km/s and exits the PDE engine generating a pressure rise of around 20 bar and a specific impulse of around 2000 s, when measured relative to fuel mass.

7. The final stage before the cycle repeats is purging, during which the exhaust products are ejected from the cylinder by injecting fresh air without fuel, in order to insure that the fresh mixture has the best chance of burning fully and with little chance of ignition taking place due to the heat of the exhaust gases from the previous cycle, known as end ignition.

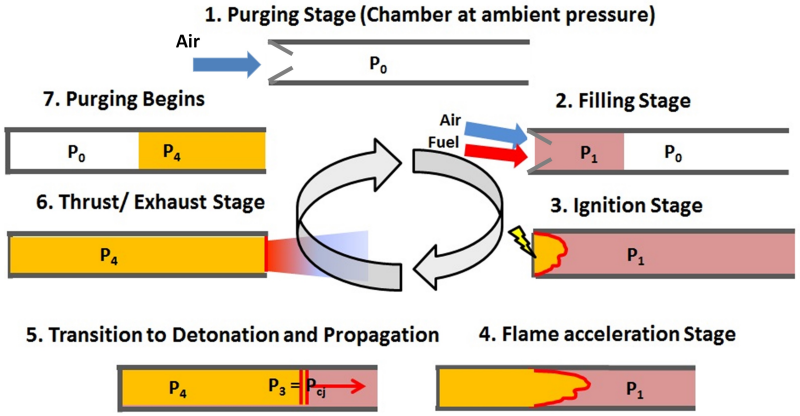

FIGURE 1.4: PDE cycle diagram adapted from the work of UTA [28]

1.3.1 Frames of reference

Frames of reference are critical when observing, measuring and modelling flows in PDEs. Without the correct frame of reference the flame speed could be measured with an error of several orders of magnitude. The classically defined turbulent flame speed differs from the flame front speed in PDEs or shock tubes, where the flame is accelerating towards the exit in an already moving gas. The flame front speed is defined as the local turbulent flame speed plus the speed of the expanding gas behind the flame front and is the observable flame front speed relative to the tube frame of reference. The flame front speed increases during flame acceleration until the gas behind the flame front is roughly equal to the speed of sound in the combustion gases, at which point the bunt gases break the speed of sound while venting through the PDE. This is the point at which detonation can take place if conditions permit DDT, Ciccarelli et al. discuss this in great detail [29], although the reason for detonation occuring is not simply that the gaseous products have reached the sonic velocity. The energy contained in premixed gas ahead of the flame must be greater than the ignition energy for hot spots to ignite, promoting detonation under favourable condtions.

1.4 Comparison with other engine cycles

The pulse detonation engine differs from other commonly used aero engines in that is mode of combustion is not based around the constant pressure Brayton cycle as in the case of the turbojet, turbofan or other constant pressure combustion engines such as the ram jet or scram jet. The pulse detonation engine operates with a cycle pressure approaching the contact volume Humphrey cycle with an alternative cycle known as the detonation cycle, sometimes called the Ficket Jacobs cycle. It is important to note that the pulse jet's Humphrey cycle combustion process is subsonic deflagration which is limited to the adiabatic combustion pressure for the mixture. In contrast the pulse

detonation engine's Ficket Jacobs cycle combustion pressure is the ideal detonation pressure, P_{CJ}, which is approximately double the adiabatic combustion pressure. In addition the PDE detonative combustion process takes place at approximately twice the speed as the pulse jets combustion cycle, which allows the tube to be filled at higher frequencies. Litke et al. have compared the PDE cycle with the pulse jet cycle in detail [30]. The pulse jet cycle is similar to the PDE cycle as described in Figure 1.4, with the main difference being that stage 5 would be removed, so the engine would generate a deflagration rather than a detonation.

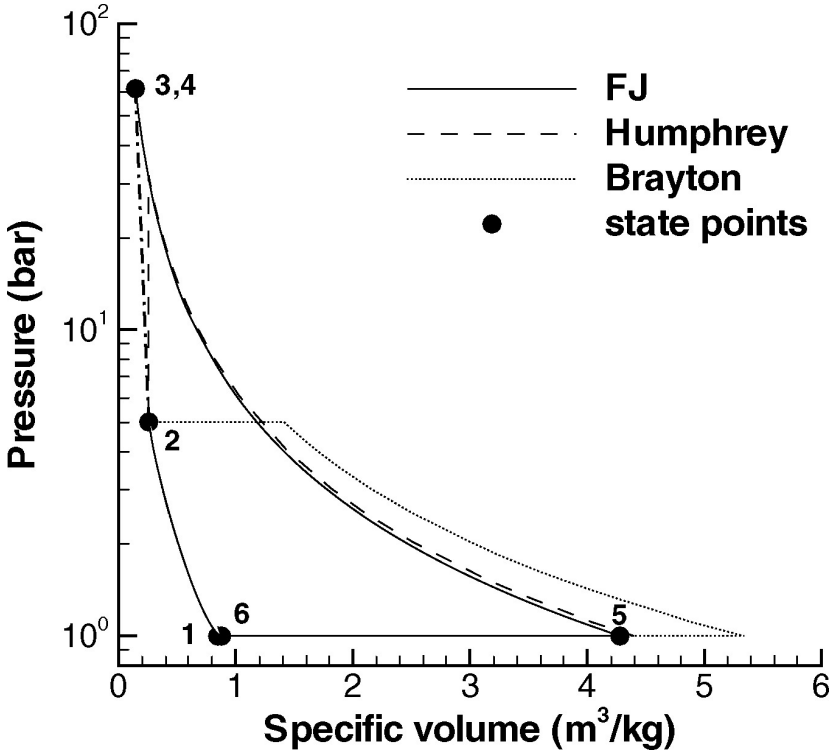

FIGURE 1.5: P-V diagram for various combustion cycles from the work of Wintenberger et al.[31]. Humphrey (Isochoric, pulse jet), Brayton (Isobaric, turbojet/gas turbine) Ficket Jacobs (detonation, PDE). The bold dotted and dashed line between point 2 and point 3,4 represents detonation, which increases the pressure as well as reducing the specific volume of the mixture on account of the detonation shock which provides compression to this novel cycle.

Figure 1.5 from the work of Wintenberger et al. [31] shows the clear difference between the isobaric Brayton (turbojet), isochoric Humphrey (pulse jet) and detonation Ficket-Jackobs (PDE) cycles. The main observed difference between the isochoric (constant volume) and isobaric (constant pressure) cycles is that the combustion process occurs at constant volume and constant pressure respectively. Expansion and compression are both assumed to be adiabatic in both cases. The main difference between the ideal Humphrey cycle and the ideal Brayton cycle is that the Humphrey cycle peaks at around 25 bar, whereas the detonation cycle peaks at 50 bar or so for the mixture in question. Detonation also compresses the reactant volume during combustion due to the

shock waves present in the detonation process, leading to a higher density immediately after the detonation wave. It can be clearly seen that the volume under the curve, which is equal to the energy available from the cycle is larger for the Ficket Jacobs Cycle than for the Humphrey Cycle, as such detonation is more energy efficient than subsonic constant volume combustion.

1.4.1 Thrust Generation

Figure 1.6 which is adapted from the work of Chao et al. [32] shows the expected pressure variation within the PDE cycle. In an ideal detonation cycle the ideal detonation pressure, the Chapman-Jouguet detonation pressure, P_{CJ} is reached at the thrust wall end of the tube and then the detonation traverses along the tube. Figure 1.6 is drawn from the perspective of a stationary observer sitting at the closed end of the tube. First of all the observer sees a high pressure Von Neuman spike, as the detonation's shock wave and flame complex passes and after a very small increment in time the pressure decreases and proceeds to a plateau of pressure is reached before the detonation travels towards the open end of the PDE tube. Once the detonation wave exits the tube there should be no further fuel to combust with the air and an expansion wave passes through the PDE tube with its accompanying pressure decay until the gas in the tube reaches atmospheric pressure (if operating in a standard atmosphere), or slightly lower. Thrust is generated in the PDE engine by a combination of the pressure acting over the exhaust area and the velocity of the exhaust gases escaping from the closed tube. Assuming that there are no obstacles in the tube to create drag, this is the same as a the pressure at the thrust wall of the tube. The impulse per unit volume for the PDE tube is inversely proportional to the detonation velocity, V_{CJ} and proportional to the plateau pressure,P_3. Thrust, T, can be calculated using Equation 1.1 for known values of s and specific impulse, I_v, frequency, f and tube internal volume, V. Equation 1.2 can be used to calculate the specific impulse per unit volume which can then be substituted in to Equation 1.1 to calculate the thrust. Careful observation of these two equations shows that P_3, f and V of the PDE are major contributors to the thrust generated by the engine which can be controlled. V_{CJ} and c_3 are properties of the fuel air mixture and cannot easily be controlled once the mixture is chosen. P_3 will change, depending on the degree of obstruction along the tube in the practical PDE engine. Thrust is inversely proportional to the detonation velocity, V_{CJ} and c_3 the speed of sound in the combustion products, which can be found using NASAs CEA software [33]. In this case α_1 and β_1 are empirically derived constants calculated by Wintenberger et al. [34, 31] which describe the decay of the Taylor expansion across the exhaust section of the cycle, which is clearly shown in Figure 1.6 after the plateau at P_3

$$T = I_v V f \quad (N) \tag{1.1}$$

Impulse per unit volume can be calculated using equation 1.2 which relates the impulse to the experimentally measurable variables P_3,V_{CJ} and c_3, the speed of sound in the combustion products. α and β are experimentally determined constants which are described in the work of Wintenberger et al. [35].

$$I_v = \Delta P_3 \left[\frac{1}{V_{CJ}} + (\alpha_1 + \beta_1) \frac{1}{c_3} \right] \quad (Ns/m^3) \tag{1.2}$$

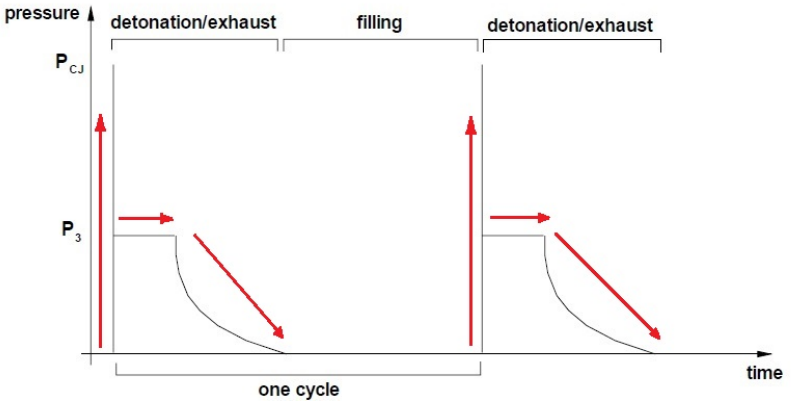

FIGURE 1.6: PDE pressure-time graph addapted from the work of Chao et al. [32]

Analysis of equations 1.1 yields that a higher PDE tube volume, greater impulse and higher frequency will produce more thrust. Further insight from Equation 1.2 for the impulse per unit volume yields that the thrust will also be greater when the plateau pressure, ΔP_3 is greater and when the speed of sound in the products, c_3 and the Chapman Jouguet detonation velocity is respectively smaller.

1.4.2 Thrust Specific Fuel Consumption

Thrust specific fuel consumption (TSFC) can be calculated using equation 1.3 where the numerator represents the fuel mass flow rate per second and the denominator is the thrust delivered by the engine. Y_f is the fuel mass fraction, which for stoichiometric propane-air is 0.0641, or 0.0662 for stoichiometric JP10-air, a common aviation fuel proposed for use in PDEs [32]. Mixture density, ρ_u will be close to 1.221 kg/m^3 for JP10-air or 1.202kg/m^3 for propane-air, both at 300 K and 101325 Pa. Impulse per unit volume, I_v, for JP10-air mixtures is given as 1372.5 Ns/m^3 or 1360.2 Ns/m^3 by Wintenberger et al. [34] thus providing a specific impulse of 0.212 kg/Nhr for JP10-air which, according to Hill and Peterson[36] is comparable with TSFC for a ram jet.

$$TSFC = \frac{fY_f\rho_u V}{fI_v V} = \frac{Y_f\rho_u}{I_v} \quad ((kg/s)/N) \tag{1.3}$$

1.4.3 Specific Impulse

Specific impulse, or impulse per unit mass can be calculated using Equation 1.4 which relates specific impulse to impulse per unit volume, I_v, the uniform gravitational field of the earth, g_0 (9.81 m/s^2) and ρ_u, the density of the initial mixture mass.

$$I_{sp} = \frac{I_v}{g_0\rho_u} \quad (s) \tag{1.4}$$

Specific impulse for several different types of engine is shown on in Figure 1.7, from the University of Texas at Arlington Aerodynamics Research Centre [28] which clearly illustrates the benefits of PDE engine powered flight. This graph compares different engine cycles as well as comparing hydrocarbon fuels or hydrogen for fuel. It is evident from this graph that the PDE engine performance predictions show the PDE generating greater specific impulse than any other engine up to Mach 5, where velocity is taken as the speed of the air vehicle containing the PDE engine. As such, this engine has great merit for study as a device for aerospace propulsion. It is worth noting that hydrogen is a difficult fuel to store, and as a gas it has a very low volumetric energy density. As a compressed liquid, hydrogen has a volumetric energy density of 8.4 MJ/l [37] when in its liquid form at -253 $^\circ C$. In comparison, Jet A-1 has a volumetric energy density of 35.1 MJ/l when stored at 15 $^\circ C$ in an atmospheric pressure tank [38]. The change in the thrust generated by each fuel is a function of the relative energy density of each fuel, which is approximately three times greater for hydrogen (120MJ/kg) [37] than for Jet A-1 (42.8MJ/kg) [38]. As a result of these physical properties, it is much easier to work with a liquid fuel on practical airborne platforms.

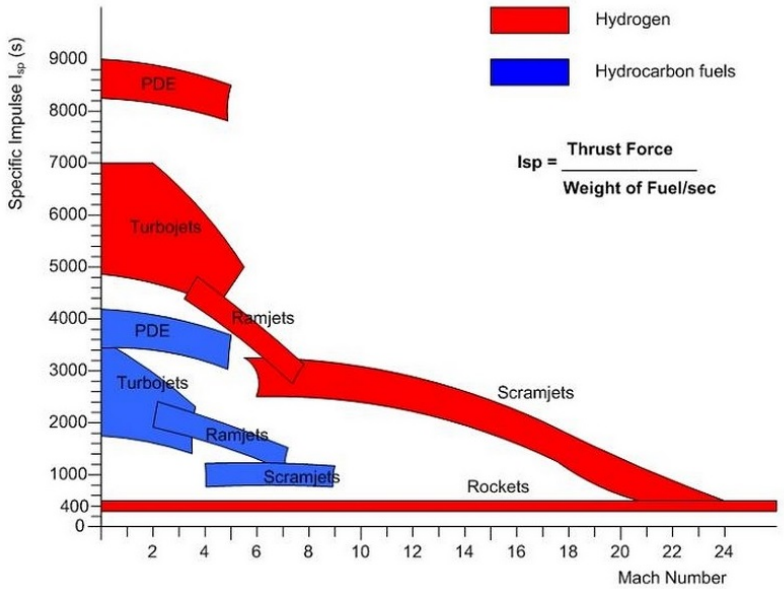

FIGURE 1.7: Specific impulse diagram for various combustion cycles from the Aerodynamics Research Centre at UTA [28]

Chapter 2

Literature Review

2.1 Theoretical Approach to PDEs

2.1.1 Synopsis

This literature review provides a theoretical background for understanding flame acceleration, turbulence; DDT and detonation which is then built on by the addition of analytical methods for assessing flame acceleration in PDEs. To give a rounded background in flames, flame acceleration and DDT the literature review will begin by describing the laminar flame and its structure, followed by various types of laminar flame instability. After detailing premixed laminar flames the literature review expands into the field of turbulence and premixed turbulent flames exploring the concepts of turbulent length scales and their interaction with the flame length scales. The interaction of turbulence and flame length scales is described in a section on turbulent flame regimes and a range of non-dimensional numbers are explored which help to classify limits of these regimes. After describing the stationary laminar and turbulent premixed flames, the concepts of flame front speed, the double discontinuity problem and deflagration to detonation transition (DDT) are explored. The DDT process is explained in some detail with the help of high speed photography from the literature. The section on the fundamental science of flames, flame acceleration and detonation finishes with a description of the detonation wave, its structure and in its various modes of propagation. To follow on from fundamental combustion science a more practical section on experimental methods introduces a variety of approaches to building test rigs for experimental flame acceleration and DDT studies, detailing different approaches to these

complex multifaceted problems. Numerical modelling of PDE is explored detailing the fundamental equations of fluid motion for reacting flow. Current state of the art detonation modelling results are discussed, followed by discussion of existing analytical and semi-empirical modelling methods which describe the acceleration of the flame. Key factors which govern the performance of PDE engines are explored in detail to provide information which help to make well informed decisions when designing PDE systems and choosing their fuels and preferred operating conditions. A gap analysis of the literature concludes the literature review by tabulating work carried out using each experimental method explored in detail within the literature review and others not discussed. The first section of the gap analysis contains details of tube geometries, fuel mixtures, blockage type and instrumentation to carefully inform experimental design. The second section of the gap analysis contains DDT details for a range of fuels and PDE combustion chamber geometries.

2.1.2 Laminar Flame Speed

Laminar flames tend to have flame thickness in the order of 10^{-4}m and reaction zone thickness in the order of 10^{-5}m and a typical flame speed, S_L of less than 0.5m/s for most hydrocarbon-air mixtures other than Hydrogen-Air and similar highly reactive gases [29]. The basic structure of a laminar flame is determined as illustrated in Figure 2.1 which shows the preheat zone, δ_{PR}, and reaction zone δ_{CH} and the overall laminar flame thickness, δ_l. Figure 2.1 is shown relative to the flames frame of reference. It is evident that time is taken to preheat the reactants from the unburnt temperature. T_u, to the stage at which the chemical reaction becomes self-sustaining, and further time until the adiabatic flame temperature,T_b. T_b is reached at the point all the reaction is complete and is shown as the plateau at the top right of Figure 2.1. Figure 2.1 illustrates the process of combustion in the laminar flame which is initiated by preheating, relative to the flame's frame of reference. As the flame changes the temperature of reactants in the reaction zone, a density gradient is generated across the flame. This density gradient promotes a gas velocity in the products exiting the flame which is greater than the reactant velocity in, from the flame reference. σ is defined as the ratio of the density of unburnt reactants to burnt products and S_L is the laminar flame speed. During the preheating phase heat from the flame is conducted and radiated into the preheat zone which increases the reactant temperature prior to ignition. The reaction

rate in this zone is negligible and as a result the reactants have not yet undergone any chemical change. As the reactants approach the chemical reaction zone their preheating temperature reaches the point at which reactions begin to take place according to the available enthalpy in the system and each reactions Gibbs free energy. These reactions are on a small scale at first, only involving smaller radical molecules, later building to larger chain reactions with larger molecules. A traverse from left to right across the flame would reveal exothermic reactions taking place increasing the heat release throughout the reaction zone allowing further reactions to take place. Molecules with larger positive Gibbs free energy are broken down and oxidized releasing further heat until the reaction rate reduces as the available chemical energy is burned and the adiabatic flame temperature for the given mixture is approached. The bulk of the reactions occur as the flame temperature asymptotically approaches the adiabatic flame temperature after which point the reaction rate begin to reduce. Only the reactions with Gibbs free energy less than the enthalpy in the system may occur, all other reactions will remain incomplete. In the context of the PDE the laminar flame occurs before significant turbulence is available to penetrate the flames chemical reaction zone.

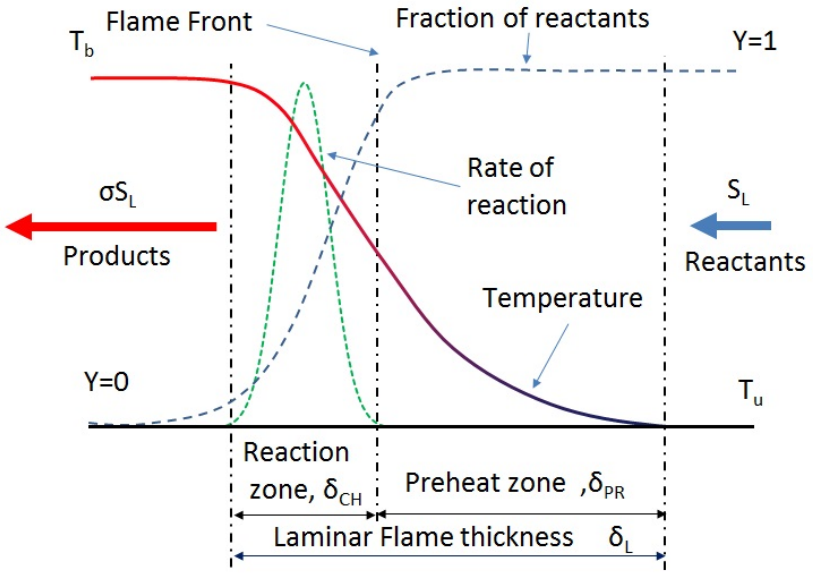

FIGURE 2.1: Laminar Flame Schematic, showing temperature, reaction rate and reactant fraction against location within the flame addapted from [29]. The diagrams frame of reference is centered on the laminar flame with gas flow through the flame from right to left.

The laminar flame thickness, δ_l can be calculated using Equation 2.1 where λ_{th} is the thermal conductivity of the fuel air mixture at the mean flame, ρ_u is the unburnt

mixture density S_L is the laminar flame speed and c_p is the specific heat capacity at constant pressure for the unburnt reactants. Typical values for the laminar flame thickness in hydrocarbon flames such as propane calculated using this figure are of the order of 2 $\times 10^{-4}$ m in length [29].

$$\delta_l = \frac{\lambda_{th}}{\rho_u S_L c_p} \quad (m) \tag{2.1}$$

Furthermore, due to the early work of Zeldovich and Frank-Kamenetzki in 1938 it is possible to calculate the size of the chemical reaction zone length, δ_{CH} using the Zeldovich number for the laminar flame, β which can be calculated using Equation 2.2. E_a in Equation 2.2 is the activation energy of the reaction, T_b is the maximum flame temperature, T_u is the unburned reactant temperature and R_g is the gas constant. A typical value of β for the typical hydrocarbon flame would be around 10 [39].

$$\beta = \frac{E_a(T_b - T_u)}{R_g T_b^2} \quad (dimensionless) \tag{2.2}$$

Once the Zeldovich number is known the chemical reaction zone thickness can be calculated using Equation 2.3, indicating that a typical chemical length scale in laminar hydrocarbon flame would be approximatley 2 $\times 10^{-5}$ m in length [29].

$$\delta_{CH} = \frac{\delta_l}{\beta} \quad (m) \tag{2.3}$$

2.1.3 Laminar Flame Instabilities

There are a number of instabilities which can cause non planar laminar flame shapes relative to the flame frame of reference, changing reaction rates on a local and macro flame scale. For the purpose of work within the field of PDEs these are likely to take place in the initial phase of FA. As planar laminar flames become more unstable their surface becomes cellular, that is to say wrinkled, this can take place before the flame has become turbulent [29].

2.1.3.1 Darreius-Landau Instability

The Darreius-Landau, (DL) instability causes a push-pull effect on the flame, driven by small perturbations in the premixed gas ahead of the flame. This theory was discovered independently by both Darreius [40] and Landau [41] around 1945. This effect is illustrated in Figure 2.2. When the flame is curved by any small change in mixture, temperature or pressure of upstream gas the flame decelerates or accelerates accordingly, generating a curvature in the flame front. Once the flame has curved in a convex manner each point along the convex flame front diverges, conversely in a concave section of the flame front the flame will continue to converge in an increasing manner [29]. The combination of these effects leads to an increasingly wrinkled flame surface. In practice, small wavelengths are damped out due to the diffusion effects prevalent at this length scale [42], whereas wavelengths which scale much larger than the laminar flame characteristic dimension- flame thickness, are stabilised due to the non-proportional increase in convex and concave sections of the flame [43].

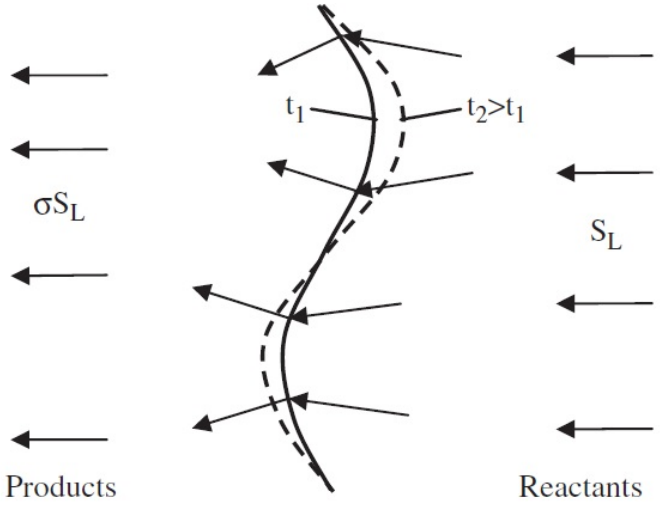

FIGURE 2.2: Schamatic of the Darrieus-Landau Instability [29] t_1 refers to the initial state of the flame, and t_2 refers to the state of the flame at an instant in time later than t_1. This diagrams frame of reference is centred on the mean planar flame location, with flow moving through the flame from right to left

2.1.3.2 Diffusive Flux Instability

In addition to the Darreius-Landau (DL) instability, diffusive fluxes also affect the stability of the planar flame front. The ability of the flame to maintain a uniform planar front is limited by the thermal diffusivity, χ (m^2/s), and the limiting reactant,

D_L which both interact with the Darreius-Landau instability as can be seen in Figure 2.3. This effect changes depending on the ratio of molecular diffusivity to thermal diffusivity, which can be characterised by the flames Lewis number Le. Lewis number is a non-dimensional number quantifying the ratio of molecular to thermal diffusivity across the flame. In this case thermal diffusivity refers to the ability for heat in the flame to diffuse away from the flame in order to heat new reactants, preparing them for combustion in the reaction zone. Thermal diffusivity is a term used specifically within flame physics to refer to heat transfer acting across the flame from the chemical reaction zone into the flame preheat zone. In flames controlled by limiting molecular diffusivity rather than thermal diffusivity, with $Le \leq 1$ in convex sections of the flame the local combustion temperature increases as the low thermal diffusivity does not allow heat to be conducted or radiated away faster than the limiting reactant enters the reaction zone. This creates an increased convex flame surface as shown in the top left part of Figure 2.3. Conversely, in concave sections of the combustion front the local flame temperature decreases as the reactants are taken from a smaller volume ahead of the concave section of the flame. This leads to a lower flame temperature and reduced flame velocity which perpetuates the problem of instability for $Le \leq 1$, leading to increased flame wrinkling. The opposite effect takes place in flames with $Le \geq 1$ which have increasingly stable flame surfaces and reduced wrinkling after the flame passes a mixture change or perturbation in the oncoming gas, from the flames frame of reference. These thermal diffusive effects were explored further during the 1970s by Shivashinski [44], Joulin and Calvin [45], as well as by Lazarev et al. [46].

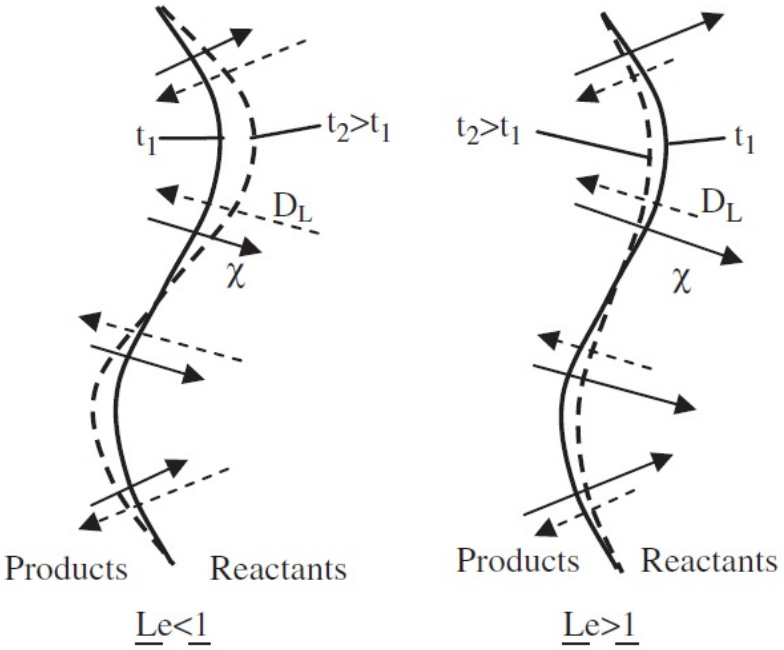

FIGURE 2.3: Schamatic of the Diffusive Flux Instability [29]. t_1 refers to the initial state of the flame, and t_2 refers to the state of the flame at an instant in time later than t_1. χ and D_L refer to thermal diffusivity and molecular diffusion of the limiting reactant respectively.

2.1.3.3 Cellular Flames

Thermal-diffusion effects can either amplify or dampen the underlying DL instability, creating either greater or lesser flame instability, depending on the flames Lewis number. For an unstable flame (with Le $\leq$ 1), the flame only becomes unstable once the ratio of the flames radius to its thickness becomes critical. This is to say that for a given premixed flame cellular instabilities originate once the radius is larger than a certain value. The ratio of the flames radius to its thickness is defined as the Peclet number or Pe, and the critical value at which this generates a cellular flame for unstable mixtures is denoted as Pe_{cr} [47]. The process of cellular flame propagation is described in detail by Markstein [42] and is analysed in further detail by Joulin and Calvin [45] and Peclet and Calvin [48].

2.1.3.4 Flame Stretch

If a flame is subject to aerodynamic forces from turbulence larger than the flame length scale the flame surface undergoes flame stretch. Flame stretch rate, α, can be defined

by Equation 2.4 which originated from the work of Karlovitz [49]. In this case A_f refers to the flames area.

$$\alpha = \frac{1}{A_F}\frac{dA_F}{dt} \quad (s^{-1}) \tag{2.4}$$

Flame stretch occurs in two primary modes, stretch and curvature as shown by Equation 2.5. Diagrams 2.4 and 2.5 illustrate the difference between flame strain, α_s and flame curvature, α_c respectively.

$$\alpha = \alpha_s + \alpha_c \quad (s^{-1}) \tag{2.5}$$

The addition of flame stretch due to curvature and strain together form the total flame stretch α, as illustrated in Figure 2.6. Flame strain is said to occur due to inhomogeneity in the upstream flow [29]. Each of these figures illustrate a change in area over time, and Figure 2.6 shows that S_n the stretched flame speed normal to the flame surface will change in most cases of flame stretch. The magnitude of the change of S_n will depend on the Markstein length of the flame, which will be introduced more fully later.

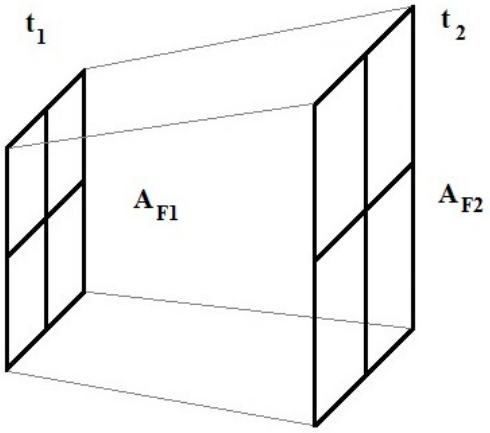

FIGURE 2.4: Schematic of flame strain, α_s the window representing the flame surface. t_1 and t_2 are taken to be two time instants with time difference δ_t, A_1 and A_2 are taken as two areas with difference δ_A

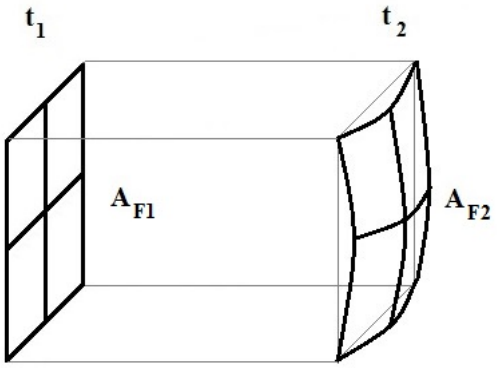

FIGURE 2.5: Schematic of pure flame curvature α_c,the window representing the flame surface.t_1 and t_2 are taken to be two time instants with time difference δ_t, A_1 and A_2 are taken as two areas with difference δ_A

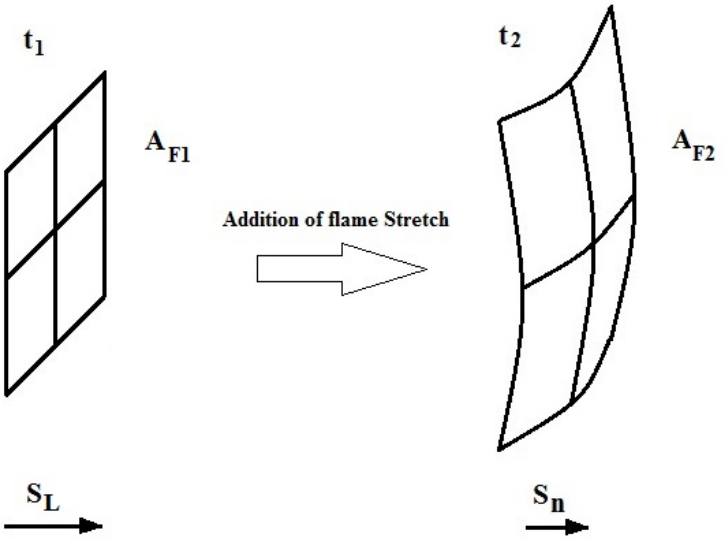

FIGURE 2.6: Schematic of flame stretch α with the window representing the flame surface composed of pure flame stretch, α_s, and pure flame curvature, α_c.t_1 and t_2 are taken to be two time instants with time difference δ_t, A_1 and A_2 are taken as two areas with difference δ_A, where the change in area due to stretch is composed of both scaling in the planar and curvilinear coordinates

2.1.3.5 Markstein number and the effect of flame stretch

Markstein [42] characterized flame stretch analytically using Equations 2.6 and 2.7 which can be used to relate the curvature or stretch of a flame to the change of velocity due to stretch using the Markstein Length, L_M. In this case S_n is the normal propagation rate of the curved flame surface and the R_F is defined as the flame's radius

of curvature. Markstein length is not a length which can be measured geometrically on the surface of the flame, however it can be calculated by dividing the difference of S_L and S_n by the flames stretch rate, α as seen in Equation 2.7. L_M can hold either positive or negative values depending on the flame's reaction to stretch. Markstein further non-dimensionalised L_M, normalising it by the laminar flame thickness, δ_l, which is also known as the thermal thickness of the flame. The normalisation of L_M by δ_l is shown in Equation 2.8, which produces the Markstein number, Ma [42]. Ma can be used to characterize a flames reaction to stretch at different fuel-oxidiser mixtures and initial conditions and is often used to report experimental findings for turbulent flame explosion measurements in fan stirred bomb reactors [50, 51, 52, 53, 54, 55, 56]. If a reactive mixture has a positive M_a, the flames speed will decrease when subjected to flame stretch,α, causing the flame to decelerate and stabilise [57, 57, 45] as it progresses along the tube as indicated by Equation 2.9, which relates the ratio of S_n and S_L to M_a to α and δ_l . This stabilisation process leads to reduced flame wrinkling and results in a lower overall rate of reactant consumption. In contrast, when a flame with negative M_a is stretched by perturbations the flame will become more wrinkled and accelerate due to an increased flame area as shown by Dorofeev et al.[58] and work carried out by the OECD nuclear energy agency [59].

$$S_L - S_n = S_L \frac{L_M}{R_F} \quad (m/s) \tag{2.6}$$

$$S_L - S_n = L_M \alpha \quad (m/s) \tag{2.7}$$

$$M_a = \frac{L_M}{\delta_l} \quad (dimensionless) \tag{2.8}$$

$$1 - \frac{S_n}{S_L} = Ma \frac{\delta_l}{S_L} \alpha \quad (dimensionless) \tag{2.9}$$

2.1.4 Turbulent Flames

Turbulent flows can be characterized by their mean velocity, u and the root mean square of the fluctuating velocity, u', as shown in Figure 2.7. This fluctuating velocity can be

a much larger percentage of the main flow velocity, u, than illustrated here, and has a large impact on the design of premixed combustors such as PDEs as u' changes certain flame characteristics. Note that u' may be superimposed on a decreasing or increasing trend in u as shown by the lower line in Figure 2.7, which will be the case in PDE combustion as the combustors reactant and product flows are continually fluctuating during the combustion cycle [60]

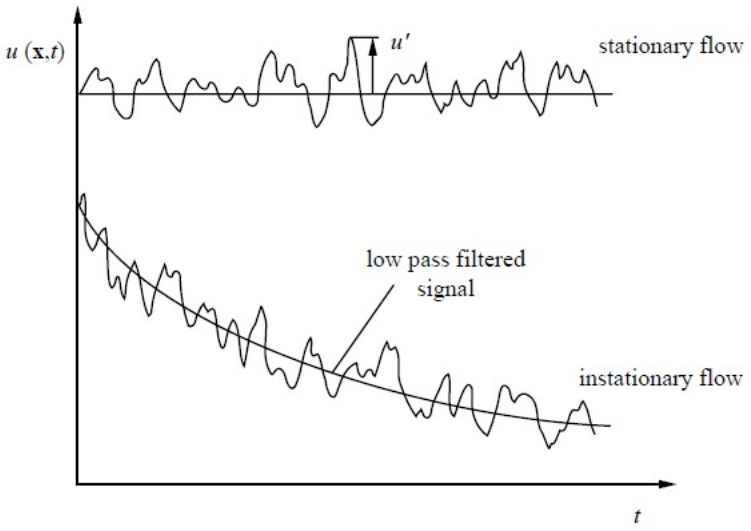

FIGURE 2.7: Turbulent velocity, u' from the work of Peters [60]

It is well known that both the scale and intensity of turbulence effect local flame speed and hence FA. The effect of turbulence has an impact in both PDEs and other accelerating flames, such as those considered for industrial safety reasons or exploding gas clouds, such as those analysed by Bradley [61].

As a flame accelerates along a single open ended obstacle filled channel, the flame is initially folded by the obstacles. This process can be observed in Figure 2.8. Flame folding occurs at low flame front speeds, where the flow is not controlled by gas dynamic effects. Flame folding occurs as a result of the interaction of the obstacle geometry with the fluid flow and flame front location. The volume between each obstacle contains a rotating torus of flow generated by the higher speed core flow. Between the core flow and the rotating torus a shear layer exists which enhances the local turbulence intensity and generates faster local turbulent flame speeds. The rotating flow within this free volume interacts with the flame, entraining flow into the core flow at on the downstream face of an obstacle, and pulling the flow away from the core flow at as it approaches

the next obstacle. As the core flow velocity increases in keeping with the acceleraring flame front velocity, the flame front moves towards the core further upstream within this void than at lower speeds. This geometric interaction of the flame front surface with the bulk flow velocity is not a turbulence driven phenomenon, but relies heavily on the rotating torus shaped vortex between each obstacle. The effect of flame folding is to increase the surface area of the flame front and the overall rate of energy release. This in turn generates a faster flame front propagation at the tip due to the expansion rate of the gas accross the flame front.This folding process increases the area of the flame front and increases the flame front speed [62, 63]. Unburnt pockets of gas behind the flame front burn later, creating a volumetric flow away from the closed end of the tube which forces the flame to propagate faster through the obstacle array.

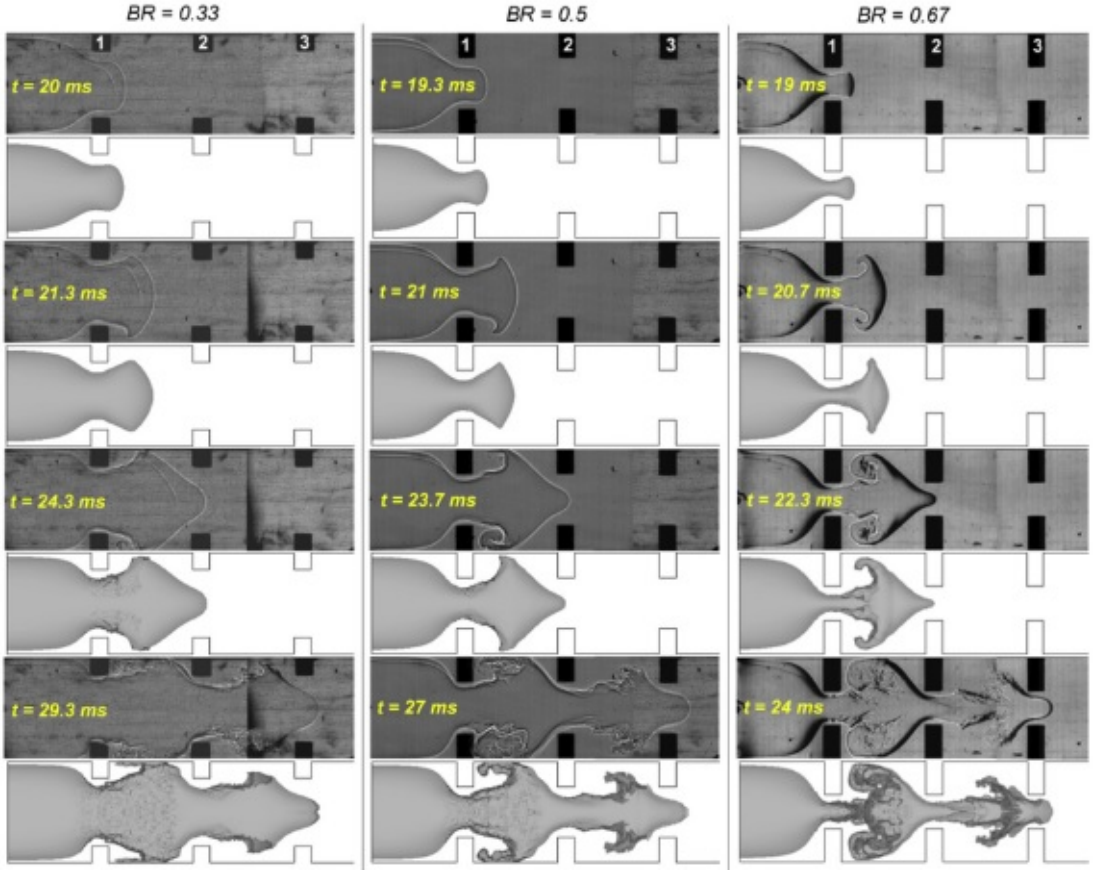

FIGURE 2.8: Illustration of flame folding from experimental schlieren images and numerical LES modelling. From the work of Johansen and Ciccarelli [64]. Obstacle blockage ratio is shown at the top of each column, time of each frame is shown in yellow

In addition to this flame folding process, turbulence in the upstream air is generated ahead of the flame as it is forced through obstacles by the volumetric gas expansion due

to the density gradient across the flame. The turbulence generated ahead of the flame increases the local flame speed relative to the moving gas frame of reference as the fresh turbulent mixture is consumed. Changes in turbulence intensity and pressure increase due to compressibility effects from upstream shock waves can promote extremely fast local turbulence flame speeds and where the channel has sufficient run up length and diameter for detonation to occur. This process can promote shock formation followed by detonation. This section will provide a detailed explanation of those factors affecting turbulent flames and some methods for analysis of such flames. Unconfined gas explosions and confined explosions in industrial plant or PDEs differ in that the flame-turbulence feedback mechanism only begins after the flame reaches a certain radius in the absence of initial turbulent conditions. A greater degree of confinement and interaction with turbulence generating obstacles leads to greater the potential for DDT within a short distance.

Both PDEs and accidental industrial explosions can often have strong degree of confinement from obstacles, pipe networks or even trees [65]. The result is that flame and gas ahead of the flame is unable to move through obstacles without being effected by localised turbulence. It is thought that the Buncefield Incident involved DDT as a result of FA along a tree lined avenue filled with a hydrocarbon-air vapour cloud which was ignited when the cloud drifted into a pumping station which was not correctly hermatically sealed. A major industrial explosion took place which is likely to have resulted in DDT and detonation. It was thought that the tree lined avenue may have caused significant FA to take place due to the turbulence generated by small branches and leaves.

Turbulent flames have many different structures within them which depend heavily on turbulence flame interactions, since turbulence is highly non-uniform and very difficult to predict on a local scale as can be seen by observing Figure 2.9 from the work of Buschmann, [66]. The image shown here illustrates OH radical concentration across the flame, a good indicator of the flames reaction progress with the fresh premixed reactants flowing up from the Bunsen towards the flame. The image shown here was taken at a turbulent Reynolds number of 755, the mean stream velocity is 8.7m/s and the fluctuation of this velocity due to turbulence is 1m/s.

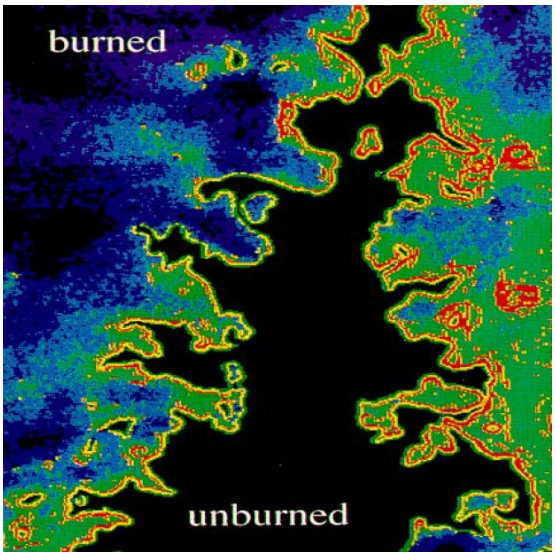

FIGURE 2.9: OH radical concentration from the work of Buschmann, Reynolds number 755, u' is 1m/s, U is 8.7m/s [66]

The relationship of turbulence in the reactants to the flame length scales can be characterised by u' and the integral length scale of local turbulence, ℓ_0. Kuznetsov et al. [67] performed a series of experiments with hydrogen and a range of mixtures of oxidizing mixtures, exploring the effects of obstacle size and geometry on flame acceleration. Their experiment was performed with circular shaped orifice obstacles known as orifice plates, as seen in Figure 2.10. The ratio of the orifice's blocked surface area to the area of its opening is known as the blockage ratio, BR, and is described by Equation 2.10.

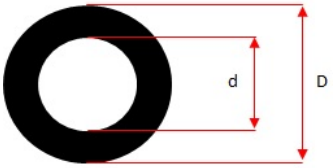

FIGURE 2.10: Orifice dimensioning conventions

$$BR = 1 - \left(\frac{d}{D}\right)^2 \quad (dimensionless) \tag{2.10}$$

Kuznetsov et al. [67] explored the relationship between blockage ratio, BR and ℓ_0. It was found that ℓ_0 depended directly on certain orifice dimensions depending on the value of BR, as illustrated in Figure 2.11. For BR in the range $0.3 \leq BR \leq 0.6$, ℓ_0 was

equal to D, the pipe diameter. For BR ≤ 0.1 ℓ_0 was found to be equal to the obstacle height, h. When BR ≥ 0.9, ℓ_0 was found to be d, the inner orifice diameter.

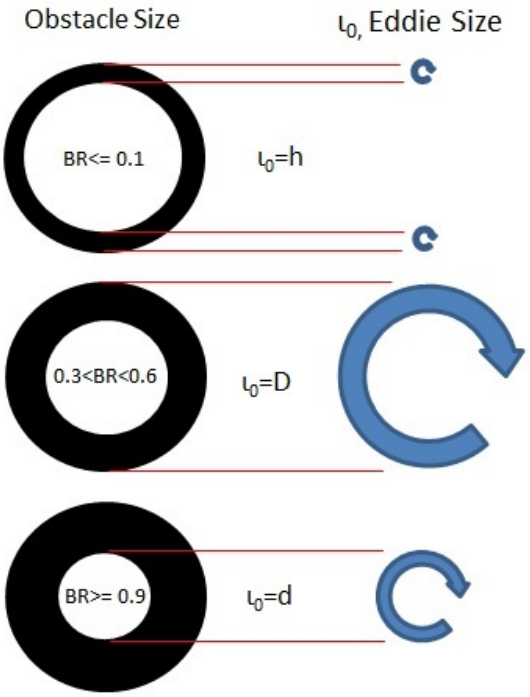

FIGURE 2.11: Turbulent Eddie integral length scale,ℓ_0 for different blockage ratio orifice plates. Derived from the work of Kuznetsov et al. [67]

Using Equation 2.11 it it possible to determine the time scale of the turbulent eddies,τ_0, as described by Law, [68].

$$\tau_0 = \frac{\ell_0}{u'} \quad (s) \tag{2.11}$$

The integral length scale is the largest length scale of the turbulent eddies. As the energy in an eddy dissipates according to the kinematic viscosity of the eddy, ν , the size of the eddy reduces, with smaller and smaller amounts of energy available to the eddy in a turbulence cascade until the smallest scale of eddy is reached at the cut off length scale, known as the Kolmogorov length scale, ℓ_κ . The Kolmogorov length scale, or cut of length scale for turbulence is determined by the magnitude of energy and scale of turbulence injected into the cascade at the largest length scale, the integral length scale.

The turbulent fluctuating velocity at the integral length scale is given by Equation 2.12 [68].

$$u'_0 = \left(\bar{u'^2}\right)^{1/2} \quad (m/s) \tag{2.12}$$

Furthermore the turbulent kinetic energy of flow, k can be described using Equation 2.13

$$k \approx \frac{3{u'_0}^2}{2} \quad (J/kg) \tag{2.13}$$

In addition it is possible to calculate the turbulent energy dissipation rate at the inertial subrange, ϵ, using Equation 2.14

$$\epsilon \approx \frac{k^{3/2}}{\ell_0} \quad (J/(kg.s)) \tag{2.14}$$

Once u'_0 and ℓ_0 are known the Reynolds number of the integral length scale can be calculated using ν, the kinematic viscosity of the fluid where $\nu = \mu/\rho$, and μ is the fluids viscosity. This Reynolds number is a measure of the ratio of inertial to viscous forces, and an indication of the turbulence intensity of in the fluid overall [68]. Equation 2.15 defines the turbulent Reynolds number at the scale of ℓ_0

$$Re_0 = \frac{u'_0 l_0}{\nu} \quad (dimensionless) \tag{2.15}$$

Once Re_0 has been calculated for the integral length scale it is possible to relate ℓ_0 to ℓ_κ using Equation 2.16.

$$\left(\frac{\ell_0}{\ell_\kappa}\right) \approx Re_0^{3/4} \quad (dimensionless) \tag{2.16}$$

Chaudhuri et al. [69] found theoretically that for a flame in isotropic turbulence, the flame Reynolds number can be related to the ratio of the laminar to turbulent flame speed. This relationship can be described by Equation 2.17. This theoretical relationship has also been verified experimentally by Chaudhuri et al. [70], as shown in Figure 2.12. It was found that expanding turbulent flames accelerate as a result of their increasing largest length scale, and decreasing smallest length scales. The larger

length scales increase as a result of surface area growth and geometric expansion of the flame, whereas the smaller Kolmogorov length scales become increasingly smaller as a result of the pressure gain form the expanding flame. These two processes increase the integral of the flame surface scalar dissipation spectrum, by increasing the range of turbulent length scales acting on the flame. This result is practically significant because it means that the range of eddies available to stretch and mix the flame with fresh reactants increases as the expanding turbulent flame propagates and generates greater pressures in the PDE. This law holds true for expanding spherical flames subject to isotropic turbulence and is expected to hold true for supernova explosions too, which are subject to the same conditions and transition through DDT in a similar manner to the way a PDE generates a detonation. Turbulence in PDEs is probably not isotropic in the case of orifice plate obstacles [71], which generate axisymmetric eddies at the integral length scale. This should be the case unless the obstacles used in the study generated isotropic turbulence, which could affect FA differently. In this equation S_T is the turbulent flame speed, S_L is the laminar flame speed, S_{L^0} is the original laminar flame speed at initial conditions, ℓ_0 is the integral length scale of turbulence and δ_l is the laminar flame thickness.

$$\frac{S_T}{S_L} \approx \left(\frac{u'}{S_{L^0}}\frac{\ell_0}{\delta_l}\right)^{1/2} \quad (dimensionless) \tag{2.17}$$

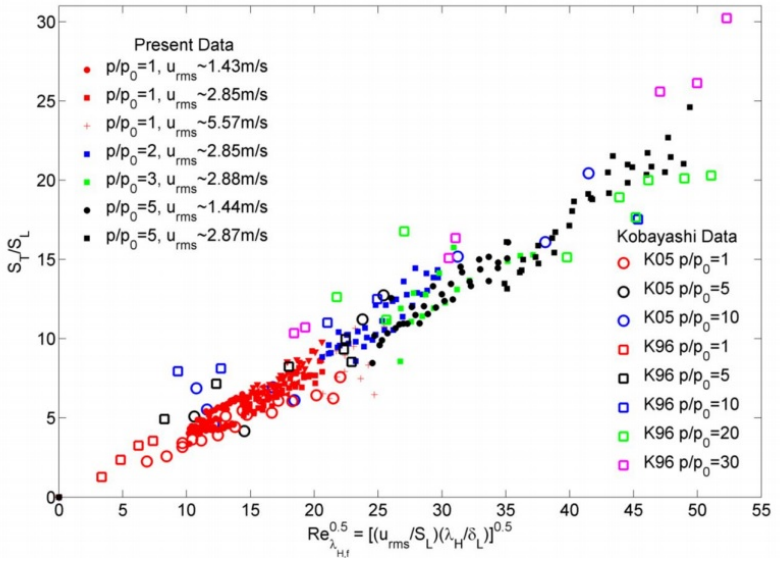

FIGURE 2.12: Data from the work of Chaudhuri et al. which shows that Methane-Air flames with 0.9 ϕ fits well with the prediction from Equation 2.17 [69]. Note that this at covers a range of pressures from p/p_0 1 to 30.

2.1.4.1 Flame Regimes

The Kolmogorov length scale is particularly useful for determining interactions between turbulence and the flame thickness, δ_l, which can be penetrated and disturbed by turbulence if the smallest turbulent length scale is able to interact with the flame due to its size. If $\ell_\kappa \leq \delta_l$ then the smallest structures in the turbulence cascade can interact with the length scales of the flame and as a result enhance the local turbulent flame speed. This statement is true unless the scale and intensity of the turbulence is small enough and powerful enough respectively to generate sufficient flame stretch, or sufficient mixing of cold reactants into the flame reaction zone to quench the flame. The process of flame quenching has been studied in detail by the Combustion Group at Leeds University [72, 73, 51, 74] with respect to the issue of flame stretch and extinction. This research has been carried out in fan stirred bomb reactors for a range of fuels, pressures and levels of turbulence. As such these results can be used to build empirically derived models for turbulent flame speed in the presence of a range of turbulence intensities at a range of different pressures. One potential use for such a model would be to determine flame speed in PDE FA.

Investigation has also been carried out by Dorofeev into the effect of turbulence mixing pockets of unburnt reactants into the flame [75], which concluded that only the smallest quenching pockets of gas are controlled by Kolmogorov scale turbulence. Dorofeev's analytical model showed that the larger thermal quenching pockets of gas were governed by mixture properties, such as Le, σ and β. Dorofeev's work also claims to be able to predict the difference between strong and weak FA, at least qualitatively, however the model is in its infancy and does not give a full quantitative description of FA behaviour.

It is important to remember that the flame thickness calculated for a turbulent flame regime is usually calculated using Equation 2.18, where ν is the kinematic viscosity. Equation 2.18 for the flame thickness within a turbulent flame front differs from the definition for the laminar flame thickness in the laminar regime shown in Equation 2.1.

$$\delta_l = \frac{\nu}{S_L} \quad (m) \tag{2.18}$$

The length scale of the flames reaction zone is roughly 10% of the total flame thickness in hydrocarbon air flames [29], with the rest being made up of the preheat zone. The

interaction between the flame's structures and length scales and the length scale of turbulence can be characterized as follows.

- When the Kolmogorov length scale is larger than the flame length scale the flame is said to be a thin flame and is likely to be corrugated, i.e. the turbulence wrinkles the flame sheet but does not penetrate the flame preheat zone or chemistry zones.
- If the Kolmogorov length scale is smaller than the preheat zone turbulent kinetic energy is able to interact with the preheating of the flame, generating a thick flame
- If the Kolmogorov length scale is small enough to penetrate the flames chemical reaction zone, δ_{CH} the flame is said to have turbulent chemistry and a distributed reaction zone [29]

Ciccarelli and Dorofeev [29] follow a similar analysis for flames using time scales instead of length scales wave numbers. In this analysis the flames characteristic time scale, τ_f is defined using Equation 2.19 compared with the life time of the dissipating eddy time scale using Karlovitz number, Ka, and the integral length time scale using Damköhler number, Da, as shown in Equations 2.21 and 2.20. τ_0 and τ_κ are the time periods of integral and Kolmogorov scale eddies respectively. It is important to note that the flame regimes discussed in Figure 2.66 are limited to the classification of flame regimes when $Da \geq 1$.

$$\tau_f = \frac{\delta}{S_L} \quad (s) \tag{2.19}$$

$$Da = \frac{\tau_0}{\tau_f} \quad (dimensionless) \tag{2.20}$$

$$Ka = \frac{\tau_f}{\tau_\kappa} \quad (dimensionless) \tag{2.21}$$

These states are then compared with the axes of a flame state diagram known as the Borghi diagram as shown in Figure 2.13, which plots flame states relative onto a map of u'/S_L against ℓ_o/δ_l. The thin flame regime is called the laminar flamelet regime

here, and is bounded by the $u'/S_L = 0$ and $Ka = 1$. Flames which fall between the bounds of $Ka \geq 1$ and $Da \geq 1$ are said to be thick flames. These flames have turbulent premixing zones and may have turbulent chemistry however the characteristic flame time scale is still faster than the characteristic time of the larger scale turbulence in the integral length scale, i.e. $Da \geq 1$. In extremely intense turbulence where $Da \leq 1$ the turbulence is so intense that the reaction cannot proceed fast enough for combustion to continue. Flame quenching is said to occur when the Reynolds number based on the integral length scale is greater than 250 [76].

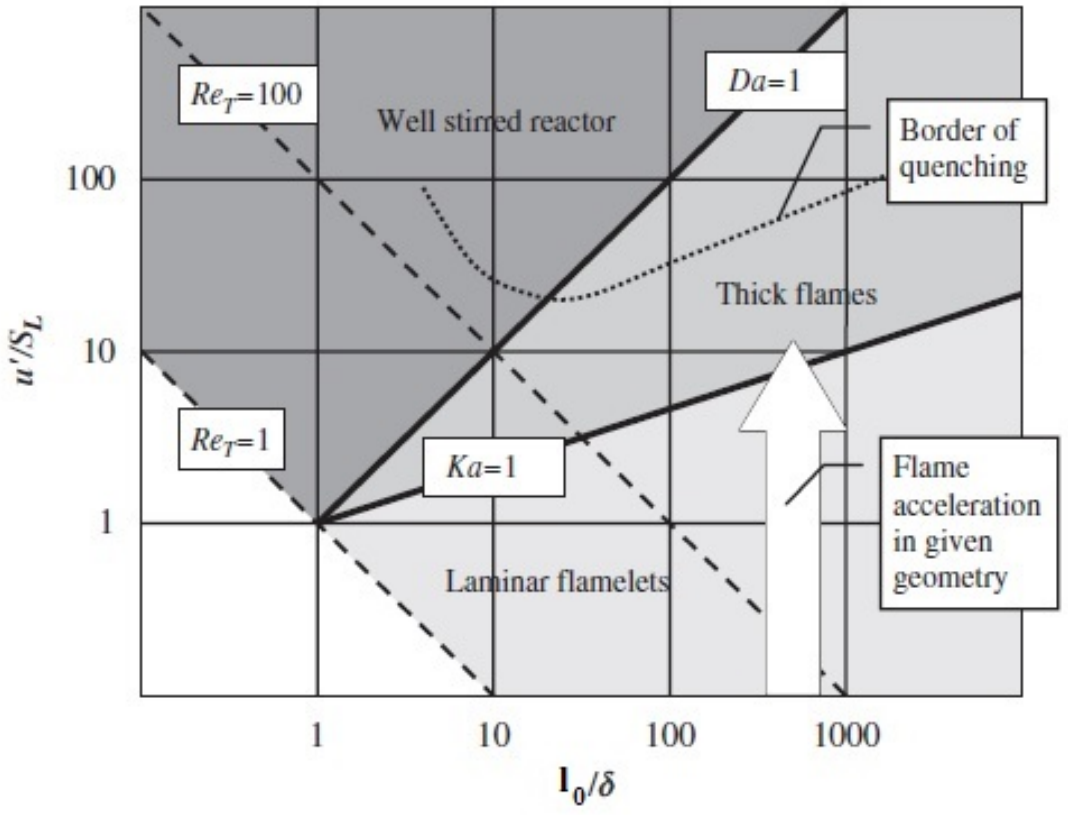

FIGURE 2.13: Borghi diagram from the work of Ciccarelli et al. [29]

2.1.5 Flame Front Speed

Flame front speed (burning rate), S_f, is defined as follows:

$$S_f = \sigma(A_f/a_d)u_{tm} \quad (m/s) \tag{2.22}$$

Where σ is the gas expansion ratio across the flame, the ratio of burnt gas to unburnt gas density ($\rho u/\rho b$), A_f/a_d is the ratio of flame area, A_f, to the cross sectional area of the duct, a_d, and is the same as the fractal dimension of the flame surface. u_{tm} is the mean local turbulent flame speed. Flame expansion ratio is determined by mixture content i.e. fuel mixture choice and equivalence ratio, and tends to be around 7-8 for most hydrocarbon fuels burning under stoichiometric conditions in air.

For FA to successfully transition to DDT it is necessary to maximise each of the terms of Equation 2.22. Flame surface area initially grows as the periphery of the flame touching the tube wall is subject to the no slip boundary condition at the wall. Volumetric expansion across the flame leads to a finger shaped flame with an accelerating core, burning slower at the walls than the centre line. This initial flame is enhanced in a PDE by obstacles; as such the tube wall should not be smooth if fast FA is desired. This will only happen successfully if a flame can stretch effectively without quenching. Turbulent flame speed, u_{tm} , is determined by laminar flame speed u_l, and local turbulence intensity u' as well as the length scales of the turbulence. Laminar flame speed is determined by fuel choice, initial pressure and temperature in addition to mixture stoichiometry. Many relationships between premixed turbulent flame speed and turbulence intensity have been suggested [77, 78, 79, 80, 81, 82], although detailed experimental data flame speed can be scarce for some fuels, particularly at the very high pressures investigated during detonation modeling.

2.1.6 The Shock-Flame Double Discontinuity

The double discontinuity is a name given to describe the stage of flame acceleration which can be described as having a separate shock and flame front before detonation has taken place. The first flow discontinuity is the shock, followed by the second discontinuity, the flame, both of which are separated by some distance. Often these conditions are created by flames accelerating through obstacle filled tubes, such as those described in the work of Ciccarelli et al. [83, 63], although this can also take place in smooth walled tubes. One common parameter used to describe the tube geometry in such experiments is the variable X/D, or non-dimensional tube length measured relative to tube diameter. Detailed experiments of FA without DDT have been undertaken by Ciccarelli [63], shown in Figure 2.14, which show flame location

against flame speed as the flame passes through three different obstacle arrays with three separate obstacle geometries, which are classified by blockage ratio. Ciccarelli's experiments were conducted within the range of $0.43 \leq BR \leq 0.75$ with $0 \leq X/D \leq 13$ using stoichiometric propane-air mixtures in a 0.14m diameter 3m long tube at a temperature and pressure of 300K and 1atm respectively. This single shot experiment used a vacuum pump and recirculation system after the reactants were injected to increase mixture homogeneity.

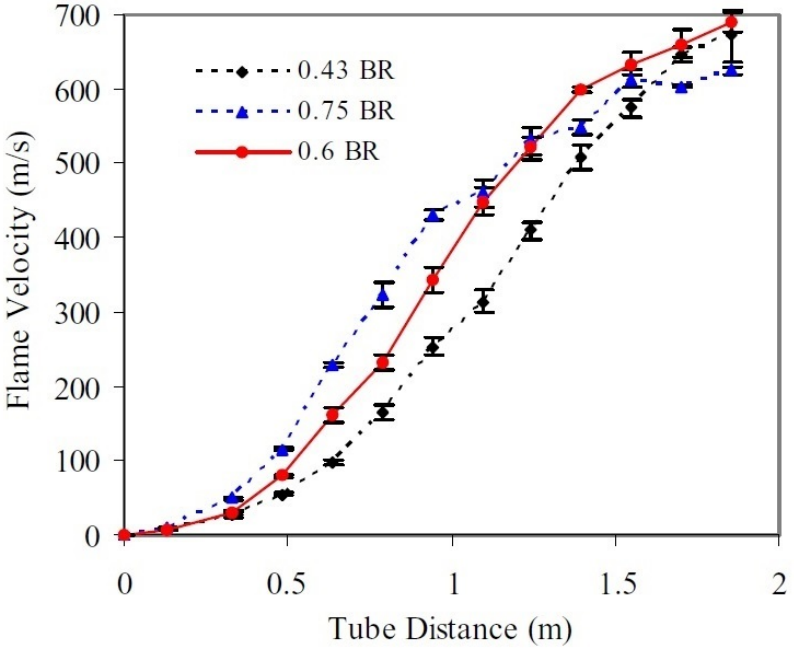

FIGURE 2.14: Experimental Data from Ciccarelli for stoichiometric propane-air and $0.43 \leq BR \leq 0.75$ at 0.14m diamter [71]

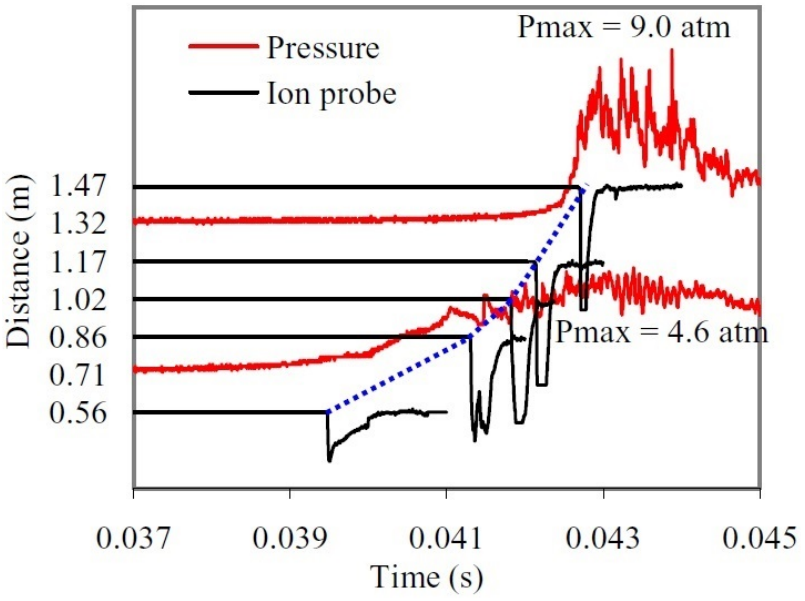

FIGURE 2.15: Ion Probe and Pressure data vs. time from ignition for stoichiometric propane-air, $0.43BR$ at 0.14m diameter [71]

The results in Figure 2.14 show rapidly increasing flame speeds until an inflection point at around the sonic velocity in the reactants. After this point the acceleration decreases until a velocity of around 700-800m/s at which point the flame speed becomes steady as X/D increases. It should be noted that DDT was not observed within this experiment. Ciccarelli used propane-air mixtures as a surrogate for JP-10 air mixtures which is a favoured PDE fuel, as both of these mixtures have similar FA and DDT properties. It can also be seen from Figure 2.15 that the flame time of arrival is difficult to determine from the pressure signal alone, and that ionisation probes or similar sensing equipment must be used to determine flame time of arrival in order to calculate flame speeds.

In a practical PDE, a set of obstacles similar to this arrangement is often used as a pre-detonator. The pre-detonator is smaller in diameter than the main detonation chamber, which enhances FA and reduces the run up distance. Because the pre-detonator uses the fuel's chemical enthalpy to drive FA and DDT the ignition energy can be considerably reduced in comparison with direct detonation initiation [84]. As a result most practical PDE engines will need to make use of a pre-detonator to run up to detonation using the fuels energy rather than a prohibitively weighty ignition system.

2.1.7 Shock-Flame Interactions

Figures 2.16 to 2.18 show the complexity of shock flame interactions which take place within the PDE environment. These results are from experiments carried out by Ciccarelli et al. [83] which focused on the effect of shock waves on the advancing flame front traveling behind the shock prior to detonation. Each of the experiments shows flame acceleration in a stoichiometric propane-air mixture which is burning within a 76mm cross section square channel with optical access for schlieren equipment which is used to measure density gradients in the gases traveling along the duct. A strong dark line at the right hand side of each frame indicates the presence of the lead shock wave, which is followed by a series transverse shock waves in each case. The transverse shocks are followed in turn by the reacting combustion front. This can be seen as an area of intense wrinkling which is present due to the change in density as combustion takes place. Figure 2.18 shows the 0.33 BR case, which illustrates compressive shock waves traveling with relatively little obstruction in comparison to the 0.5BR and 0.67BR cases seen in Figures 2.17 and 2.18 respectively. The two later cases illustrate much stronger compressive shock waves, which refract out towards the wall with a progressively near spherical shape as the degree of restriction increases from 0.33 BR to 0.67 BR. It is also interesting to note that behind each of the orifice plates there is a strong recirculating vortex formed on the trailing edge of the orifice lip. This vortex is much more visible in the 0.67BR case. The later cases exhibit considerable losses to the shock wave, which reduce the ability of the shock wave to sufficiently compress the reactant mixture and therefore decrease the reaction rate.

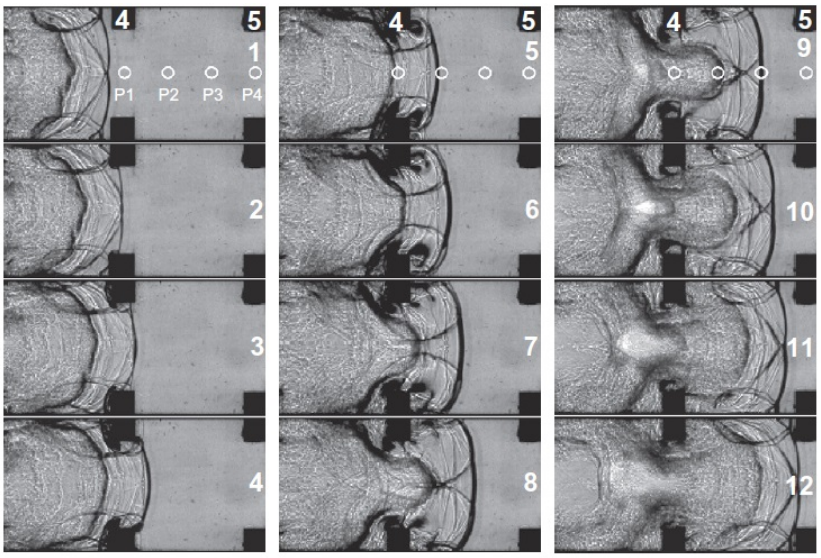

FIGURE 2.16: Experimental schlieren data from Ciccarelli for stoichiometric propane-air and 0.33BR in a 0.076m square channel from the work of Ciccarelli [83]. Interframe time 33μs

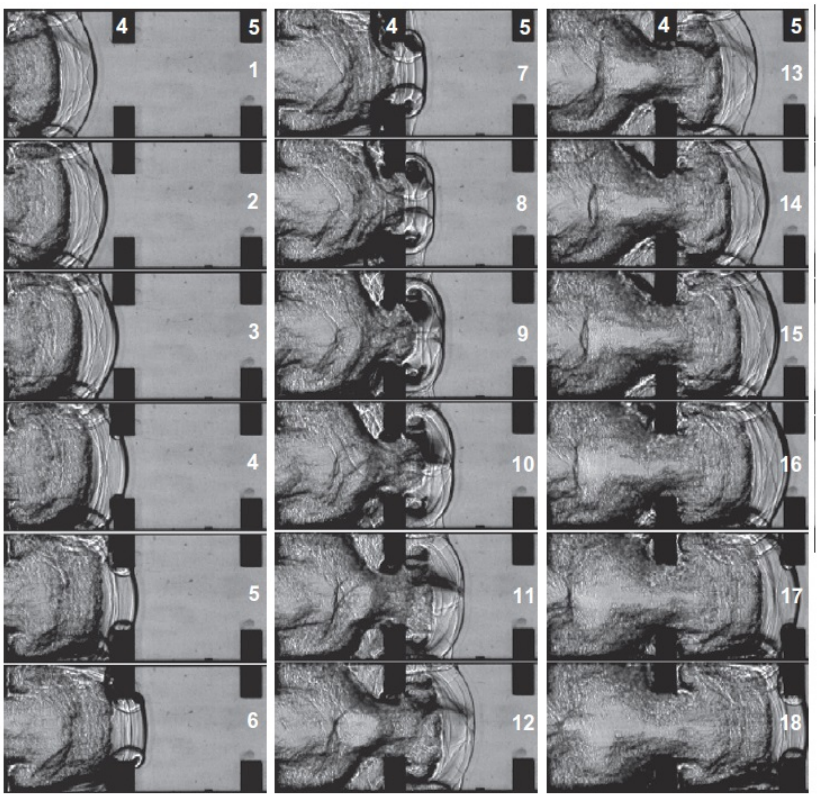

FIGURE 2.17: Experimental schlieren data from Ciccarelli for stoichiometric propane-air and 0.5BR in a 0.076m square channel from the work of Ciccarelli [83]. Interframe time 33μs

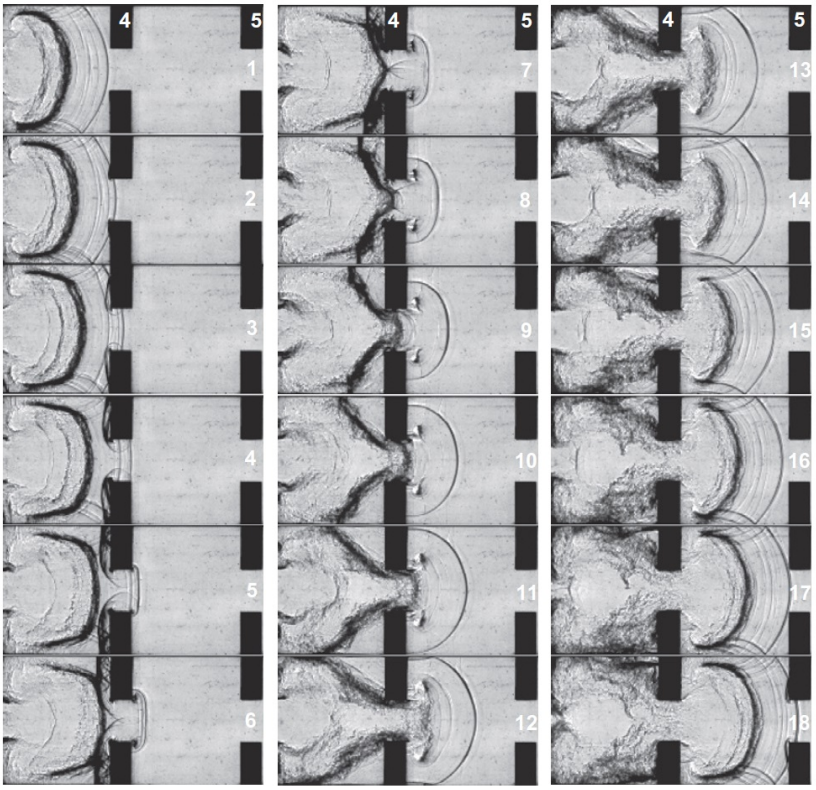

FIGURE 2.18: Experimental schlieren data from Ciccarelli for stoichiometric propane-air and 0.67BR in a 0.076m square channel from the work of Ciccarelli [83]. Interframe time 33μs

These schlieren images were also taken in conjunction with flame speed measurements calculated made by means of a time of flight (TOF) measurements between ion probes. These ion probes detected the presence of the chemically reacting flame front as soon as it conducted ions between two charged electrodes mounted in the channel. As the distance between sets of electrodes was known, the TOF flame velocity measurements between each ion probe could be calculated by dividing this distance by the time of flight between the two probes. It was found that the 0.33 BR case allowed for the flame to reach a flame speed plateau of 750m/s before accelerating further to approximately 900m/s by the end of the 3.66m long tube. The higher blockage ratio cases did not exhibit this velocity jump, but plateaued at around 600m/s and 700m/s respectively. It is thought that Richtmeyer-Meshkov flame instabilities caused by rearward propagating shock waves reflected off of forward obstacles were interacting with the flame in the 0.33BR case, but that this was not possible in the cases with higher blockage ratios. These instabilities known to accelerate the turbulent flame speed [83]. These results can be seen in figures 2.19 to 2.21. The solid red and black lines in these figures represent

the flame speed observed along the tube by ion probe TOF measurements. The green data with a large variation around the ion probe data is a record of the instantaneous flame speed recorded with high speed video at 120,000 fps.

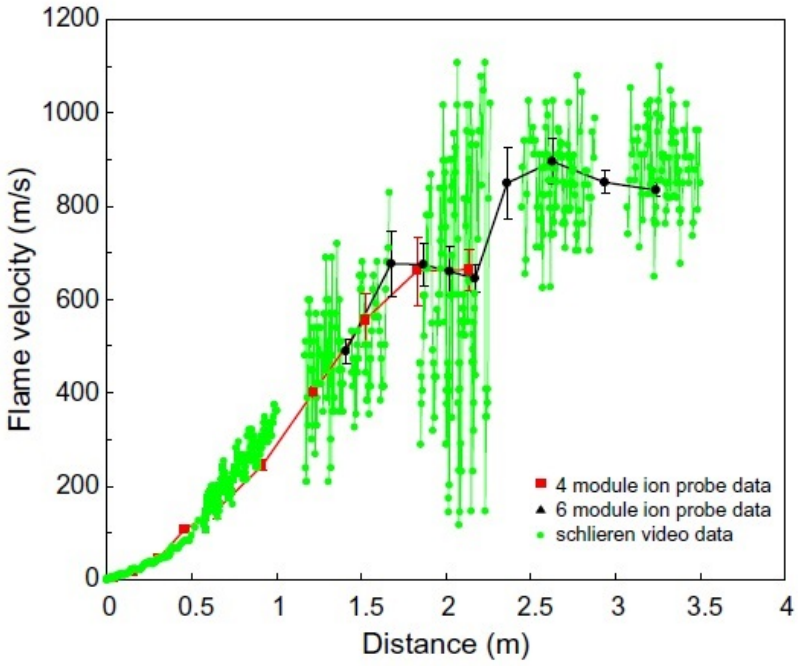

FIGURE 2.19: Experimental ion probe and schlieren data from Ciccarelli for stoichiometric propane-air and 0.33BR in a 0.076m square channel from the work of Ciccarelli [83].

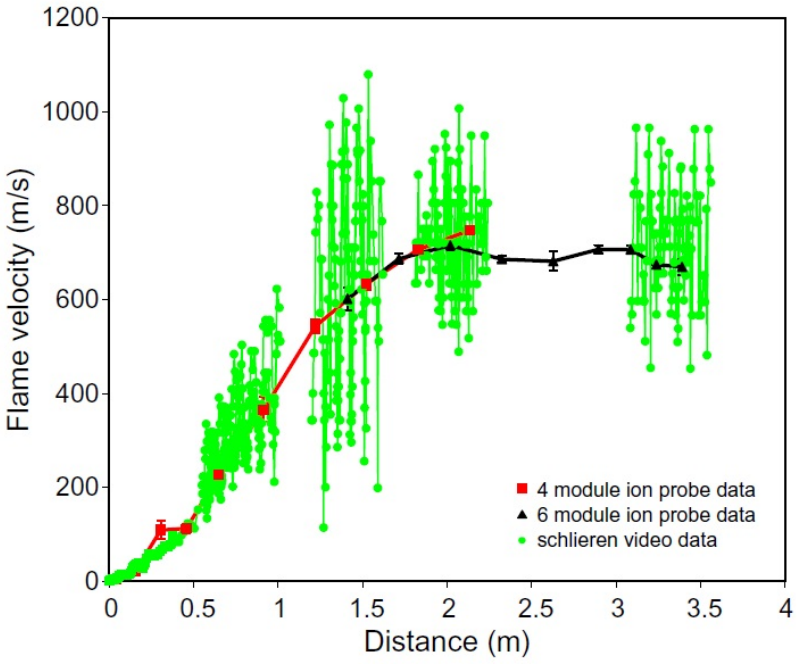

FIGURE 2.20: Experimental ion probe and schlieren data from Ciccarelli for stoichiometric propane-air and 0.5BR in a 0.076m square channel from the work of Ciccarelli [83].

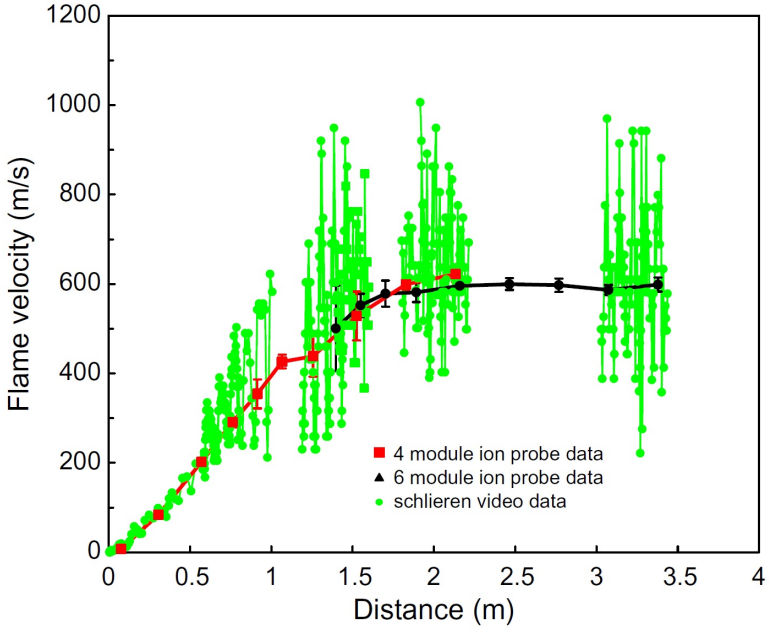

FIGURE 2.21: Experimental schlieren data from Ciccarelli for stoichiometric propane-air and 0.67BR in a 0.076m square channel from the work of Ciccarelli [83].

Figure 2.22 shows a set of compound schlieren images for these orifice plates in the same tube. It can be seen that the larger orifice plates obscure the passage of the flame from the pockets of unburned gas inside of these deeper orifice plate bounded pockets.

This is because the rotating shear layer left behind after the passage of the shock wave moves at a slower rate than the small intense shear layers in the 0.33BR and 0.57BR case, resulting in a reduced rate of mixing between the flame front and the unreacted gas held within these pockets. The result of this unburnt gas being left behind is that the flame takes much longer to burn through the entire mixture of the tube.

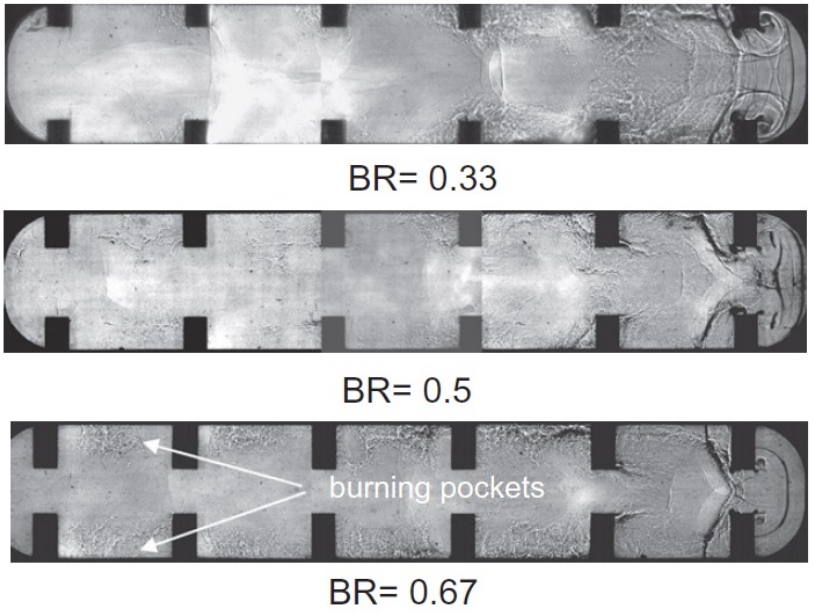

FIGURE 2.22: Composite experimental schlieren data from Ciccarelli for stoichiometric propane-air and a range of orifice BR, as indicated above. The channel used in each case was 0.076m and sqaure in cross seciton, from the work of Ciccarelli [83].

2.1.8 Deflagration to Detonation Transition

2.1.8.1 What is DDT?

DDT, or the explosion within the explosion occurs when the reactants ahead of the flame are subject to conditions which generate hot spots due to the shock wave ahead of the flame. For such hot spots to be generated the flame must first be traveling at a high enough speed to generate a shock wave ahead of the flame due to the speed of the gas venting. Schlieren imaging is a technique often used by researchers exploring the effect of shock waves and density gradients on flames. The image is created by shining a high intensity light through an area of interest with an expected density gradient, such as a shock or flame then refracting the image which is received on a knife edge before passing the remaining image to a camera where the density gradients are recorded to

show regions of higher and lower density. The schlieren image in Figure 2.23, [85] clearly illustrates the different fluid dynamic sections in a fast deflagration, namely the turbulent flame brush (left) and the shock wave (right) sometimes known as the 'double discontinuity' due to the distinct separation between the flame and the shock wave. The flame shown in this Figure is traveling at approximately $V_{CJ}/2$, the speed of sound in the combustion products. $V_{CJ}/2$ is the maximum flame speed possible for a turbulent deflagration before detonation occurs, and can only be obtained if the detonation tube is long enough to allow FA to occur for long enough to reach this pace. If this condition is maintained for a sufficiently long time, and the induction length between the shock and the flame is sufficiently long, DDT is likely to occur.

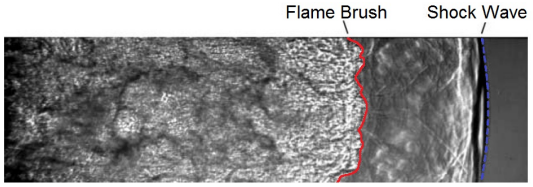

FIGURE 2.23: Schlieren image of a fast deflagration traveling at approximately 800m/s from the work of [85] This image is taken from the tube wall frame of reference

Figure 2.24 from the work of A.K Oppenheim [86] shows the process of the turbulent flame front approaching the lead shock over time during FA.Time intervals of 5 μs between frames are recorded here in a hydrogen oxygen flame.

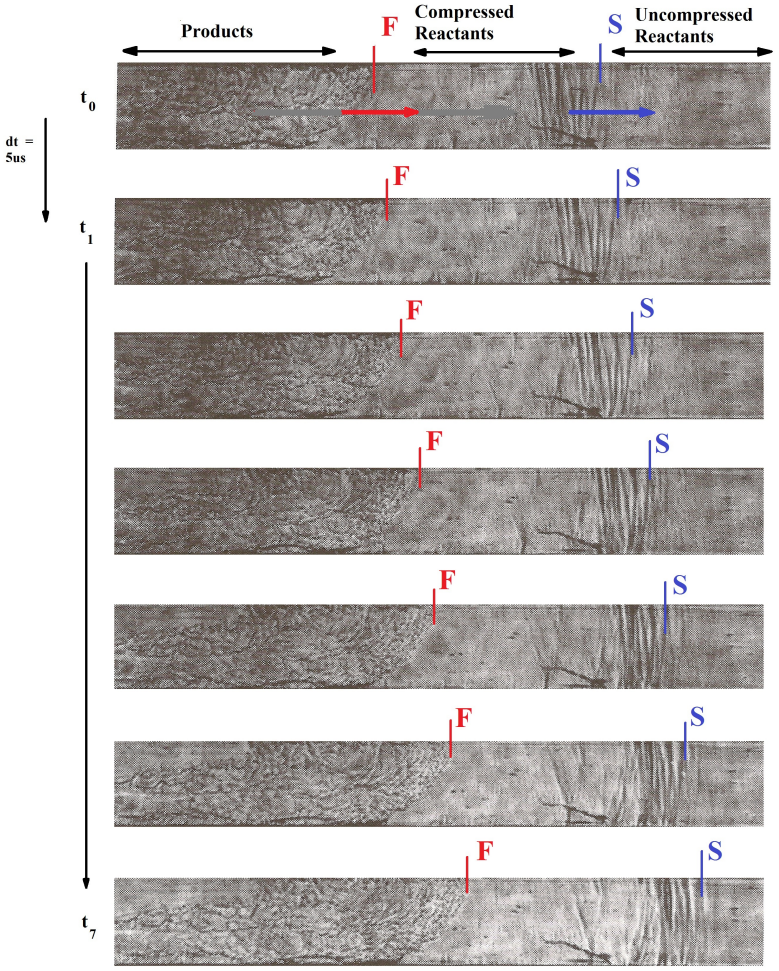

FIGURE 2.24: Schlieren image of a fast deflagration adapted from the work of Oppenheim [86] S represents the most forward location shock front, F represents the most forward location of the flame front. Arrows indicate the shock and flame direction of movement, taken from the tube wall frame of reference. Time difference between frames

Figure 2.24, also from the work of Oppenheim, [86], shows the later stages of FA. By the second frame the shock wave refractions behind the lead shock can be seen to interfere with the flame front at the lower corner of the flame where it meets with the turbulent boundary layer. After the next 5 μs interval this effect has generated two distinct hot spots, each with their own distinct flame fronts, shown by two dark rounded shadows on the schlieren image. By the fifth frame, only 10 μs later, a new hot spot has been generated at the boundary of these two hot spots. This hot spot has been generated by the raised pressure formed by the two new combustion hot spots and their associated pressure waves. After this point the new hot spot generates a tube wide DDT event, which may or may not form a stable detonation after decaying

from the initial overdriven detonation, depending on the fuel type and mixture, tube geometry and other operating conditions.

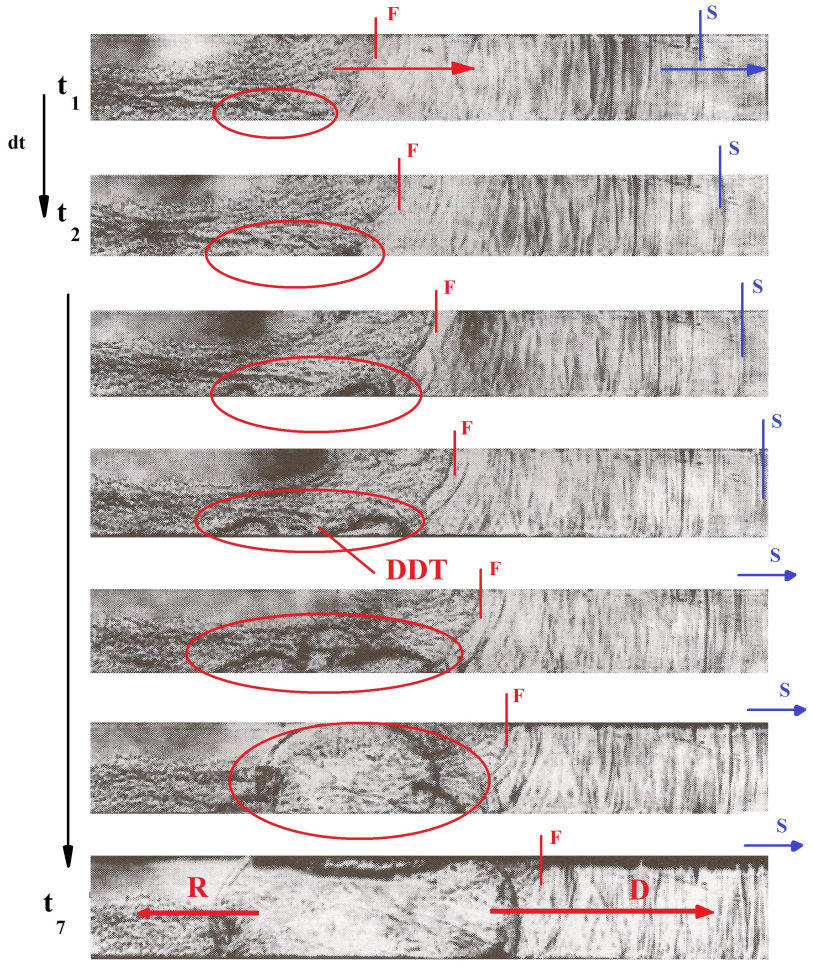

FIGURE 2.25: Schlieren image of DDT onset from a shock reflection in the boundary layer adapted from the work of Oppenheim et al. [86] both the detonation wave, D, and retonation wave, R, back into the products can be seen here. F and S represent the flame and shock fronts respectively, note that for the final three frames the shock has exited the field of view indicated by the arrow. Blue and red arrows indicate the direction of the shock and flame travel. This schlieren image is taken from the tubes frame of reference with a stationary schlieren camera

2.1.8.2 Processes leading to DDT

There are many different processes which can lead to detonation via flame acceleration in ducts. The main processes are described in detail in the work of Lee [86] using images reproduced from the work of Meyer et al. [87] who performed an extensive laser schlieren imaging study of accelerating hydrogen oxygen flames and their transition to

detonation in tubes with one end closed. Routes to DDT have been grouped into those close to the flame and those closer to the shock.

DDT in the turbulent flame brush Meyer et al. studied the case of DDT in the turbulent flame brush [87], which was pre-compressed by means of the shock present from previous flame acceleration and gas expansion. Interestingly, Meyer et al. found that the shock wave ahead of the flame was insufficient in strength to generate autoignition in the reactants. This conclusion was reached after carrying out a detailed particle path analysis for the particle which eventually became the centre of the explosion within the explosion which produced a temperature and pressure plot for this particle. As a result it was possible to integrate the ignition delay time over time along the particle path with known temperature and pressure. Meyer et al. conclude that it is not possible for the centre of the explosion within the explosion to occur as a result of autoignition because only 4 % of the total autoignition delay was completed by the time the explosion within the explosion had begun. Meyer et al. state that other means of local DDT triggering are responsible for the transition to detonation, namely the heat and mass transfer properties of the flame.

Furthermore Meyer et al. speculate that the physical processes driving this phenomenon of DDT in the turbulent flame brush are due to the transfer of free radicals ahead of the flame, shown in Figure 2.1 as the front edge of the reaction zone, or by heat transfer ahead of the flame as a result of radiation, although this speculation is not explored further by Meyer. Liberman et al. [88] have recently investigated the effect of radiation on propagating flames, finding that radiation can enhance FA by increasing the flame speed ahead of the flame, or generate a direct DDT event. Liberman et al. assume that the gas phase is transparent to radiation and that dust in the unreacted gas absorbs and then re-emits the radiation to surrounding reactants, generating a thermal time lag between the reaction front source emission and the reactants heating. The effectiveness of radiative heat transfer depends on the wavelength of radiation generated, and on the medium absorbing the radiation ahead of the flame, whether hydrogen as modelled in the paper or another fuel. It is speculated that this mechanism may also have a large impact on dust explosions where particles ahead of the reaction front could readily absorb thermal radiation, generating faster FA rates or

DDT ahead of the main reaction zone. This is a new field of study which warrants further numerical investigation, particularly as the effect of radiation in mixtures without suspended dust particles was not explored in detail. Work in this field has also been completed by Karlin [89] who specifically investigated radiation in tulip shaped flames and wrinkles which concentrated radiation in small pockets of unreacted gas. Karlin states that radiation can trigger DDT in the gas phase directly, by means of generating a temperature gradient ahead of the flame. Karlin did not model particles in the flow, only the gaseous phase. Clearly, this is a field which warrants further study from both experimental and numerical perspectives.

DDT in shockwaves There are a number of mechanisms responsible for the generation of DDT within shock waves further away from the vicinity of the flame [86]. One example of the explosion within the explosion taking place is within the foot of a precursor shock wave ahead of the flame, which creates a hot spot close to the wall. This hot spot then propagates becoming the explosion within the explosion which travels across the channel as well as upstream (retonation) and downstream (detonation). Furthermore another mechanism for DDT generation can take place at the location of the contact surface between two shock waves, where two merging precursor shock waves generate a detonation.

2.1.9 Detonation

2.1.9.1 Planar Detonations

In order to have a good reference point for understanding the detonation phenomenon it is important to know where detonation occurs in relation to deflagration and when DDT might occur. Pierre-Henri Hugoniot (1851 - 1887) [90] was a French Engineer who worked extensively for the French Navy and undertook research regarding gaseous detonation in canons. Hugoniot also developed a system of equations based on the continuity of mass, momentum and energy upon which the continuity equation, Navier-Stokes and energy equations were later built. The Hugoniot curve can be seen in Figure 2.26 [29, 91] and is plotted against relative density and pressure to allow the engineer to visualise the pressure loss or pressure gain effects of combustion at the same time as visualising density. Point 1 is the origin of the combustion process on the Huginiot

curve. Points on the Huginiot curve between P and C represent subsonic deflagration, in the subsonic regime. Points between P and V are physically impossible to obtain and which are crossed during DDT. Points between V and J represent supersonic combustion within the sonic regime, with J representing the CJ detonation state, and points above J are overdriven detonations with velocities and pressures in excess of the steady CJ detonation values. Points closer to C than P represent strong deflagration and points closer to C than J represent strong detonation. Detonation strucure is often defined in terms of the detonation cell width, λ, which is essentially the width of the pattern generated by transverse detonation waves and the detonation lead shock as they intersect and the and longitudinal waves as they propagate during the detonation phenomenon. The shape produced is usually akin to a fish scale, with the convex curces aimig in the direction of detonation propagation.

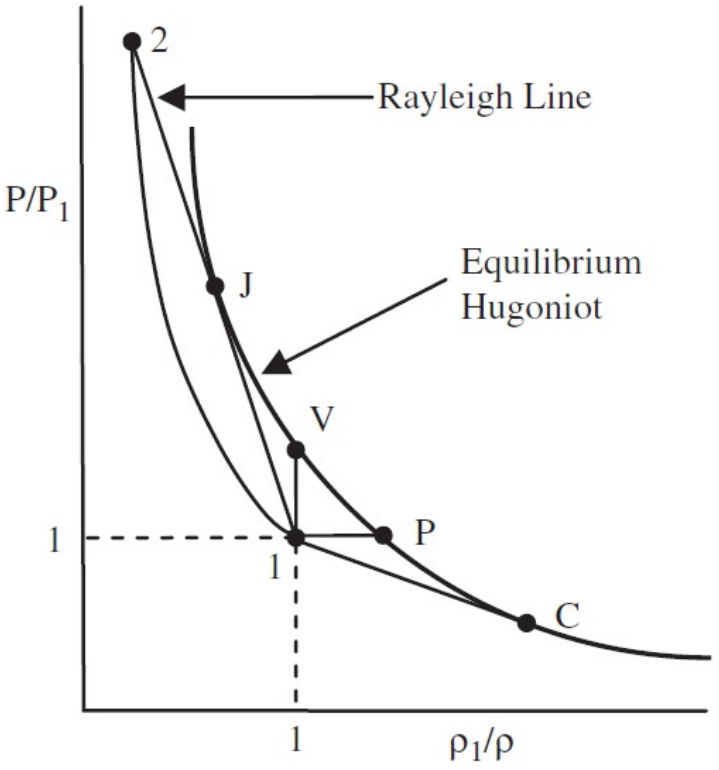

FIGURE 2.26: Hugonoit curve expressing combustion properties of subsonic and supersonic combustion [29]

Figure 2.27 [92] shows the various routes to detonation with path a being very unlikely to achieve without reactions at every point along the curve, path b represents fast chemical kinetics, path c represents slow chemical kinetics and path d represents zero

chemical energy release within the shock wave. Furthermore the peak of pressure in each curve represents the Von-Neuman spike behind each shock wave. Using this method of analysis, it is possible to determine whether a detonation has taken place, or not.

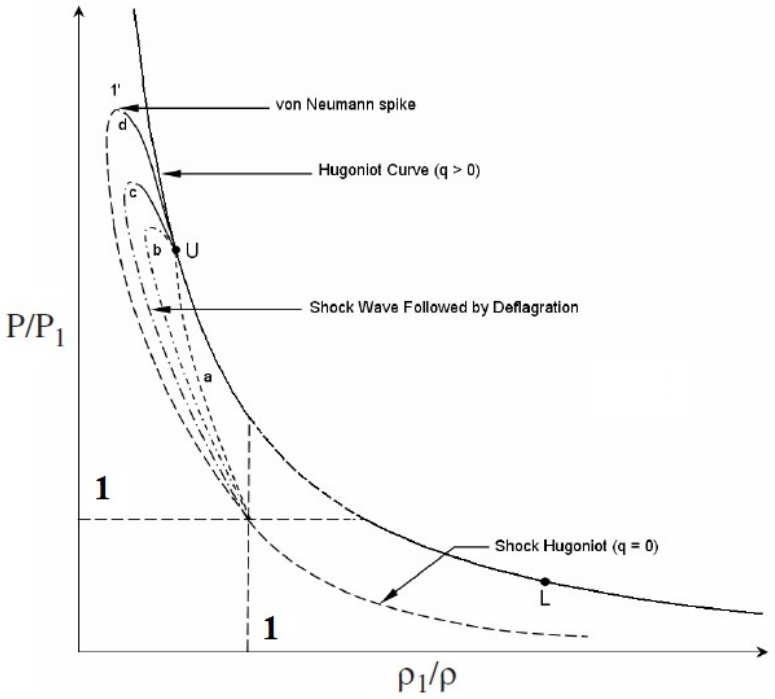

FIGURE 2.27: Possible scenarios during DDT plotted on the Hugonoit curve [92]

Planar detonations have a repeating structure which can be seen on soot foil records in detonation tubes as repeated detonation cells, often with the same or similar characteristic dimension- particularly in the case of a stable CJ detonation. These cells have a fish scale like appearance which is created by the crossing of trajectories of longitudinal and transverse shock waves coalescing at triple points as can be seen in the soot foil record in Figure 2.28 and 2.29. Each different mixture has a different cell size, and in this case the mixture cell fills one tube diameter which is the limiting structure for the tube in question according to the tube diameter detonation cell size criterion. In this case the soot foil record can clearly be seen to be repetitive in the X and Y axes, which indicates that he detonation structure is traveling in one plane and is therefore a planar detonation rather than a spinning one. The numerical simulations of Sugiyama in 2.28, [93] match remarkably well with the shape of detonation soot records taken for a different case shown in Figure 2.29 (2H2, O2 and 70 % Argon at 70 torr) from the

original work of Strehlow in the 1960's [94]. This comparison serves as an illustration of recent advancements in numerical modelling of detonation structures.

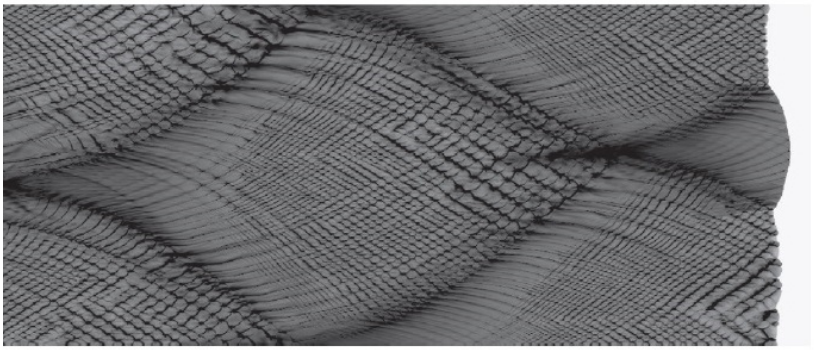

FIGURE 2.28: Numerical Simulation of a soot foil record for the limiting case of cell size in a detonation tube [93]

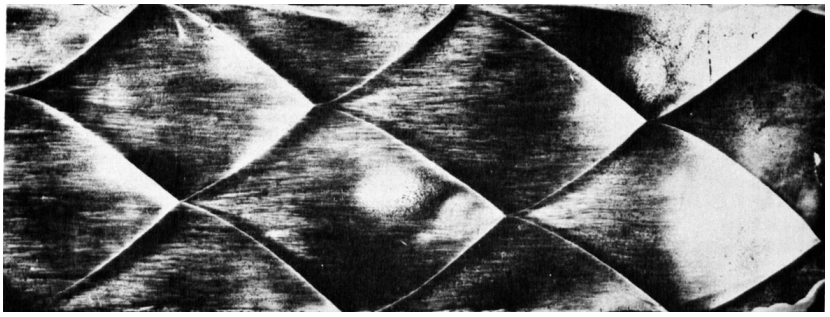

FIGURE 2.29: Experimental soot foil record in the planar mode (2H2, O2 and 70 % Ar at 70 torr) [94]

The work of Ishii et al. [95] in Figure 2.30 shows that soot records match with schlieren imagery in the same situation, and also that these records tie in with high speed measurements taken of light self-emission from the flame. In this case the white circles highlight the triple points the two transverse waves and longitudinal wave meet and the dotted line highlight the slip line caused by micro-vortices which trail behind the triple point as colliding gas paths meet.

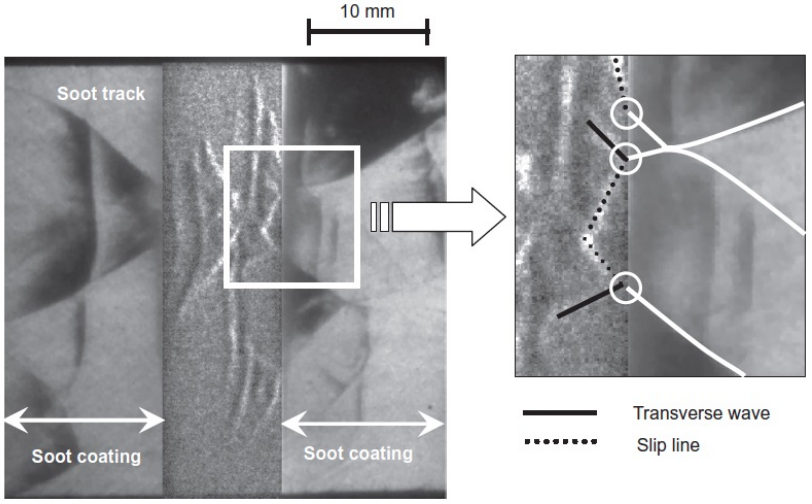

FIGURE 2.30: Experimental soot foil record compared in line with schlieren images (2H2, O2 and 7 Ar at 40kPa) [95]

2.1.9.2 Spinning Detonations

Continuous spin detonations have been the interest of several recent investigations in the literature as they provide relatively constant thrust over a short duration from continually spinning detonations between two annuli Bykovskii et al. [96]. Spinning detonations are known to take place at the limiting geometric conditions for detonation to take place, i.e. at the limiting tube diameter. This process has been investigated by Frolov et al., where detonation has been seen to transition in a limiting diameter smooth tube after having being accelerated to an adequate velocity using specially shaped obstacles [97, 98].

2.2 Experimental Approaches to PDEs

Many experimental approaches have been taken to the problem of generating a reliable detonation for the purpose of creating PDEs powered propulsion devices for the aerospace propulsion. Approaches range from instantaneous detonation generation methods to geometric or electrical DDT methods in addition to novel geometric DDT methods. It has been determined that the most energy efficient manner of generating detonations for use in aerospace propulsion is via geometric DDT devices due to weight and space constraints.

2.2.1 Classification of FA Regimes

In order to determine whether a detonation has been achieved experimentally dynamic pressure, photodiode and ion probe signals are often used to determine the speed of shock waves and flame reaction zones respectively. It is important to be able to interpret these graphs to classify the different combustion modes. According to Kuznetsov et al. [67] there are at least four main regimes for FA in obstacle filled tubes. Kuznetsov et al. have illustrated the different results in X-t plots which record amplified analogue signals of the pressure, light intensity and ion current present in the flame as it traverses along the tube. These regimes are described as follows:

Unstable/Quench In this case, the flame is travelling at a speed slower than the speed of sound in the combustion reactants and with an unstable flame speed. Typically this sort of flame will quench as the flame travels along the tube, leaving a portion of the reactants mixed with products in the tube.

Unstable/Slow In this case the flame speed is travelling slower than the speed of sound in the combustion products and the pressure developed is far less than the adiabatic combustion pressure for complete combustion of the mixture. The flame speed is also unstable, galloping, or changing as the flame propagates along the tube. This galloping is not the result of pressure oscillations in the tube, but the result of local quenching of the flame and re-ignition sending a propagating combustion wave both upstream and downstream. One example of the unstable/slow regime is shown in Figure 2.31 in which case the flame speed accelerates to 156m/s and then decelerates to 2m/s. The maximum observed pressure in this case was only 1.25atm and the orifice blockage ratio was set at a constant BR=0.3. Increasing the orifice BR with a similar mixture of H_2 and air was seen to yeild a faster, yet still unstable flame in Figure 2.31. The flame propagation chart observed in Figure 2.32 illustrates flame quenching followed by re-ignition and flames travelling both forwards and backwards along the tube.

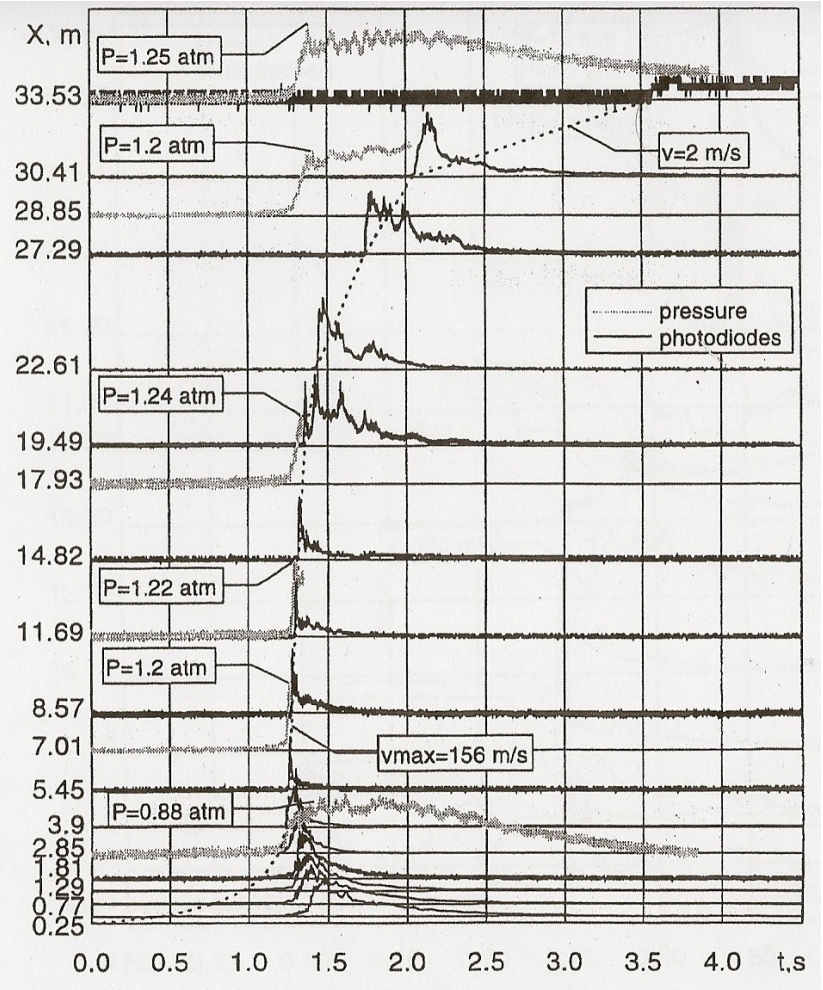

FIGURE 2.31: Experimental X-t plot from a slow/unstable flame reproduced from the work of Kuznetsov et al. [67]. Results here show flame propagation in a tube with an internal diameter of 520mm filled with BR=0.3 obstacles and a 10% H_2:air mixture.

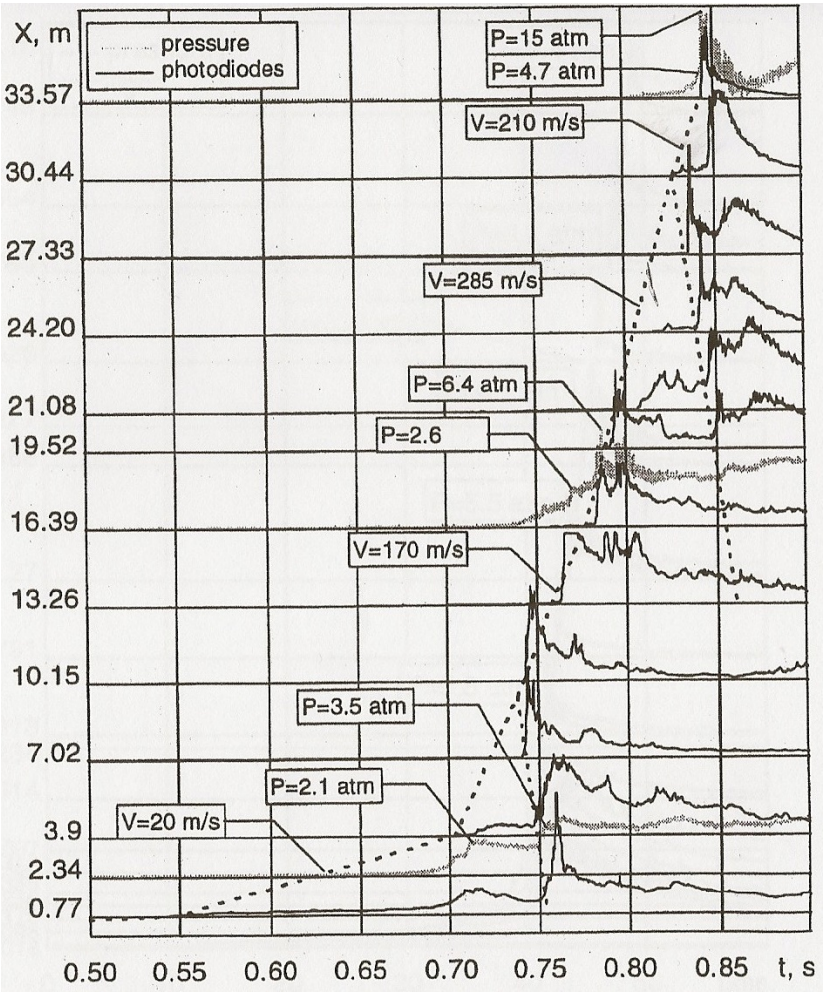

FIGURE 2.32: Experimental X-t plot from a slow/unstable flame from the work of Kuznetsov et al. [67]. Results here show flame propagation in a tube with an internal diameter of 520mm filled with BR=0.6 obstacles and a 9.5% H_2:air mixture (by mass)

Choked Flames A chocked flame is a flame travelling at a soinc speed, close to the isobaric speed of sound in the combustion products. Such flames are said to propagate with steady speed. An example of a choked flame is shown in Figure 2.33.

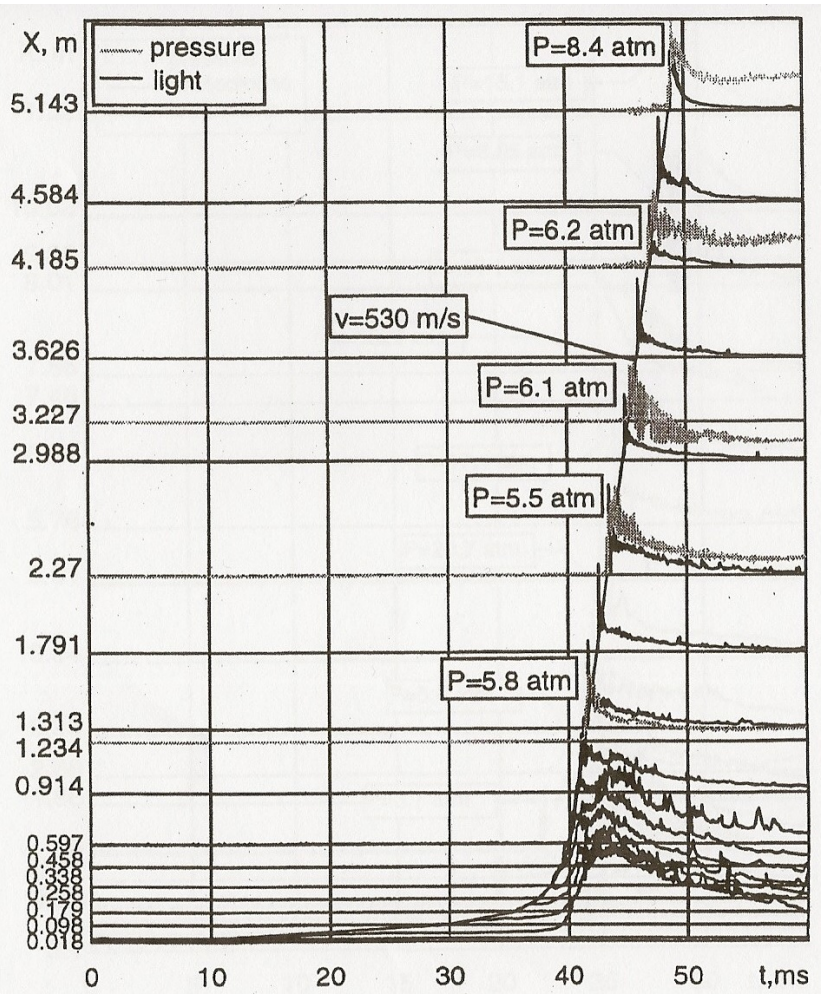

FIGURE 2.33: Experimental X-t plot illustrating the sonic or choked flame regime form the work of Kuznetsov et al.[67]. Results here show flame propagation in an 80 × 80mm channel filled with BR=0.6 obstacles and a 13% H_2:air mixture

Quasi-detonations Quasi detonations are the fastest of all the FA regimes occuring within obstacle filled tubes, with overpressures comparable to P_{CJ} and steady flame propagation speed somewhat slower than V_{CJ}. The detonation velocity is not achieved as a result of momentum losses which are proportional to BR. An example of a quasi-detonation is shown in Figure 2.34.

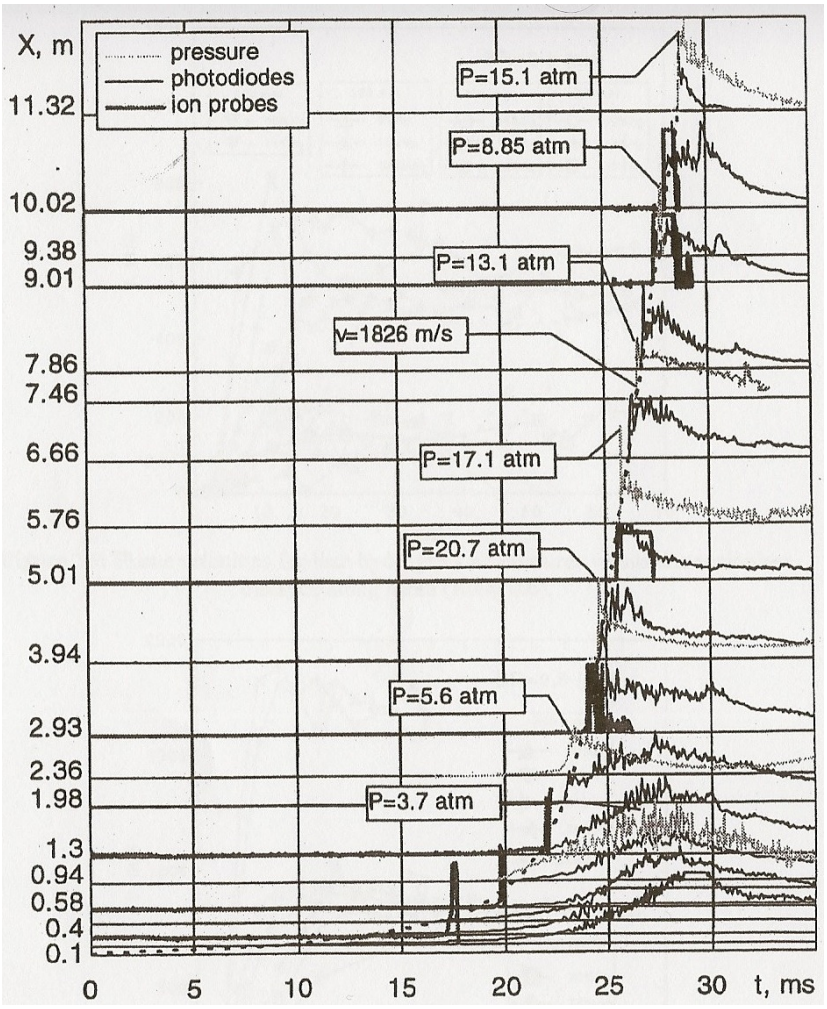

FIGURE 2.34: Experimental X-t plot for a flame propagating in the quasi-detonation regime, reproduced from the work of Kuznetsov et al. [67]. Results here show flame propagation in a tube with an internal diameter of 174mm filled with BR=0.3 obstacles and a 60% H_2:air mixture

Spinning Detonations Spinning Detonation results from the work of Frolov et al. were produced when detonating natural gas-air (natural gas was over 98% methane in this case) mixtures in a 94mm duct, which is the limiting tube diameter for this mixture [98]. Pressure results from this study can be seen in figure 2.35. Spinning detonations were observed in this experiment showing a strong shock wave from the spinning detonation head, followed by several smaller decaying pulses of similar duration. The cause of these decaying after pulses is that the leading detonation head spins along the tube as it travels and is followed by a structure of shock waves which spin down the tube in the products, generating decaying pulses of pressure. The pressure waves occur at fixed period intervals as

a result of the fixed geometry of the spinning shockwave 'screw' geometry, which shows a fixed angle relative to the tube wall of around 45° [86]

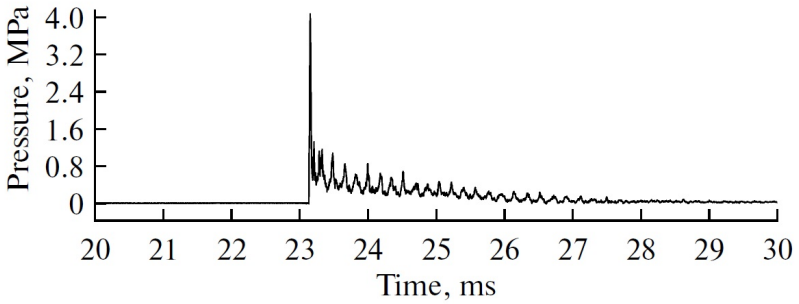

FIGURE 2.35: Experimental pressure time plot for a propagating spinning detonation, reproduced from the work of Frolov et al. [67]. Results here show flame propagation in a tube with an internal diameter of 94mm filled with specially shaped convergent-divergent obstacles and a stoichimetric natural gas:air mixture [98]

2.2.2 Statistical Methods used in FA and DDT

The goal of most practical PDE research is to ensure that detonation is reached reliably within a minimum distance within a minimum time. Researchers such as Schauer [99] Rolling [100] have investigated the percentage chance of detonation success achieved using statistical methods. This research has been conducted to determine the likely chance of the detonation flame regime being achieved for given experimental conditions. It is of upmost importance to consider the statistical distribution of flame acceleration and DDT in experiments which could yield detonations, as in a practical engine only a well developed detonation will propel a vehicle at the design conditions. Schauer's research [99] shows that percentage chance of detonation in liquid hydrocarbons has a strong dependency on the fuel temperature within the PDE, as illustrated in Figure 2.36. Similar methods will be employed in this current work to determine whether the experimentally determined flame speeds are easily reproducible at a variety of different conditions.

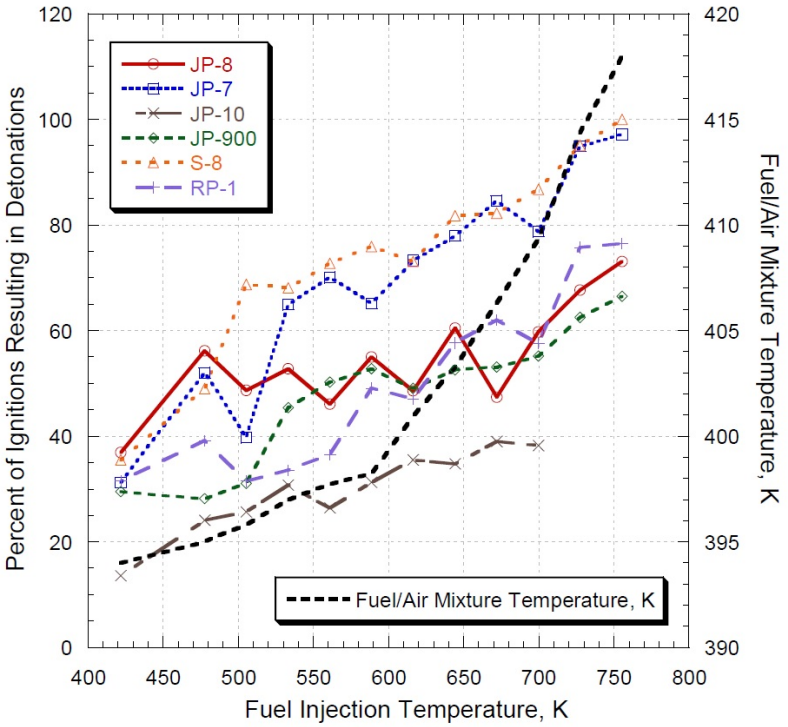

FIGURE 2.36: Experimentally determined % chance of detonation for a variety of difference liquid hydrocarbons at a range of different fuel-air temperatures. Reproduced from the work of Schauer [99]

Rolling used a constant sample size of 10 ignition cycles to determine whether the detonation was likely to occur in the detonation cross over tubes studied. Some of these cycles were ignored due to sensor malfunction, or flame speeds in excess of 3000m/s. This process allowed a large variety of different geometries to be explored and compared with each other directly to determine which was the most reliable way to ignite a mixture with a detonation wave. Rolling's report is useful in that both the mean and standard deviation of the flame speed were reported, so that the average detonation reliability and deviation from this value could be determined. In addition, the percentage difference in the flame speed from the theoretical Chapman Jouguet conditions for the mixture were also reported, along with the pressure each at a series of different locations.

2.2.3 Geometric DDT devices

There are a number of different DDT devices which have been adopted to increase flame acceleration rates in PDEs via the flame folding and the turbulence feedback

mechanism. Two common devices, the Schelkin spiral and the orifice plate are shown in Figure 2.37. These devices provide additional surface roughness to the tube wall which allows turbulence to interact with the flame as it accelerates. The distance for DDT to occur is shown in the diagram here as around 3 meters. This is obviously impractical for use in aircraft engines as the length of the DDT section is similar to that of a large civil airliner engine. Optimisation of the DDT device could lead to reduced detonation transition length and a more practical DDT device. One common way to determine the degree of obstruction caused by a flow obstacle is the blockage ratio, BR, as shown in Equation 2.10, and also in the illustration. BR should not be used alone to provide a direct comparison of effectiveness however, as obstacles will perform differently depending on their geometry, and spacing.

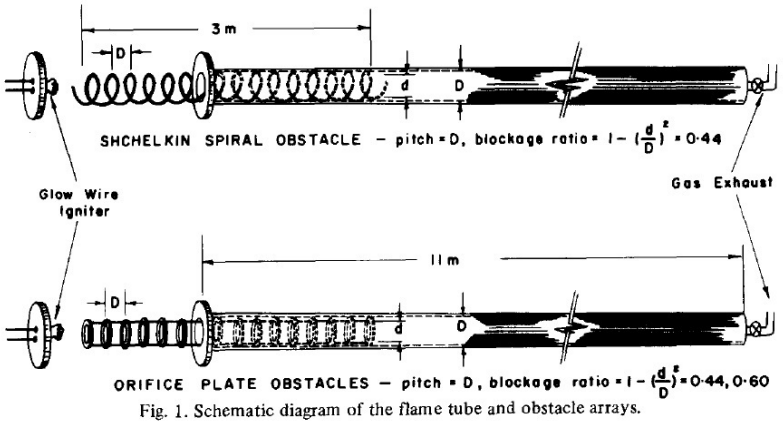

FIGURE 2.37: Illustration of experimental Shchelkin spiral and orifice plate blockages as used by Lee et al. [101]

The effect of changing the blockage ratio of orifice plate obstacles has been studied in detail by Ciccarelli et al. and Kuznetsov et al. [71, 102, 67] furthermore this effect has been modelled by Dorofeev [103]. These orifice diameters were changed in batches rather than selectively choosing the best fit orifice. Ciccarelli ran experiments with three different BR configurations, each with the same separation, S, of 0.14m, or one tube diameter. Three different orifices BR cases are investigated in this work, namely 0.43, 0.6 and 0.75. The results of these experiments show that the FA is faster in the 0.75 BR case until an inflection point when the flame reaches an axial distance 1m, after which the 0.6BR case gains pace much faster, illustrating that there is a balance to be obtained between allowing expanding gaseous products to escape the obstacles and

producing enough turbulence to feed further flame acceleration. Rather than mounting these devices as a separate physical module inside of the PDE combustion chamber, New et al. [104] have investigated the effect of changing the internal geometry of the pipe wall by machining this away to reveal an obstacle.

Experiments have been carried out to investigate orifice spacing such as those conducted by Ciccarelli [105, 29], Teodorczyk et al. [106], Dorofeev et al. [103], and others [107, 108, 109, 110, 111, 112] to name a few. These experiments have been carried out in a variety of tube cross sections and diameters, most of which are less than 0.2m in diameter, and each containing repeated obstacles classified by obstacle BR. Fuels in each of the above experiments are gaseous, as this allows for a premixed flame to be generated with greater ease, and the fuel gas ranges from propane to hydrogen. Ciccarelli found that the orifice spacing was of little significance to the run up distance, the distance for the flame to become supersonic, unless the orifice blockage ratio was high, such as the 0.75BR case. In this case a spacing of 1.5D allowed run up to occur in 1 tube diameter less than the 1D spacing case.

Another common blockage type which has been investigated is the perforated plate, a plate with multiple through holes [113, 114]. Such plates generate a strong turbulent field with much smaller length scales than the standard single hole orifice plate. Sexton's experiments [113] showed that a perforated plate can generate intense turbulence and enhance FA. It was found that a trade-off should be achieved between shock wave intensity and shock speed which could be controlled by the hole size. In this experiment the tube diameter was 101.6mm, and the orifice contained 24 holed with a range of hole sizes. It was found that the best hole size for this particular experiment was 3mm in diameter, although 4mm diameter holes also provided beneficial flame speed enhancements. Smaller hole sizes quenched the flame as it travelled through the orifice. The purpose of these obstacles was to generate intense turbulence, with a BR of around 0.95 to 0.98 in the best performing cases at the beginning of the tube. This has been shown to produce greater FA in the initial stages of PDE experiments, but according to the work of Ciccarelli, does not make a great difference thereafter [105]. It is important to note that severe restriction of the flow to generate small turbulence length scales with a BR of over 0.90 would be very impractical in a practical PDE, due to the requirements for filling the tube with flow rates of over 100m/s.

Furthermore Roy et al. [115] have reviewed recent progress in PDE development. Specific developments in the field of PDE geometry recorded in this modern review include internal PDE nozzle design with conical transition obstacles, valveless PDE pre-detonator design with two concentric low paths and design of PDEs including optimal distribution of tubulising chambers along the PDE length as well as novel injection techniques for practical liquid fuels such as JP-10. In addition to this, laser diagnostics and real time control of engine injection systems are also investigated in the text [115].

2.2.4 Fractals

Fractal orifice shapes such as those illustrated in Figure 2.38 have been investigated by Abou El-Azm Aly et al. [116] as cold flow orifice devices which were suggested for implementation as replacements for flow metering orifice plates which can reduce pressure losses across the orifice plate. It was found that fractal shapes can reduce dynamic pressure loss with higher fractal dimension in comparison with circular orifice plates and orifice plates with lesser fractal numbers for a given flow area. Abou El-Azm Aly et al. state that the change in pressure drop is due to a wider range of smaller turbulent velocity scales generated by the fractal orifice plates in comparison with standard circular orifice plates. Interestingly, the authors note that one diameter after the orifice plate, the pressure loss across the triangular fractal and circular cases is identical, whereas the pressure loss across the star shaped orifice case is 14% less than the circular case. In each case the generation of smaller turbulent velocities increased for the fractal case over the standard orifice. Hurst and Vassilicos have compared a range of fractal grids with differing fractal dimension (Figure 2.39) in comparison with uniform, single scale square and I grids for the generation of turbulence [117]. Hurst and Vassilicos found that fractal grid generated turbulence was highly dependent on fractal dimension, mesh size and the ratio of the largest to smallest length scales. Furthermore Hurst and Vassilicos found that the turbulence intensity and turbulent Reynolds number were higher for the low blockage ratio (BR=0.25) fractal grid than for higher blockage ratio grids without fractal geometries.

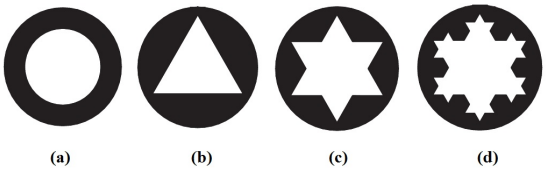

FIGURE 2.38: Illustration of experimental apparatus used by Abou El-Azm Aly et al. for fractal generated turbulence. Adapted from the work of Abou El-Azm Aly et al. [116] (a) represents a standard orifice, (b), (c) and (d) show respectively increasing degrees of fractal geometry

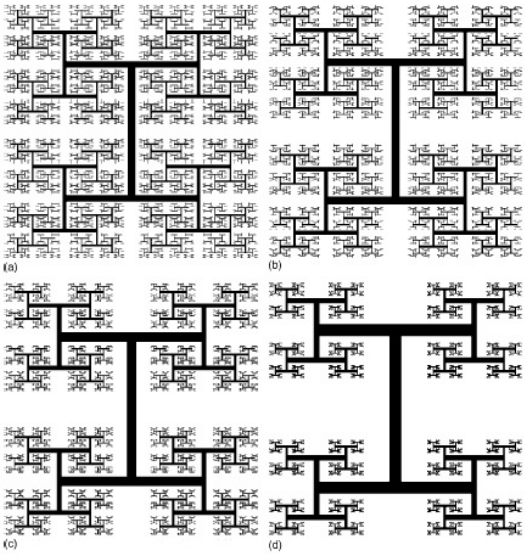

FIGURE 2.39: Illustration of experimental apparatus used by Hurst and Vassilicos for fractal 'I' grid generated turbulence [117]

Furthermore, the application of fractal turbulence generating grids to premixed combustion has been investigated by Sponfeldner and Soulopoulos et al. [118] ad Soulopoulos and Kerl et al. [119] in addition to Goh and Giepel et al. [120, 121], from Vassilicos' and Lindstedt's respective groups at Imperial College London. Sponfeldner and Soulopoulos et al. found that fractal grids generated greater flame wrinkling, faster turbulent burning velocities and more intense flame corrugation when compared to square non-fractal grids [118]. Fractals grids were also found to allow for the independent manipulation of turbulence length scales irrespective of the r.m.s. fluctuation velocity of u'.

Although the use of fractals has been applied to premixed flames they have not yet been applied to flame acceleration in PDEs, and as such fractal obstacles for enhanced turbulence and local flame speed merit investigation. Direct measurement of the turbulent length scales generated by obstacles is not reported in PDE related literature as length

scale measurements are very difficult to make within high temperature, high pressure environments with standard measurement equipment such as hot wire anemometers. This is because direct measurement by intrusive measurement methods would destroy the instrumentation deployed within the combustion environment.

2.2.5 Novel DDT techniques

In this section a range of different DDT devices has been investigated which promote the reduction of X_{DDT}, the axial location of the DDT length.

2.2.5.1 Mixed Geometric Devices

In recent years research in DDT has begun to diverge from using one type of obstacle or blockage and has begun to focus on optimization of the obstacle within the PDE. Such research has started by mixing types of obstacles such as the work of Huang [122] which mixed Schelkin spirals, orifice plates and shock focusing obstacles in order to generate detonations in Jet-A air mixtures in less than one meter at frequencies of 20-60Hz. This engine is clearly approaching a more acceptable detonation engine for use in the aerospace industry, as it will generate a high thrust and also uses a valveless air inlet system. Huang et al. have solved many of the problems associated with PDE design and have built a series of test rigs to compare different obstacle combinations as can be seen in Figure 2.40. Huang's engine has successfully detonated kerosene-air mixtures in less than 1 meter, with a combustor diameter of 29mm, which is smaller than the minimum diameter of a single propane or kerosene detonation cell width, λ, of around 52mm, but larger than the detonation cell size criterion of λ/π. This detonation engine must be generating a fast flame within the DDT section of the tube, and with a detonation occurring inside the obstacle as the pressure generated by this detonation engine at the location X_{DDT} shown in the papers records of pressure is in excess of 40 bar. The exit wave speed was around 900 to 1000m/s in most of these cases with an exit pressure of around 20 to 25 bar at a frequency of 20Hz and around 5 bar at 60Hz, the limiting frequency for this experiment. This work is clearly of great interest and should be drawn from in the design of the PDE experiment during this thesis. Clearly the effect of reducing tube diameter has a great effect on the length of the transition to detonation within the PDE tube.

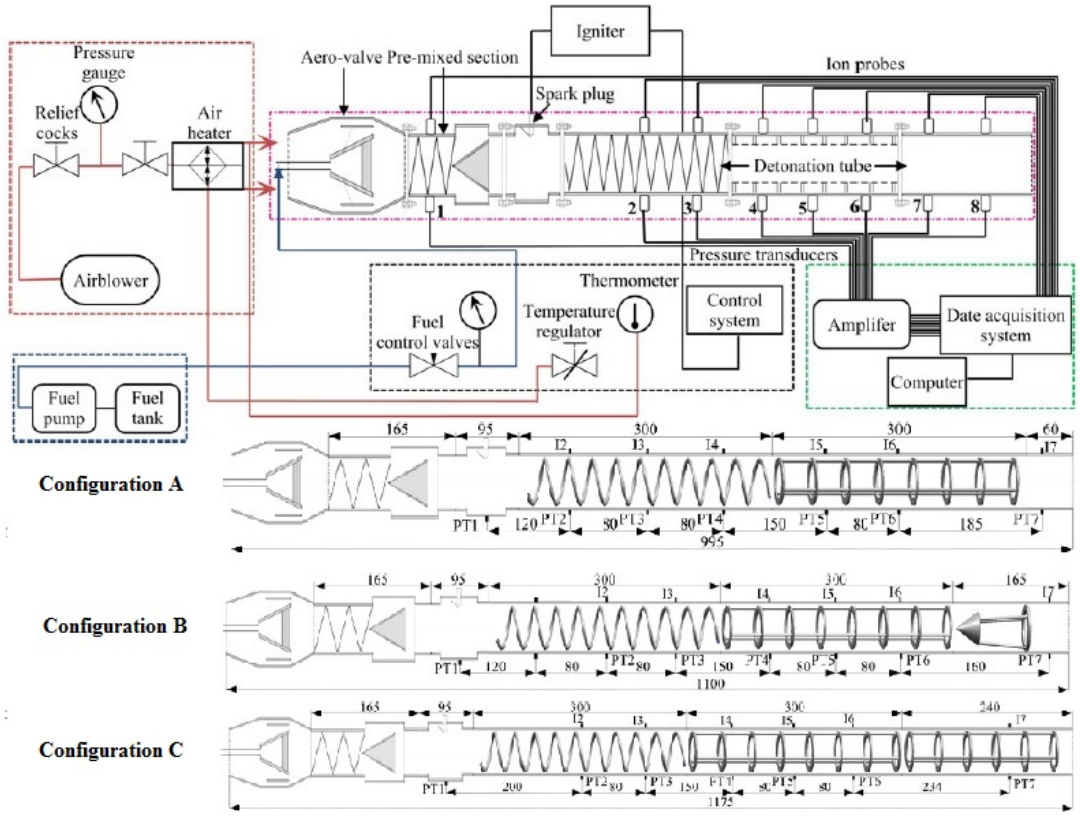

FIGURE 2.40: Illustration of experimental apparatus used by Huang et al. to investigate the effect of mixing obstacle geometry on flame acceleration in Kerosene:Air fuelled PDE engines [122]

2.2.5.2 Sequential Spark Ignition

Ciccarelli et al. and Frolov et al., [71, 123] have completed experiments with sequential spark ignition along the tube axis to ignite small pockets of flame ahead of the main reaction zone as this traversed away from the closed end of the tube, as shown in Figure 2.42. These experiments have proven to be very productive and have changed the course of PDE development in this period. The use of distributed ignition can reduce tube length considerably, changing X_{DDT} from several meters to around one meter. From the perspective of an engine developer this is indeed very helpful, as detonation can occur over a length which is acceptable from the point of view of an air frame designer. The method for accomplishing this is to trigger ignition using a pressure signal from the lead shock wave ahead of the combustion front, so that the ignition closely follows the pressure wave, enhancing the coupling between the two. This method has been used with good success and Frolov et al. have refined their design to reduce the number

of ignitors from seven to two as can be seen in Figure 2.42. There is however a need to carefully control the voltage and energy discharged with such a system depending on the concentration of the fuel and the altitude at which the system is operating. This electrical control system relies on the use of very high voltages and large storage capacitors which may be deemed impractical on some aircraft, and are certainly more complex than an alteration in the tube geometry. A detonation was sustained within this device whilst running on liquid fuels in less than one meter with a 28mm diameter detonation tube, one of the shortest tube lengths of any PDE experiment, evidently this technology is highly effective.

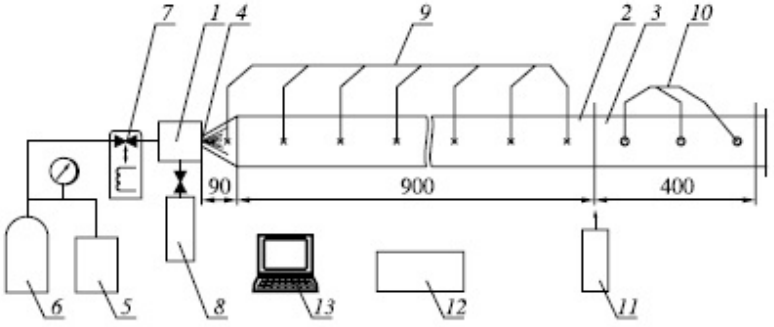

FIGURE 2.41: Illustration of experimental apparatus using sequentially triggered traveling ignition points to enhance ignition (shown as point 9) [124]

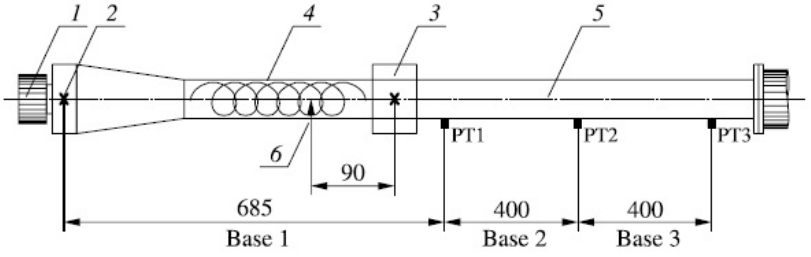

FIGURE 2.42: Illustration of experimental apparatus using sequentially triggered traveling ignition points to enhance ignition, similar to Figure 2.41 with only 2 ignitors in a 28mm diameter tube [124]

Figure 2.43 shows the effect of distributed ignition on the flame acceleration profile from the work of Ciccarelli [71], in comparison with a baseline case with no distributed ignition and another case with a bank of three sequential perforated plates which provided intense turbulence at the closed end of the combustor. It can be seen that the distributed ignition system adds some benefit in accelerating the flame more rapidly in the initial run up to a choked flame, but that this is not stable and is quickly reduced

after the igniter is removed. The benefit in Frolov's work generated a much faster run up to detonation and accelerated the flame speed past the choked flame velocity as a result. This increased flame speed could be due in part to Frolov's variable ignition delay system, which deposits energy in the flow at an optimized time. In addition Frolov used different ignition energies which were also optimised in his study. As such Frolov's PDE demonstrator provided a much more thorough invesigation of distributed ignition than Ciccarelli's work.

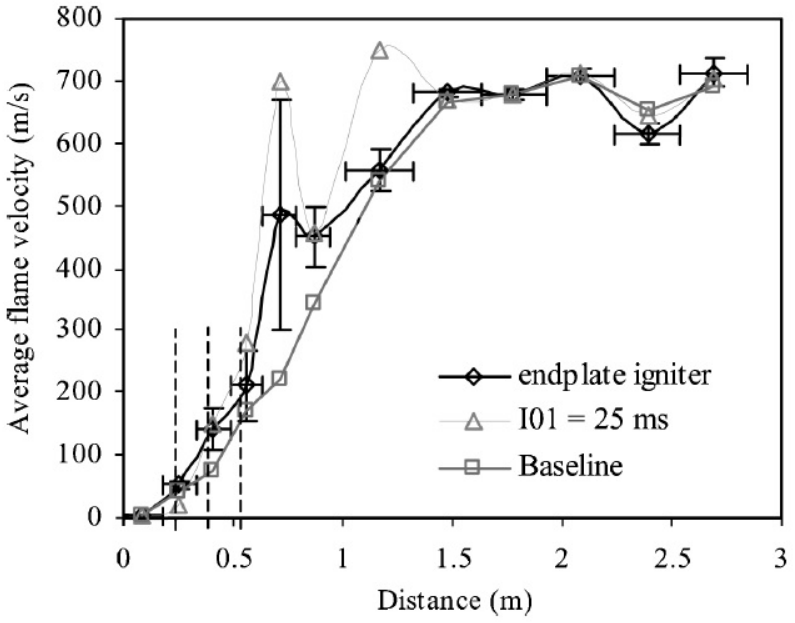

FIGURE 2.43: Illustration of experimental results for distributed ignition system from the work of Ciccrelli [71] showing the baseline case and the case for an ignition delay after a first bank of ignitors of 25ms, IO1 =25ms. The endplate ignitor case used three perforated plates situated at the location of the vertical dashed lines and only used ignition at the end plate

2.2.5.3 Shock Wave Focusing and Reflection

Shock wave focusing has the potential to reduce the deflagration to detonation transition distance by focusing the shock waves pressure over a small area ahead of the accelerating flame, enabling the formation of a hot spot and strong shock wave in the same location, which could lead to detonation. Early work in this field includes the research of Chan, who investigated orifice plates and backwards facing wedges in combustible atmospheres in shock tubes with an inlet shock velocity of Mach 2.2 [125]. Chan argues that strong shock waves can create local hot spots which promote strong ignition in localised unburned pockets of gas which can promote localised blast waves,

i.e. a shock wave propagating supersonically from an explosive region. If this local blast wave coalesces with other blast waves, or reflections from the wall of sufficient strength DDT is likely to occur.

Witt et al. [126] have experimented with the use of shock reflecting obstacles to increase the pressure in a localised pocket of gas ahead of the flame in order for DDT to occur over a shorter distance than would usually be possible with a pre-detonator alone. Witt et al. experiment with the use of cones at the end of the pre-detonator as well as obscured orifice plates with shock reflecting obstacles in their path in ethylene oxygen tests within a 0.14m diameter tube. Witt's experimental apparatus can be seen in Figure 2.44, clearly illustrating the orifice laden section responsible for flame acceleration and the reflection obstacle responsible for DDT triggering.

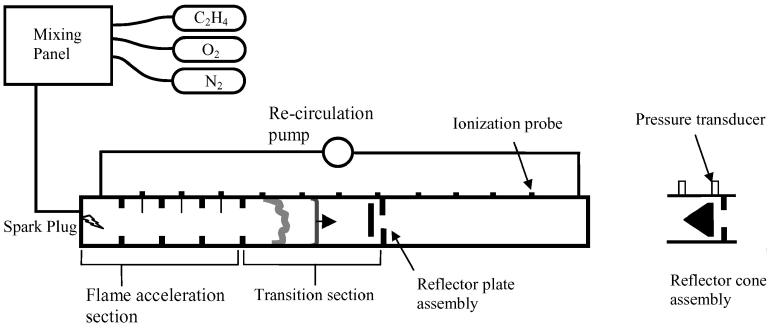

FIGURE 2.44: Illustration of experimental apparatus using shock focusing plates reproduced from the work of Witt et al. [126]

Frolov et al. have also experimented with the use shock focusing techniques such as u-bend tubes and specially shaped repetitive shock focusing obstacles [127]. Frolov's u-bend tubes can be seen in Figure 2.45. The main effect of using u-bend tubes to focus these shock waves is that the X_{DDT} can be reduced considerably, notably the parabolic obstacles show marked increase in FA in comparison to standard orifice plate obstacles, reaching approximately 20 % further along the PDE flame acceleration section in the same time interval.

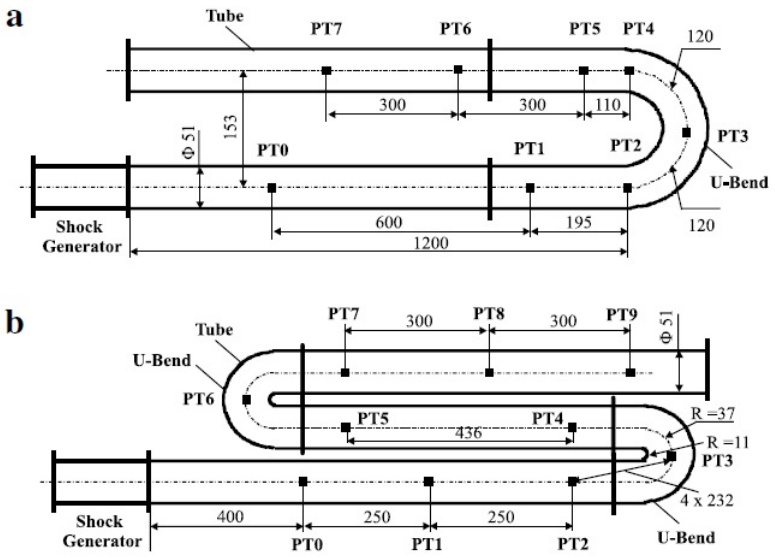

FIGURE 2.45: Illustration of experimental apparatus using shock focusing u-bend tubes reproduced from Frolov et al. [124]

In addition to u-bend tube experiments, Frolov et al. have investigated the effect of shock focusing in order to promote fast transition to DDT using specially shaped obstacles [128]. This obstacle has been designed to produce fast DDT by adding a shock focusing obstacle to the end of a standard flame accelerating obstacle array. The experiment carried out in Figure 2.46 shows apparatus used to test the shock focusing geometry in a 4.5m long 51mm diameter tube. The shock focusing obstacle divergent section was 30mm long, reaching its narrowest point at 27mm in diameter, followed by a 450mm divergent section. It was found that the inlet flow velocity required to transition to detonation after the obstacle reached a critical cut off limit at 680m/s $\pm$ 20m/s or approximately Mach 2 relative to the upstream conditions. These experiments were all carried out with stoichiometric propane air mixtures and the shock wave was initially generated using a solid propellant shock wave generator with a diaphragm which bursts between 500 and 1500 atmospheres, allowing control of the primary shock wave through burst disc control and weighing of the solid propellant sample.

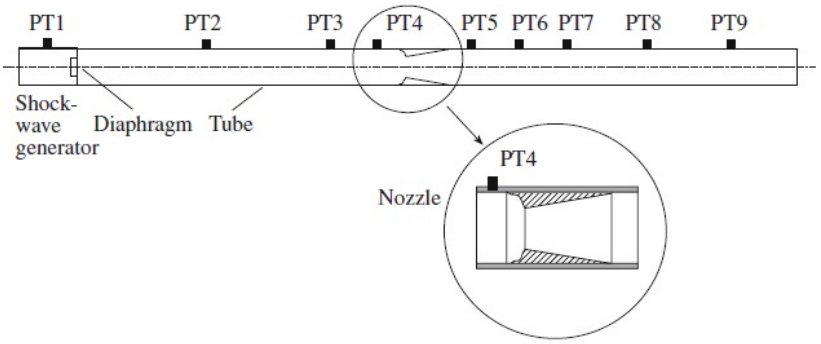

FIGURE 2.46: Illustration of experimental apparatus using shock focusing obstacle for fast DDT with an inlet speed of $\geq$ 680m/s $\pm$ 20m/s reproduced from Frolov et al. [128]

Frolov, Aksenov and Berlin have patented a number of inventions relating to fast DDT in pulsed detonation engines [129, 130, 131]. These devices typically include a shaped obstacle which aids the transition of accelerating deflagrations to detonation by focusing the compressive shock wave which is ahead of the flame until transition to detonation is achieved. A number of different methods have been investigated, including axisymmetric obstacles mounted on the tube centreline with shock focusing geometry (Fig. 2.48), conical nozzles with shock focusing geometry (Fig. 2.49) and repetitive parabolic shaped obstacles which promote shock focusing (Fig. 2.47) and are the subject of a number of Frolov's papers [127, 132, 133]. Frolov devised and carried out a test to determine whether the parabolic obstacles are more successful in aiding transition do detonation with a typical flame speed of 1070m/s $\pm$ 20m/s, typical of the flame velocity generated by 12 or more diameters of Schelkin spiral [127] during which he substituted the Schelkin spiral of the combustor with a high pressure chamber (HPC) filled with a propylene-air mixture at a pressure of five atmospheres. The mixture of propylene air was ignited using a standard automotive spark plug which increased the pressure in the HPC until a burst disk perforated generating a shock traveling along the axis of the detonation test section. After the HPC the shock traversed into a low pressure chamber (LPC) buffer section filled with air with a length of 0.6m and a diameter of 70mm. Once the buffer section had been traversed the shock then entered a square sectioned test section (100mm in width and height) which was filled with a mixture of propylene-air after which the shock flowed into the exit section which was 0.8m in length and constructed from a smooth 70mm diameter tube. The test section opposed

wooden obstacles which were either orifice shaped or a specially shaped parabolic obstacle, as shown in Figure 2.47. Frolov's experimental results show a great difference between the shock focusing obstacles and the orifice plates, with a marked difference between the exit velocity of 600m/s, showing that the orifice plates decelerated the shock then recovered the shock velocity, however the parabolic obstacles accelerated the shock velocity promoting DDT.

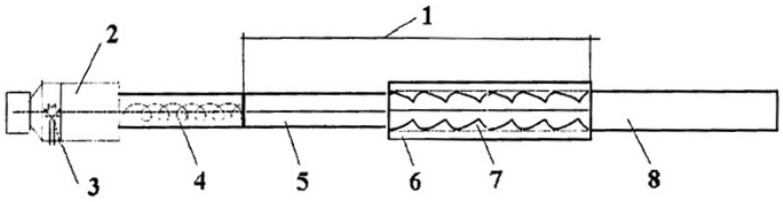

FIGURE 2.47: Illustration from patent filed by Frolov et al. for an array of parabolic obstacles used to focus shock waves and promote fast DDT[129]

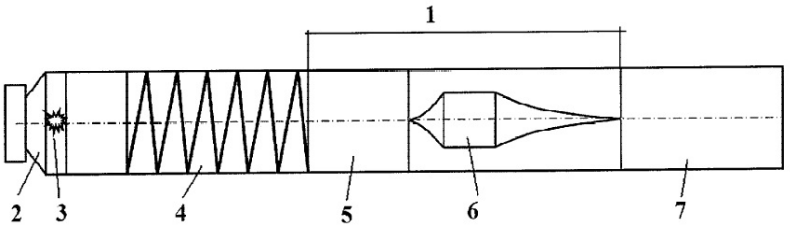

FIGURE 2.48: Illustration from patent filed by Frolov et al. for a single bullet shaped parabolic obstacle for shock focusing and fast DDT [130]

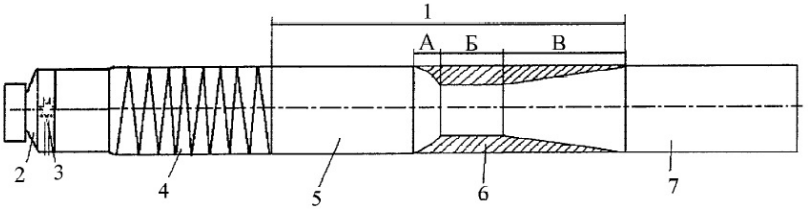

FIGURE 2.49: Illustration from patent filed by Frolov et al. for a single parabolic nozle obstacle for shock focusing and fast DDT [131]

The test section and other geometry was modelled using a 2D Navier stokes based CFD model [127] which showed a high temperature core flow region 10mm in length and 3mm in width was generated with a maximum temperature of 2250K and 2100K, which was separated by a small island of 2050K gas. Frolov et al. discovered that the reaction front propagated rapidly along this high temperature volume generating a blast wave wave which then coupled with a similar explosion above the sixth obstacle

generating a detonation. The result of this numerical experiment can be seen in Figure 2.50. These results seem to provide an unfair test, as the orifices used to compare with the specially shaped obstacles are much thicker (in the axial length) than standard orifices. This would affect the vena contracta, and generate less fine scale turbulence as the orifice is not sharp edged.

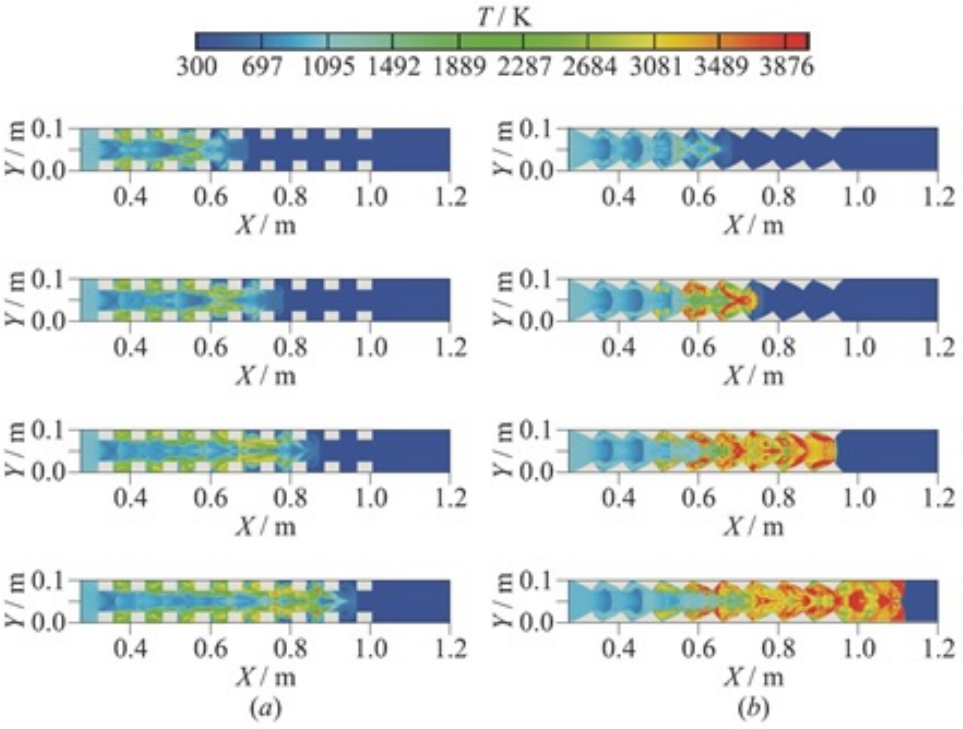

FIGURE 2.50: Numerical comparison of specially shaped obstacles with orifice plates [127]. The upper snapshot was taken at a time of 480 μ seconds, other snapshots are taken at intervals of 100 μ seconds

2.2.6 Initiation by combusting gaseous jets

Detonations can also be generated by the use of combusting gaseous jets, which flow from one detonation in a small tube to a larger tube, generating highly turbulent conditions in the larger tube and initiating detonation. Studies by Chao et al. [134] show how this can be achieved with a variety of tube geometries and diameters (300mm x 300mm channel and a 150mm diameter pipe) containing a pre-detonator and detonation section, a perforated plate which generates extremely intense turbulence from the incoming detonation and another detonation section. The apparatus from Chao's experiment can be seen in Figure 2.51

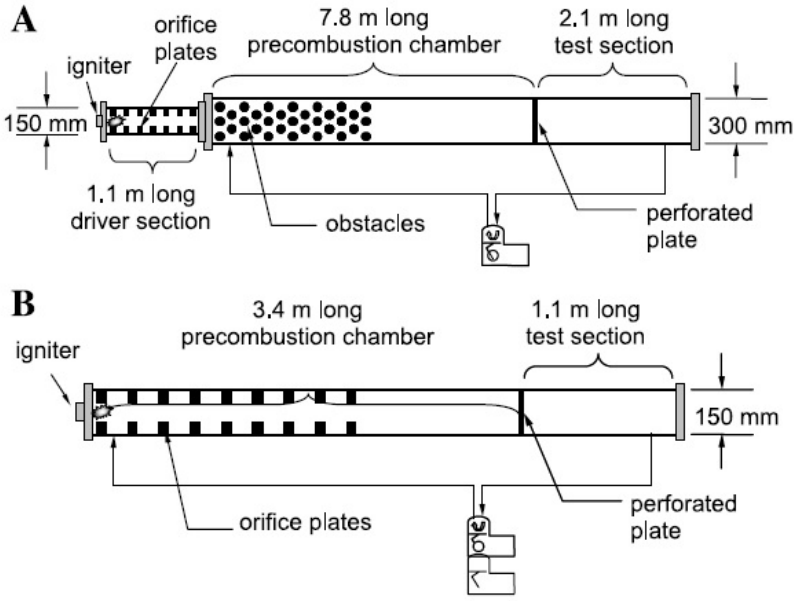

FIGURE 2.51: Illustration of experimental apparatus for ignition using highly turbulent jet flows from the work of Choa et al. [134]

2.2.7 Direct Detonation Initiation

A great deal of recent research has been invested into the development of direct detonation initiation, resolving the problems of DDT by inserting a large amount of energy into the system via novel ignition systems. The limits of direct detonation initiation have been experimentally and numerically determined in a by a number of authors, Bartenev [135], Vasil'ev [136], Yao [137] Most of these approaches make use of specialist ignitors, such as plasma ignitors [115, 138, 139], high voltage ignitors [140, 141, 142], explosive charges [143, 144] in order to overcome the detonation activation energy instantaneously and negate the need for a PDE pre-detonation tube. Each of these concepts concentrate on generating an instantaneous detonation, however with each concept there is also the need to provide extra energy and weight costing alternative technologies to the propulsion system, which Ciccarelli argues is not realisable in a practical PDE engine [71]. As such these technologies have been deemed beyond the scope of this thesis, which will focus on geometric means to study DDT.

2.3 Numerical PDE Modelling

2.3.1 General Equations of fluid motion

The general equations of motion for reacting compressible multicomponent fluids are detailed in table 2.1, which lists each term according to its type. Equations in the first column are associated with rates of change of the quantity referred to, for example the rate of change of mass, and are therefore required for transient fluid dynamics analysis. Equations in the second column are responsible for the net momentum and energy fluxes (i.e. convection) out of the volume with positive flux indicating a loss form the volume. Column three represents the diffusive terms of the represented equations. Column four represents the pressure tensor which has been contracted twice with respect to the divergence of the velocity in each direction. This term represents the conversion of flow kinetic energy to thermal energy in the flow, which is important to consider in supersonic flows, particularly in the viscous effects present in boundary layers present at the wall [68]. In subsonic flows this term can be simplified considerably. Column five represents the body force in the momentum and energy equations, or the mass reaction rate in the species equation which can be related to the molar reaction rate, $\hat{w}_i$ and species molar mass, W_i using equation 2.27. These equations have are described in detail in the work of Law [68].

Eqn	Equations					
of:	(1)	(2)	(3)	(4)	(5)	Eq. No
Mass	$\frac{\partial \rho}{\partial t}$		$+\nabla \cdot (\rho \vec{v})$		$= 0$	(2.23)
Species	$\frac{\partial \rho Y_i}{\partial t}$		$+\nabla \cdot \left[\rho \left(\vec{v} + \vec{V_i}\right) Y_i\right]$		$= w_i$	(2.24)
Momentum	$\frac{\partial \rho \vec{v}}{\partial t}$	$+\nabla \cdot (\rho \vec{v} \vec{v})$	$= -\nabla \cdot \vec{P}$		$+ \sum_{i=1}^{N} Y_i \vec{f_i}$	(2.25)
Energy	$\frac{\partial \rho e}{\partial t}$	$+\nabla \cdot (\rho \vec{v} e)$	$= -\nabla \cdot \vec{q}$	$-\vec{P} : \nabla \vec{v}$	$+ \sum_{i=1}^{N} Y_i \vec{f_i} \vec{V_i}$	(2.26)

TABLE 2.1: General Equations of Fluid Motion from the work of Law [68]

$$w_i = W_i \hat{w}_i \tag{2.27}$$

2.3.2 The Navier Stokes Equations

In order to successfully model FA and DDT in PDEs it is necessary to solve the equations of fluid motion in at least two dimensions, with inclusion of a heat release term for combustion and the energy equation. The equations appear as shown in Equations 2.28, 2.29, 2.30, 2.31 and 2.39. In these equations ρ is density, u_r is velocity in r, u_θ is velocity in the θ direction and u_z is velocity in in the z direction. τ is shear stress, Re is Reynolds number and Pr is the Prandtl number. These equations are adapted from the work of Bird et al. [145] as presented by Kuo [146].

Transient Compressible Continuity in Cylindrical Co-ordinates:

$$\frac{\partial p}{\partial t} + \frac{1}{r}\frac{\partial\left(\rho r u_r\right)}{\partial r} + \frac{1}{r}\frac{\partial\left(\rho u_\theta\right)}{\partial \theta} + \frac{\partial\left(\rho u_z\right)}{\partial z} = 0 \tag{2.28}$$

Transient Compressible Equation of Motion in Cylindrical Co-ordinates

r-component:

$$\begin{aligned}\rho\left(\frac{\partial u_r}{\partial t} + u_r\frac{\partial u_r}{\partial r} + \frac{u_\theta}{r}\frac{\partial u_r}{\partial \theta} - \frac{{u_\theta}^2}{r} + u_z\frac{\partial u_r}{u_z}\right)\\ = -\frac{\partial p}{\partial r} + \left(\frac{1}{r}\frac{\partial}{\partial r}\left(r\tau_{rr}\right) + \frac{1}{r}\frac{\partial \tau_{r\theta}}{\partial \theta} - \frac{\tau_{\theta\theta}}{r} + \frac{\partial \tau_{rz}}{\partial z}\right) + \rho B_r\end{aligned} \tag{2.29}$$

θ-component:

$$\begin{aligned}\rho\left(\frac{\partial u_\theta}{\partial t} + u_r\frac{\partial u_\theta}{\partial r} + \frac{u_\theta}{r}\frac{\partial u_\theta}{\partial \theta} + \frac{u_r u_\theta}{r} + u_z\frac{\partial u_\theta}{u_z}\right)\\ = -\frac{1}{r}\frac{\partial p}{\partial r} + \left(\frac{1}{r^2}\frac{\partial}{\partial r}\left(r^2\tau_{r\theta}\right) + \frac{1}{r}\frac{\partial \tau_{\theta\theta}}{\partial \theta} + \frac{\partial \tau_{\theta z}}{\partial z}\right) + \rho B_\theta\end{aligned} \tag{2.30}$$

z-component:

$$\begin{aligned}\rho\left(\frac{\partial u_z}{\partial t} + u_r\frac{\partial u_z}{\partial r} + \frac{u_\theta}{r}\frac{\partial u_z}{\partial \theta} + u_z\frac{\partial u_z}{u_z}\right)\\ = -\frac{\partial p}{\partial z} + \left(\frac{1}{r}\frac{\partial}{\partial r}\left(r\tau_{rz}\right) + \frac{1}{r}\frac{\partial \tau_{\theta z}}{\partial \theta} + \frac{\partial \tau_{zz}}{\partial z}\right) + \rho B_z\end{aligned} \tag{2.31}$$

Where the shear stresses are given by:

$$\tau_{rr} = \mu \left[2\frac{\partial u_r}{\partial r} - \frac{2}{3} (\nabla \cdot \vec{v}) \right] \tag{2.32}$$

$$\tau_{\theta\theta} = \mu \left[2 \left(\frac{1}{r} \frac{\partial u_\theta}{\partial \theta} + \frac{u_r}{r} \right) - \frac{2}{3} (\nabla \cdot \vec{v}) \right] \tag{2.33}$$

$$\tau_{zz} = \mu \left[2\frac{\partial u_z}{\partial z} - \frac{2}{3} (\nabla \cdot \vec{v}) \right] \tag{2.34}$$

$$\tau_{r\theta} = \tau_{\theta r} = \mu \left[r\frac{\partial}{\partial r} \left(\frac{u_\theta}{r} \right) + \frac{1}{r} \frac{\partial u_r}{\partial \theta} \right] \tag{2.35}$$

$$\tau_{\theta z} = \tau_{ztheta} = \mu \left[\frac{\partial u_\theta}{\partial z} + \frac{1}{r} \frac{\partial u_z}{\partial \theta} \right] \tag{2.36}$$

$$\tau_{zr} = \tau_{rz} = \mu \left[\frac{\partial u_z}{\partial r} + \frac{\partial u_r}{\partial z} \right] \tag{2.37}$$

$$\nabla \cdot \vec{v} = \frac{1}{r} \frac{\partial}{\partial r} (r u_r) + \frac{1}{r} \frac{\partial u_\theta}{\partial \theta} + \frac{\partial u_z}{\partial z} \tag{2.38}$$

$$\frac{\partial E_T}{\partial t} + \frac{\partial u E_T}{\partial x} + \frac{\partial v E_T}{\partial y} + \frac{\partial w E_T}{\partial z} = -\frac{\partial up}{\partial x} - \frac{\partial vp}{\partial y} - \frac{\partial wp}{\partial z} + \frac{1}{RePr} \left(\frac{\partial q_x}{\partial x} + \frac{\partial q_y}{\partial y} + \frac{\partial q_z}{\partial z} \right) + \frac{1}{Re} \left(\frac{\partial}{\partial x} (u\tau_{xx} + v\tau_{xy} + w\tau_{xz}) + \frac{\partial}{\partial y} (u\tau_{xy} + v\tau_{yy} + w\tau_{yz}) + \frac{\partial}{\partial z} (u\tau_{xz} + v\tau_{yz} + w\tau_{zz}) \right) \tag{2.39}$$

Equations 2.28 to 2.39 are defined for unsteady three dimensional fluid flow with heat transfer. When running computational fluid dynamics modelling simulations, it is necessary to form assumptions about the type of flow which occurs in the real environment to simplify the calculations taking place. For example, Equations 2.29 to 2.31 all include Reynolds stress terms which cannot easily be resolved, so numerical methods are applied to simplify these equations, allowing the problem to be solved using the Reynolds Averaged Navier Stokes (RANS) equations or Large Eddy Simulation (LES) to name a few possible solution options. In most cases the Navier Stokes equations

can be simplified using a 2D axi-symmetric approximation with unsteady flow and the energy equation in the case of PDE combustion, that is to say that the equations can be reduced to take account of only two axes in the Cartesian or cylindrical co-ordinate system. Axi-symmetric simulation boundary conditions can also allow for swirl, i.e. velocity in the angular direction. This method allows modelling engineers to predict PDE flows with much greater ease, considerably reducing computational time and effort in setting up the numerical problem.

2.3.3 Boussinesq Viscosity

In order to mathematically close the Navier Stokes equations, it is necessary to make assumptions about the nature of Reynolds stress tensors, τ_{ij}. The Boussinesq viscosity assumption [147] can be used to approximate these, and assumes that the Reynolds stress tensors are proportional to the mean strain rate tensor, S_{ij}. The assumtion is expressed in Eqaution 2.40, where μ_t and k are the eddy viscosity and turbulent kinetic energy of the flow respectively.

$$\tau_{ij} = 2\mu_t S_{ij} - \frac{2}{3}\rho k \delta_{ij} \tag{2.40}$$

This equation then requires the use of a turbulence model to approximate the generation and destruction of turbulcence, and the eddie viscosity. S_{ij} can be calculated as a property of the fluid flow.

2.3.4 OpenFOAM Explosion Modelling

OpenFOAM is an open source numerical solver which can be applied to CFD and other numerical modelling applications. It contains a series of models and solvers developed by the open source software community, and can be accessed for free under the terms of the GNU General Public Licence [148]. Open foam contains a toolbox which is suitable for compressible combustion, XiFoam which is also openly accessible from a GNU liscence. Several researchers have successfully modelled detonation progression and DDT using OpenFOAM software, such as Wen and Heidari [149, 150, 151] who have modelled both hydrogen-air and propane air detonations and sucessfully validated

the results against experimental results. As such OpenFOAM offers an acesible and scalable method of solving reactive compressible CFD equations in the field of DDT and detonation.

2.3.4.1 The $k-\omega-SST$ turbulence model

OpenFOAM recomends the use of the k-ω-SST (Shear Stress Transport) model for both incompressible and compressibe flows with Reynolds Averaged Stress modelling. As such it has been studied here for application to the modelling of FA problems. Equations 2.41 to 2.47 express this model in analytical form, which were originally proposed by Menter [152]. Equation 2.41 shows the calculation of the kinematic eddy viscosity. Numerical constants for these equations are tabulated in table 2.2. In addition this model is capable of switching from incompressible to compressible flow.

$$\nu_T = \frac{\alpha_1 \kappa}{max(\alpha_1 \omega S F_2)} \tag{2.41}$$

Turbulence kinetic energy is given by the Equation 2.42.

$$\frac{\partial k}{\partial t} + U_j \frac{\partial k}{\partial x_j} = Pk - \beta^* k\omega + \frac{\partial}{\partial x_j}\left[\nu + \sigma_k \nu_T \frac{\partial k}{\partial x_j}\right] \tag{2.42}$$

Specific dissipation rate is characterised by Equation 2.43

$$\frac{\partial \omega}{\partial t} + U_j \frac{\partial \omega}{\partial x_j} = \alpha S^2 - \beta \omega^2 + \frac{\partial}{\partial x_j}\left[\nu + \sigma_k \nu_T \frac{\partial k}{\partial x_j}\right] + 2\left(1 - F_1\right)\sigma \omega^2 \frac{1}{\omega}\frac{\partial k}{\partial x_i}\frac{\partial \omega}{\partial x_i} \tag{2.43}$$

Where F_1 is given by Equation 2.44, F_2 is given by Equation 2.45, P_k is given by Equation 2.46 and CD_{kw} is given by Equation 2.47

$$F_1 = tanh\left[\left[min\left[max\left(\frac{\sqrt{k}}{\beta^* \omega y}, \frac{500\nu}{y^2 \omega}\right), \frac{4\sigma \omega^2 k}{CD_{k\omega} y^2}\right]\right]^4\right] \tag{2.44}$$

numerical constant	value
α_1	5/9
α_2	0.44
β_1	4/30
β_2	0.0828
β^*	9/100
σ_{k1}	0.85
σ_{k2}	1
$\sigma_{\omega 1}$	0.5
$\sigma_{\omega 2}$	0.856

TABLE 2.2: Table of $k-\omega$-SST numerical constants from the work of Menter [152]

$$F_2 = tanh\left[\left[max\left(\frac{2\sqrt{k}}{\beta^*\omega y}, \frac{500\nu}{y^2\omega}\right)\right]^2\right] \tag{2.45}$$

$$P_k = min\left(\tau_{ij}\frac{\partial U_i}{\partial x_j}, 10\beta^* k\omega\right) \tag{2.46}$$

$$CD_{k\omega} = max\left(2\rho\sigma_{\omega 2}\frac{1}{\omega}\frac{\partial k}{\partial x_i}\frac{\partial \omega}{\partial x_i}, 10^{-10}\right) \tag{2.47}$$

2.3.4.2 OpenFOAM CFD combustion modelling

OpenFOAMs XiFOAM toolbox makes use of the Weller combustion model. In its simplest form, the one equation Weller combustion model is expressed using Equation 2.48, from the work of Weller [153]. In this case, the value of A_{wel} given for propane is 0.62. This equation is used to model flame wrinkling, and the effect of turbulence on the flame surfact area. It must be used in combination with a transport model for Ξ, such as Equation 2.49 which can be used in the most basi cases. The regress variable, b is defined in Equation 2.50, where f is the current fuel mass fraction and f_b and f_u are the burnt and unburnt fuel mass fractions respectively. The full detail of this model can be found in Wellers report [153].

$$\Xi_{eq} = 1 + A_{wel}\left(\frac{u'}{S_L}\right) = \frac{S_t}{S_L} \tag{2.48}$$

numerical constant	value
W	0.446
η_g	0.12
ξ_g	4.95
α_g	1.77
β_g	-0.2

TABLE 2.3: Gulders laminar flame speed model constants for propane [154]

$$\frac{\partial}{\partial t}(\rho b) + \nabla \cdot (\rho \vec{u} b) - \nabla \cdot (\rho D \nabla b) = -\rho_u S_L \Xi |\nabla b| \tag{2.49}$$

$$b = \frac{f - f_b}{f_u - f_b} \tag{2.50}$$

Furthermore, it is also necessary to have a model for the laminar flame speed, for which XiFoam uses the Gulders flame speed correlation [154], which is expressed in Equation 2.51. The equations constants for propane are listed in table 2.3.

$$S_L = W \Phi^{\eta_g} exp\left[-\xi_g (\Phi - 1.075)^2\right] \left(\frac{T}{T_0}\right)^{\alpha_g} \left(\frac{P}{P_0}\right)^{\beta_g} \tag{2.51}$$

2.3.5 Current State of the Art

Recently the problem of modelling detonation has been investigated to great effect with novel simulations generating novel valuable insight into the processes behind DDT and detonation waves. Oran [155, 156, 157] has produced much of the leading work in this field in recent years, with others such as Johansen and Ciccarelli [64], Nikitin[158] adding to this using both 2D or 3D numerical simulations based on LES and RANS computational fluid dynamics

The recent 2D modelling work of Gamezo and Oran [156] shown in Figure 2.52, carried out with stoichiometric hydrogen air mixtures using one step Arrhenius kinetics has shown that detonation can take place by a number of different mechanisms depending on obstacle geometry. It was found that for closely packed obstacles, flame acceleration occurred much faster than for widely spaced obstacles, conversely detonation favoured the wider obstacle spacing which allowed refraction of the detonation wave between

obstacles during transit. The results and conclusions of the paper can be interpreted differently to postulate that obstacle spacing should be graded from dense spacing at the closed end to to sparse spacing at the open end. This may enhance initial flame acceleration, then promote effective transition to detonation towards the open end. This work also found that the fastest route to DDT was to stagger obstacles on one side of the tube then the other at a spacing, S, of double the tube width, in which case a resonant mode was achieved which reduced X_{DDT} from 46cm to 36. Clearly, detonation modelling, even in 2D with incomplete chemical resolution can provide valuable lessons for the experimentalist.

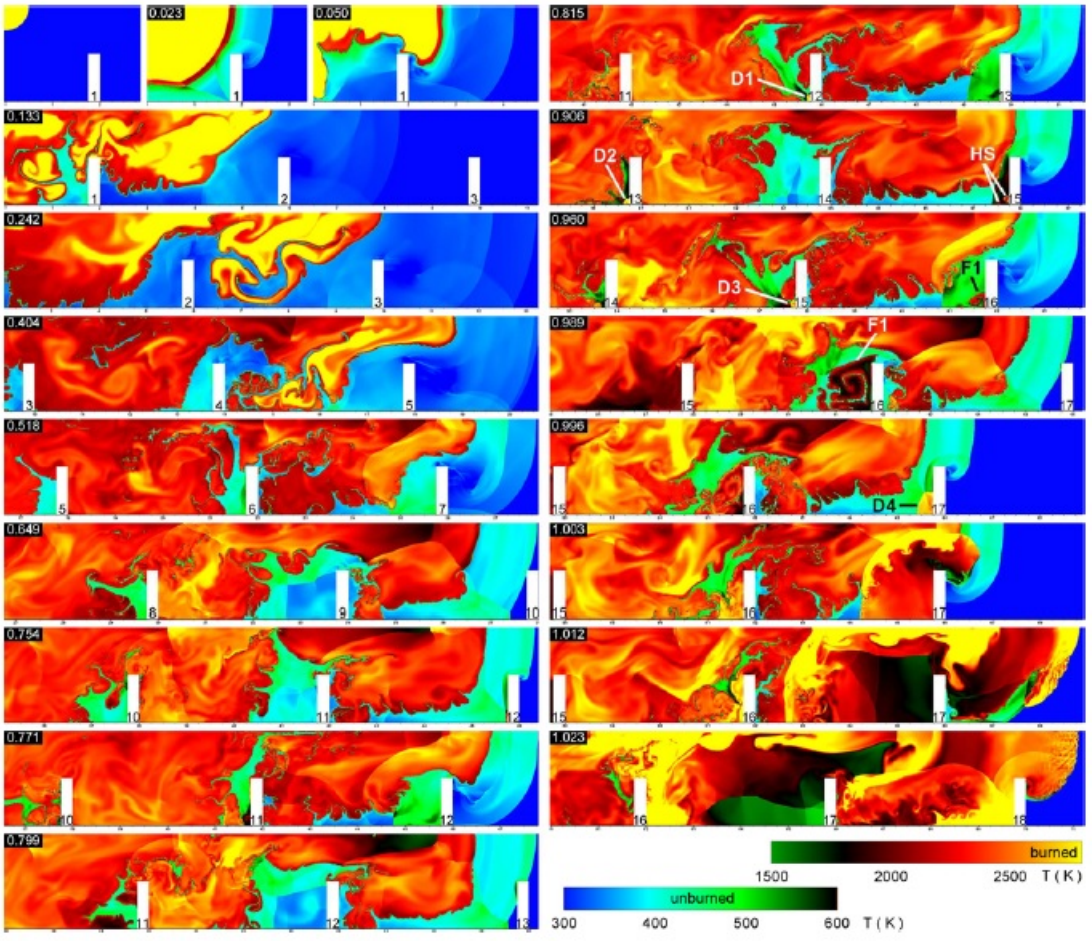

FIGURE 2.52: Numerical DDT modelling from the work of Oran [156] in Stoichiometric hydrogen-air mixtures with a channel width of 2cm and an obstacle spacing of 4cm. HS: Hot Spot, F1: New Flame, D1-4: Detonations. Time in milliseconds is shown above each frame

Furthermore, Johansen and Ciccarelli [64] have successfully modelled FA within orifice plates as shown in Figure 2.53. This model was built using flame surface density models and LES closure to the Navier Stokes equations in a similar manner to the work of Di

Sarli [159], Gubba [160], Wang [161], Masri [162] and Wen [163]. It can be seen from this figure that the flow around each orifice plate is captured well and reproduced in circumstances matching the experimental flow almost exactly. Clearly this is a very complex time dependent chemical reacting flow.

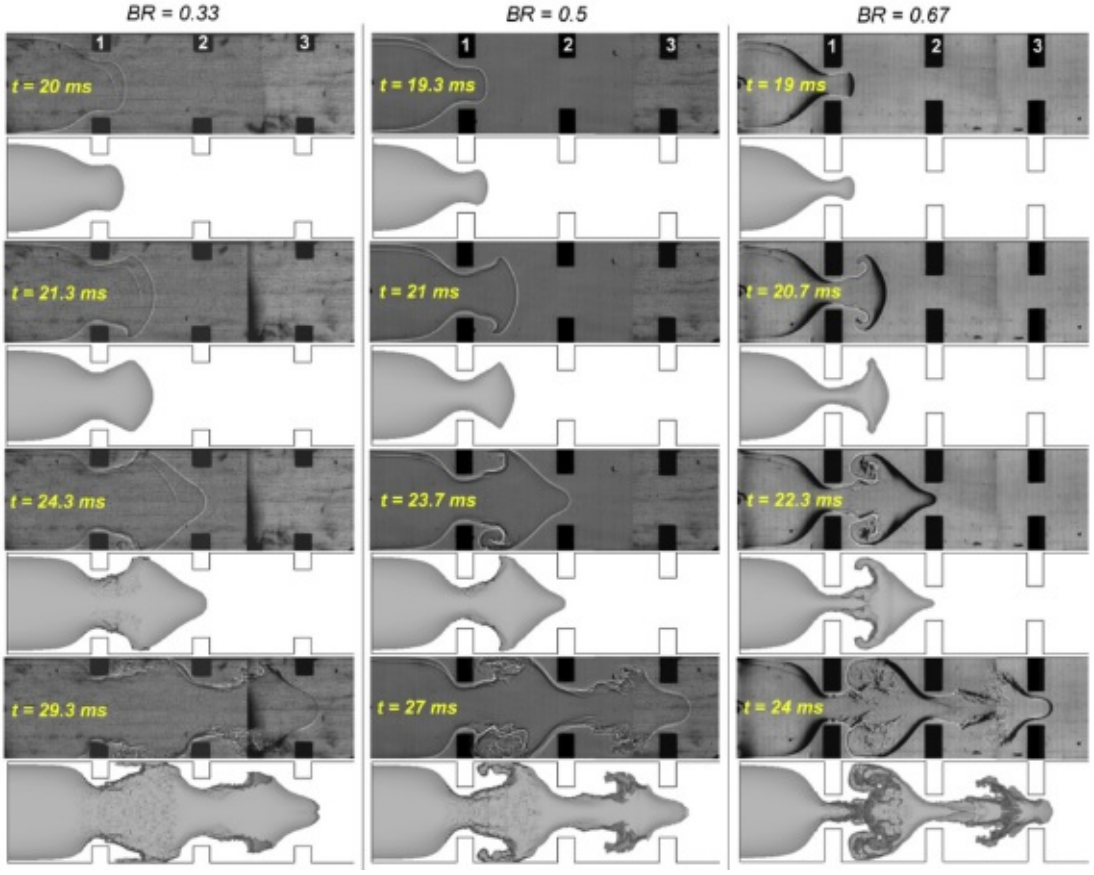

FIGURE 2.53: Experimental vs. Numerical LES modelling comparison of FA within obstacle arrays from the work of Johansen and Ciccarelli [64], obstacle blockage ratio is shown at the top of each column, time of each frame is shown in yellow

2.4 Existing Analytical FA Models

Previous work from the literature has been investigated to identify models which can predict flame acceleration using semi-empirical flame acceleration models in one or two dimensions and time. These models are largely useful because they can be solved rapidly with little computational effort. Veser [107] predicts the point at which the flame becomes sonic in obstacle laden tubes, but does not provide information regarding the development of the flame over time. Veser's model predicts that the flame will

transition to DDT given that the venting flame is choked for long enough to allow for autoignition to occur after the compressive shock.

2.4.1 Silvestrini's Model

Silvestrini's work [164] predicts the development of the flame speed relative to X/D, Eq. 2.52-2.54 and can also be used to predict flame acceleration in time as well as X_{DDT} in smooth tubes. A, B, ϵ in Equation 2.52 are empirically determined factors which were chosen over a range of fuels by Silvestrini et al. A, B, ϵ are given the values 6.5, 0.0061 and 0.4 respectively. Silvestrini's model can predict X_{DDT} location with an accuracy of $\pm$ 40 % when compared to experimental data across a variety of fuels and tube diameters. The model can predict X_{DDT} in obstacle laden tubes as well as smooth tubes. Silvestrini's model predicts that DDT will occur when the flame speed is equal to half of V_{CJ}, the Chapman Jouguet ideal steady detonation velocity. Other models such as that of Sorin, [165], also focus on the run up length to detonation without providing full detail of the intermediate steps.

$$V_f = A\sigma u_l e^{B(\sigma-1)\left(\frac{X}{D}\right)\left(\frac{D}{0.15}\right)^{\epsilon}} \quad (m/s) \tag{2.52}$$

$$\left(\frac{X}{D}\right)_{DDT} = \frac{1}{A(\sigma-1)}\left(\frac{0.15}{D}\right)^{\epsilon} \ln\left(\frac{BV_{CJ}}{\sigma u_l}\right) \quad (dimensionless) \tag{2.53}$$

$$\left(\frac{X}{D}\right)_{DDTBR} = \frac{1}{1+15BR}\left(\frac{X}{D}\right)_{DDT} \quad (dimensionless) \tag{2.54}$$

Initially a flame in a smooth tube accelerates after ignition due to wrinkling of the laminar flame caused by the Landau-Darreius (LD) instability. Additional thermal diffusion effects can change the flames stability which may in turn result in the flame becoming cellular and promote further FA. At this point the development of a flame between a smooth walled tube and an obstructed channel diverges. In the case of the smooth walled tube, the flame accelerates largely due to the interaction of the flame

front with a growing boundary layer ahead of the flame and a compression wave which builds to form a shock wave at some point along the tube [29]. In comparison, FA in obstacle laden tubes is controlled largely by the geometric interaction of the obstacle with the flow field ahead of and around the flame, known as flame folding. The flame folding phenomenon changes the FA process considerably in comparison to the smooth walled tube case. As the FA process begins after ignition, the LD instability and thermal diffusion effects lead to a cellular flame, which then rapidly stretched by the interaction of the expanding gas with the obstacles in the channel in the flame folding process. Towards the end of FA as the flame approaches the choked regime where compressibility effects and shock reflections play an important role in the nature of the flames behaviour.

As a result of the physical differences between FA in smooth channels and obstacle laden channels Silvestrinis' FA model (Eq. 2.52,2.53) is only valid for flame acceleration in smooth walled tubes. However an equation for X_{DDT} in blockage laden tubes is also given (Eq. 2.54), but without the prediction of the developing FA prior to this point. Silvestrini's model can clearly be used for the prediction of FA in smooth tubes and could be helpful for PDE combustor design length, although these predictions are based on the assumption of exponential growth of turbulence in the boundary layer and are incapable of providing detailed developments of the flame speed against time and distance. This model might possibly be investigated and developed to further understand the initial flow in obstacle enhanced flame acceleration.

2.4.2 Bradley's Double Discontinuity Model

Bradley et al. [166] have built an analytical model which predicts the flow of venting gas explosions along ducts. The venting gas velocity, V_g, can be determined for a known flame front area, A_f, turbulent flame speed, u_t, cross sectional duct area, a_d, and combustion density expansion ratio, σ, as shown in Equation 2.55. V_g is used to calculate c the explosion venting number. Venting number is calculated (Eqn. 2.56 for a known ratio of specific heats, γ, and sound velocity in the products, a_b. Venting number, c, can be related to the Mach number of the shock, M_1 (Eqn. 2.57). The shock Mach number can then be used to solve Equations 2.58 and 2.59 for the shock temperature and pressure ratios which are used to find the post shock pressure and

temperature. Bradley et al. have used this theoretical model to determine the gas speed at which DDT could occur through autoignition. This autoignition relies on sufficient duct length to provide an adequate residence time after the autoignition conditions have occurred before the shock leaves the detonation tube.

$$V_g = u_{tm}\frac{A_f}{a_b}(\sigma - 1) \quad (m/s) \tag{2.55}$$

$$c = V_g\left(\frac{\gamma + 1}{2a}\right) \quad (dimenesionless) \tag{2.56}$$

$$M_1 = \left(\frac{c}{2}\right) + \left(\frac{1 + c^2}{4}\right)^{1/2} \quad (dimensionless) \tag{2.57}$$

$$\frac{P_2}{P_1} = \left(\frac{2\gamma M_1}{1 + \gamma}\right) - \left(\frac{\gamma - 1}{\gamma + 1}\right) \quad (dimensionless) \tag{2.58}$$

$$\frac{T_2}{T_1} = \left(\frac{2\gamma M_1^2(\gamma - 1)}{\gamma + 1}\right)\left(2 + \frac{(\gamma - 1)M_1^2}{(\gamma + 1)M_1^2}\right) \quad (dimensionless) \tag{2.59}$$

2.4.3 Bychkov's flame propagation model

There has been significant recent work to analyse low speed flame acceleration using a novel analytical approach. The model proposed by Bychkov, Valiev, Eriksson, Akkerman and Law as can be seen in Figure 2.54 [167, 62, 168, 169] was initially derived for incompressible flow which was seen to be valid for flames in weakly compressible flow, up to Ma =10^-3. Bychkov's model predicts the effect of different obstacle blockage ratios on the initial stages of flame acceleration as a result of the volume of gas between the obstacles and the local turbulent flame speed S_t.

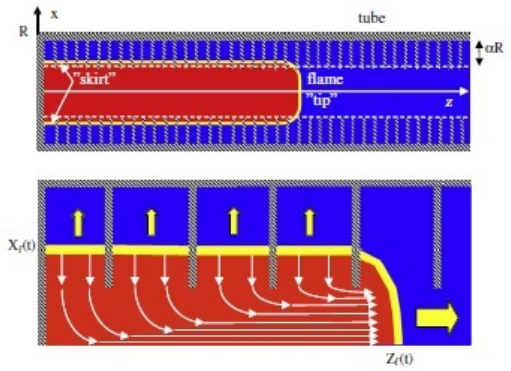

FIGURE 2.54: Schematic of flame propagation in an obstacle laden channel according to Bychkov's models [168]

Bychkov et al. propose that for incompressible flame acceleration due to burning in pockets between the obstacles can be characterised using Equation 2.60 [62], where Z_f is the location of the flame tip, α_β represents the ratio of the diameter of the internal tube to the external tube. R in this case is the largest internal radius of the combustion chamber and σ is the ratio of unburnt reactant density to burnt product density. The scaled acceleration rate is represented by $\theta_{By} = (\sigma - 1)/(1 - \alpha)$

$$\frac{Z_f}{(1-\alpha_\beta)R} = \frac{\sigma}{\sigma - 1}[exp\,(\theta_{By} U_f t/R) - 1] \quad (dimensionless) \tag{2.60}$$

It can be seen that the flame location increases exponentially with respect to time, flame tip speed and scaled acceleration rate, and is exponentially inversely proportional to the radius of the tube. Acceleration is seen to be stronger with larger thermal expansion across the flame, σ and larger blockage ratio. This model does not predict the instantaneous rate of flame acceleration as accurately as a computational fluid dynamics (CFD) model would, however it is capable of predicting the average flame acceleration profile which the flame takes over a series of repeated obstacles. The work carried out by Bychkov et al. for incompressible flows [62] was later extended for weakly compressible flows [168] using a more advanced equation for the flame tip location which included terms relating to the flow Mach number and resulted in reduced acceleration rate with increasing Mach number.

2.4.4 Bradley's Empirical Turbulent Flame Model

Furthermore, Bradley [52] has investigated turbulent flames experimentally over an extensive range of pressures. Turbulence was varied up to the point of flame quenching. The experimental data was then used to derive empirical correlations for the prediction of turbulent flame speed, u_{tm} [52]. Markstein number, Ma_{sr}, was calculated from the Karlovitz stretch factor, $Ka_{0.8}$. This relationship is valid within the range -3$\leq Ma_{sr} \leq$11. The ratio of u_{tm} to u' (rms turbulence velocity of premixed reactants) can be calculated using Equation 2.62. Empirical factors α and β from Equations 2.63 and 2.64 [52] have been found for stoichiometric propane air mixtures. In Bradley's work u' is chosen as a maximum value prior to quenching which occurs at $Ka_{0.8}$. Once the ratio u_{tm}/u' is known it is possible to find u_{tm} using Equation2.65 where u' is known. The area of the turbulent flame front can then be found with Equation 2.66. It is then possible to calculate V_f using Equation 2.67 as well as V_g from Equation 2.55. The work of Bradley et al. [166, 52] does not link u' generation to geometrical obstacle geometry, however to u' required for maximum flame stretch to occur. This allows the maximum theoretical flame speed of a mixture to be calculated, for a given mixture. The use of this model in practical terms for engine design however is somewhat limited to theoretical limits of flame speed. This is because the models does not contain a link between obstacle geometry and u' generation for use as a predictive tool for optimization of obstacle geometry.

$$Ma_{sr} = \left(\frac{34.4}{Ka_{0.8}}\right)^{\left(\frac{1}{1.8}\right)} - 4 \quad (dimensionless) \tag{2.61}$$

$$\frac{u_{tm}}{u'} = \alpha_B Ka_{0.8}^{\beta_B} \quad (dimensionless) \tag{2.62}$$

$$\alpha_B = 0.022(30 - Ma_{sr}) \quad (dimensionless) \tag{2.63}$$

$$\beta_B = 0.0105(Ma_{sr} - 30) \quad (dimensionless) \tag{2.64}$$

$$u_{tm} = \left(\frac{u_{tm}}{u'}\right) u' \quad (m/s) \tag{2.65}$$

$$\frac{A_f}{a_d} = 1 + \frac{u'}{u_l} \quad (dimensionless) \tag{2.66}$$

$$V_f = \sigma \left(\frac{A_f}{a_d}\right) u_{tm} \quad (m/s) \tag{2.67}$$

Bradley et al. determine whether a flame is likely to transition to detonation based on the auto-ignition delay time at the post shock conditions given using the shock Equations (Eq.2.56 and 2.57). It is worth noting that this work does not predict the run up distance or time, only whether detonation is possible. Bradley's models are used in the literature to predict V_{CJ} for a given mixture. This flame model cannot be used to predict the effect of turbulence generating obstacles on the flame in its current state. Perhapse the model could be modified to incorporate u' generation, and used as a design tool.

2.5 Key Factors Governing PDE Performance

2.5.1 Tube diameter

It is important to distinguish between the processes involved in FA and DDT, for example for strong FA it is necessary for combustion to take place within a tube diameter at least two orders of magnitude larger than the laminar flame thickness [29], in addition there must be strong turbulent mixing present to provide the critical feedback path for flame acceleration. Once the flame has reached a sufficiently fast speed that detonation is possible, it is necessary to consider the best environment for detonation, whether within the turbulence producing obstacles, or within the smooth section of the tube.

Tube diameter effects on the success of DDT have been investigated since the early 80s with key work combining the effect of tube diameter and stoichiometry being carried out by Peraldi et al. [170]. In his paper Peraldi finds that DDT occurs readily in tubes

with a diameter to cell size ratio, λ/d of thirteen. This figure is given irrespective of wall roughness and will transition to detonation readily providing the equivalence ratio is roughly stoichiometric. Peraldi determined that smaller tube diameters produced reduced post DDT overpressure and a narrower the band of acceptable equivalence ratios for effective DDT than larger tube diameters.

Further to the early work of Peraldi and Oppenheim [170], recent work has extended the limits of the minimum tube diameter for detonation. Ciccarelli and Dorofeev [29] report that for detonation to occur within a smooth tube, the external tube diameter D must obey $D \leq \lambda/\pi$, where λ is the detonation cell size. For example, in the case of stoichiometric propane-air with a cell size of 56mm, the critical tube diameter will be 17.8mm. If the detonation takes place within an obstacle laden tube, the critical dimension becomes the internal diameter of the blockage, d, which must obey $d \geq \lambda$, so in the case of stoichiometric propane-air an internal orifice diameter of 56mm is required for detonation to occur within the orifice section of the tube. Zipf et al. have investigated the detonation limits of methane-air flames in a 73m long,1.05m diameter tube with orifice blockages and a variety of different stoichiometric mixtures [171]. This experiment was designed to investigate the effect of methane build up in mine shafts in order to investigate the risk associated These experiments show that even small diameter tubes representing mine shafts are likely to promote DDT under approximately stoichiometric conditions with sufficient run up length and confinement.

Clearly, if detonation is required to transition within the FA blockage of a PDE the tube diameter must be much greater in size than in the case of transition in a smooth tube. This poses a problem for PDE designers as the ideal flight capable PDE would be as short as possible and may need to fit within a small streamlined package with a minimal cross section.

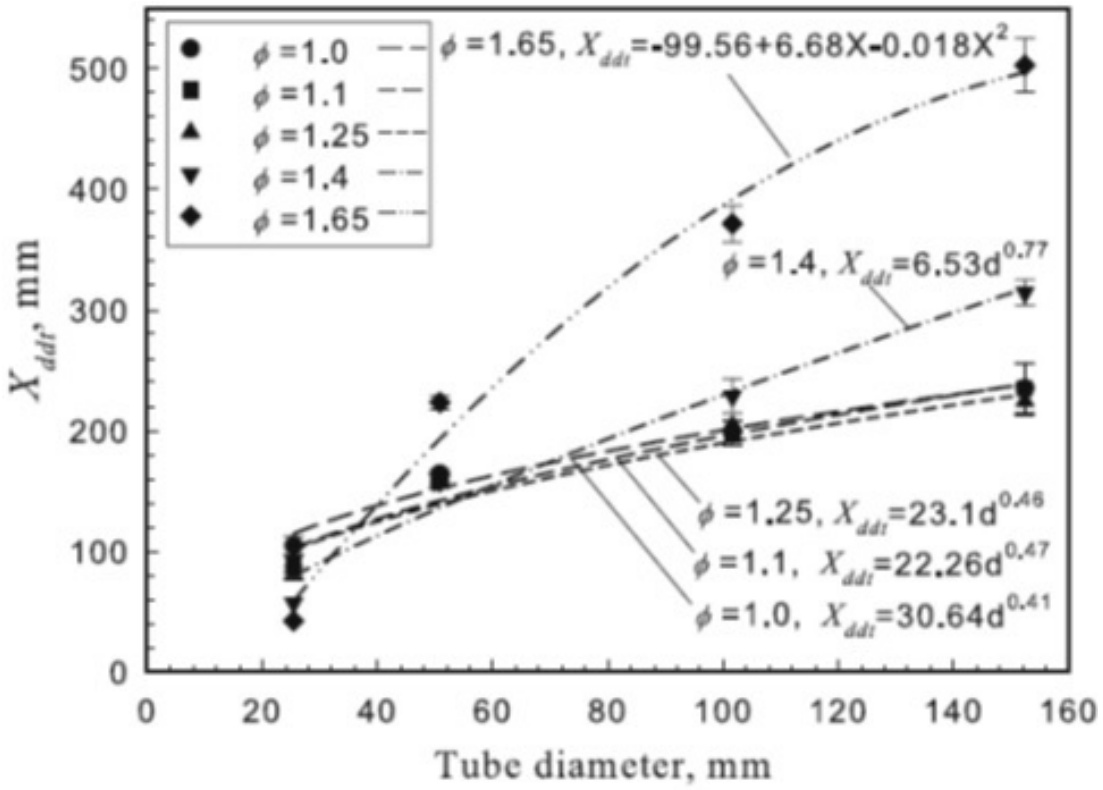

FIGURE 2.55: The effect of changing diameter or equivalence ratio on X_{DDT} the run up length, from the work of Li et al. [172]

One solution to this problem is to accelerate the flame through a blockage with a smaller internal diameter than λ in order to gain fast FA, then progressively reduce the blockage ratio until a higher flame speed comparable with the isobaric speed of sound in the reactants has been reached, at which point the obstacles could be removed entirely allowing the flame to detonate in a tube with a small diameter comparable with $\lambda/\ \pi$. In this way, the FA section of the PDE (pre-detonator) and the thrust chamber can maintain the same external diameter throughout, allowing a streamlined small cross section engine to be built.

Bychkov et al. [167] investigated the acceleration of flames in obstacle free, smooth walled tubes theoretically. Bychkov found that the flame acceleration rate of the flame such a tube is inversely proportional to the Reynolds number of the flow for large values of the Reynolds number ($Re \gg 4\ \sigma$, greater than 36 in the case of propane). Bychkov et al. further investigated the effect of obstacles on flame acceleration and DDT in ducts [62, 168]. The same relationship can be used in orifice laden tubes [67], where the turbulence length scale is determined by the tube diameter, D,for orifice blockages

with $0.3 \leq BR \leq 0.6$. The effect of diameter on flame acceleration will therefore have a large effect on the run up distance to a supersonic flame in addition to the 'go', 'no go' condition determining the possibility of detonation due to the detonation cell structure.

Li et al. [173] investigated the effect of diameter on the degree of over driven detonation generated immediately after the DDT event takes place and found that larger tube diameters generated higher factors of detonation overdrive. This knowledge is useful as a design consideration for use in a ground based test bed to avoid rupturing the detonation tube wall, and in flight test beds to limit the wall thickness and keep engines light by reducing the size of the detonation tube immediately after DDT, perhaps transitioning to a larger diameter once a stable CJ detonation has been established.

2.5.2 Obstacle Blockage Ratio and Length

Blockage ratio and length have a coupled effect on flame acceleration such that for a flame to accelerate enough to reach X_{DDT} both criterion for blockage ratio and blockage length should be considered together. Ideally the blockage should be long enough that the flame accelerates to a speed sufficient to allow further FA and DDT, but not too long as this will cause unnecessary drag and decelerate the shock wave. Altering the blockage length can make a great difference to the final flame speed as can be seen by the comparison of Figures 2.56 and 2.57 in a 2" ID tube, with 9.5 and 27 tube diameters of spiral length, respectively [174]. Figure 2.56 shows strong FA with little deviation from the FA trend and a clear transition from deflagration to detonation wave at around 5 X/D, which stabilises at approximately V_{CJ} and continues at this speed for the full length of the PDE tube. In contrast, Figure 2.57 shows a large amount of scatter on a small negative FA trend from 5 to 30 X/D. This is because the flame accelerates early but the flame and shock become unstable. This instability is caused by obstacle induced drag which obstructs the propagating detonation wave from an unsteady overdriven detonation state with speeds of up to 2700m/s to around about 1500m/s. This deceleration is caused by the shock decoupling and recouping with the reaction front several times along the length of the PDE tube, leading to an unsteady detonation wave speed.

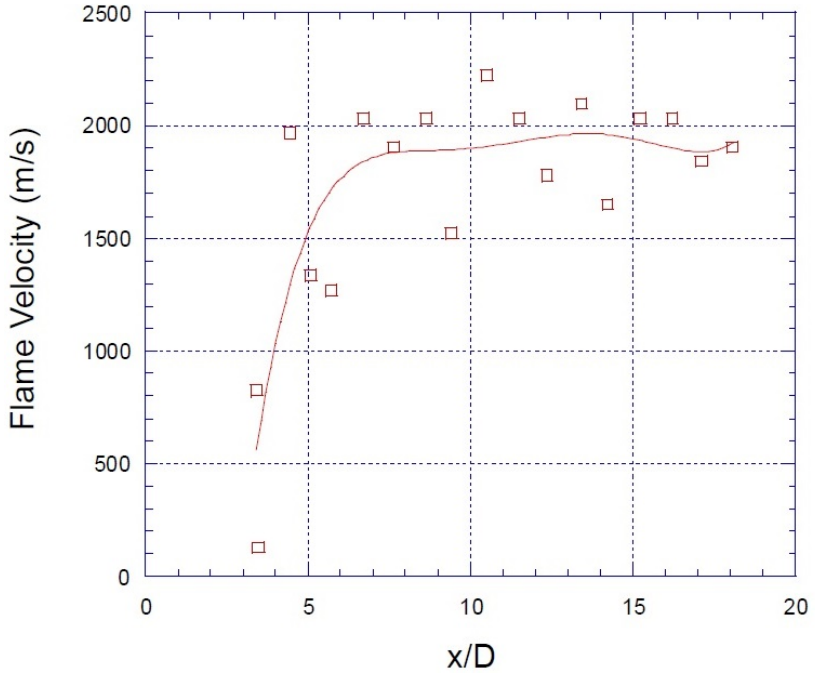

FIGURE 2.56: 9.5 x/D Schelkin spiral length flame speed history[174]

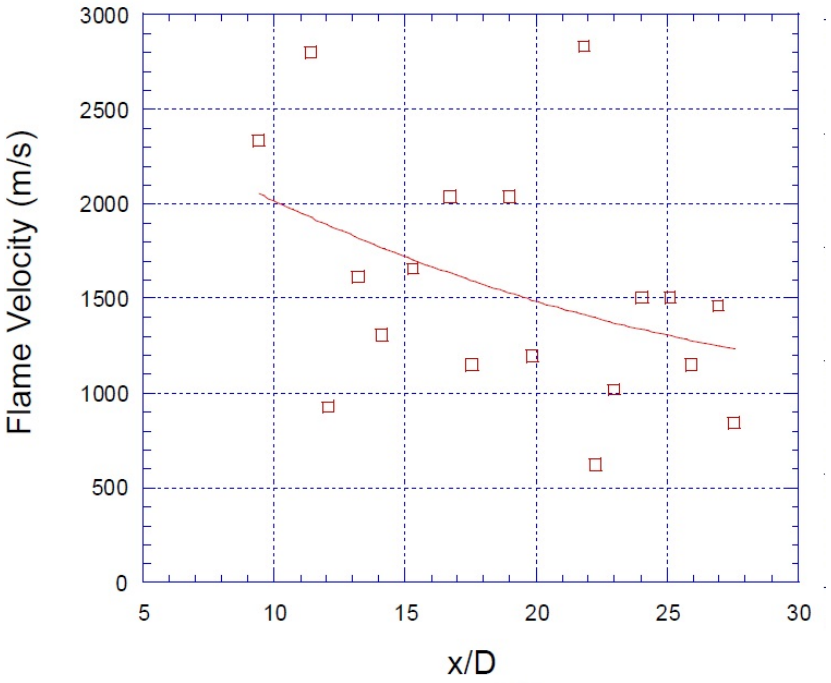

FIGURE 2.57: 27 x/D Schelkin spiral length flame speed history[174]

New et al. [104] have investigated the effect of obstacle geometry, investigating Schelkin spirals, embedded helical groves, circular groves and convergent-divergent nozzles with an obstacle length to diameter ratio of 6.6 showing that the effect of obstacles can be detrimental if the obstacle length is too short. In comparison the earlier work of New

et al. [175] shows that with longer obstacle length such as a length to diameter ratio of 12.5 conditions for stable, reliable and high pressure detonations are achievable. Similar obstacle lengths can be found in the work of Smirnov (12.3 L/D) [176] and Ciccarelli (13 X/D) [105]. The early work of Lee et al. utilized blockages with a length of around 60 L/D [101], which is more than sufficient to generate a chocked flame, but would generate unnecessary drag on the wall during the filling process of a practical PDE.

The work of Li et al. [177] summarises well the effect of obstacles on flame acceleration, showing how different blockage ratios and lengths can affect the run up to DDT and FA over distance. Li et al. [177] draw on the work of Sorin et al., Peraldi and Lee et al. [165, 178, 179] to draw conclusions about possibilities available to an accelerating flame, depending on the degree of constriction (BR), length of the obstacle and the tube diameter. Figure 2.58 illustrates these relative options. In Mode One, the flame accelerates through the flame acceleration stage, reaches the choking point at which point DDT occurs within the obstacle then an over driven detonation is generated which decays to a stable CJ detonation state at a velocity of V_{CJ}. In Mode Two, the flame accelerates past the point of choking but is not able to form a stable detonation due to flame-shock interactions with the obstacles which generate drag and slow the detonation wave down to the quasi-detonation regime, which is well documented in the work of Ciccarelli and Cross [83, 180]. Once the quasi detonation passes the end of the obstacle, the flame accelerates to the overdriven detonation state, which again decays and forms a steady state detonation which propagates the rest of the fuelled tube length.

Conversely in Mode Three, the choking velocity is reached after which point the flame immediately exits the obstacle array, which reduces the strength of the flame feedback mechanism generating a flame which has insufficient energy to propagate to a quasi-detonation or over driven detonation as the obstacle was too short to promote the necessary conditions in the flame. In Mode Four, the obstacle was over constrained with a pitch which was too small, this generated a weak flame propagating below the sonic regime in the reactants, as a result the drag is too great for the flame to accelerate to the choking point at which DDT occurs.

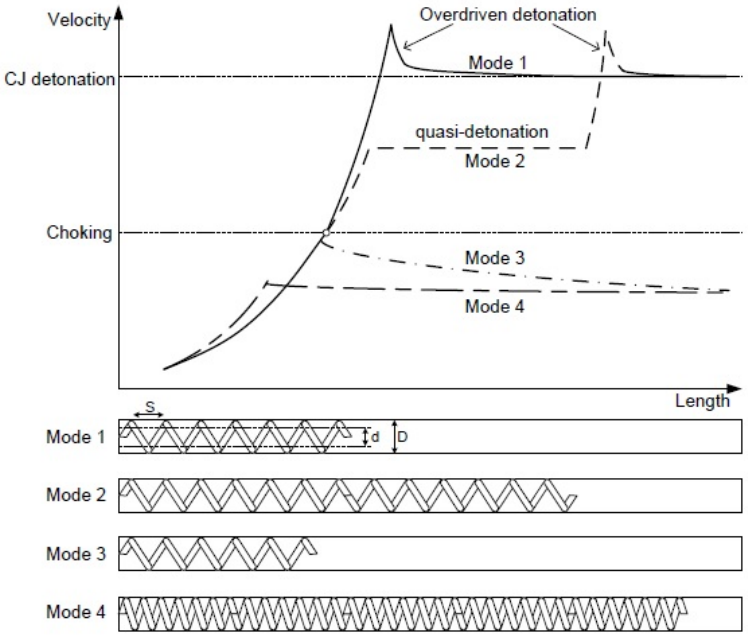

FIGURE 2.58: Classification of the effect of obstacles on run up from the work of [177], addapted from [165, 178, 179]

2.5.3 Combustor Length

For a flame to accelerate to the point of DDT and successfully transition into a stable detonation the flame front speed must first reach a velocity approaching the speed of sound in the burnt products. At this point the flame is said to have choked [71, 181]. After this point is reached the flame must be allowed to run up to detonation which takes approximately 7λ or more [29], where . This process of flame acceleration to the choked flame has been investigated both numerically and experimentally in the work of Sorin [165], Veser [107] and Dorofeev [182], described succinctly using Equation 2.68, which is used to predict the point at which the gas velocity is 95% of the velocity sound in the combustion gases. This model is based on the assumption that the turbulent flame speed S_t is likely to be around 10 times the laminar flame speed. Equation 2.68 has been formed by assuming that the flame takes on a conical formation with a wrinkled surface which can be expressed as a function of the blockage ratio of an orifice obstacle, as such the formula is valid only for fixed blockage and spacing orifice plate arrays within a parallel walled tube.

$$\frac{X_s}{D}\frac{(20(\sigma-1)S_l)}{a_b} \approx a_v \frac{(1-BR)}{(1+b_v BR)} \quad (dimensionless) \tag{2.68}$$

This equation is valid for 0.3≤BR≤0.75 and has been validated both experimentally and numerically, where σ, the expansion ratio is the unburnt to burnt gas density ratio, a_v and b_v are fitting coefficients 2 and 1.5 respectively. Determining the sonic velocity for a burnt mixture, a_b is easily achieved in combustion software such as NASA's Combustion Equilibrium with Applications (CEA) code [33].

For propane-air combustion with a_b equal to 900m/s [33], S_L given by 0.42m/s [183] and σ of 8 Equation 2.68 provides the non-dimensional run up distances shown in Figure 2.59 below. It can be seen that increasing BR decreases the non-dimensional run up distance X_s/D considerably from nearly 20 diameters for 0.3 BR to approximately 4 diameters at 0.7 BR.

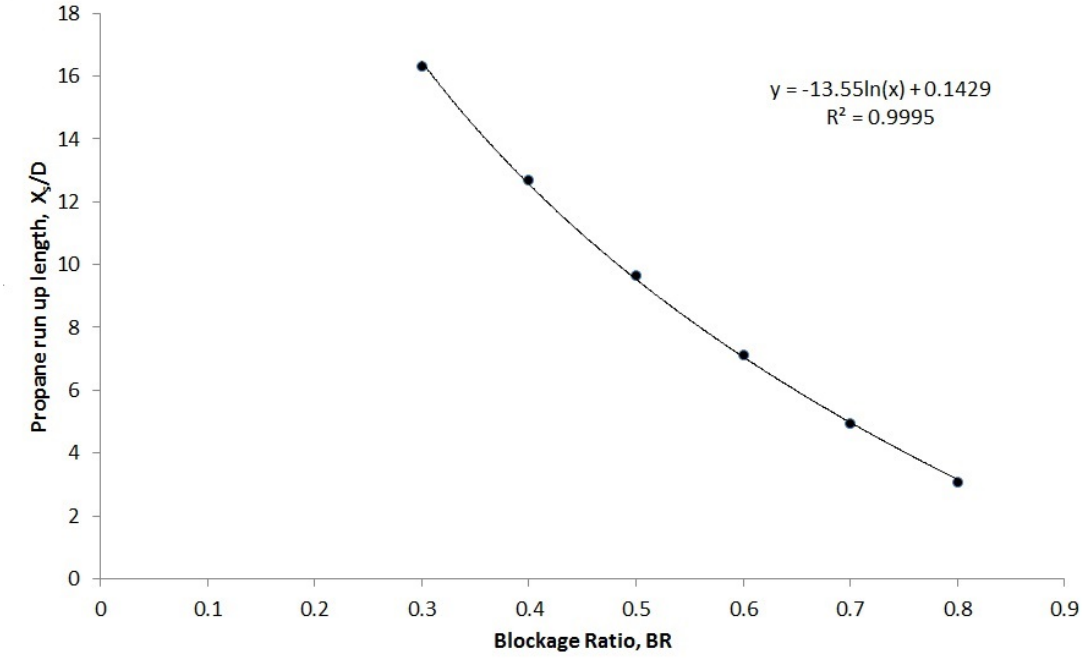

FIGURE 2.59: The effect of changing BR on run up length to the supersonic flame X_s the run up length, using equations from [182]

Once this point has been reached the flame must be given time to run up to detonation. Different authors use differing methods for the calculation of run up to detonation, some of which vary dramatically, indicating that the run up to detonations still not well enough understood, quantitatively at least.

Sorin et al. have measured the success of detonation run up in an obstacle laden tube after the flame has reached the sonic velocity of the combusted gases. This figure can be used to determine the run up length

2.5.4 Critical Geometric Duct Length

Dorofeev et al. have explored the effect of length on a range of different H_2-O_2-N_2 mixtures and geometry sizes in the 32 × 2.2 × 2.3 m^3 scale RUT and 1:50 scale MINIRUT [103]. These experimental facilities consisted of a series of instrumented, interconnected rooms for explosion studies. The critical geometry length, L, is defined in Equations 2.70 to 2.71. In the case of repeated obstacles with the same separation distance S, and channel height, H, L_1 is given by Equation 2.70.

$$L = \frac{L_1}{(1-\alpha_D)} \quad (m) \tag{2.69}$$

$$L_1 = (S+H)/2 \quad (m) \tag{2.70}$$

$$\alpha = \left(\frac{d}{D}\right)^{1/2} \quad (dimensionless) \tag{2.71}$$

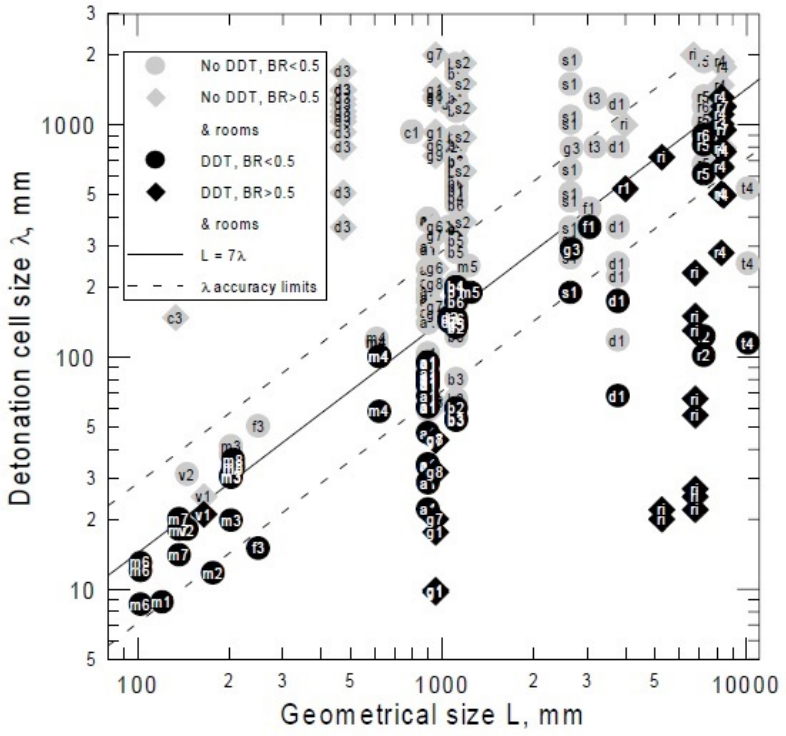

FIGURE 2.60: Effect of scale on DDT 'GO' and 'NO GO' conditions [103], L ≤ 7λ

It can be seen that where L $\leq 7\lambda$ detonation can take place, but where L is greater than this limit detonation is not likely. This length corresponds to the longest length from downstream corner of the orifice plate with the wall to the centre line of the tube. This equation will be of critical importance when designing any PDE tube geometry.

2.5.5 Fuel

2.5.5.1 Fuel type

Fuel considerations are crucial for generating fast flame acceleration (FA) to the point of mixture detonation. The main criteria are that the flame generated must readily accelerate when under high turbulence, high pressure conditions, within an adequate tube diameter and length so that a detonation is generated as rapidly as possible, allowing high cycle frequencies for thrust generation. There are several factors to consider when choosing a fuel for flame acceleration. These factors may differ from the fuel used after detonation, depending on PDE design. For instance, if a rapid detonation is intended within a short distance a small quantity of more volatile fuel may be used in FA leading to detonation than the main bulk fuel for PDE thrust such as that used by Frank Schauer in the USAF PDE demonstrator [184]. It was determined by Ciccarelli et al [63] that the best fuel to replicate kerosene air mixtures for detonation at room temperature was a stoichiometric propane-air.

2.5.5.2 Fuel Stoichiometry

Fuel stoichiometry must be chosen carefully to promote maximum FA, and must be accurately controlled for the duration of the filling cycle to produce a well-mixed homogeneous mixture throughout the length of the FA obstacle in order to promote detonation. Figure 2.61 [185] illustrates the effect of changing tube diameter on the length of transition to detonation and the degree of overdriven detonation resulting after DDT occurred in propane-oxygen mixtures of varying stoichiometry, showing that for a larger tube diameter X_{DDT}, is longer, with an increasing trend in X_{DDT} with increasingly rich fuel mixtures. Once normalised by tube diameter raised to the power 0.44, the transition length to detonation shows direct dependence on equivalence ratio for propane-oxygen mixtures.

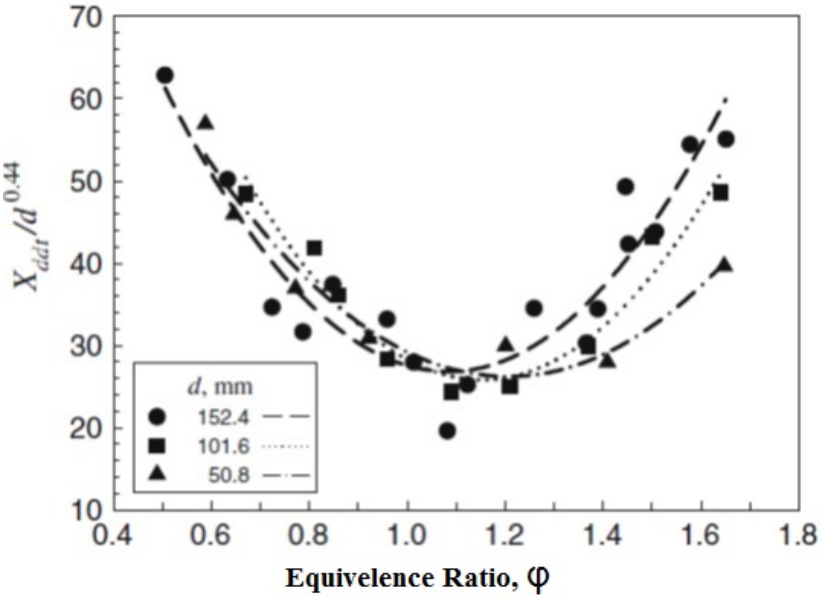

FIGURE 2.61: The effect of changing equivalence ratio on X_{DDT} the run up length, reproduced from [185]

Stoichiometry has a coupled effect with diameter on the ability of a mixture to detonate. Stoichiometry effects detonation cell size dramatically and this effect varies from one fuel to the next. Figure 2.62 clearly illustrates the effect of stoichiometry for Acetylene, Ethylene and Propane, showing a decreasing trend with increasing stoichiometry until approximately $\phi = 1$ for most fuels, apart from Acetylene which maintains a small detonation cell size for a large range of $0.8 \leq \phi \leq 2.8$.

Generally, if detonation is possible at one tube diameter with a fixed stoichiometry it is possible to achieve detonation over a wider stoichiometric range by increasing the tube diameter, providing the flame speed entering the tube cross section has the same velocity. The effect of tube diameter on DDT has been known for some time [170, 185] and is determined by the detonation cell pattern after DDT. Cell size varies with fuel stoichiometry and for a successful detonation to sustain it must be able to self-organise in such way that the detonation chamber has λ/π detonations within the minimum tube diameter for a spinning detonation. Tubes with smaller diameter than the cut off limit will not sustain the minimum detonation cell pattern and will stop the detonation front from forming, leaving a fast sonic flame with no detonation front.

In a practical PDE, fuel stoichiometry must be carefully controlled so that DDT is successful and the generated detonation can sustain its self once generated. For a PDE

TABLE 2.4: The effect of changing pressure on M_a in stoichiometric propane-air mixtures [52, 55]

Pressure (bar)	u_l (m/s)	M_a
1	0.397	7.01
2.5	0.375	5.62
5	0.321	2.81
9	0.31	0.26
14	0.25	-1.39

to work well it must control the mixture carefully and reliably during the filling step so that the PDE will continue to operate within its limits whenever the operator desires.

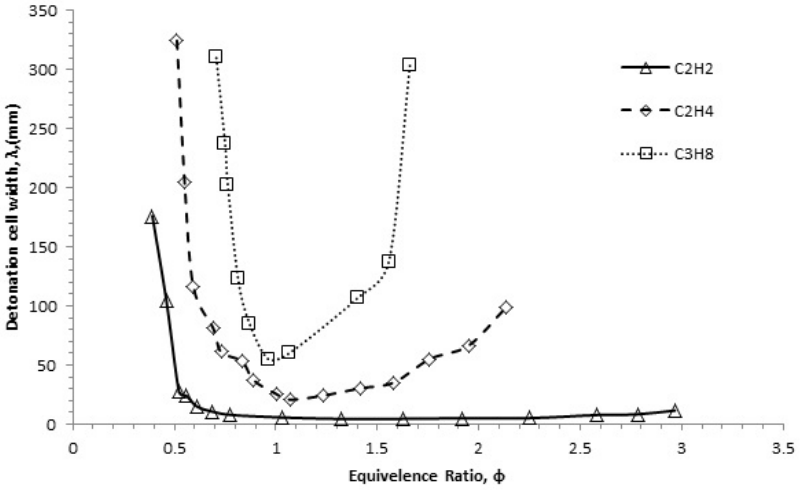

FIGURE 2.62: The effect of changing equivelence ratio on the detonation cell size, λ, from Knystautas et al. [186]

2.5.5.3 Markstein Number

Markstein Number is defined as the flame stretch rate over the flame strain rate and is an indicator of a flames response to instabilities approaching the flame front. It is understood that Markstein number can be used as an indicator of a flames ability to accelerate [165, 29, 166].

Bradley et al. have used empirical Markstein number relations to determine the speed of a detonating flame and its response to turbulence (Bradley et al. 2008) and have gathered a large body of experimental data for explosions in high pressure fan stirred bomb reactors [52, 187]. Examples of typical Markstein numbers for propane air and hydrogen air flames can be seen in table 2.4.

Flames with a high Markstein number exhibit the ability to become stable flames even during high stretch rate environments created by extreme turbulence. Flames which exhibit a low, or negative Markstein number are unstable, and will consume more mixture by stretching rapidly in increasingly turbulent conditions. Markstein number is a function of pressure, temperature and fuel stoichiometry in a premixed flame, like the PDE. The Markstein number of a fuel under a particular condition can be used to determine the turbulent to laminar burning velocity ratio which can be used to predict the flame speed relative to the moving gas frame of reference.

M_a can be controlled by choosing the reactant mixture and initial reactant conditions. Applying this knowledge to PDEs indicates that the choice of fuel air mixture is critical to determining PDE DDT performance and will also inform geometric design for detonation to occur. For example, it may be possible to find a fuel such as hydrogen with a high magnitude negative Markstein number which will detonate with relative ease. In contrast to kerosene, a traditional gas turbine fuel, hydrogen will provide a very limited aircraft range for the same storage volume, or require much more complex and impractical storage system to keep the fuel compressed on board an aircraft. Since the pressure of the reactants at each stage of combustion cannot be controlled directly, the reactant mixtures can be chosen on the basis of the Ma response to pressure and the geometry of obstacles must be designed to optimize flame. The PDE designer must control the degree of confinement and intensity of the turbulence feed back into the flame in order to insure that the flame continues to accelerate. This can be achieved by careful obstacle design and the correct choice of fuel-air mixture which allows the flame to accelerate as the pressure increases. If a flames M_a decreases rapidly with an increase in pressure, this reactant mixture is likely to generate rapid FA in confined tubes with the correct obstacle arrangement.

2.5.5.4 Expansion Ratio

A flames ability to accelerate along a tube is largely determined by the expansion ratio, σ, of the gases expanding as the flame burns. If the expansion ratio is high then the flame speed will be further augmented in the tube frame of reference, allowing more turbulence to be generated as the air ahead of the flame accelerates across the upstream baffles. Once turbulence has been generated the flame consumes the turbulent mixture,

which governs the local flame speed with respect to the gas frame of reference. The effect of expansion ratio has been investigated thoroughly by Kuznetsov et al. [67] who found that fuel mixtures which exhibited an expansion ratio of less than 3.75 ± 0.25 were unable to generate high speed flames during FA and transition to detonation. Mixtures with higher expansion ration accelerated much more readily and transitioned to detonation, provided that the geometry of the flame duct was sufficiently large to allow for detonation to occur as discussed in the work of Dorofeev et al. [103].

2.5.5.5 Practical PDEs

In recent years there has been a strong drive to create PDEs with practical use on aerial platforms. For this reason there has been strong interest in the use of liquid fuels due to their higher energy density. The use of liquid fuels on board PDE powered aircraft is probably the quickest route to application for such engines, as this fuel handling technology is well understood and already in use. Several research teams have investigated the use of liquid fuels such as Card et al., Fan et al. and Frolov [188, 189, 124].

2.5.6 Filling and Inlet Design

The filling process is controlled predominantly by the internal geometry of the engine (which generates a pressure loss) and the upstream air delivery pressure at the engine inlet. In order to increase the flow rate of the practical PDE it is necessary to reduce loss coefficients in all of the components within the PDE flow path to generate faster filling time, as long as the detonation run up length is not compromised.

The internal tube geometry is designed to prioritise flame acceleration after ignition in the first instance, in order for the engine to generate thrust after successful detonation, however, in order to increase the limiting frequency of operation to higher orders of magnitude, careful attention must be given to limit filling drag. Since the detonation tube must be filled with a much lower pressure than the pressure seen during combustion (up to 50 times less) internal drag across DDT obstacles promotes a much smaller flow rate and longer residence times while filling than while detonating. Often, it would appear that great consideration is given to the optimise FA and DDT in the PDE,

however an equally crucial criteria for achieving high thrust values is the frequency of detonation [31]. Since the filling velocity of a PDE cycle is often slow, the filling period is often the longest of the cycle periods. As a result, low inlet/valve pressure drop, along with high inlet mass flow are crucial for generating a high frequency PDE engine. High frequencies are neccessary to generate large amounts of thrust for a practical device.

A number of concepts have been investigated to combat the problem of slow PDE filling times, such as using a pre-detonator to generate the detonation separately from the main combustor. A pre-detonator feeds a detonation chamber or thrust chamber with a detonation in order to trigger a bulk detonation across the whole thrust chamber. Generally the pre-detonator can be filled separately to the thrust chamber, with minimal flow resistance in the detonation chamber to allow high frequency operation [190, 7] More refined PDE geometry alternatives include the use of concentric cylindrical flow paths [191] with the internal void used for filling and the external concentric void used to generate detonation, triggering detonation in the internal bulk flow. Investigation has been made into side filling PDEs in order to further increase cycle timing, as the main limitation of end filling tubes is the maximum area of the inlet, which can be much larger than the end if side wall filling is applied. The side filling concept has been explored by Carter et al. and the group from University of Texas at Austin [192]. Partial filling has also been investigated, as the PDE fuel charge expands during combustion which results in some amount of the mixture being expelled from the open end of the tube during combustion. The application of partial filling has been researched by Li et al, Mawid et al. and Ma et al. in addition to Chen et al. [193, 16, 194, 195].

In the practical PDE consideration must also be made for the changes in upstream pressure, temperature and volume during flight conditions which alter the filling, deflagration, detonation, and purging of the PDE depending on flight altitude, Mach number and humidity of the inlet air and the pressure at the outlet. There is a large body of recent work on PDE ejectors which generate thrust augmentation for the practical PDE. In addition to ejectors variable geometry spike inlets have been investigated in order to convert sonic inlet flow into subsonic flow with higher pressure, in order to allow high altitude, high Mach number PDE flight [196]. Other key technologies include nozzle and ejector design used to augment thrust generated by PDEs by focusing the jet efflux from the exhausted detonation [184, 194]

Extensive research has been carried out into the area of valveless PDE concepts, such as those described in the work of Shimo and Heister [197], Choi et al. [198], Wang [199], and Lu et al. [200]. This method of valving would allow PDE manufacturers to design PDEs with very few moving parts which would in turn reduce maintenance cost and increase reliability, assuming the system works effectively.

2.5.7 Nozzles

Nozzles have been shown to improve the thrust performance of PDEs by Allgood et al. [201], Yan [202] and Chen [195] who have investigated diverging/converging and converging/diverging nozzles. Nozzles can augment thrust and are capable of increasing the detonation chamber pressure during run up which results in shorter run up length and smaller detonation cell size. As such nozzles are a key aspect of PDE miniaturisation. Allgood et al. [201] investigated the effect of partial filling on nozzle performance. Fill fraction, ff was defined as the fraction of the PDE tube filled with combustible mixture when the valves had closed. Allgoods findings state that nozzles are not effective for PDEs operating with ff less than 0.5, but that PDEs with ff greater than 1 benefit from converging nozzles [201].

2.5.8 Liquid fuels

In practice a detonation engine would be much more likely to run using liquid fuels rather than gaseous fuels as a result of the fuel density and its subsequent impact on aircraft range during flight. Considerable effort has been made by researchers such as Tucker [203] since the early work carried out in shock tubes on kerosene detonation such as the work of Kling et al. [204]. Kailasanath et al have investigated liquid fuel detonation [205], concluding that if the droplet size was less than 10 μm, detonation will propagate at the same speed as in a hydrocarbon gas mixture. It is also stated here that detonations are possible in droplets around the order of a millimetre in size, as the lead shock can shatter and strip the droplet into smaller droplets which are more readily burnt [205]. Frolov et al. have extensively investigated liquid hydrocarbon detonation in a number of papers [133, 206, 127, 124, 190] and have developed a system for creating a detonable droplet/ vapour mist which is capable of detonating the Russian analogue

Fuel	Cell Size, mm
IPN - air[1]	8.18
PO - air[1]	6.19
n-Hexane - air[1]	11.34
petrolium ether - air[1]	12.28
n-Decane - air[1]	17.76
n-Heptane - air[1]	17.80
JP-10-air[2]	45

TABLE 2.5: Cell size measurement for liquid hydrocarbons. [1] minimum cell size taken at an equivalence ratio of approximately 1.2 from the work of Yao et al. [137][2] taken from the work of Austin [208], which was measured at atmospheric pressure and a temperature of 373K. *IPN*: Iso-propanol nitride, *PO* propylene oxide

of Jet-A1, TS-1[1]. Frolov's experimental rig diagram is illustrated in Figure 2.63, The pre-vaporiser wall temperature is recorded here as 190 ± 20 °C, which allows the mixture to detonate more readily and reduces the detonation cell size.

A great deal of recent work has been carried out on liquid hydrocarbon detonation engines, along with recent interest in liquid hydrocarbon cell size data such as the data shown in Table 2.5. One recent example of hydrocarbon detonation cell size is the work or Yao [137], which was carried out in a 6.5 meter long 0.20m diameter tube. Yao et al. investigated the cell size for a range of liquid hydrocarbon air mixtures across a wide range of equivalence ratios whilst also exploring the minimum ignition energy by changing the amount of hexogen in an industrial detonator used to ignite the hydrocarbon- air mixtures.

[1]Notes regarding Kerosene: The main differences between Jet-A1 and TS-1 are the freezing point and flash point. TS-1 has a freeze point of -60°C, whereas Jet A-1 has a freezing point of -47°C. The flash point of TS-1 is 28 °C, in comparison to that of Jet A-1, which is 38°C. These differences are a result of the difference in standard operating temperatures in different parts of the globe. [207]. Furthermore Jet A, which is often used in the US, has a reduced limitation on the maximum freezing point of -40°C. Jet A's flash point is the same as that of Jet A-1. Kerosene is often referred to in the literature without specifying which particular product quality of kerosene is used. As such, kerosene is specified throughout this literature review in a number of locations without knowing the specific grade of kerosene used, as kerosene quality ranges from heating oil products to jet fuel.

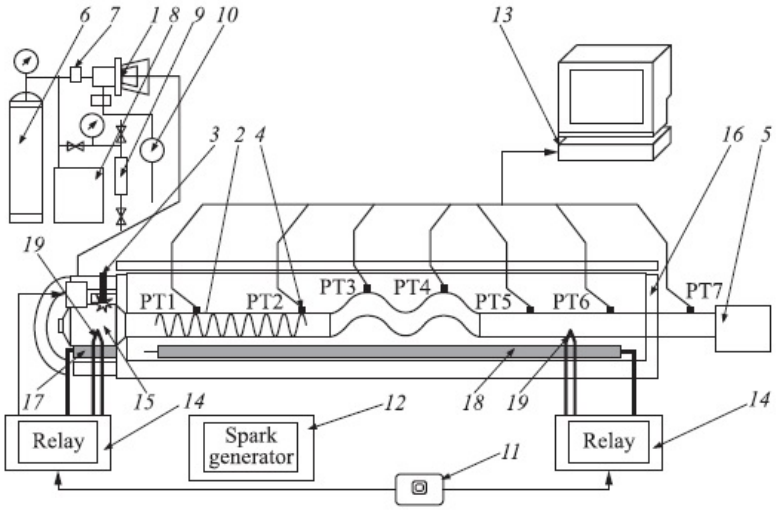

FIGURE 2.63: Diagram of liquid hydrocarbon detonation system [133] 1: injector, 2: detonation tube, 3: igniters, 4: pressure transducers, 5:detonation arrestor, 6: Air bottle, 7: fuel valve, 8: air compressor, 9: kerosene tank, 10: fuel filter, 11: digital controller, 12:Power Supply, 13: PC, 14: control relay, 15: pre-vaporiser, 16: thermostat, 17 &18: electrical heaters, 19: thermocouples

Wen et al. have investigated the effect of initial temperature and equivalence ratio of JP-8-Oxygen mixtures on X_{DDT} in a 1.143m long tube with a diameter of 101.6mm [209], as illustrated in Figure 2.64. It can be seen clearly that as the initial mixture temperature increases from 393 to 413K the trend for X_{DDT} reduces dramatically. It is noteworthy that there is a steep decline in X_{DDT} in the range $1 \leq \phi \leq 1.2$, particularly after an initial mixture temperature of 413K. This data will prove very useful for those interested in designing practical PDE systems as such engines require fuel to be carried in an energy dense form such as liquid JP-8 rather than a gas such as most of the earlier work on detonation using propane, hydrogen and ethylene as well as others.

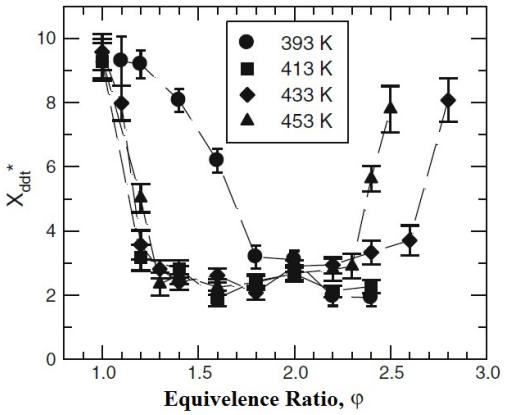

FIGURE 2.64: Effect of temperature and equivalence ratio on X_{DDT}, reproduced from [209]

2.5.8.1 Supersonic orifice flow

Torizumi et al. have run a series of experiments to determine the mass flow across a range of orifice flow conditions, from sub-critical (subsonic at the throat) to super-critical (supersonic at the orifice throat) [210]. These experiments were performed using a 50mm diameter pipe through which a high mass flow of air was passed through an orifice. The flow across the orifice was metered at static conditions before and after the orifice plate in order to determine the pressure drop across the orifice plate. This experiment was conducted to determine the orifice mass flow so that existing mas flow prediction calculations could be extended beyond the theoretical limit of choked orifice flow. Super-critical flow is only possible because the location of the vena-contra in the flow downstream of the orifice plate moves downstream close to the sonic condition, allowing more gas to pass through the orifice than would usually be the case.

The general equation for mass flow through an orifice is defined in Equation 2.72, where $\dot{m}$ refers to the mass flow passing through the orifice plate, α_o is the orifice flow coefficient and ε_o is the orifice expansion factor. A_N is the area of the orifice opening, ρ_1 and P_1 are the orifice inlet density and pressure respectively. The only unknowns in this equation were α_o and ε_o, which were found experimentally to be characterised by Equation 2.73

$$\dot{m} = \alpha_o \varepsilon_o A_N \left[2\rho_1 P_1 \left(1 - r\right)\right]^{1/2} \tag{2.72}$$

Equation 2.73 contains a list of measureable quantities,M_1, the upstream Mach number, β_0 the diameter ratio of the orifice internal to external diameter, the static pressure ratio accross the orifice plate, r and the ratio of specific heats, γ.

$$\left(\alpha_o \varepsilon_o\right) = \frac{M_1}{\beta_o^2} \left(\frac{\left[2(1-r)\right]}{\gamma}\right)^{-1/2} \tag{2.73}$$

This information could be used to calculate the pressure drop across an orifice plate for any known orifice mass flow, given the other conditions were known.

2.6 Rig Design Considerations

2.6.1 Material temperature limits

Frolov et al. record the tube wall temperature of a tube undergoing repetitive detonation cycles can reach temperatures of 500 °C [97] in a natural gas fired pulse detonation burner developed for industrial power. In contrast, elements of the burner exposed to the deflagration-shock wave complex waves only reached temperatures of approximately 300 °C.

2.6.2 Instrumentation

Instrumentation used in the literature to record flame acceleration and detonation falls into two main categories:

Dynamic Pressure Measurement Dynamic pressure measurement instrumentation is used to measure the explosion overpressure with high temporal resolution at discrete spatial points. This type of instrumentation is responsible for the generation of dynamic pressure plots as seen in many PDE papers, and is used in the majority of the flame acceleration and detonation experiments in the literature [67, 109, 83, 171, 97, 98, 176, 193, 211, 212, 213, 105, 29, 102, 84, 214, 128, 215, 189, 122, 133, 208, 216, 203]. Key factors influencing the effectiveness of this instrumentation include the natural response time of the sensor and the geometric diameter of the sensor head [217], which determine the ability of the device to measure shocks.

Flame Speed Measurement Flame speed measurement can be achieved by a number of means. Some of these methods, such as ion probes, are applicable to engine demonstrators and more fundamental studies alike and are used widely in the literature for time of flight measurements between port locations [67, 109, 83, 177, 211, 212, 213, 63, 105, 29, 203]. An alternative, robust, point based optical method used for tracking flame speed is to use equally distributed photodiodes along the PDE tube for the measurement of flame speed as used by a large proportion or authors in the literature [67, 83, 171, 97, 98, 105, 29, 102, 122, 216]. Wider measurements of the entire flow

field can also be made, such as schlieren (for density measurements) [83, 84], Laser Induced Fluorescence (LIF), for the measurement of OH radicals in the flame front and Particulate Image Velocimetry (PIV) as well as Laser Doppler Anemometry (LDA) lend themselves to more fundamental studies of flame acceleration and detonation due to the complexity of setting up experimental apparatus such as laser light sheets, not to mention the optical access issues which can become a real issue with cylindrical combustion chambers due to the distortion of light travelling from the flame through curved volumes with different refractive indices. As such these experiments tend to be set up in laboratories with laser tables and conducted with single shot rigs. One potential circuit for use with ion probes with a single electrode (using the PDE tube as the second electrode) is displayed in Figure 2.65. This ion probe circuit is based around the traditional 741 operational amplifier, which is connected as a current to voltage converter. A bias voltage is applied between the tube wall and the central electrode of the ion probe, which encourages an ion current to flow between the two electrodes. This ion current is then converted to a voltage and amplified using the operational amplifier, generating a signal which can be read by DAQ equipment.

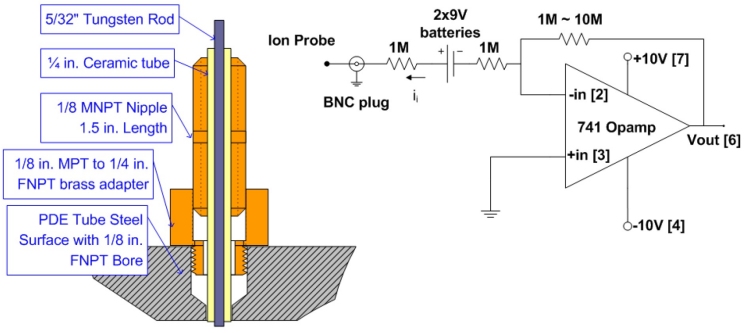

FIGURE 2.65: Ion probe illustration and circuit: Reproduced from the work of Panicker, [217]

2.6.3 Data Acquisition and control

DAQ systems for use with PDE or detonation studies must be capable of recording signals at a high enough sampling rate to surpass the Nyquist frequency, which is double the maximum frequency which should be measured. Preferably the measurement frequency should be even higher than this in order to determine the shape of the pulse adequately. Table 2.6 shows the sampling rate and instrumentation used to measure detonations in various studies, complete with references to the work. It should be

Sensor	Natural Sensor Frequency (kHz)	DAQ Sampling Frequency (kHz)	Reference
SINOCERA CY-YD-205	≥ 200	200	[199]
-	-	5000	[179]
PCB Model 111A24	450	100	[175]
PCB Model 111A24	450	240	[104]
PCB Model 111A24	450	2000	[192]

TABLE 2.6: Dynamic pressure sensor measurement frequency and sampling frequency table. - refers to unavailable data.

noted that the Nyquist Frequency criterion is not adhered to in some cases, which will have limited the maximum frequency resolution of the measurements made to half that of the sampling frequency, such as the first and third dynamic pressure measurement in the table. Some of the references also note that the data is only sampled for 10 seconds, presumably to avoid buffering issues which would affect the transfer of data from the DAQ system to storage on a hard disk [175]. This should be noted when deciding on a data acquisition system for use with high speed instrumentation for the measurement of shock waves and flames. Many of these experiments also used load cells for the measurement of thrust, which were also sampled at the same frequency as the pressure transducers in each experiment. In addition some of the experiments used ion probe measurement systems to determine flame speed by means of time of flight (TOF) measurement techniques. These detectors are built in house using spark plugs, and amplified using off the shelf electronic components to build amplifiers as discussed in section 2.6.2

2.7 Gap Analysis of Previous Research

2.7.1 Thoughts on turbulence generation

A review of the literature in section 2.2.3 showed that intense small scale turbulence can be beneficial in the early stages of the FA process. It should be noted, however, that high BR obstacles with blockage ratios in excess of 0.9BR are not practical for use in real PDE engines due to filling requirements which state that the tube should be filled at hundreds of cycles per second, or filling rates in excess of 150m/s for a meter long PDE tube, depending on the fill cycle duration. As such, it is thought

that intelligent obstacle design should optimize turbulence length scales generated by carefully controlling the obstacle geometry and BR, to improve the trade off between drag and introduction of smaller turbulent flame speed enhancing length scales along the tube.

Figure 2.66 clearly illustrates the relationships of different turbulent wave numbers (inverted length scales) as discussed by Nicolleau and Matthieu [218] relative to the energy available in the turbulent energy spectrum. It is clear that the large majority of the energy in turbulence can be found close to the integral length scale of turbulence. After turbulent kinetic energy has been injected into the flow by obstacles in the PDE, this turbulence is transferred through the inertial subrange to the dissipation range at the Kolmogorov length scales which determine the flame regime. Figure 2.66 (a) represents the thin flame regime where corrugation and wrinkling occur, Figure 2.66 (b) represents the thick flame regime and Figure 2.66 (c) represents the turbulent chemistry regime with distribution of the reaction zone.

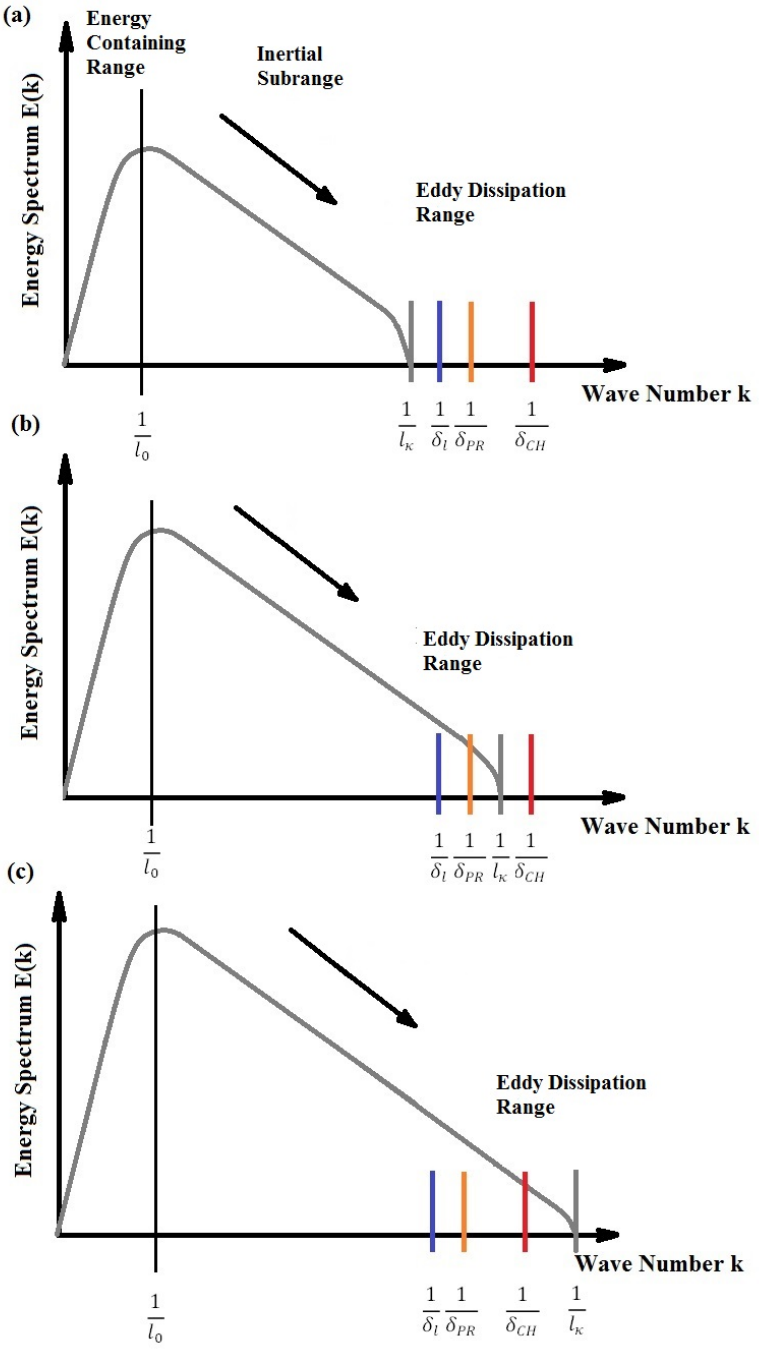

FIGURE 2.66: Flame Regimes depending on the Kolmogorov turbulence length scale, l_κ, and the flame lengths δ_l,δ_{PR} and δ_{CH} generating corrugated laminar flames, thick flames and distributed reaction zones respectively adapted from the work of Nicolleau and Matthieu [218] The integral length scale and Kolmogorov length scale wavelengths are shown, along with the intermediate inertial subrange

Most of the obstacles discussed in the literature contain geometries which generate turbulence at one integral length scale due to one defining length scale, examples include perforated plates with one hole size or orifices with one single hole size, as discussed in

Section 2.2.3.One potential method for increasing the intensity of small scale turbulence would be to use fractal obstacle shapes, similar to fractal grid geometry discussed in Section 2.2.4. Such a device for use in the PDE environment would need to be able to withstand strong shock waves without sustaining structural damage. Consequently it is thought that a fine fractal shape could be used to enhance FA and increase the isotropic nature and of the turbulence. Such a fractal obstacle could also force the turbulence cascade towards larger wavenumbers, with smaller Kolmogorov length scales. This turbulence enhancement would hopefully increase the rate of mixing at smaller scales relevant to the flame and shift the flame from the corrugated laminar regime or thick flame regime to a distributed reaction zone with a high turbulent flame speed. The scale and intensity of turbulence could be controlled by design, thus enhancing FA in a PDE combustor. As discussed in Section 2.2.4 the size of these length scales cannot be measured directly in the PDE combustor due to instrumentation limitations (without the use of prohibitively expensive optical techniques).Their effect on overall flame acceleration could be determined by flame speed measurement. Such experiments could be the basis of a qualitative study on the effects of turbulence generation by fractal obstacles on FA.

2.7.2 Thoughts on DDT modelling

Section 2.1.8.2 explored several possible routes to DDT, finding that there are many different paths to generating DDT in propagating flames. As a result, it is not possible to create a model which will predict all DDT events using a single method. This is because the routes to DDT vary greatly and the run up to the explosion in the explosion cover a wide range of temporal and spatial scales. Turbulent eddies for example exhibit a highly random, unrepeatable nature, when averaged over a small time frame such as the time taken from ignition to detonation. In comparison, flows in constant pressure premixed combustion can be treated with the assumption of having constant, repeatable turbulence characteristics as the flow has steady boundary conditions and is constant over time. Modelling DDT accurately therefore requires the full range of scales to be taken into consideration. Instead of modelling FA and DDT it may be more useful for FA studies to simply model FA before detonation, due to the complex nature of DDT. This could be achieved using parts of Bradleys model for the shock-flame double discontinuity model coupled with Bradleys empirical flame models. As discussed in

Section 2.1.8 it would be interesting to explore the effect of radiation on DDT triggering, although it is thought that this is likely to be to time consuming and complex to undertake within the scope of this work whilst carrying out modelling and experimental work.

2.7.3 Thoughts on statistical results analysis

In the literature researchers tend to present mean data for flame speeds and shock speeds. Sometimes they present data for the standard deviation, or very occasionally a histogram including experimental conditions with percentage changes of success for detonation. Whilst presenting the data accurately, this method of analysis does not allow the reader to see the full spectrum of data clearly, as discussed in Section 2.2.2 of the Literature Review. This could be achieved more thoroughly through the use of frequency band analysis, where each of the data sets for a given experimental condition are gathered into discrete bands of pressure amplitude, for example, and the number of occurrences within the given band are counted. The results can then be plotted in a histogram or a probability density function (pdf) including the full set of the results. This means of analysis presents the full data set for a given condition, allowing the reader to gather information about the likelihood of occurrence of a given result magnitude.

The vertical axis of a pdf indicates the probability of occurrence, and the x axis is used to record the range of values of statistical interest, such as dynamic pressure, for instance. The area under a pdf is equal to a probability of occurrence of 1, i.e. all possible measured instances fall under the curve. Values beyond the extremities of the curve are deemed highly unlikely, unless the experimental sample size was too small. The probability of a range of occurrences happening could be calculated by dividing the area under the curve between the two values of interest on the x axis, by the total curve area to give a percentage chance of occurrence. As such, it was decided that measurements in this thesis should be analysed using the pdf statistical method with frequency bins, to detail the full range of experimental results and allow the reader to determine the relative effectiveness of experimental conditions on flame acceleration.

Fuel	Tube diameter(m)	Tube length(m)	Orifice plates	Schelkin spiral	Alternative obstacle	Shock focusing	Pressure probe	Ion Probes TOF	Photodiodes TOF	Schlieren	Thermal imaging	Detonation observed	Reference
H2-air*	range	range	X	-	-	-	X	X	X	-	-	X	[67]
H2-air†	0.15	3.4	X	-	-	-	X	X	X	-	-	X	[67]
H2-air†*	0.08	5	X	-	X	-	X	X	-	-	-	X	[109]
CH4-air	0.076^{ch}	3.66	X	-	-	-	X	X	X	X	-	-	[83]
CH4-air	0.3	73	X	-	-	-	X	-	X	-	-	X	[171]
CH4-air	0.15	5.5	X	-	-	-	X	-	X	-	-	X	[97]
CH4-air	0.094	4.8	X	-	-	-	X	-	X	-	-	X**	[98]
C2H4-air	0.024	1.24	-	X	-	-	X	-	-	-	-	-	[176]
C2H4-air	0.063	1-2	X	X	-	-	X	X	-	-	-	X	[177]
C2H4-O2^{ip}	0.076	1.01	?	?	-	-	X	X	-	-	-	X	[211, 212]
C2H4-O2^{ip}	0.045	0.25	-	-	X	X	X	X	-	-	-	X	[213]
C3H8-air	0.14	3.05	X	-	-	-	X	X	-	-	-	-	[63]
C3H8-air	0.14	3.05	X	-	X^{p}	X^{el}	X	X	X	-	-	-	[105]
C3H8-air*	0.14	3.05	X	-	-	-	X	X	X	-	-	-	[29]
C3H8-air*	0.14	3.05	X	-	-	-	X	-	X	-	-	-	[102]
C3H8-air	0.051	1.5	-	-	-	X^{el}	X	-	-	X	-	X	[84]
C3H8-air	0.051	2.4	-	-	-	X^{sf}	X	-	-	-	-	X^{sg}	[214]
C3H8-air	0.052	4.5	-	-	-	X^{sf}	X	-	-	-	-	X^{sg}	[128]
C3H8-O2	1.016	1.14	-	-	-	-	X	-	-	-	-	X	[215]
C6H14-air	0.028	1.49	-	-	-	X^{el}	X	-	-	X	-	X	[84]
C8H16-air	0.03	2	-	X	-	-	X	-	-	-	-	X	[189]
C8H16-air	0.05	1	-	X	-	-	X	-	-	-	-	X	[189]
C8H16-air	0.056	2	-	X	-	-	X	-	-	-	-	X	[189]
Kero-air	0.029	1.0	X	X	-	-	X	-	X	-	-	X	[122]
Kero-air	0.029	1.1	X	X	-	-	X	-	X	-	-	X	[122]
Kero-air	0.029	1.18	X	X	X	X	X	-	X	-	-	X	[122]
TS-1‡	0.051	3	-	X	-	X^{sf}	X	-	-	-	-	X	[133]
JP10-air	0.028	7.3	0	-	-	-	X	-	-	-	-	X	[208]
range[1]	0.026	2.6	-	X	X^{p}	-	X	-	X	-	-	X	[216]
range	0.053	1.52	-	X	-	-	X	X	-	-	-	X	[203]
C3H8-air	0.038	1.21	X	-	-	-	X	X	-	-	X	?	CW
C2H4-air	0.038	1.21	X	-	-	-	X	X	-	-	X	?	CW

TABLE 2.7: Instrumentation Gap Analysis: X^{el}: shock focusing by electronic means. *CW*: current work, as chosen from the gap analysis. Kero: Kerosene. X^{sf}: shock focusing from tube bends or special obstacles X^{p}: perforated plates at the inlet to the blockage. ^{op}: tests carried out at inlet pressures other than atmospheric ^{op}: channel cross section (square) $-^{0}$: experiments carried out with no obstacles, direct detonation initiation. Yes^{sg}: detonation achieved with shock wave generator. [1]: different blends of fuels specified to change λ to 10mm. *: other fuels were also used. **:near limit case, spinning detonation observed here. †: range of equivalence ratios investigated ‡: TS1 is a Russian analogue of Jet A-1

2.7.4 Analysis of the critical diameter for DDT

Table 2.8 is a comparison of various different PDE engines operating in detonation mode with successful near CJ detonation conditions. Each of the engines tube lengths, obstacle lengths, obstacle blockage ratios and detonation transition distances are recorded when given. In order to compare detonation performance with cell size each engines fuel mixture has also been compared with the literature available for detonation cell size at the same initial conditions for temperature, pressure and mixture equivalence ratio where possible. It is found that some PDEs operate with tube diameters below the critical tube diameter for transitions occurring within the obstacle array, so the transition must occur outside of the obstacle in the smooth tube section of the PDE. Such engines include those designed by Frolov et al. fuelled by stoichiometric methane air mixtures for use as power generators [98], which Frolov states is a near limit case of detonation transition and the results of this study clearly show a spinning detonation taking place in the PDE tube. Interestingly this methane powered pulse detonation burner has the shortest transition length of any of the engines as X_{DDT} occurs within 8-10 λ of the ignition point, where lambda is given from the work of Tiesen et al. [219]. This engines combustion chamber is 94mm in diameter, and the limit cell size is 305mm. The critical diameter for transition in a smooth tube is given by λ/π which is 97mm in this case, inferring that the $d_c = \lambda/\pi$ rule is approximately true (perhaps the operating conditions differed slightly for each experiment).

Other engines also demonstrating this behaviour for transition under the cell size include those in the work of Huang et al. (Section 2.2.5.1) operating on kerosene [220, 122] and Lindestedt's original experiments on DDT promoted by Schelkin spirals in butane air mixtures [221] for example. Interestingly, some of the experiments recorded here transition from within the obstacle array, such as the results of Lindstedt [221] in stoichiometric butane-air and the results of Tangirala [222] in hydrogen - air mixtures and ethylene-air mixtures. Both Lindstedt and Tangirala used similar blockage ratios in their experiments with either Schelkin spirals or orifice plates. This shows that Lindestedt's experiments with butane transitioned within a diameter of 38.35mm (accounting for blockage ratio) within the Schelkin spiral, breaking the $d_c = \lambda$ for the critical diameter within an orifice plate , as the internal diameter of the Schelkin spiral is half that of the butane cell size at the same conditions. As a result it must be stated

that the Schelkin spiral is better suited to generating a detonation in a small diameter tube than the orifice plate. Perhaps this is due to the Schelkin spiral interacting with the limiting mode of detonation propagation, the spinning detonation. It may be the case that the Schelkin spiral amplifies the shock waves which coalesce to form the spinning detonation, and help to sustain this within a diameter less than the critical blockage diameter. It is of great significance that the during the spinning mode of detonation, the spinning head follows a 45° trajectory angle at the tube wall (relative to the tube axis) [86]. The Schelkin spiral used in Lindstedt's experimental campaign had a very similar helical angle of approximatley 45° (calculated to be 41.5° at the tube wall and 49.85° at the internal diameter of the Schelkin spiral). In contrast the two dimensional planar orifice plate will not allow any spinning motion to be transferred through its boundary, particularly close to the wall where the Schelkin spiral would be able to channel high speed flow along its coils, generating a hot spot as observed by Schauer et al. in a quartz PDE tube [223].

2.7.5 Thoughts on experimental geometries

Table 2.7 shows previous research which has been carried out in the area of FA and DDT combined with measurement methods and tube dimensions. Interestingly, there has been no investigation in the literature into the effect of changing the obstacle BR throughout the PDE length, which will impact on the pressure lost to the obstacles, the turbulence added to the flow, flame folding and shock flame interactions along the tube. Unless otherwise stated, all experiments were carried out under stoichiometric conditions. The tube geometry of the current work was chosen to represent a similar tube geometry to that of Huang et al. [122], who achieved DDT in kerosene air mixtures within a 29mm diameter tube, with a length of less than one meter. The investigation will focus on stoichiometric propane-air mixtures, which have comparable cell size to kerosene-air mixtures. The experimental tube geometery will contain an instrumented section 12 diameters in length to replicate the work of Ciccarelli et al.[63]. The tube diameter will be smaller than that used by Ciccarelli et al. and therefore to investigate the tube diameters effect on FA, and DDT if possible. This plan for a novel test will be complimented with pressure probes for the measurement of dynamic pressure and shock time of flight and ion probe flame sensors to measure flame time of flight. In addition, thermal measurements will also be made of the tube wall whilst operating the

PDE to determine the effect of different obstacle geometries. Frolov et al. state that detonation can be measured by the high steady state wall temperature was measured as approximately 500 °C, rather than 300 °C for a deflagration.

Fuel	Cell Size, mm	Cell Size Reference	PDE Tube ID, mm	BR	Obstructed Length, m	X_{DDT},m	X_{DDT}/ tube ID	PDE Reference
Kero-Air	45[1]	[208]	29[2*]	0.43	0.9	0.51	17.6	[122]
Gasoline-Air	18[3]	[137]	60	0.46	1.276	≤1.276	≤21	[200]
$C_4H_{10} - Air$	75	[224]	50.8*	0.44	1.5	1.4	27.6	[221]
$C_3H_8 - Air^{\dagger}$	48[†]	[143]	52	N/A	N/A	N/A	N/A	[84]
$C_3H_8 - Air^{\dagger}$	48[†]	[143]	38*	0.43	1.5	No DDT	No DDT	[225]
$C_3H_8 - Air^{\dagger}$	48[†]	[143]	50.8	N/A	1.22	1.105	21.3	[226]
$C_3H_8 - Air^{\ddagger}$	78[‡]	[227]	50.8*	N/A	1.22	≤1.22	24	[223]
$C_2H_6 - Air$	50	[219]	50.8	0.44	1	1.2	23.6	[221]
$C_2H_4 - Air^{\dagger}$	26[†]	[143]	62.7	0.43	0.9	0.815	13.0	[177]
$C_2H_4 - Air^{\dagger}$	26[†]	[143]	51	0.43	1.02	0.867	17.0	[222]
$C_2H_4 - Air^{\dagger}$	26[†]	[143]	76.2	0.43	1.016	No DDT	No DDT	[225]
$C_2H_4 - Air^{\dagger}$	26[†]	[143]	100	0.43	3.1	1.2	12	[188]
$C_2H_2 - Air$	9	[227]	24	0.498	0.3	≤0.6	≤25	[176]
$C_2H_2 - Air$	9	[227]	100	0.43	3.1	0.75	7.5	[188]
$CH_4 - Air^{\dagger}$	305	[219]	94**	N/A	1.2	2.5-3	26.6-31.9	[98]
$H_2 - Air$	10.6	[143]	350	0.6	N/A	1.75	5	[67]
$H_2 - Air$	10.6	[143]	51	0.43	1.02	0.485	9.5	[222]
$H_2 - Air$	10.6	[143]	50.8	0.43	0.413	0.483	9.5	[228]

TABLE 2.8: Cell size:PDE engine comparison with tube diameters for detonation "GO" rather than "NO GO" conditions, unless otherwise stated. All experiments carried out at atmospheric pressure and temperature unless otherwise stated. [1]; cell size taken for JP-10 at 378K. [2] kerosene at 388K, exact kerosene composition for the PDE experiment not given. [3]; results taken at 293K, 1.1 bar. [†] cell length/cell width taken as 1.5 [‡] propane equivalence ratio 0.9, interpolated from [227] * tube diameter less than the reported cell size. ** tube diameter less than reported cell size and close to the limit cell width.

Chapter 3

Analytical Model

3.1 Background

During the process of DDT the FA feedback mechanism increases flame speed incrementally. A negative flame Markstein pressure gradient is a good indicator of a fuel's ability to detonate via DDT, as pressure from a venting flame will increase flame stretch and therefore the flame-turbulence feedback mechanism will be enhanced. Fuel mixtures such as air with hydrogen, ethylene or acetylene all exhibit negative Markstein-pressure gradients, favouring FA and DDT. Other critical conditions such as the tube diameter and length must also be within acceptable limits for DDT to occur and form a stable detonation. Detonation chamber diameter is determined by the cell size criterion as summarized in Section 2.5.1 of the literature review.

Blockages in FA and DDT studies are widely characterized as having a blockage ratio, BR, defined as the ratio of blocked to total cross sectional area of the obstacle. BR has become a key metric to compare an obstacles ability to enhance FA and DDT. Another common metric used in detonation studies is the non-dimensional axial flame displacement X/D. X/D is the ratio of a flames axial displacement from the closed tube wall, X, and the tubes internal diameter, D.

In a practical PDE, a set of obstacles similar to this arrangement is often used as a pre-detonator. The pre-detonator is usually smaller in diameter than the main detonation chamber, which enhances FA and reduces the run up distance, as FA is a function of the tubes aspect ratio. This concept is covered in more detail in Section 2.5.3 of the

literature review. Because the pre-detonator uses the fuels chemical enthalpy to drive FA and DDT the ignition energy can be considerably reduced in comparison with direct detonation initiation.

3.2 Aims

This model has been developed for the following purposes:

- To provide a semi empirical, quick method of modelling time dependent flame acceleration. This is in contrast to the work carried out in the literature which tends to one of two extremes, either incredibly complex and expensive to run state of the art numerical simulations (as presented in 2.3.5) or much more simplistic analytical models which are not sufficiently detailed to model strong compressible flow (as presented in Section 2.4.3). The state of the art CFD simulations are still not capable of predicting DDT effectively, and need to be trained to experimental results by altering ignition delay properties of the mixture.
- To model post shock pressure and temperature as well as flame speed, to calculate the likelihood of a DDT event occurring.
- To provide insight into the physical processes involved in FA in turbulent flames. This can be viewed as an improvement to advanced CFD calculations, as physical models are solved from simplified algebraic equations each of which can be understood individually, unlike the Navier Stokes equations. As such the impact of each term in the algebraic models can be quantified, and compared with other terms if necessary. This could form the basis of a sensitivity analysis.
- To determine whether improvements in flame speed could be possible with particular orifice plate arrangements. Examples might include reducing or increasing the BR along the tube axis.

3.3 Two Novel Modelling Approaches

In this chapter two distinct modelling approaches were developed for the purpose of modelling 1D FA. The first model was built on derivations from Silvestrini's FA model

and the second from Bradley's shock and flame models. These models were developed to address the issues with previous analytical models developed in the literature, as discussed in Section 2.4. The first approach, The Modified Silvestrini Model (MSiM) is based on the work of Silvestrini [164] which was adjusted to predict orifice enhanced FA by differentiating the expanded version of Equation 2.54. The second approach, the conjugate flame acceleration model (CFAM) utilizes shock dynamic equations and empirical flame data from Bradley's work [166, 52] with additional experimental data for high pressure flames from Kitagawa [55] to model FA. These results are tabulated in the Literature Review, Table 2.4. Both models predict V_g and V_f in obstacle laden tubes at a given axial location using data from the previous time step allowing the development of the flames properties to be mapped against time and distance. The predicted flame speeds of these models were then compared experimental results from Ciccarelli's experiment with propane-air combustion in orifice laden tubes [71] for validation.

Figure 3.1 illustrates the difference between FA modelled by the Silvestrini Model in a smooth walled in comparison with Ciccarelli's experimental data, as presented in Section 2.1.6. This model assumes all conditions are identical with the exception of 0.6BR orifice plates spaced at 1D. This comparison suggests the need for Silvestrini's FA model to be adapted to predict FA whilst taking the effect of obstacles into account. The first modelling strategy applied to FA was to adapt these equations for the prediction of FA with blockage laden tubes is to modify Eq. 2.52 using the additional BR coefficient which used to scale Eq. 2.53 in Eq. 2.54. Eq. 2.54 can be differentiated to produce a new model predicting V_f with terms for BR.

Bradley's model can be used to model detonations; however FA has not yet been studied with this model. FA could be an area to explore with Bradley's model in order to produce a modelling system which can be solved quickly for a range of PDE internal geometries, requiring only a small computational resource. This model could be used as a predictive tool to scope the range of PDE geometries such as tube diameter and investigation of different blockage ratios or fuels for parametric design studies. The driver for developing this model was to reduce the number of experimental tests during the engine prototyping stage.

Bradley's current models for turbulent flames and combustion in single closed end tubes shown in Sections 2.4.2 and 2.4.4 of the Literature Review, are currently incapable of

predicting the instantaneous flame acceleration along a tube. The logical next step here would be to include a turbulence generation sub-model which could predict turbulence generation as a function of obstacle geometry. This turbulence could then link Bradley's double discontinuity model with his flame speed model. The novel model could then be operated in an iterative manner to predict the effect of changing BR along the tube on the FA process as it develops. This model would predict FA in spatial and temporal co-ordinates.

3.3.1 Modified Silvestrini Model- MSiM

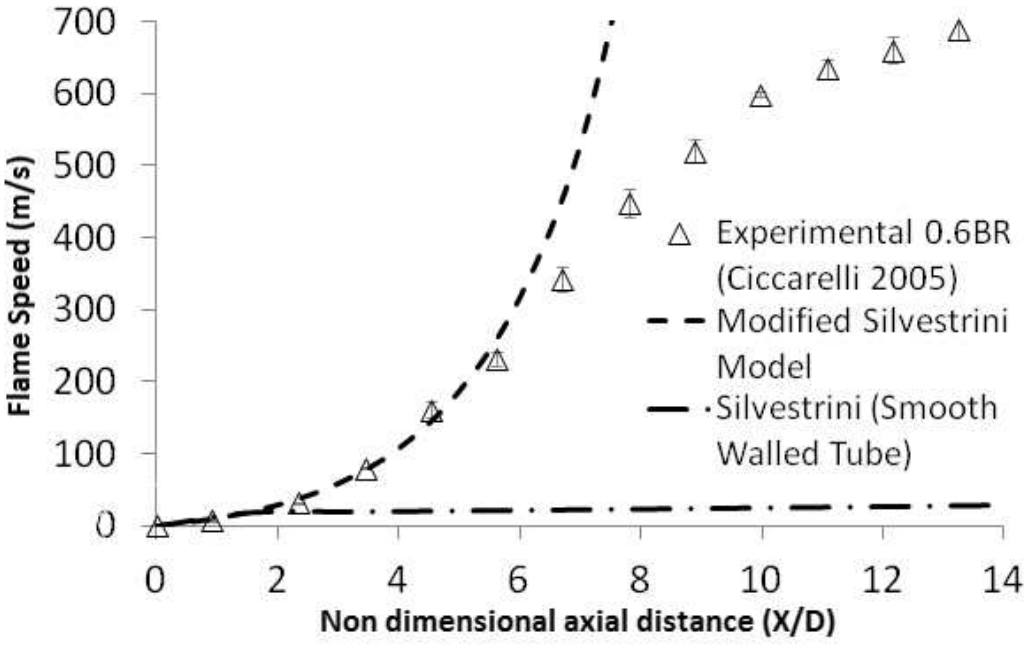

FIGURE 3.1: Silvestrini and Modified Silvestrini model comparison with Experimental Data for 0.6BR at 0.14m diamter [71]

Silvestrini's FA model, as shown in Equation 3.1 was investigated to determine how well it could function as a model for FA in obstructed tubes by differentiating the functions for distance to detonation in obstructed tubes. Eqs. 3.2 is derived from Equation 3.1 by making X/D the subject of the equation, then setting V_f as $1/2V_{CJ}$. This provides an approximate transition point for DDT to occur, as determined in the work of Silvestrini et al. [164]. These equations are suplemented by an empirical model which was validated againstFA in a range of fuels, tube geometries and orifice plate BR shown in Equation 3.3, also from Silvestrini's work [164].

numerical constant	value	units
A	6.5	(-)
B	0.0061	(-)
ϵ	0.4	(-)
σ	8	(-)
u_l	0.46	(m/s)

TABLE 3.1: Table of Modelling constants for the MSiM model

Equation 3.3 provided a value for an extra term for blockage ratio, (1+15BR), in comparison to the predicted run up length in the smooth tube. In the current work, this extra term was added to the initial Equation for V_f given in Equation 3.1 by taking inserting equation 3.2, setting velocity 1/2 V_{CJ} back to V_f to predict for all cases of X/D and solving for V_f (1/2 V_{CJ} had been substituted in by Silvestrini to predict the axial location of DDT).The new formulation is shown in Equation 3.4, which is presented here for the first time. This equation adds to the previous work by predicting FA in orifice laden tubes in both temporal and spatial co-ordinates in Section 2.4 of the Literature Review. Results for the MSiM are shown in Figure 3.1. It can be seen that the model is capable of predicting FA up until approximately 6 X/D , when V_f is approximately equal to the sonic velocity in the reactants,a_1. Modelling constants for the MSiM model are shown Table 3.1. The model assumes zero initial flame speed, starting from zero X/D.

$$V_f = A\sigma u_l e^{B(\sigma-1)\left(\frac{X}{D}\right)\left(\frac{D}{0.15}\right)^{\epsilon}} \quad (m/s) \tag{3.1}$$

$$\left(\frac{X}{D}\right)_{DDT} = \frac{1}{A(\sigma-1)}\left(\frac{0.15}{D}\right)^{\epsilon} \ln\left(\frac{BV_{CJ}}{\sigma u_l}\right) \quad (dimensionless) \tag{3.2}$$

$$\left(\frac{X}{D}\right)_{DDTBR} = \frac{1}{1+15BR}\left(\frac{X}{D}\right)_{DDT} \quad (dimensionless) \tag{3.3}$$

$$V_{fBR} = A\sigma u_l e^{(1+15BR)B(\sigma-1)\left(\frac{X}{D}\right)\left(\frac{D}{0.15}\right)^{\epsilon}} \quad (m/s) \tag{3.4}$$

Observations of V_f vs. X/D in Figure 3.1 show that the MSiM diverges from experimental results at $V_f \approx a_1$. Shock flame interactions which begin around Mach 1 in the

combustion reactants and take place towards the end of the flame acceleration process, as the flame approaches the choked regime cannot be taken into account using this simplistic exponential model. It was decided that the MSiM model should only be used to model flow for the first orifice plate, as after the initial orifice plate flame folding takes place which defies the original assumption of the exponentially growing boundary layer in smooth tubes discussed above. One possible approach to address this deficit was to model the compressive shock wave using Bradley's model from Section 2.4.2 of the Literature Review, which takes account of compressibility in the reactants ahead of the flame. Bradley's model can then be combined with an orifice model applicable to compressible flow which is capable of calculating pressure loss which generates turbulence in the reactant gases ahead of the flame.

3.4 Conjugate Flame Acceleration Model Description and Equations

A novel simple analytical model, the CFAM was developed to address the compressibility issues discussed with the MSiM FA model. The CFAM assumes compression is generated with a single planar shock which increases the pressure and temperature in the reactant mixture. Turbulence is then generated accross the orifice, assuming that the post shock conditions are seen by gas on the downstream side of the orifice. The CFAM uses Bradley's work on explosions and DDT discussed in Sections 2.4.2 and 2.4.4 of the Literature Review, with an empirical supercritical orifice flow model derived by Torizumi as described in Section 2.5.8.1 of the literature review. Torizumis model provides an estimate of the post shock pressure attenuation generated by the orifice plates. Torizumi's orifice mass flow model has been re-arranged to form Equation 3.10, where A_o is area of the internal passage through the orifice. This pressure ratio can be used to calculate the dynamic pressure loss across the orifice, ΔP_{23}, which is proportional to an increase in rms turbulent velocity, $\Delta u'$. For the purpose of this model, it is assumed that u' at initial conditions is zero. u' is approximated using Equation 3.12 which is derived Bernoulli's equation for dynamic pressure. This model is primarily built on others research, the novelty of this model lies in the colation of several sub-models in a manner not previously carried out. New equations in the model include the MSiM

equation, the modification of Torizumi's empirical supercritical orifice flow equations and the CFAM u' model (Equations 3.4,3.10 and 3.12 respectively)

Initial and Boundary conditions and mesh size are presented in Table **??** and 3.3 respectively. The model assumes isothrmic heat conditions at the walls. The model also assumes that there is no residual turbulence left from the injection process, i.e. u'_0 is zero before combustion takes place. The CFAM constant is trained to fit the experimental data for initial data sets, then interpolated for future work. One CFAM constant has been used for each dataset, remaining the same for each orifice step, irrespective of the flow velocity, pressure or flame speed.

Numerical constant	Value	Description	Units
mesh size	S	orifice spacing	(m)
a_0	340	initial speed of sound in reactants	(m/s)
C_{CFAM}	trained to data	Empirical modelling constant	(-)
V_{g0}	MSiM V_g	V_g predicted by MSiM at X/D = 1	(m/s)
u'_0	0	Initial rms turbulent velocity	(m/s)
P_0	1.01235	Initial mixture pressure	bar
T_0	288	Initial mixutre temperature	K
σ	8	Expansion ratio	(-)
γ	1.4	Ratio of specific heats	(-)
β	$(1 - BR)^{1/2}$	Orifice dia. ratio	(-)

TABLE 3.2: Table of initial condition modelling constants for the CFAM model

Numerical constant	Value	Description	Units
step size	S	Orifice spacing	(m)
C_{CFAM}	Trained to data	Empirical modelling constant	(-)
P_1	1.01235	Pre-shock reactant pressure	bar
T_1	288	Pre-shock reactant temperature	K

TABLE 3.3: Table of boundary condition modelling constants for the CFAM model

The first step of the CFAM model takes V_{fBR} from Equation 3.4 in order to predict the incoming gas velocity for the first orifice plate, V_{g0}, which is calculated for X/D in the MSiM model. MSiM constants, A, B and ϵ in this case are 6.5, 0.0061 and 0.4, as specified in Section 2.4.1 of the Literature Review. This equation is only used once in order to predict the initial conditions for the CFAM model. Each of the equations from Equation 3.5 to 3.21 are then calculated in order to predict the mean flame speed between the first orifice and the next orifice, given the inlet gas speed and subsequently generated turbulence from the fluids interaction with the first orifice plate. After the first iteration of each of these equations, the final value of V_f from the previous iteration

is used to calculate the gas speed approaching the current orifice plate being analyed using Equation 3.5.

$$V_g = V_{fBR}\frac{(\sigma - 1)}{\sigma} \quad (m/s) \tag{3.5}$$

Variables c,and M_1 the non-dimensional explosion venting number and mach number of the venting gas were calculated using Equation 3.6 and 3.7, presented in Section 2.4.2 of the Literature Review from the work of Bradley et al.

$$c = V_g\left(\frac{\gamma + 1}{2a}\right) \quad (dimenesionless) \tag{3.6}$$

$$M_1 = \left(\frac{c}{2}\right) + \left(\frac{1 + c^2}{4}\right)^{1/2} \quad (dimensionless) \tag{3.7}$$

Post shock pressure and orifice head loss were accounted for at the flame front using Equations 3.8 and 3.9, also presented in the work of Bradley et al. Post shock reactant density, ρ_2, was calculated using Boyle's law for ideal gases, based on the pre-shock conditions for P_1 and T_1 presented in Table 3.2.

$$\frac{P_2}{P_1} = \left(\frac{2\gamma M_1}{1 + \gamma}\right) - \left(\frac{\gamma - 1}{\gamma + 1}\right) \quad (dimensionless) \tag{3.8}$$

$$\frac{T_2}{T_1} = \left(\frac{2\gamma M_1^2\,(\gamma - 1)}{\gamma + 1}\right)\left(2 + \frac{(\gamma - 1)\,M_1^2}{(\gamma + 1)\,M_1^2}\right) \quad (dimensionless) \tag{3.9}$$

Torizumi's supercritical orifice mass flow model has been rearranged to make the pressure ratio the subject, shown in Equation 3.10.

$$\frac{P_3}{P_2} = 1 - \left(\frac{V_g \rho \gamma \beta^2}{8M_1}\right)\left(\frac{P_2}{\rho_2}\right)^{1/2} \tag{3.10}$$

Equation 3.12 is based on the Bernoulli equation for incompressible gas flow, Equation 3.11. Bernoullis famous equation has been rearranged to find u', adding a linear constant, C_{CFAM} in order to provide a modelling parameter used to fit experimetnal data for flame speed whilst training the model.

$$P_d = \frac{1}{2}\rho V^2 \tag{3.11}$$

$$u' = \left(2C_{CFAM}\frac{\Delta P_{23}}{\rho_2}\right)^{0.5} \tag{3.12}$$

Experimental turbulent flame speed measurements reported in table 2.4 of the Literature Review were modified for use within the CFAM flame model. Equation 3.13 was used to presdict $K_{0.8}$ as a function of reactant pressure at the just ahead of the flame, P_3, in Equation 3.13. Furthermore an empirical equation relating u_l to flame pressure was calculated using data from the same table, which produced Equation 3.14. Markstein number was then predicted, based on the results of Equation 3.13 using Equation

$$K_{0.8} = 0.0334(P_3)^2 - 0.0707(P_3) + 0.534 \tag{3.13}$$

$$u_l = 0.3862e^{-0.035P_3} \tag{3.14}$$

$$Ma_{sr} = \left(\frac{34.4}{Ka_{0.8}}\right)^{\left(\frac{1}{1.8}\right)} - 4 \quad (dimensionless) \tag{3.15}$$

Bradley's empirical flame speed model as seen in Equation 3.18 was used to calculate local turbulent flame speed as the flame moves thought the gas between orifice plates. Constants for this model are calculated based on empirical equations, 3.16 and 3.17, also from the work of Bradley et al., which took the value of Ma_{sr} calculated using Equation 3.15. Additionaly, Equation 3.13 was used to provide the value of $K_0.8$ used in equation 3.18.

$$\alpha_B = 0.022(30 - Ma_{sr}) \quad (dimensionless) \tag{3.16}$$

$$\beta_B = 0.0105(Ma_{sr} - 30) \quad (dimensionless) \tag{3.17}$$

$$\frac{u_{tm}}{u'} = \alpha_B K a_{0.8}^{\beta_B} \quad (dimensionless) \tag{3.18}$$

The local turbulent flame speed, u_{tm} was then calculated using Equation 3.19, which took recently calculated values of (u_{tm}/u') and u'.

$$u_{tm} = \left(\frac{u_{tm}}{u'}\right) u' \quad (m/s) \tag{3.19}$$

The ratio of the flame surface area relative to the tube cross sectional area was then approximated using Equation 3.20, which took u_{tm} from Equation 3.19.

$$\frac{A_f}{a_d} = 1 + \frac{u'}{u_l} \quad (dimensionless) \tag{3.20}$$

The result of Equations 3.20 and 3.19 were then substituted into Equation 3.21 with σ, the expansion ratio for propane, to calculate the flame speed. This equation allowed for the calculation of the average flame speed between the current orifice and the next.

$$V_f = \sigma \left(\frac{A_f}{a_d}\right) u_{tm} \quad (m/s) \tag{3.21}$$

Once all of the these equations had been calcualted based on the inital value passed from the MSiM model, V_f from Eqaution 3.21 was substituted into Equation 3.5 and the cycle was repeated between the 2nd and 3rd orifice plates. This process was continued untill the end of the orifice laden section of the tube.

3.4.1 Solution Algorithm

The solution algorithm for the CFAM is presented in Figure 3.2. Initial conditions for flame acceleration such as P, T, D and BR were assigned before starting the simulation. In this case initial pressure and temperature were taken to be 1atm and 288K respectively. Empirical constants were chosen from the Silvestrini model as described in Section 2.4.1 of the Literature Review and applied to the MSiM. The MSiM was used to generate the initial flor up to the the first orifice. This values for V_f and V_g were used to initiate the CFAM model flow for the second and all subsequent orifice

plates. This process was necessary as the CFAM model is not capable of generating a pressure increase and resultant change in flame speed with no initial flow. The CFAM model then takes over from the MSiM model after the first orifice, as can be seen in Figure 3.3.

The main iterative computational loop of the CFAM model uses V_f from the previous iteration to predict V_g for the next time step and orifice location using equations 2.67 and 2.55. Post shock pressure and temperature, P_2 and T_2 are computed using Equations 2.55 to 2.59 from Bradley's model. The pressure drop across the current orifice plate is then determined using Equation 3.10 and subtracted from the post shock pressure to give P_3. Flame properties were calculated at the current orifice using Equations 3.14 and 3.13. Once the orifice pressure loss ΔP_{23} was known, u' was estimated using Equation 3.12 and substituted into Equations 2.62 and 2.65 to give the turbulent flame speed u_t. Equation 2.66 was used to calculate the flame surface area, A_f for known tube D, u' and u_t. Equation 2.67 was then used to calculate the flame speed V_f. This flame speed was used to calculate a flames time of flight between orifice plates then differentiated across all of the orifice plates to find the rate of FA. As the simulation iterates through each numerical loop the orifice plate number is increased sequentially and is recorded against the sum of the time of flight values, V_f and each of the other variables. The model terminates when the modelled flame reaches the end of the computational domain which is the equivalent to the location of the last orifice plate.

3.5 Results

Figure 3.3 shows the development of the flame relative to the axial distance travelled. The current model predicts flame acceleration along the length of the tube throughout which the flame speed was measured by Ciccarelli et al. shown in Section 2.1.6 of the Literature Review. The modelled shock raises the pressure to approximately 8 bar (absolute) at the point which the flame leaves the end of the domain. This pressure is one bar less than the pressure reported by Ciccarelli et al.. Post shock temperatures also increase with the gas speed up to a shock temperature ratio of around 2, giving rise to a post shock temperature of around 700K. These temperatures and pressures

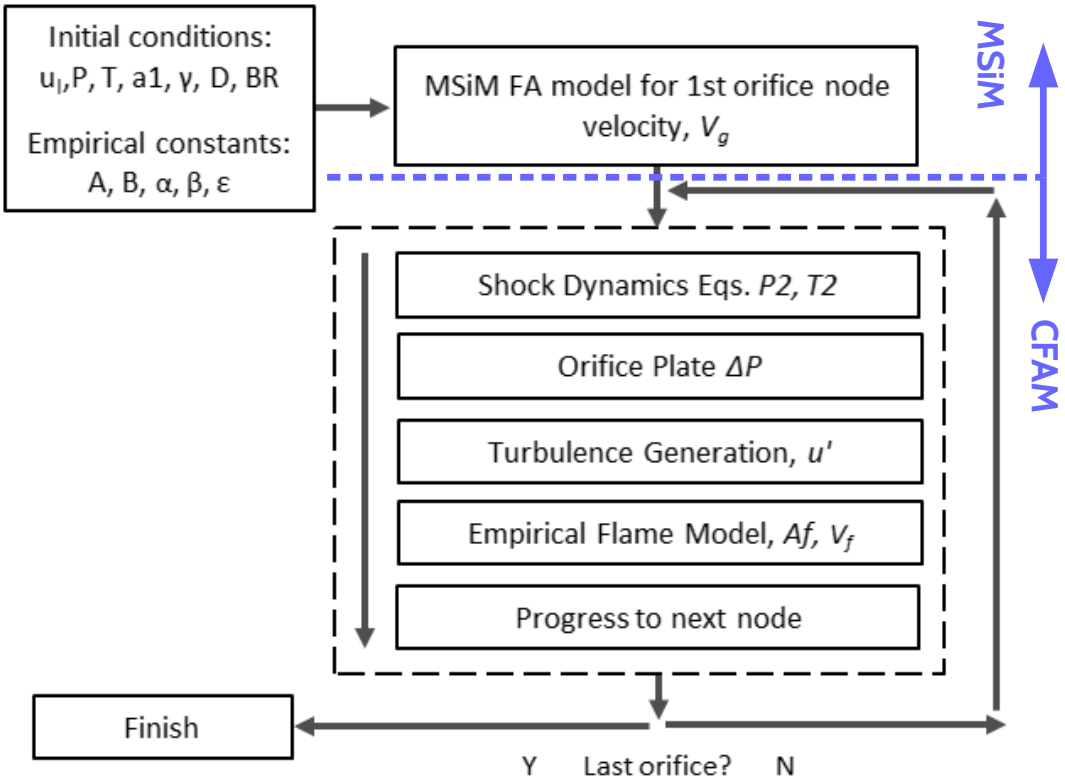

FIGURE 3.2: Solution Algorithm for the CFAM. The MSiM model is used to initialise the main CFAM loop. Cange over from one MSiM to CFAM models illustrated by the blue dashed line.

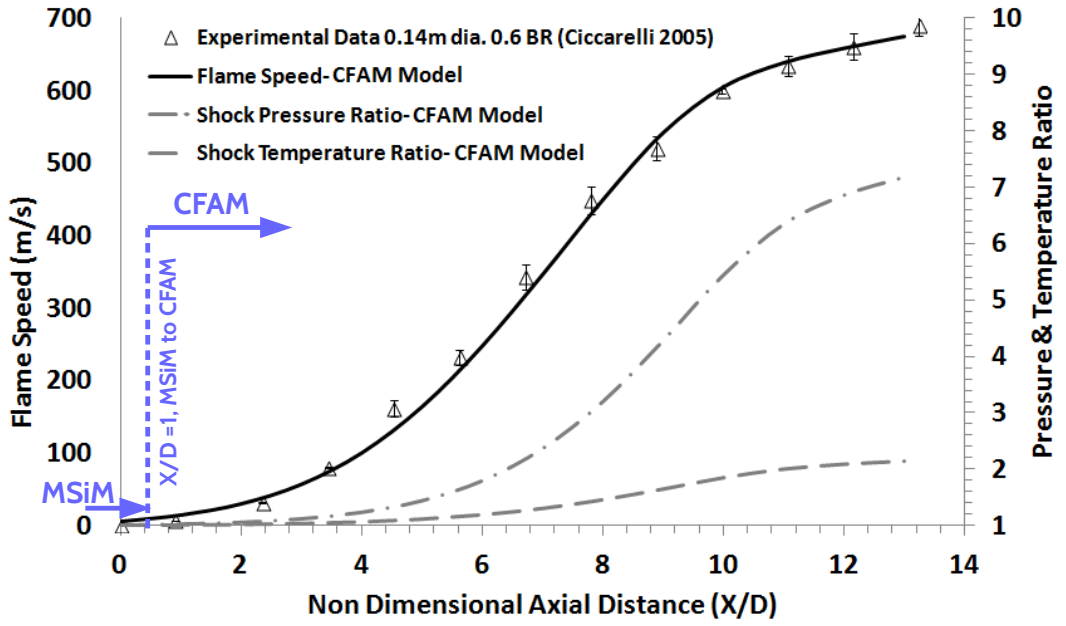

FIGURE 3.3: CFAM Model results, Triangles: Experimental data from [71] for 0.6BR 0.14m diameter tube. Solid Black: Flame Speed (V_g), Alternate dashed grey: Shock Pressure Ratio, Long dashed grey: Shock Temperature Ratio. The change over from the MSiM to CFAM FA model is illustrated by the blue dashed line.

are insufficient for autoignition to occur on a large scale across the tube in the shock compressed gas.

Figure 3.4 compares Ciccarelli's experimental results with the CFAM modelling results for the 0.14m diameter tube with a variety of different blockage ratios for orifice plate blockages, as presented in Section 2.1.6 of the Literature Review. These experiments were all conducted with the same initial conditions and mixture composition. The model was run using the same solution algorithm for each condition, changing only the value of BR and C_{CFAM} for each orifice set. C_{CFAM} was found for each experimental condition using a least squares fit on the flame acceleration curve. The results show an increasing initial flame acceleration in the first 6 orifice plates with increasing BR, which matches well with results from the literature. Each of the three simulations matches the FA profile for the same experimental data set. The general trends in FA are reproduced by the model well. For instance the final flame speed in the 0.75BR case falls behind the 0.6 and 0.43BR cases. The 0.6 BR simulation matches experimental data very closely, however the 0.43 simulation over estimates the flame speed for most of the mid-section of the FA data set, even though the gradient of the velocity curve is matched well. It is interesting to note that the point of inflection in each case occurs around the location which V_g becomes sonic with respect to a_1 in the CFAM model. This shows that the model is capable of capturing the effect of compressible gas flow on orifice pressure loss and turbulence generation and its subsequent effect on the FA process. This suggests that the inflection in FA curves is due to compressibility effects which take place as the orifice vents and which have a direct effect on the turbulence generation at the orifice.

Furthermore, it can be seen from figure 3.4 that each of the numerical models reach a steady state solution at between 14 and 25 X/D. The steady state solution of the 0.75BR result is reached within the experimental data set however the other two data sets have not. Further analysis for this case can be seen in figure 3.5 by plotting normalised $dV/d(X/D)$, $dM/d(X/D)$, $dP/d(X/D)$ and $d^2M/d(X/D)^2$ alongside the gas velocity Vg with respect to non-dimensional axial distance, X/D. It can be seen that the change in flame velocity with respect to distance is driven by the change in the second derivative of the Mach number. As the second derivative of Mach number with respect to distance peaks the gradient of the velocity with respect to distance begins to decrease, then peaks and decreases. This occurs at a gas speed of around

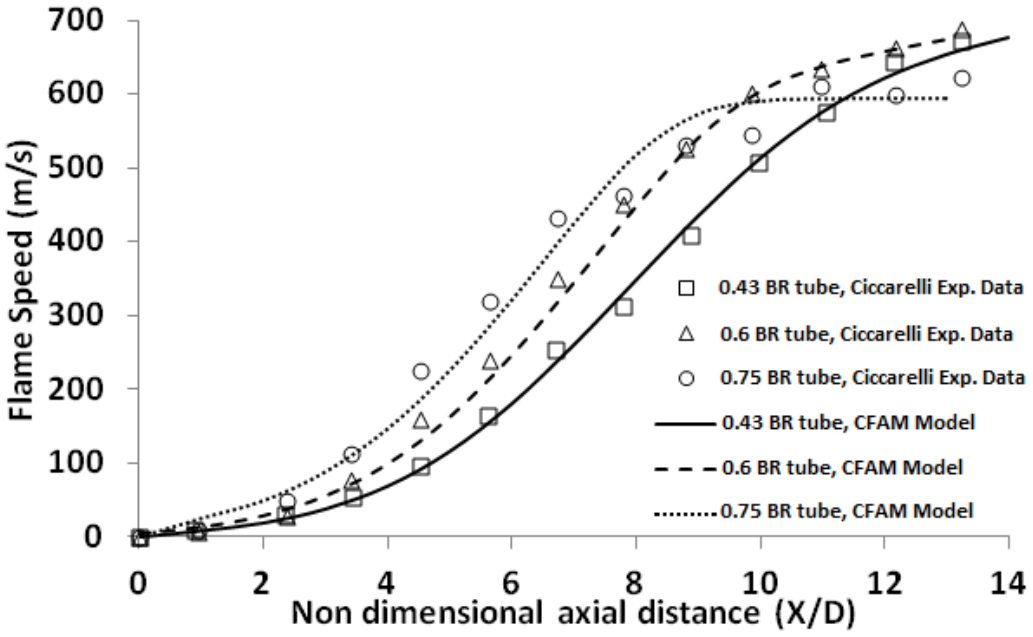

FIGURE 3.4: CFAM results for propane-air wth an equivalence ratio of 1, Blockage ratios of 0.43, 0.6 and 0.75BR in a 0.14m D tube accelerating over 13 X/D compared with experimental data from Ciccarelli for the same conditions [71]. Solid lines show the modelled results, experimental results are shown by open symbols

the sonic velocity, 340m/s. The clear dependence of the flow velocity on the flow Mach number indicates that compressibility has a large effect on both the pressure loss and turbulence generation which feeds the flame speed feedback mechanism. Once the sonic velocity for a given set of orifice plates has been reached, the flow begins to decelerate.

Figure 3.5 clearly shows $dP/D(X/D)$ peaks at the same axial location that V_g reaches the sonic velocity. This is due in part to the inverse relationship with pressure loss. It is also evident that the modelled turbulence generation becomes steady state before the normalised Mach number, M_1 becomes steady state. This occurs at a turbulent flame speed of around 8-9m/s which holds with similar values in the literature for the maximum turbulent flame speed observed. This reduction in turbulence intensity is driven by a reduction in the local pressure loss form the orifice model, $dPloss$, as can be seen by the change in gradient of the normalised $dP_{loss}/d(X/D)$ curve. This curve follows almost exactly the same path as the $dM_1/d(X/D)$ curve, showing that there is a strong dependence within this model upon the Mach number, M_1, of the reactants at the shock which is driven directly by the gas expansion.

During experimental flame acceleration tests such as those carried out by Ciccarelli,

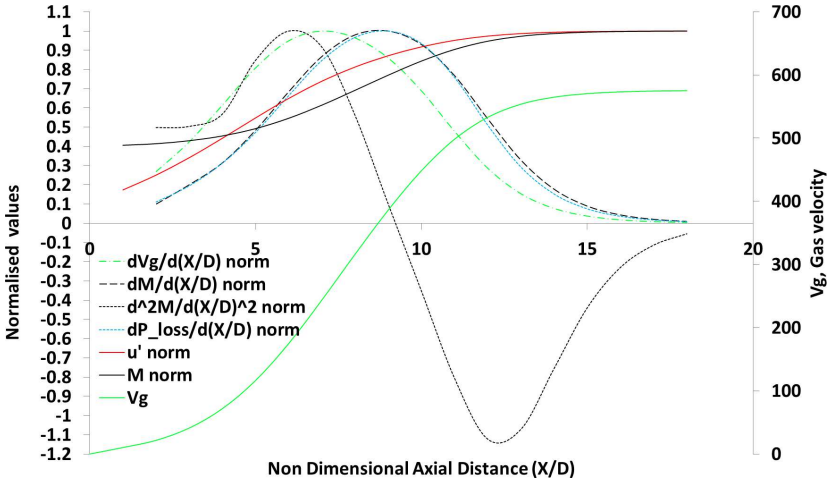

FIGURE 3.5: Normalised $dV_g/d(X/D)$, $dM_1/d(X/D)$, $dP_{loss}/d(X/D)$, $d^2M_1/d(X/D)^2$, u' and M_1 with V_g plotted against non-dimensional axial distance X/D along the combustion chamber

researchers tend to build their own flame sensing equipment to measure flame speed via time of flight measurements. In this case each flame speed sensor must be able to determine when the flame passes at a high temporal resolution in order to provide suitable measurement accuracy. Typically, where detonations are concerned this triggering rise time must be reliably less than 1 μs in order for the detonation to be tracked with little variation in the measured time of flight. This rise time depends on maximum expected flame speed, V_{CJ}, or greater and sensor separation distance. A possible alternative to this method would be to use the shock equations from Bradley's work to predict the post flame speed for a given measured shock pressure using the shock relations in equations 2.58 and 2.59. The results of these calculations can be seen in Figure 3.6 illustrates expected shock and flame conditions for a given shock pressure.

Once known, the post shock conditions can be used to calculate auto-ignition delay times based on either empirical or numerical data at the given post shock temperature and pressure to calculate whether DDT is likely to occur before the arrival of the flame front. Figure 3.6 can also be used as a validation to the rough rule of thumb given in the respective works of Silvestrini and Veser et al. in Section 2.5.3 of the Literature Review, for detonation to take place at approximately $V_{CJ}/2$.

Based on the assumption of DDT starting at around $V_{CJ}/2$, indicated by the red dashed line in Figure 3.6 this suggests that a shock pressure of around 11-12 bar would be necessary and would produce a post shock temperature of 800-900 Kelvin at a gas venting speed of approximately 800m/s, corresponding to a flame speed of

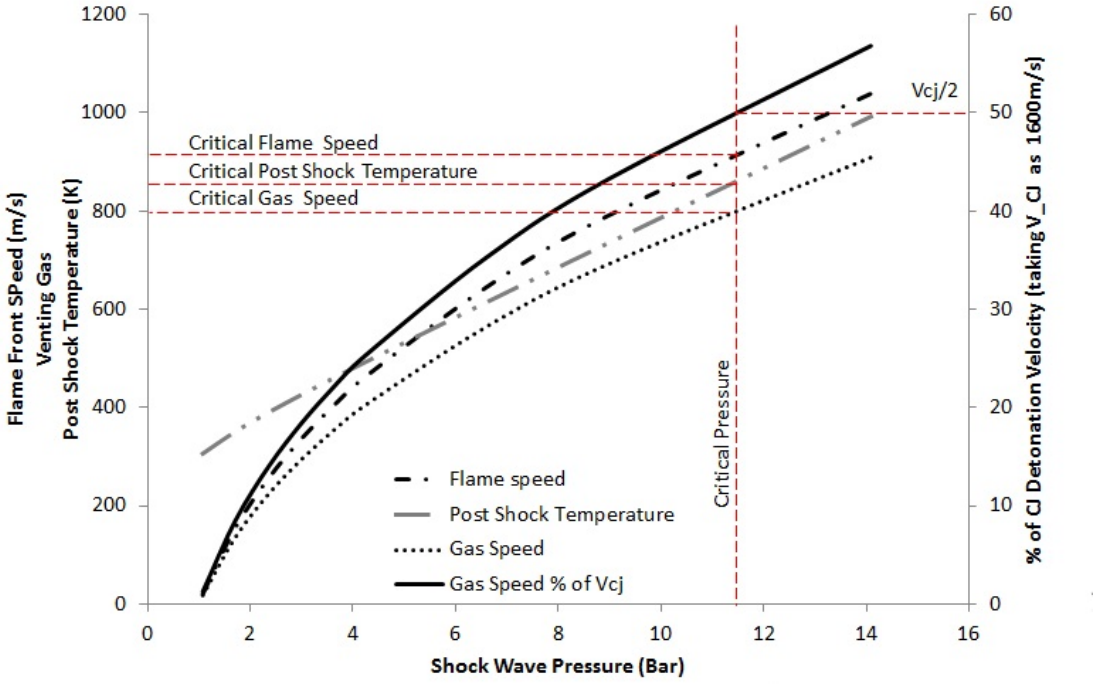

FIGURE 3.6: Prediction of post shock conditions for a given shock pressure, showing results of sock speed, flame speed and temperature. Dotted red lines indicate estimated DDT event conditions

about 900m/s. In this case Ciccarelli's experiments were on the verge of generating a detonation, with sufficient residence time to generate the appropriate autoignition delay time.

3.6 Further Analysis

From this experiment we were able to find the correlation between the CFAM constant, C_{CFAM} ,and blockage ratio for the 0.14m diameter tube. Furthermore the same method has been applied to 0.076m hydraulic diameter cross section duct from the work of Ciccarelli et al. Figure 3.7 shows the effect of tube diameter on the CFAM constant. Note that this constant is not the only factor affecting flame acceleration, and the result cannot be interpreted as having a direct effect on the rate of flame acceleration in different tubes without taking into account the pressure loss equation which is affected by blockage area and orifice β ratio. Furthermore, it was found that by plotting C_{CFAM} multiplied by tube diameter against orifice BR in one continuous line resulted. This infers that the C_{CFAM} constant should contain a maximum length scale term. This could be the subject of further work. The physical significance of

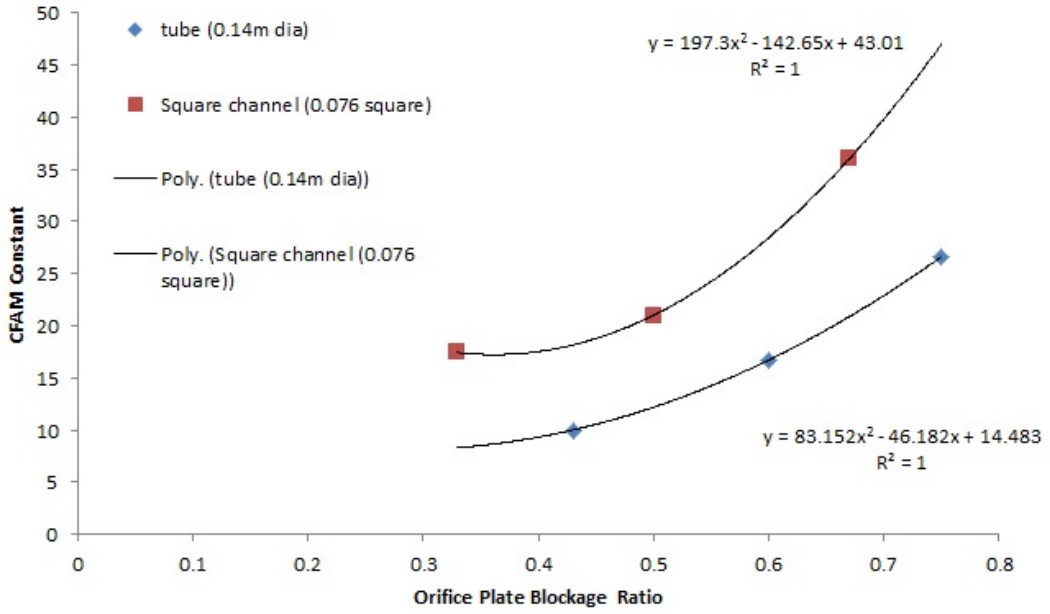

FIGURE 3.7: C_{CFAM} constant plotted against orifice blockage ratio for two different sets of experimental data.

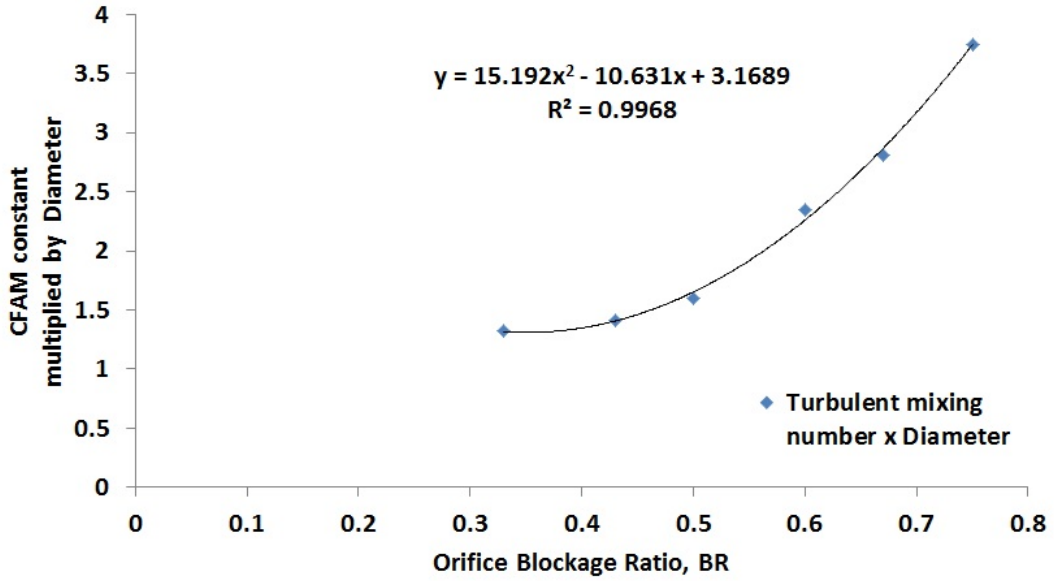

FIGURE 3.8: C_{CFAM} constant multiplied by diameter and plotted against orifice blockage ratio for two different sets of experimental data

this finding is that turbulence feedback into the flame is smaller in tubes or ducts with larger geometric length scales, this infers that the feedback mechanism is. The result of this multiplication of C_{CFAM} and D can be seen in figure 3.8 which shows that higher blockage ratio orifice plates will always produce a larger C_{CFAM} figure. These results can then be used in combination with the existing model to predict the effect of changing the orifice plate BR along PDE axis.

3.7 Hypothesese

It was considered that by changing the flow constricting, turbulence generating effect of orifice blockages along the tube the flame could be either retarded or accelerated further, when compared to a fixed orifice BR.

Hypothesis 1 Gradually increasing the blockage ratio of obstacles in the PDE along the tube from the closed end will increasingly constrict the flow, reflecting a larger portion of the shock wave and transmitting a smaller proportion of the shock wave. If detonation is not caused by the shock wave (which cannot be predicted by this model), FA will slow down as a result of the energy lost by the shock wave, and the reduced post shock pressure. This will generate a reduced flame speed in the obstacle filled section of the tube. It is hypothesised that faster gas velocities result in larger pressure loss across the orifice plate where a large orifice plate is inserted in the flow at a later stage of flame acceleration. In contrast if a high BR orifice plate is inserted earlier on in the flame acceleration process it is less likely to hamper the venting gas as the gas is traveling at a slower velocity. On the contrary a high BR orifice plate inserted close to the closed end of the tube is likely to promote flame acceleration further as a greater amount of turbulence is generated promoting faster flame acceleration.

Hypothesis 2 Conversely, a gradual decreasing of the obstacle blockage ratio along the PDE tube axis from the closed end will reduce the flow constriction, reducing the amount of pressure lost by the shock wave as it progresses along the tube. At the same time, the smaller BR orifices will be more effective for turbulence generation at higher speeds, increasing the flame speed further and generating a wider internal diameter which promotes detonation, provided the diameter is large enough to sustain DDT. In this obstacle order, the high BR orifice plate generates a high initial turbulence intensity which promotes flame acceleration, followed by less flow restriction from smaller later orifice plate BR which promotes increased shock strength and faster flame acceleration overall.

These hypotheses were tested using the CFAM mode in the same manner described in Section 3.4 in conjunction with the relevant C_{CFAM} constant for other blockage ratios, changing the orifice constants in each of the other parts of the model at the same time. For this model, the PDE was approximated by a 0.14m internal diameter, 1.26m long

tube with nine orifices in three sequential sections with three orifices each. The orifice conditions were altered as shown in table 3.4. For this test a 0.03175 m diameter tube was used, as this was used in an experimental test campaign, so that the results could be compared with experimental test data.

Case	Section 1 BR	Section 2 BR	Section 3 BR
1	0.75	0.57	0.42
2	0.42	0.57	0.75

TABLE 3.4: Modelled orifice BR conditions. Section 1 contains 5 orifice blockages, section 2 contains 4 orifices and section 3 contains 5 orifices respectively.

3.8 Modelled Results

It can be seen from figure 3.9 that the initial flow restriction produces a rapid flame acceleration, as shown by the fine dotted line, which is followed by a gradual reduction in the gradient of, V_f, the flame speed as the orifice BR changes from 0.43BR to 0.57BR. This trend is reflected in the u' trend and u_{tm} which also show a decrease in the gradient at this point. Post shock pressure, P_2, Orifice pressure drop, P_{23} and gas speed, V_g follow the same trends at this stage. The gradient of these curves is followed until the ninth orifice, where the orifice blockage ratio undergoes a step change from 0.57BR to 0.42BR. The modelled change in u', V_f and u_{tm} is a direct result of the change in modelling boundary conditions at the ninth orifice plate, as the CFAM constant, and blockage area change at this location which impacts directly on u' generation first, then the turbulent flame speed which is followed by the flame propagation speed. This order is reflected at the first BR transition, from 0.75BR to 0.57BR, although the results are less visible in this graph. After the second transition the model shows a strong decreasing trend, which propagates from the flame propagation speed and the local flame speed into every other variable at the next orifice plate. This is due to the fact that the other variables are coupled to turbulence generation at the next orifice plate following a change in flame speeds. The final flame speed observed at the end of the tube is around 500m/s with a post shock pressure of approximately 5 bar, and a local u_{tm} of 4.5m/s with u' about 8m/s.

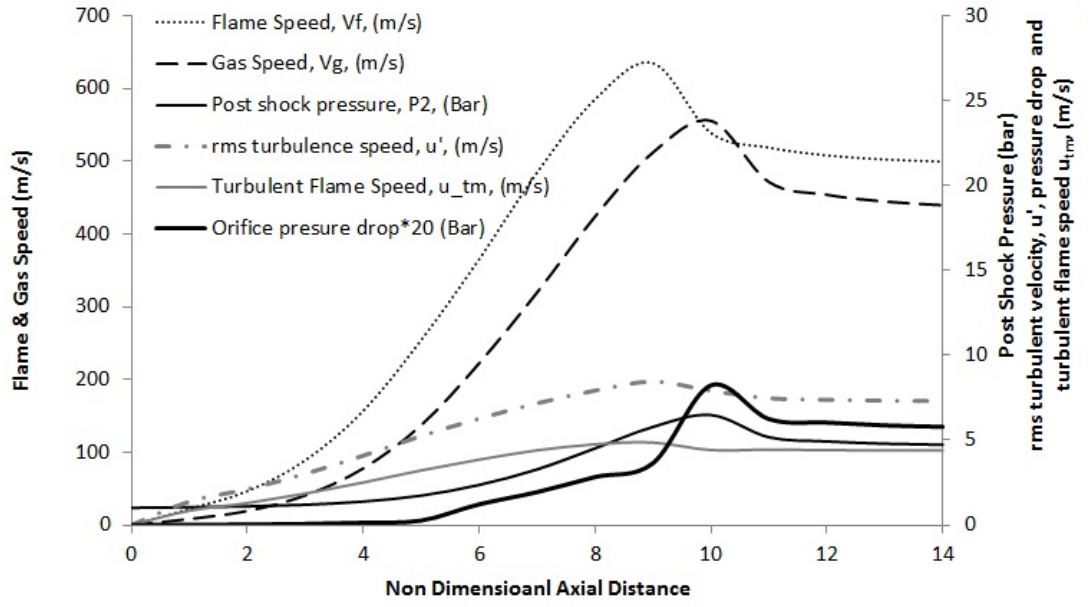

FIGURE 3.9: Test case 1, reducing BR. BR = 0.75, 0.6, 0.43 in batches of 5, 4 and 5 orifice plates respectively.

In comparison with figure 3.9, if blockage ratio increases, as shown in figure 3.10 the overall trend shows a peak in V_f at around the ninth orifice plate, which then plateaus in each of the modeling variables, reaching a steady state. The flame speed at this location is shown to be between 650 and 700m/s. All other plotted variables follow a similar trend, which illustrate slower flame acceleration in the initial stages of flame propagation than the decreasing case. After the ninth orifice plate u', V_f, u_{tm} and P_{23} each reach an plateau where the CFAM constant and orifice internal area step change in their value. This drives the gas speed and post shock pressure to remain constant, which maintains a constant Markstein Number and the burning rate plateaus until the exit which exhibits a steady flame speed $\leq$ 770m/s and a post shock pressure of around 7.5 bar gauge. This supports the argument that reducing the orifice blockage ratio along the tube increases initial FA, however surprisingly the modelled flame speed decreases with increasing distance after the initial rapid acceleration. In the model this is due to insufficient turbulence generation, or shock strength to further increase FA. These results will be compared with experimental results for the same conditions to validate the model.

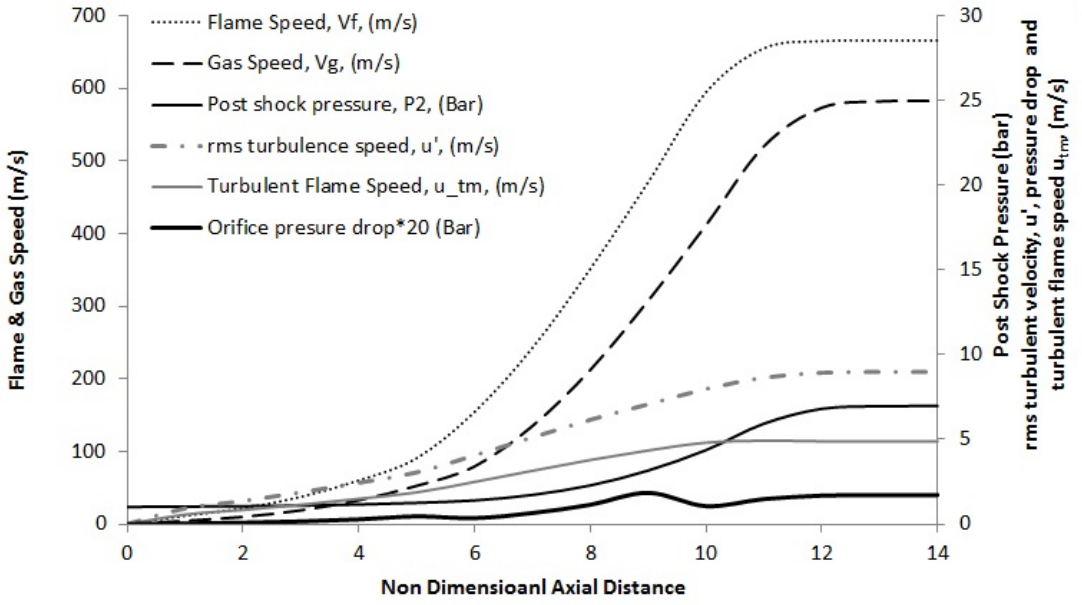

FIGURE 3.10: Test case 2, increasing BR. BR = 0.43, 0.6, 0.75 in batches of 5. 4 and 5 orifice plates respectively.

3.9 Conclusions

Empirical flame acceleration models have been investigated for the purpose of predicting run up and X_{DDT} in PDEs. Prediction of run up time can be used to determine the fining cycle period with additional information regarding filling, purge and detonation blow down. The PDE cycle period is of crucial importance in a practical PDE as this determines the limiting engine cycle frequency which directly influences the engines maximum thrust. If a PDEs run up time can be reduced it would be possible to increase an engines cycle frequency and thrust as a result. Furthermore, if the pre-detonation section of a PDE can be shortened by reducing the run up distance the PDE filling and purge volumes also reduce which in turn reduces the necessary cycle filling and purge periods, which allow further frequency and thrust gains. In addition, a method of predicting flame and shock speed has been developed which is based upon the shock relations published by Bradley which gives further theoretical insight into experimental pressure measurements where direct flame speed measurements are not possible. After training the model using experimental data, further predictions have been made for alternative experimental configurations which have been tested using the model. Result of this test suggest that reducing the BR along the tube length

could increase initial flame acceleration but would result in a lower final speed than increasing BR.

3.10 Summary

The model shows good correlation with experimental data across three experimental datasets, indicating the increasing flame acceleration trend. The CFAM model simulates FA in tubes in a temporal and spatial manner simultaneously with significant V_f modelling improvements over previous models. This is particularly evident once the flame is traveling above the sonic velocity in the reactant gases. In addition the model has several other benefits which help to understand the FA process in obstacle enhanced flame acceleration:

- u' prediction, and the interaction of turbulence generation with the local turbulent flame speed and flame acceleration as a result of this local flame speed interaction with the venting gas.
- Shock pressure and temperature ratio prediction, from Bradley's venting model [166] which can be used to determine the autoignition delay time and predict the length of tube required for a detonation to begin. This capability extends the current ability of models used to predict the location of X_{DDT}. This capability provides insight into the effect of compressibility on FA.
- Prediction of the run up time, and flame speed relative to time which would impact the maximum frequency in a PDE and could be useful to determine strain in both industrial safety and PDE applications
- Novel method for investigation of flame speed based on experimental pressure measurements using the work of Bradley et al. [166]

The model is currently limited to one set of experimental results for propane-air mixtures with an equivalence ratio of unity. Future work includes extending the model to be used with a wider range of detonation chamber diameters, multi-shot PDE cycles and other fuels.

Chapter 4

Pulse Detonation Engine Ground Test Rig Design

4.1 Design Requirements

The design of any fluid dynamic system is subject to various design constraints from a number of different perspectives. Such design considerations call for careful optimisation of all of the variables whilst compromising as few as possible. During the design of the University of Sheffield PDE (UoSPDE) the following design requirements were set:

- Regular, reliable injection of a fuel air mixture of known quantities and be able to control fuel stoichiometry through the control of:
  - injection timing
  - synchronization of air and fuel injection streams
  - flow metering to quantify equivalence ratios, fill factors and purge fractions
- Capability to demonstrate FA
  - suitable obstacle design to promote each stage of FA through:
  - sufficient flame accelerating tube length
  - tube diameter larger than the flame quenching diameter

- Capability to demonstrate DDT with:
  - DDT section diameter greater than d_c, the critical tube diameter
- Provision a safe vessel to contain explosions by controlling:
  - Wall thickness
  - Material choice
  - Fatigue design
- Sufficient instrumentation to measure steady operating conditions and dynamic shock/flame conditions with:
  - Data acquisition hardware
  - Data acquisition software
  - Design of high speed flame sensing equipment
  - calibration of transducers
  - ranging of transducers
  - choice of flow meters
  - data post processing

4.2 Fuel Choice

Fuel choice was investigated in section 2.5.5.1 of the literature review. It was found that propane-air mixtures are often used in the literature to replicate Kerosene-air detonation conditions due to the similar detonation cell width and ease of handling. As such this fuel was used to carry out the PDE experiments at the University of Sheffield's Low Carbon Combustion Centre (LCCC).

4.3 Geometric Factors

There are a number of Geometric factors which must be considered in the design of the PDE tube from an internal flow perspective, particularly the tube length and diameter, obstacle geometry, obstacle BR and length. Obstacle BR must be chosen to increase

FA but reduce drag. Tube diameter and obstacle internal diameter must be chosen to be larger than the minimum diameter criterion for DDT, should the PDE designer aim to generate detonation within the obstacle array. There must also be additional length for the detonation to propagate along the tube after successful detonation. The PDE designer may wish to generate quasi detonations within the obstacle prior to transmission of the quasi detonation into the tube. Conversely the designer may wish to run up to a choked flame within the obstacle then transition to detonation outside of the obstacle laden section, so that detonation takes place in the smooth walled tube. This process is described in sections 2.5.2 and 2.5.3 of the literature review. The length and diameter of the obstacle as well as the tube play a major role in FA and DDT studies, as such the ability to adjust these incrementally will be useful from an experimental design perspective. Lengths of the tube and obstacles are much easier to adjust than the internal diameter of the tube or the external diameter of the obstacle, as the lengths of sections can be flanged to fix on to one another as is commonplace in PDE experiments in the literature.

4.3.1 FA and Run-Up to DDT

Flame acceleration up to X_s can be calculated using Veser's formula for flame acceleration as described in 2.5.3. Using these formulas it is possible to predict to within an accuracy of $\pm 40\%$ whether flame acceleration is likely to reach the choking point within a certain distance. Figure 4.1 clearly shows that Vaser's run up model is closer to the detonation run up length observed experimentally across the range of fuels, tube diameters and orifice BRs discussed in table 2.7. References for the results from the literature can be found in table 2.7. This result suggests that detonation is likely to occur at X_s plus 7λ, rather than X_s, the point at which the flame chokes. Table 4.1 summarises the effects of fuel choice on the run up to the sonic flame and to detonation, providing that the operating conditions are standard temperature and pressure in addition to the tube diameter being larger than the diameter criterion, d_c.

Fuel (mix.w air)	S_l (cm/s)	a_p (m/s)	λ (mm)	X_s (D)	7λ (D)	X^*_{DDT} (D)	X_{DDT} from Lit. (D)
C_4H_{10}	38	990	75	12.6	10.3	22.9	27.6
C_3H_8	36	993	48	13.7	6.6	20.37	24
C_2H_6	41	994	50	11.7	6.9	18.59	23.6
C_2H_4	62.5	1004	26	7.95	3.6	11.57	17
C_2H_4	62.5	1004	26	7.95	2.9	10.85	13
C_2H_4	62.5	1004	26	7.95	1.8	9.77	12
C_2H_2	122	1025	9	4.16	0.6	4.79	7.5
CH_4	40	997	305	11.74	22.7	34.45	27
H_2	200	1088	10.6	2.69	1.45	4.14	9.5
H_2	200	1088	10.6	2.69	1.45	4.14	9.5
H_2	200	1088	10.6	1.63	0.14	1.78	5

TABLE 4.1: Prediction of Flame acceleration in PDEs: * represents X_s plus the 7λ rule as suggested by Ciccarelli in [29]. D represents the number of tube diameters along the tube axis to the point of interest, such as flame choking.

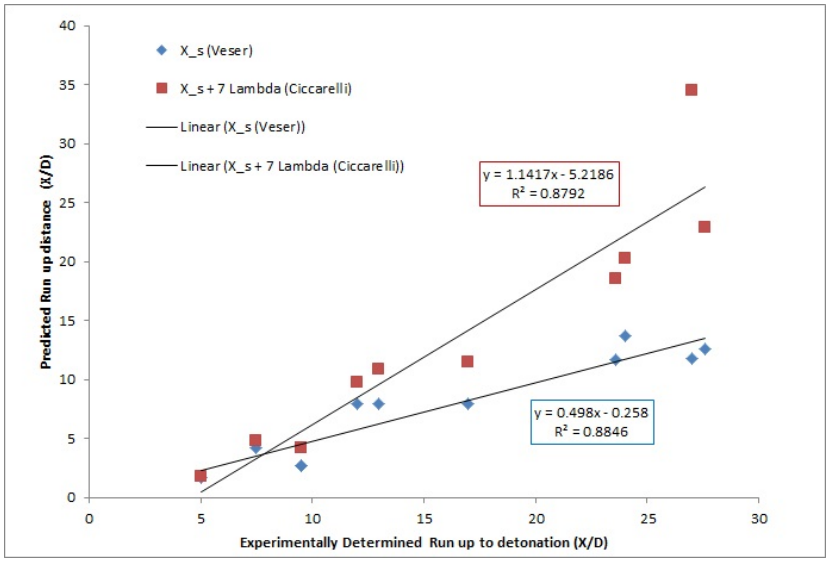

FIGURE 4.1: Experimental and predicted run up distances predicted using Veser's run up distance model (Veser) and Ciccarelli's run up plus 7 λ criterion

4.3.2 DDT

In order for DDT to occur, FA must first take place, however after FA has accelerated the flame to 50 % of V_{CJ} the flame will be likely to transition to detonation within a short distance providing the tube diameter meets the DDT criterion for detonation in tubes. There are two conditions to this criterion depending on whether the tube is smooth or rough, having the surface obstructed with obstacles such as Schelkin spirals,

orifice plates or some other sort of blockage. The effect of the blockage on the tube diameter is to reduce the characteristic dimension of the tube for detonation.

In the case of a smooth tube, detonation is only likely to occur when the internal diameter of the tube $D \leq \lambda \ / \ \pi$, or 15.27 in the limiting case for propane in a smooth tube. In the case of a tube with a rough wall, obstructions such as orifice plates interfere with the formation of the DDT process and therefore reduce the minimum passage diameter, d, through which the core of gas can accelerate and generate a detonation. In this case detonation is likely to occur as long as $d \leq \lambda$ or 48mm. As a result, in order for detonation to occur it is necessary to accelerate the flame to a state at which it is traveling at the speed of sound within the combustion products inside of the obstacle filled section of the tube. The flame can then transition to detonation in a the smooth walled section of the tube, provided that the diameter is larger than the $D \leq \lambda \ / \ \pi$ rule in order to allow detonation to take place. This design practice may allow DDT to occur within the shortest distance possible provided that the tube diameter is large enough for the mixture to detonate.

Fuel type	λ (mm)	d_c (mm)
C3H8	48	15.27
C2H4	26	8.28
C2H2	9	2.86

TABLE 4.2: Cell width limitations on PDE design

4.4 Inlet Air Flow

In order for the PDE to produce the correct mixture of air and fuel for each cycle it was necessary to inject purge air followed by filling air for the fuel air mixture. A nominal purge air fraction, pf, of 50% of the tube volume was chosen in order to separate the fresh mixture from the heated end gas from the previous cycle. The nominal fill fraction, ff, for all of these experiments was 1, ensuring that the PDE was filled with fuel and to allow comparison between all experiments. The required inlet air flow can be calculated using Equation 4.1. Density was calculated using the ideal gas law, as the flow was incompressible during filling.

$$m_{fill} = (ff + pf)\left(\rho \pi r^2 L\right) \quad (g) \tag{4.1}$$

Furthermore, the filling frequency can be incorporated into this equation to calculate the mass of air required for the PDE to operate per second. This could be calculated using Equation 4.2.

$$\dot{m_{fill}} = f(ff + pf)\left(\rho\pi r^2 L\right) \quad (g/s) \tag{4.2}$$

Table 4.3 illustrates the mass of air required for the final PDE tube design iteration.

Frequency (Hz)	Air mass flow (g/s)	Fuel mass flow (g/s)	Comments
1.00	2.27	0.10	Frequency too low for VSD
2.00	4.54	0.20	Frequency too low for VSD
3.00	6.81	0.29	Frequency too low for VSD
4.00	9.08	0.39	Within range
5.00	11.35	0.49	Within range
6.00	13.62	0.59	Air mass flow unatainable
7.00	15.89	0.68	Air mass flow unatainable
8.00	18.16	0.78	Air mass flow unatainable

TABLE 4.3: PDE filling conditions with a fill factor of 1.5 at a range of operating frequencies assuming STP exit conditions.

4.4.1 Valve design

Valve design is one of the most critical components of designing a successful PDE. As building an engine valve system is a complicated procedure it was decided that a donor engine cylinder head should be used in order to produce the correct air quantity and timing for the University of Sheffield PDE. In order to assess the available amount of air from the PDE valves, calculations were performed using equations from Heywood's work relating to internal combustion engines [229]. An illustration of valve lift can be seen in figure 4.2. The cylinder head cam shaft contains a series of lobes such as the one illustrated in this figure which force valves open, whilst compressing a spring which later returns the valve to its closed position.

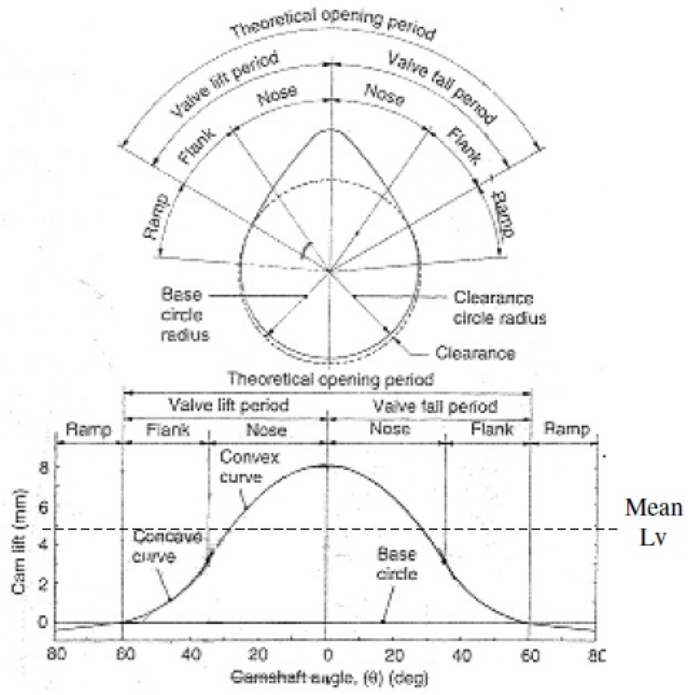

FIGURE 4.2: Illustration of valve lift profiles reproduced from the work of Heywood [229]

The valves used in the current PDE have been re-arranged to allow the engine cylinder head to open both exhaust and inlet ports simultaneously. This valve timing alteration was achieved by opening the twin overhead cam cylinder head and rotating the interlocking cam drive gears until the timing was as closely synchronized as possible. Figure 4.3 illustrates how the cam pulley angle used to drive the valves corresponds to the air mass flow passing through the valves with a pressure of 9800 Pa, whilst operating the fan at 40Hz (80% of its full speed). During this particular cold flow experiment the 1m long 0.089m internal diameter tube was connected to the PDE cylinder head with one functioning set of valves for a single cylinder. There were no obstructions in the PDE tube and the PDE rig was connected to the atmospheric air delivery line. The atmospheric conditions were 0.102100 MPa and the ambient temperature was 21 $^{\circ}$ C. It can be seen from these cold flow experimental results that the valve air mass flow closely approximates two valves overlapping with a small fall in amplitude at the centre of the plot. In practice this valve will be spinning, which will lead to a lag in the inlet flow conditions at the beginning of the valve opening period and a slight increase in the flow velocity at the closing conditions. Quantification of these dynamic effects were seen to be beyond the scope of this thesis.

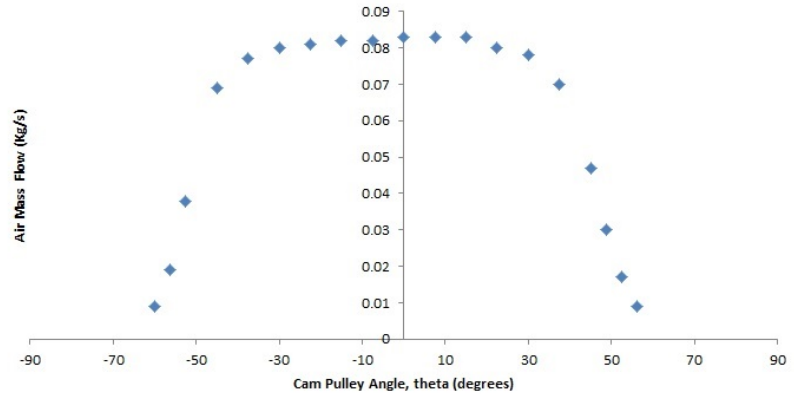

FIGURE 4.3: Cold flow testing results on the cylinder head for air mass flow with the 89mm PDE tube attached

Figure 4.3, also shows that the valves open for approximately 120° of their 360° full rotational cycle, or 1/3 of the cycle period when the valves rotate. This infers that the flow rate through these valves is at least three times the mass flow rate through the upstream mass flow meter due to the dynamic nature of the valve filling cycle. As a result the air receiver volume up stream of these valves was specified to be at least three times larger than the average mass flow per second multiplied by the operational frequency of the engine. This relationship is expressed in terms of mass to overcome the difference static pressure before and after the valves in equation 4.3 This equation assumes that the flow is incompressible, which is reasonable as the inlet air flow is only pressured to 0.15 bar during the filling cycle.

$$dotm_{cylinder} = 3f\left(\rho\pi r^2 L\right) \quad (g/s) \tag{4.3}$$

4.4.2 Air delivery system description

Air is delivered to the PDE by means of an atmospheric pressure line which is equipped with a British Standard orifice plate designed in accordance to BS:5167 [230]. The air delivery apparatus can be seen in Figure 4.4. This orifice plate is capable of measuring mass flow within an accuracy of ± 0.5 %, as rated by BS:5167. The majority of this error is as a result of the error in the discharge coefficient, with a much smaller error present from the expansion factor, which was calculated to be two orders or magnitude smaller over the range of flows of interest (0 to 40g/s air). This line operates at a

maximum pressure of 0.2 bar gauge and approximately 300K ± 3K. Once air has passed though the atmospheric pressure line it flows through two parallel 254mm diameter 1000mm long (100 Litre) cylinders constructed from PVC polymer sanitary tubing which where used to provide sufficiently large volumes of pressurized air to the back of the cylinder head valves. These cylinders were originally sized around the 88.9mm diameter 1000mm long PDE tube, which allowed the 6 Litre tube volume to be filled up to 16.9 times a second. These air receivers serve the purpose of providing the following valve system with a steady delivery pressure in order to reduce dynamic effects in the air delivery system.This was achieved by storing large volumes of low pressure air as close to possible to the cylinder head valve inlet. The tubes were connected together using moulded ABS fittings which formed a T-junction which was connected to the 152mm internal diameter atmospheric pressure line by means of a 76mm diameter flexible rubber hose and steel conical reducer section.

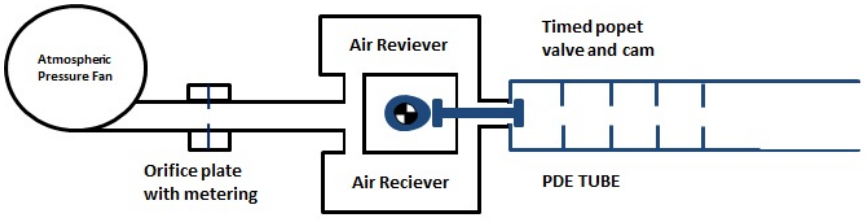

FIGURE 4.4: Original PDE Air Delivery System

Once air had passed through the air receivers it entered the valve system which was reclaimed from an automotive cylinder head. The cylinder head valves were dismantled and packed with grease to allow operation without oil, making the system much simpler and cleaner to operate over short running durations. The cylinder head was driven by a three phase speed controller and electrical motor which was coupled by means of a cam belt to the cylinder head and also to a timing pulley which drives the timing shaft. The timing systems can be seen in Figures 4.5 and 4.6.

4.4.3 Fuel delivery

Initially a rotary peristaltic valve was designed using a purpose built offset bearing which was essentially used as a brake to stop propane flow flowing through a flexible process line. The timing diagram for this apparatus can be seen in Figure 4.5. This apparatus was used for early development work and it was soon realised that the

peristaltic valve design was not sufficient to withstand 4 bar propane pressure as well as the eccentric loading provided by the peristaltic pump bearing. Over time the hose delaminated due to fatigue from the mechanical load and created a small leak which was shut off immediately using a remotely operated solenoid valve. After initial experiments it was decided that the fuel delivery system would be updated to an electronic solenoid valve. This new injection timing system can be seen in Figure 4.6, which illustrates the replacement of the peristaltic pump with an injection timing circuit.

The injection timing system was activated by means of a rotary light gate attached to the timing shaft along with the ignition timing rotor. Both injection delay and duration could be determined by rotating the rotors giving a phase offset to the relevant system. That injection rotor was designed to provide a range of fuel injection sweep which were between 60° and 120°. The duration of the airflow inlet system was set to 120°, and the fuel injection sweep was set to 90° so that the purge air fraction was 50%

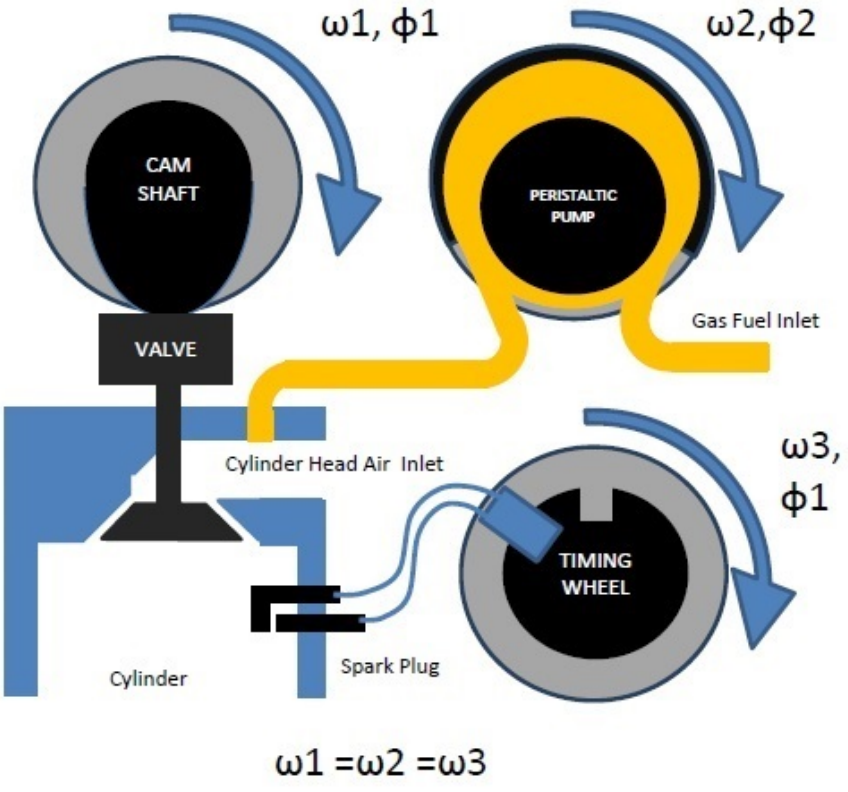

FIGURE 4.5: Original PDE Injection Timing System

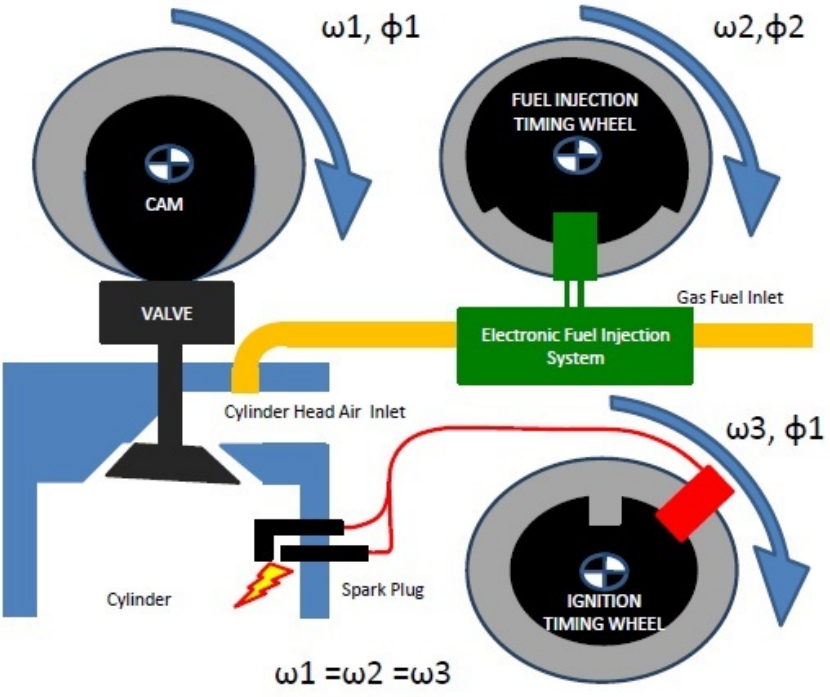

FIGURE 4.6: Final PDE Injection Timing System

The combustion injection system can be seen in Figure 4.6. All of the timing wheels rotate at the same angular frequency and rotate in phase with one another once set up, as they're attached by a system of shafts and pulleys. This allows the timing delay for fuel and ignition to be set easily using two variable timing rotors and strobe light to determine the relative timing delay.

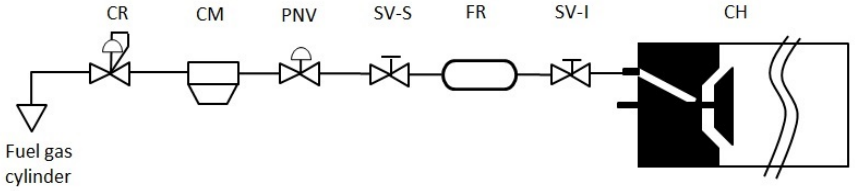

FIGURE 4.7: Fuel injection system from propane regulartor to delivery at he valve port. CR: Regulator, CM: Coriolis meter, PNV: Pneumatically actuated Needle valve, SV-S: Safety Shut off Solenoid Valve, FR: Fuel Receiver,SV-I: Injection Solenoid Valve CH: Cylinder head valve port

Figure 4.7 illustrates the fuel injection system flow path from propane cylinder regulator to the delivery system on the PDE. First fuel flowed from a cylinder and regulator housed externally (for safety reasons) through a dedicated propane hose, into a Coriolis flow meter (Micromotion CMF010). The accuracy of the Coriolis meter calibration curve was calculated to have an R^2 value of over 95% for the linear curve fit to the

data in each case. The flow then passed through a pneumatic needle valve which was controlled via an electronically actuated air pressure controller which was removed from the locality of the fuel pipe in case of possible leaks. The fuel then passed through a safety shut off solenoid valve another process line and a fuel receiver. The fuel receiver was designed to contain sufficient fuel so that the pressure in the receiver remained constant during the filling cycle. After the receiver the fuel injection timing was controlled by twin parallel Hana A type injectors which were connected using a twin Hana fuel injector manifold and controlled using a driver circuit designed in-house by Christopher Grigson, an instrumentation engineer at the department of Mechanical Engineering, The University of Sheffield.

4.4.4 Synchronisation and timing

Each of the air, fuel and ignition systems must run in synchronisation with the other systems, with a set phase difference and the same operating frequency in order for the PDE to operate at the correct operating condition. Figure 4.8 shows the timing diagram for the full PDE cycle. For each of the experiments run with this PDE, the purge fraction was set to 50 %. As a result, the tube was purged with air amounting to 50 % if its full volume before being filled with fresh reactants, then closing the valves. The time allowed for this injection process was approximately 67ms. A delay was applied to the spark igniter of 80ms after valve closure to allow the mixture to settle before ignition. This Figure was determined experimentally. After ignition the mixture was allowed to accelerate through FA, detonate if possible and then blow down whilst the combustion wave was inside the tube. Once the combustion wave had exited the tube, the burnt products were allowed to expand for a short while before purging began for the next cycle. The time allowed for the last two stages was approximately 55ms.

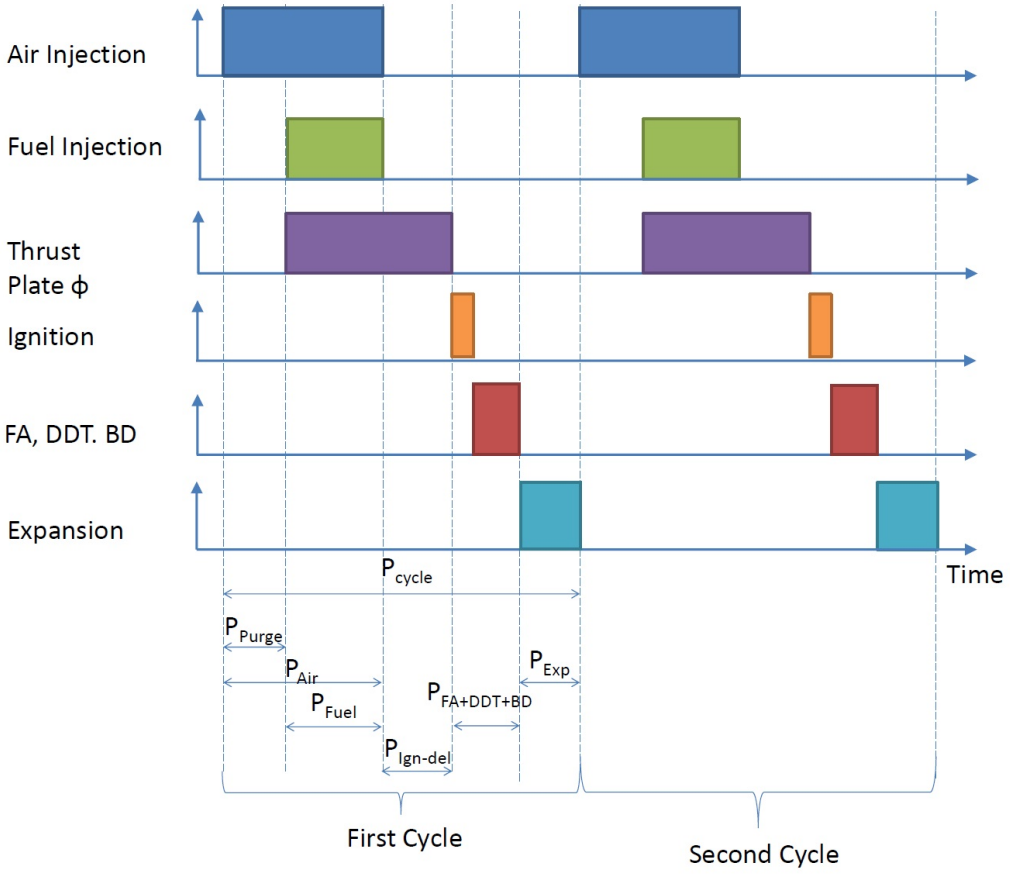

FIGURE 4.8: Injection timing diagram. Events vs. time. P_{cycle}: cycle period, P_{purge}: Purge period, P_{Air}: Air filling period, P_{Fuel}: Fuel filling period, $P_{Ing-del}$: Ignition delay period, $P_{FA+DDT+BD}$: Flame acceleration, DDT and blow down period. P_{Exp}: Expansion period

4.5 Test Rig Mechanical Design

4.5.1 Tube geometry

4.5.1.1 First Iteration

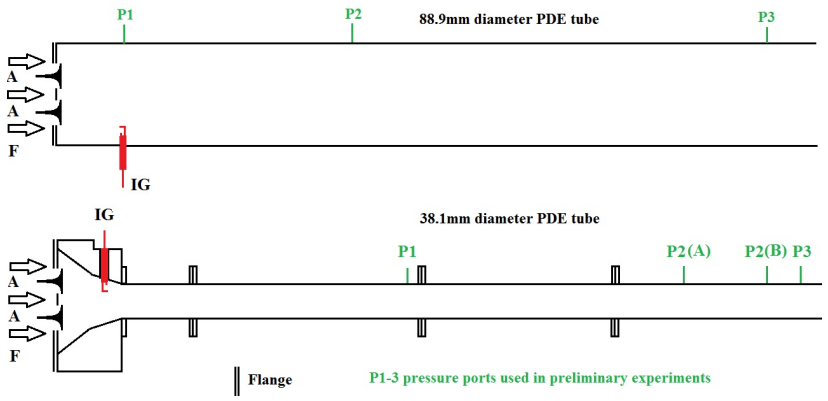

FIGURE 4.9: Top: initial PDE design diagram, the PDE tube is 1000mm long with a 0.0889m internal diameter. Ports are mounted at 0.1m, 0.4m and 0.9m. The Ignitor is side mounted at 0.1m from the thrust plate. Bottom: final PDE design diagram, main tube diameter 0.0381m. Some tests were run with an insert in the obstacle filled section which restricted the working diameter to 0.0318m. Ports mounted at regular intervals as described by Figure 4.10.The ignitor in the latter case was mounted 0.05m from the thrust wall.

The initial PDE tube design can be seen in figure 4.9 which illustrates the valve block on the far left followed by the valve and then the main PDE tube. The PDE tube was 1m in length with an internal diameter of 0.0889m. Instrumentation ports were located at 0.1m, 0.4m and 0.9m from the valve wall or thrust plate. The ignition system used a side igniter at 0.10m from the thrust plate on the bottom of the tube, diametrically opposed to the first instrumentation port. This tube, the valve system and obstacles were inherited from the work of previous students working on PDEs [231, 232, 233, 234, 235, 236]. There were a number of problems with the tube including inadequate wall thickness for long duration tests due to fatigue issues and port bosses which had incorrect thread sizes for the preferred instrumentation. The bosses were changed and a series of short tests were carried out using these tubes before they were retired. These tests included work on orifice plate diameter and Schelkin spirals.

An appraisal of the tube geometry was made after completing a small number of tests and the following issues were identified with this tube:

- There were too few ports to study flame acceleration in depth
- Studies on the effect of PDE tube length were not possible
- DDT was not observed in the experiments
- The tube could not be flanged and extended due to limitations of the atmospheric line air delivery system

4.5.1.2 Second Iteration

After the first set of tests proved that detonation was not possible with propane-air mixtures in a 88.9mm internal diameter, 1m long tube, it was decided that the PDE tube aspect ratio should be increased. Since the volume of the combustion chamber was a limiting factor due to a low pressure air delivery system, it was decided that the diameter should be reduced rather than increasing the combustion chamber length. The aspect ratio was chosen to be 29 according to the equations explored in Section 2.5.3 which according to equation 2.68 should be long enough for the run up length for a sonic flame. The combustion chamber diameter was chosen to be 38.1mm, which according to Section 2.5.1 and information gathered from the gap analysis 2.8, is large enough to sustain a spinning detonation. This is because the diameter is greater than λ/π, but smaller than λ, the cell width, which is 46mm for propane. A diagram of the second tube geometry is shown in Figure 4.10 which illustrates the modular, flanged design of the second PDE tube.

The first section of the new PDE tube, as shown in Figure 2.64 consisted of a 77mm long reducer section, reducing from 88.9 mm to 38.1mm diameter flow cross section, which housed a spark plug at an axial distance of 38.1mm from the thrust wall. The ignition system and spark plug are derived from a standard automotive ignition system with no modifications to ignition energy. Timing was provided by a Wessel ignition unit designed to be fitted to motorcycles, which triggered using a magnetic Hall effect transducer and magnet attached to a rotor. Once the flow had exited the reducing section the mixture passed into the obstacle laden section of the PDE tube, consisting of four separately flanged tubes as can be seen in Figure 4.10. The sequential tube lengths are 4, 8, 8 and 9 diameters, 1.182m in total when including the reducer section.

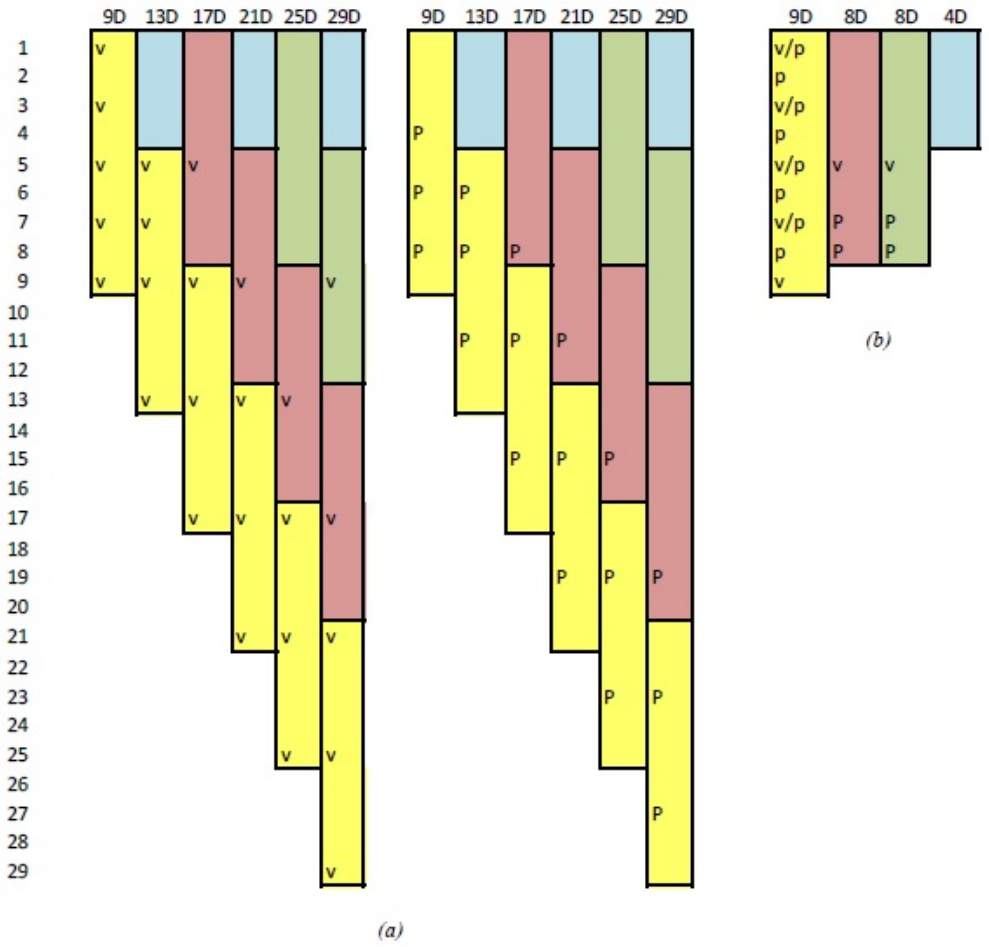

FIGURE 4.10: PDE tube assembly options. P represents a pressure port, V represents a flame speed port. D refers to one tube diameter, hence 9D is a 9 diameter long tube. a) tube assembly length options: 9D, 13D, 17D, 21D, 25D and 29D. b) port locations.

Orifices could be mounted into the tube by means of bars with spacers as shown in Figure 4.11, or using orifice cages which the plates slotted into as shown in Figure 4.13. All orifice blockages were spaced equally at 1D from the start to the end of the orifice blockage with a range of orifice multiples, depending on the test. High speed dynamic pressure transducers were inserted at a range of locations throughout this experiment, depending on the preference for the experiment in question as can be seen from Figure 4.10, which includes suggestions for the final test. The fractal orifices and modular tube were both designed in conjunction with Thomas Black, an MEng final year project student, using the same geometry as Abou El-Azm Aly et al., as shown in Figure 4.12.

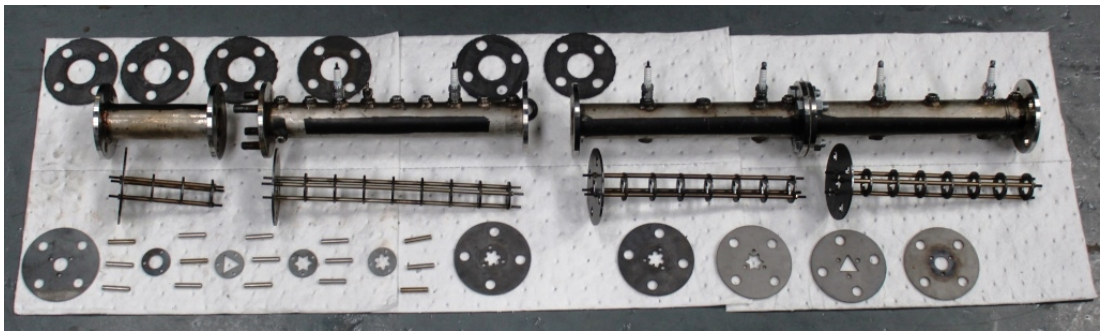

FIGURE 4.11: Dismantled PDE tube and fractal orifice assambly.

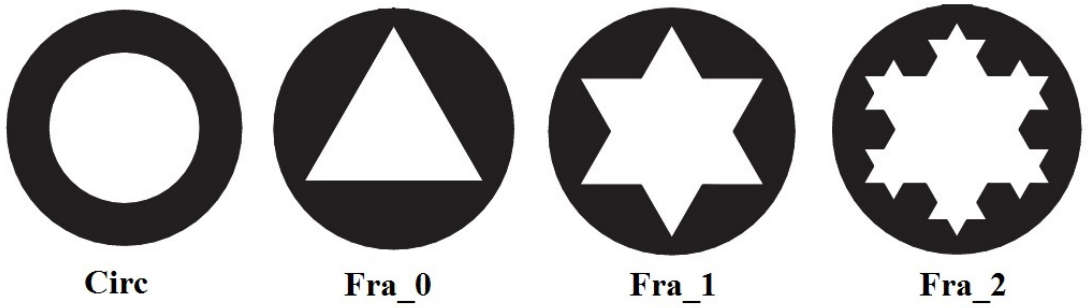

FIGURE 4.12: Fractal orifice hole shapes

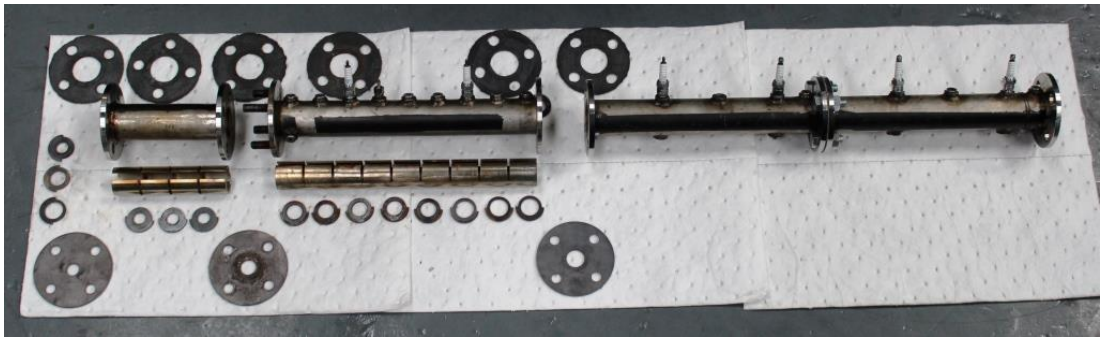

FIGURE 4.13: Dismantled PDE tube and orifice cage assambly used in variable orifice diameter experiments. Spark plugs are mounted in the locations used in the stratified orifice experiments. Diametrically opposing ports were also used in this (chronologically) final set of experiments.

In a number of the preliminary tests the full range of instrumentation was unavailable as there were only three or four working pressure transducers. Preliminary tests were therefore carried out with transducers placed in strategic locations to determine whether it was possible to move the port location between experiments for one case. Figure 4.14 shows and early test which used Kistler dynamic pressure transducers (green wiring). Ion probes are not shown in this picture as it was taken at a point in

the testing campaign before these were developed, however the electrode locations can be seen in Figure 4.13.

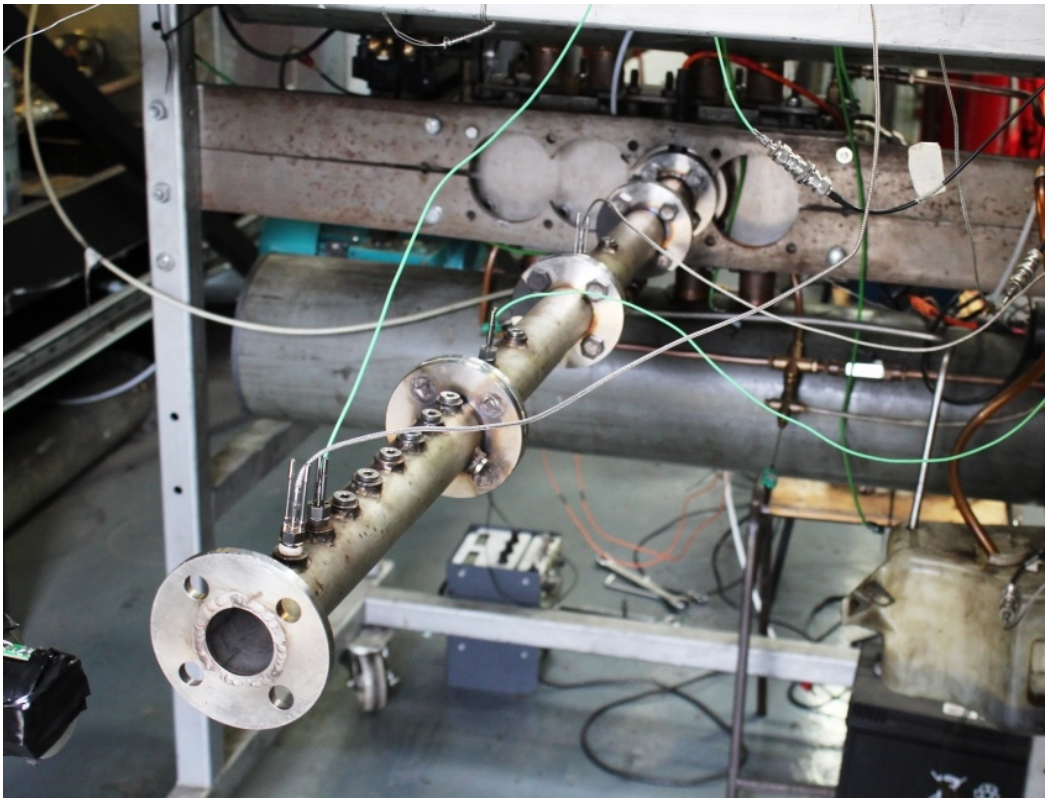

FIGURE 4.14: Assembled 38.1mm diameter PDE tube with Kistler pressure transducers.

4.5.2 Control

It was decided early on in the project that the PDE should be controlled wherever possible using National Instruments (NI) LabView (LV) control software which was to be programmed specifically for this task. Fuel flow and air flow were controlled using a combination of digital and analogue control outputs so that the atmospheric airline fan and fuel solenoids could be switched on (or isolated) when necessary. An equivalence ratio set point could then be reached by setting analogue dials on the LV computer screen control panel until the equivalence ratio readout read out the correct value. The PDE valves were controlled manually, as the process of integrating with the motor speed controller was deemed too lengthy.

In addition to the analogue and digital outputs and manual control required to achieve the correct operating conditions flow metering devices were used to measure the flow

rates of both fuel and air mass flow. A Micromotion CMF010 Coriolis meter was calibrated prior to each experiment with a range of 0-2 g/s so that the mass flow of fuel could be measured from the devices voltage output. An orifice plate with D and D/2 pressure tapings and an upstream thermocouple were used to give readings for air mass flow which were then interpreted using specialist in-house LV code programmed to according to an industrial standard for orifice plate flow (BS 5167). The test operator controls the flow of fuel and air until the air flow matches the required mass flow to give sufficient purge and fill air then increases the fuel flow until the desired stoichiometry is required. In this case, the overall stoichiometry is 2/3 of the stoichiometry during filling, as in each of the tests detailed in this thesis a purge fraction of 0.5 was chosen. The reason for choosing a purge fraction of 0.5 was that the air delivery system could only supply a maximum pressure of 0.15 bar, which was insufficient to fill at higher rates. The air delivery was supplied by means of a 30m long 101.5mm internal diameter process line which had BS 5167 standard orifice plate flow meter installed after 14 diameters along the line allowing for the measurement of mass flow to an industrial standard. This system is known as the atmospheric pressure airline, as the delivery pressure is close to atmospheric pressure. The atmospheric line was unable to deliver sufficient air to fill 100% of the tube volume after purging the same tube volume at the minimum cycle frequency. As a result, the purge fraction was reduced until a reasonable amount which stopped end ignition from the previous mixture, as determined by empirical methods using some of the early ion probe designs to determine which direction the flame was traveling.

High speed data logging systems were used to measure the pressure and ion probe data used in these experiments, but as these systems were measuring signals at 1Ms/s, the data could not be read to the screen at the same time as the data was logged in a meaningful way. This resulted in the rig being run blind, followed by post processing. The results of post processing then determined how each test condition had performed.

4.5.3 Dynamics

Early versions of the PDE rig operated with a large bore fuel valve, which was capable of operating for short durations before the valve's compressible pipe was destroyed, as described in section 4.4.3. This allowed high fuel mass flows to be achieved with little

pressure loss across the valve, or dynamic lag during the filling time. As a result the mass flow of fuel was able to match the mass flow of air delivered during the time the engine was operating. As this system was unreliable and had a low inherent robustness due to high dynamic loading and friction within the fuel valve, the system was deemed unsafe and replaced with electronically controlled gas valves. A manifold coupled to twin Hana A type LPG fuel injection valves was used which were switched using an in-house circuit capable of switching up to 2 amps at 10 volts was used to time the flow of gas into the back of the injection system. This system was capable of delivering fuel up to a pressure of 4 bar before the injectors locked up due to overpressure. During the commissioning of the Hana injection system it was found that there was insufficient mass flow delivered to the PDE cylinder during the filling cycle. It was thought that this could be due to flow restrictions in the line before the new injection system. This problem was overcome by installing a 0.6L fuel receiver directly up stream of the injectors, with the capacity to deliver one seconds worth of fuel at a frequency of 5 Hz, so that the dynamic filling of the receiver inlet was fast enough to maintain the reservoir pressure whilst the valves were actuated dynamically. If the rig was to be operated at higher frequencies, this fuel receiver would need to be larger still.

4.6 Test Rig Electrical and Instrumentation Design

4.6.1 Ignition system

The electronic ignition timing system was fitted using an off the shelf 12V motorbike ignition timing system with a phase adjustable magnetic rotor, transistor box and spindle. The circuit diagram for this system can be seen in Figure 4.15, from the OEM website [237].

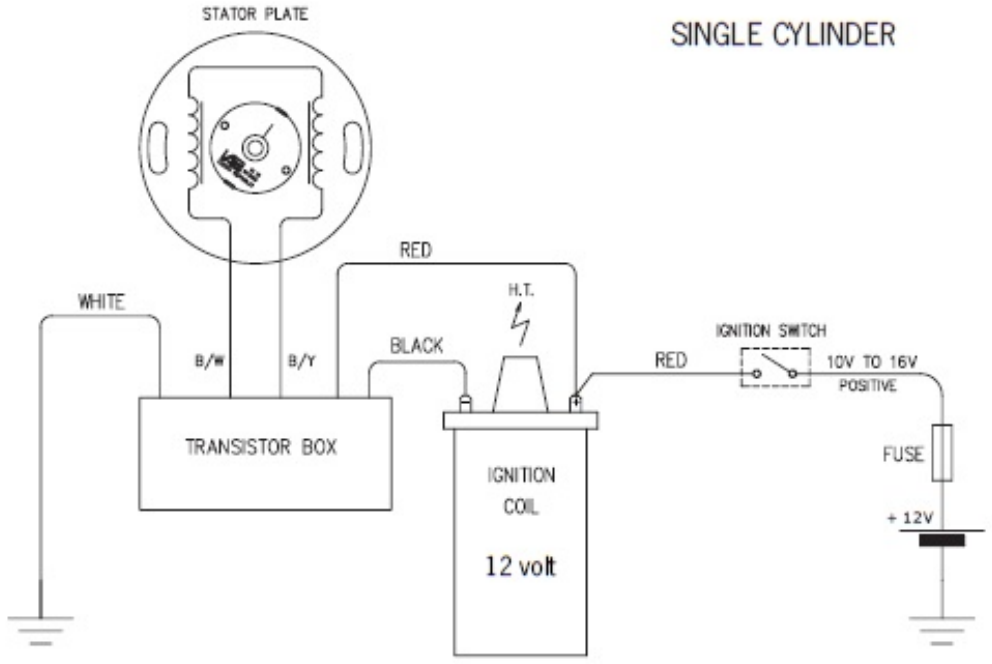

FIGURE 4.15: Outsourced ignution circuit manufactured by Wassel [237]

The circuit diagram described in Figure 4.15 was left unmodified with the exception of the second timing pin on the magnetic rotor. This was removed so that the rig only fired once per revolution, to reduce the change of generating misfires if the timing of the valves were accidentally set up incorrectly. The ignition switch in the above diagram was connected to a relay which was controlled by a switch and power supply at the control computer. This allowed the ignition to be controlled from a distance while running tests.

4.6.2 Injection system

An initial fuel injector driver circuit was built which failed to supply a high enough output current to activate the electromagnetic coil in the injector. After this initial circuit failed to work reliably a second prototype was built in collaboration with in-house instrumentation technician, Christopher Grigson at the Department of Mechanical Engineering. The circuit design can be seen in Figure 4.16 which illustrates the light gate, U1 which is triggered when the gates rotary wheel allows light to pass through. Field effect transistor Q1 allows for amplification of the signal generated by the light gate to drive the Hana injection solenoid, RL1, with a current of up to 2 Amperes. This

circuit and injection system provided a reliable, robust system for fuel gas to the PDE cylinder head, which was injected behind the poppet valve as soon as it had opened, as shown in Figure 4.6.

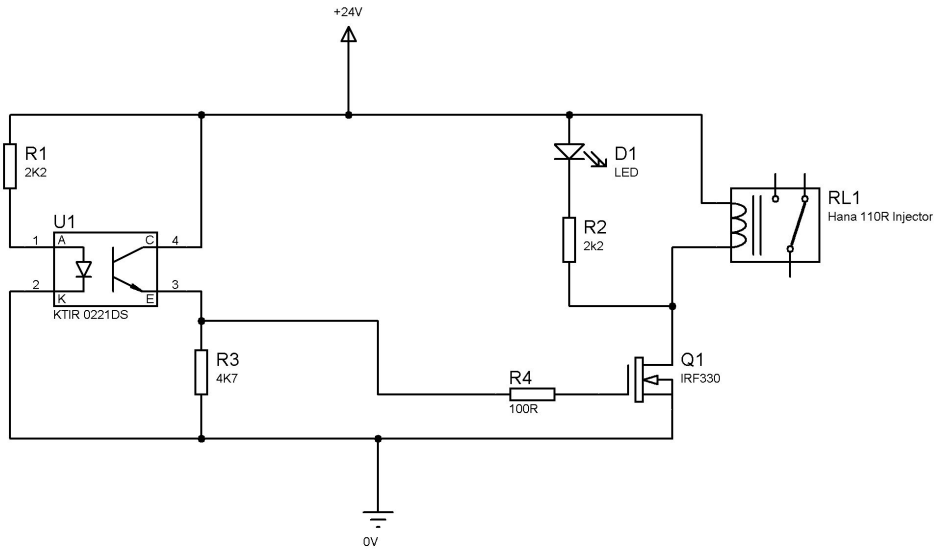

FIGURE 4.16: Injector driver circuit, for use with a rotary light gate. In-house designed, tested and built by Chris Grigson

4.6.3 Pressure instrumentation

All of the preliminary tests were completed using high speed, high pressure Kistler dynamic pressure transducers as shown in Figure 4.17. The dynamic pressure transducers were Kistler 6061A transducers with a natural frequency of 90kHz, a sensor head width of 10mm and a maximum operating temperature of 250°C at the sensor surface. The charge amplifiers used were Kistler 5037A charge amplifiers. A similar system was used for three additional PCB pressure transducers in the later experiments which were carried out. The PCB pressure transducers used were three PCB 113B26 pressure transducers with a natural frequency of over 400kHz and a maximum soak temperature rating of 136°C (flash temperatures of over 1500°C were also allowed). As this temperature limit was very low the experiments were controlled to switch off if the sensor thread adapter reached a surface temperature of 80°C, which was measured on each thread with a K-type thermocouple per adapter. The PCB pressure transducers had built in amplifiers, so there was no need for a charge amplifier to amplify the charge generated by the quartz crystal externally. An external signal conditioner was used to

power the transducers and process the output signal before it was carried along CAT 5 screened data cable to the NI 9223 DAQ modules and their respective cDAQ.

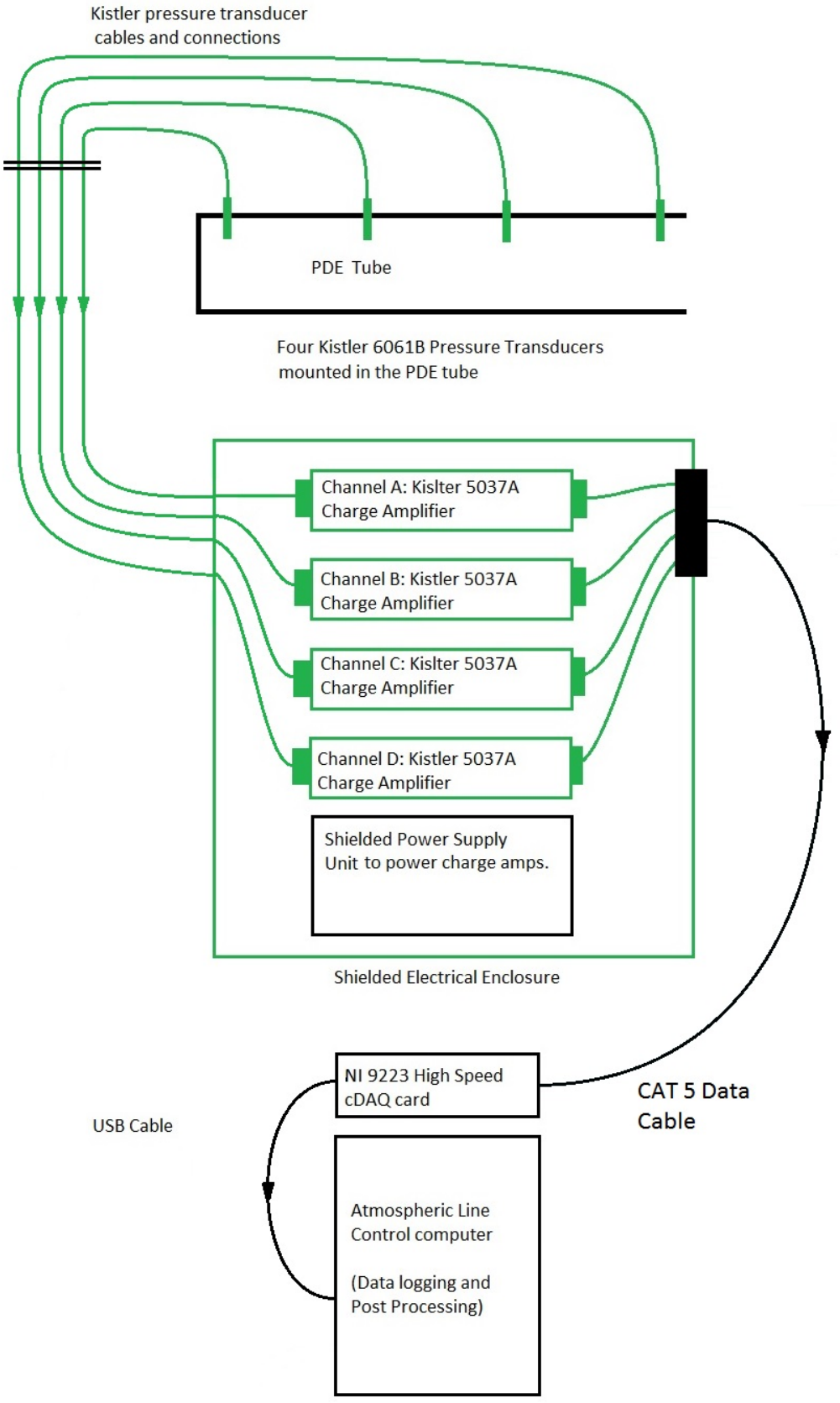

FIGURE 4.17: Kistler Pressure transducer instrumentation arrangement as used in preliminary experiments

4.6.3.1 Error of a Single Pressure Measurement

Kistler Dynamic Pressure Measurement There are a number of sources of error in the Kistler instrumentation. These include errors from the sensor (Kistler Model 6061A) uncertainty and linearity which had a maximum value of ±0.35% of the reading and ±0.43% of the full scale respectively. The linearity error was calibrated at a range of 0-5 bar, 0-50 bar and 0-250 bar, with the maximum value quoted here, from the 0-5 bar range (the 0-50 bar range had a maximum error of ±0.1%, so this is the worst case scenario). There was an additional uncertainty in the measurement of the charge by the charge amplifier (Kistler Model 5037A), which was quantified as ±0.05%. These figures were obtained by means of external calibration services provided by Trescal. In addition to the sensor and charge amplifier, there were also uncertainties in the measurement of the charge amplifier voltage by the NI9223 analogue to digital converter, which had an offset error of ±0.40% of the full range and a gain error of ±0.40%. These errors propagate by means of addition as each of the systems multiply the signal from the previous subsystem. For example the charge amplifier amplifies the charge produced by pressure transducer which produced by the pressure the piezoelectric quartz crystal at the tip of the pressure transducer. As a result each of the above gain errors can be added to generate an overall gain error measurement for Kistler pressure measurements of ±0.8% of the indicated value. In addition to this error, there is another compound error from the offset and linearity errors which are a function of the maximum scale of the measurement for both the DAQ and the pressure transducer. In this case the DAQ offset error is ±0.40% of full scale (FS), which is 10V. 10V equates to 20 bar in this case, so ±0.40%FS is ±0.08 bar. The maximum error in transducer linearity was recorded as ±0.43%FS at 5 bar, so ±0.0215 bar. These two additional errors add to give an additional error of ±0.1015 bar, so the maximum error is calculated using Equation 4.4.

$$KistlerPressureError = \pm 0.8\% IndicatedValue \pm 0.102 \quad (bar) \tag{4.4}$$

In order to simplify the statement of error in Kistler based pressure measurements in this work, an indicated value of 18 bar will be assumed. This is the maximum error

which could be experienced if a detonation were to occur. As such the maximum error in Kistler based pressure measurement is given as ±0.25 bar.

PCB Dynamic Pressure Measurement As with the Kistlers there were a number of error sources for PCB based pressure transducers. The linearity error for PCB transducers (PCB Model 113B26) had a maximum value of ±0.3% FS, where the FS reading was 34.5 bar. This error equated to 0.1036 bar. The uncertainty error for the transducer calibration curve was ±1.3%. The signal conditioner (PCB Model 482C05) had an uncertainty error of ±0.2% in the gain, no other error was reported in the calibration document for this device. These pressure measurements were converted into digital signals by the NI 9233 Modules with the same gain uncertainty and offset error as quoted for Kistler pressure measurement. The error for PCB pressure measurements can be calculated using Equation 4.5.

$$PCBPressureError = \pm 1.9\% IndicatedValue \pm 0.1836 \quad (bar) \tag{4.5}$$

To simplify the statement of error in PCB sensor pressure measurements in this thesis, an indicated value of 18 bar will be applied to Equation 4.5. As such the maximum error in PCB based pressure measurement is given as ±0.53 bar.

4.6.4 Flame sensor instrumentation

4.6.4.1 Early Ion probes tests

Initial ion probe designs were based on the similar circuits to the work of Panicker in his thesis on the development of a ground based PDE demonstration engine, as referred to in section 2.6.2, with an operational amplifier connected as a micro-ammeter current to voltage converter circuit. This circuit was capable of amplifying nA currents to a signal of 8 volts, depending on the strength of the ion field in the flame. Initial results from tests with this circuit are shown in Figures 4.18 and 4.19. These figures both show a great deal of noise in the signal, which obscures the start of the gradient in the sensor output signal, rendering the signal impossible to read using automatic software and difficult to read by eye. A series of measurements were made based on different

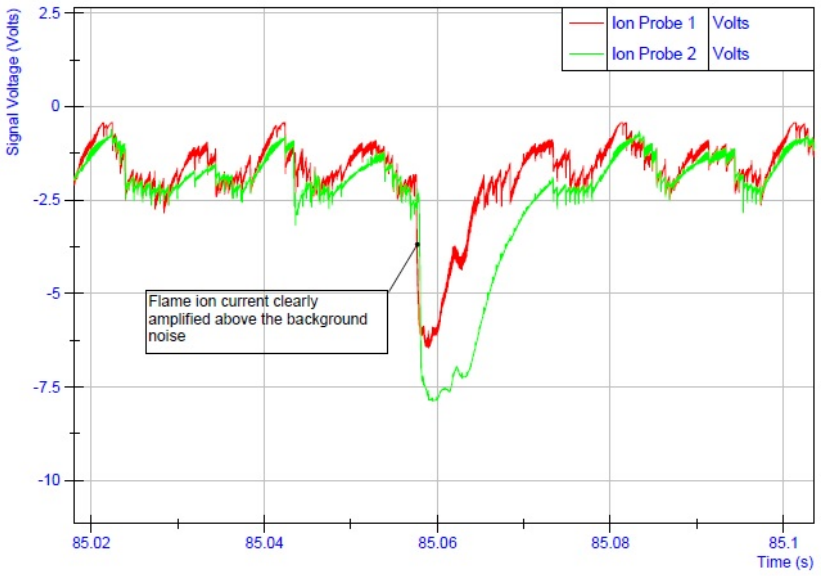

FIGURE 4.18: Ion Probe graph plotted for two channels in voltage (V) vs. time (s). Time resolution in the x axis is 20ms per division, voltage resolution in the y axis is 2.5V per division. Noise clearly obscures the signal. Probe locations at 1010mm and 1160mm from the thrust wall.

techniques to determine whether these signals could be read in a repeatable manner. These methods included measurement by eye on NI Diadem software, measurement of the gradient using in-house NI LV software and measurement of the peak using in-house NI LabVIEW software. The results of these tests can be seen in Figure 4.18 , which illustrates that the noise in the signal is creating a large error in readability of the measurement. Figure 4.19 illustrates that the flame speed measured by this developmental stage circuit could be as fast as 405m/s, based on the time difference between the signal falling edge and the distance between the probe locations. This test was completed using two NGK CR9E spark plugs as ion probes mounted in ports at 1010mm and 1160mm along the tube, separated by 0.152m

4.6.4.2 Ion Probe Development

The final ion probe circuit was developed by Ben Kitchener, an in-house instrumentation technician, for the purpose of measuring PDE flame speeds. The circuit diagram can be seen in Figure 4.20, which is a design modified from the work of Panicker discussed in section 2.6.2, with digital conversion of the signal. This circuit illustrates an operational amplifier which amplifies the ion current and converts this into a voltage,

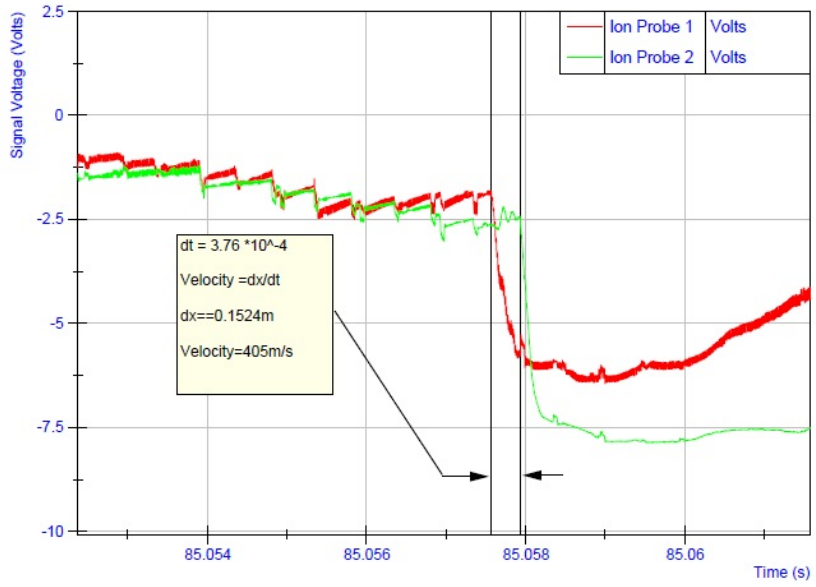

FIGURE 4.19: Ion Probe graph plotted for two channels in voltage(V) vs. time(s). Time resolution in the x axis is 2ms per division, voltage resolution in the y axis is 2.5V per division. Noise clearly obscures the start of the signals rising gradient. Probe locations at 1010mm and 1160mm from the thrust wall

followed by two CMOS Schmitt triggers (from a 7414 hex Schmitt trigger chip) connected in series for a fast rise time on a very small voltage, saturating the output of the circuit to the full 5V signal with a very small signal. The response time of the operational amplifier is 80ns after which a slew rate of $7V/\mu s$ begins. Once the output of the operational amplifier reaches a value of 1.3volts the Schmitt trigger output begins to rise, which takes 15ns, or a maximum value of 22ns. The same process occurs with the second Schmitt trigger, increasing the sensitivity of the amplifier circuit. No data is provided for the variation of response time in the operational amplifier, so a maximum value of twice the quoted value is assumed for the response time. The real value cannot be any larger than this as the lower response time cannot be less than 0, as the operational amplifier would be amplifying a signal before it was present on the input. As such the variation in response time is assumed to be 80ns. The slew rate of the operational amplifier is quoted to be a stable $7V/\mu s$ with a supply voltage of +5V and -0V, or $9V/\mu s$ with +15V and -15V, so it is assumed that this remains constant.

Figure 4.21 illustrates the maximum timing error achieved using this circuit. The timing accuracy value between sequential ion probes would be double the value indicated in the figure, 212ns. If the ion probe ports are separated at a distance of four diameters, or 150 +/-1mm and a flame speed of 1800m/s is assumed (the CJ detonation velocity for

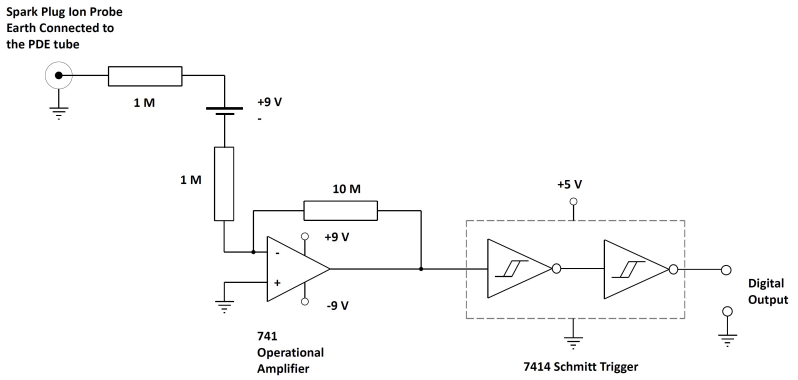

FIGURE 4.20: Ion Probe Circuit Diagram.

stoichiometric propane-air), then the error in flame speed measured would be 24m/s. This is much more accurate than most detonation experiments as a digital recording device is being used to measure the signal at a sampling rate of 160MHz, rather than the standard 1-5MHz sampling rate usually used in such experiments.

Figures 4.22, 4.23 and 4.24 show the results of tests on three ion probe circuits operating in parallel attached to three NGK CR9E spark plugs were mounted at 725mm, 1030mm and 1144mm stations along the tube from the thrust wall. For the duration of this experiment the PDE tube was filled with 14 0.6BR orifice plates mounted in a 31.75mm diameter tube insert, which then opened up to the full 38.1mm diameter of the tube after the last orifice plate, located at 610mm. The experiment was performed using a propane/butane- air mixture from a plumbers blow lamp and mixed with air in the PDE whilst the valves were not turning. Ignition was provided through an open port in the rig close to the thrust wall in order to ignite the mixture without providing undue electrical or RF noise from the spark plug during ignition. Later experiments were performed with the spark ignition system and with the valve motor spinning to investigate whether further RF screening was necessary, which proved not to be the case. Each figure shows the output of the final ion probe circuit from the output of the second Schmitt trigger, i.e. a 5 volt digital signal. The relative time resolutions for Figures 4.22.4.23 and 4.24 were 10ms per division, 5ms per division and 1ms per division. When there was an increased ion density between the probe electrode and ground (the tube wall) the ion probe circuit amplified this current sufficiently to the saturation voltage. Each of the plots are triggered on channel 1 (the top channel) which was located at 725mm, closest to the thrust wall. The scope was then set to a range

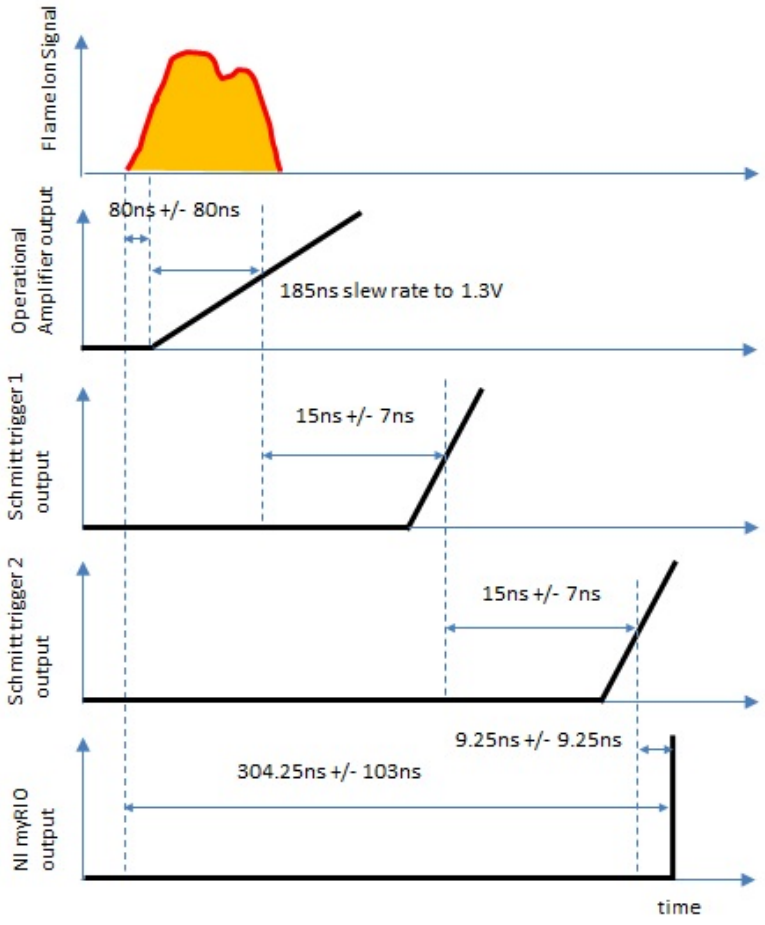

FIGURE 4.21: Ion Probe Flame instrumentation test. Ignited from the closed end of the tube. Oscilloscope triggered on the upper trace. The middle and lower traces are located at 1010 and 1160mm from the thrust plate, with 0.150 +/-1mm between the ports. 10ms/Div in x, 5V/Div in y for every channel.

of different time division durations to investigate the signal over a range of durations. Figure 4.22 shows the three separate circuit 'high' pulses which were the result of the flame passing along the PDE tube and flickering past the ion probe three times, just after the end of the orifice plates. Each of these three pulses was approximately 5ms in duration. The second trace illustrates a single pulse, with a duration of approximately 10ms. The final pulse illustrates a short duration spike which is thought to be a shock wave due to its extremely short duration and timing which shows a high state before the beginning of the previous trace. This spike is followed by a short duration pulse approximately 5ms in length, thought to be the flame. Figure 4.23 shows the same event with a temporal resolution of 5ms per division in the x axis. Figure 4.24 illustrates the same signal zoomed in to 1ms per division in the x axis. It is evident

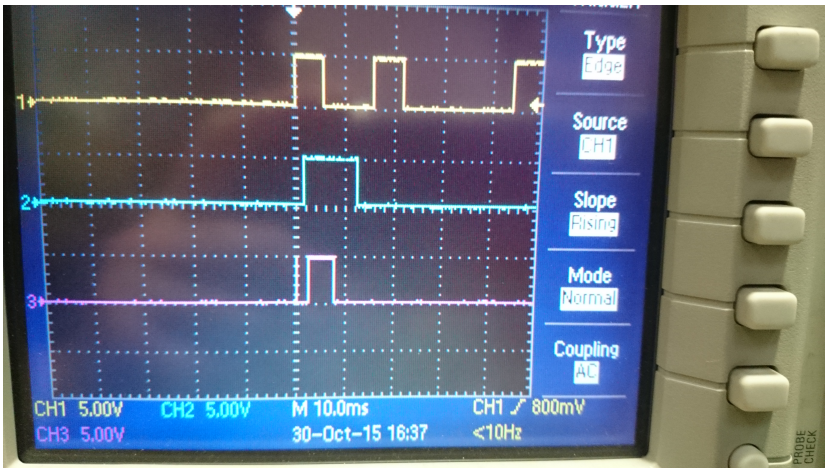

FIGURE 4.22: Ion Probe Flame instrumentation test. Ignited from the closed end of the tube. Oscilloscope triggered on the upper trace. The middle and lower traces are located at 1010 and 1160mm from the thrust plate, with 0.150 +/-1mm between the ports. 10ms/Div in x, 5V/Div in y for every channel.

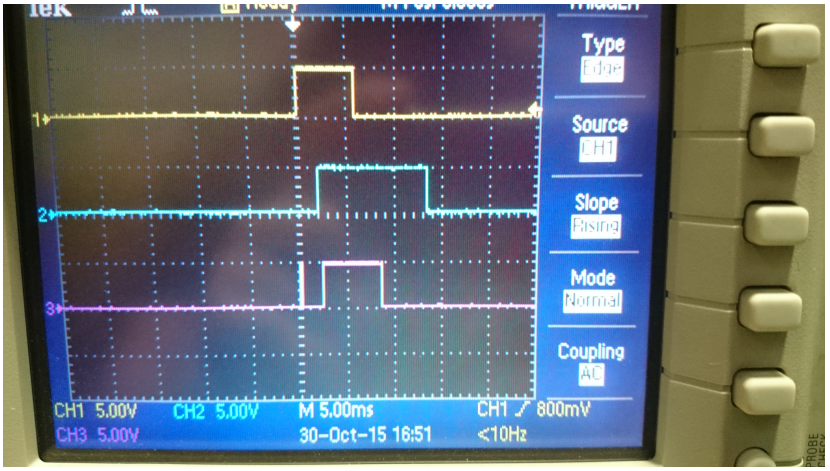

FIGURE 4.23: Ion Probe Flame instrumentation test. Oscilloscope triggered on the upper trace. The middle and lower traces are located at 1010 and 1160mm from the thrust plate, with 0.150 +/-1mm between the ports.. 5ms/Div in x, 5V/Div in y for every channel.

that the duration of the shock wave pulse on channel 3 was approximately 0.25ms in length. The difference between rise times for channel one and two was measured using a measurement function on the oscilloscope to be 1.9ms providing a flame speed of 160m/s. The time of flight between probe 2 and 3 was measured as 280μs, providing a flame speed of 544m/s, and the distance in the time of arrival between the spike and the flame on channel three was 2.2ms.

Figure 4.25 illustrates the effect of intentional end ignition, providing a quick functional check on the sensors and proving that the the instrumentation is capable of registering

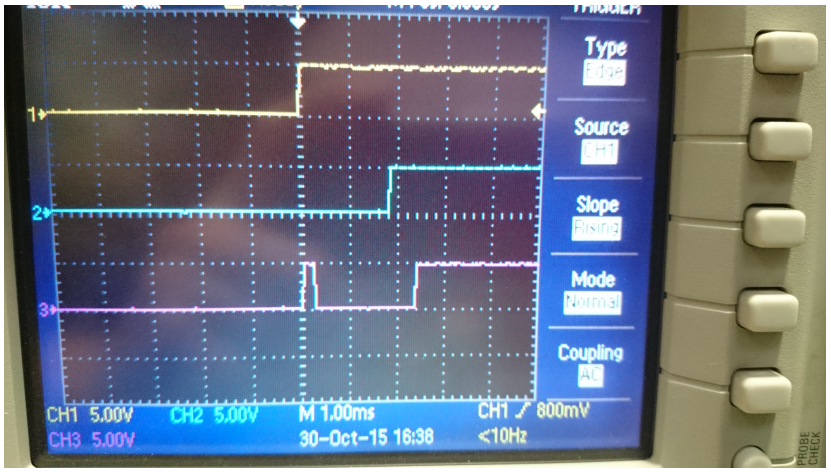

FIGURE 4.24: Ion Probe Flame instrumentation test. Oscilloscope triggered on the upper trace. The middle and lower traces are located at 1010 and 1160mm from the thrust plate, with 0.150 +/-1mm between the ports.. 1ms/Div in x, 5V/Div in y for every channel.

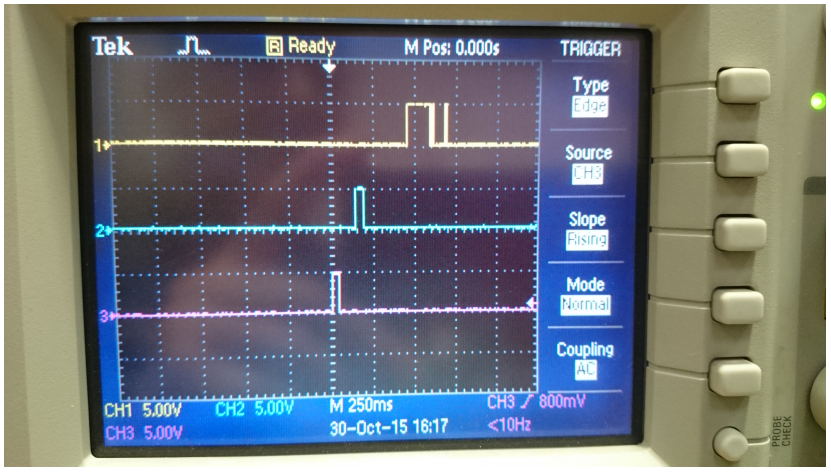

FIGURE 4.25: Ion Probe Flame instrumentation test. Oscilloscope triggered on the lower trace, channel 3. The middle and lower traces are located at 1010 and 1160mm from the thrust plate, with 0.150 +/-1mm between the ports.. 250ms/Div in x, 5V/Div in y.

when the rig is firing in reverse. This test was operated by triggering the oscilloscope on the third transducer, located closest to the end of the tube.

Figure 4.26 shows the data from one shot which was recorded using the high speed ion probe instrumentation and analysed in NI LabView's Diadem system. It can be seen from this data that the flame speed fluctuated dramatically as the shot progressed, untill a velocity of 822m/s was reached. By this point a DDT event had occurred downstream close to the final pressure transducer, generating a flame signal before the natural progression of the deflagrating flame had reached the end of the tube.

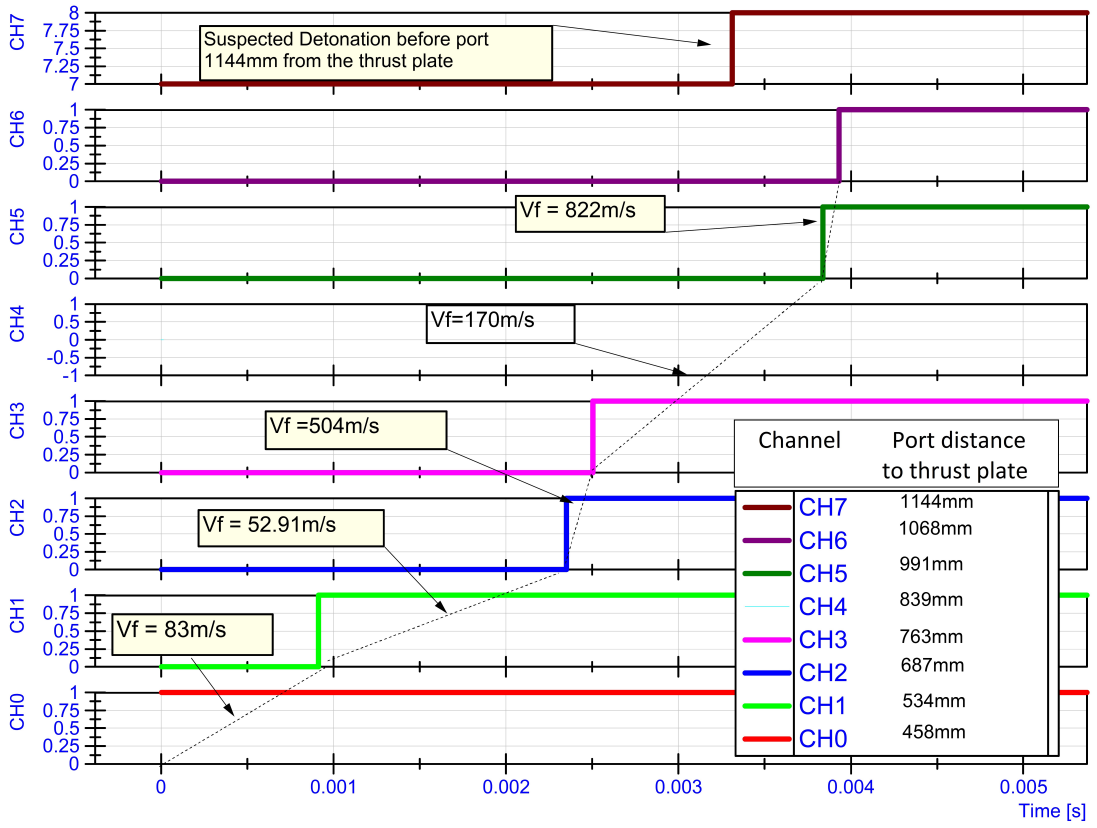

FIGURE 4.26: Ion Probe Flame instrumentation test.8 channels tested simultaneously, with port locations and channel names indicated in the key. Flame speed, Vf is also calculated and presented. Note, channels are not separated at equal intervals. Detonation was suspected at the tube exit, before the 28th port location.

Once the ion probes and amplifiers had been tested, bespoke software was designed to operate on the NI myRIO microcomputer which recorded the digital output from the amplifier circuit. The amplifier circuit contained two back to back Schmitt triggers after the operational amplifier voltage to current converter to convert the small amplified signal to a full 5V digital signal. This signal was sampled at a sampling rate of 160MHz, giving a single sample period of 9.25μs. A full schematic of the final PDE ion probe system can be seen in Figure 4.27, which illustrates the spark signal used to trigger a 100ms recording window on the NI myRIO system. After this window was triggered, a series of up to four high-low pulses could be recorded for up to eight digital channels. The data for each of these pulses was stored relative to the spark circuit triggering time. Ion probes were mounted in the locations shown in Figure 4.28, 345 +/-1 mm, 534 +/-1 mm, 69 8+/-1 mm, 851 +/-1 mm, 1010 +/-1 mm and 1160+/-1 mm from the thrust plate.

A summary of several instrumentation tests can be seen in Figure 4.29. Each of the

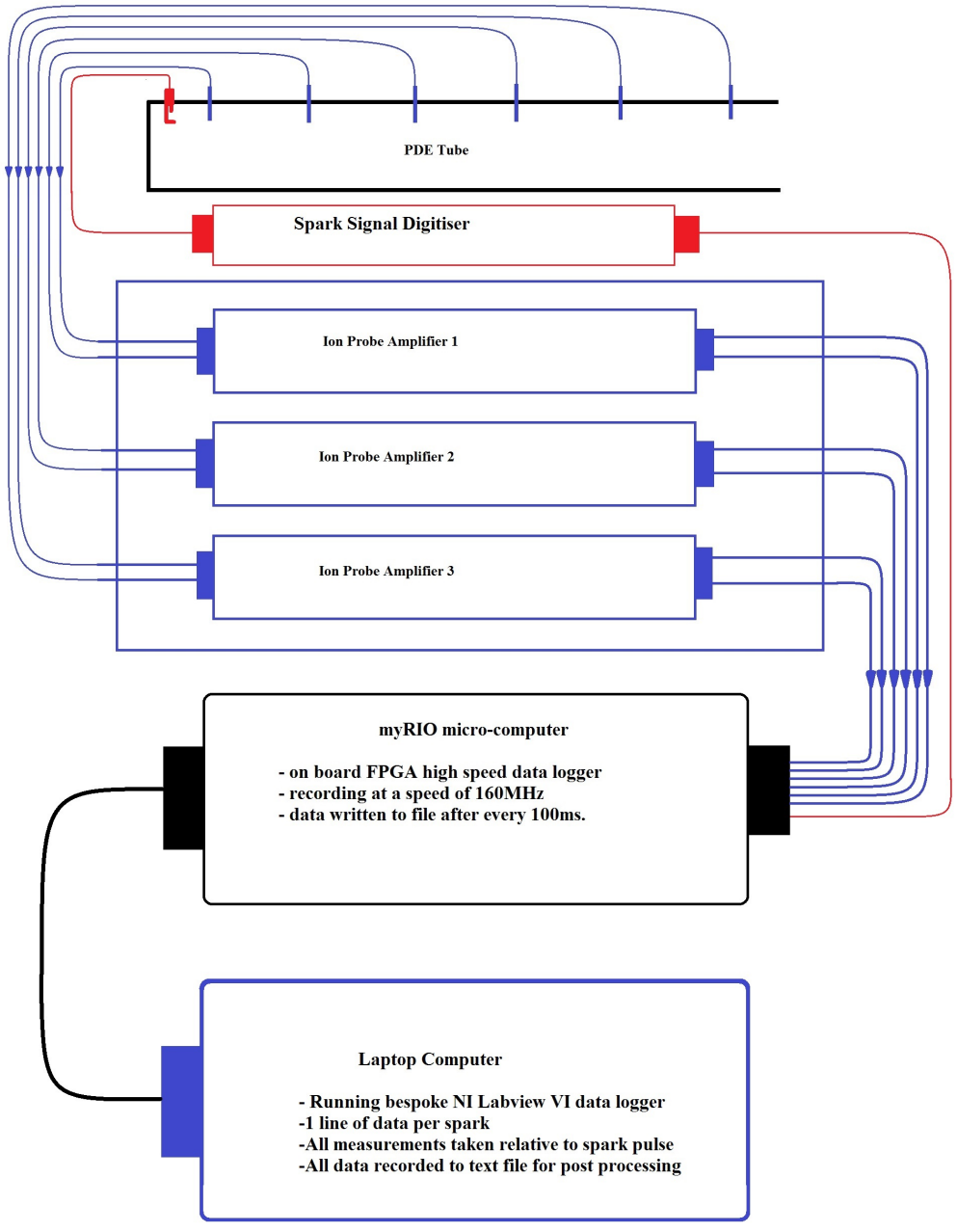

FIGURE 4.27: Finalised ion probe system schematic

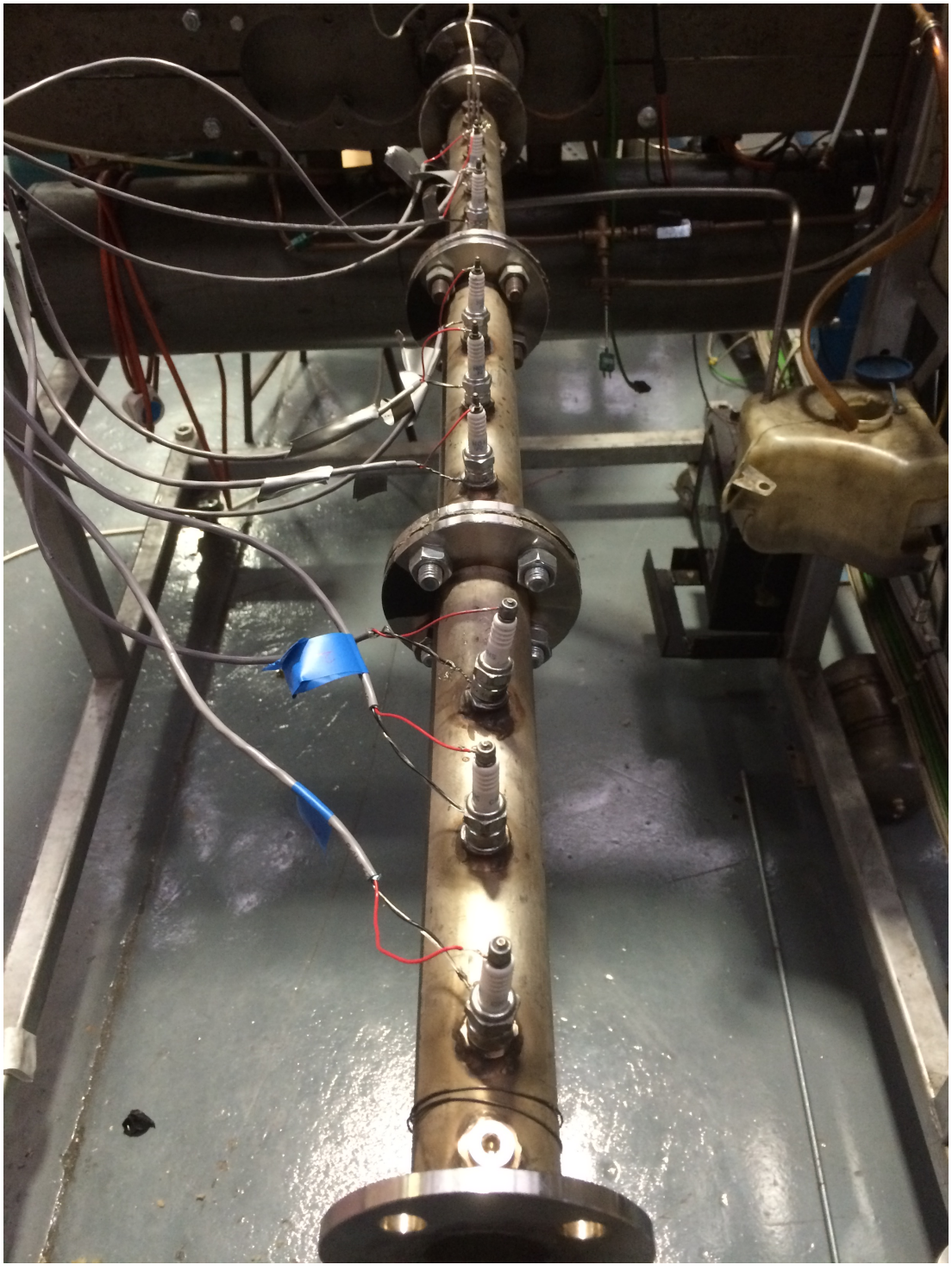

FIGURE 4.28: A photograph of the PDE rig with ion probes fitted into various ports.

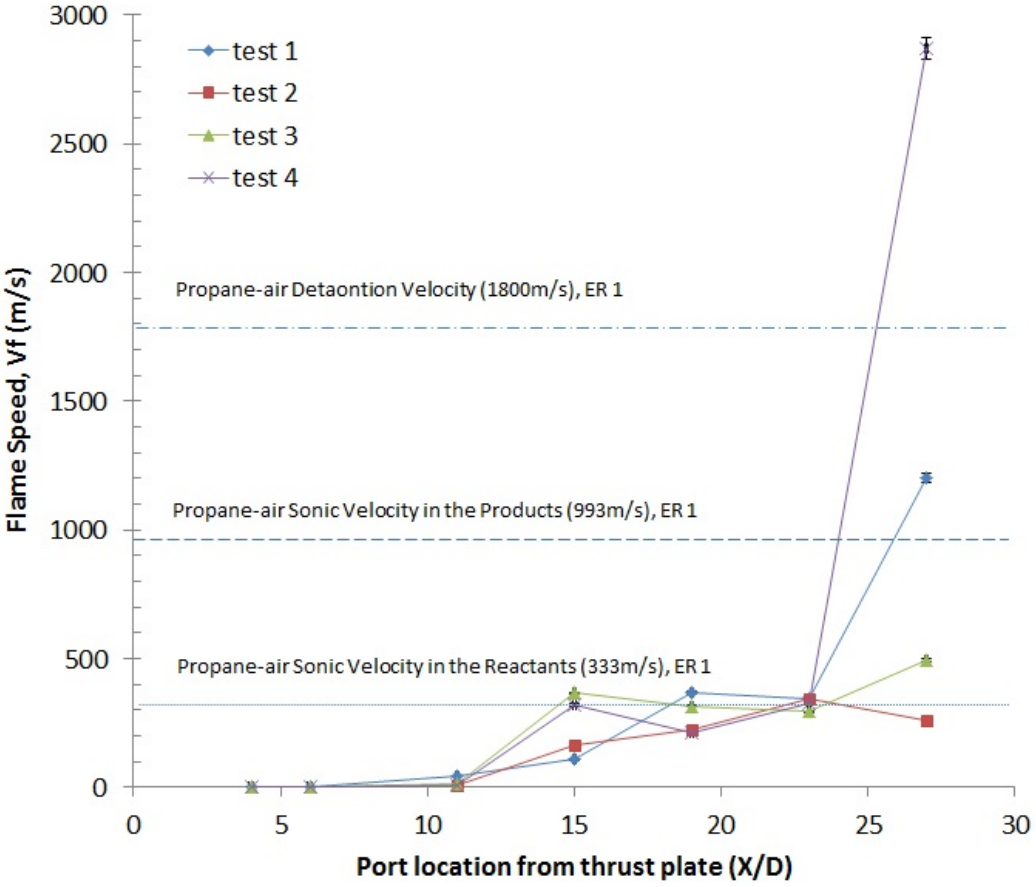

FIGURE 4.29: Ion Probe Flame instrumentation tests with 6 channels tested simultaneously. Ignition was located at the 4th diameter, probes were located at 345 +/-1 mm, 534 +/-1 mm, 69 8+/-1 mm, 851 +/-1 mm, 1010 +/-1 mm and 1160+/-1 mm from the thrust plate. Detonation is clearly observed in tests 1 and 4.

shots recorded were ignited with a spark ignition system located at 305mm diameter along the PDE tube from the thrust plate. Further instrumentation ports fitted with Ion probes were located at 345 +/-1 mm, 534 +/-1 mm, 69 8+/-1 mm, 851 +/-1 mm, 1010 +/-1 mm and 1160+/-1 mm from the thrust plate. As such the first two ion probes were located inside of the orifice laden section of the tube, which was filled with 15 0.6BR orifice plates spaced at 1D. The spark plugs used were each flush with the wall after a number of experiments with longer spark plugs failed when the ceramic fractured due to the extreme force from shocks and high speed flow passing the protruding plug. This caused the ion probe circuits to produce a false high reading. As such all of the ion probes were switched for smaller flush spark plugs so that the experiments could be carried out in a repetitive manner without having to replace ion probe sensors regularly. A picture of the rig with ion probes mounted can be seen in Figure 4.28

These tests were then combined with pressure transducer recordings in the final set of experiments using stratified orifice plates. It can be seen from the plot in Figure 4.30 that a great deal of information can be presented regarding the flame speed at different locations using the combination of pressure sensors for shock wave location and peak measurements, in addition to the flame speed measurements. It must be noted however, that some of the data for flame speed showed unrealistically high flame speed measurements which were thought to be caused by spurious noise triggering the flame speed sensors. Even small amounts of noise could trigger the flame speed sensors due to the high sensitivity of the amplifiers and schmit trigger signal digitisers. Such noise can also be seen in the experimental work carried out by Kuznetsov et al. as shown in the analogue ion traces from figure 2.34. This noise was only present just before the flame approached the ion probe, as also shown in figure 4.30, and was not present at any other time before the the flame arived after spark was ignited. Only four high-low pulse cycles could be recorded by this system in the time frame of one ignition cycle with the memory available on the myRIO. It would have been advantageous to be able to see the anologue output trace of the amplifiers, however there were too few anologue inputs available for in the high speed DAQ system. As a result the system was designed around a high speed digital recording system. Shots with these high flame speed measurements were removed from the data set, and treated as poorly recorded data. Future development of this system could see the trigger threshold of the Schmit trigger ciruit increased by reducing the gain of its preamplifier. In this manner only a true flame would trigger a sensor. This sensor optimisation activitiy was deemed to require resources beyond those available for this work, and so the digital system was used as it is presented here.

The data presented in Figure 4.31 is the raw, calibrated data read directly from the data storage file. It can be seen that there is a large degree of random noise on the pressure signal curves, which distracts from the true shape of the curve. As a smoothed plot of the data is presented in figure

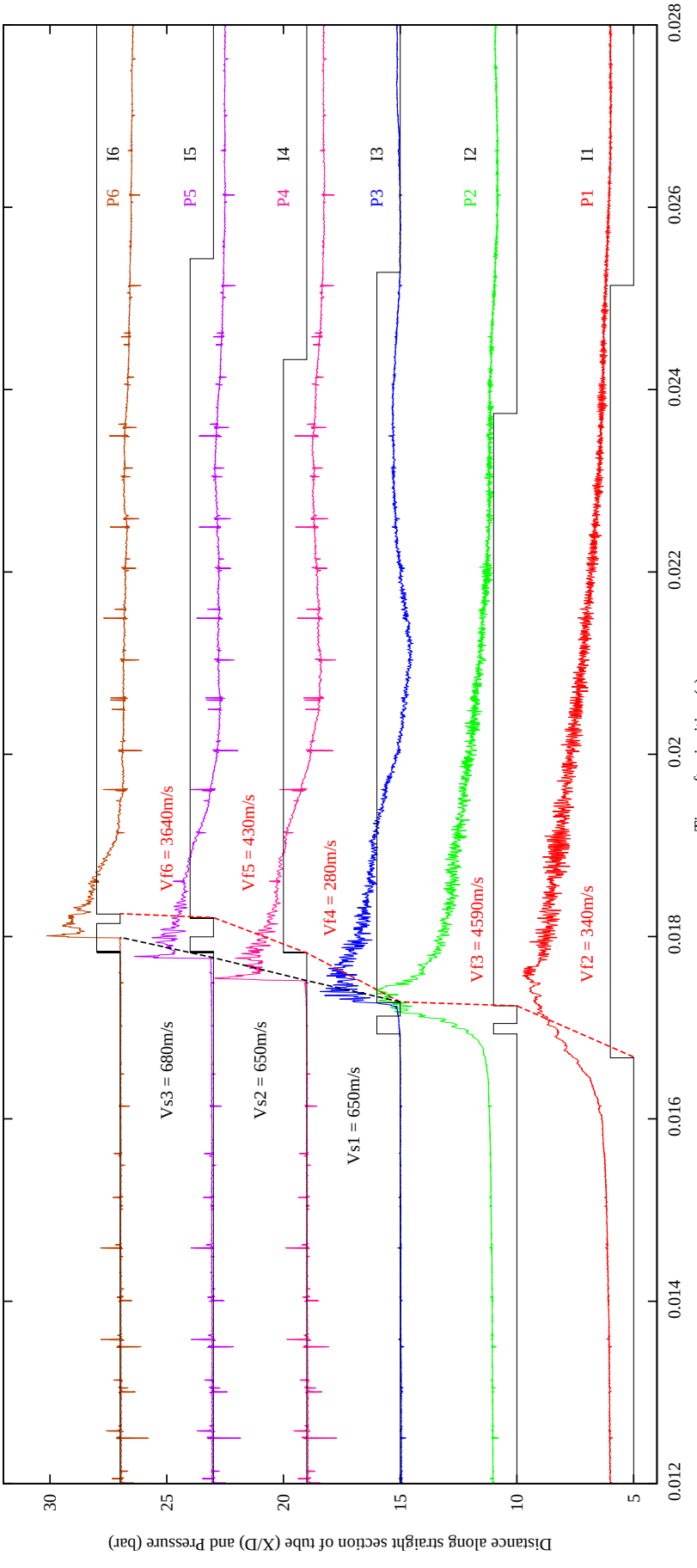

FIGURE 4.30: Orignial data 0.57BR DDT showing explosion within the explosion but not detonation.The equivalence ratio for this shot was recorded as 0.999. The plot starts 12.37ms after ignition.

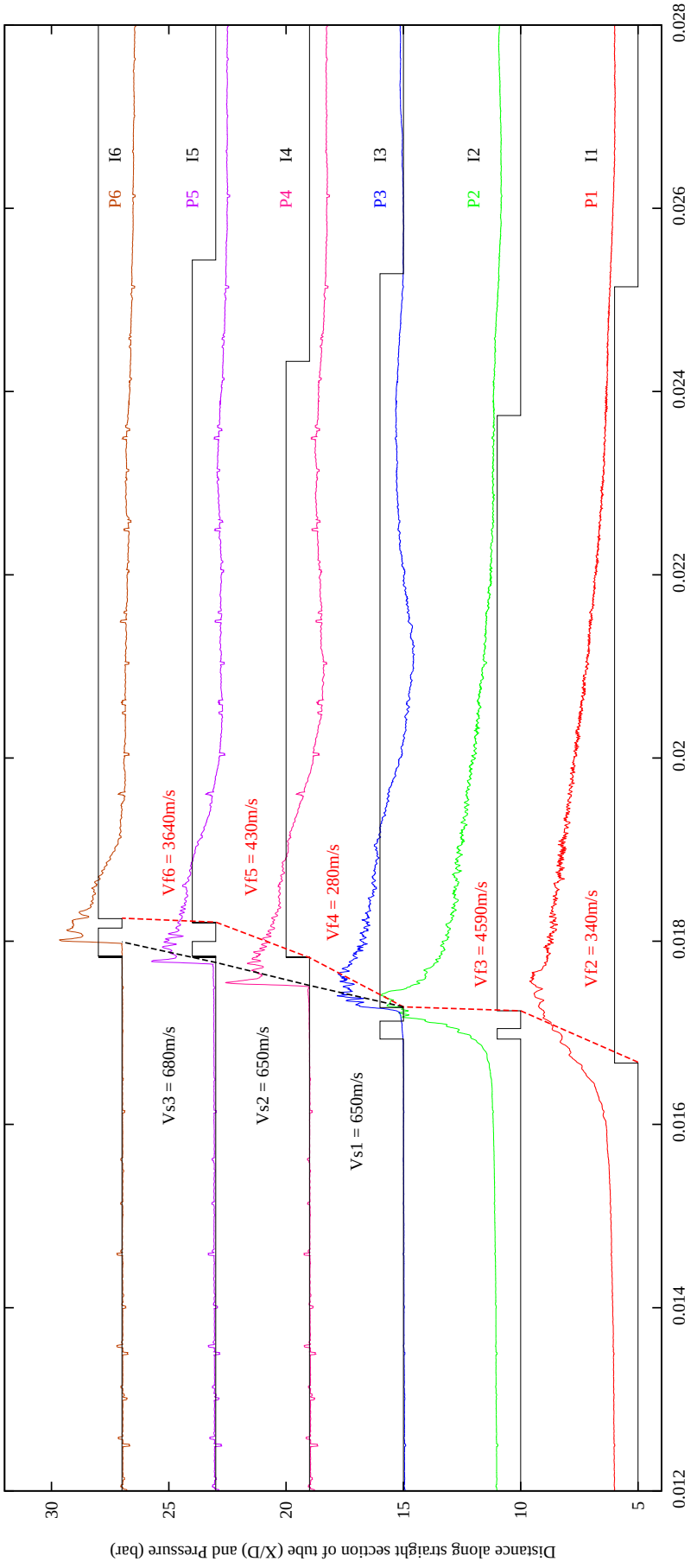

FIGURE 4.31: Smoothed pressure traces. 0.57BR DDT showing explosion within the explosion but not detonation.The equivalence ratio for this shot was recorded as 0.999. The plot starts 12.37ms after ignition.

4.6.4.3 Photodiodes

Photodiode flame sensors were investigated after the initial failure of the first prototype ion probe circuit. Ben Kitchener developed an ion probe circuit which was capable of detecting a flame from a cigarette lighter. This circuit as also tested using an LED as a light source, to determine the rise time in comparison to the LED current rise time, as shown in Figure 4.32. The response time was characterised as 200ns from the time voltage was applied to the LED until the photodiode detector circuit reached an output value of 0.5V. The photodiode circuit's peak output value of 5V was reached after a 350ns delay.

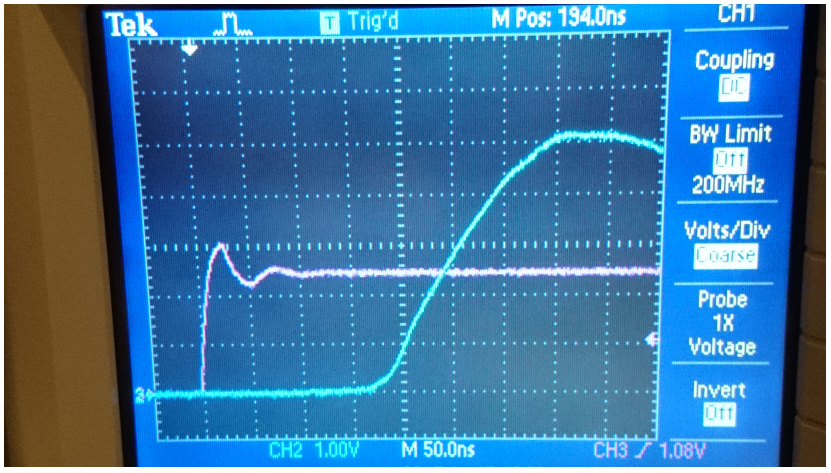

FIGURE 4.32: Response plot for the photodiode and amplifier circuit output in blue and the LED driver circuit signal from a signal generator in yellow .The LED circuit rises first followed by a delay and then an increased measured voltage output on the photodiode circuit output

Figure 4.33 gives an indication of the circuit size, which was designed to be housed within a 25.4mm diameter housing which was designed to be thermally isolated, electrically isolated and pressure resistant. This circuit was mounted in a housing which was isolated from the combustion system by means of a sapphire window, as shown in Figures 4.34 and 4.35. The distance between the combustion chamber and the window was sufficient that the window was kept at a relatively cool temperature and the photodiode was cool enough not to melt its plastic optical housing. This system was tested, however the infra-red photodiode was not sensitive enough to the flames spectra to generate a useful output voltage. It was decided that later work would be carried out with ultra-violet photodiodes or photo-transistors which have a much higher gain.

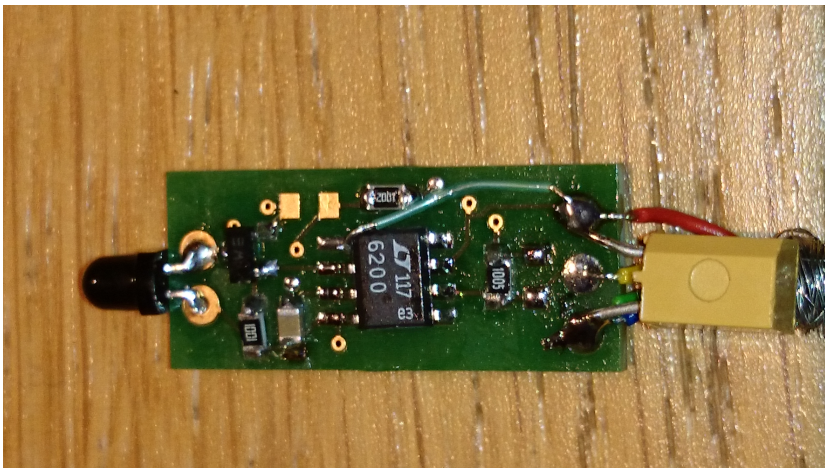

FIGURE 4.33: Picture of the circuit mounted Photodiode circuit design

FIGURE 4.34: Picture of the dissassembled photodiode mounting system.

FIGURE 4.35: Picture of the assembled photodiode mounting system

4.6.5 Data Acquisition and Control

Experimental data acquisition and control (DAQ) was achieved using National Instruments(NI) LabView (LV) 2012 software in combination with a NI SCXI chassis and NI cDAQ (compact Data Acquisition and Control) chassis set up according to table 4.4. After setting up the experimental equipment, all of the data was recorded using in-house software which records at two distinct frequencies. Background data, such as inlet temperature, pressure and mass flows of the fuel and air streams were all recorded at 3S/s, whereas the dynamic pressure transducer voltage was read and recoded using a data logging system which uses LV's inbuilt TDMS (technical data management streaming) functions to record data up to the maximum frequency of the NI cDAQ-9171 card (1 MS/s). The low recording frequency of the operating condition data was a direct result of complex iterative calculations adopted from the orifice plate standard which had to converge before one loop was complete. As a result the recording frequency of the rigs operation conditions were all simultaneously limited by the main loop of the LV software to around 3Hz. This method allows high speed data acquisition to effectively monitor the PDE pressure and log this data stream whilst controlling the operating conditions safely. The logging software was set up to query the test engineer about the test configuration before running each test so that the engineer has a second data storage point when post processing results.

NI Part Number	Name in NI Max	Example Channels
NI SCXI-1001	SC1	Operating Conditions/Control
NI SCXI-1102	SCMod1	Thermocouple Card
NI SCXI-1102C	SCMod3	Rig Static Pressure
NI SCXI-1102C	SCMod4	Rig Static Pressure
NI cDAQ-9171	cDAQ1	Dynamic Pressure Chassis
NI cDAQ-9223	cDAQ1Mod1	Kistler Dynamic Pressure Transducers
NI cDAQ-9171	cDAQ2	Dynamic Pressure Chassis
NI cDAQ-9223	cDAQ2Mod1	PCB Dynamic Pressure Transducers
myDAQ	cDAQ2	UOS FSS1

TABLE 4.4: National Instruments Data Acquisition System hardware set up

Figure 4.36 clearly illustrates the PDE DAQ and control environment observed by the test operator when operating the PDE. It should also be mentioned that whilst navigation to this screen where the test can be begun, two mandatory screens which cannot be avoided request the details of the test and save all of the information in a

separate text file named test-config.txt. Options are chosen from a set of drop down menus and text boxes with questions forcing the test operator to fill in the test details every time the software is run. In this way the data recorded by the test engineer in the PDE test log book can be verified against an electronic copy which stores all of the test configurations in one place. This file saves information such as the fuel type, stoichiometry, orifice number, BR, and type of orifice plates, as well probe location automatically prior to every test. When each test is started a new folder is opened which saves all of the test data, including the configuration file, the operating condition data text file which is recorded at 3S/s and the high speed data logging file which is recorded at 500KS/s or more. Each of the files are stored in a folder which automatically references the time and date of the start of the test, so that the high speed data, operating condition data and test conditions are stored safely and routinely using the same folder name format.

Instrument calibration files were stored automatically in text file format for each instrument, and indexed to the most recent part of the file using LabVIEW programs which had been previously written. This data was then uploaded from the file into the NI LV PDE operating program whilst running and used to convert voltage or current signals at the NI DAQ to a meaningful physical reading to be read by the operator and logged. Whenever a new calibration was carried out, the data and linear calibration curve constants were stored in the file for the relevant transducer. Calibrations were carried out at least once per year, or after re-ranging the instrument, which ever came first. Static pressure transducers were calibrated using a Druck pressure calibrator unit, which is used for all in house pressure calibrations. This unit is externally calibrated once a year by external calibration company Pennine instruments. Dynamic pressure transducers were purchased calibrated or calibrated at the start of this work using external supplier Trescal.

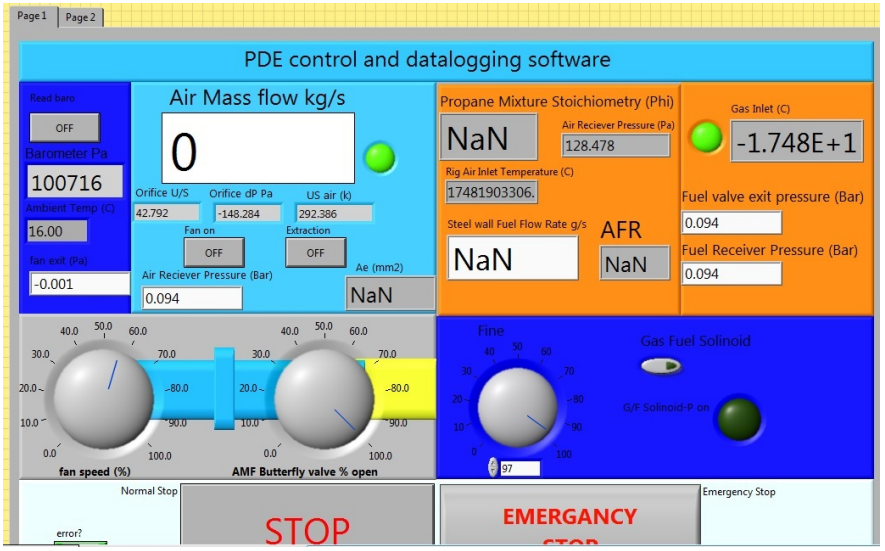

FIGURE 4.36: LabView PDE Experimental DAQ VI- controlling and recording operating conditions whilst logging high sampling rate channels simultaneously

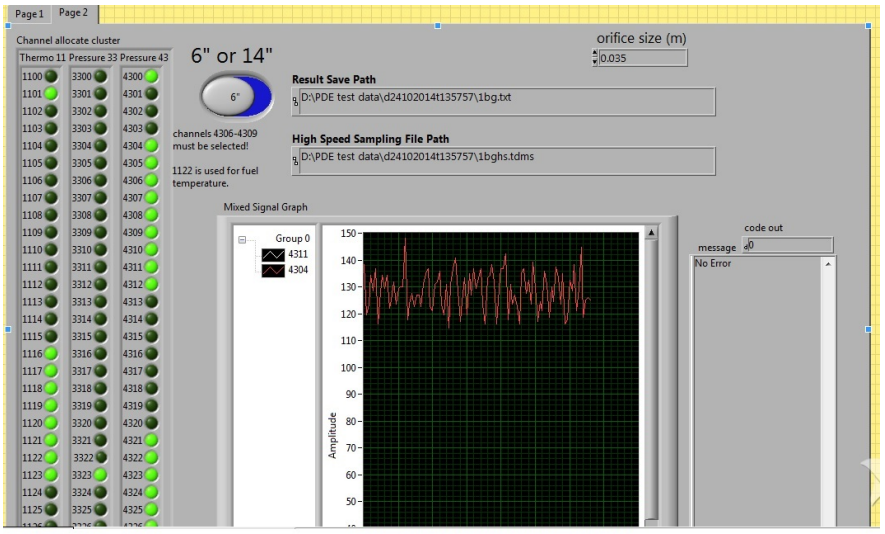

FIGURE 4.37: LabView PDE Experimental DAQ VI channel allocation set up.

After these files are generated the main test can begin, and the test operators screen is activated, as shown in Figure 4.36.

4.6.6 Results Post Processing

High speed data logging software has been used to record data at sampling rates of 500KS/s and with the capability to record on 8 channles at a frequency of 1MS/s in combination with NI high speed DAQ systems. A limited amount of this code can be seen in AppendixA A.1 to A.18.

4.6.6.1 Pressure peak evaluation software

All pressure and operating conditions data were post processed using in-house LV code, due to the large size of the each TDMS pressure logging file, which was of the order of 1Gb for less than five minutes of testing time. To conserve the amount of computer memory used in post processing the number of TDMS data points assessed at any one time was 20kS. This number was carefully chosen to correspond to the approximately one tenth of the period between ignition points in the dataset with a PDE firing rate of 5Hz. Each sequential 20k data points were interrogated using a LV waveform function which recorded any data points over 0.25 bar and registered this as the beginning of a peak. The value of 0.25 bar was used to filter out any unwanted noise in the signal, which tended to be a single sample in length (1/500,000 seconds) but provided a source of error to the post processing operation. This waveform function then parsed 1k data points after the initial peak to a waveform peak finding function which recorded the absolute value of the peak and logged this against the sample number. This functionality can be seen in Figure 4.38, which shows the output of the earlier system which did not incorporate signal filtering. At this stage of processing only the voltage peak was calculated, the instrument calibration is applied later on within the next stage of the software. A later version of the software, which was used for all of the figures in this thesis made use of a triangular filtering function, which reduced the noise significantly in the pressure trace, as can be seen in Figure 4.39. This software also outputs a zoomed in plot, as shown in Figure 4.39, which was selected using a trigger threshold and sample width of 3000.

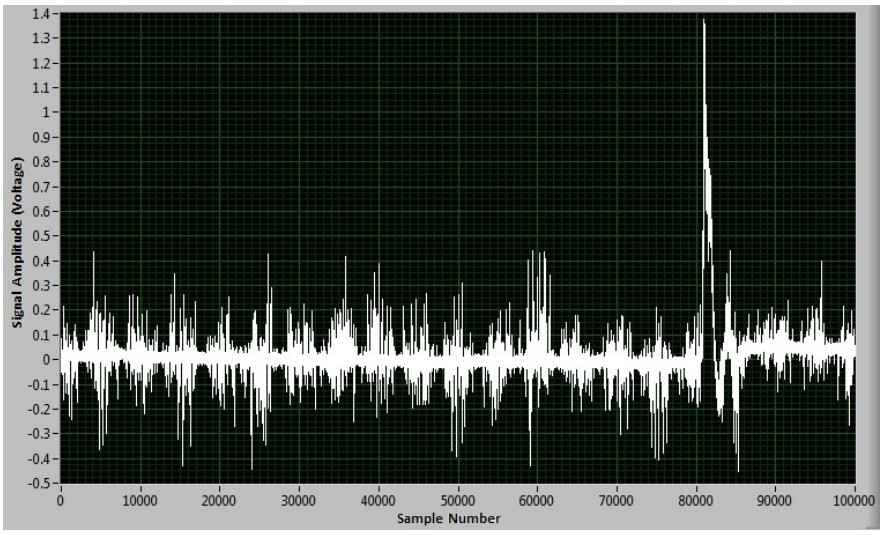

FIGURE 4.38: Unfilterer High Speed Pressure Peak Finder Post Processing VI output

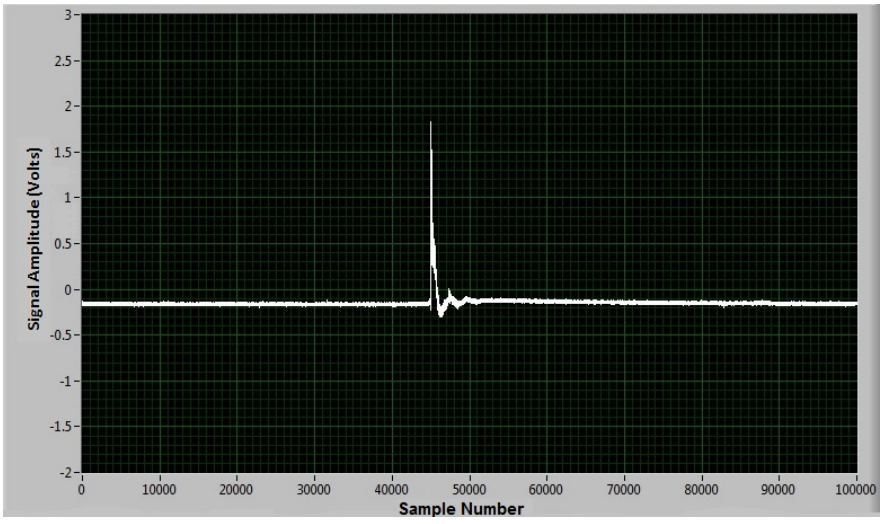

FIGURE 4.39: High Speed Pressure Peak Finder Post Processing VI output, with filtering incorporated. Large sample width output.

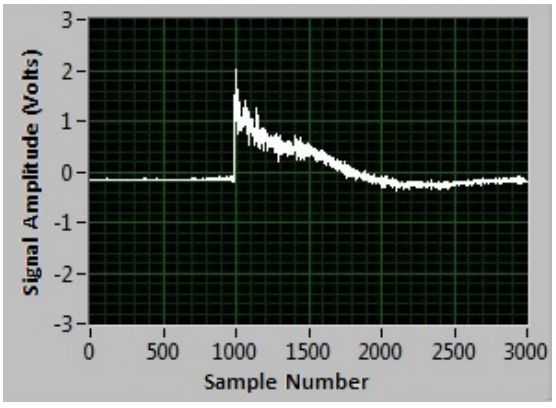

FIGURE 4.40: High Speed Pressure Peak Finder Post Processing VI output, with filtering incorporated. Small sample width plot output.

To understand how this software operates in greater detail it is necessary to look at the LV software block diagram shown in Figure A.19. To the left of the figure we can see automatic manipulation of the file path which determines the save path for the text file containing the LV softwares results. This programmed system determines the channel name (Kistler1, 2, 3 or 4) which is controlled from the 'channel names' drop down selection box on the front panel. This string is concatenated with the TDMS file path which has been reduced, removing the file name type and replacing this with the string 'peaks' along with an optional save path string which allows the operator to find data more easily if the operation needs to be carried out repeatedly. Once complete, the TDMS file is opened, then the properties are listed (such as which channel is being read), the selected channels properties are then parsed into the the TDMS file reader which runs in a for loop extracting 20k samples within the main programs for loop. Once the for loop is complete, this data is parsed into the second half of the software shown in Figure A.20.

Figure A.20 shows the post processing analysis side of the in-house peaks finder software. Firstly, the data is parsed from the for loop into a smoothing filter which is used to help reduce noise for triggering the data. This smoothing filter is not applied to the main data stream which is used for saving data, but only to help reduce erroneous noise which is usually only one or two samples in length. Due to the short noise duration the smoothing filter uses a triangular moving average with a half width of one hundred samples (0.2ms), which was chosen by trial and error. Once the filtered stream is triggered on a rising edge with a value greater than 0.25 bar gauge, the main data stream is interrupted and a subset of 1000 samples were extracted from the waveform. This subset is then parsed onto an amplitude measuring VI which measures the maximum amplitude of the subset. A further check is applied to determine whether the signal is definitely a pressure signal and not a spike in noise. This check samples the value of the waveform for four consecutive samples 300 data points into the 1000 samples recorded after the trigger. If each of these values is greater than 0.1 bar, the event is determined to be valid. It should also be mentioned that the running average of the baseline pressure before the triggered value is also subtracted from the pressure peak, so that the true pressure is recorded, not a biased pressure. This amplitude and sample or index number is then recorded, as long as saving conditions are met. A further saving condition is that the start of the sample subset must be below 0.1 bar to ensure

that the subset is not measured part way into a peak, but from zero pressure to the maximum peak amplitude. The peak finding VI also has the capability to count the number of peaks as they are being analysed to help the operator determine whether the run was successful or not at a glance.

Once the pressure data had been post processed to find peaks above 1.0 bar and the corresponding data point the data was output into a text file and then the next 20k data points were interrogated until the end of the TDMS file was reached. The TDMS file start time was then passed on manually to a separate LV program (VI) which was used to link the operating conditions, or back ground data such as the fuel and air mass flow for each point. This was a complex process as the pressure data was interrogated for sample number and the operating conditions were interrogated against operating system time, so the operating conditions VI interpolated between each second and the 3 data points stored within each second of recording time to find the appropriate operating conditions for each pressure peak.

The respective functionality of these two pieces of software were then combined into one VI which handled all of the data from each test condition and searched for file names automatically, as they were stored automatically according to a uniform system across all data sets. This increased the speed of post processing data considerably. This VI's LV block diagram can be seen in Figure A.21. This process is carried out within a while loop, logging each one of the triggered pressure peaks until the end of the TDMS file is reached, after which the true/false case structure is activated to run the in-house peaks-operating condition linking software: OC-HSP LINK CODE VI.

4.6.6.2 Other software

Similar software was designed for this project and is listed below:

Shock speed measurement Software has been developed which is capable of measuring the shock speed between two consecutive dynamic pressure transducers. This software used the derivative of the pressure signal in time with a trigger threshold set just above the background noise in the pressure derivative signal to detect shock waves passing. The rest of the software was very similar to the

pressure peak measurement software, only that it was duplicated so that the difference in the time stamp between two consecutive signals could be measured. This allowed the time of arrival for each shock wave to be detected and processed in the same manner as the peak dynamic pressure results

Operating condition time stamp matching software It was necessary to write software to link the operating condition file to the time stamp of the pressure peaks, shock waves and flame speed measurements in order to select results which were gathered at the correct operating equivalence ratio. This software took the time stamp from the data file of interest and interpolated the same time from the back ground operating conditions file, which had been recorded at 3Hz. The results were then saved to a comma separated text file which could be read into Microsoft Excel for post processing.

First spark time detector In order to match data from the ion probe results with the operating conditions file it was necessary to find the first spark signal for a given experiment. Each spark was recorded on both high speed data logging cards as well as the myRIO so that all of the signals could be synchronized and matched in time for each ignition. This allowed for direct comparison of flame speed and pressure data for every single ignition event when this system was installed in the later tests. The software found the first spark time as recorded by the NI DAQ system, this was then passed onto the operating condition time stamp matching software, which synchronised flame speed data with operating condition data

myRIO high speed digital flame ionisation data logger This software was responsible for recording the high speed flame data on board the NI myRIO platform. The system was designed and built specifically for this project by Ben Kitchener, an Instrumentation and Control Technician at the University of Sheffield in the Department of Mechanical Engineering. The software was programmed to sample up to eight high speed digital inputs which operated with 0-5 volt signals at a frequency of 160MS/s, simultaneously. This allowed for a timing error of 9.25ns for each signal. This system was programmed into the core of the microprocessors FPGA (Field Programmable Gate Array) as regular higher level programming was not fast enough to operate at these speeds on this hardware.

This software was capable of recording up to four pulses per channel for a maximum window of 100ms per ignition, and output this data at high speed to a text file which was buffered through a USB cable to further software on board a remote laptop. Data was recorded in tics of the software loop, so each tic was 9.25ns in length.

Flame speed measurement software As the data generated by the myRIO system was recorded in time only, this needed to be converted into a velocity by counting the number of tics between a valid flame signal on one port to the next. This software only recorded flame signals which lasted longer than 10ms, as there were a large number of signals which were generated by noise at the ion probe surface. The flame speed was calculated by dividing the measured port separation distance by the time difference between each flame trigger. The speed of transition between of the ports was then recorded against the ignition time pulse difference from the first ignition of the test run. This data was stored in a text file format. Once recorded the data was further processed as discussed above to match the data with the operating conditions and pressure data for the same ignition.

4.6.6.3 Instrumentation summary

The final PDE system was instrumented using the following instrumentation shown in table 4.5:

Instrument Type	Purpose
Kistler 6061B	Four dynamic pressure transducers
Kistler 5037A	Four individual charge amplifiers for K6061B
PCB 113B26	3 dynamic pressure transducers
PCB 2 482C05	4 channel signal conditioner
UOS FSS1	Six In-house flame speed sensors
NI cDAQ-9171	DAQ chassis
NI cDAQ-9223 (1)	High speed analogue DAQ module 1 (Kistler & Spark)
NI cDAQ-9223 (2)	High speed analogue DAQ module 2 (PCB & Spark)
myDAQ	High speed flame ion detector digital DAQ system (Ion Probe & Spark)

TABLE 4.5: National Instruments Data Acquisition System hardware set up

4.6.7 Summary of Rig Changes

The third and final iteration of the University of Sheffield PDE rig during this work had the following aims:

- To continue to operate with sufficient degree of reliability in respect to injection valve timing, ignition timing and fuel air mixture to create measurable results for the purposes of this experiment.
- To replicate conditions present in Ciccarelli's FA experiment presented in Figure 2.14 of Section 2.1.6, at the same time as promoting detonation, if possible.
- To measure flame acceleration in such a way that it could be reported well by means of regularly interspersed flame speed sensors using time of flight(TOF) measurements as well as pressure transducers to measure the shock wave speed and pressure peaks during FA, DDT and Detonation blow down if the later stages of the DDT process are observed.
- To determine whether the hypotheses about accelerating flames through varying BR orifice arrays are correct or not with a sufficient degree of statistical accuracy (i.e. small enough measurement error at the relevant speed) to determine whether there are differences between each test case and to determine the size of this difference.
- To gather sufficient information regarding the operating conditions of the rig with appropriate accuracy in both time and measurement quantity to be able to determine whether the results are of statistical significance.

System upgrade	Prior Art	1st Iteration	2nd Iteration	3rd Iteration
88.9mm diameter, 1000mm long combustor	X	X	-	-
Peristaltic mechanical fuel injection	X	X	-	-
Mobile combustion unit to allow for use at the LCCC	-	X	X	X
Calibrated air and fuel flow measurement	-	X	X	X
Kistler 90kHz pressure instrumentation	-	X	X	X
High speed data acquisition system (NI 9223)	-	X	X	X
38.1mm diameter 1200mm long combustor	-	-	X	X
Modular combustor geometry	-	-	X	X
Mechanically timed electrical fuel injection	-	-	X	X
Time of flight measurement with Kistlers	-	-	X	X
Diametrically opposed ports	-	-	-	X
PCB 400kHz pressure instrumentation	-	-	-	X
Time of flight measurement with ion probes	-	-	-	X

TABLE 4.6: Documented upgrades of the UOS PDE system installed at the LCCC

4.6.8 Standard Operating Procedure

1. Check the flow metering orifice is the correct one and that it is installed in the correct direction, change if necessary. Ensure that the LV PDE software has the correct orifice value recorded in the set up page

2. Check that the Coriolis meter is set and calibrated for the flow range of interest using the Haart instrument calibrator

3. Set the motor speed controller to the desired frequency and start the PDE valve motor spinning.

4. Switch on the PDE igniter solenoid to ensure any gas remaining in the system is ignited.

5. Press the start button in the NI LV PDE control and DAQ software to start the test software operation.

6. Fill in test configuration boxes.

7. Ensure that all of the correct transducers are selected in the set up panel of the front end (see 4.37)
8. Start the atmospheric line fan.
9. Set the atmospheric line fan control valves to the desired value
10. Wait for mass flow to reach the desired value from table 4.3 for the set operating frequency.
11. Set the fuel valve to zero.
12. Switch on the fuel solenoid.
13. Increase the fuel mass flow until the Equivalence Ratio indicator reads 0.66 (bearing in mind the fill factor is 1.5, so 0.66 refers to ϕ=1).
14. The rig will then start to fire.
15. Wait for two minutes, maintaining $\phi = 1$.
16. Switch off the fuel supply solenoid.
17. Switch off the ignition.
18. Switch of the atmospheric line fan once the rig has cooled.
19. Press the regular Stop button on the software interface.

4.6.9 Emergency shutdown procedure

If at any point in this procedure an incident occurs, such the occurrence of a fire in an unwanted area or the loss of valve control, the PDE emergency stop button, or the e-stop on the side of the rig should be pressed. Either of these buttons will immediately stop the flow of fuel to the rig by stopping all of the fuel solenoids in the line. Once the e-stop circuit has been activated, the e-stop circuit must be reset by resetting the e-stop switch prior to the rig being operated again.

4.7 Preliminary Results and Discussion

A series of preliminary tests were carried out on the 88.9mm diameter tube and compared later with results from the 38.1mm diameter tube. The premise for manufacturing the second, smaller tube was that flame acceleration process should be able to take place over a shorter length, providing a more practical engine size for propulsion on small airborne platforms.

4.7.1 88.9mm Diameter PDE ignition delay experiment

Figure 4.41 shows the effect of changing the ignition delay time on the success of audible ignitions, recorded using a microphone. A fire or misfire event could be clearly determined by the presence or absence of the regular explosions at the chosen cycle frequency, which allowed the percentage chance of success to be recorded for each of the ignition delay conditions, cycle frequencies an equivalence ratios. This test was carried out prior to the installation of calibrated pressure measurement instrumentation to find the optimal ignition delay on the rig, which was chosen to be 140ms. It was thought that the scatter reduced with increased ignition delay as a result of increased homogeneity in the mixture, as greater time was given for the mixture to be fully mixed after injection and before ignition near to the closed end of the tube. This test was carried out with nine $0.6BR$ orifice plates in the 1m long, 88.9mm internal diameter PDE tube.

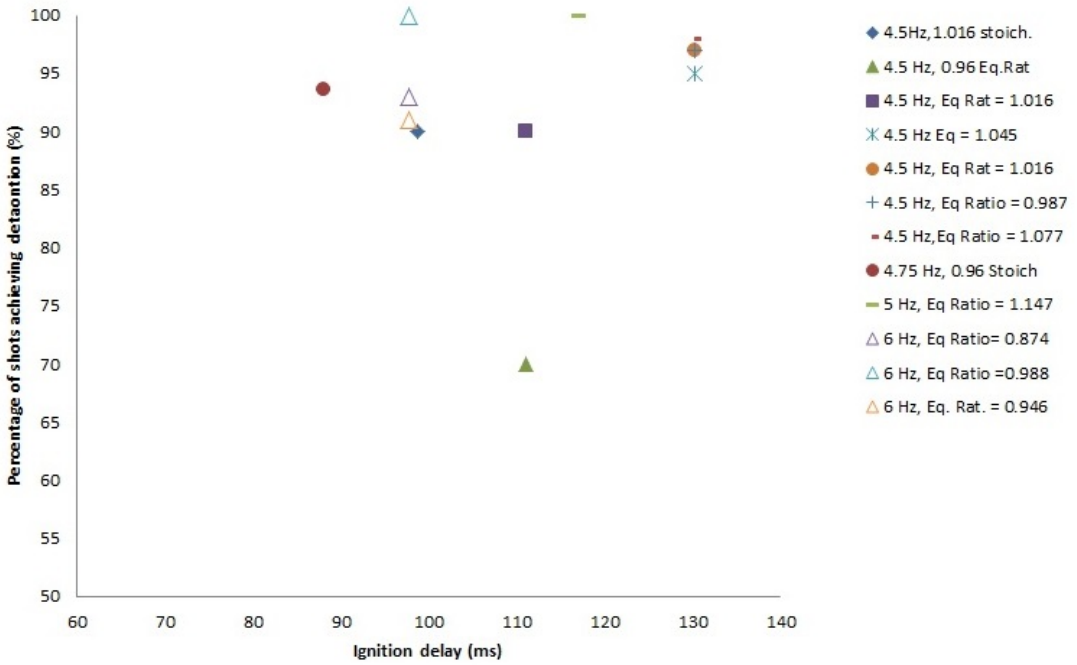

FIGURE 4.41: Results from the initial commissioning tests- ignition probability vs ignition delay

After installing calibrated Kistler charge amplifiers and pressure transducers into the PDE a series of tests were carried out using a range of orifice plate dimensions. This PDE tube and the plates had been manufactured by previous students, but had not been tested appropriately under the correct conditions, as insufficient instrumentation had been used in previous tests.

4.7.2 88.9mm Diameter PDE Dynamic Pressure Measurements

The test illustrated in Figures 4.42 to 4.45 were carried out with nine orifice plates in each case in the initial 88.9mm PDE tube illustrated in the top half of Figure 4.9.

In order to fully represent the range and frequency of different pressure results at each port location statistical density functions have been used as discussed in the Literature Review Gap Analysis, Section 2.7.3. This is the first time data has been plotted in this fashion, and hopefully represents a fuller picture of the data generated by PDE FA experiments. Usually the mean and standard deviation of the results are plotted in FA and PDE experiments, presenting the reader with a reduced picture of the experimental results.

Frequency distributions have been used to plot the likelihood of each pressure as a portion of the whole set of data for each port location. Port locations along the tube are shown in the x-axis, as well as probability. The pressure has been recorded along the y-axis and is common to each port location. It can be seen from these initial experiments that there is a wide range of data outside of the standard deviation of the results, and that the data is not symmetric about the mean, as symmetric standard deviation error bars would portray the data.

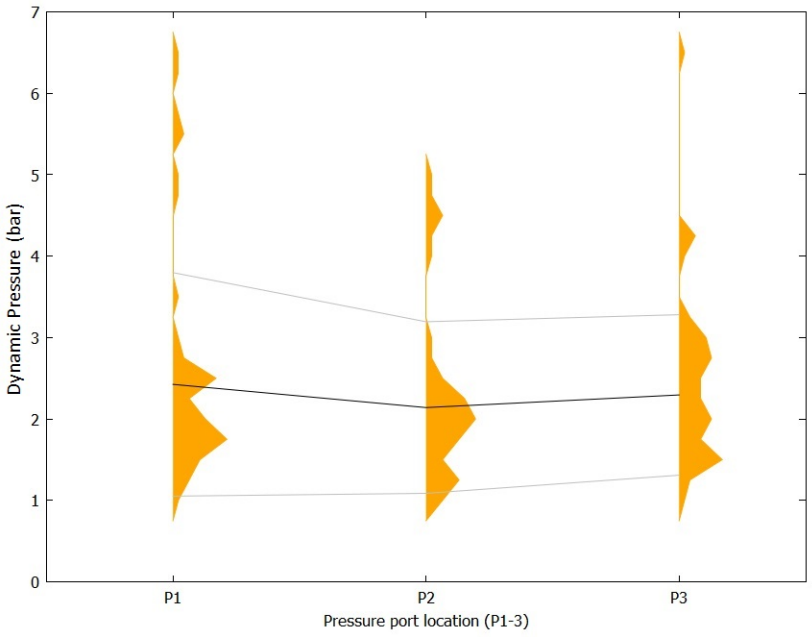

FIGURE 4.42: Results for 88.9mm internal diameter PDE tube with 140 degrees ignition delay and 9 0.46 BR orifice plates spaced at 88.9mm between each orifice plate. Port locations at 100mm, 400mm and 900mm

Figure 4.42 plots the dynamic pressure of the 0.46BR case against the port location. This figure shows that the bulk of the data contains low dynamic pressure shock wave peaks, and a mean value of around 2 to 2.5 bar at each port location along the tube. There are a number of outliers at higher pressures closer to the adiabatic flame pressure in propane, close to 9 bar in this case. The mean pressure reduced between the first and second port locations, and then increased again by the final port location. The standard deviation reduced all of the way along the tube.

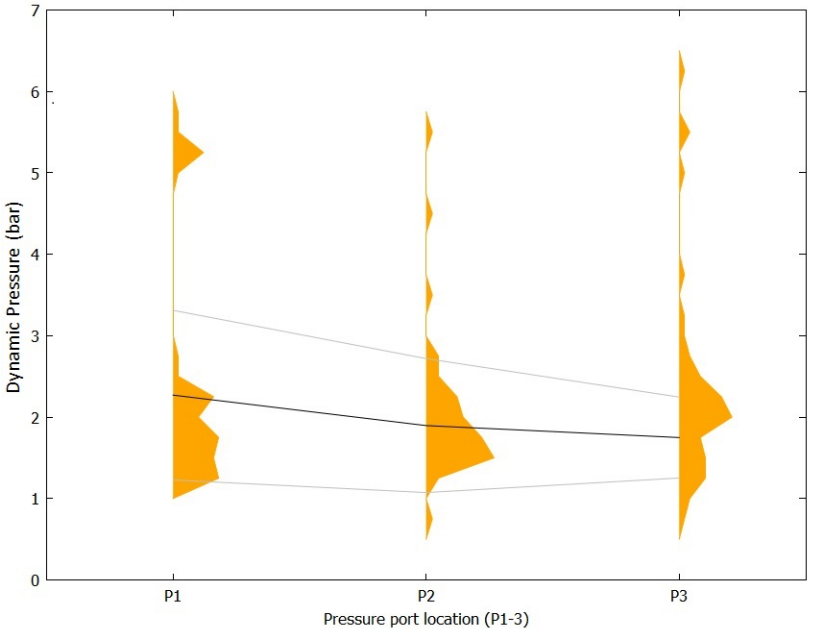

FIGURE 4.43: Results for 88.9mm internal diameter PDE tube with 140 degrees ignition delay and 9 0.6 BR orifice plates spaced at 88.9mm between each orifice plate. Port locations at 100mm, 400mm and 900mm. Eqivelence ratio band $0.942 \leq \phi \leq 1.028$. Mean ϕ: 0.977, ϕ standard deviation: 0.022

Figure 4.43 plots dynamic pressure against port location for the 0.6 BR case. This case exhibits similar patterns to the 0.43 BR case, however the mean values are lower in this case and the trend of the mean pressure is a reducing rather than an increasing one. This case also exhibits a number of high pressure shots which are close to the adiabatic combustion pressure for the propane- air mixture being studied here.

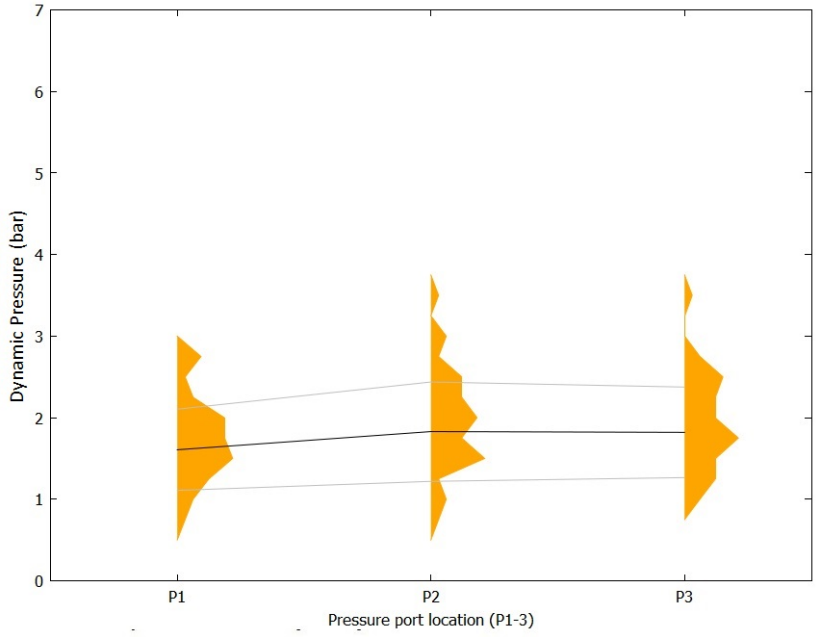

FIGURE 4.44: Results for 88.9mm internal diameter PDE tube with 140 degrees ignition delay and 9 0.75 BR orifice plates spaced at 88.9mm between each orifice plate. Port locations at 100mm, 400mm and 900mm. Equivalence ratio band $0.942 \leq \phi \leq 1.028$. Mean ϕ: 0.983, ϕ standard deviation: 0.029

Figure 4.44 illustrates dynamic pressure vs. distance along the tube for the 0.75 BR case, which exhibits much lower initial mean pressures than the earlier, lower BR cases. The spread of data reduced in this case, in comparison with lower BR results. By the time the shock had reached the second and third port, the mean pressure, standard deviation and spread of results from the frequency distribution had become relatively constant. The final pressure was comparable with the earlier two cases.

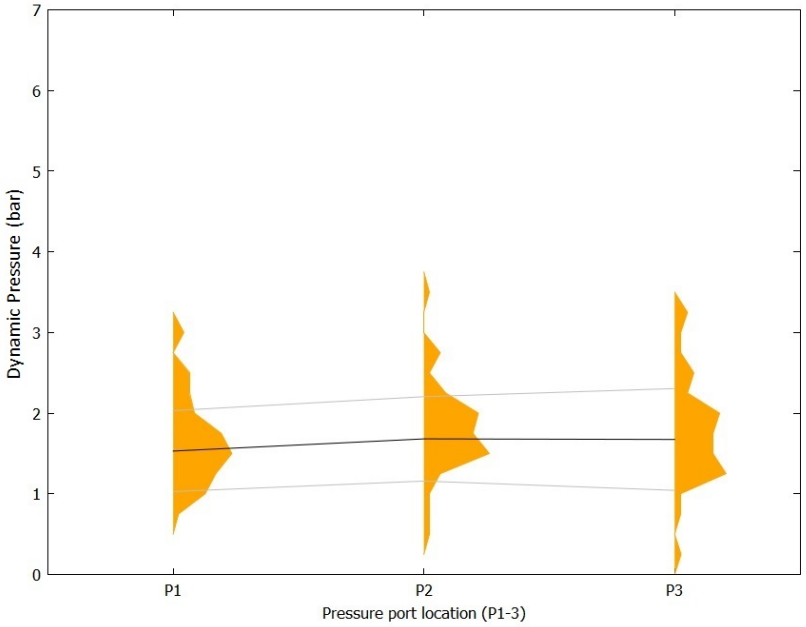

FIGURE 4.45: Results for 88,9mm internal diameter PDE tube with 140 degrees ignition delay and 9 0.86 BR orifice plates spaced at 88.9mm between each orifice plate. Port locations at 100mm, 400mm and 900mm. Equivalence ratio band $0.766 \leq \phi \leq 0.872$. Mean ϕ: 0.843,ϕ standard deviation: 0.029

Figure 4.45 shows dynamic pressure vs. port location for the 0.86BR orifice condition. These results are very similar to the 0.75BR case, with a tightly packed distribution of results and a low mean at each port location. The trend of the mean data is also similar, with a lower initial mean and slightly larger mean dynamic pressure values at the second and third port locations.

4.7.3 Comparison of Results

Figure 4.46 compares results with the same equivalence ratio for the 88.9mm diameter tube and the 38.1mm diameter tube filled with a variety of orifice plates. Both tubes are similar in length with the larger diameter tube being 1m in length and the smaller diameter tube being 1.18m long. Case conditions are noted below the figure for reference. It can be seen that much larger over pressures can be developed by FA in smaller diameter tubes in a similar number of tube diameters. To see a direct comparison of the same orifice plate blockage ratio, it is possible to compare flame acceleration for the 0.75BR case at both tube diamters. Both cases are recorded with tubes filled with orifice plates. The port locations are slightly different (10D in the 88.9mm case, 12.5D in the 38.1mm case), but not significantly so. The mean overpressure developed in the

0.75BR 38.1mm case more than double the mean overpressure developed in the 88.9mm case at a similar number of diameters, and a considerably smaller overall length. This could be because the length scale of the turbulence is much smaller, allowing the turbulence to cascade down to smaller Kolmogorov length scales and penetrating the laminar flame length scales faster than in the larger geometry case.

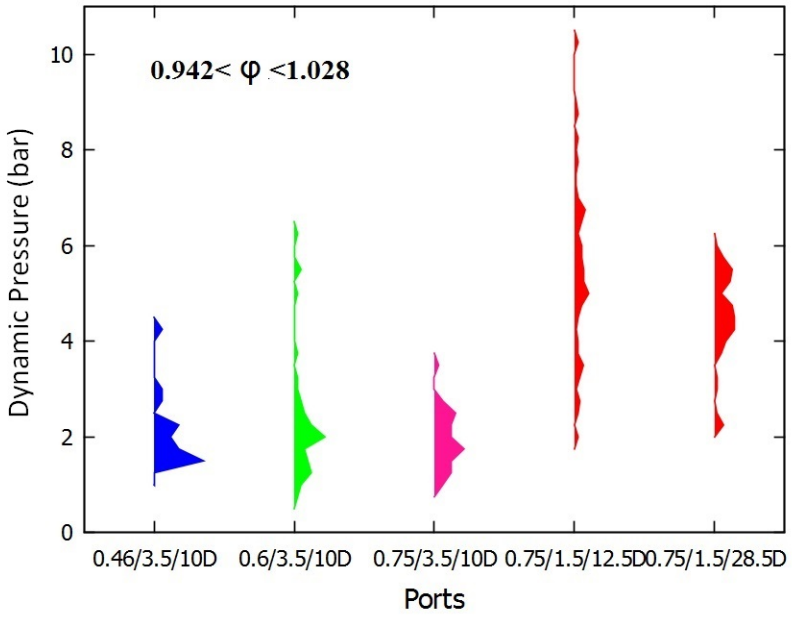

FIGURE 4.46: A comparison of different tube diameters and blockage ratios over the same range of equivelence ratios (0.946≤ϕ≤ 1.028) 0.46/3.5/10D: 0.46 BR 88.9mm diameter port at 900mm or 10D. 0.6/3.5/10D: 0.6 BR 88.9mm internal diameter port at 900mm or 10D. 0.75/3.5/10D 0.75 BR 88.9mm internal diameter port at 900mm or 10D. 0.75/1.5/12.5D 0.75BR 38.1mm diameter tube port at 12.5D or 540mm from the thrust plate. 0.75/1.5/28.5D 0.75BR 38.1mm diameter tube port at 28.5D or 1140mm from the thrust plate

4.7.4 Experimental Repeatability

As there are only 3 high temperature capable (250deg C) Kistler 6061A pressure sensors with matching charge amplifiers it was necessary to move the pressure sensors between ports during these experiments to determine the pressure at every location along the PDE tube. The error associated with this method was determined by running an experiment with one stationary pressure sensor, which remained in the same port throughout all of the experiments whilst the other two pressure sensors were moved according to the locations of interest. All of these experiments aimed to maintain a constant equivalence ratio where possible, and the stationary pressure sensors were compared with one another during the analysis procedure to determine whether results were comparable.

4.7.4.1 Statistical Measurement of Error

An example of a preliminary experiment designed to prove out this concept can be seen in Figure 4.47 which was taken for the same equivalence ratio with the same port location. It can be seen that the overall profile of the statistical distribution of pressure is the same between case one and case two, although some of the shots in case one are failing to fire correctly, leaving a small number of low pressure (1 bar) shots which reduce the mean value in case one. Case two has less of these low pressure shots, and therefore the mean is slightly higher. The mean pressure for case one is seen to be 4.94 bar (Standard deviation = 0.417 bar) with 170 shots, and case two had a mean value of 4.87 bar (Standard Deviation= 0.478 bar) and 178 shots.

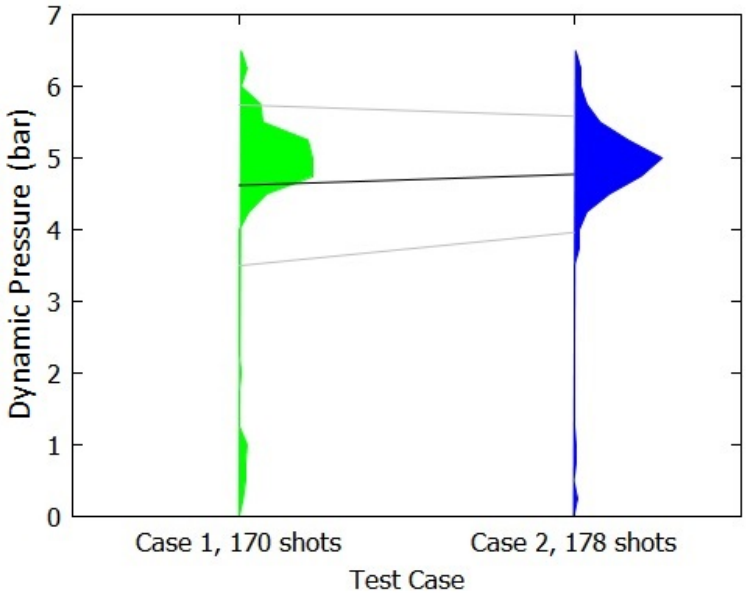

FIGURE 4.47: Comparison of two separate experiments with ports in the same location to check repeatability, black line: mean value, grey outliers: one standard deviation from the mean.

These results were compared further by overlaying the statistical distributions on top of one another and plotting the difference in the statistical distribution, as can be seen in 4.48. It can be seen that the mean value is altered by the low pressure shots at the bottom of the plot, where case one and two differ from each other. A higher number of cycles could have been measured to reduce this difference.

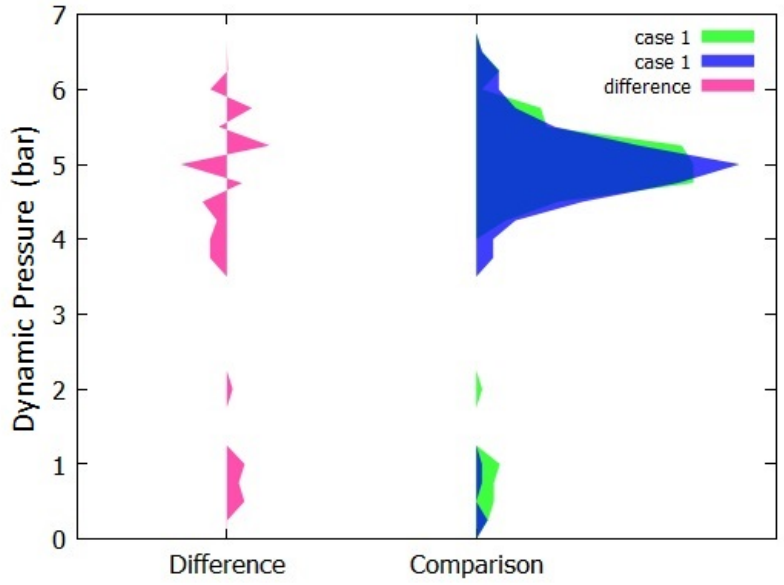

FIGURE 4.48: A comparison of two separate experiments with ports in the same location to check repeatability. Pink shows the difference in case one and case two, green and blue show the statistical distribution of results overlaid on each other for comparison.

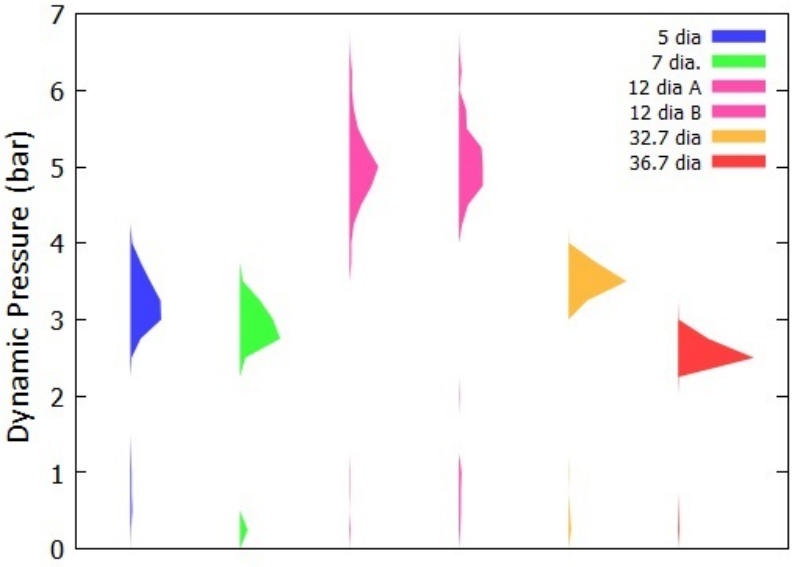

FIGURE 4.49: The full set of data for two tests with one stationary port, taken for 14 0.57BR orifice plates

4.7.5 Data processing error

The error in data processing techniques has been quantified for a real set of experimental data. Seventy shots were assessed by eye using NI DIAdem for amplitude, from the

horizontal part of the pressure curve before ignition until the peak pressure was reached. The error in automatic measurement after the filters were applied was ± 2.4 %.

Furthermore, the automated time of flight measurements for exit velocity with measurements made by eye using NI DIAdem. This software had an error of ± 3 % due to discrepancies in the gradient of the curve at which the eye read the start of a pressure pulse and the softwares automatic gradient detection trigger, which had to be set a little higher to keep from being triggered by small amounts of noise.

4.7.6 Operating conditions

The atmospheric line fan operating conditions impose a limitation on the maximum mass flow through the PDE rig which then impose limitations on the maximum PDE firing frequency, as can be seen in table 4.3. With the second stage of PDE development, the 38.1mm diameter tube is able to operate with a tube length of 29 diameters and the tube reducer up between firing frequencies of 4 and 5Hz. At lower frequencies than 4 Hz the variable speed drive and motor are incapable of turning over the cylinder head valves, even with weaker valve springs fitted. At higher frequencies than 5 Hz it is not possible for the atmospheric line to provide sufficient pressure to deliver enough mass flow to the PDE to operate with a full charge of air, as the line is only capable of delivering 1.15 bar of air when the fan is operating at 50Hz.

4.7.7 Video

A video of the PDE operating with fractal orifice plates can be seen in slow motion below if this document is being viewed in adobe pdf reader with a recent version flash player installed, or in still pictures in Figure 4.50 which illustrates three sequential exhaust plumes:

A high speed central jet can be observed, surrounded by a larger torus of rotating gas. This pattern does not appear to display visible evidence of shock waves, although these would be very difficult to see at this resolution and frame rate. Interestingly the products of a secondary external explosion appear to be flying to the left in Figure 4.50(a), which shows three diverging streaks to the extreme left of the frame. These do not appear in later frames, although the overall pattern of a central jet of exhausting gas surrounded by a torus is present in Figures 4.50(b) and 4.50(c).

.

(a) a

(b) b

(c) c

FIGURE 4.50: (a): first explosion, (b): second explosion and (c): third explosion

Chapter 5

Stratified Orifice Experiments

5.1 Synopsis

5.2 Experimental Design

Each of the orifice plates were mounted in an orifice cage which allowed notched orifices to slot into a notched barrel, which was then inserted into the PDE tube. The internal diameter of this barrel was 1.25", or 31.75mm. This system allows rapid interchangeability of components to test alternative configurations with as little time taken as possible in order to speed up the experimental process at the same time as locating the orifices in the correct location every time.

5.2.1 Hypotheses

Hypothesis 1 and 2: It was hypothesised in Chapter 3 that the reduction in orifice blockage ratio will produce a reduction in flame speed and an increase in blockage ratio will produce a reduction in flame speed. This hypothesis will be tested with all other conditions equal to determine the effect of the hypothesis.

If this hypothesis is correct it will prove that significant back pressure from orifice plates has a greater effect than the increased effect of turbulence from initial blockage according to the CFAM model

Test of Hypothesis 1 and2: In order to test Hypothesis 1 a section of orifice plates shall be installed into the PDE with increasing and reducing BR. Flame speed TOF and pressure instrumentation will be installed in the tube to detect any difference in the pressure, shock speed and flame speed generated by these novel obstacle geometries. The results will then be processed using frequency distributions to plot the probability of each of the results occurring.

Hypothesis 3: If a spinning detonation can be obtained in a smooth walled tube with diameter D $\leq \lambda/\pi$ then it stands to reason that the beginning of the tube could be filled with obstacles such that flame acceleration is achieved in the obstacle filled section. Transition from deflagration to detonation can then be achieved in the smooth walled section provided that the tube is long enough for this reaction to occur.

Test for Hypothesis 3: Fill a tube with diameter D $\leq \lambda/\pi$ with obstacles sufficient to generate a choked flame at approximately $V_{CJ}/2$, then leave the rest of the tube clear of obstacles, but with sufficient length to initiate DDT after the obstacle array. For a propane-air flame this length should be a total tube length of at least 24 X/D.

5.3 Stratified orifice test

After carrying out preliminary tests the results were observed, finding that there were differences between flame acceleration in decreasing and increasing BR orifice arrays. It was decided that further instrumentation should be built and installed on the PDE rig to determine the flame speed at regular intervals along the tube to track the progression of the flame speed. Further pressure based instrumentation was also installed at regular intervals to determine the local dynamic pressure properties at regular intervals along the PDE tube. The new instrumentation system allowed for comparisons of flame speed and dynamic pressure at each stage of FA, giving a clearer picture of the physics controlling the accelerating flame. Firstly, the instrumentation port locations and test matrix are presented in section 5.3.1, followed by detailed experimental results in sections 5.3.3 to 5.3.11. A summary of the main points from the data is presented in Section 5.4, which presents each of the results in one place, and later in Section 5.4.5 which compares the mean flame speed, as well as pressure at each port along the tube for each of the cases in this Chapter.

5.3.1 Instrumentation plan

Ports are located as evenly as possible with the existing hardware using the port locations listed in Table 5.1. All of the port locations in this figure are measured relative to the thrust plate, where the vales are situated at the entrance to the combustion chamber. A small number of tests cases were selected to investigate the effect of increasing and reducing the orifice plate BR along the tube to determine whether reducing or increasing the number of orifice plates could benefit the flame speed and reduce X_{DDT} for propane air mixtures within this tube. These tests are shown in Table 5.2, which shows the orifice array BR for each set of orifices, the port locations and instrumentation type installed. There are initially five orifice plates of type $BR1$, then four orifices of type $BR2$, followed by five orifices of type $BR3$, making a total of fourteen orifices located immediately after the end of the reduction section of the PDE tube. It can be seen from Table 5.2 that there are a number of cases operating with 0.57BR orifice plates installed. The first of these, case 2, was run in a separate test campaign to the all of the other tests. All of the other tests were completed within one week, in a single test campaign to reduce unnecessary decommissioning and changes to the rig between tests.

Port Number (PL)	Straight tube Dia's †	Distance from thrust plate (mm)
PL1	6	307 ±1
PL2	7	345 ±1
PL3	11	497 ±1
PL4	12	535 ±1
PL3*	10	460 ±1
PL4*	11	498 ±1
PL5	15	698 ±1
PL6	19	851 ±1
PL7	23	1010 ±1
PL8	27	1160 ±1

TABLE 5.1: Port Locations. [c2] represents the port locations used in the 0.57BR first test run, case 2. † straight tube diameters are the number of tube diameters from reducer exit.

Case	BR_1	BR_2	BR_3	PL 1	PL 2	PL 3	PL 4	PL 3*	PL 4*	PL 5	PL 6	PL 7	PL 8
1	0.42	0.42	0.42	-	f	f	k	-	-	k/f	p/f	p/f	p/f
2^{c2}	0.57	0.57	0.57	-	f	-	-	k*	f*	k/f	p/f	p/f	p/f
3^2	0.57	0.57	0.57	-	f	f	k	-	-	k/f	p/f	p/f	p/f
4^{SI}	0.57	0.57	0.57	-	f	f	k	-	-	k/f	p/f	p/f	p/f
5	0.75	0.75	0.75	-	f	f	k	-	-	k/f	p/f	p/f	p/f
6^i	0.42	0.57	0.75	-	f	f	k	-	-	k/f	p/f	p/f	p/f
7^d	0.75	0.57	0.42	-	f	f	k	-	-	k/f	p/f	p/f	p/f

TABLE 5.2: Cases: 1-3 are base line cases with constant blockage ratio. All test cases are to be run with stoichiometric propane-air. Blockages are inserted in sets of 5 for BR_1 and BR_3, however BR_2 required 4 orifice plates. All experiments in this section used end ignition unless otherwise stated.BR_x, blockage ratio of x. ^{1}, the first case taken at the 0.57BR condition.^{2}, the second case taken at the 0.57BR condition. ^{SI}, Side ignition port. ^{i}, increasing blockage ratio.^{d}, decreasing blockage ratio.PL, port location. k, Kistler pressure transducer. p, PCB pressure transducer.f, ion probe flame sensor.*, PL and order of these ports has changed. S-, ports blanked off.

Figures 5.1 and 5.2 show the different port locations used between tests when combined with Tables 5.2 5.1. Case 2 was run during a separate test campaign to all of the other cases. After testing Case 2 it was realised that the pressure transducer mounted at 460mm from the thrust plate (10d from the reducer) was in a different location to tests in other chapters. As such, the test was repeated with the pressure transducer in the port at 535mm from the thrust plate.

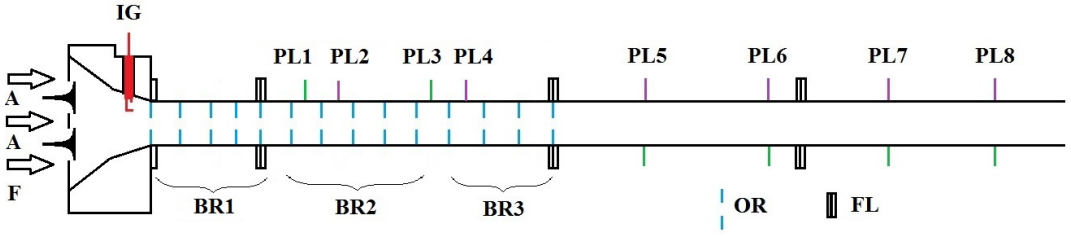

FIGURE 5.1: PDE DIAGRAM: IG: ignitor, PL: port location, OR: orifice, A: air, F: fuel and BR: blockage ratio, FL: Flange. This setup was used for 0.57 end ignition, case 2

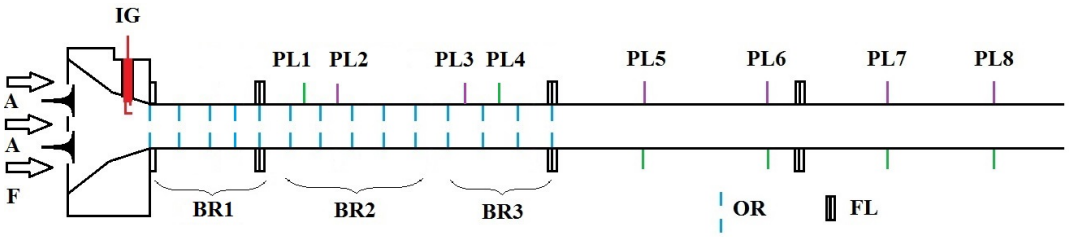

FIGURE 5.2: PDE DIAGRAM: IG: ignitor, PL: port location, OR: orifice, A: air, F: fuel and BR: blockage ratio, FL: Flange. This setup was used for all tests other than 0.57 end ignition, case 2.

5.3.2 Test Overview

Table 5.3 provides an overview of all data gathered for the shots within the correct equivalence ratio range which has been selected for all experiments within this thesis (0.964-1.027). The mean equivalence ratio, $\overline{\phi}$, its standard deviation σ_ϕ, mean fill factor, $\overline{\text{ff}}$ and mean purge factor $\overline{\text{pf}}$ have been calculated for all of the shots which were analysed in the data. In addition the sample size for each case, N_{shots} is recorded. For each of these cases, a greater number of shots than those recorded here were fired. All of the ignition events which were fired within the required equivalence ratio band were selected for analysis so as not to select the data artificially and bias the results. It is important to note that the 0.43 BR condition did not ignite within the set range of equivalence ratios, purge factors and fill factors. As such this test condition was left out of the analysis.

Due to the nature of operating a low pressure compressed air line and fuel supply, there was a degree of variation of air and fuel flows which meant that it was difficult to predict the number of ignitions fired within the required band for equivalence ratio. This is why the sample size for the number of shots analysed varied. In the proceeding sections for each test condition the number of ignitions fired for each test is recorded, and a breakdown of misfires, sensor failures and other factors affecting the number of shots analysed has been tabulated. A misfire was determined as a shot which with a recorded ignition signal but no readable flame speed or pressure gain. Possible causes of misfired ignitions will be discussed in the discussion section.

Case	Test Condition	$\overline{\phi}$	σ_ϕ	$\overline{\text{ff}}$	$\overline{\text{pf}}$	N_{shots}
1	0.43BR	N/A	N/A	N/A	N/A	N/A
2	0.57BR*	0.994	0.022	1.110	0.555	74
3	$0.57BR^{REP}$	1.007	0.013	1.082	0.541	49
4	$0.57BR^{SI}$	0.999	0.018	1.067	0.534	40
5	0.75BR	0.978	0.015	1.087	0.544	202
6	Increasing BR	0.989	0.021	1.054	0.527	94
7	Decreasing BR	1.008	0.016	1.054	0.527	344

TABLE 5.3: Test Operating Condition Summary. ^{SI} represents the case which used the side ignition port as opposed to the end ignition port used in each of the other cases.^{REP} indicates that this case was repeated, after decommissioning and recommissioning the rig onto the atmospheric pressure air line. * sensors PL3 and PL4 moved in this experiment, please see table 5.1

5.3.3 Case 1: 0.42 BR results

Data for the 0.42BR condition was not available as the standard mixture was unable to fire at this operating condition. As such there is no statistical analysis for this data.

5.3.4 Case 2: 0.57 BR end ignition results

In this section 0.57 BR results are presented. Some of the results have been omitted from this section where data was not complete for the full suite of sensors. For example, in 30 of the 104 shots fired with a mixture of the correct of equivalence ratio (0.964-1.027) there were negative or very high indicated values of flame speed. Where this data indicated high speed, it often indicated a time of flight of one clock pulse of the flame speed instrumentation. Such value were far from realistic, and must have been generated by electrical noise as it is much higher than any overdriven detonation results in the literature. This value occurred three times within the 0.57BR data set, and was deemed to be due to noise or deterioration of the ion probe spark plug sensor ceramic. This ceramic was seen to deteriorate over time producing more of the same results over time, and warranted regular replacement of the spark plugs to prevent false readings. A sensible range for detonation velocities recorded by Rolling et al. was defined as 0-3500m/s for all data with the range of FA and DDT, Detonation and overdriven detonation. In this case a number of cases which were larger than 3500m/s

were recorded and so have been included, where these seem reasonable. An arbitrary cut-off was made at 13000m/s to include as much data as possible.

Other 'false' results were indicated with negative flame speeds, making up the remaining 27 false shots. Approximately half of these negative flame speed results were thought to be the result of electrical noise. These are discounted for the same reason as the erroneous positive large flame speeds. The remaining 13 results were flames with slow to sonic negative velocities, ranging from -400m/s to -700m/s, which took place across the last sensor at the end of the tube. It is thought that these velocities could be a true reading of negative velocity from the slow/unstable flame regime and that the ignition source of these negative flame speeds could be the reflection of the shock from the PDE tube exit. These results are omitted from the following statistical analysis, and can be quantified by observing Table 5.4.

Type of shot	Number of shots	% data within range
Total in ϕ Band	107	100
Misfires	2	1.9
Good	74	71.2
Nagative flame speed	13	12.5
Faulty sensor	18	16.8

TABLE 5.4: Data Quality for the constant 0.57BR test

5.3.4.1 Statistical Pressure Analysis

It can be seen from Figure 5.3 that the pressure throughout the orifice laden section of the tube increases from an average of 3.33 bar at PL1 to nearly 4.54 bar after PL4 (at the 10th orifice) near the exit. This increasing trend indicates healthy FA in this section of the PDE tube. After the flame exits the orifice plate, a decrease in pressure is observed from nearly 4.54 bar at PL4 to 3.47 bar at the PL5, directly after the last orifice plate. By the time the shock wave has reached the next pressure sensor at PL6 it is evident that a DDT event has started and failed, as the pressure form some of the shots has increased in the smooth section of the tube, but not up to P_{CJ}. Normally the pressure would decay in a smooth tube without extra shock reflection of turbulence

generation from orifice plates or other obstacles. Possible reasons for failed transition into a stable detonation wave will be discussed in the discussion chapter.

The average pressure at PL6s 4.62 bar, which then decays as the shock travels along the tube to an average of 3.92 bar at PL7, then up again to an average of 4 bar at PL8. It is interesting to note that there is a large degree of scatter in the pressure at PL6, with a standard deviation of 0.74 bar, larger than the standard deviation in any of the other results. This is likely to be due to the unpredictable nature of DDT, which is highly dependent on the local mixture, turbulence and geometric conditions.

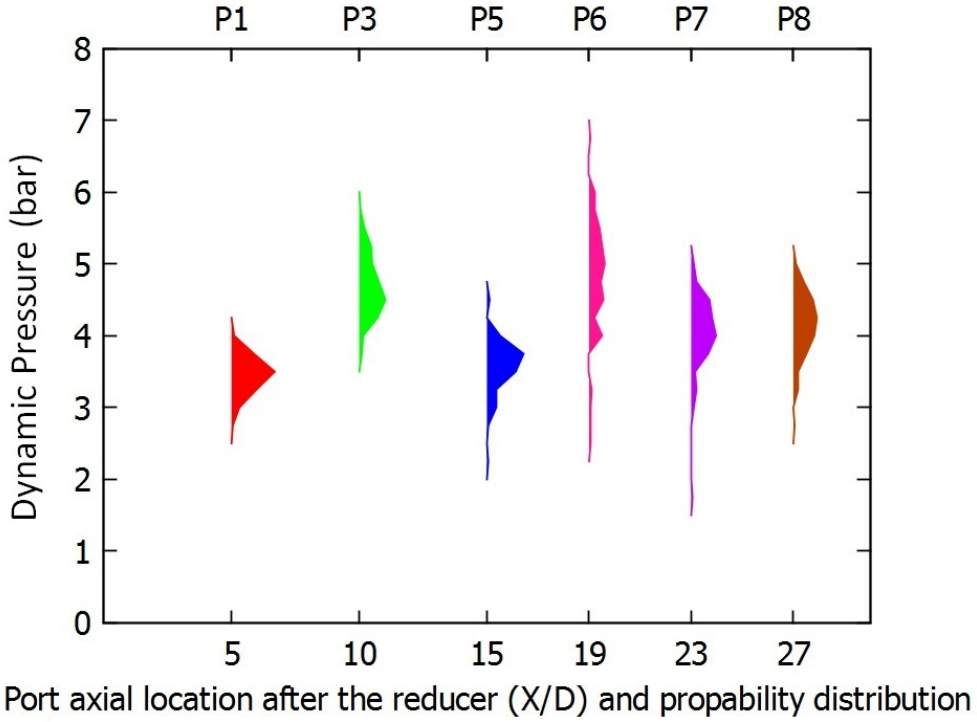

FIGURE 5.3: Statistical Distribution of pressure at each port taken with 0.57BR orifice plates installed throughout.

5.3.4.2 Statistical Shock Speed Analysis

Figure 5.4 shows the increase in the shock wave speed, measured using the TOF method. The horizontal axis shows length along the tube in the number of straight diameters after the reducer measured from the last pressure transducer used to calculate the TOF measurement. The shock speed pdf at PL6-7 shows a relatively tightly grouped band of shock speeds, with an average of approximately 575m/s and a range of 450m/s to 625m/s. By the time the shock reached PL7-8 the median shock speed had accelerated

by approximately 100m/s, however the range of the shock speed pdf had also increased, with a number measurements of shocks in excess of 800m/s, and some as slow as 660m/s.

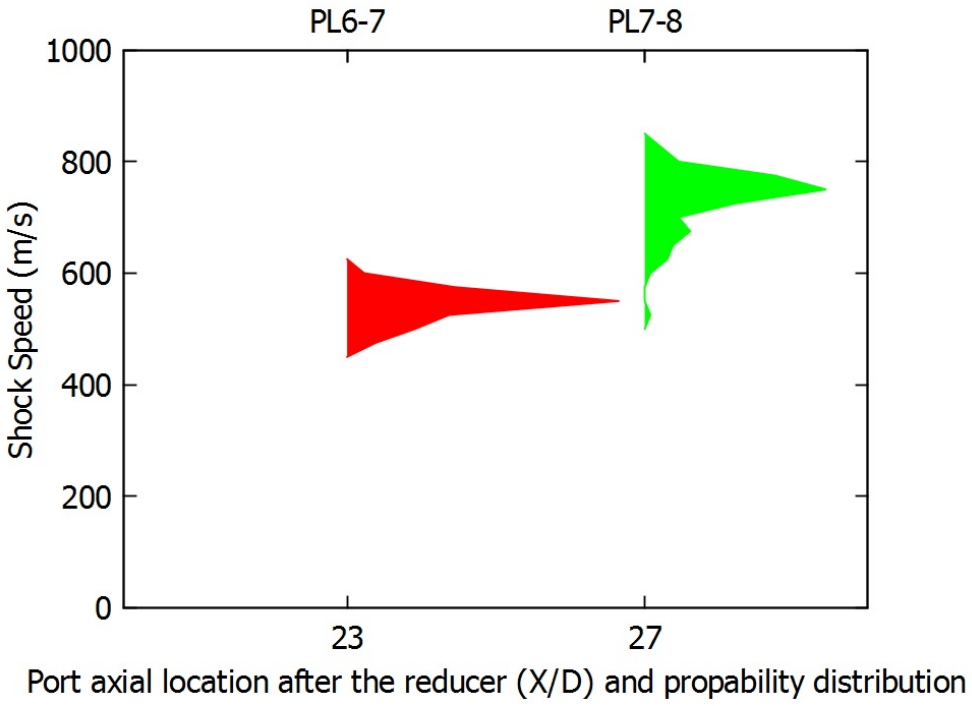

FIGURE 5.4: Statistical Distribution of shock speed for the last three pressure transducers taken with 0.57BR orifice plates installed throughout.

5.3.4.3 Statistical Flame Speed Analysis

Figure 5.5 and 5.6 illustrate the flame speed measured between ion probes for the good quality data indicated in table 5.4. An arbitrary cut off velocity on the y-axis of 4000m/s was chosen to allow the detail of the lower flame speed probabilities to be seen in greater detail, as these lower speeds accounted for most of the data. This is plotted in Figure 5.6. It is important to note that this data excludes all of the misfires, negative flame speeds and sensor errors in the data. The remaining 71.2 % of the data indicates that flame acceleration between sequential ion probes and was recorded at 160 MS/s in order to determine the flame speed with a high degree of accuracy. Between the spark and PL2, the indicated flame speed forms a tight band of velocities with a standard deviation of 2m/s on an average of 17m/s. By PL4, the flame speed has reached an average velocity of 335m/s with a standard deviation of 72m/s.

Between PL4 and PL5, the flame speed accelerated dramatically, and in some cases exceeded the detonation velocity. The bulk of flame speeds at this location are less than

the speed of sound in the products (993m/s for stoichiometric propane-air). About 35 % of the results exceed the speed of sound in the product at this location. The mean V_f TOF at this location is 1360m/s with a standard deviation of 1288m/s . By the time the flame has reached the next port, PL6, the flame speed has decelerated significantly to and average 519m/s with a much smaller standard deviation of 216m/s. This pattern of deceleration continues to the next port, PL7 at which the average flame speed is 413m/s with a larger degree of scatter producing a standard deviation of 346m/s at this port. Interestingly, by the time the flames have reached the final port they begin to accelerate again, with a mean V_f TOF between PL7 and PL8 of 1997m/s and a very large scatter, producing a standard deviation of 1607m/s.

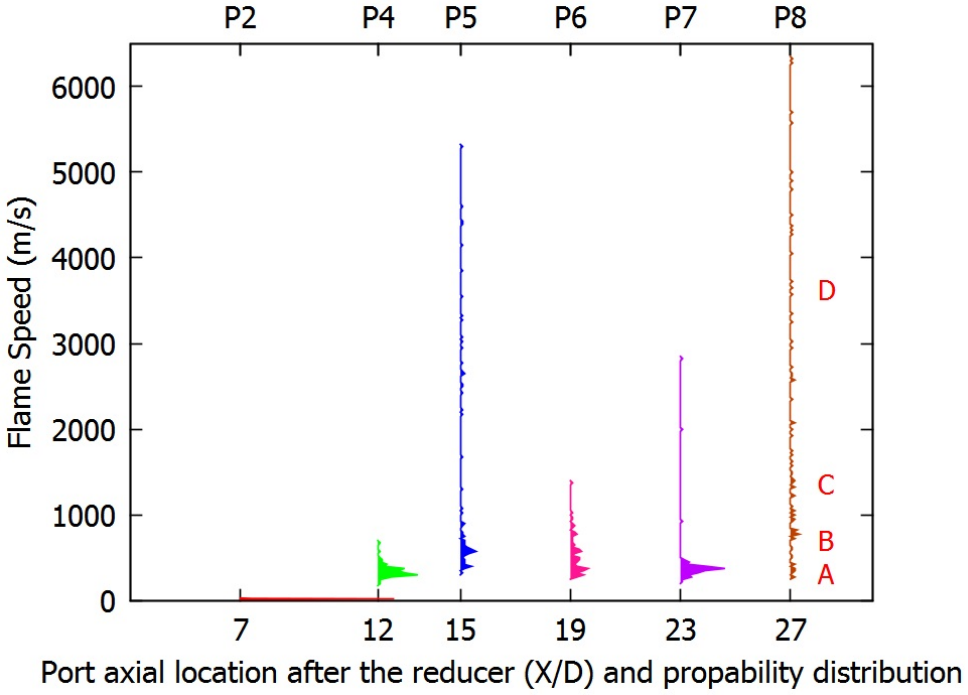

FIGURE 5.5: Statistical Distribution of flame speed at each port taken with 0.57BR orifice plates installed throughout.

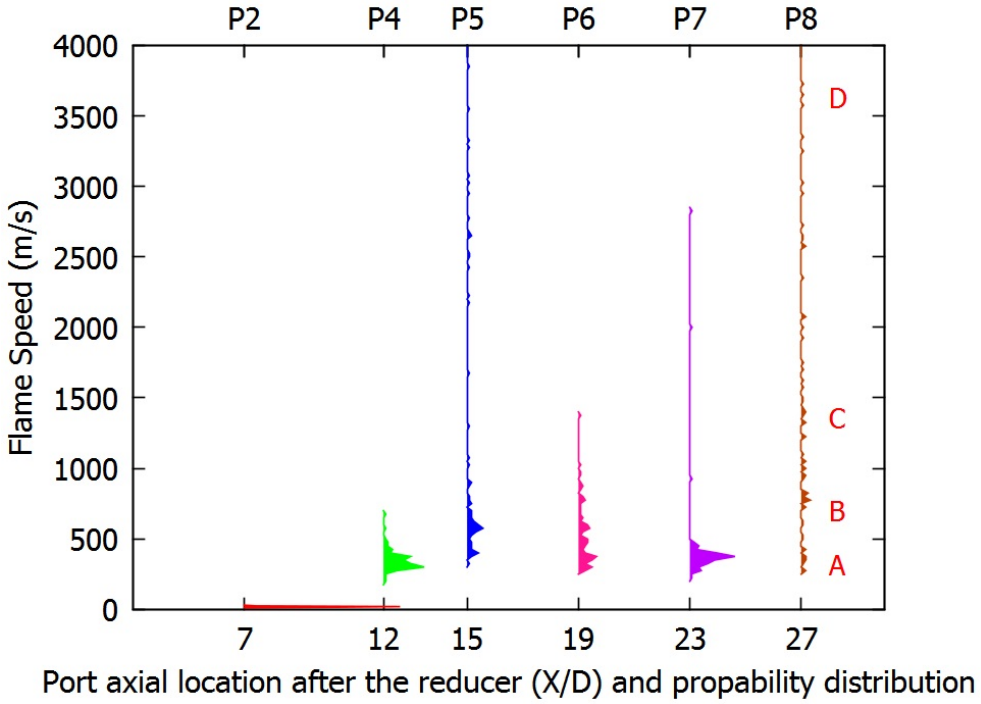

FIGURE 5.6: Statistical Distribution of flame speed at each port taken with 0.57BR orifice plates installed throughout. This plot is cut off at 4000m/s to give a clearer indication of the low speed data, which provides the statistical bulk of the data at most sensor locations.

5.3.5 Key flame regime plots

Key flame regimes have been selected according to the average velocity of the group of shots between key flame velocities. For example, Plot A contains data from the average shot velocity within the velocity band 0-340 m/s, the sonic velocity in propane-air mixtures. Table 5.5 lists each of the bands and the number of shots within that band in addition to the average velocity of the shot within each band. A shot with an exit velocity similar to this figure was chosen in each instance, giving a reasonable representation of the average shot from within this velocity band.

Each band was chosen to represent a key flame regime. Band A represented slow speed flames (from stationary to the sonic velocity in the reactants, 340m/s). Band B represented flames which were travelling above the sonic speed in the reactants but below the speed of sound in the products (990m/s). Band C represented flame speeds traveling above the sonic speed in the products but below the mixtures' CJ detonation velocity, V_{CJ}, 1800m/s. Band D represented average overdriven flame velocities, where the flame speed was greater than the CJ detonation velocity, with no upper bound.

This banding is similar to that used in the literature review to characterise different flame regimes, as discussed in Section 2.2.1 of the literature review.

Band	Figure	Lower V_f (m/s)	Upper V_f (m/s)	Average data V_f (m/s)
A	5.8	0	340	301
B	5.9	340	993	701
C	5.10	993	1798	1371
D	5.11	1798	N/A	3637

TABLE 5.5: 0.57 BR Velocity Bands

5.3.5.1 Band A Observations

Figure 5.7 illustrates FA in the slow regime, with a flame speed remaining less than the speed of sound along the full tube. The dynamic pressure can be observed on the y axis of this chart using the coloured traces, with both Pressure and non-dimensional axial distance plotted along the same axis. The digital trace from the flame speed measurements has been plotted as a solid black line, which is one y unit higher during the presence of a charge ionic field. Noise can also be seen to affect these measurements on some of the later plots, which will be explained in greater detail within the discussion chapter. Trends of the shock front and flame front are plotted in dashed black and red lines respectively, with TOF velocities presented beside each dotted flame or shock front location. Significantly, each individual explosion recorded within this test was different as the turbulence and mixing occuring with each shot was stochastic in nature, producing a range of pressure and ion trace results. Turbulence, for instance is a highly stochastic process, which means that no two turbulent flows are identical, even under the same initial and boundary conditions. As such, no two explosions generated in a turbulent mixture are identical, and must be analysed using statistical methods rather over a suitable sample size rather than a one, or a small number of explosions.

Figure 5.7 illustrates FA in the slow regime, with a flame speed remaining less than the speed of sound along the full tube. The dynamic pressure can be observed on the y-axis of this chart using the coloured traces, with both pressure and non-dimensional axial distance plotted along the same axis. The digital trace from the flame speed

measurements has been plotted as a solid black line, which is one y unit higher during the presence of a charge ionic field.

When this experiment was conducted high frequency back ground noise was recorded simultaneously with the pressure signal data, which distracts from the pressure trace when reading the graph. In order to clarify which parts of the pressure data were signal and which were noise, a selective low pass filter was applied to sections of the pressure data which had a low gradient, as seen in Figure 5.8. This smoothed the pressure data when no overall change in dynamic pressure was observed over a period of time. The full, unsmoothed signal was displayed when a peak was detected in order to show the sharp gradients present in the pressure wave. Data presented in Figure 5.7 and 5.8 was processed from the same shot, with the latter figure presenting smoothed pressure data. This was achieved by means of an in-house programmed LabView post processing code. The code smoothed the data using a 300 point central average, taking 150 points before the data point of interest, and 150 points after, then calculated the mean of the 300 points and recoded this. When the gradient of the line, as sampled over the same 300 data point surpassed a limit trained on this data set, the original data was recorded with no smoothing applied. This resulted in an output file with smoothed data either side of the pressure peaks.

For the remainder of this thesis pressure data will be presented in its smoothed form where the average signal is determined to have a gradient close to zero. This was achieved using the process outlined above to remove the noise spikes from the signal. The smoothing threshold gradient remained identical for all other datasets, using the same software throughout.

Ion probe data is also plotted on these graphs. A short duration pulse was often detected in advance of the pressure wave, which is physically impossible at the speeds considered.Even in the case of a detonation, the shock always precedes the flame. The short pulse was usually very short in duration (less than 200 μs). Consequently, the short pulse was treated as noise and neglected when plotting the propagation of the flame front.

Due to the high gain of the ion probe amplifier, some noise was observed in the ion probe signal before the main pulse due to the flame. This is possibly due to the presence of earth loops in the ion probe circuit, which have triggered ion probes in the proximity

of those near to the flame. This usually results in a short pulse before the main pulse of interest due to the flame. This problem was not fully understood whilst carrying out the experiments, and as a result should be corrected in further work. Possible solutions which require further investigation include reduction of the amplifier gain and elimination of earth loops by individually earthing each of the components to the same earth connection with similar earth wire lengths. The noise pulse is only present when other ion probes have already produced a high signal upstream of the sensor with a short duration noise pulse. This infers that the problem is not due to random noise, otherwise the signal would trigger instantaneously, but that it is likely to be due to small currents flowing through earth loops in the system once an ion probe has been triggered in close proximity to the probe which produces a noisy signal.

Given these assumptions, a red dotted line is drawn along the rising edge of the long pulse to indicate the location of the flame front and time of its incidence. Flame speed, V_f is indicated adjacent to each respective section of this line in m/s calculated based on time of flight measurements. The same process has been repeated for to follow the location of the shock wave front, using a black dotted line. The shock speed V_s is indicated adjacent to the respective dotted line, also calculated using time of flight measurements.

Observations of Figure 5.8 show that this particular shot developed a relatively low pressure across the obstacle laden section of the tube, with a maximum pressure of 3.6 bar reached at PL1 (P1). The P1 trace reveals a gentle gradient with no distinct spike at the front indicating the presence of a shock wave. The flame speed between port location 5 and 10 was seen to be 200m/s, which is subsonic relative to the velocity of the reactants. At this port location, the flame front reaches the sensor whilst the pressure gradient is still increasing, but before the pressure peak. This is a vented, subsonic deflagration. By the time the flame has reached the next port, PL 4, the corresponding pressure trace gradient has increased considerably, in keeping with the flame speed which is 360m/s, of the order of the speed of sound in the reactants . The maximum pressure at PL3 has reduced by this point to 3.4 bar. At this location, the pressure wave has begun to accelerate in front of flame, and the peak of the pressure wave reaches the sensor location at approximatley the same time as the flame is detected. The high speed gas flow ahead of the flame cannot vent fast enough to maintain an

equal pressure throughout the mixture, resulting in compressible gas flow and pressure piling.

After exiting the orifice laden section of the tube, the pressure follows a decreasing trend from a peak of 1.9 bar at PL5 to 1.7, 1,5 and 1.5 bar at PL6,7 and 8 respectively. The flame speed trace is seen to briefly accelerate through the last portion of the orifice plate laden section of the tube, then decelerate as it enters the smooth walled tube section. This is because the turbulence and gas mixing enhancing effects of the orifice plate are relatively localised. Once the flame has propagated past the orifice plate, the reactant mixture entering the flame front will have a lesser degree of turbulence. This will promote lower flame speeds as the flame adjusts the the change in local turbulence length scales and intensity. Throughout this section of the tube, the shock wave preceeds the flame, moving along in the form of a double discontinuity, but not a detonation.

Towards the end of the tube, the flame speed begins to build again reaching a speed of 320 m/s by the end of the tube. When comparing all of the pressure waves together it is evident that the gradient of the pressure wave increases with respect to time as it travels down the tube. By the 19th straight tube diameter a peak begins to form, which subsequently develops into a more obvious shock wave by the last pressure transducer. Time of flight comparison of these pressure peaks yields an increasing trend in the shock wave speed from 420m/s to 490m/s before the flame exits the tube.

5.3.5.2 Band B Observations

Figure 5.9 shows FA for a flame with an exit V_f calculated using the TOF method, of 700m/s, which represents the average shot in band B. The first pressure trace, P1, taken at PL1 has a shallow gradient similar to that of P1 in Figure 5.8. Again, this reflects the same pattern as a vented subsonic deflagration, with the flame arriving before the pressure peaks maxima, and an initial flame velocity of 310m/s, close to the sonic velocity in the reactants. The maximum pressure here is 3.75 bar, which is slightly higher than that for the band A plot. P2 measured at PL3 has a much steeper gradient than P1 and reaches a maximum pressure of 4.79 bar by which point the flame is traveling at a speed of 310m/s, just below the speed of sound in the cold reactants. As the flame passes through the last orifices it is seen to accelerate from

310m/s to 610m/s, with the pressure peak accelerating past the flame front as the venting explosion becomes sonic relative to the speed of sound in the reactants, and is classified as being in the sonic regime. The pressure measured at PL5, after the last orifice reduced by the time it reached this point to a maximum value of 2.92 bar. It is worth noting that the separation time between the shock and the flame at this location is approximately 0.1ms, with a separation between the shock and flame of 2.92 Diameters or 110mm. After this point the time and spatial separation between the shock and the flame begins to grow until the flame leaves the tube, as the flame acceleration enhancing orifice plates have been passed by the flame. The main cause of turbulence after the orifice plates have been passed is the interaction of the high speed gas with the PDE tube wall. The P4 pressure trace at PL6 shows that a clearly defined lead shock wave has formed by this point, and the shock speed has reached at an average TOF speed of 550m/s. This shock continues to travel throughout the rest of the smooth section of the tube from PL6 to PL8. The amplitude of the shock wave does not change between PL6 and PL7, but grows to 3.38 bar by PL8. The flame speed decreases considerably after PL5 from 610m/s to 490m/s by PL7. By PL8 the flame speed has decreased further to 350m/s. Interestingly, at the last pressure transducer, a flame speed of 700m/s can be observed.

It should be noted that a considerable amount of false triggering of the ion probe signal occurs prior to the flame reaching the location of the ion sensor in this graph, and others with fast flame acceleration. Observations of these false triggers across a range of different transducers shows that the rising edge form one pulse often matches up with the rising edge of the pulse on the next transducer along the tube. As this sometimes occurred in more than two locations at the same time ($\pm$ 0.5 μs or so) and so was very unlikely to be due to the flame triggering all of these locations at once. As a result, only the longest pulse on each ion probe channel was recorded as a flame in the flame speed calculating software, and the same practice has been used for the red dotted line denoting the flame path and speed. When comparing these pressure traces with those displayed in Figure 5.8, the latter case exhibits much steeper rising edge gradients, particularly in the later port locations PL6, PL7 and PL8.

5.3.5.3 Band C Observations

Figure 5.10 shows the FA propagation of a flame with an exit V_f of 1360m/s. P1 measured at PL1 shows a slight increase in pressure from the previous graph, reaching a peak of 3.58 bar with a similar profile to Figures 5.8 and 5.9, but a slightly steeper gradient. By the time the flame reached the next port, PL3, it had reached a flame speed of 560m/s and the pressure at this location, P2 has a peak value of 4.66 bar. The flame is clearly travelling as a vented sonic deflagrating explosion at this port location. The flame speed then undergoes a short lived rapid acceleration by to 4150m/s, after which the flame decelerates to 330 m/s after the orifice plates between the 15th and 19th diameters, this rapid deceleration may be due to the reduction of flame acceleration enhancing turbulence feedback from the orifices, which have been traversed past by this point. If this high flame speed is correctly indicated, the result is due to an over driven detonation. It is worth noting that the natural frequency of the pressure transducers for P1-3 is only 90kHz, so if there was a von Neumann spike in this flow, due to detonation, it might not be detected even when present. The flame and shock traces at the next port, PL5 indicate that the shock and the flame are traveling along the tube together with no visible separation shown on this plot. The peak pressure in P3 at PL5 was seen to be 3.13 bar and a clear shock wave was shown in the pressure trace at this location. From PL5 to PL6 the pressure increases to 3.88 bar whilst the flame speed decreases to 330m/s with a corresponding shock speed of 550m/s, clearly the suspected DDT event has failed and results in a sonic vented deflagration propagating along the rest of the DPE tube.. A pronounced spike is seen in this pressure trace which wasn't evident in the previous trace, P3. This could be due to the fact that the final three pressure transducers have a natural frequency greater than 400kHz, which is capable of detecting the Von Neumann spike of a detonation if present. By PL7 the peak dynamic pressure measured as P5 has decreased further to 2.94 bar and the corresponding shock and flame speeds are seen to be 700m/s and 300m/s respectively. Finally, at PL8 the dynamic pressure peak begins to increase again to 3.33 bar and the flame begins to accelerate again reaching a flame speed of 1360m/s but still remaining 0.2ms behind the shock which was traveling at 690m/s by this point. This is not a detonation but likely to be the start of an incomplete DDT event.

5.3.5.4 Band D Observations

Figure 5.11 shows FA for a flame with an exit velocity, V_f of 3637m/s. P1 measured at PL1 shows a peak pressure of 3.75 bar, which is the largest P1 pressure of any of the plots for this case. The gradient still follows a similar pattern to earlier plots, with a slow rise in pressure which peaks after the passing of the flame. The flame and shock complex travelling along the tube at this location can be classified as a sonic vented deflagration. The flame speed between this port location and the PL3 is 340m/s. P2, measured at PL3 reaches a peak of 4.91 bar as measured by the slower dynamic pressure transducers. After the peak, the negative pressure gradient decreases rapidly before reducing to a shallower gradient. This is a similar pattern to the two earlier chart P2 trace profiles. The velocity between this port and the next then accelerates to 4590m/s and couples with the shock wave before reaching the next transducer at PL5. This high speed flame and shock wave an be classified as a short lived overdriven detonation, as a DDT event has occured. This DDT event fails before the detonation reaches the next port, after the last orifice plate. P3 which is measured at PL5 reaches a peak of 3.45 bar, showing a marked decrease in pressure from the previous pressure transducer, which mirrors the fact that the flame and shock fronts decouple at this location. By this location the flame and shock are travelling as a double discontinuity along the tube and can be classified as a vented explosion, which is initially subsonic. The shock speed between PL5 and PL6 is 650m/s and the flame speed has decelerated considerably to 280m/s, below the speed of sound in the reactants, the flame is now travelling behind the pressure peak. The pressure trace for P4 at PL6, shows a sharp rise in pressure indicating the presence of a shock wave, which overshoots, reaching a peak of 4 bar then decreases. The shock speed between PL7 and PL7 is 650m/s again, with a flame speed between the same port locations of 430m/s which is sonic relative to the reactants. At PL7 the pressure, P5, reaches a peak of 3.33 bar, which 0.7 bar smaller than the previous pressure measurement. Between PL7 and PL8 the flame progression accelerates rapidly, generating a flame speed of 3640m/s. The accompanying shock speed at this location is 680m/s, suggesting that this is not a detonation and that DDT has not occured at the end of the tube. Perhapse if the tube length was slightly longer than DDT would occur, as the trajectories of the flame and shock would meet in a short distance if they continued with the same velocities. By the time the shock wave has reached PL8 the pressure peak reaches a value of 4.04 bar.

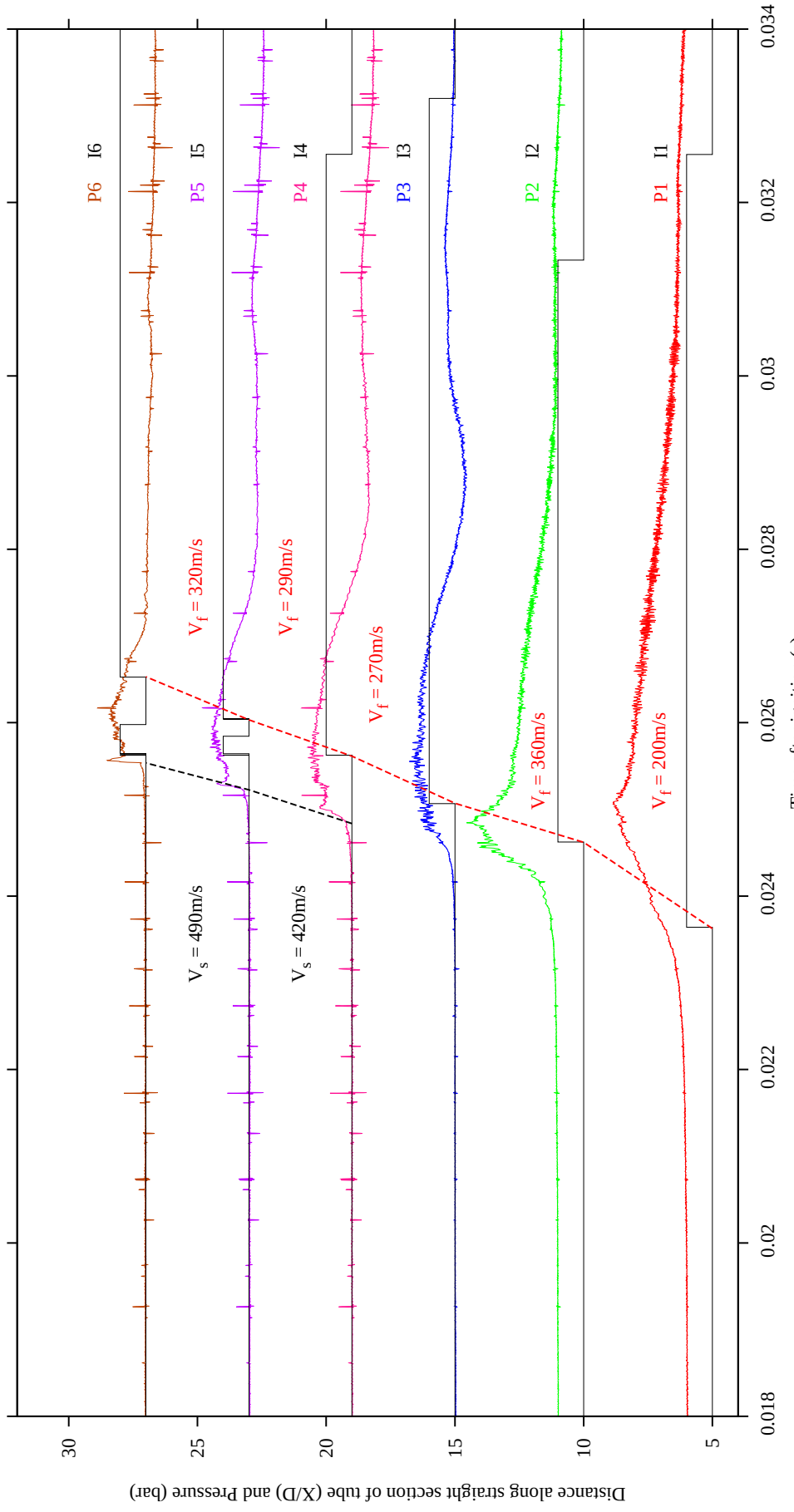

FIGURE 5.7: Shot A: 0.57BR oringinal, unsmoothed pressure and ion probe plot.

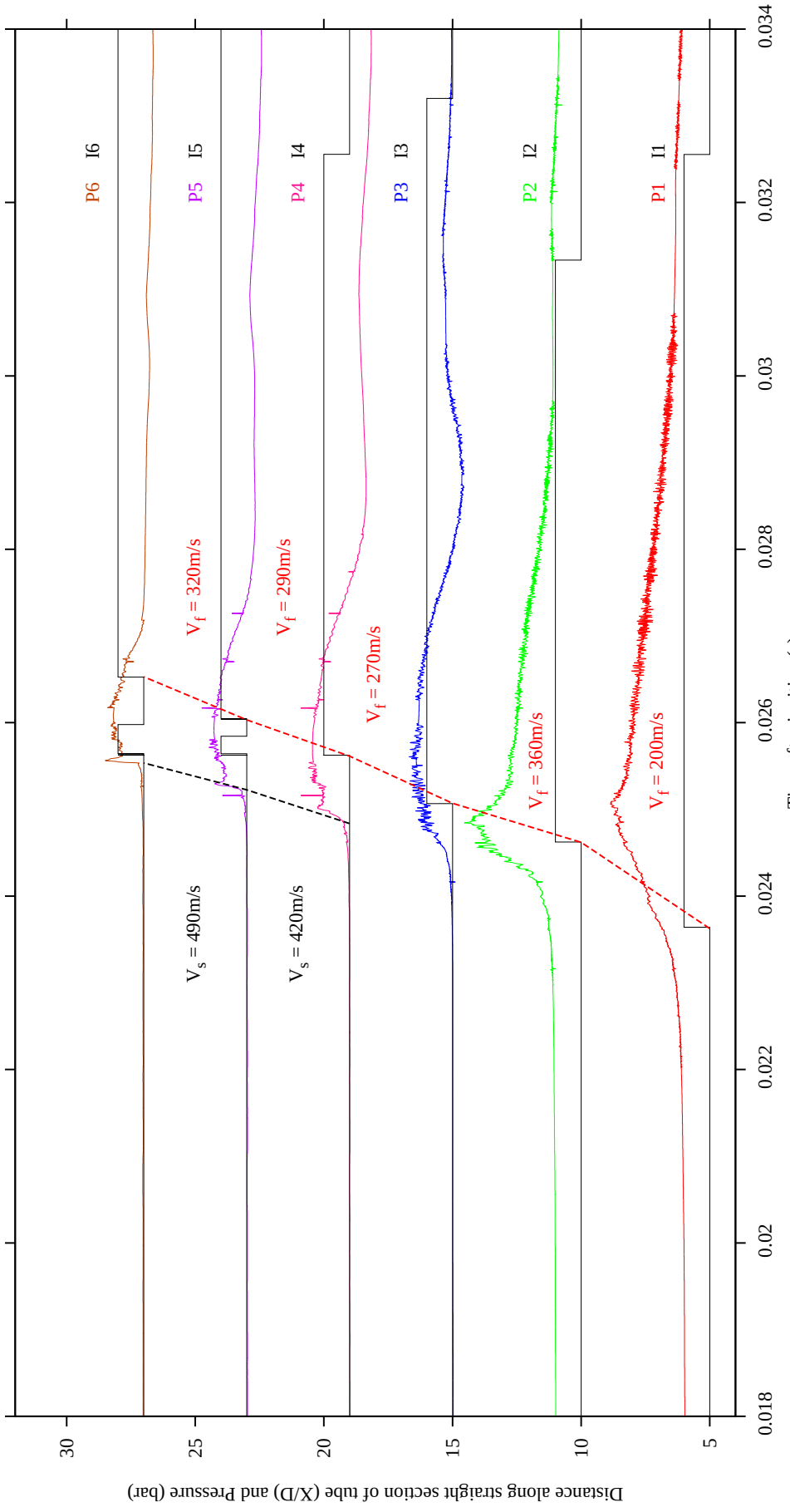

FIGURE 5.8: Shot A: 0.57BR setlectively smoothed pressure and ion probe plot.

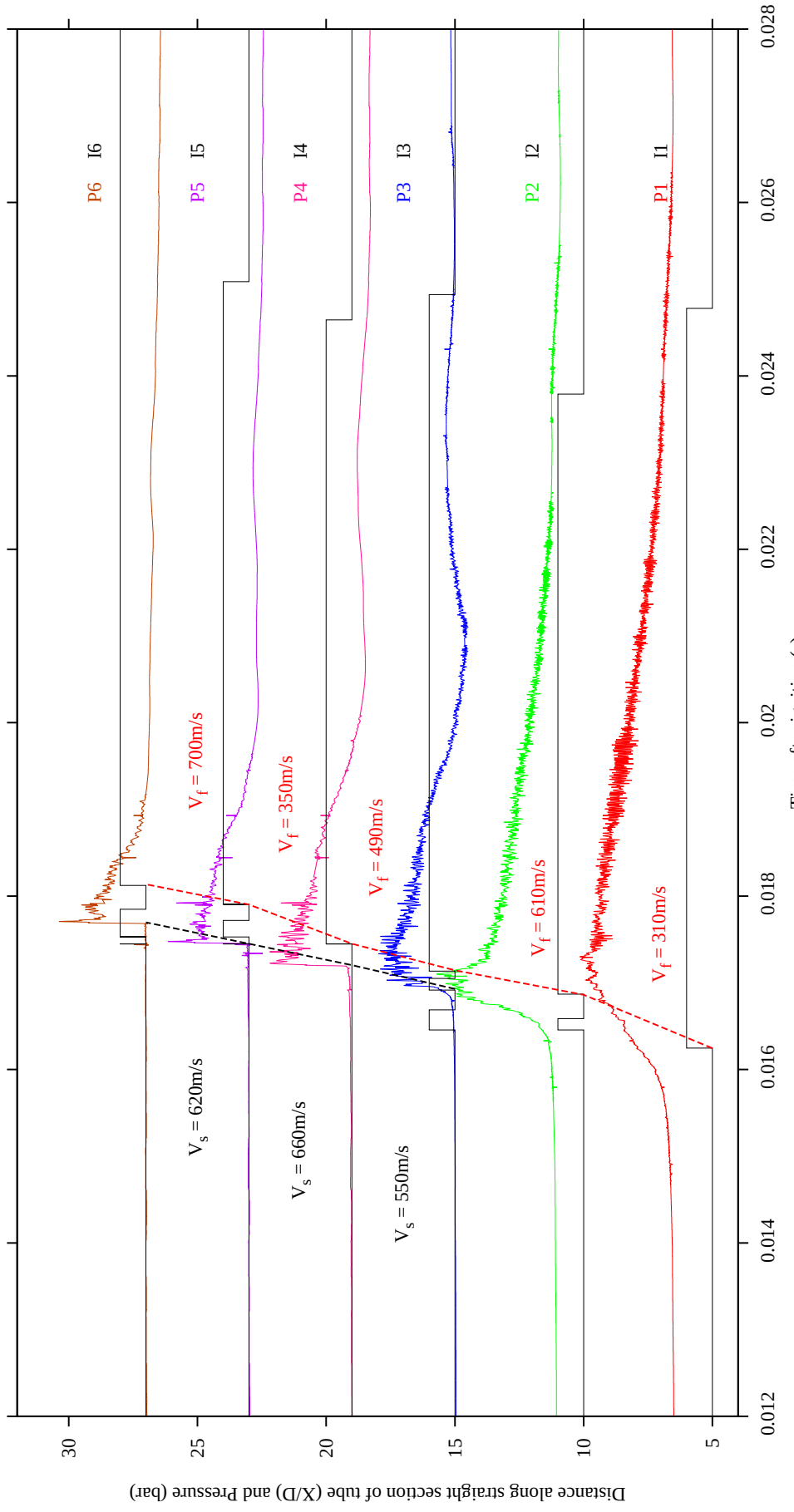

FIGURE 5.9: Shot B: 0.57BR setlectively smoothed pressure and ion probe plot.

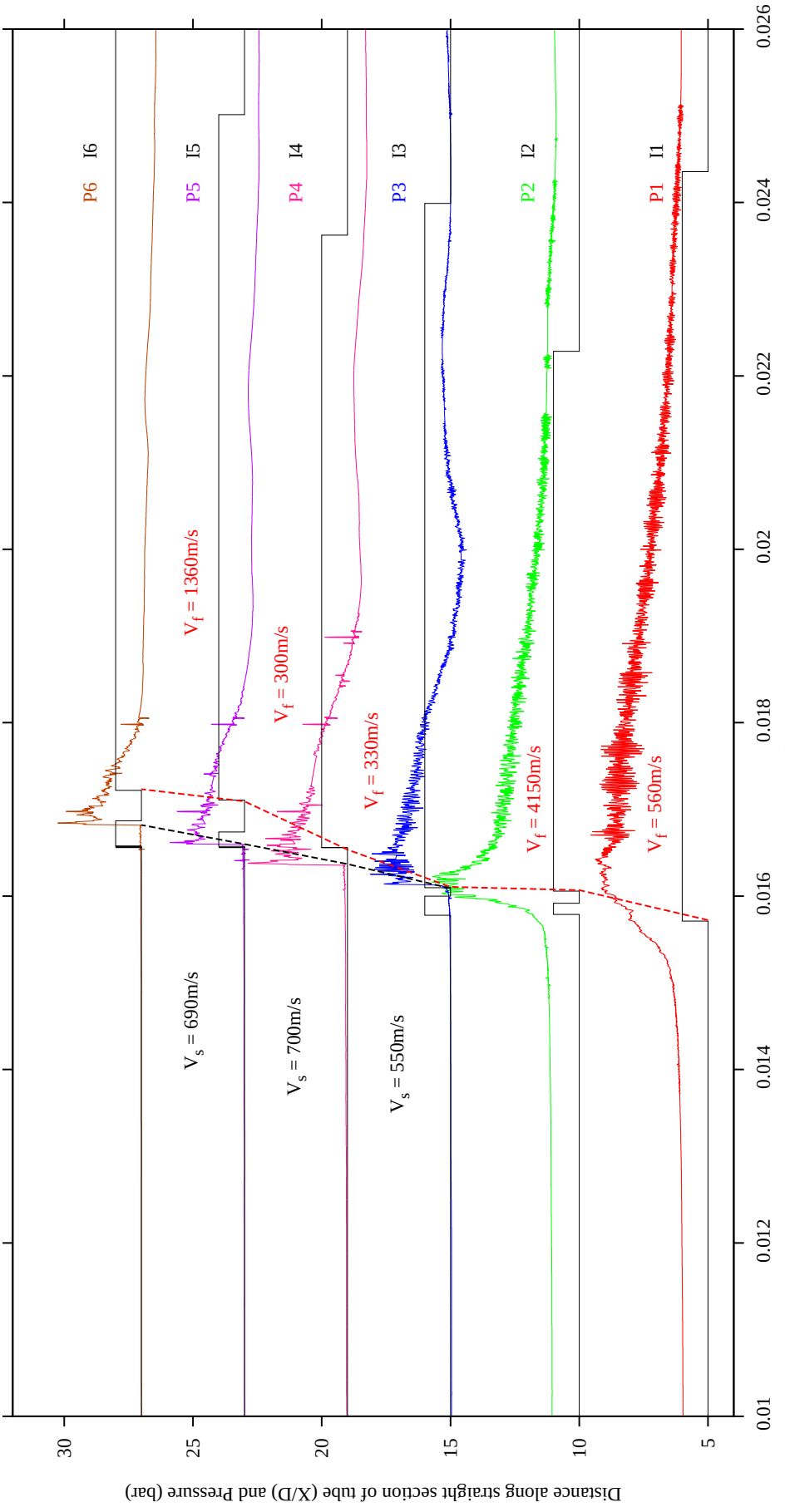

FIGURE 5.10: Shot C: 0.57BR setlectively smoothed pressure and ion probe plot.

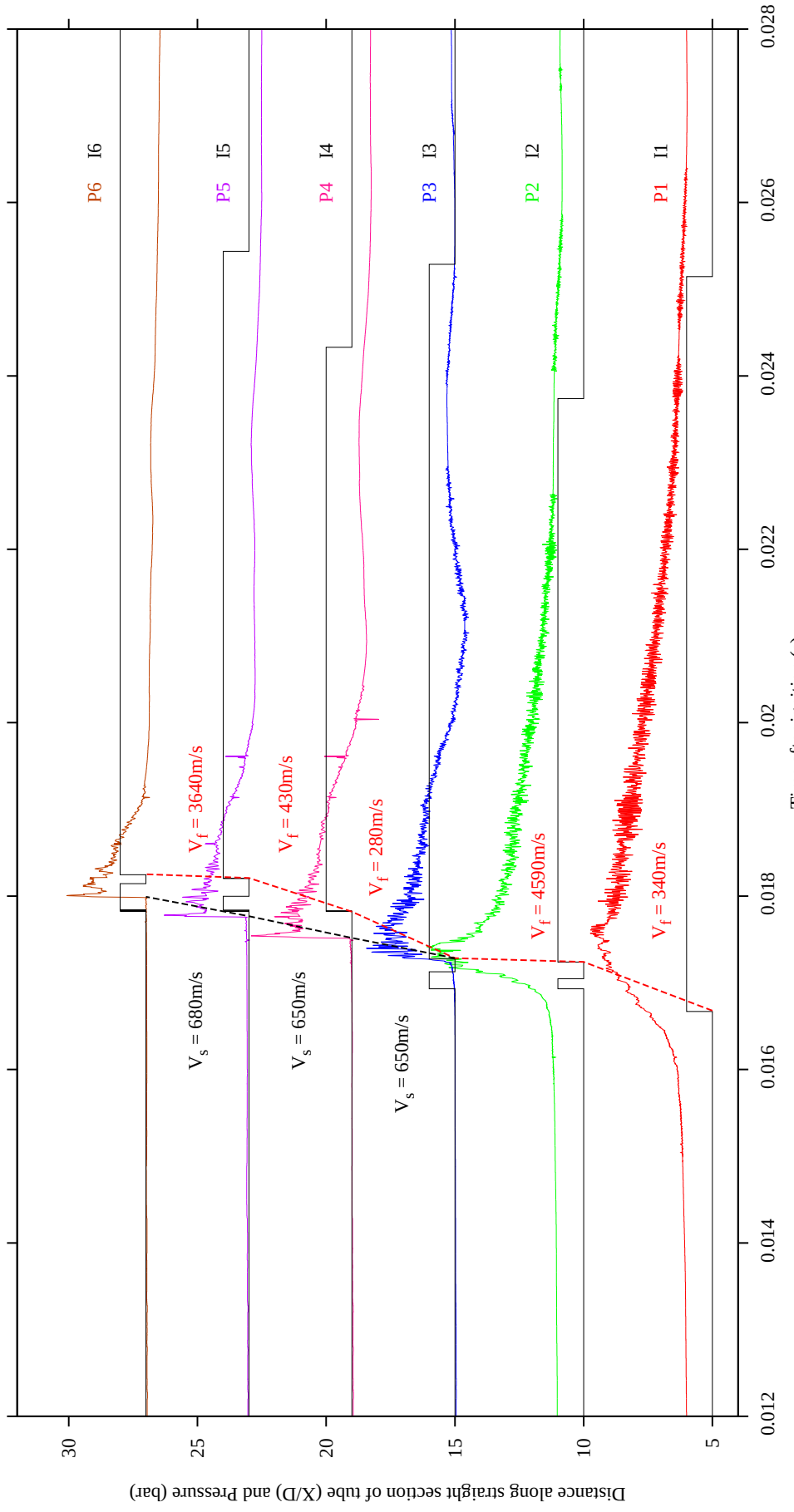

FIGURE 5.11: Shot D: 0.57BR smoothed pressure and ion probe plot.

5.3.6 Repeated 0.57 BR end ignition results

Type of shot	Number of shots	% data within range
Total in ϕ band	245	100
Misfires	96	39.2
Good	49	20.0
Nagative flame speed	45	18.4
Faulty Sensor	55	22.5

TABLE 5.6: Data Quality for the constant 0.75BR test

It can be seen from table 5.6 that there were a number of negative indicated flame speed results. This was the last test to be completed on the rig, so the negative flame speeds were thought to be the result of increasing sensor failure, as the ion probe ceramics had begun to fracture by this test. When this happened with other tests the ion probe spark plugs were changed after the test and the preceding test showed only positive flame speeds.

5.3.6.1 Statistical Pressure Analysis

Figure 5.12 illustrates the statistical distribution of pressure along the PDE tube taken from the repeated 0.57BR test case. It should be noted that the first pressure transducer failed after the initial 0.57BR test and as such these readings are excluded from all other tests. The first pressure reading, P2, taken at PL4 shows a mean pressure value of 5.60 bar, with a standard deviation of 0.45 bar. After PL4 the pressure is seen to drop severely by nearly 2 bar to a mean of 3.76 bar in P3 at PL5. This rapid reduction in peak pressure corresponds with the orifice plate exit. The standard deviation in P3 is seen to be slightly smaller at 0.26 bar. Each of these pdf's for pressure appear to be skewed to the right, indicating that pressures lower than the pdf centre line are more regularly attained than higher pressures with the mean being off centre to the right. P4 measured at PL6 indicates a rise in pressure from PL5. The mean peak value at P4 is 4.86, with a standard deviation of 0.32, maintaining a right skewed pdf. This pressure then reduces by PL7, with the mean peak pressure in P5 being 3.43 bar and standard deviation of 0.025. The standard deviation in pressure is much smaller at

this port location than any other. By the time the shock wave has reached PL8, the pressure measured by P6 has begun to increase to a mean value of 3.64 bar with a standard deviation of 0.19 bar.

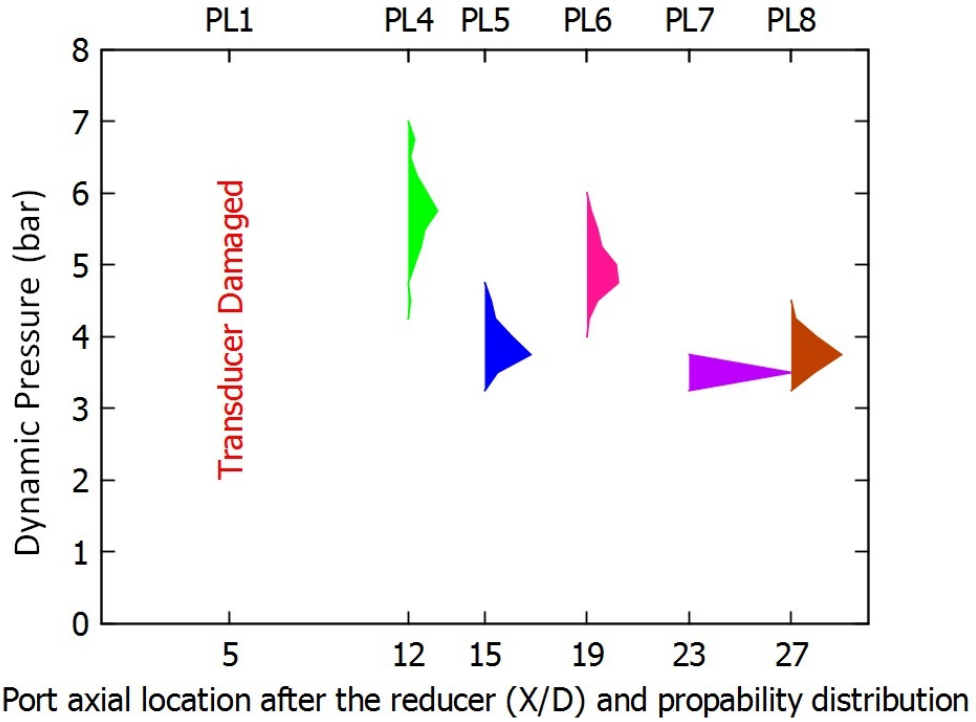

FIGURE 5.12: Statistical Distribution of peak shock pressure at each port taken with 0.57BR orifice plates installed throughout, repeated test.

5.3.6.2 Statistical Shock Speed Analysis

Figure 5.13 shows the shock speed between ports PL6-PL7 and PL7-PL8. There is a strong increase in the average shock speed from the first to the second reading, with an average increase in the shock speed from 600m/s with a standard deviation of 18m/s up to 705m/s with a standard deviation of 18m/s between PL7 and PL8.

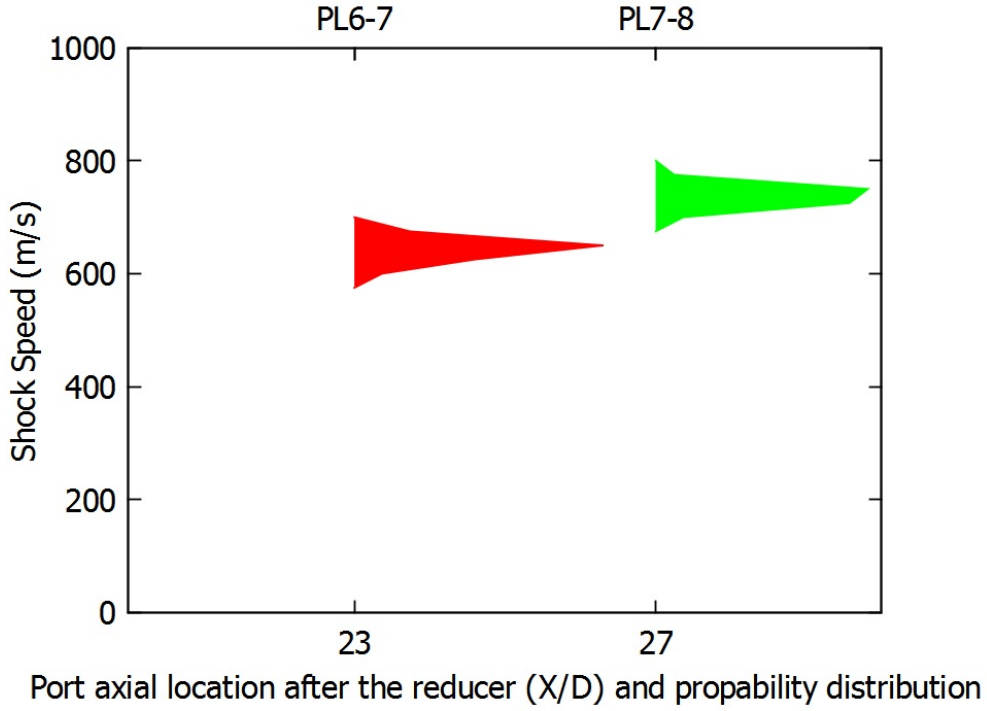

FIGURE 5.13: Statistical Distribution of flame speed at each port taken with 0.57BR orifice plates installed throughout, repeated test.

5.3.6.3 Statistical Flame Speed Analysis

Figure 5.14 illustrates the statistical FA progression along the tube for the 0.57 BR repeated test case. The initial flame acceleration between the igniter and PL2 is seen to produce a flame speed of 17m/s with a standard deviation of 2m/s. By PL4 the flame speed is seen to increase to a mean value of 886m/s with a standard deviation of 459m/s. By PL5 the average flame speed has reduced to 762m/s with a standard deviation of 439m/s. This trend of decreasing flame speeds continues, as by PL6 the flame speed has reduced further to 664m/s with a standard deviation of 234m/s. Again, by PL7 the flame speed drops further to a mean value of 401m/s with a standard deviation of 64m/s. At the final ports TOF measurement, PL8, the flame speed increases to 573m/s with a standard deviation of 550m/s. It should be noted that high speed outliers exist in the PL3-PL6 locations as well as the PL8 Location, but that because the proportion of the data at these velocities is small, the mean is only affected to a small degree. In contrast to the 0.57 BR initial end ignition case discussed in Section 5.3.4, the flame speed measured at port 11 is much higher, with a larger proportion of detonations than

the later cases, indicating much faster initial FA, which then reduces further along the tube, until it begins to occur again in the outliers across the last measurement section.

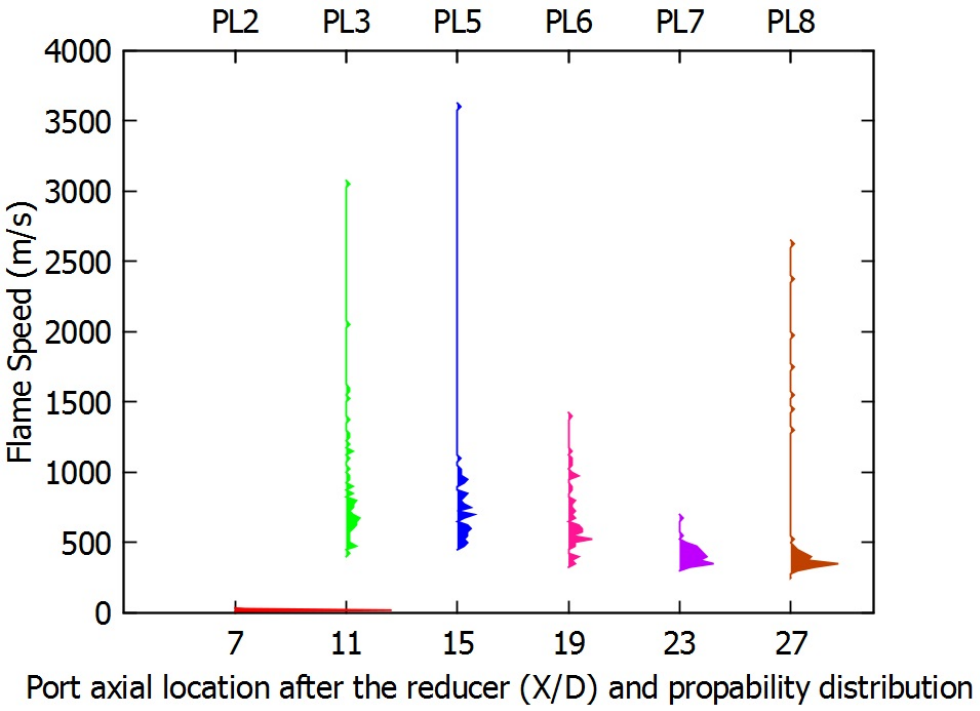

FIGURE 5.14: Statistical Distribution of flame speed at each port taken with 0.57BR orifice plates installed throughout, repeated test.

5.3.7 0.57 BR side ignition results

This side ignition case was included in the results to compare this group with other tests carried out in the rest of the experimental data across this thesis, each of which used the side ignition port. It can be seen that the ignition port location has a large impact on the firing reliability, with a relatively large number of misfires indicated for this case. The breakdown of the number of shots can be seen in table 5.7.

Type of shot	Number of shots	% data within range
Total in ϕ band	248	100
Misfires	170	68.6
Good	40	16.1
Nagative flame speed	10	4.0
Faulty Sensor	28	11.3

TABLE 5.7: Data Quality for the constant 0.75BR test

5.3.7.1 Statistical Pressure Analysis

Figure 5.15 illustrates the statistical pressure distribution along the PDE tube for 40 shots taken across the test equivalence ration band. The first pressure reading, P2, taken at PL4 is seen to have a tightly bounded pdf with a standard deviation of 0.38 bar and a mean value off 5.34 bar. By P3, which is measured at PL5, the pressure reduced by 1.6 bar to 3.69 bar with a standard deviation of 0.28 bar. PL5 was located just 2.5 diameters after the final orifice plate, in the smooth walled section of the tube. By P4, located at PL6, the pressure reached a mean value of 4.65 bar with a standard deviation of 0.27 bar, indicating an increase of 0.96 bar. By the next port location, PL7, the pressure P5 reduced again to a value to 3.35 bar with a standard deviation of 0.17 bar. The final pressure, P6, measured at PL8 increased again to 3.56 bar with a standard deviation of 0.21 bar.

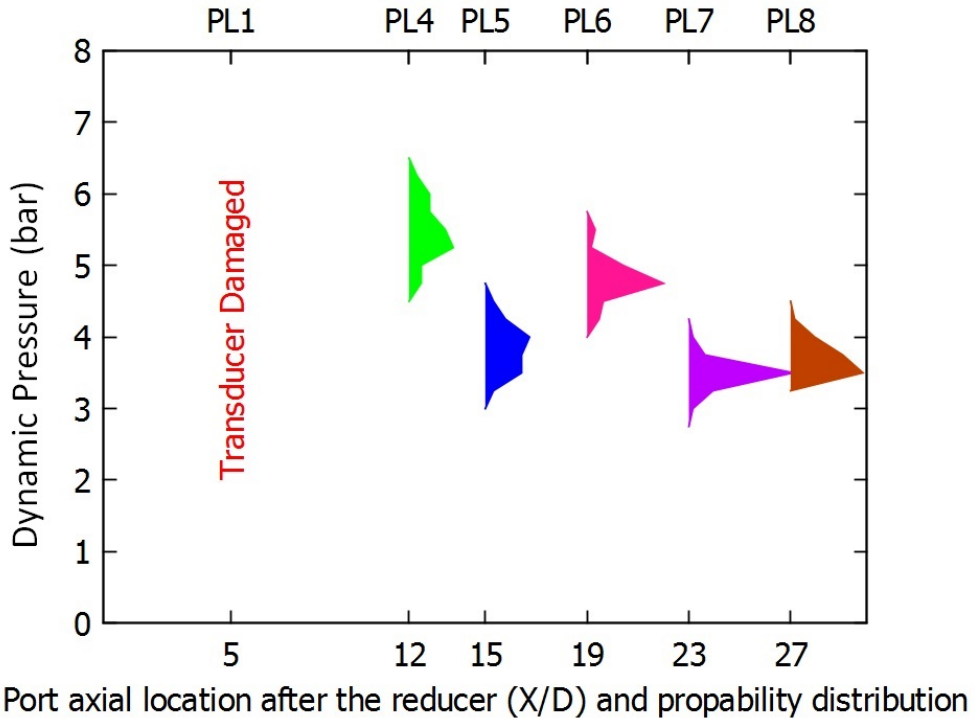

FIGURE 5.15: Statistical Distribution of peak shock pressure at each port taken with 0.57BR orifice plates installed throughout, side ignition test.

5.3.7.2 Statistical Shock Speed Analysis

Figure 5.16 shows a marked increase in shock speed from a mean value of 610m/s between PL6 and PL7 to 680m/s between PL7 and PL8. The respective standard deviations of these shock speeds are both 10m/s.

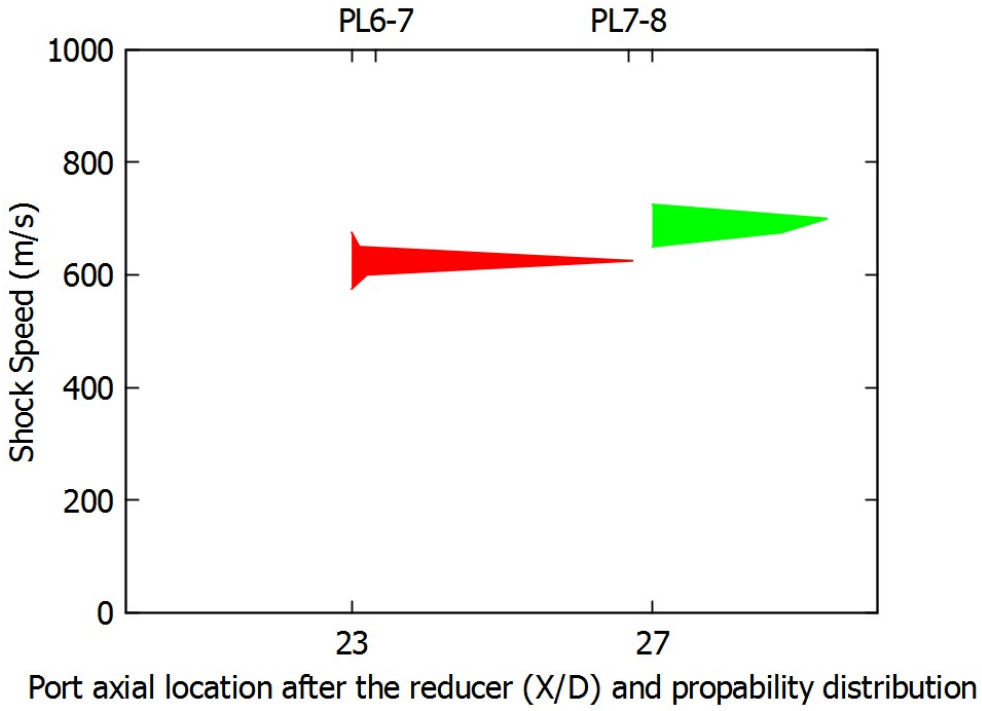

FIGURE 5.16: Statistical Distribution of flame speed at each port taken with 0.57BR orifice plates installed throughout, side ignition test.

5.3.7.3 Statistical Flame Speed Analysis

Figures 5.17 and 5.18 show the flame acceleration pdfs for the 0.57 BR orifice side ignition case. The flame speed measured between the ignition port and PL2 at the 7th tube diameter has an average value of 17m/s with a standard deviation of 3m/s. By the next port, PL3, the spread of results has increased dramatically from a minimum value of around 150m/s to a maximum of over 8km/s. The mean flame speed at PL3 was calculated to be 1215.80m/s which was affected to a large degree by four shots which had a velocity greater than 3000m/s. The median value here is probably closer to 600m/s, although this is difficult to observe from Figure 5.17. It is much easier to determine the difference in figure 5.18, which shows at three distinct velocity groupings at around 500m/s, 600m/s and 900m/s. Above the velocity of 900m/s the flame velocities are sparsely populated and spread over a large velocity range, with several shots distributed between 100m/s and 1600m/s. By the 15th diameter at PL5 the lower flame speed limit is approximately 500m/s, and the maximum velocity in this range is limited to around 1400m/s. The pdf at PL5 shows that the bulk of the flame velocities fall below the 800m/s value, with a strong skew to the lower velocity

range as shown in other flame velocity pdf plots. The mean value at this location is 703m/s with a standard deviation of 171m/s. The next pdf for flame speed at the PL6 location shows that the range of velocities is very similar to the PL5 location, however the bulk of flame velocities have reduced from a range of 500m/s to 800m/s down to a range of 400m/s to 700m/s, showing a stronger skew to the lower flame velocity. The mean flame speed at this location was calculated as 584m/s with a standard deviation of 203m/s. PL7 and PL8 illustrate a rapid reduction in flame speed, coupled with a strong reduction in the range of flame speeds. By PL7 and PL8 no flame velocities above 600m/s were registered by the ion probes. The mean flame speed at PL7 was calculated as 324m/s with a standard deviation of 34m/s. By PL8 the mean flame speed had dropped to 285m/s with a standard deviation of 32m/s.

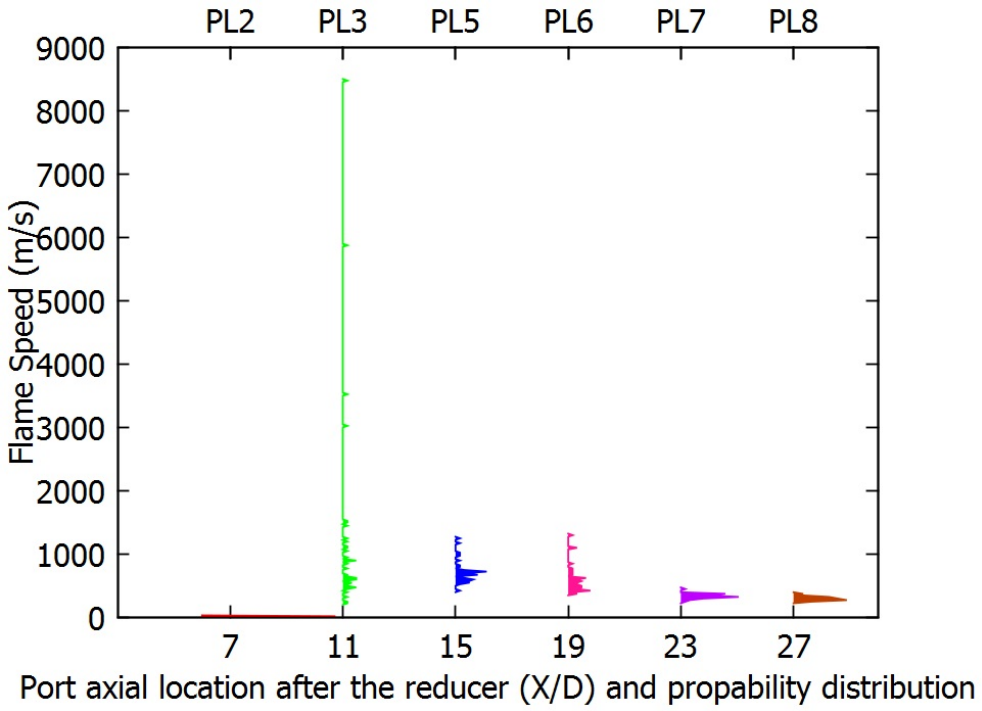

FIGURE 5.17: Statistical Distribution of flame speed at each port taken with 0.57BR orifice plates installed throughout, side ignition test.

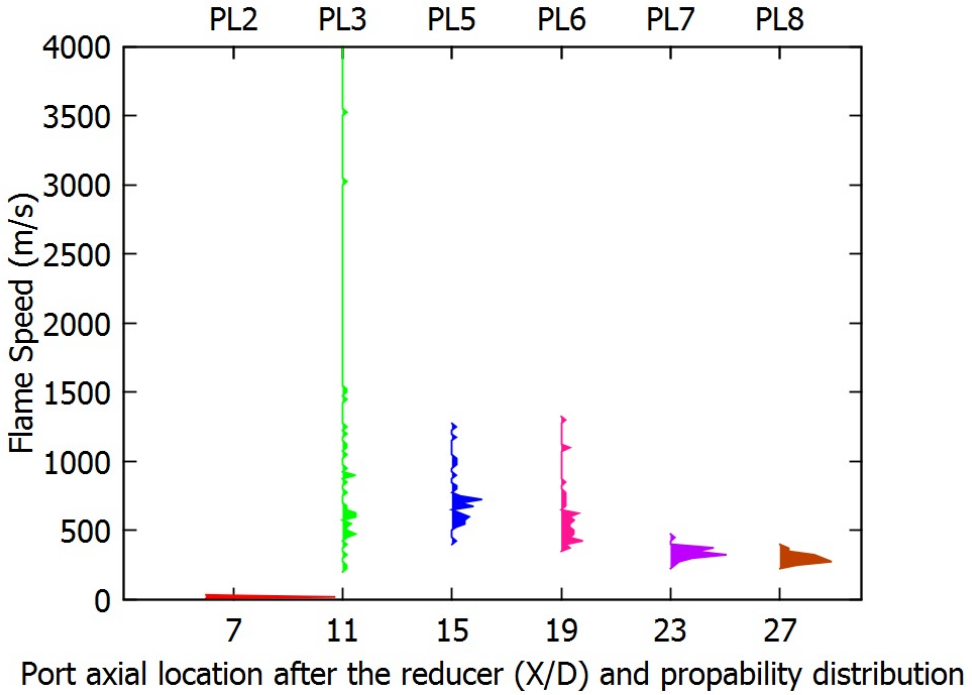

FIGURE 5.18: Zoomed in Statistical Distribution of flame speed at each port taken with 0.57BR orifice plates installed throughout, side ignition test.

5.3.8 0.75 BR end ignition results

Type of shot	Number of shots	% data within range
Total in ϕ band	368	100
Misfires	143	38.9
Good	176	47.8
Nagative flame speed	44	12.0
Faulty Sensor	5	1.4

TABLE 5.8: Data Quality for the constant 0.75BR test

5.3.8.1 Statistical Pressure Analysis

Flame pressure pdfs for the 0.75BR test case can be seen in Figure 5.19. It can be seen that the pressure at this PL4 is distributed across a a wide spectrum of pressures from 1 to 6 bar. The mean pressure at this location is 4.04 bar with a standard deviation of 0.57 bar. From this location onwards the pressure was seen to decrease rapidly, and unlike other cases the pressure did not increase further down the tube. Pressures measured from PL5 to PL8 all shared the same wide pressure range as the pressure measured at PL4, however the range had been shifted by approximately -2 bar. The mean pressure steadily dropped as the shock wave progressed along the passage. The mean value of pressure at PL5 to PL8 was 2.16 bar 2.13 bar 1.77 bar and 1.73 bar respectively. The standard deviation in the pressure from PL5 to PL8 was seen to be 0.48 bar, 0.70 bar, 0.62 bar and 0.69 bar respectively. The pressure pdf distributions at PL6 and PL8 still exhibit a small peak at the high pressure side of the pdf, around 3 bar. This indicates that a small number of shocks are gaining pressure at these particular ports relative to PL5 and PL7, however this is only a small fraction of the whole. Interestingly, each of these pressure pdfs exhibit the opposite skew to previous graphs, skewing to the higher pressure end of the spectrum and tailing off to the lower pressure end. It was initially thought that this could have been a processing error which may have resulted from a change in the threshold value of pressure set on the waveform trigger function. This hypothesis was disproved by repeating all of the post processing at this particular condition however no change was indicated in the results.

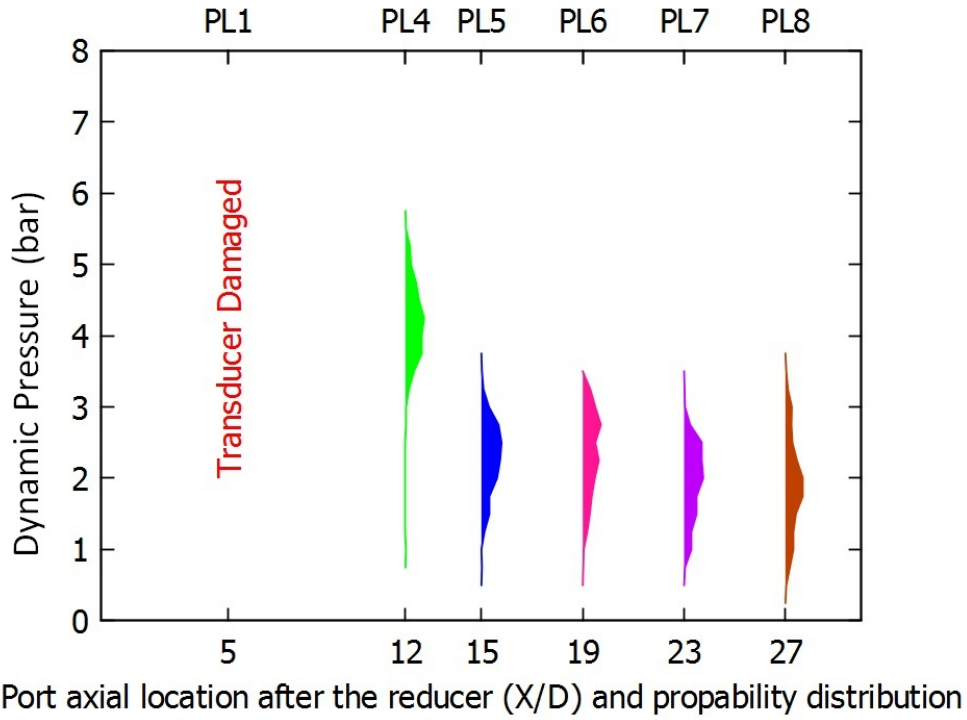

FIGURE 5.19: Statistical Distribution of pressure at each port taken with 0.75BR orifice plates installed throughout.

5.3.8.2 Statistical Shock Speed Analysis

Shock speeds between PL6 and PL8 are recorded as pdfs in figure 5.20. The shock speeds measured between PL6 and PL7 have a mean value of 490m/s and a standard deviation of 60m/s. In comparison, the shock speed measured between PL7 and PL8 has a mean value of 510m/s and a standard deviation of 100m/s. The shock speed pdf here shows a wide spectrum of different shock speeds, which is much larger in range than any of the other shock pdfs for cases analysed previously.

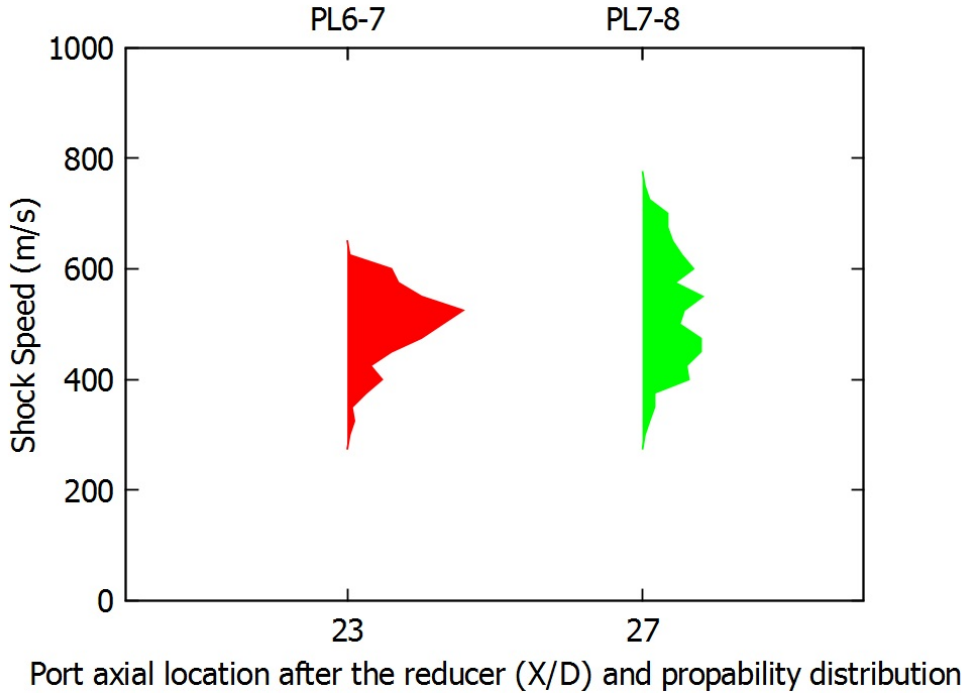

FIGURE 5.20: Statistical Distribution of shock speed using TOF calculated shock speeds taken with 0.75BR orifice plates installed throughout.

5.3.8.3 Statistical Flame Speed Analysis

Figures 5.21 and 5.22 show the flame speed distribution for the 0.75BR end (thrust wall) ignition port case. Initial flame acceleration is seen to be slow, with no high speed outliers showing DDT velocities until PL6, which is much later than previously analysed data. The flame speed between the igniter and PL2 had a mean value of 18m/s and a very narrow standard deviation of 1m/s. By PL3 the flame speed has accelerated to a mean value of 147m/s with a standard deviation of 39m/s. The flame speed at PL5 mean value was calculated to be 464m/s with a standard deviation of 156m/s. This increasing trend of FA continued through PL6 to PL7 with mean V_f values of 728m/s and 1202m/s respectively before decreasing to half this value, 654m/s by PL8. The standard deviations in V_f from PL6 to PL8 were 2233m/s, 2307m/s and 817m/s respectively. This pattern of slow FA and reduction in flame speed at the last port breaks the trend in earlier results for other cases, which exhibited initially rapid FA, a decrease in the flame speed and further FA between the last two ports, PL7 and PL8.

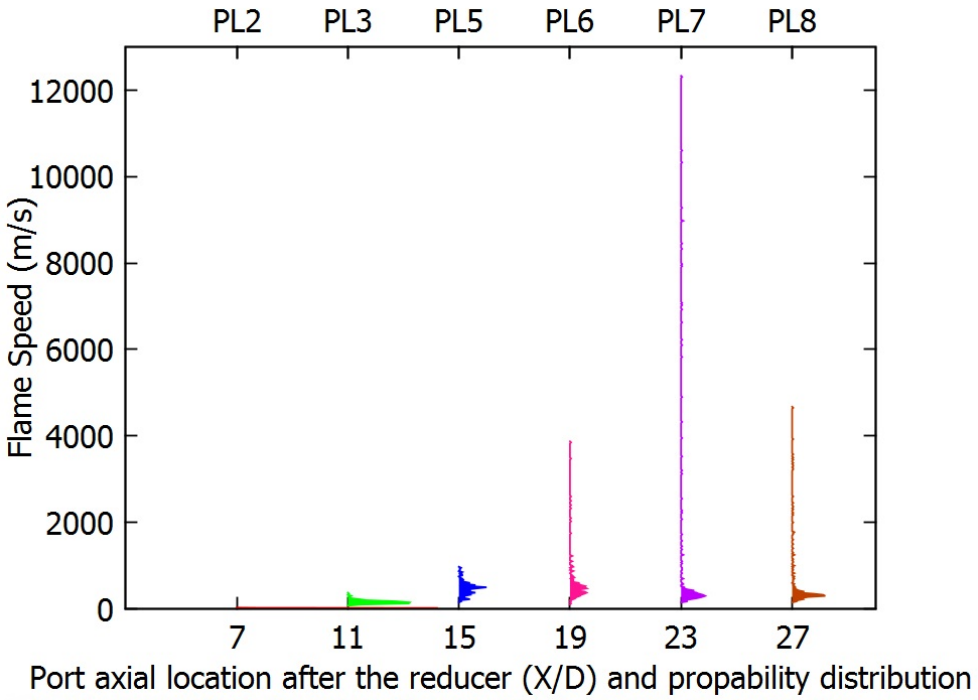

FIGURE 5.21: Statistical Distribution of flame speed at each port taken with 0.75BR orifice plates installed throughout.

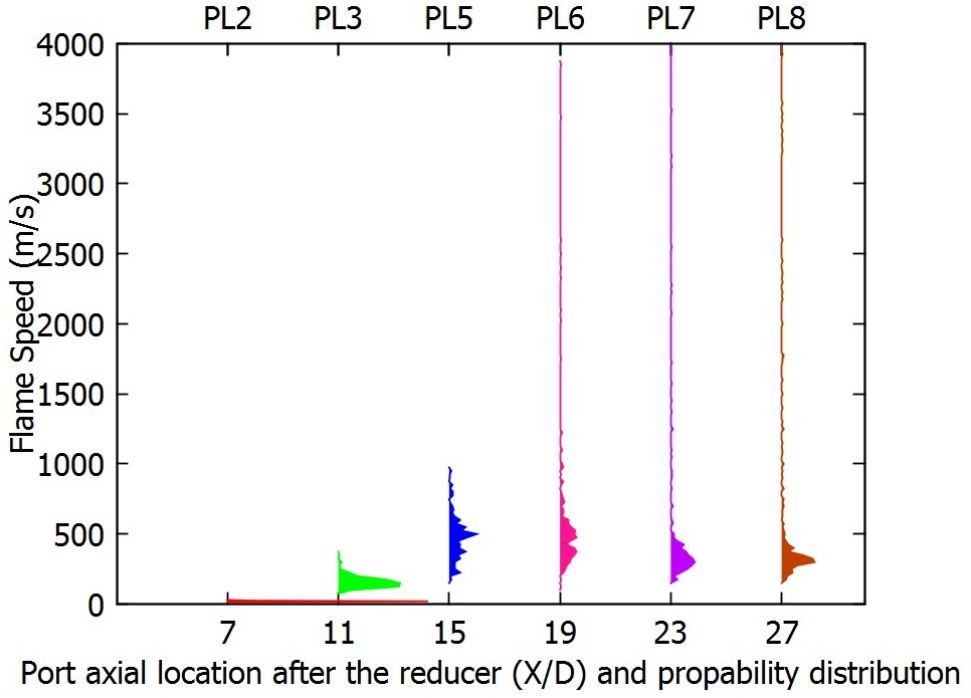

FIGURE 5.22: Statistical Distribution of flame speed at each port taken with 0.75BR orifice plates installed throughout. This plot is cut off at 4000m/s to give a clearer indication of the low speed data, which provides the statistical bulk of the data at most sensor locations.

5.3.9 Increasing BR end ignition results

It should be noted that the number of misfires for this condition was the lowest for any of the conditions, as can be seen in table 5.9. The number of negative flame speeds was very low for this case, at 1 %.

Type of shot	Number of shots	% data within range
Total in ϕ Band	91	100
Misfires	0	0
Good	90	99.0
Negative Flame Speed	2	1.0

TABLE 5.9: Data Quality for the inccreasing BR test

5.3.9.1 Statistical Pressure Analysis

Statistical pdfs for the shock wave pressure generated by increasing BR orifice plates as described in Table 5.2 can be seen in Figure 5.23. The pressure distribution seen in this figure is generally similar to that of the earlier conditions seen in sections sec:0.57res to 5.3.7. The pressure seen at PL4 has a mean value of 4.97 bar with a standard deviation of 0.37 bar. The pressure than falls to 3.19 bar at PL5, with a standard deviation of 0.25. A pressure rise is observed between PL5 and PL6, to a mean value of 3.61 bar with a standard deviation of 0.25 bar. This peak shock wave pressure then decreases by 0.5 bar to a mean value of 3.10 bar at PL7 with a standard deviation of 0.2 bar before increasing again at PL8. The final mean value at PL8 is seen to be 3.41 bar with a small standard deviation of 0.16 bar.

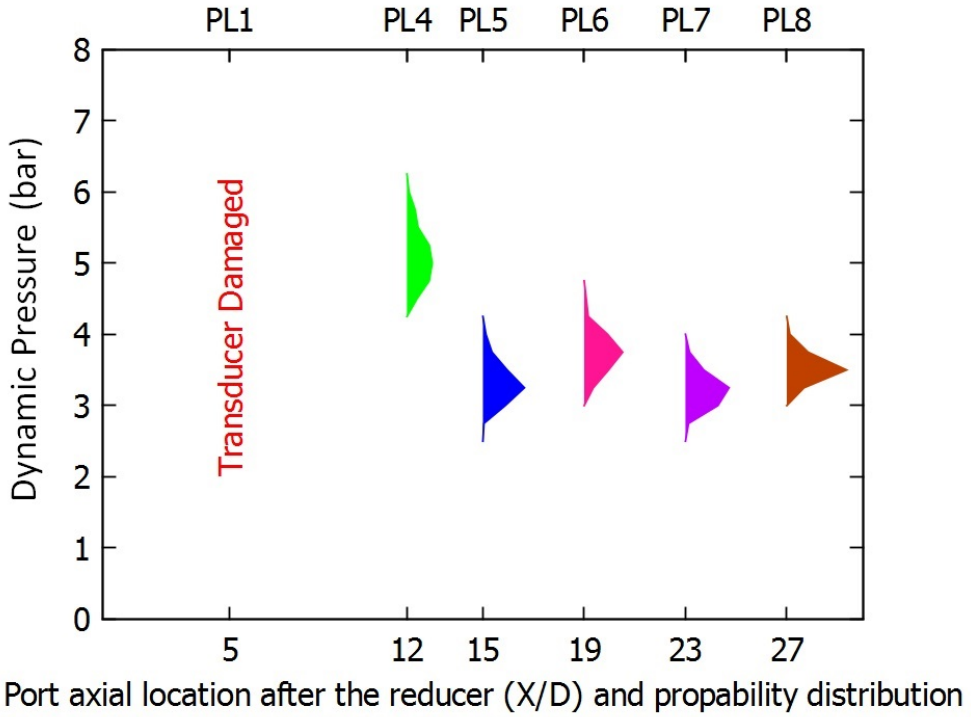

FIGURE 5.23: Statistical distribution of pressure at each port taken with increasing BR orifice plates installed.

5.3.9.2 Statistical Shock Speed Analysis

Figure 5.24 shows the statistical shock speed distribution for shocks produced by FA across the increasing BR obstacle section. The mean velocity for the shock speed from PL6-PL7 was calculated to be 630m/s with a standard deviation of 20m/s. Between PL7 and PL8 the mean shock velocity was recorded as 760m/s with a standard deviation of 30m/s.

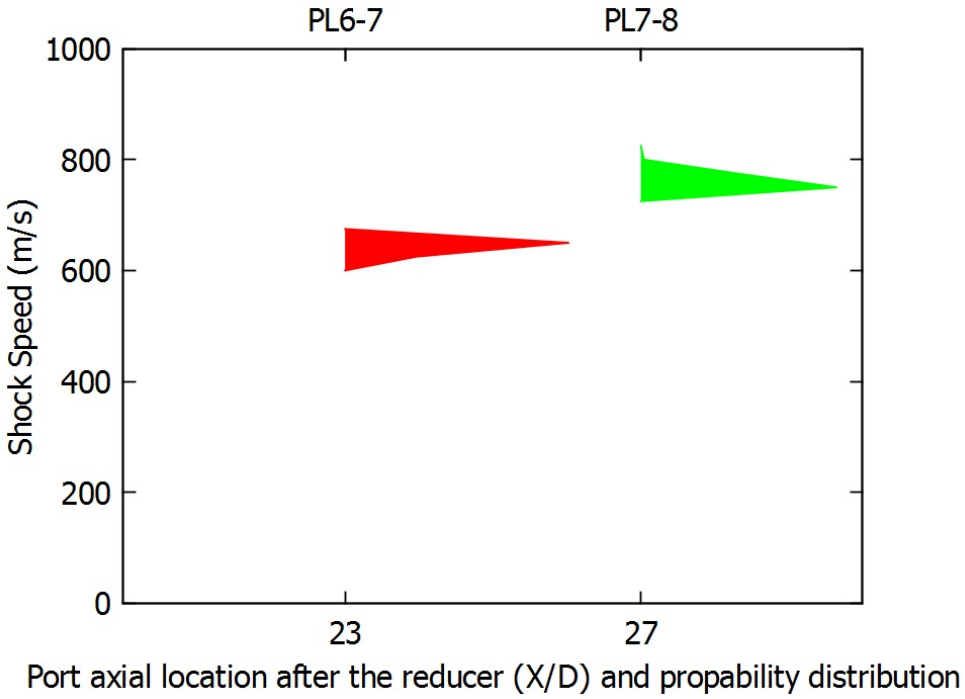

FIGURE 5.24: Statistical distribution of shock speed between PL6-7 and PL7-8 with increasing BR orifice plates installed.

5.3.9.3 Statistical Flame Speed Analysis

Figure 5.25 shows the statistical distribution of flame speeds along the tube for the Increasing BR case. The mean initial flame speed recorded from the igniter to the first port, PL2, was 22.5m/s with a standard deviation of 1.65m/s. Between PL2 and PL3 the flame speed increased to a mean value of 485m/s with a standard deviation of 89.94m/s. A small number of outliers were indicated in the pdf at around 1000m/s flame speed for this location. Between PL3 and PL5 the flame speed increased to a mean value of 627m/s with a standard deviation of 351.0 m/s. By this port location the pdf indicates that the bulk of the flames are traveling at at velocities below the sonic speed in the products, however there are a portion of flames traveling at around 900m/s and one or two occasional outliers at very high speeds. By PL6 a small fraction of the pdf is distributed around the detonation velocity at approximately 1500m/s with one shot reaching a velocity of around 3500m/s. The bulk of the flames travelling between PL5 and PL6 are however much slower, between 300m/s and 700m/s with a mean flame velocity for this port location of 648.65m/s and a standard deviation of 403.2m/s. By the time the flame had traversed to PL7 the mean flame speed had fallen to 341m/s with a standard deviation of 51.89m/s. This is reflected in the figure by a strong deceleration

and reduction in the range of the flame speed pdf. By PL8 the mean flame speed had further decelerated to 280.9m/s with a standard deviation of 32.56m/s. It is interesting to note that there are no high speed flames measured along the last two port locations.

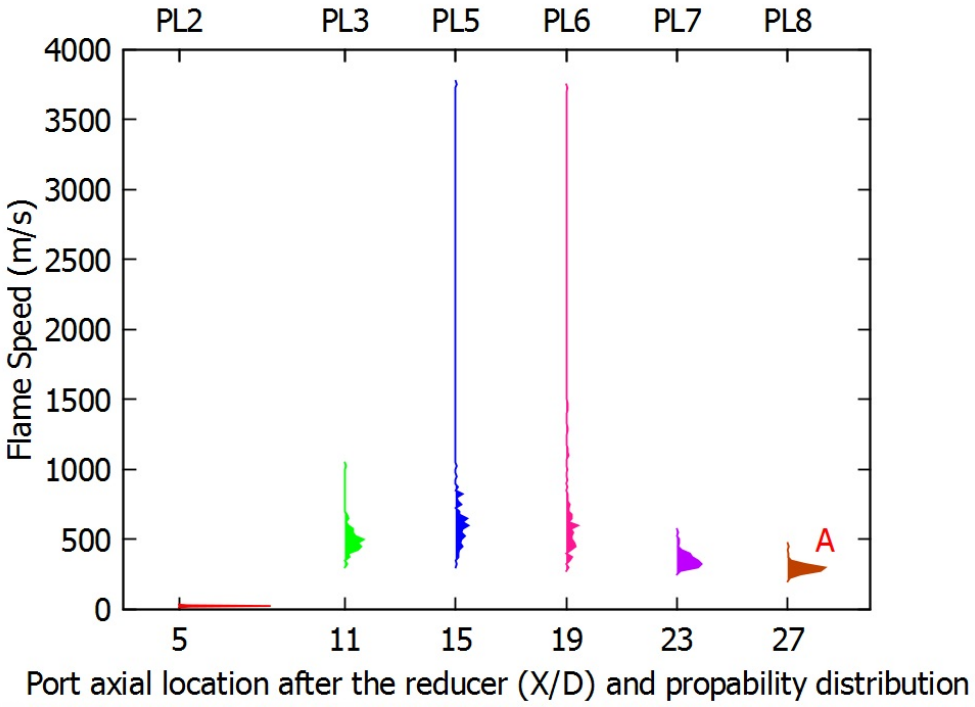

FIGURE 5.25: Statistical Distribution of flame speed at each port taken with Increasing BR orifice plates installed

5.3.10 Key regimes

Only one velocity band has been chosen for this case as 97% of the data fell within the slow regime, with the flame exit speed being less than the sonic velocity in the products. There were only three shots in ninety-four above this threshold. The fastest data above this threshold a velocity at the end of the tube of 439m/s and the average velocity across this extra band would have been 390m/s. Because this data is so rarely achieved, no further analysis will be carried out on the 3% above this value for this particular case.

Band	Lower V_f (m/s)	Upper V_f (m/s)	Average data V_f (m/s)
A	0	340	277

TABLE 5.10: Velocity Bands

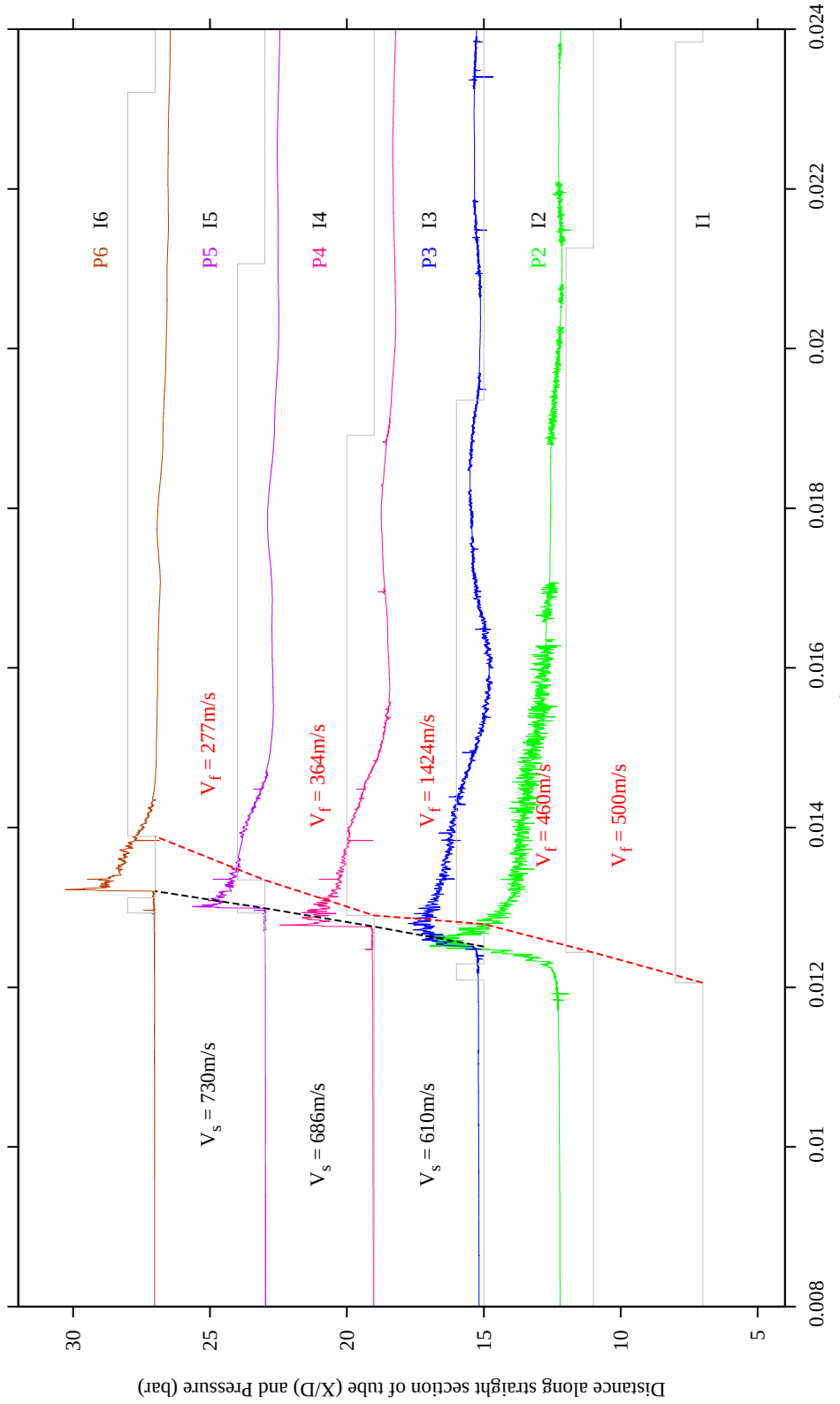

FIGURE 5.26: INCBR setlectively smoothed pressure and ion probe plot for the average velocity taken at point A.

5.3.11 Decreasing BR results

Type of shot	Number of shots	% data within range
Total in ϕ band	404	100
Misfires	31	7.7
Good	344	85.1
Nagative flame speed	16	4.0
Faulty Sensor	13	3.2

TABLE 5.11: Data Quality for the decreasing BR test

5.3.11.1 Statistical Pressure Analysis

Figure 5.27 shows the statistical distribution of pressure for the shock waves generated by FA in the decreasing BR orifice case. The mean peak dynamic pressure measured at PL4 was 4.54 bar with a standard deviation of 0.58 bar. The pressure pdf measured at this port showed a strong skew top, with a large mass of results at the higher pressure range up to approximately 5.5 bar. By PL5 the mean pressure had reduced to 3.33 bar with a standard deviation of 0.28 bar. The spread of the pdf reflects the reduction in the standard deviation at this location. The pressure pdf taken at PL6 shows a similar pattern to the pdf taken at PL4, with a strong skew towards shock peak pressures, and a waxing tail to the right, lower portion of the pdf. The mean peak dynamic pressure measured at this port location was 4.12 bar with a standard deviation of 0.53 bar. The peak dynamic pressure measured at PL7 had mean value of 3.16 bar with a standard deviation of 0.31 bar, exhibiting a tighter pdf with a short tail proceeding to approximately 1.75 bar. By the final pressure transducer, which was mounted at PL8, the mean pressure reached a value of 3.37 with a standard deviation of 0.31 bar.

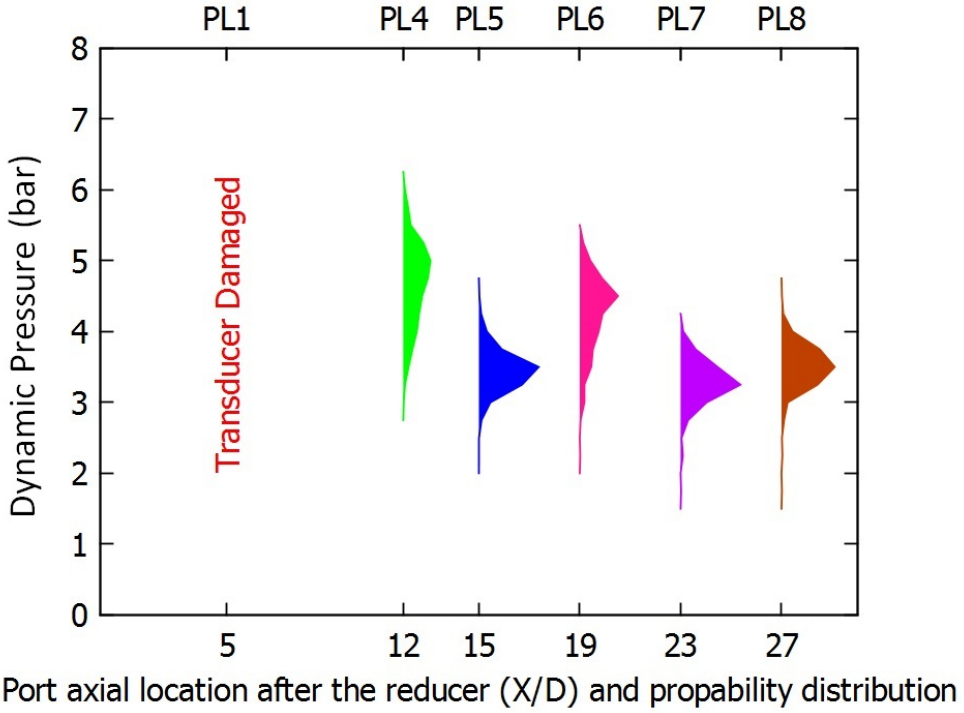

FIGURE 5.27: Statistical Distribution of pressure at each port taken with decreasing BR orifice plates installed.

5.3.11.2 Statistical Shock Speed Analysis

The statistical pdf of shock speed for the decreasing BR condition can be seen in Figure 5.28. The mean shock speed between PL6 and PL7 was calculated as 630m/s with a standard deviation of 40m/s. The mean shock speed between PL7 and PL8 was calculated and found to be 740m/s with a standard deviation of 40m/s.

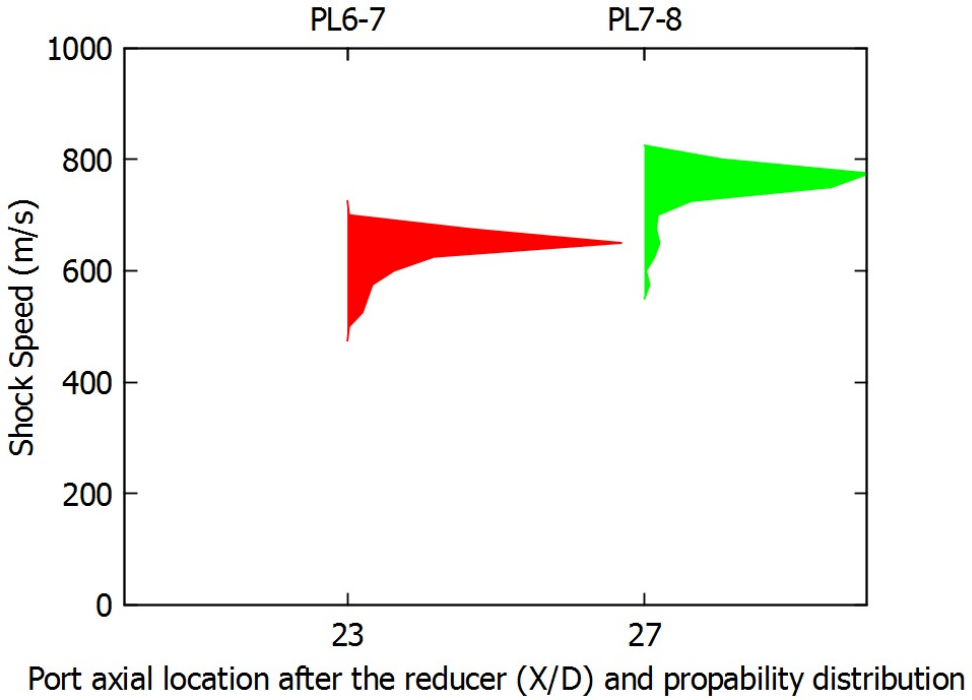

FIGURE 5.28: Statistical distribution of shock speed accross PL6-7 and PL7-8 taken with decreasing BR orifice plates installed.

5.3.11.3 Statistical Flame Speed Analysis

Figures 5.29 and 5.30 illustrate the flame speed pdfs for the decreasing BR orifice blockage case. It can be seen that the initial flame speed between the igniter at the thrust wall and the first port PL2 is low, as usual, with a mean flame speed of 18.4m/s and a standard deviation of 1.2m/s. Between PL2 and PL3 the TOF measured flame speed increases rapidly to a mean value of 482.7m/s with a standard deviation of 868.4m/s. Between PL3 and PL5 the flame accelerates further, on average, to a mean value of 970.8m/s with a standard deviation of 1333.2m/s. Between PL5 and PL6, the flame begins to decelerate to a mean flame speed of 545.1m/s with a standard deviation of 145.4m/s. The mean flame speed between PL6 and PL7 was measured as 454.9m/s with a standard deviation of 229.8m/s. By the last port the flame had begun to accelerate again to a mean value of 582.9m/s with a standard deviation of 598.6m/s.

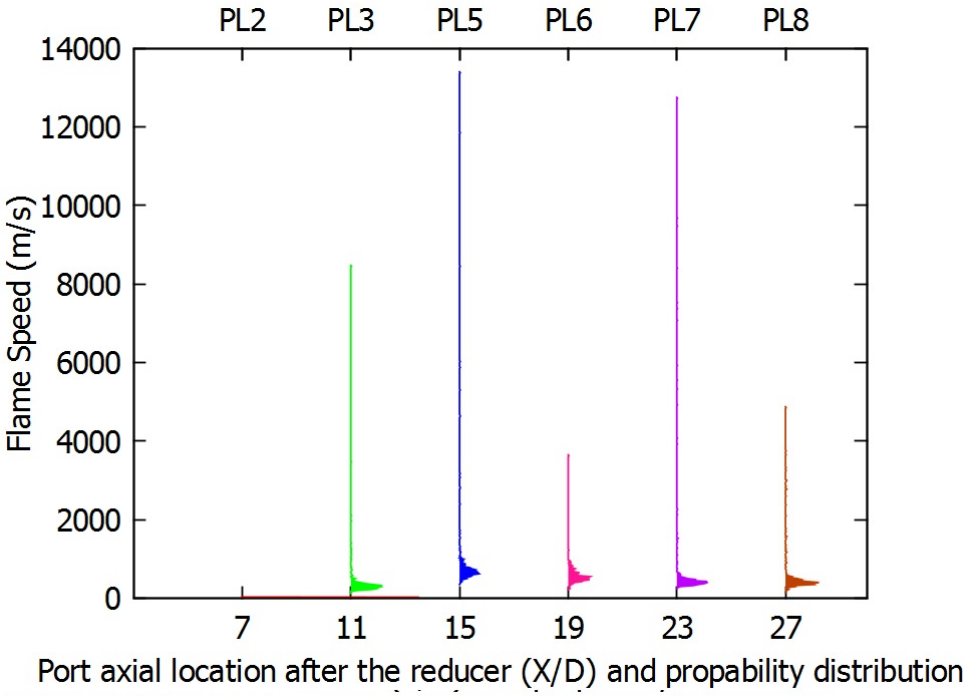

FIGURE 5.29: Statistical Distribution of pressure at each port taken with decreasing BR orifice plates installed.

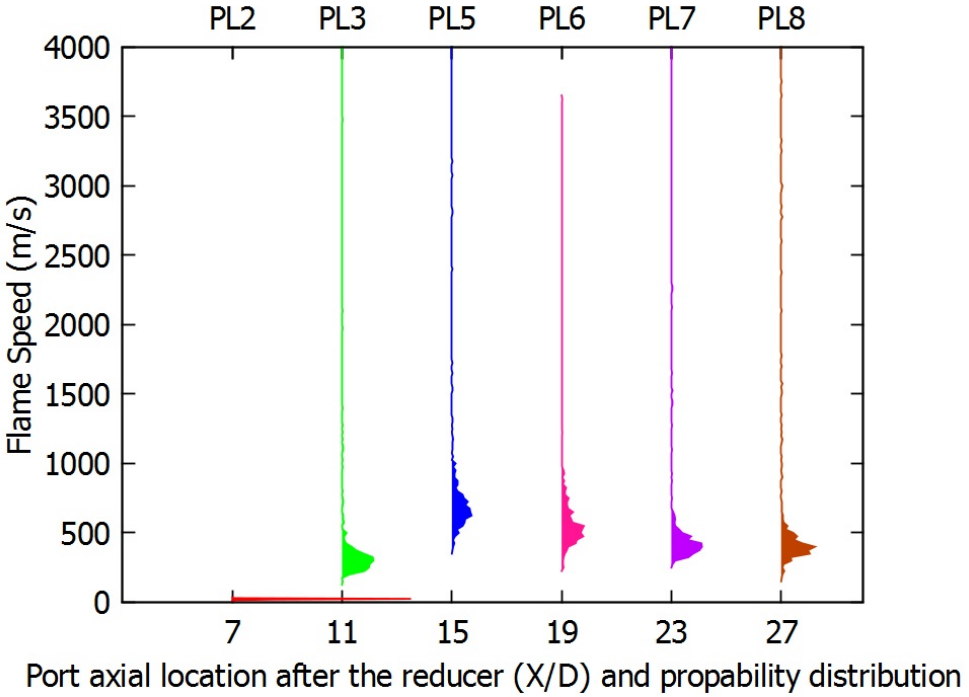

FIGURE 5.30: Statistical Distribution of flame speed at each port taken with decreasing BR orifice plates installed throughout. This plot is cut off at 4000m/s to give a clearer indication of the low speed data, which provides the statistical bulk of the data at most sensor locations.

5.3.12 Key regimes

Band	Lower V_f (m/s)	Upper V_f (m/s)	Average data V_f (m/s)	$N_{Band}/N_{s-total}$ %
A	0	340	298	21.2
B	340	993	434	70.6
C	993	1798	1345	4.1
D	1798	N/A	3080	4.1

TABLE 5.12: Decreasing BR Velocity Bands

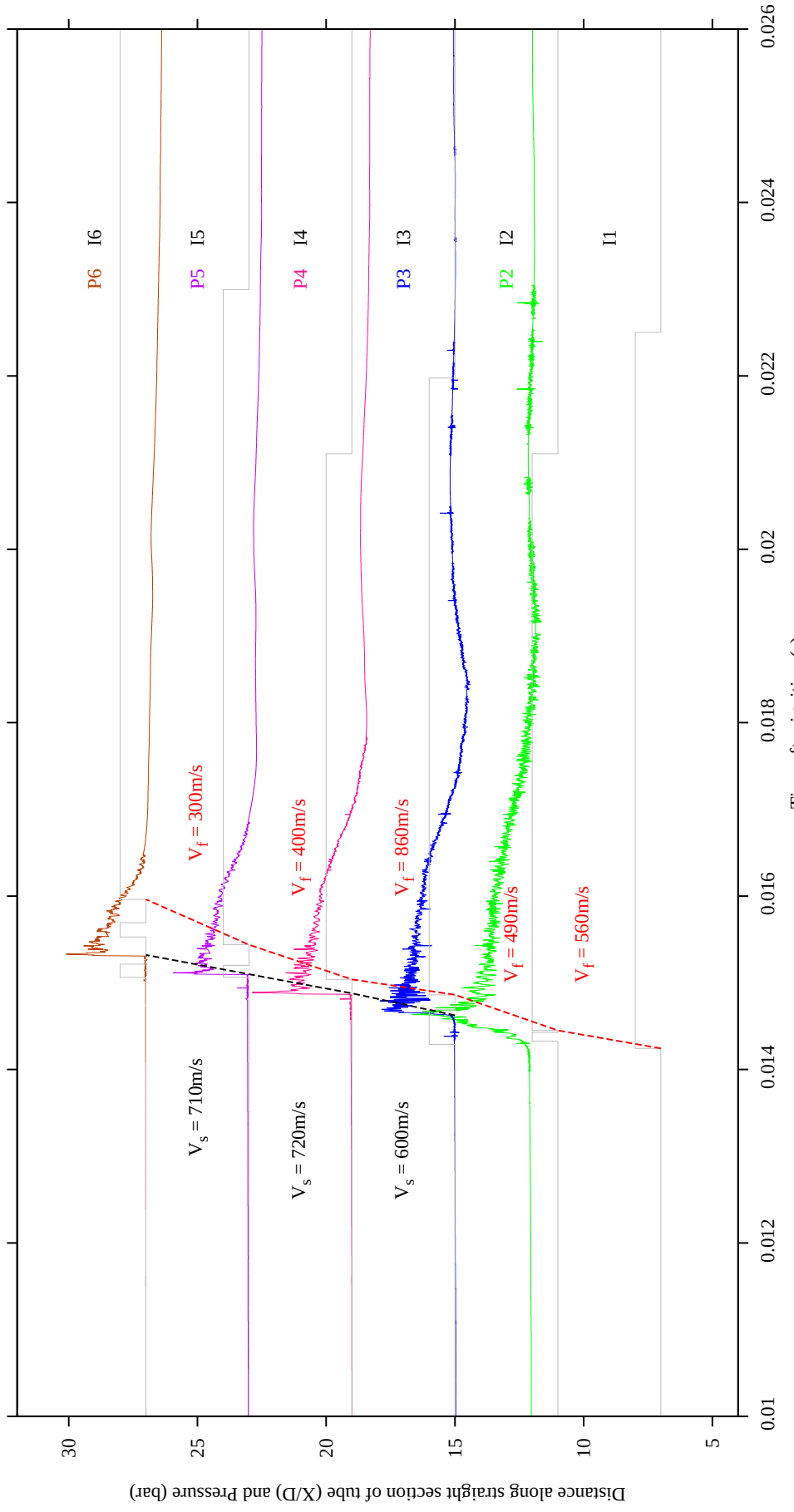

FIGURE 5.31: Shot A: Decreasing BR setlectively smoothed pressure and ion probe plot.

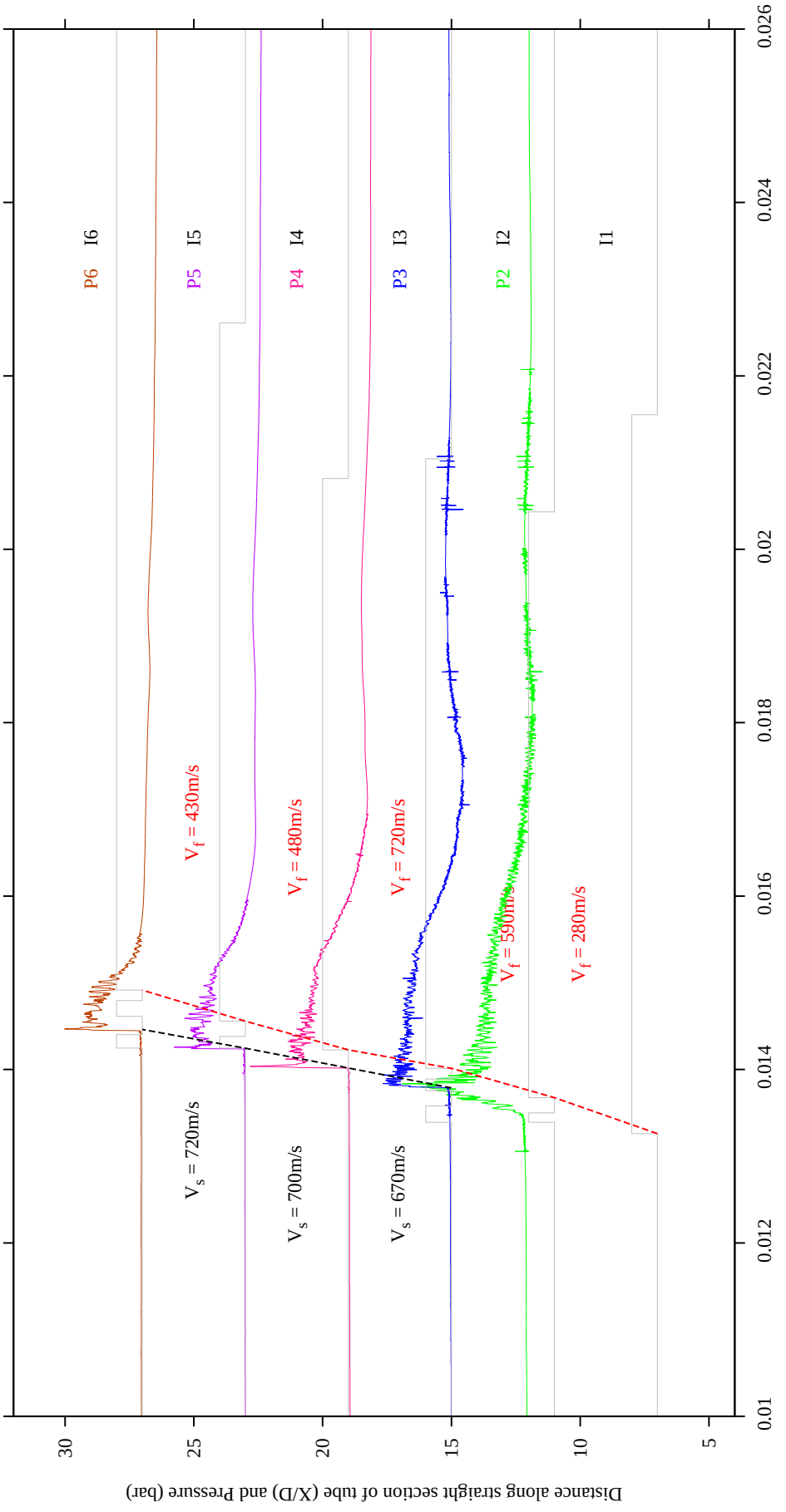

FIGURE 5.32: Shot B: Decreasing BR setlectively smoothed pressure and ion probe plot.

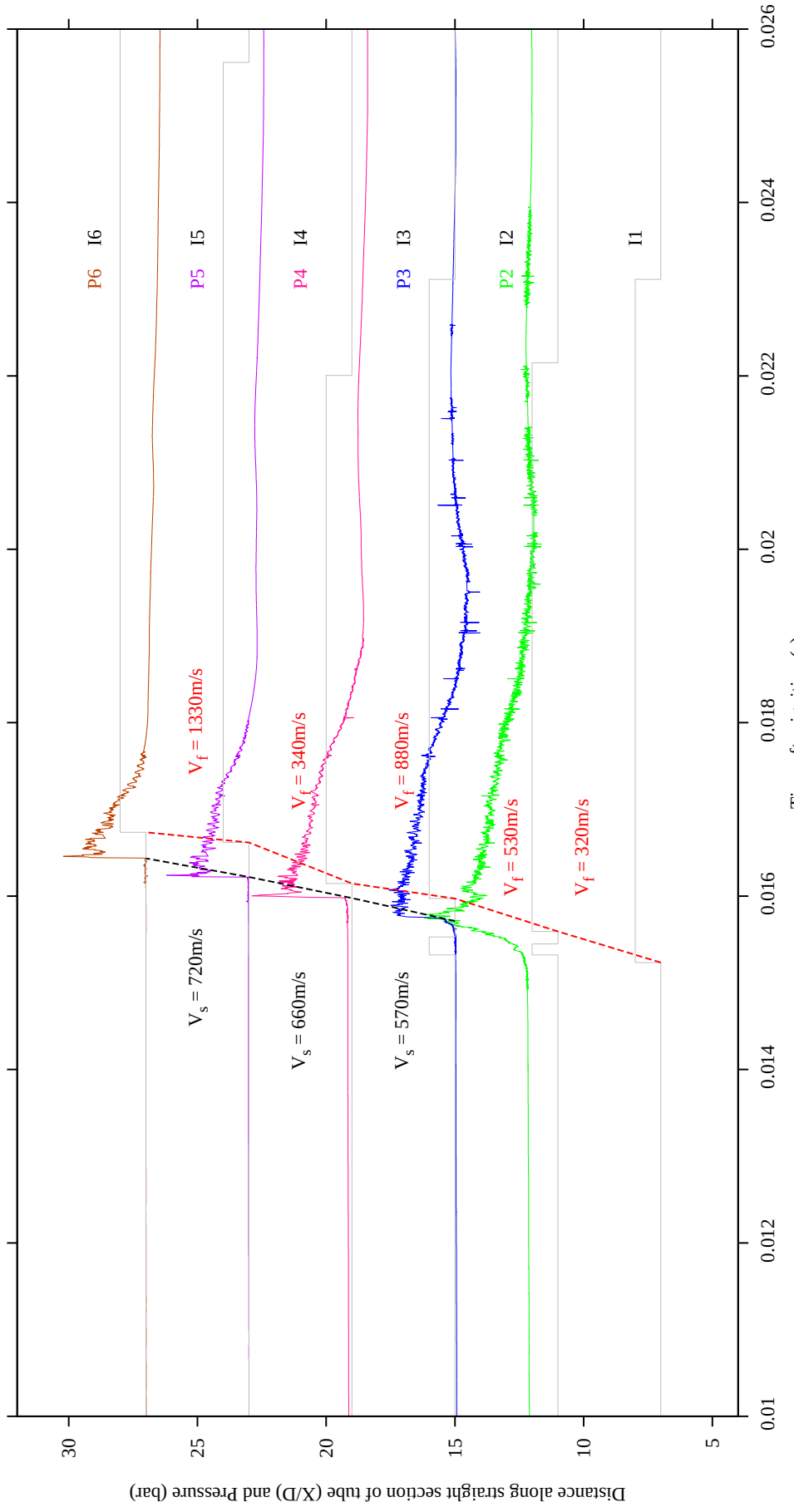

FIGURE 5.33: Shot C: Decreasing BR setlectively smoothed pressure and ion probe plot.

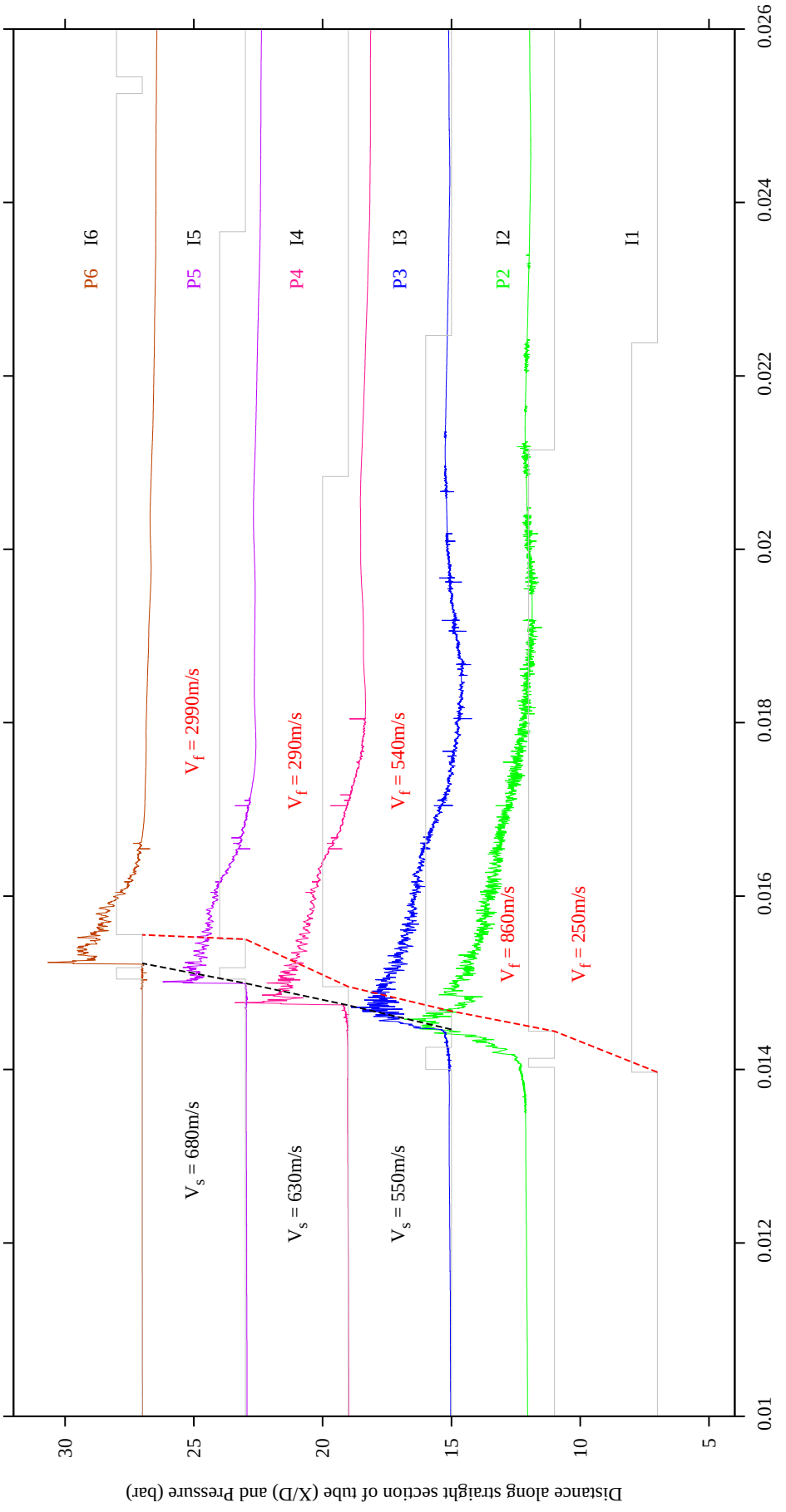

FIGURE 5.34: Shot D: Decreasing BR setlectively smoothed pressure and ion probe plot.

5.4 Case Comparisons

Figures 5.35 and 5.36 show the data quality and breakdown of different velocity bands for each of the cases. It can be seen from Figure 5.35 that very few of the 0.57 BR end ignition and 0.57 BR side ignition shots could be analysed with good quality data. This is because the majority of the 0.57 BR side ignition shots were misfires (over 60 %) while around 40 % of the 0.57 BR end ignition shots were misfires, an additional 40% were negative flame speeds or faulty sensor readings. It should also be noted that the 0.75 BR data contained around 40 % misfires and an additional 10% of the data was neglected due to faulty sensor readings or negative flame speeds, which may have also been sensor failure. The remaining three cases exhibited over 80% good quality data with very few misfires, particularly in the increasing BR case.

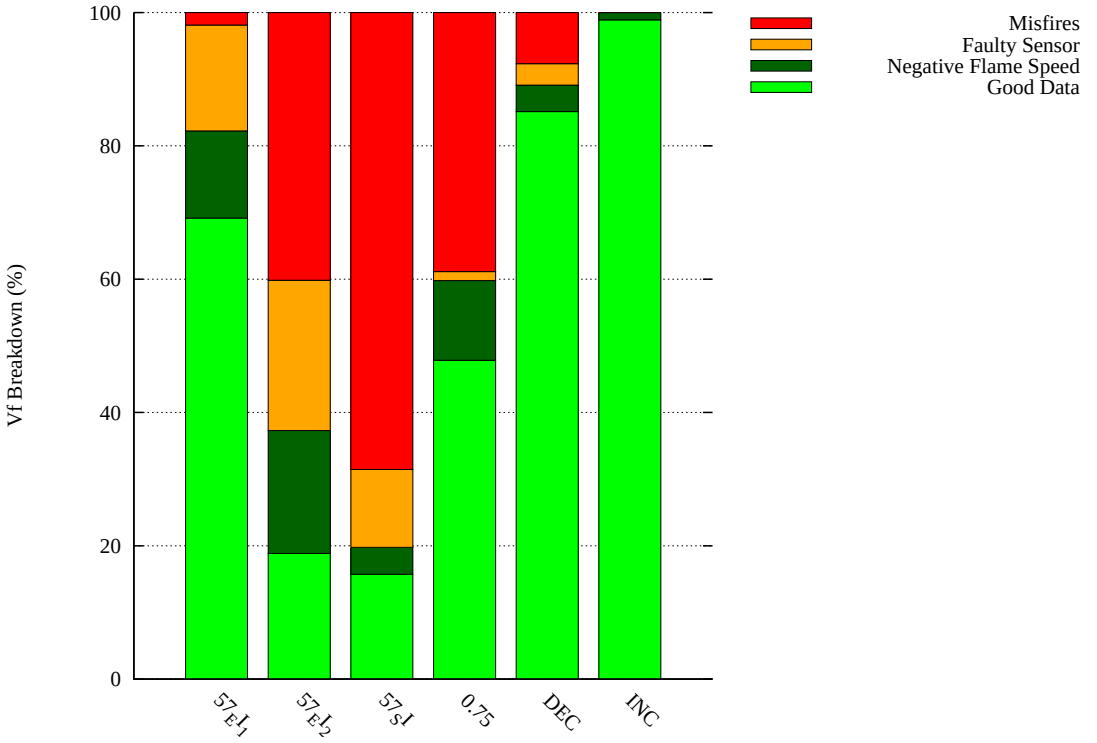

FIGURE 5.35: Ignition reliability and data quality percentage breakdown.

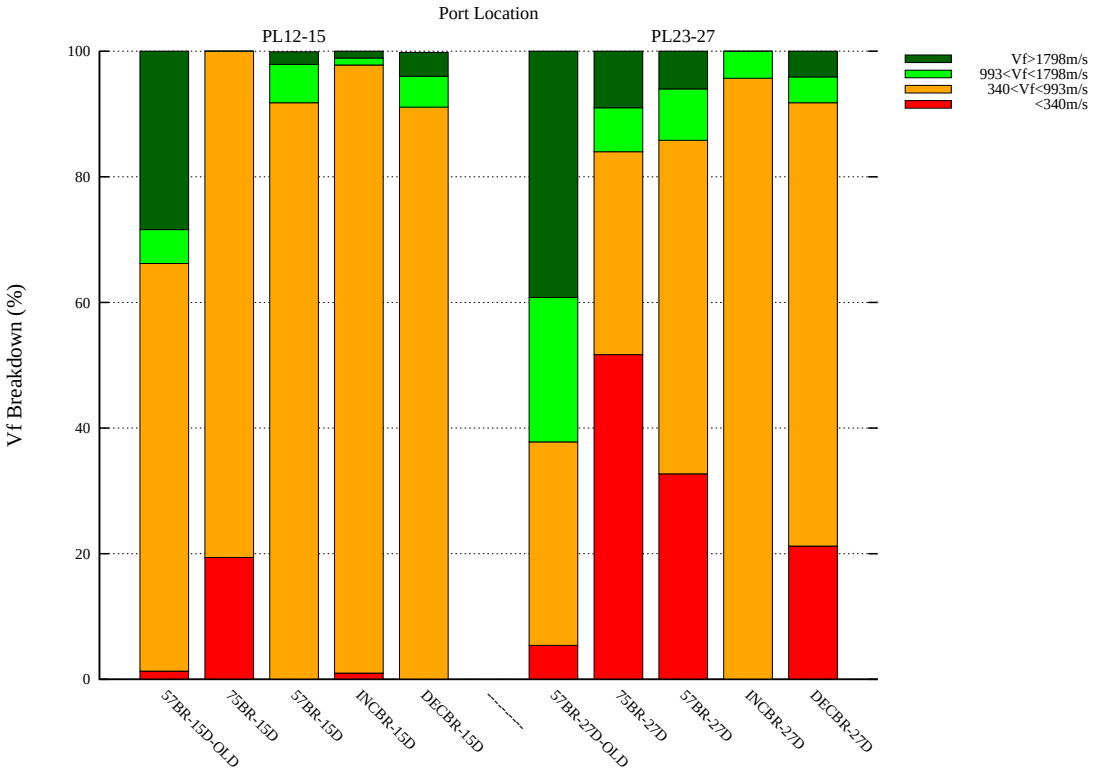

FIGURE 5.36: Percentage breakdown of flame speed ranges across each of the different test conditions.

5.4.1 Shock wave pressure peak pdfs

Figures 5.37 illustrate each of the the plots for statistical pressure distribution on the same page to aid direct comparison of the results. It can be see that the maximum pressure measured within the orifice plates can be seen in the repeated 0.57 BR orifice condition, for PL4. The next highest shock wave pressure was generated by the 0.57 BR side ignition case, then the increasing BR case followed by the decreasing BR case. In general the shock wave pressure decayed as it travelled along the smooth walled section of the tube, however in all cases apart from the 0.75 BR case and to some extent the decreasing BR case, there was considerable pressure gain around the 19th diameter after the reducer, at PL6. This pattern is particularly evident in any of the 0.57BR cases as shown in Figures 5.37, 5.38 and 5.39, and also to some extent in the increasing and decreasing BR cases, as shown in Figures 5.41 and 5.42. Interestingly, towards the end of the tube, most of the last two pressures measured at ports PL7 and PL8 are very similar in amplitude but with a slightly increasing gradient along

the tube. This appears to occur in every case apart from the 0.75 BR case, shown in Figure 5.40.

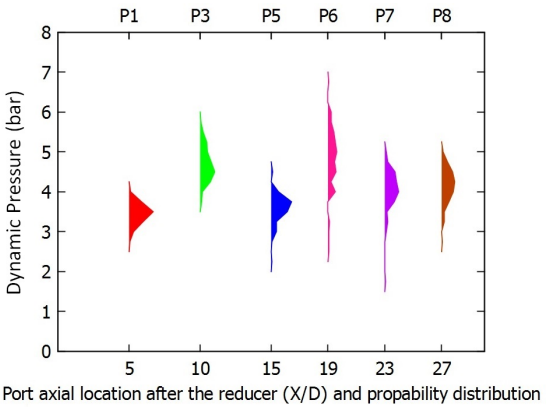

FIGURE 5.37: 0.57 BR orifice plate statistical pressure distribution

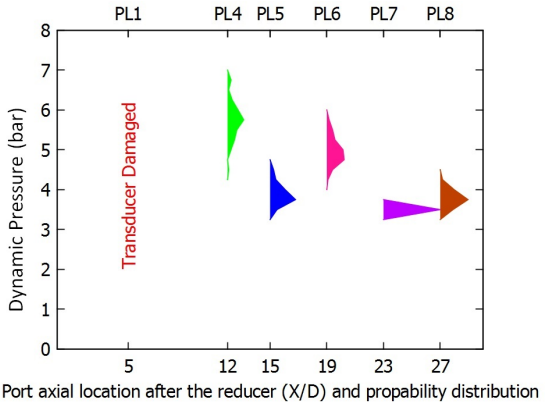

FIGURE 5.38: Repeat 0.57 BR orifice plate pressure distribution

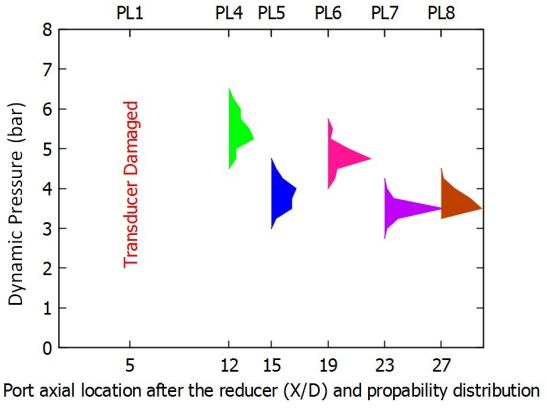

FIGURE 5.39: 0.57 BR orifice plate side ignition pressure distribution

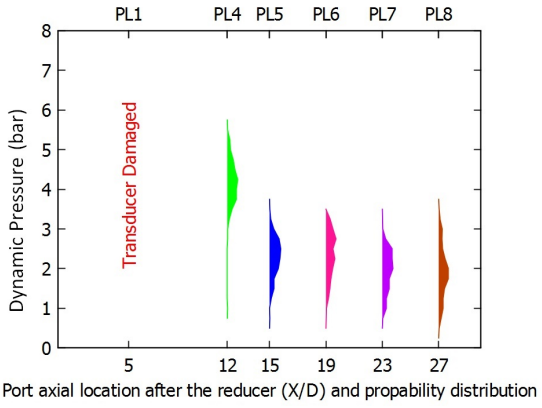

FIGURE 5.40: 0.75 BR orifice plate statistical pressure distribution

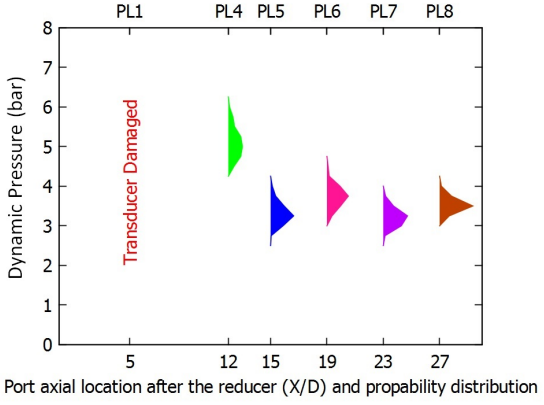

FIGURE 5.41: increasing orifice plate BR statistical pressure distribution

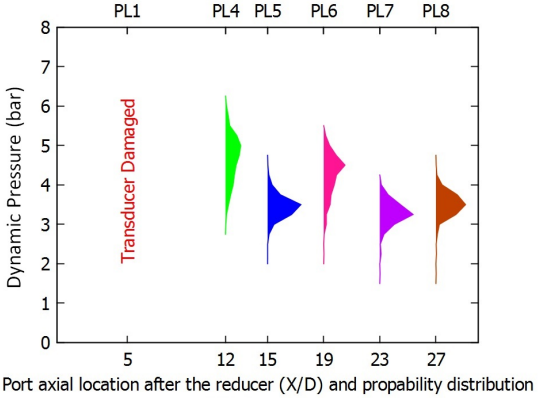

FIGURE 5.42: decreasing orifice plate BR statistical pressure distribution

5.4.2 Shock wave speed pdfs

The tube exit shock speeds measured from PL6 to PL7 and PL7 to PL8 are illustrated in Figures 5.43 to 5.48. It can be seen that most of these pdfs exhibit similar patterns and flame speed ranges, apart from the 0.75BR case, which exhibits a much wider range of shock velocities than the other cases. The first 0.57 BR case and the decreasing BR case also exhibit a relatively wide spread of results in comparison with the three remaining cases. The fastest shock TOF velocities at between PL7 and PL8 are shown by the repeat 0.57 BR case and the decreasing BR case. The decreasing BR and first 0.57 BR case exhibit the highest shock speed at the uppermost extremity of their pdf, however the lower range of these two cases reduces the mean shock speed value. The side ignition 0.57BR case exhibits a slightly slower mean shock speed (around 50m/s) than the fastest cases with a similarly very small pdf width.

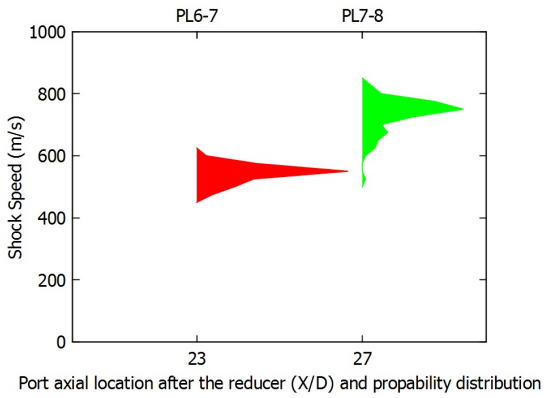

FIGURE 5.43: 0.57 BR orifice plate statistical shock TOF distribution

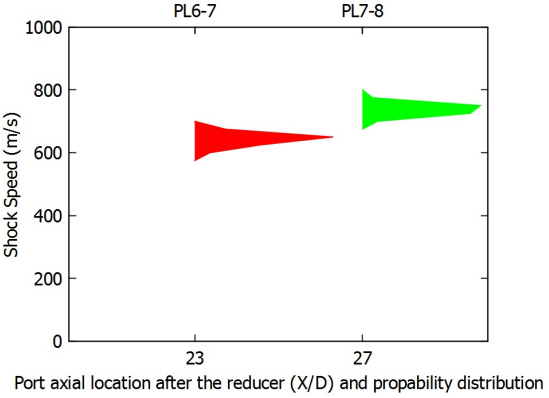

FIGURE 5.44: Repeat 0.57 BR orifice plate shock TOF distribution

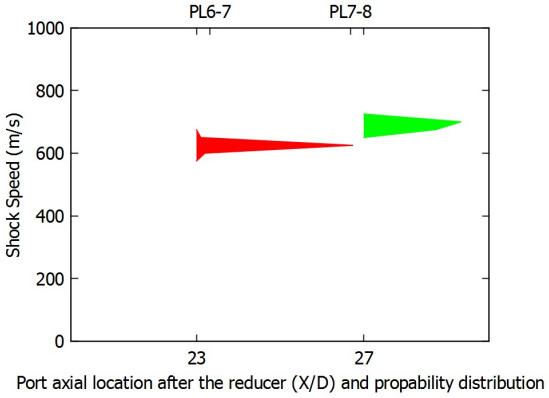

FIGURE 5.45: 0.57 BR side ign. orifice plate shock TOF distribution

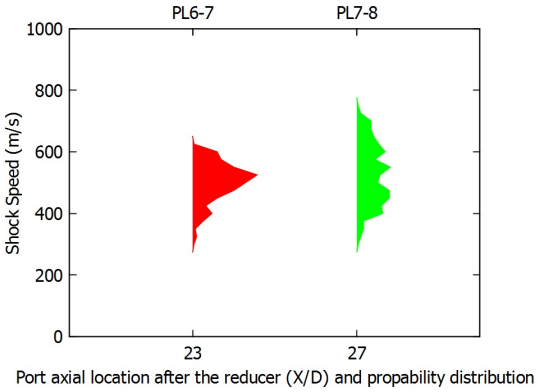

FIGURE 5.46: 0.75 BR orifice plate statistical shock TOF distribution

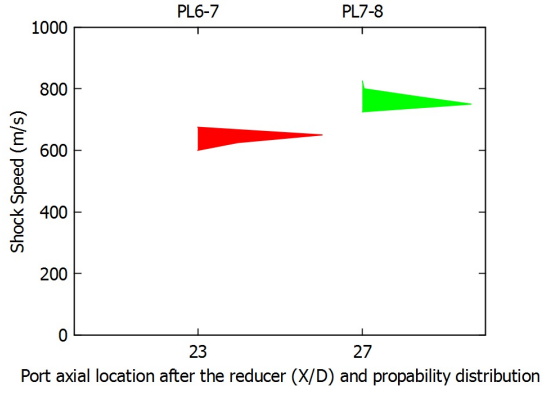

FIGURE 5.47: increasing orifice plate BR statistical shock TOF distribution

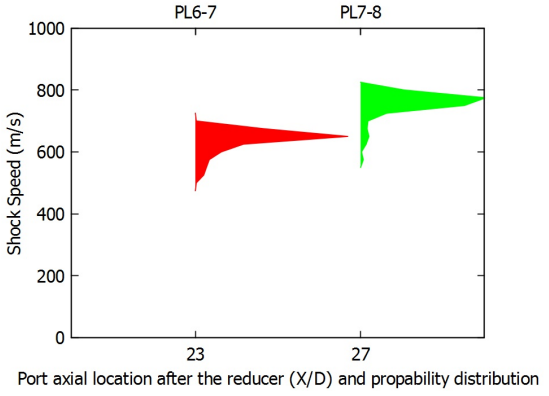

FIGURE 5.48: decreasing orifice plate BR statistical shock TOF distribution

5.4.3 Full flame speed pdfs

Figures 5.49 to 5.54 show the pdfs for flame speed along the tube in each of the six different cases considered in this chapter. The full range of velocities is included for these data sets as to provide the information without reducing its size more than

necessary. In this subsection the maximum range of the data will be discussed. This however presents a problem when comparing the low speed data, due to changing y-axis scale values, so to see the majority of the data up to a cut off limit of 4000m/s please view Figures 5.55 to 5.60.

It can be seen from Figure 5.49 that the flame speed increases dramatically from PL2 through to PL5 where a number of very high speed outliers begin to present themselves. This pattern can also be observed in the 0.57BR repeat test case, shown in Figure 5.50. The increasing BR and decreasing BR cases also show the same patterns in Figures 5.53 and 5.54 respectively. In contrast the side ignition 0.57 BR test and 0.75 BR test do not exhibit this rapid initial acceleration causing a small number of high speed outliers in by PL5. The side ignition case shown in Figure 5.51 shows very fast initial flame acceleration up until PL3. The bulk of the medium flame speeds (1000-1500m/s) are still present by the next port, however all of the detonation velocity flame speeds have disappeared by PL5.

Comparing the results for the later parts of the smooth walled section of the pipe, from PL6 to PL8 it is evident that the 0.57BR original case outperforms all of the other cases with many more high speed shots for this condition by the time the flame has reached PL8. This case exhibited deceleration over the full pdf range, between PL6 and PL7. By PL8, many of the flames had accelerated to beyond the detonation flame velocity, with a wide flat pdf distribution. Each of the other cases exhibits a strong population of shots around the sonic velocity in the reactants at PL8, whereas the 0.57BR original case does not.

The repeat 0.57 BR orifice case shown in Figure 5.50 shows a strong decreasing trend from PL6 to PL7, and for the majority of the shots at PL8. There were, however, a small number of high speed outliers at velocities above 1300m/s at PL8 in this case. The 0.57 BR side ignition case shows a strong deceleration from PL6 to PL8, with no outliers presented at PL8. This may be due to the small sample size for this particular case, which was only 40, and would reduce the chance of observation of sporadic high flame speeds. A similar pattern of deceleration was observed in the increasing BR orifice case shown in figure 5.53. Both the 0.75 BR case and the decreasing BR case showed similar patterns, with a strong population of slow flame velocities below the DDT triggering velocity, 990m/s, in both PL7 and PL8 port locations. Both of these

cases, illustrated in figures 5.52 and 5.54 show a relatively large number of widely distributed, high speed outliers above the 990m/s cut-off limit too.

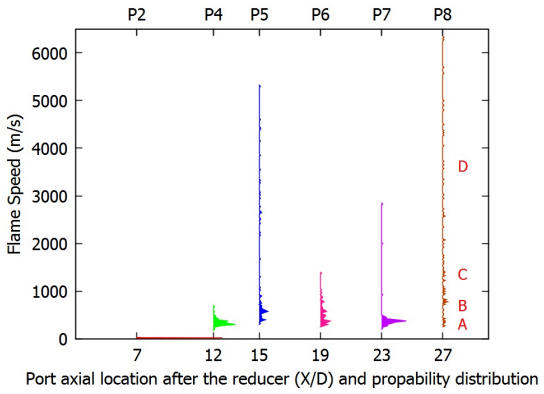

FIGURE 5.49: First 0.57 BR orifice plate statistical flame TOF distribution

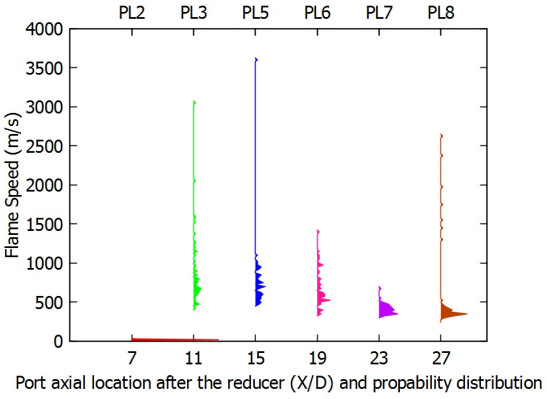

FIGURE 5.50: Repeat 0.57 BR orifice plate statistical flame TOF distribution

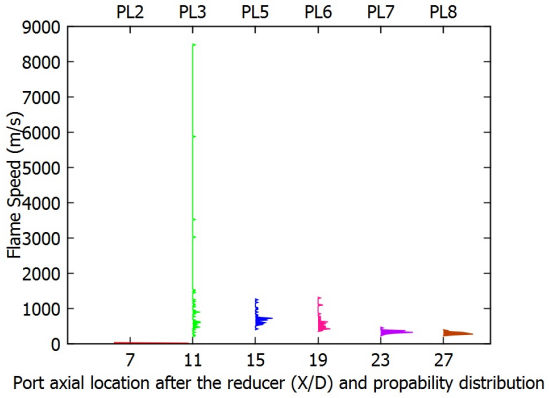

FIGURE 5.51: Side Ign. 0.57 BR orifice plate statistical flame distribution

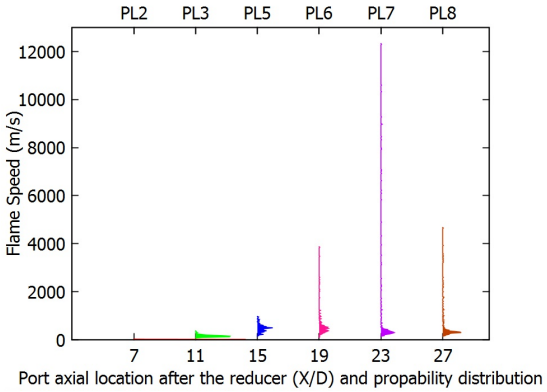

FIGURE 5.52: 0.75 BR orifice plate statistical flame TOF distribution

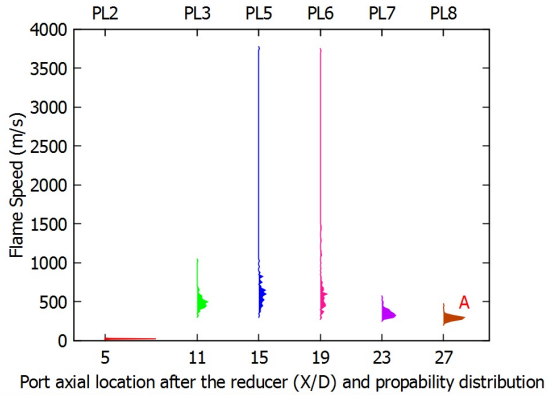

FIGURE 5.53: increasing orifice plate BR statistical flame TOF distribution

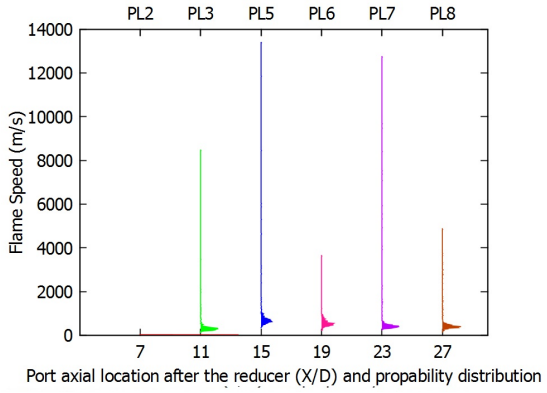

FIGURE 5.54: decreasing orifice plate BR statistical flame TOF distribution

5.4.4 Zoomed in flame speed pdfs

To compare the flame speed pdfs with a similar y-axis scale and observe trends in the median data, it was necessary to scale each of the graphs from 0 to 4000m/s flame speed. The result of this scaling can be seen in Figures 5.55 to 5.60. The flame speed between the igniter and PL2 for each case is seen to be very slow and evenly distributed for each case. Between PL2 and PL3, the flame speed varies dramatically depending on the case, with the 0.57 repeat (Fig. 5.56) and 0.57 side ignition (Fig 5.57) cases both showing a wide range of flame speeds from 500m/s to 3000m/s in the first case and 250m/s to over 4000m/s in the second case. The increasing BR orifice case and 0.57 BR original case both exhibited a mean flame speed of around 500m/s with a small pdf distribution around this point. The majority of the data for the 0.75 BR and increasing BR cases were below 500m/s, apart from a very small fraction of data in the increasing BR case which exhibited a much higher flame speed.

Flame speeds measured between PL3 and PL5, across the exit to the orifice show a wide variation of results too. The pdf for flame speeds at this port location for the 0.75 BR case indicate that very few shots exceed 1000m/s. The side ignition 0.57 BR case shows a similar pattern here, but with a positive shift between 200 and 300m/s. The repeat 0.57 BR case, the increasing and decreasing BR cases each exhibit similar patterns, with the lower range of the pdf at approximately 300m/s with the bulk of the data finishing by around 1000m/s however both of these cases exhibit occasional distributed outliers at higher flame velocities in excess of 3000m/s. Again, the first 0.57 case shown exhibits a much wider, faster range of flames at this location, with the bulk of the flame speed data between 400m/s and 1000m/s but a relatively large proportion of data distributed widely above this.

By the time the flames have travelled to PL6 the first three cases (Figures 5.55 to 5.57) exhibit an absolute pdf range from approximately 300m/s to 1500m/s. The rest of plots (Figures 5.58 to 5.60) exhibit the same pattern for the bulk of the data but with very occasional outliers up to speeds of 3500m/s. These outliers constitute less than 5% of the data at this location.

In each case PL7 shows a marked deceleration form PL5, with most cases presenting the bulk of the flame speed data below 500m/s. Exceptions to this rule include the

occasional high speed flame which can be seen in the first 0.57 BR, 0.75 BR and decreasing BR cases.

A distinct pattern emerges from the data at PL8, with the first 0.57 BR case showing distributed shots from a range of different velocities, at least half of which exceed 990m/s. The repeat 0.57 BR, 0.75 and decreasing BR cases also exhibit the same pattern, but with less high speed shots. The remaining 0.57 BR side ignition and increasing BR cases show flame deceleration with no high speed flames generated at this location.

It was decided that analysis by pdf was useful but difficult to make direct comparisons with, so Figures 5.61 and 5.62 show plots of the mean flame velocity and pressure at the full range of ports along the tube.

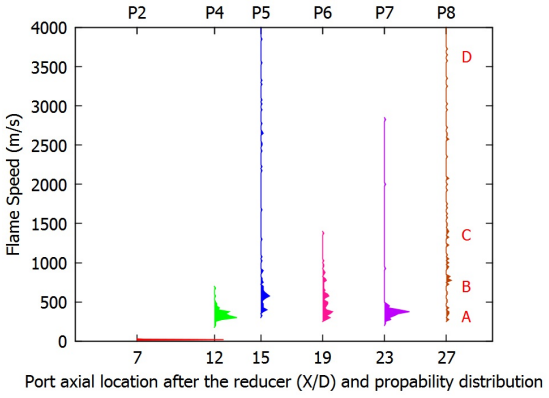

FIGURE 5.55: First 0.57 BR orifice plate statistical flame TOF distribution.

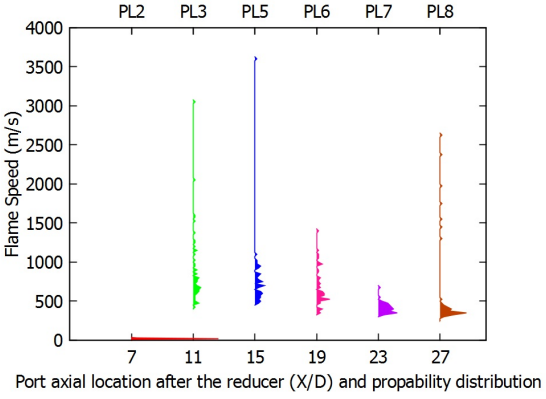

FIGURE 5.56: Repeat 0.57BR orifice plate statistical flame TOF distribution.

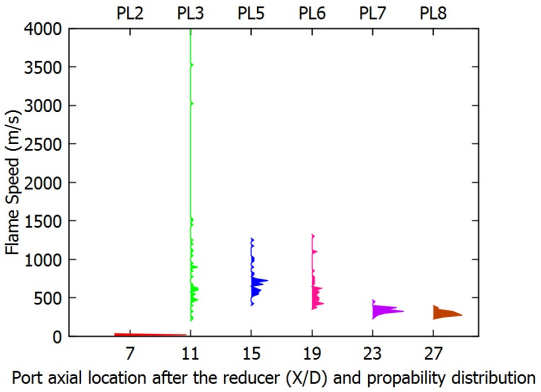

FIGURE 5.57: Side ignition 0.57 BR orifice plate flame TOF distribution.

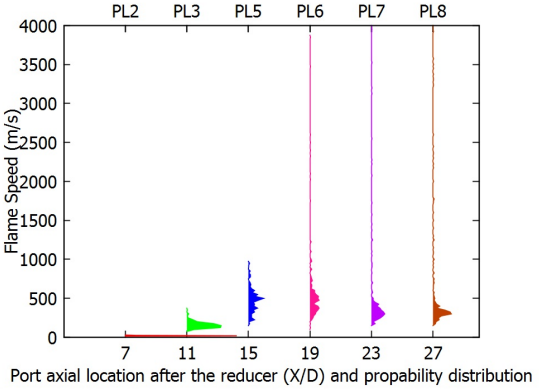

FIGURE 5.58: 0.75 BR orifice plate statistical flame TOF distribution.

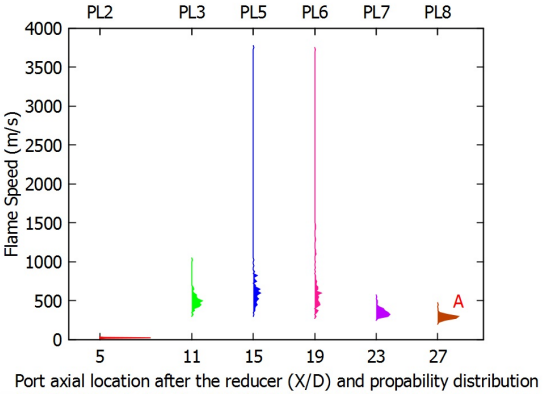

FIGURE 5.59: increasing orifice plate BR statistical flame TOF distribution.

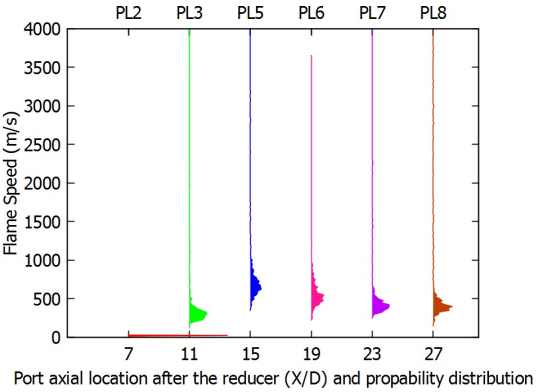

FIGURE 5.60: decreasing orifice plate BR statistical flame TOF distribution

5.4.5 Mean Case Performance

5.4.5.1 Measurements at the orifice exit

Figures 5.61 and 5.62 show the flame speed and pressure for each case respectively. Observations of Figure 5.61 at PL5 yield the flame speed generated by the orifice obstacle array. There is a notable difference between the flame speeds of each of the cases at this location, and the ranking is somewhat different to that inside of the obstacle array, as seen at PL3 or PL4*. The fastest mean flame speed of any of the cases the orifice exit was generated by the old 0.57 BR case (0.57 BR EI OLD), at around an average flame speed of 1500m/s. This was followed by the decreasing BR case (DEC BR), at a mean flame speed of approximately 1000m/s, so 50% of the flames generated were travelling at or above the sonic speed in the products. This is the most successful of the new cases, as measured at the orifice exit. Next followed the new 0.57 end ignition case (0.57 BR EI NEW), which showed a flame speed less than the sonic speed in the products, followed by the side ignition 0.57BR case (0.57 BR SI NEW), the increasing BR case (INC BR) and finally the 0.75 BR orifice case (0.75 BR).

Mean pressures at this port location fall into two main bands, one around 4 bar and one around 2. The 0.75 BR case falls into the 2 bar case, whereas all other data sets are closely distributed at around 4 bar.

5.4.5.2 Measurements at the tube exit

By the end of the tube, the majority of the flame speeds have reduced considerably through the smooth section of the tube, decaying as the flame progress along the tube, to around 600-750m/s at PL6. By PL7 the mean flame velocity drops to below 500m/s in each case, with the exception of the 0.75BR case, which has a mean flame velocity of over 1000m/s. By the time the flames have reached the tube exit, three main bands form. These bands are flames which travelling at about 300m/s, the sonic speed in the reactants, those which are travelling at around 600m/s and those which are reaching DDT velocities at least 50% of the time. The decreasing BR and 0.57 BR side ignition cases fall into the first of these bands. The 0.57 end ignition, decreasing BR and 0.75 BR cases fall into the second band. Lastly, the 0.57 BR end ignition old case falls into the high speed band.

Mean pressures at the exit show a falling trend from the orifice exit in each case, with most of the cases having a mean dynamic exit shock pressure of 3-4 bar. The 0.75 BR case, in contrast exhibits a mean shock wave pressure of less than 2 bar.

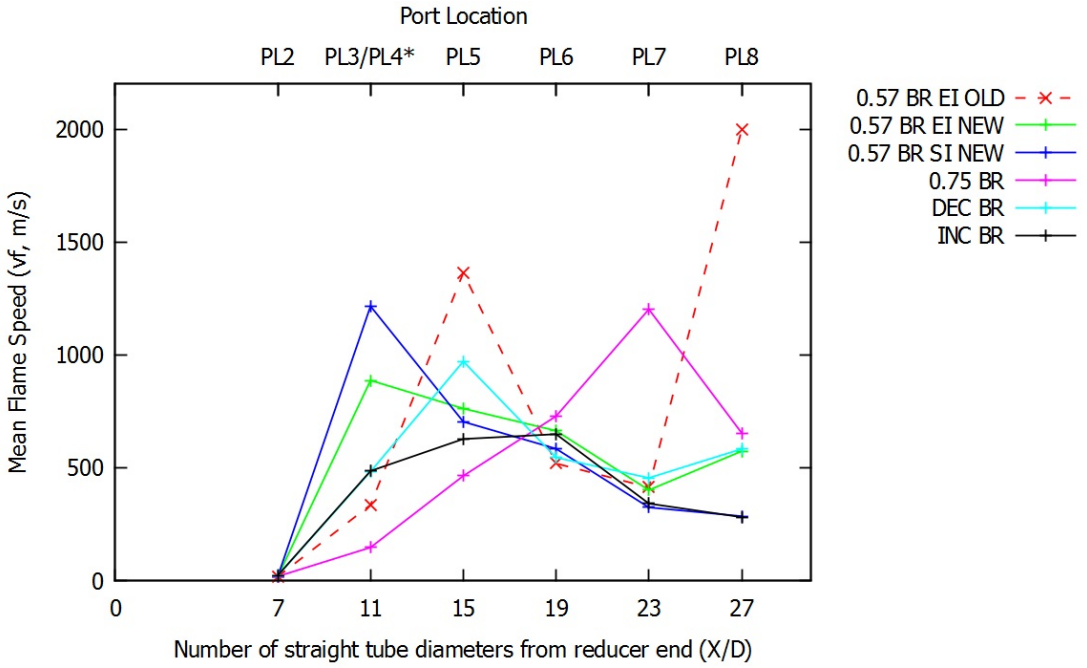

FIGURE 5.61: Mean flame speed at each port location for the full range of obstacles tested. The old data has been dashed to indicate that it is likely to have been taken at a different equivalence ratio, or potentially with a mixed fuel source. SI indicates side ignition port use, to compare with other data; EI indicates end ignition port use. PLx* denotes the port location used for the old data case, as indicated in Table 5.1

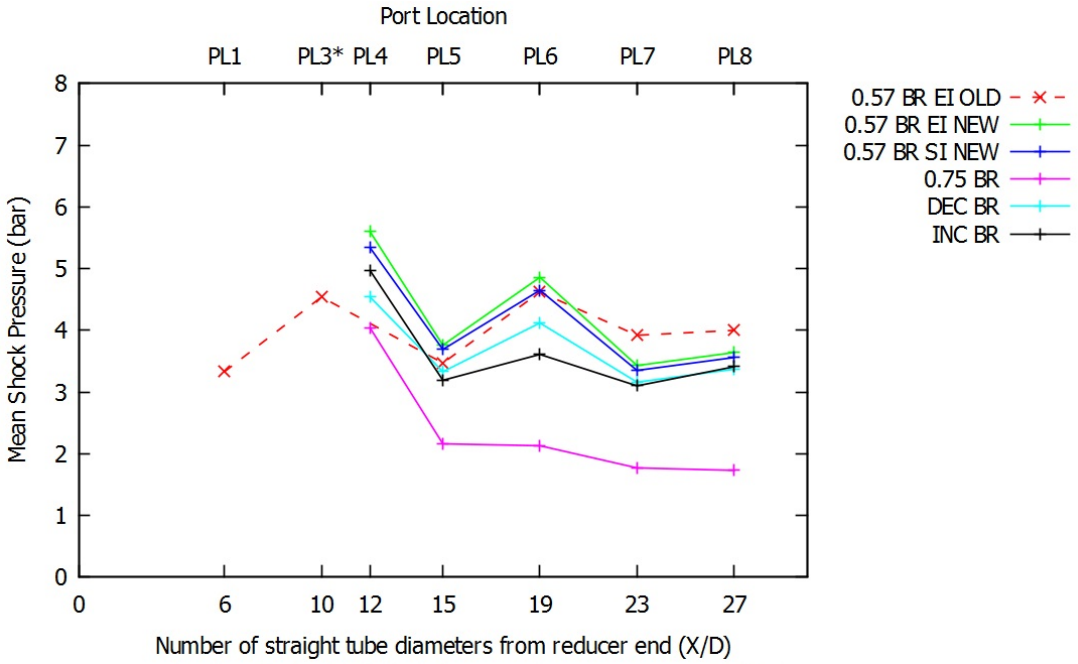

FIGURE 5.62: Mean flame speed at each port location for the full range of obstacles tested. The old data has been dashed to indicate that it is likely to have been taken at a different equivalence ratio, or potentially with a mixed fuel source. SI indicates side ignition port use, to compare with other data; EI indicates end ignition port use. PLx* denotes the port location used for the old data case, as indicated in Table 5.1

Chapter 6

Fractal Orifice Experiments

6.1 Synopsis

In this experiment the application of fractal orifice shapes have been tested in a PDE engine in order to increase the pre-detonator exit pressure and reduce the run up distance to detonation. Fractal geometries are known to change the way fluids interact with their boundaries, generating turbulence at a wide range of length scales [116]. In this experiment the effect of varying the fractal dimension with a constant orifice BR of 0.75 has been studied to determine whether finer fractal geometries can be used to enhance turbulence and directly increase FA. The effect of fractal orifice geometries has been investigated with a series of experiments. It should be noted that these experiments were completed before flame speed measuring equipment was available, and that the results chapters are not presented in chronological order. As such it was only possible to explore shock wave speed and pressure for the range of fractal experiments presented here. The shape of the fractal orifice internal opening is reflected in the Figure 6.1 which has been modified from the work of Abou El-Azm Aly et al. [116].

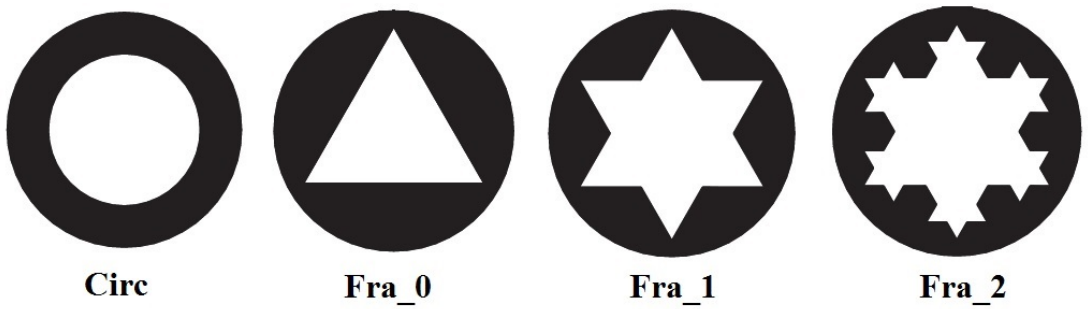

FIGURE 6.1: Fractal orifice hole shapes, addapted from the work of Abou El-Azm Aly et al. [116]

Twenty orifice fractal dimension comparison Three different orifices were tested using a 38.1 mm diameter (D, 1.5") 1.18m long tube with 20 orifices spaced equally at 1D. The orifices were circular, *circ* (standard), triangle von Koch fractal with dimension 0, $fra0$ (triangular) and von Koch fractal with dimension 1, $fra1$ (star). The results show that fractal obstacles with higher fractal dimension generate up to 10% higher pre-detonator exit pressure than lower fractal dimensions or standard orifices. Furthermore it is also shown that the PDE exit shock speed is sometimes much greater with lowerfractal dimension orifices, the exit shock speed is highly stochastic however with a standard deviation of $\pm$ ~100m/s around a mean figure of 700m/s. The $fra1$ and *circ* results show mean and standard deviation results of 100m/s and 50m/s respectively. It is thought that this is a direct result of smaller length scales generated by fractal geometries which produce greater mixing within the flames structure and greater flame acceleration rates. It is also thought that faster flame speed is likely to result in higher flame exit pressure at the test conditions with the greatest fractal dimension. This has direct implications for PDE pre-detonator length reduction as deflagration to detonation transition (DDT) takes place much more rapidly at higher pressure and flame speed.

28 orifice fractal dimension comparison In this section the effect of increasing the length of the obstacle laden section of the tube to 28 diameters was investigated for a range of fractals. Only shock speed data was analysed for this case. It was found that changing the length of the number of fractal orifice plate had an effect on the shock speed ranking of different fractal orifice types. The fastest data was

gathered for the fra_0 case followed by the fra_2 case, the *circ* and fra_1 cases which exhibited very similar shock speeds.

Changing the number of fra_2 orifices Pressure and shock speeds were analysed for fra_2 fractal orifice plates. The number of orifice plates ranged from 12 to 28. It was found that increasing the number of fra_2 orifice plates changed the shock exit speed mean value by up to 100m/s, and the mean dynamic pressure was altered by up to 1.25 bar. The highest exit pressure was exhibited by the 12 orifice obstacle blockage. Larger numbers of obstacles increased the pressure measured at the tube exit. The observed shock exit speed remained relatively constant, not exhibiting such a large change in speed between 12 and 28 orifices.

Twelve orifice graded fractal comparison Twelve orifice plates were assembled in a variety of patterns, in groups of four orifices. The fractal dimension remained the same all of the way along the tube in three experiments, but changed along the tube in the other two experiments. Both exit shock speed and peak dynamic pressure were measured. It was found that the increasing and decreasing fractal dimension results performed worse than the constant fractal cases. An promising finding was discovered for the fra_2 case as the mean shock speed for this case was higher than any of the other results with a tightly banded set of results for shock speed. This case exhibited similar pressures to the circular orifice plate, but with higher shock speed results and should be considered for further investigation

6.3 Results

6.3.1 Twenty Orifice Fractal Comparison

Table 6.1 shows that there is little deviation from the desired equivalence ratio of 1 throughout all of the following experiments. This insures that the experimental conclusions for fractal effects on flame acceleration are independent of equivalence ratio. Each of the equivalence ratio values from the experiment were ranked then limited within the range of $0.943 \leq \phi \leq 1.028$. This process limited each set of experimental conditions to match the smallest range of equivalence across all each data set to provide a fair comparison across different test conditions. This was necessary as controlling the

TABLE 6.1: Mixture Equivalence Ratio and Number of Samples

Orifice	$\bar{\Phi}$	$\Phi\|\sigma\|$	N Samples
circ	0.986	0.0333	64
fra1	0.971	0.02715	143
fra2	0.986	0.0662	259

equivalence ratio proved to be difficult, even with the 600 ml fuel receiver tank fitted. The following results were taken from data with the following propane- air mixture at 30 degrees C.

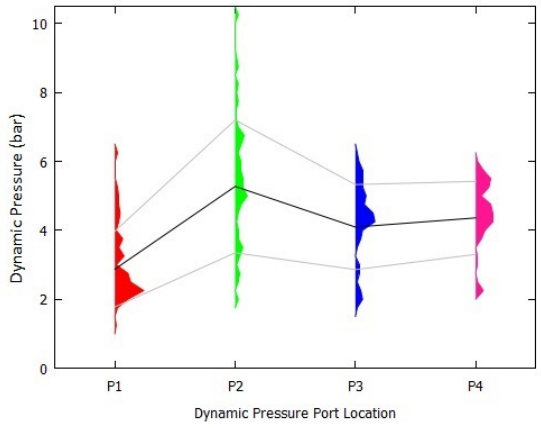

FIGURE 6.2: *Circ* peak pressures

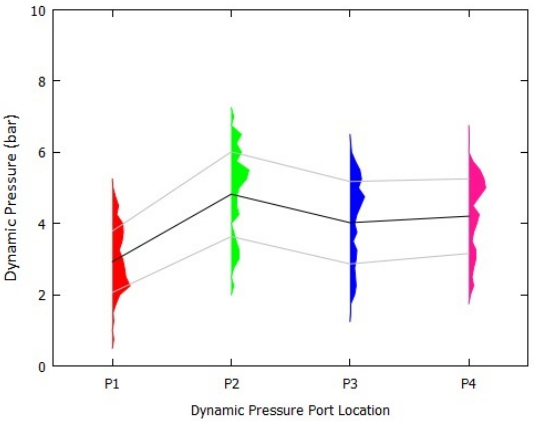

FIGURE 6.3: *Fra*0 peak pressures

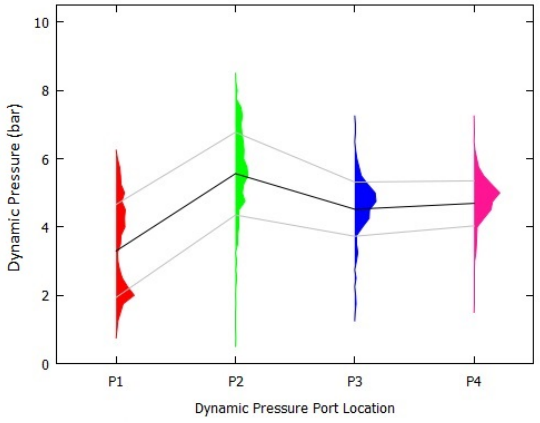

FIGURE 6.4: *Fra*1 peak pressures

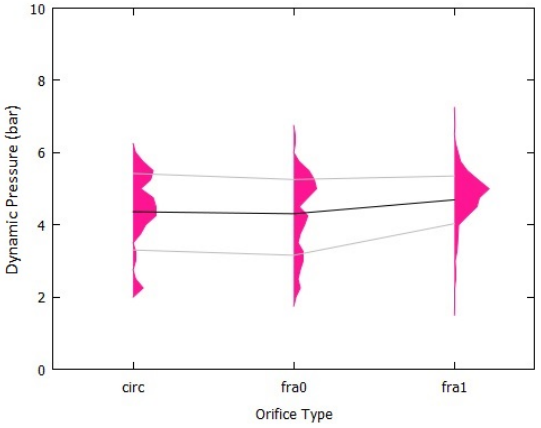

FIGURE 6.5: P4 vs. orifice type

The results of these experiments have been plotted with mean and standard deviations of dynamic pressure against Kistler location in Figures 6.2, 6.3, 6.4. K1-4 are measured at 508mm, 698mm, 1080mm and 1118mm from the rear thrust wall. Figures 6.2, 6.3 clearly show that there is little difference between the pre-detonator exit pressure between the circular and triangular orifice geometries (*circ* and $fra1$ respecively).

It is evident however from Figure 6.4 that the second fractal iteration orifice case, $fra1$, generates a higher exit pressure across the same range of operating conditions at K3 where the flame exits the PDE pre-detonator. Interestingly, the results for the first $Fra1$ data set show a higher primary peak pressure at K1 between the values of 3 and 7.85 bar, as shown in Figure 6.2, which then reduces by K2 to a maximum pressure of 5.5 bar at 1 standard deviation. This is a similar result to the pressure shown for $Fra0$ at K2 in Figure 6.3. $Fra1$ differs again here, as pressure K2 ranges from 3.7 to 5.5 within the limits of 1 standard deviation.

Figure 6.5 directly compares the exit pressures from the pre-detonation tube at K3 against the different orifice geometries, *circ*, $fra0$ and $fra1$ respectively. Figure 6.5 clearly shows that the exit pressure is greatest for the orifice with the highest fractal dimension. Interestingly, the exit flame pressure does not vary greatly between the circular orifice and the triangular orifice cases, *circ* and $fra0$ respectively.

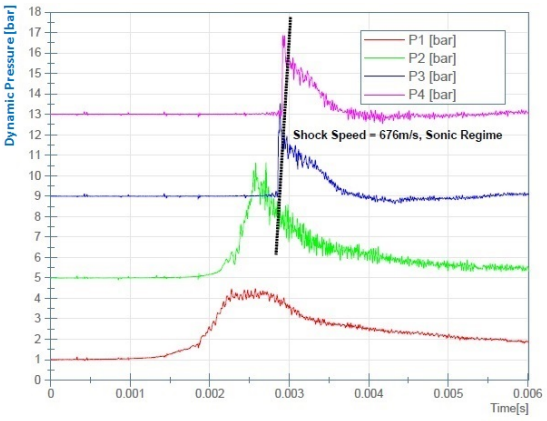

FIGURE 6.6: *Circ* pressure-time plot for K1-K4

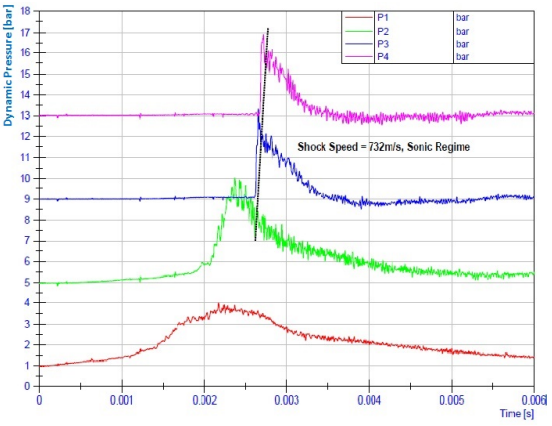

FIGURE 6.7: $Fra0$ pressure-time plot for K1-K4

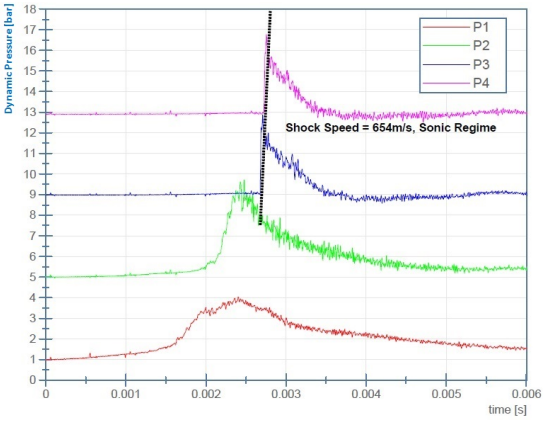

FIGURE 6.8: $Fra1$ pressure-time plot for K1-K4

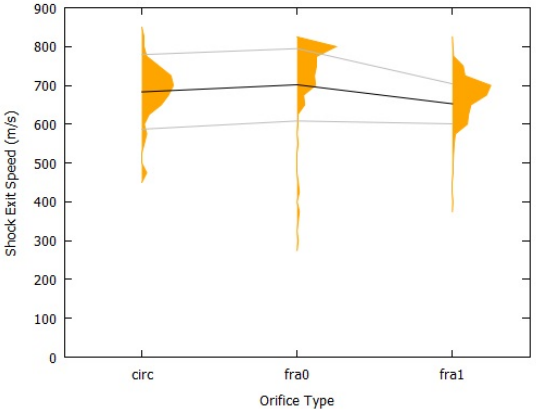

FIGURE 6.9: TOF shock speed, different fractals.

Figures 6.6, 6.7 and 6.8 each refer to a typical explosion for *circ*, $fra0$ and $fra1$ orifices chosen respectively for their proximity to the average pressure at K2. K2 pressure was chosen as this represented the closest condition to the exit of the turbulence generating orifice bank, and therefore should be a good measure of the maximum amount of energy release in this particular shot. It can be seen from these figures that each of the shots is within the sonic regime, prior to detonation at the exit plane from the PDE. The *circ* shot exhibits the highest dynamic pressure at K2 as shown in earlier results with a steep gradient and slow decay after the combustion wave has passed, which is indicated by the large degree of disturbance on the tail end of the pressure signal. The fra_0 and $fra1$ results follow the trend of earlier results from Figures 6.7 and 6.8 so the chosen results match well with each analysed data set. We can see from each of the pressure plot figures that the shock exit pressures are very similar in each case however when inspecting these values closely the time of flight data reveals that the triangular orifice plate provides an advantage in the shock exit velocity from Figure 6.9.

Time of flight data shows that the $fra0$ orifice provides a faster mean shock exit velocity of 737m/s, but with a large degree of variation in shock exit speed. Interestingly the $fra1$ results show a slower mean shock exit velocity of 652m/s, breaking the pattern of higher shock exit speeds with higher fractal dimension. The standard orifice plate provides an mean exit shock speed of 683m/s, between the value produced by the other respective orifice plates.

Figure 6.10 plots the mean shock pressure for each of the cases mentioned against the minimum length scale of the orifice, so the fractal with the smallest length scale is on the left hand side, and the largest length scale is on the right hand side of the graph (fra_1 and *circ* fra_0 respectively). It can be seen that as the minimum geometric length increases, the flame speed increases but the pressure developed at both P2 and P4 is less. The difference generated in mean flame speed from the smallest length scale obstacle to the highest length scale obstacle was an increase of approximately 50m/s. The reduction of mean dynamic pressure from the two extremes, smaller to higher minimum length scale was approximately 0.5 bar.

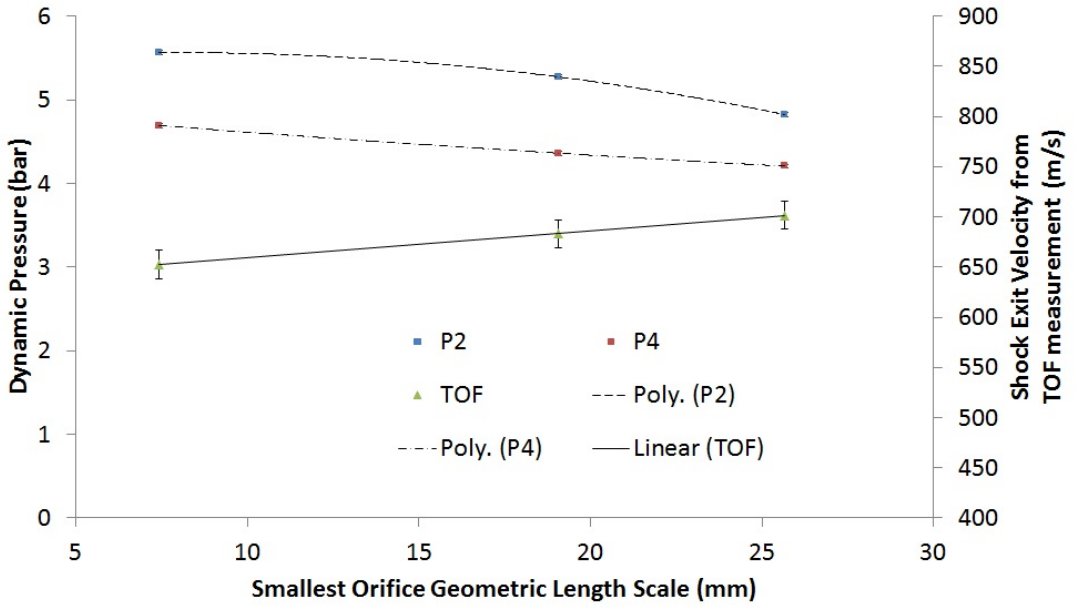

FIGURE 6.10: PDE pre-detonator P3 P4 and TOF shown against the minimum geometric scale length of the orifice (in oder fra0, circ, fra1)

6.3.2 Twenty eight orifice fractal comparison

Further experiments were carried out with 28 orifice plates placed at a separation distance of one tube diameter, filling the entire combustion tube with orifice plates. Time of flight results revealed the same pattern for faster flame acceleration here also, indicating that this faster flame speed must be taking place within the orifice plate laden section of the tube as well as within the smooth tube walled section. Table 6.2 shows the equivalence ratio of the reactants in each case as measured from the upstream inlet conditions to the rig.

Orifice	$\overline{\phi}$	σ_ϕ
circ	0.970	0.0307
fra0	0.972	0.0190
fra1	0.978	0.0237

TABLE 6.2: Experiemental mixture equivelence ratio conditions for the 28 orifice case experiments

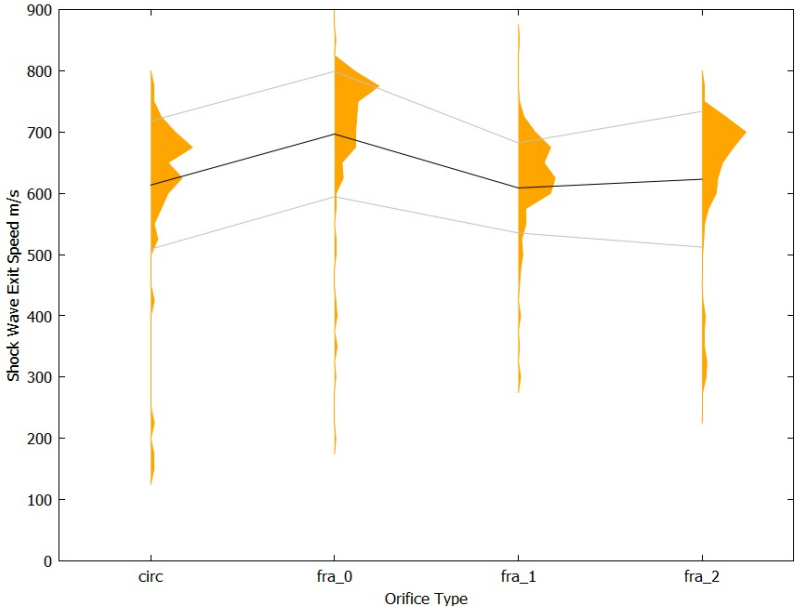

FIGURE 6.11: Exit shock speed for different fractals with 28 orifices (based on TOF data)

6.3.3 Changing the number of $fra2$ orifices

Once experiments on the type of orifice had been completed for a range of fractal dimensions the number of orifices was also tested to determine the effect of a greater or fewer numbers of orifice plates in the tube. $fra2$ orifices were chosen to perform these experiments as this shape of orifice plate has not been reported in the literature yet, and as such the experiments are a novel investigation into the number of fractal orifice plates present in a tube and their effect on FA.

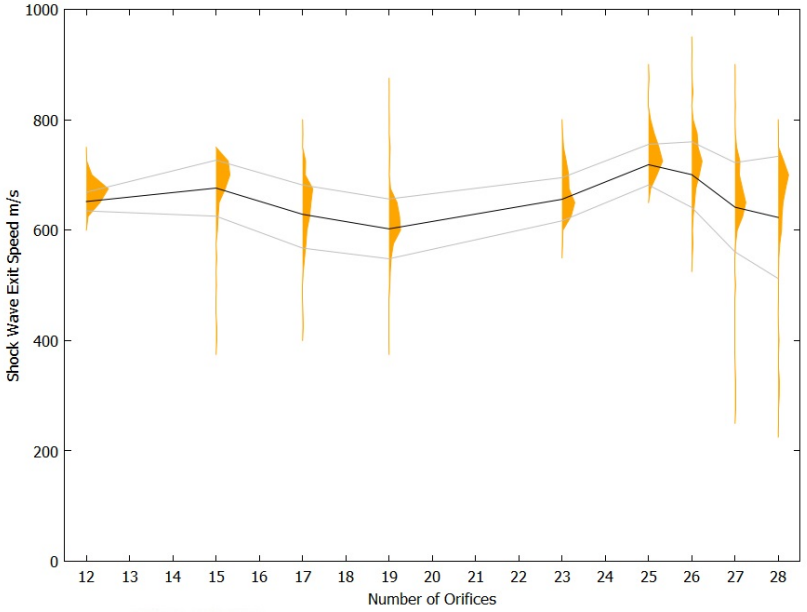

FIGURE 6.12: PDE pre-detonator shock exit TOF measurements taken with fra2 fractal

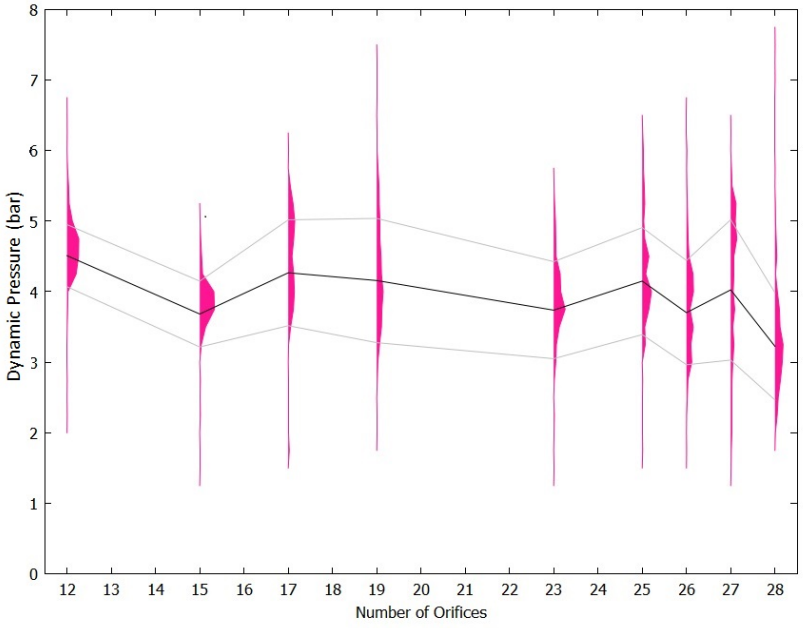

FIGURE 6.13: PDE pre-detonator exit pressure measurements taken with fra2 at P4 fractal

Figures 6.12 and 6.13 show the effect of changing the number of orifice plates when the fra_2 fractal orifice is chosen. It can be clearly seen that 12,15, 25 and 26 orifice plates each produce fast shock speeds results however the iterations between these produced slower shock speeds. Observations from Figure6.13 yield that the trend for the mean

peak dynamic pressure decreases with increasing number of orifice plates inserted along the tube. This data can be used to choose the optimum number of orifice plates for the tube length, with the best compromise between flame speed and exit pressure to increase the likelihood of detonation occurring. It would seem that 12 orifices appears to give the best combination of both shock exit speed and peak shock pressure.

6.3.4 Twelve orifice graded fractal comparison

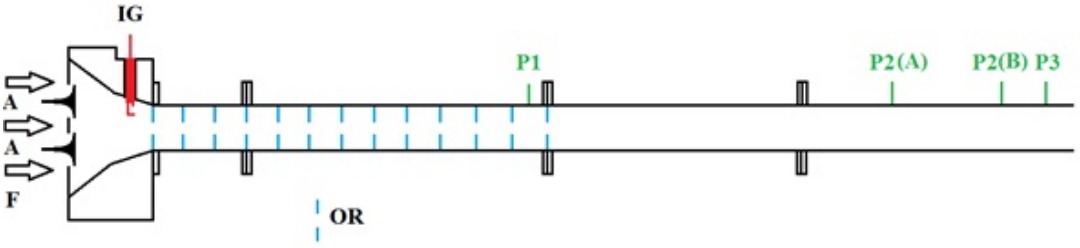

FIGURE 6.14: 12 orifice fractal experiment

In the light of the results above, it was decided to further explore the effect of changing the fractal dimension, stratifying or grading it along the length of the tube, with the 12 orifice plates as this was indicated as the optimum number of orifice plates for the best combination of TOF speed and dynamic pressure. Figure 6.14 shows the experimental apparatus set up. By this point in the experiment one of the charge amplifiers had begun to malfunction, providing erroneous results with little amplitude which were physically unlikely as the pressure reported either side of this port location was showing much larger pressures. Moreover, the pressure port was swapped with another at identical conditions and the pressure was seen to be larger in the functionality check, so this charge amplifier was deemed to require maintenance. Due to the high cost of such experimental equipment, and the lead time in repair (several months) it was decided to carry on the experiments with only three pressure transducers placed at strategic locations. Firstly, one pressure transducer was placed close the upstream side of the last orifice as possible, half way between the 11th and 12th orifice plate, then the other orifice plates were located at the end of the tube to measure the speed of the shock escaping from the smoothed walled tube. Location P2(A) was used in most cases apart from the data earlier collected for $fra2$ from the orifice number test as this provided a larger port separation between the two time of flight measurement ports. This larger separation introduced a greater time of flight, which in turn produces a

smaller error in the experimental results as the measured time of flight is a greater number of multiples of the natural period of the pressure sensors and DAQ equipment.

Orifice	$\overline{\phi}$	σ_ϕ
circ	0.991	0.022
fra0	0.973	0.020
fra2	0.984	0.021
fra012	0.981	0.20
fra210	0.988	0.22

TABLE 6.3: Experimental mixture equivalence ratio conditions

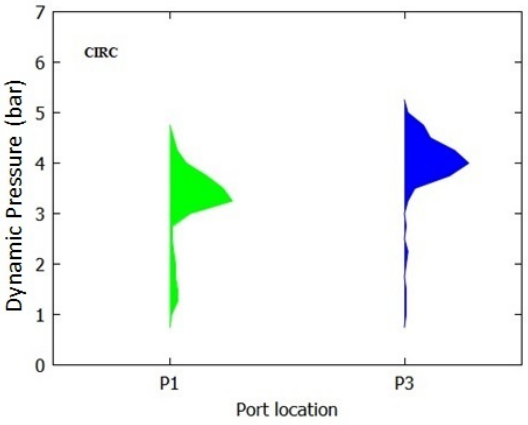

FIGURE 6.15: *circ* pressure-port plot for P1 & P3

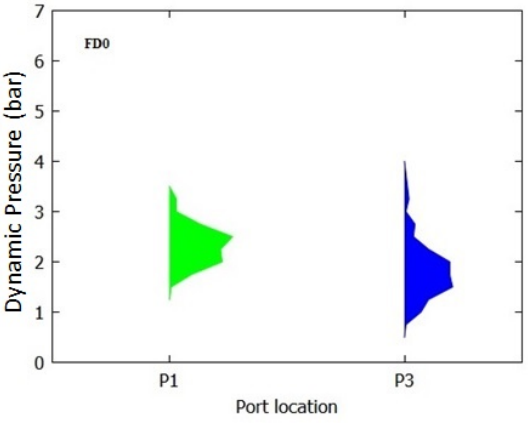

FIGURE 6.16: $fd0$ pressure-port plot for P1 & P3

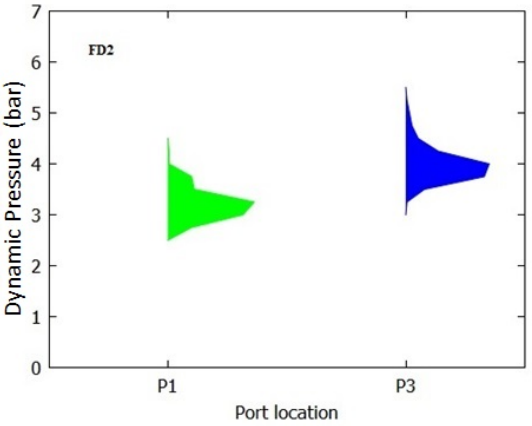

FIGURE 6.17: $fd2$ pressure-port plot for P1 & P3

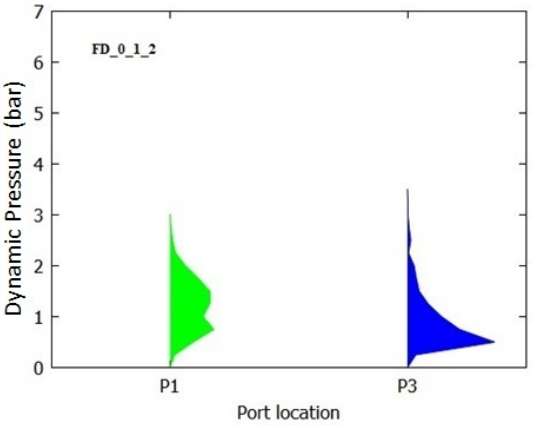

FIGURE 6.18: $fd012$ pressure-port plot for P1 & P3

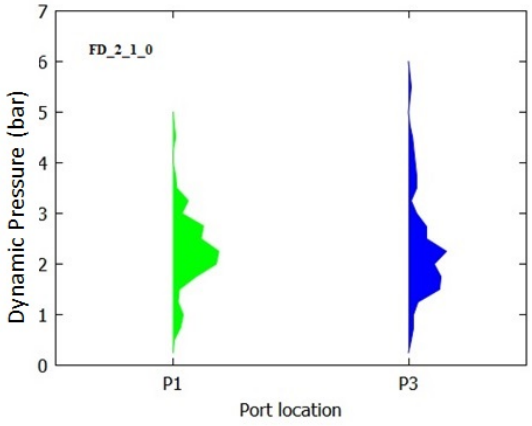

FIGURE 6.19: $fd210$ pressure-port plot for P1 & P3

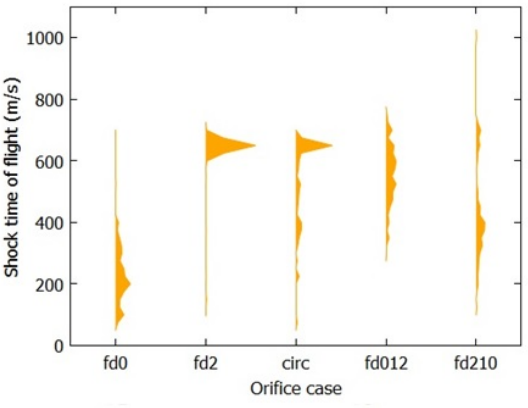

FIGURE 6.20: TOF data from P2 & P3 for each of the cases consided above

6.5 Discussion

Observations of the experimental results show that the greater the fractal order orifice plates enhances shock wave pressure across the last dynamic pressure transducer, but produce surprising results regarding the flame speed. All other conditions remained the same in this test campaign except from the orifice type, so the orifice shape is the only other factor effecting turbulence generation and its interaction with the flame as hypothesised in the literature review.

It was noted that the primary pressure measured at K1 in the circular orifice case, *circ*, produced the highest pressure which then reduced as the flame travelled along the length of the tube to produce a relatively weak exit pressure at K3. In comparison the highest order fractal case, $fra1$ generated the lowest primary dynamic pressure peak measured at K1, and the highest exit dynamic pressure, measured at K3. This effect could be due to the scale of the geometry generating the turbulent length scales. For instance, the smallest length scale on the circular orifice, the orifice diameter, is 19.05mm and the smallest scale in the triangular orifice case, the length of one side of the triangle is 25.66mm. In comparison, the smallest length scale in the star shaped orifice, $fra1$ is 7.41mm.

To compare these results, we would expect to see a faster flame speed and higher dynamic flame pressure with the smallest length scale orifice, $fra0$. In this case, the smallest length scale is 38% of the smallest length scale in the circular orifice plate and 29% of the smallest length scale in $fra0$, the triangle. However, 7.41mm is still much larger than the length scale expected for a stoichiometric propane-air flame however, which is sub millimetre in length. The likely reason for this benefit is that the turbulence cascades between each orifice plate producing smaller and smaller turbulent eddies of increasing frequency and reducing scale. The greater number of small scale geometries in the $fra1$ case will generate smaller scale eddy cascades more rapidly than the larger scale orifices. It is possible that these eddies are able to survive between orifice plates but not after one orifice barrier due to flow disturbances when crossing an orifice plate. This could be the reason why the *circ* and $fra0$ cases don't generate smaller length scales.

This increase in pressure at the exit port could possibly be explained by turbulence generation length scales, but this did not explain the higher pressure at K1 in the circular orifice case. It was found by Abou El-Azm Aly et al [116] that the pressure lost across circular orifice plates in cold flow experiments was larger than that lost across Von Koch fractal orifice plates with fractal dimension ranging from 0-3. This large pressure loss will generate large scale eddies which promote large scale mixing in the initial stages of flame growth through flame folding. The advantage of these eddies are only realised at the initial stages of flame growth as the developed flame which can be seen by ports K2 and K3 can only be accelerated by mixing on a smaller scale which penetrates the flame front (preheat and reaction zone).

This is the first finding of its type with fractal orifice plates used in PDEs, showing a faster flame acceleration is possible with triangular orifice plates than circular ones

Furthermore the effect of changing the number of fractal fra_3 orifice plates has been investigated between 12 and 28 orifice plates. It was found that 12, 25 or 26 orifice plates each produced strong shock pressures and fast shock exit velocities, but that blockages with other numbers of orifice plates generated only subsonic shock speeds at the orifice exit. This effect is still somewhat evident with 13 orifices but is still considerably reduced. It is thought that the 12 orifice case leaves enough time for the double discontinuity flame and shock to grow in strength before reaching the tube exit. In comparison the tube length may be insufficient for this to happen with the intermediate obstacle lengths between 13 and 24, until the blockage reaches 25 diameters in length with 25 orifice plates when the orifice enhanced flame acceleration becomes so strong that the sonic flame regime is encountered. The same behaviour is exhibited with a blockage containing 26 fra_3 orifice plates, however when 27 or 28 orifice plates are present it is clear that the shock exit speed has reduced considerable, possibly because there is insufficient unobstructed tube for a shock to develop between the pressure transducers used to measure the shock speed at 27 and 28 D. This doesn't appear to be the case with $circ$, $fra1$ or $fra2$ orifices however so this effect could be a connected to the type of orifice plate in use.

When experiments were conducted with 20 orifices and a range of fractal dimensions a strong correlation was found between increasing exit pressure from P1 to P3 and the exit time of flight from the smooth walled section of the tube. Interestingly, when

comparing the $fd0$ results with the $fd2$ and *circ* results the $fd0$ case generated a reducing trend in pressure and a statistically smaller TOF speed with an average well below half of the other two fixed orifice geometry cases.

Comparing the 20 diameter and 28 diameter data reveals generally similar profiles with similar mean shock speeds. It is interesting to note that the $fra2$ orifice results from the 28 diamter loing obstacle case are comparable to the *circ* orifice for the same case, indicating that the fractal obstacle dimension should be higher than the $fra2$ case to enhance the flame speed.

Comparing across the twelve orifice graded fractal comparison yielded that fd_2 (highest fractal density) fractals were generated the highest combination of both pressure and shock speed for orifices with 12 fractals in length. The next best results came from the *circ* orifice case, which exhibited slightly higher exit pressures at P4, but a wider distribution of shock speeds below 600m/s which weren't present in the fd_2 case. The $fd0$ (triangle) case produced the lower shock pressures than any of the other single fractal dimension blockages and the lowest flame speeds of any of the test cases with this number of orifices. The $fd012$, increasing fractal density case produced the lowest shock pressure of any of the results, decaying along the tube from P2 to P4. The shock wave speed for this case was the third highest of all of the cases. In comparison, the decreasing fractal blockage test showed an increasing range of pressures along the tube. A split in the data for shock wave speed could also be observed, with one band around 750m/s and a lower band around the sonic velocity in the reactants (200-400m/s). Clearly for short lengths of obstacle filled tube, intricate fractal geometries produce high shock wave pressures as effectively as circular orifice plates, and generate more uniform shock wave speeds than circular orifices.

Chapter 7

Discussion

7.1 Areas of interest from the Gap Analysis

The gap analysis presented in section 2.7 summarised some of the key findings of the literature review. These items are presented below, to form a framework for discussion.

Turbulence Length Scales In section 2.1.4 the effect of turbulent length scales was discussed, stating that turbulence with a smaller Kolmogorov length scales produced faster turbulent flame speeds. These length scales are known to be affected by the local turbulent Reynolds Number and integral length scale, as stated in equation 2.16.This infers that for higher turbulent Reynolds numbers, flames will be faster. This will have a direct effect on flame acceleration, generating faster FA with more intense turbulence for instance. Section 2.2.4 discussed the effect of Fractal geometries on the generation of turbulence. No literature was found regarding FA through fractal obstacles, but that a number of experimental studies had been carried out on fractal grid generated turbulence for cold flows and those involving stationary premixed turbulent flames. It was suggested that the effect of fractal obstacles could be investigated to determine whether these geometries had a beneficial effect on FA.

Modelling Whilst it was found that modelling DDT could be incredibly complex do to several different routes to DDT, it was decided in the gap analysis that Bradley's double discontinuity model could be adapted for use with his flame model and

turbulence generation models for the prediction of FA with orifice type obstacles, drawing on the work of Torizumi for sub and supercritical orifice plate flow.

DDT diameter Hypothesis A hypothesis was generated regarding the critical diameter for detonation within an obstacle filled tube. It was hypothesised that the critical internal obstacle diameter should be larger than λ, i.e. $d \geq \lambda$ in orifice plate filled tubes, but that it could be smaller in the case of Schelkin spirals. This hypothesis was formed around others experimental work which illustrated no detonation has occurred in the literature within orifice blockages which are smaller than the critical obstacle diameter criterion, but this has occurred within Schelkin spirals. It is thought that the reason for this is because a Schelkin spirals pitch can match the pitch of the spinning detonation head in the limiting diameter detonation mode, allowing the pressure wave to traverse along the Schelkin spirals path with no obstructions. It was decided that experiments on Schelkin spirals would not be undertaken as the Schelkin spiral could not easily be modelled in a 1D analytical model which would allow for its optimisation. This is largely because little data for Schelkin spiral drag coefficients could be found in the literature, whereas data for pressure drop across orifice plates had been studied in great detail by a number of authors including Chapman, Torizumi and others.

Variable BR Orifices Variable BR orifice arrays were chosen as an area of investigation which had not previously been studied in the literature. A strategy was proposed to explore the effect of changing obstacle geometry both experimentally and using analytical models, then compare the results of both types of obstacles and explore whether FA could be enhanced by changing or grading the blockage along the tube axis.

7.2 A Review of rig design

The existing rig was iteratively optimised to study the effect of different obstacle geometries on FA within the PDE tube. It was discovered that the initial PDE 3.5" PDE tube was incapable of producing a detonation within the tube length. It was decided that the reason no DDT events were observed was because of an insufficient tube

length to diameter ratio, with the help of rules of thumb developed in the literature for FA. These models, discussed in the Literature Review in Section 2.5.3 were used to predict when flame choking would occur, and therefore predict when detonation was likely to be triggered in the PDE. Furthermore, the same rules of thumb, together with observations about the critical tube diameter for detonation were used to specify tube dimensions for a new PDE tube which had and internal diameter of 1.5" and a length of 29 D, after the reduction section of the PDE tube which reduced the PDE tube diameter from 3.5" to the 1.5" required for the new tube. This tube was designed to be modular so that smaller lengths can be bolted together in different orders, allowing for ports to be moved around into areas of interest.

Other developments were made to the original PDE rig. These changes included the addition of accurate fuel and air flow measurement instrumentation, pressure instrumentation and ion probe instrumentation which took considerable time and effort to develop and are detailed in full in Table 4.6. The reliability of the rig was dramatically improved by the addition of an electro-mechanically timed fuel injection system which triggered gas injectors reliably over a series of test campaigns for 3 years with no sign of failure. The previous fuel injection system based on a peristaltic pump required regular maintenance whenever friction de-laminated or burst the mechanically deformed hose. In addition, the degree of precision and control in fuel timing gained by changing to a mechanical wheel and light gate in the new system was much greater than the previous study. This new system also allowed for brief investigation of ignition-injection timing, and could be investigated further in future studies. Similar electrical valve systems are used in other experimental rigs discussed in the literature. Whilst this information was not explored in great detail in the literature review, it formed a large portion of the work carried out on rig development during the PDE rig design phase of this thesis.

The process of analysing results has been improved by including a statistical distribution of the data gathered for each of the test cases investigated. This has not been completed in the same manner in the literature, as usually only the mean and standard deviation of the flame speed data is represented for multiple FA experiments in single shot rigs or multiple cycles in real PDE engines. This novel method of presenting flame acceleration, shock speed and shock dynamic pressure gives a fuller picture of all of the results available at a given test condition and illustrates how large the range of the data is. This also represents the statistical distribution of the experimental data. As

a result of plotting the data in this fashion, it is much more difficult to ignore results which would otherwise have been missed from the analysis. It is worth stating that FA and DDT are highly stochastic processes, which differ from one event to the next and that results should be presented in their entirety to allow for proper analysis, which this method permits.

7.3 Experimental Comparisons

7.3.1 Differences between Stratified Blockage Ratio Experiments

In this section each of the results for the different orifice plates have been compared with one another in order to determine the effect of different orifice combinations on a range of factors including the following:

- Peak dynamic pressure, as measured at regular intervals
- Shock Time of Flight as measured at the tube exit using dynamic pressure transducers
- Flame speed as measured instantaneously along the tube

Throughout this discussion the results of the first 0.57 BR orifice plate case will be ignored as it was thought that the results of this test had been affected by the presence of a liquid hydrocarbon mist in the fuel line. Observations made of the exhaust plume throughout these experiments would support this hypothesis as the plume was yellow and blue in colour, not the regular blue colour produced by a propane-air flame. This is possibly due to the line being incorrectly purged between the previous tests which used the same fuel delivery line operating with diesel. The later tests were performed after the line was purged carefully with isopropanol to adsorb the diesel, and then flushed out. Nitrogen was then used to clear the line of isopropanol which is a volatile substance at room temperature, so that the fuel was not contaminated in the later tests.

7.4 Effect of obstacle length scale on FA

7.4.1 Circular Orifices

The work of Kuznetsov et al. stated that obstacles are found to generate turbulence at the integral length scale of the tube when the obstacle BR is between 0.3 and 0.6BR. Furthermore, it is also stated that the turbulence generated by orifice plates with BR $\approx$ 0.1 is the same scale as the height of the obstacle fence, and obstacles with BR $\approx$ 0.9 generate turbulence with an integral length scale comparable to the internal orifice diameter. This suggests that the integral length scale turbulence generated by the 0.42BR, 0.57BR and 0.75BR orifice plates will be D, the tube diameter. Of course this turbulence will decay into smaller eddies over time, but it is difficult to quantify the scale of this turbulence in the combustion chambers environment within the given system. Furthermore it is also difficult to predict the effect of later orifice plates and their respective turbulence generation on the length scale as there would be a degree of gas movement before the flame reached these orifice plates, after the shock wave. This would result in a longer residence time for the turbulence to cascade to smaller length scales and begin to dissipate kinetic into thermal energy.

It is however possible to use the approximate relationship used in Equation 2.16 to link the integral length scale to the Kolmogorov length scale of the turbulence as a function of the pressure drop. This suggests that the obstacles which generate a higher u' will generate a smaller length scale. Results from the analytical modelling chapter suggest that higher BR orifice plates will generate a larger pressure drop and therefore a greater u' intensity for any given inlet conditions when compared to those with smaller BR. This implies that the higher BR orifice plates will generate smaller length scale turbulence and as a result will generate faster flame acceleration for a full tube of fresh mixture. Obstacles with a higher BR, however, will also impede the shock wave once the process of FA has accelerated the gas to speeds in excess of the sonic velocity. As such it is thought that decreasing the orifice plate BR along the tube at the correct location, around the point where FA has become sonic, could generate fast FA which would stabilise the flame and reduce viscous losses across the orifice plate at higher velocities.

The concept of varying or stratifying the orifice BR was tested in Section 5.3.11 and compared with the opposite order to test the hypothesis in Section 5.3.11. These tests performed well, showing that both the increasing BR and decreasing BR conditions produced more regular ignitions than the 0.57BR case or the 0.75BR case. The increasing BR case fired every time the mixture was ignited, whereas the decreasing case fired successfully for over 90% of the cases. Other obstacles produced between 30% 60% of the cycles reducing in successfully registered ignitions which could be recognised by the ion probe and pressure instrumentation. The remaining data produced spurious results with no flame speed registered at all and no pressure trace measured above the thresholds set in the LV software. The pressure threshold for this software was set to ≤ 0.25 bar, so any flame larger than this would be recognised. This could be a result of abnormally large proportions of combustion products being left from the previous cycle causing non-ideal reactant mixtures to be generated in the present cycle. Other alternatives include irregular vale timing, and irregular ignition energies, although these should have been the same in each test case as the experimental apparatus did not change in this respect. It is expected that these misfires are most likely to be caused by an effect of the orifice plate BR, as no other factor changed between these experiments. As such the 'purging effectiveness' of different BR orifice plates is likely to be the main contributing factor to the change in % of misfires between these experiments.

7.4.1.1 Observations at the orifice exit

The stratified BR cases exhibited the highest flame speeds at the exit of the orifice laden section of the tube, as can be seen from Figure 5.61. The mean orifice exit flame speed was higher in the case of the decreasing BR orifice plate than any of the other orifice plates for the later set of results. The next fastest flame exit speed was the 0.57 BR end ignition case, then the 0.57 BR side ignition case, the increasing BR case and finally the 0.75 BR case.

The mean shock wave pressure shown in Figure 5.62 generated at the orifice array exit was highest in the two new 0.57 BR cases, followed by the increasing BR case and the decreasing BR case. It is thought that the large exit blockage in the increasing BR case would act as a choked nozzle in this case; increasing the back pressure along the full

set of obstacle array once the gas becomes sonic at the throat. This could be the main reason that the pressure is higher in the increasing BR case at this location rather than the decreasing BR case. The 0.57BR orifice case exhibits higher exit pressures than any of the other conditions, perhaps this is because the pressure has been able to build through successive relatively high BR orifice plates from the point of ignition until the shock exited the orifice plates. The 0.75 BR case was expected to produce very intense turbulence and generate a higher flame speed due to the strong turbulence intensity. On the contrary, in practice the pressure and flame speed developed were much lower than in the comparison presented by Ciccarelli in Section 2.14 for similar orifice BR conditions. It is thought that this is a direct result of burnt products being left behind in the recirculation zone behind each orifice plate in the 0.75BR case. This result is supported by the work carried out by Ciccarelli in the literature review, as shown in Figure 2.22, which shows unreacted pockets of gas being left behind in the reacting shear layer between 0.67BR orifice plates in a 76mm cross section square channel. These pockets take much longer to burn out as the shear layer between them is far less turbulent than that of the smaller blockage ratios which exhibit the same flame forward gas speed. As a result the mixing processes taking place through flame folding in these pockets is much slower than in the smaller blockages.

The effect of these results has been found to compare well with the experimental data, showing a maximum flame speed inside of the orifice plates of 500m/s for the 0.75 BR case, where the 0.57 BR case exhibits a flame speed of around 700m/s. The decreasing BR case exhibited a flame speed of around 1000m/s in this case, indicating that reflected compressive shocks from the smaller orifice plates at the end of the tube were interacting with the oncoming flame front, as suggested by Ciccarelli. This argument is detailed briefly in the shock flame iterations section of the literature review, Section 2.1.7. It thought that the initial high BR orifice cases restrict the flow, generating localised intense turbulence and flame folding which accelerate the flame kernel. This intense turbulence generates the small length scales necessary for the flame to transition from a laminar flame propagating at a slow velocity to a distributed reaction zone which is well mixed by small scale turbulence, with similar Kolmogorov length scale to the flame front. As the flame propagates through the reduced 0.5BR blockage, the degree of restriction reduces but the flame is travelling at a higher velocity by this point. This means that a smaller orifice will still generate the required turbulence intensity, but

will provide less obstruction to the propagating shock wave which is travelling ahead of the flame front. Finally, by the time the flame has reached the last, smallest BR orifice, it is likely to be travelling at around 700m/s, as indicated by the flame speed between PL2-PL3/PL4* indicated in Figure 5.61. At these sorts of speeds, and with reduced obstruction, the reflected shock waves are able to propagate up stream into the oncoming flame and increase the flame speed dramatically, up to the 1000m/s mean velocity observed between PL3/PL4* and PL5, i.e. across the last batch of orifice plates.

7.4.1.2 Observations at the tube exit

Along the smooth section of the tube the pressure decays in most cases, except the first 0.57BR case, which will be ignored for the sake of this analysis. These results can be seen in Figure 5.62.After exiting the orifice laden section of tube most of the cases showed an increase in pressure at the PL6 location, at the 19th diameter from the reducer. The 0.75BR case was an exception which showed an initial rapid decreasing trend in pressure. From PL6 to PL7 each of the test conditions showed a decline in the peak shock wave pressure to between 3 and 3.5 bar. This pressure then increased by PL8 to around 3.5 bar in most cases, with the exception of the 0.75 BR case. In general, a decline in pressure is observed from the exit of the orifice laden section of tube.

The mean flame speed in figure Figure 5.61 also decreased in most cases, with the exception of the 0.75BR case which showed a peak in the flame speed at PL7, with a mean speed of over 1000m/s. This flame speed quickly reduced to around 600m/s by the end of the tube at PL8. This may represent a series of failed DDT events. At PL8 the flame speeds fell into two groups for each of the test cases, those traveling at the speed of sound in the reactants (340m/s) and those traveling at double the speed of sound in the reactants, around 600m/s. Each of the gradients for the 0.57BR SI, 0.75BR and INC BR cases was negative, where as the gradients in the 0.57BR EI case and the DEC BR case were increasing. Those cases exhibiting increasing flame speed gradients at the end of the tube were the flames which exited the orifice section fastest at PL5. Perhaps if the tube was longer, DDT would take place in these cases at the

furthest extremity of the tube, as would appear to have taken place in the old 0.57BR case, indicated by the dashed line.

7.5 Comparison of Analytical and Experimental Results

7.5.1 3.5" 0.75BR comparison

7.5.1.1 Result

Figure 7.1 shows the results of analytical modelling and experimental results each conducted on a 3.5", 88.9mm diameter tube which was 1000mm in length. The tube was filled with stoichiometric Propane-Air mixtures and the flame was accelerated through nine 0.75BR orifice plates each spaced at 1D.

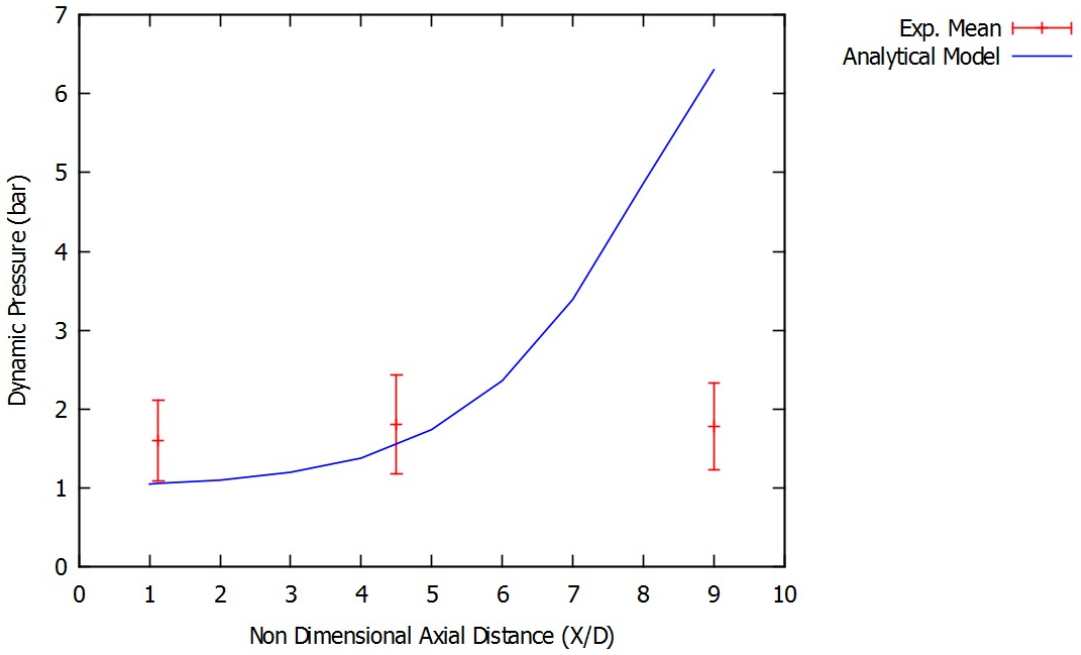

FIGURE 7.1: Experimental/Analytical Model comparison. 3.5" (88.9mm) diameter tube, 0.75 BR orifices with stoichiometric propane-air mixture. Measurements indicate peak dynamic pressure at various port locations (bar) vs. port axial location (X/D).

7.5.1.2 Discussion

As can be seen from Figure 7.1, the analytical model's results match the experimental results with reasonable accuracy at the begining of the flame acceleration process.

In fact, for the first and second port locations the results match very well, falling almost within one standard deviation of the mean at the first port location, and within one standard deviation at the second port location. By the third port location the analytical model predicted a pressure three times greater than that demonstrated by the experimental results.

A selection of possible reasons for modelling inadequacies are presented below.

- The analytical model's orifice C_{CFAM} constant could be incorrect, producing an incorrect value for the production of turbulence from a given pressure loss across the orifice plate. If too much turbulence was generated for a each respective quantity of pressure lost across an orifice plate, the flame speed and pressure would build faster in the model than in the experiment. This observation only occurs at the last port location along the tube, however, and is not reflected in the earlier port location. This suggests that if the problem is due to an incorrectly set C_{CFAM} constant, it is only incorrect at higher flame speeds present later along in the duct, as the pressure is predicted relatively well at the earlier port locations, which would be closer to the sonic velocity.

- The model could be incorrectly predicting pressure lost across the orifice plate, δP_{23}, from Equation 3.10. It is a strong possibility that the effect of shock reflections at the later stages of flame acceleration are not fully captured in this re-arrangement of the Torizumi model, as the original model only accounts for a single orifice plate. In this case the pressure lost from each orifice is subtracted from the post shock pressure after the flame passes through a given orifice plate. Unless there are strong shock reflections between each consecutive orifice plate which occur as the flame traverses in the void between the orifice plates, this is unlikely to have an effect on the flame speed, as this is determined by local conditions of pressure and turbulence and temperature for a premixed gas..

- Finally, another possibility is that the tube was not fully purged in the later sections of the tube, as $pf = 0.6$ was used in this case. This could result in a larger portion of the products remaining in the tube, which would change the reactant mixture properties rendering the empirical combustion model out of its normal range (i.e. $\phi \neq 1$.

7.5.2 Stratified Orifice Modelling Comparison

In order to compare the results of the stratified orifice tests presented in Chapter 5 with the predictive capability of the analytical model presented in Chapter 3, it was necessary to perform further modelling comparisons using the CFAM analytical model. The results of these experiments using the model with a 1.25" (31.75mm) diameter domain 15 diameters in length were combined in plots and presented below in Figures 7.2 through to 7.7.

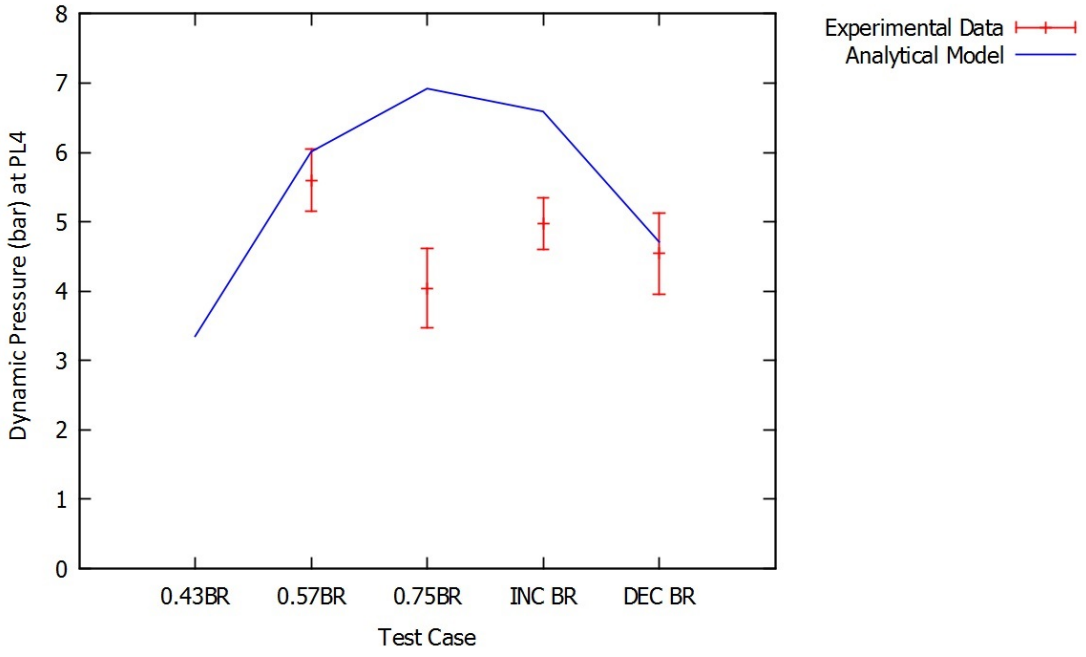

FIGURE 7.2: Experimental/analytical comparison. 1.25" (31.75mm) diameter tube, with stoichiometric proapane-air mixture. Peak dynamic pressure measurement at PL4, 12.5D after the reducer (bar) vs. orifice blockage configuration.

Figure 7.2 shows the comparison of modelled pressure data against the experimental comparison, with symmetric error bars representing one standard deviation in the measurement. It can be seen that the modelling results predict the correct order of magnitude in all of the above cases. The 0.57 and DEC BR case analytical results match the experimental data within one standard deviation. In contrast, the 0.75BR and INC BR cases show large deviations from the experimental result. It is thought that this could be the result of insufficient purging/mixing in the rotating shear layer between the larger BR orifice plates present in the 0.75BR case, and at the end of the INC BR case. This is a corollary of the cyclic nature of the experiment, in comparison with the single shot experiments on which the model was based. In the single shot

experiments carried out by Ciccarelli a perfectly fresh mixture was created before ignition each time by taking the up most care to thoroughly clean the test section with a vacuum pump every time the experiment was carried out. The fresh mixture was then re-circulated multiple times through the test section before ignition, as discussed in Section 2.1.6. In contrast, the current work uses multiple, cyclic ignitions with 0.5 pf purging in between. It is thought that this discrepancy between the 0.75BR case, the increasing BR case and the analytical modelling results is because of the difference between the mixing in the pockets of burnt products in between these orifice plates. Interestingly, there is much less discrepancy between the analytical and experimental results of the decreasing BR case.

It is hypothesised that this discrepancy is because the purging mixture has a higher concentration of fresh air as it is first injected into the tube, and becomes progressively mixed with products as it passes along the tube. This would seem to make sense, as the difficult to purge initial sections in the decreasing BR case would be purged effectively then the purge gas would progress into lesser BR orifices which would be much easier to clean due to the smaller pockets of burnt mixture in the inter orifice shear zones. In contrast, the increasing BR orifice plate array would purge more readily at the normally closed end of the tube, but as the purge gases move through the tube and become increasingly contaminated from the earlier orifice plates their purging would become less effective. This would be compounded by the confinement of the final 5 0.75BR orifice plates which trap burnt products in their recirculation zones. As the purge gases would already be contaminated by this point their ability to properly purge the last few orifices could be diminished. It is also thought that this effect could be responsible for the slightly low experimental flame speed in the 0.57BR case, in comparison with the analytical model, although because this case had a lower BR, the effect is thought to have been smaller.

This hypothesis could be tested by installing oxygen/lambda gas sensors between each of the orifice plates in the multi-cycle UoS PDE and measuring the concentration of oxygen and/or fuel in multiple locations along the tube prior to ignition. Alternatively, an analogous experimental system could be built using similar Reynolds numbers and density ratios of gases with different gas colours to investigate the effect of mixing in an optically transparent duct or tube, other non-dimensional numbers for mixing would

also need to be considered. Further more the system could be modelled numerically with varying equivalence ratios along the tube.

It is envisaged that for proper modelling of PDE FA processes in a cyclical PDE system, a mixing model for purging and filling would be extremely useful to determine the effect of larger orifice plates. This pre-combustion model could be used to predict the quality of the mixture ready for combustion before ignition took place. Such a combustion model would need to be able to account for slower S_L, S_T and different σ due to the increased proportion of combustion products in the reactants before combustion. The portion of products in between each orifice could be calculated analytically, and then passed onto the combustion model in order to predict flame acceleration. Alternatively, the whole system could be modelled in a numerical CFD package assuming that the initial mixture was generated by complete combustion of stoichiometric reactants. These reactants could then be mixed with varying proportions of purge gas and fresh reactants and ignited after a time delay and valve closure. This holistic approach could be accompanied with a chemical model which would automatically calculate the flame speed of the combustible mixture using similar chemistry to exhaust gas recirculation in internal combustion engines. To successfully build such a large model would be a huge undertaking and as a result would require many man hours, therefore an analytical model may be a more effective solution.

Figures 7.3 to 7.7 compare the experimental TOF with TOF results for the flame front generated by the analytical model. The analytical TOF data was calculated by finding the compound time of flight between several orifice plates and interpolating the results where necessary. As there was no data for the 0.43 BR case, due to its inability to ignite sufficiently and generate shock waves or flame ion probe data, there is no experimental data presented with the 0.43 BR case shown in figure 7.3.

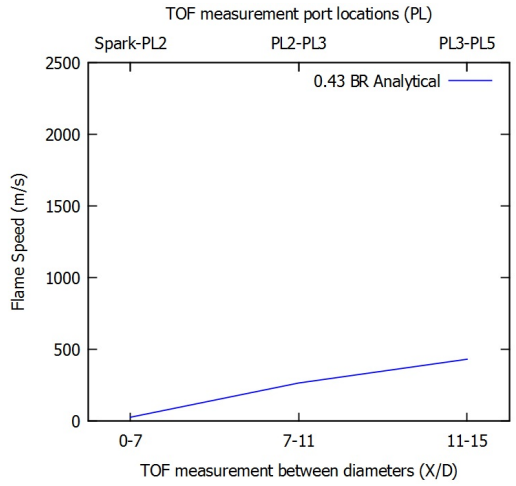

FIGURE 7.3: Experimental/analytical comparison. 0.43 BR orifice plate statistical flame TOF.

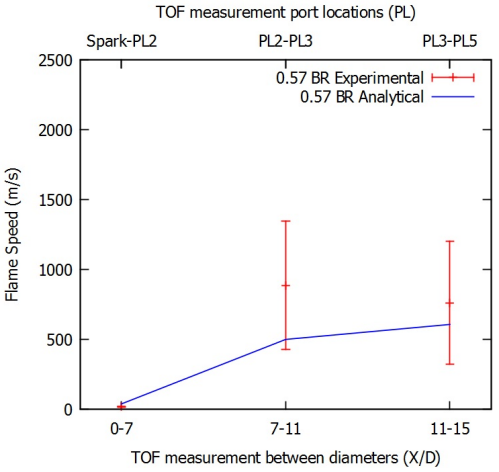

FIGURE 7.4: Experimental/analytical comparison. Repeat 0.57 BR orifice plate statistical flame TOF

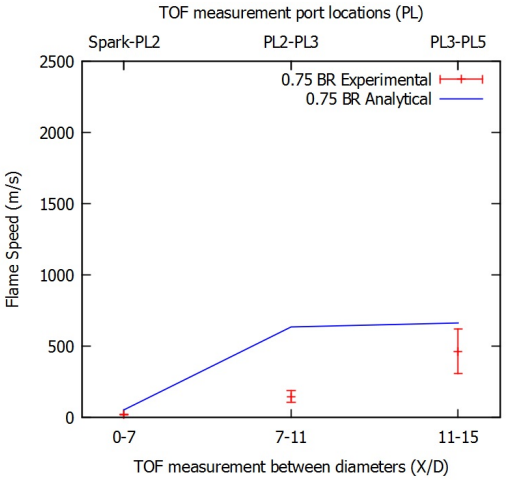

FIGURE 7.5: Experimental/analytical comparison. 0.75 BR orifice plate flame TOF

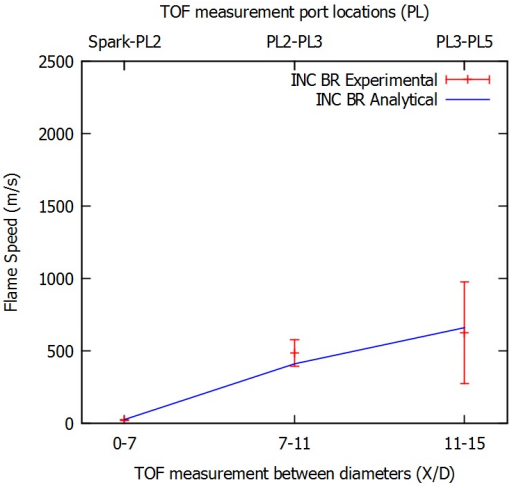

FIGURE 7.6: Experimental/analytical comparison. Increasing BR orifice plate statistical flame TOF

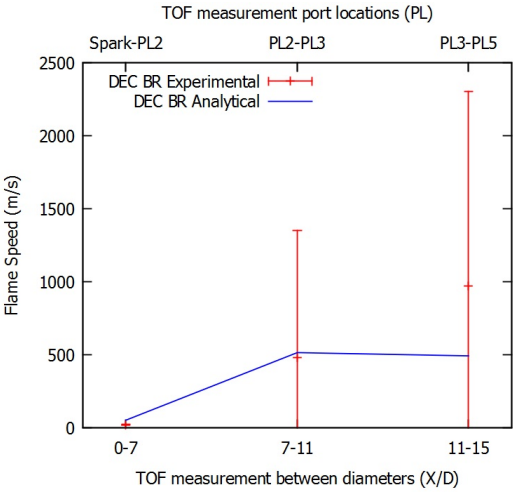

FIGURE 7.7: Experimental/analytical comparison. Decreasing BR orifice plate statistical flame TOF

The results of Figures 7.3 to 7.7 show correct order of magnitude for flame speed in each of the cases studied apart from the TOF result for the 7th to the 11th diameters in the 0.75BR case. Most of the results, with the exception of the 0.75BR orifice case show good correlation with th experimental data and fall within the error bars for one standard deviation. The 0.57 BR case under predicts the TOF flame speed, particularly between the 7th and 11th diameters. It is likely that this is because some of the flames had begun to transition to DDT, or have experienced the same Richtmeyer-Meshkov instabilities as a result of shockwaves which were also observed by Ciccarelli et al. in lower BR obstacles (discussed in Section 2.1.7). These instabilities increase the average flame speed producing a jump in flame speed, as could be seen by flame X-t plots shown in the flame speed distributions for this case in Figure 5.14. As the model was not designed to be capable of capturing these physics, this could not be predicted. Similarly, this could explain the high flame speed average encountered between the 11th and 15th diameters for the decreasing BR case in Figure 7.7, as the shock wave could interact with the flame without being heavily obstructed here too.

Another possibility is that the analytical model could be under predicting the turbulence generated by the 0.75BR case orifice plates, and that in practice the turbulence generated is so strong that the flame is being quenched. It is thought that this is unlikely however, as the flame speeds (and gas speeds) calculated for this set of orifice plates is much smaller than those of the other cases. This infers that there would be less energy available in the system to generate intense turbulence for the 0.75 BR orifice plate than the smaller BR plates, so a velocity deficit on the grounds of intense turbulence along is unlikely. In addition, this does not match with the results of Ciccarelli et al. in the literature for a 0.75BR orifice plate shown in section 2.1.6 of the Literature Review. As a result it is much more likely that the difference between the analytical model and experimental results is due to ineffective purging of the 0.75BR orifice in the experimental test, and the inability of th model to simulate purging before ignition.

The results of Figures 7.2 to 7.7 show that the analytical flame acceleration model is capable of capturing the physics of flame acceleration up until the point of detonation when the underlying physics of the model are unable to predict flame speeds. In addition it is thought that errors in prediction of the flame speed with high BR conditions can be explained by inadequate purging of exhaust products which in turn reduces the mixture equivalence ratio. The model however, is not currently able to model the

physics of the flame and shock propagating along the smooth section of tube. Both of these areas could form the basis of a future model which is capable of modelling flame acceleration in real PDE systems.

7.6 Fractal Orifice Experiments

All of the fractal orifice plate experiments were performed with 0.75BR orifice plates as this left sufficient space for mounting the orifice plates in the three rod orifice mounting system. It may be beneficial in future work to experiment with fractal orifices of smaller BR, which have proven to generate faster FA and shock speeds in the stratified orifice plate chapter of this thesis, Chapter 5. Unfortunately the flame ion probe instrumentation had not been developed by the time the experimental campaign was conducted and as a result flame speed data was unavailable for the cases involving fractal flame acceleration. As such this chapter can only serve to provide information on the shock wave generated by the combustion process and not the combustion process directly.

7.6.0.1 Changing the fractal dimension

Three separate experiments were conducted during which the orifice fractal dimension was changed. Firstly, the 20 orifice plate experiment, then the 28orifice plate experiment which only explored shock speed followed by the 12 orifice plate experiment. The first two experiments found that the fra_0 case with the triangular orifice plate produced the fastest shock speeds. In contrast, with a shorter obstacle containing only 12 orifices spaced at 1D, the fra_2 case outperformed the fra_0 case. It is thought that smaller, more refined fractal geometries have a larger effect at smaller flame and shock speeds, increasing the turbulence intensity and reducing the Kolmogorov length scale of the turbulence generated over a short distance. In contrast, obstacles with larger length scales would not be able to generate such a wide range of turbulent length scales due to their larger geometry. In contrast, with longer obstacles it is thought that the effect of smaller minimum obstacle length scales is considerably reduced as the flame will already be traveling at high speed by the time it interacts with the later obstacles.

This means that the turbulence Reynolds number would be much larger at this location due to the higher gas velocity at this point along the tube. This high Reynolds number would create smaller length scales due to the turbulence cascade, as expressed in Equation 2.16.

7.6.0.2 Number of $fd2$ orifice plates

Tests were performed using $fd2$ orifice plates to determine the optimum length of this particular orifice type. It was found that the high shock speeds could be maintained with mean shock speeds of between 600m/s and 700m/s for between 12 and 28 orifice plates. It should be noted that the standard deviation of these results changed depending on the number of orifice plates, particularly with between 26 and 28 orifice plates. The peak shock pressure showed a strong decreasing trend with the number of orifice plates inserted along the tube. A mean peak pressure of 4.5 bar could be attained with 12 $fd2$ orifice plates, however with 28 orifice plates, this figure had fallen to a value of 3.1 bar. This leads to the conclusion that increasing the number of orifice plates in the tube can be detrimental to the peak shock pressure. This reduction in pressure could be due to viscous drag on the shock wave from the orifice obstacle, which would be much larger in the case of complex fractal geometries than a regular orifice plate. It could also be suggested that with too many $fd2$ orifice plates would severely reduce the chance of detonation as the auto-ignition time of the reactants would be slower with weaker shock waves and temperature gradients.

7.6.0.3 Varying the orifice fractal dimension along the blockage

Experiments were performed changing the fractal dimension of the orifice plate which revealed that there was no major benefit of changing this along the blockage. It was found that for an orifice obstacle 12 diameters in length and with a spacing of one diameter, the best performing orifice was an $fd2$ fractal.

It is thought that this is due to the effects listed below:

- Intense, small length scale turbulence in the initial stages of flame acceleration promotes penetration of turbulence within the length scale of the flame, changing

the premixed combustion regime from a laminar flame to a thick flame and eventually a distributed reaction zone when the turbulence length scales penetrate the chemical reaction zone. This is helpful in early stages of the combustion process, which is indicated by the comparison between the $fd0$ and $fd2$ cases when 12 orifices were used in Section 6.3.4. And is also confirmed by Ciccarelli et al with his work on perforated plates, which expressed that the benefits of more intense turbulence generating obstacles are only at the beginning of the tube, for the first two orifice plates where a spacing of 1D is used.

- As the length of tube traversed by the flame increases and the flame speed increases, shock waves begin to develop as a result of increased gas speed along the tube. These shock waves are a key part of the FA process, and are affected by the presence of orifices as detailed in the work of Ciccarelli et al discussed in Section 2.1.7 of the Literature Review. It is thought that a coarse fractal shape with longer minimum length scales (such as the $fd0$ case) will provide less obstruction to the propagating shock. As a result, a shock wave with less drag will maintain a higher post shock pressure and a higher velocity overall, creating a better environment for faster FA

7.7 Fast flames but no detonation

It is noted that even thought a number of the explosions resulted in flame speeds in excess of the Chapman Jouguet detonation conditions, detonation pressures were not recorded on any of the transducers at any point throughout the experiments.

Section 2.2.1 of the Literature Review illustrates the work of Kuznetsov which clearly depicts different flame acceleration regimes in orifice laden tubes. Using the information presented here, it is possible to draw comparisons with the results produced in the current work. The flame speed in Figure 5.8 remains subsonic throughout, similar to slow/unstable flame regime depicted in Figure 2.31. Maximum pressures in the region of 1.5 bar are reached in the literature here, in comparison the current experiments exhibits a maximum pressure of 3.6 bar decaying to 1.5 bar at the exit location, where the tube is smooth. The flame speed in the literature here is 150m/s, and the flame

speed in current work, Figure 5.8, is around 300m/s. This indicates that the measurements are of similar range and are feasible. The geometric difference between these two experiments lies in the length of the orifice laden section of the tube. In the literature is full tube length, 33m, or approximately 70 diameters, in comparison to 14 diameters and around 600mm in the current experiment. In addition, the fuels are also different, however it is possible to compare the pressure developed by the flame speed in general terms, as the gas compression generated by comparable flame speed should generate a similar shock strength and compression wave. This can be shown by equations form the literature, in Equations 2.55 to 2.59 and 2.61 to 2.67, i.e. that the shock speed relates directly to the gas speed and the flame speed.

Flame speeds in excess of the detonation flame speed were observed, however, these were rarely maintained throughout the whole tube. The flame often accelerated to the detonation speed within the orifice laden section of the tube, then decelerated after the last orifice as the flame and shock decoupled. This behaviour can be seen in Figures 5.10 and 5.11, for instance.

There is sufficient length of tube for the flame to reach the choking velocity according to calculations performed in the PDE rig design Chapter, with the results displayed in Table 4.1. According to this table, the choked flame should be reached by 24 diameters, and detonation should occur at a similar location. The flame speeds recorded indicate that the flame begins to choke within the orifice laden section of the tube in both of the new 0.57BR cases, and the DEC BR case as is shown in Figure 5.61, in the mean case at least. Where the flame reaches the choking velocities before the end of the orifice plate, as is seen in the 0.57BR cases, the flame then decelerates through the orifices. This is thought to be due to the orifice diameter being smaller than λ, the critical diameter for DDT transition in an orifice laden tube, as discussed in the Gap Analysis section of the thesis, Section 2.7.4. This caused any DDT hotspots which were initiated to decelerate due to the tube being insufficiently large to contain the cell structure required for DDT to fully transition. The remaining length of the tube after the last orifice plate was 310mm, which was shorter than the 7 λ required for a detonation to transition from a choked flame by a margin of approximately one diameter.

Unfortunately, the alalysis for this section of the literature review was completed after

the design of the PDE tube, so the tube geometry could not be changed before completion of this work. There was a degree of ambiguity in the literature as to whether detonation happens as soon as the flame is choked, or 7λ later. Both Silvestrini and Vaser suggested that detonation occurred at X_s, the point of flame choking, where as Ciccarelli and Dorofeev suggested a more conservative limit of X_s plus 7λ. As such the initial tube geometry was designed around a 29 Diameter long section, which was thought to be sufficient to reach a choked flame and therefore generate a detonation. It is thought that DDT had just begun to occur at the end of the smooth section of the tube in the 0.57BR EI OLD case, as the flame speeds at this location were around 2000m/s as a mean value at the exit. The shock speed at this location was much lower, around 800m/s however, and the pressure was only 4 bar at the mean value. It is thought that DDT had been started by a high flame speed, and that the shock and flame were beginning to converge as can be seen in Figures 5.11, 5.34 and other high speed flame plots. It should be noted that this only occurred in a small percentage of the cycles ignited.

These results are similar to the findings of Kuznetsov et al. discussed in the Literature Review, Section 2.34, prior to detonation initiation in the quasi-detonation regime within obstacles. In this case the pressure prior to DDT was around 5-6 bar just before detonation which began with an overdriven pressure then decayed to a quasi-detonation state. It is be hypothesised that DDT had nearly occurred in the smooth section of the tube. IN 5.11 the flame accelerated up behind the shock, possibly approaching DDT just before the end of the tube. To test this hypothesis it would be necessary to extend the tube length and instrument the extended tube accordingly. Unfortunately, before this was possible, the PDE valves began to seize, so no further testing could be carried out. Of course this only occurred in a small fraction of cases, so it would also be necessary to investigate extending the number of orifice plates, or adding alternative obstacles such as Schelkin spirals to enhance FA further along the tube.

7.8 Industrial Explosion Safety

The results of the fractal experiments are particularly applicable to industrial explosion safety, as explosions occurring in industrial environments often contain a wide number of length scales as was briefly discussed in Section 2.1.4 of the Literature Review. The

experiments carried out in the current work here show that for an identical orifice blockage ratio, the shape of the obstacle can dramatically affect the ability of the obstacle to enhance turbulence generation, particularly in the early stages of flame acceleration simulated by the twelve orifice experiment.

This turbulence scale effect may have played an important role in the process of FA and rapid DDT which took place in the Buncefield incident [65] as the tree lined avenue which the flame front accelerated along contained trees with small characteristic length scale twigs and leaves. It could be argued that these trees represent fractal objects which would increase the generation of turbulence at a number of different length scales. It is hypothesised that the small scale of these finer fractal shapes present in the tree lined avenue, coupled with intense gas speeds due to FA would enhance the flame speed in comparison with large obstacle shapes as the turbulence generated would more readily penetrate the chemical length of the flame $\delta_C H$. This would have the direct result of enhancing the local turbulent flame speed and augment the FA process over the area with fractal obstacles present. These smaller length scales orifices also produced higher shock wave dynamic pressures in the longer obstacle tests with either 20 or 28 orifices. The shock speeds generated at these longer obstacle lengths were much more uniform, each having a mean value between 600m/s and 700m/s. All of these factors are likely to combine to enhance the flame speed and increase the likelihood of DDT occurring providing that there was sufficient space, residence time, temperature and pressure for the induction zone to auto-ignite and generate a large scale detonation.

Of course, the macro length scales of the tube geometry used in this experiment are much smaller than the macro length scales involved with the Buncefield incident and other open air explosions. To fully understand the effect of obstacles with a range of length scales on FA and DDT on industrial accidents it would be necessary to conduct experiments at realistic length scales so that Reynolds numbers and other non-dimensional numbers relevant to explosion studies were correctly scaled.

Chapter 8

Conclusions

During this work a PDE ground test demonstrator has been developed and tested at The University of Sheffield's Low Carbon Combustion Centre. This rig has been developed and instrumented in order to measure the rig operating conditions as well as high speed instrumentation which is capable of measuring shock wave dynamic pressure, shock TOF and flame TOF measurements. In addition the practicalities of developing a multi-cycle PDE fuel and air injection system have been overcome and the rigs mixture delivery system reliability has improved throughout this work.

A series of PDE tubes have been manufactured, with a range of obstacles for testing novel geometries which have not been observed elsewhere in the literature. These particular geometries are fractal obstacles for use in a PDE rig for investigation of FA, and the variable BR obstacles. The effect of different obstacle geometries on FA in stoichiometric propane-air mixtures in a 31.75mm/38.1mm diameter tube and a straight 38.1mm diameter tube has been explored in detail, with several novel findings taking place. In addition FA was also explored with standard orifice obstacles in an 88.9mm diameter tube. All of these tests were performed with close to stoichiometric propane-air mixtures and obstacle spacings of 1D. Filling parameters ff and pf were maintained close to 1 and 0.5 respectively during all of these experiments, and a standard automotive spark ignition system was used throughout.

Whilst full DDT was not observed, it is thought that the initial stages of DDT events at the end of the smooth section of the tube were observed in at least one test case.

This was indicated by average flame speeds traveling at velocities similar to those seen in detonation events, but much lower peak shock wave pressures.

Furthermore, a semi-empirical analytical model has been developed to gain a deeper understanding of the physical processes involved in FA prior to DDT. A Numerical model has also been explored for the purpose of predicting FA, although these numerical experiments were not progressed beyond preliminary investigations due to the effort required to build, test and improve the experimental rig. As a result the development of this model and its findings are not presented in this thesis. The aim of undertaking this path of work was to produce models which could be used as predictive tools for designing practical PDE engines. In particular, the semi-empirical analytical model was developed without the use of expensive, time consuming super-computers, thus allowing the PDE designer to explore a wide range of experimental conditions in a cost effective, relatively fast manner.

Both of these models have been validated against experimental results. It is thought that the analytical model is capable of predicting FA in orifice obstacle laden tubes relatively well for single shot experiments, where the propane-air mixture is both stoichiometric and homogeneous. The model appears to under-predict flame acceleration in cases where the proceeding shock wave is likely to produce flame shock interactions, such as Richtmeyer-Meshkov instabilities which can increase FA considerably when present. The model has not been modified as yet to include a sub model for prediction of FA under these conditions. It is thought that this is likely to be the reason why the model was unable to predict that FA would be faster for a reducing BR blockage along the tube length, when compared to an increasing BR obstacle.

8.0.1 Summary of experimental findings

The result of these experimental findings are summarised below.

8.0.1.1 Fractal Experimental Conclusions

12D long fractal obstacles Experiments were performed with varying fractal geometry 12D long obstacles. It was found that smaller obstacle minimum pattern

length scales produced faster shock speeds at the tube exit. Each of the blockages had the same cross sectional flow area with 0.75BR. The smallest of these obstacles produced a more uniform, high speed shock TOF than any of the other fractal obstacles and displayed a marked improvement on a circular orifice plate, which ranked next. Similar over pressures were developed in both the $fd2$ and circular fractal cases. Novel experiments were also performed to compare constant fractal dimension orifice blockages with others which changed the fractal dimension along the length. Both of these results showed higher mean TOF shock speeds than the $fd0$ case, but with much lower overpressure development.

20D and 28D long fractal obstacles At these longer lengths the ranking for flame speed changed a larger orifice fractal dimension, such as the $fd0$ case produced mean shock speeds up to 50m/s faster than other cases with 28 orifices, including the standard circular orifice plate. This trend was the same with 20 orifices, however with less difference between each case. This is thought to be a result of less viscous interaction with the shock as it passes though the orifice plates. As such, it would merit further study to investigate the effect of changing fractal dimension over a longer obstacle length

Length Scales It is thought that the benefit of smaller length scales is only advantageous at the earlier stages of FA, before the shock begins to play a major role in FA. As such a small number of high fractal dimension orifice plates at the beginning of a PDE pre-detonator could enhance FA when compared to standard circular orifice plates.

8.0.1.2 Stratified Orifice Plate Experimental Conclusions

Firing Reliability Perhaps one of the most significant findings of this section of research was that by varying the orifice blockage ratio, the reliability of ignition in the UoS PDE rig could be changed. The INC BR and DEC BR cases exhibited the best ignition reliability, in comparison to the 0.75BR case which exhibited poor reliability.

Flame speed developed within the blockage A marked improvement was made to the mean flame speed throughout the orifice laden section of tube for certain obstacle types. The 0.57 BR SI and 0.57 BR EI cases exhibited fast FA until

approximately the centre of the orifice laden section of the tube, but these flame speeds decelerated quickly towards the end of the orifice laden section. It is thought that this was the result of failed DDT due to the minimum tube diameter condition. The DEC BR case, however, exhibited a constantly increasing FA progression throughout the orifice laden tube, with the fastest exit velocity of any of the cases. This could prove to be useful in designing critical diameter PDE engines in the future

Purging It was found that the 0.75 BR orifice plate used in the stratified orifice test produced very low flame speeds. These were much lower than those found in the literature for single shot experiments, which exhibited rapid initial FA comparable to that of the 0.57BR orifice plates. It is thought that this was the result of mixing issues associated with the larger inter-orifice cavity in this case.

Order of Stratification It was found that increasing BR orifice plates performed better than decreasing BR orifice plates. This is thought to be the result of a number of factors. Firstly, initially high levels of turbulence enhance the flame speed and are thought to reduce the Kolmogorov length scales at the beginning of the tube. Once a shock has developed however, less obstruction is beneficial as this reduces the shocks viscous drag, and leaves a higher pressure environment in which the flame can burn. Lower BR orifice plates were found to promote Richtmeyer-Meshkov instabilities, which may have also occurred here. These experimental results are in keeping with Hypothesis 1 and Hypothesis 2 from the Analytical Modelling Chapter.

8.0.1.3 Detonation and DDT

It is thought that DDT and detonation were not observed due either to the tube length being insufficient to start DDT for the mixture. It is supposed that the tube could have been several diameters too short, but that detonation would be likely if the tube was extended in the higher speed cases where the flame and shock were converging.

8.0.1.4 Analytical Methods

A novel application of statistical methods to PDE engine FA results has been realized. By applying the use of frequency distributions to flame speed, pressure and shock speed results, it is possible to see the full statistical distribution of the results for a given experimental condition and compare these directly with other conditions. By using this method it is much easier to compare the full spectrum of data rather than simply using a mean and standard deviation to report experimental findings of what is by nature a very stochastic physical phenomenon.

8.0.2 Semi-Empirical Analytical Model

This semi-empirical analytical model successfully predicted the experimental overpressure developed with the orifice blockage at one location to within one standard deviation of the experimental results for both the decreasing BR case and the 0.57 BR case. It is thought that over-prediction errors of the model in the increasing BR case and 0.75 BR case were caused by inadequate purging during the multi-cyclic PDE firing experiments. This would seem to concur with the literature, which shows no significant reduction in flame speed for the 0.75 BR case over the 0.6 BR case as discussed. In addition, the model correctly predicts the TOF flame speed in three locations for the same cases to an accuracy of 1 standard deviation of the experimental results, which would seem to support this statement. The model does not however include a physical model for the prediction of direct shock flame interaction which can increase flame speeds through Richtmeyer-Meshkov instabilities in short distances with low BR orifice plates. As such the model would be improved by the inclusion of these physical mechanisms, if possible.

8.0.3 Practical PDE development design statements.

The results of these experiments and analytical modelling tests are thought to have relevance to practical PDE engine design. Design suggestions gathered from this thesis include the following:

- Initial obstacles should provide intense turbulence. These turbulence inducing obstacles could be made from fractal obstacles with a high BR in order to promote smaller, more intense Kolmogorov length scales enhancing initial FA

- Later obstacles should generate less turbulence and provide less resistance to the shock wave. This can be achieved by using low obstacle BR and possibly incorporating other shapes with longer length scales than the circular orifice plate for the same blockage ratio, such as a triangular orifice.

- A review of the literature and comparison with the limiting detonation propagation mode yields interesting results. Schelkin spirals with the same pitch as a spinning detonation allow detonation propagation beyond the $d \geq \lambda$ rule. As such the smallest diameter PDE tube could be smaller than the cell size, transition to detonation within a Schelkin spiral and propagate into a smooth tube with $D \geq \lambda/\pi$. The length of this PDE would need to allow for the detonation to run up to the choking point in the spiral laden section of the tube plus 7λ to allow for full DDT transition. The smooth section of the tube would then need to allow for the detonation to become stable, if necessary. This would be likely to represent the smallest scale of PDE engine possible, unless alternative high energy ignition systems were used to negate the use of the flame run up section. In this case a spinning detonation may start in a tube with $D \geq \lambda/\pi$ throughout. This tube length would also be the shortest, as run up is a function of tube X/D.

Chapter 9

Further Work

Naturally, with six years of time and funding invested in this project, it would lend its self to further experiments. Further work will be discussed first in terms of what is achievable with the current test apparatus following this details of possible improvements to the test rig will be laid out and a sample of experiments which could be tested with a new test rig.

9.1 Currently Acheivable Experiments

The following experiments could be investigated with the test rig as it currently stands

- Thermal imaging of the tube wall and further investigation of heat transfer properties at different filling conditions/ mixtures
- Investigation of flame acceleration for a range of gaseous fuels in dynamic conditions
- Investigation of flame acceleration with different mixture equivalence ratios
- In depth investigation of the effect of ignition delay
- Investigation of the effect of purge air fraction
- Exploration of the effect of distributed ignition with a range of voltages using standard spark plugs (with the addition of further electronic hardware)

- Exploration of the effect of reduced fuel fractions designed to minimize the amount of fuel lost out of the end of the PDE due to thermal expansion throughout the injection process- i.e. varying the fill fraction
- Determination of the effects of different combinations of timing fractions

9.2 Possible Future Improvements and Subsequent Opportunities

9.2.1 Fundamental Research

- Photodiode flame sensor development and application to the rig at regular intervals
- Purchasing of further pressure sensors applied at regular intervals for investigation of shock and detonation wave development throughout the combustor length
- Quartz glass tubes and high speed camera to study the effect of different obstacles on dynamic filling flame acceleration, DDT and Detonation propagation
- CFD modelling of obstacles to determine the effect of fractal shapes on shock reflection, transmission and turbulence generation
- CFD modelling to optimise obstacle spacing and diameter at different axial locations
- firing shocks into single obstacles to measure their reflected and transmitted shock velocities at a range of carefully controlled inlet shock Mach numbers/

9.2.2 Applied Combustion Engineering Research- Engine Development

- Variable ignition coil energy to investigate the effects of spark ignition energy on DDT
- Stainless steel air inlet system to investigate the effect of changing inlet temperature on flame acceleration and DDT

- Larger diameter longer tubes coupled with a higher fan delivery pressure to suit increased volumetric/mass flow requirements
- Flash vapoirizer / liquid fuel atomizer to investigate liquid fuel flame acceleration and DDT
- Updated air valve system with larger ports to allow more rapid filling of air at low pressures
- Development of an engine demonstrator for use onboard small UAV platforms, fueled using a liquid fuel
- Optimization of a PDE control system to control PDE firing at a range of operating conditions
- Installation of a thrust measuring device into a new PDE system, which would allow for the direct measurement of thrust at a range of firing frequencies and other operating conditions

Chapter 10

Publications

10.0.3 Conference Papers

J. N. Knapton and S.G. Blakey. A Semi-empirical 1D transient reacting flow model for prediction of flame accelerating effects of obstacles in pulsed detonation engines fuelled by propane-air mixtures. Joint meeting of The British and Scandinavian-Nordic Sections of the Combustion Institute, March 27-28, 2014, Cambridge, UK. http://www.ntnu.edu/documents/14215121/0/Joint_Meeting_Abstract/feed98b6-872e-4c5b\-b47b-d93ce1dd1cdc

Jonathan N. Knapton, Simon Blakey, and Frank Nicolleau. Understanding the Effects of Fractal Blockage Geometries on Flame Acceleration in Propane-Air Flames, AIAA 2015-4147, 51 st AIAA/SAE/ASEE Joint Propulsion Conference, Propulsion andd Energy Forum, Orlando, FL. http://arc.aiaa.org/doi/abs/10.2514/6.2015-4147

Appendix A

Labview Code

A.1 Labview DAQ Code

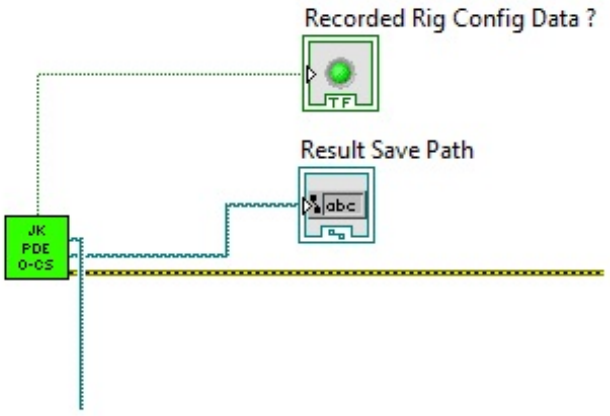

FIGURE A.1: PDE VI: calling the operating conditions saving VI.

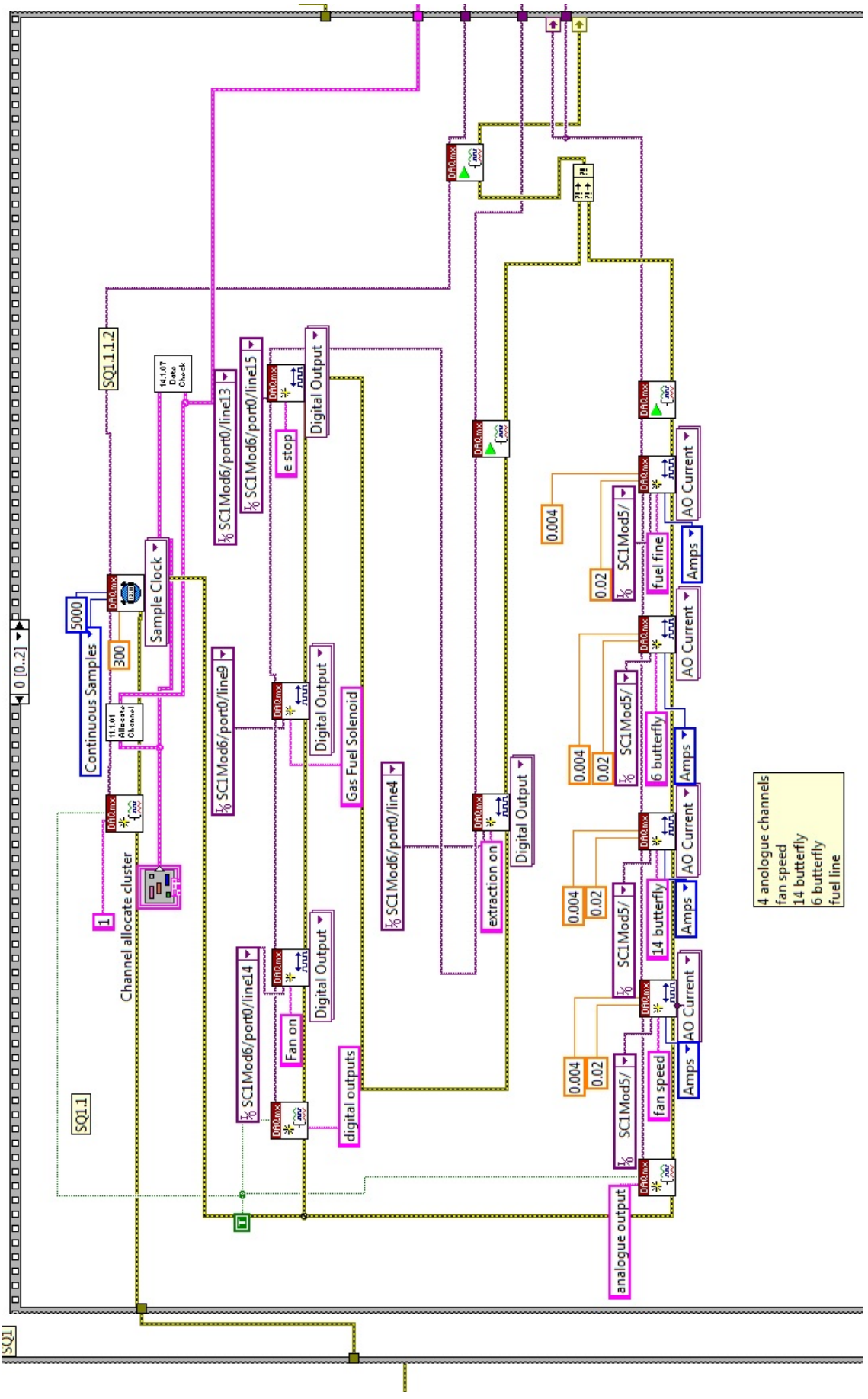

FIGURE A.2: PDE VI: allocating tasks and channels.

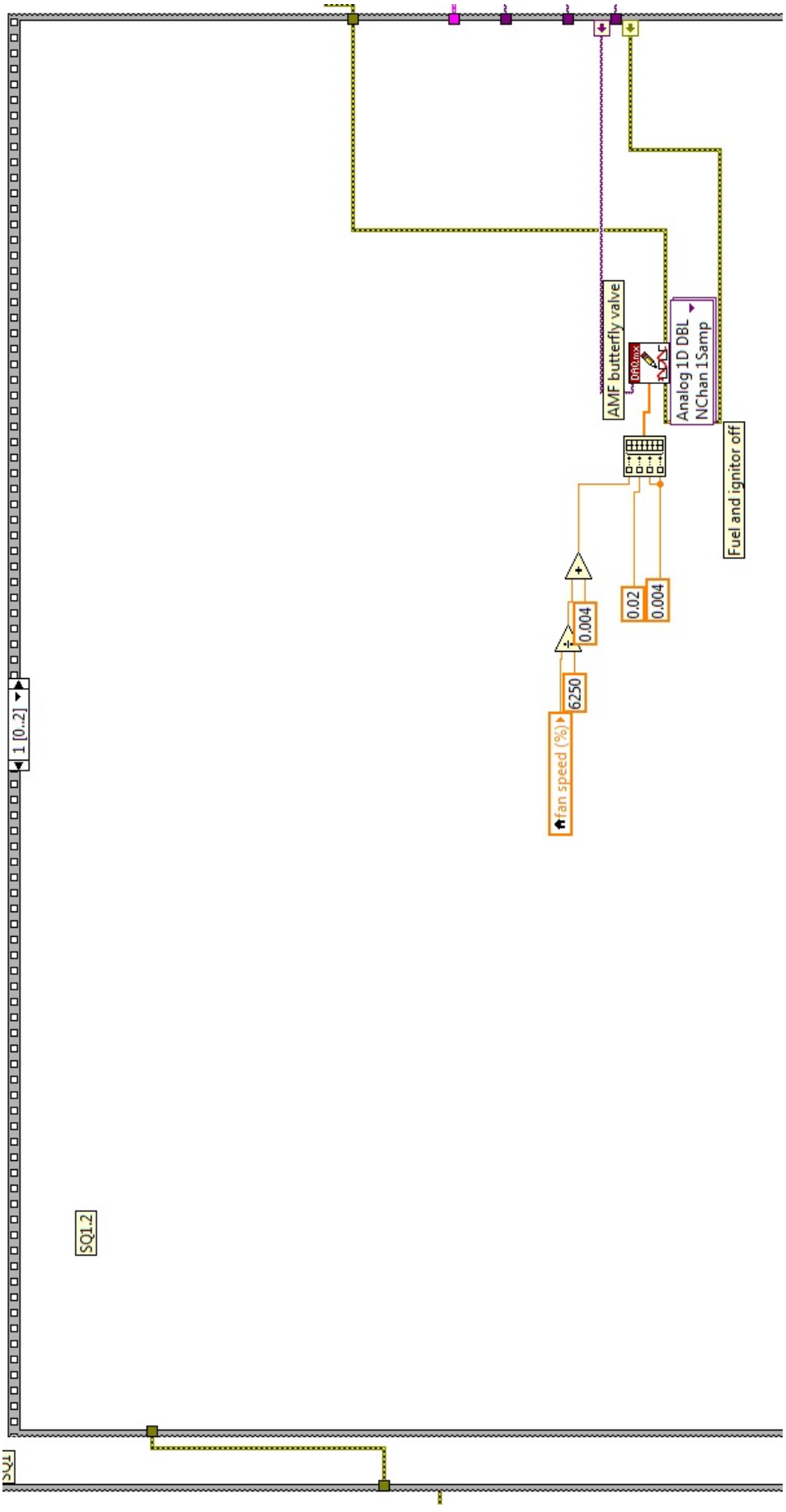

FIGURE A.3: PDE VI: Initialising anologue controller values.

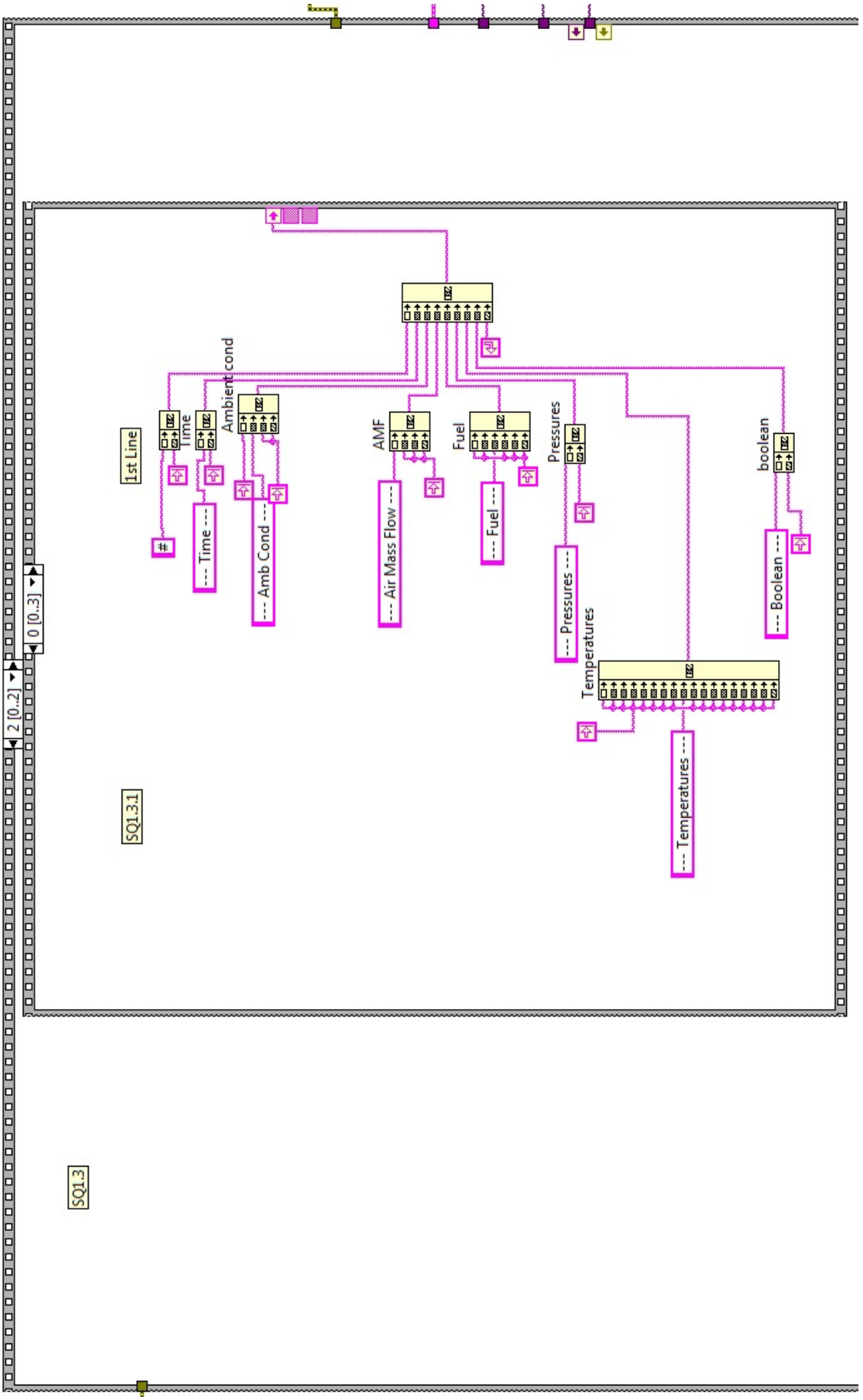

FIGURE A.4: PDE VI: File Header top line text input, groups.

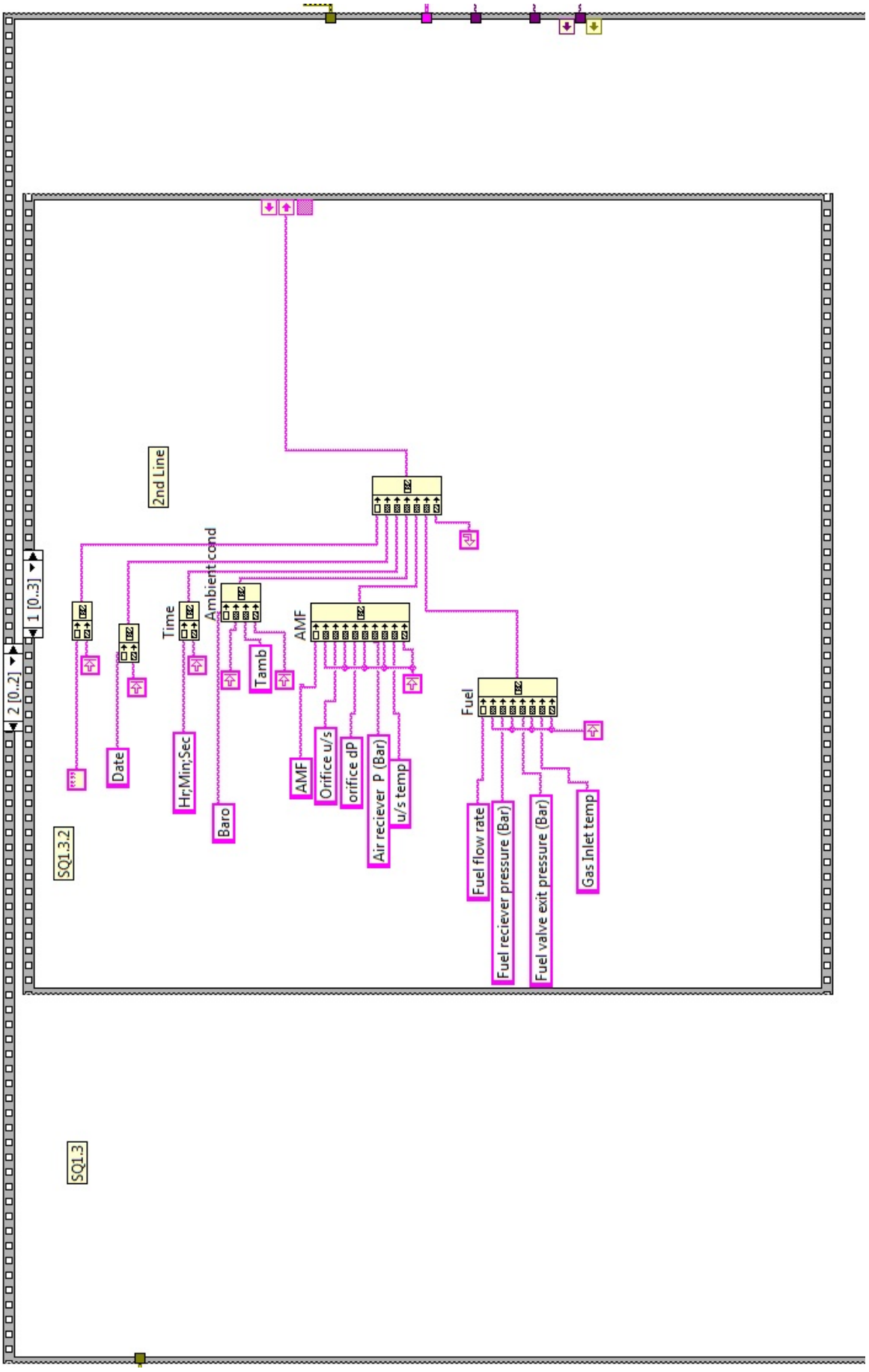

FIGURE A.5: PDE VI: File header middle line text input, measured values.

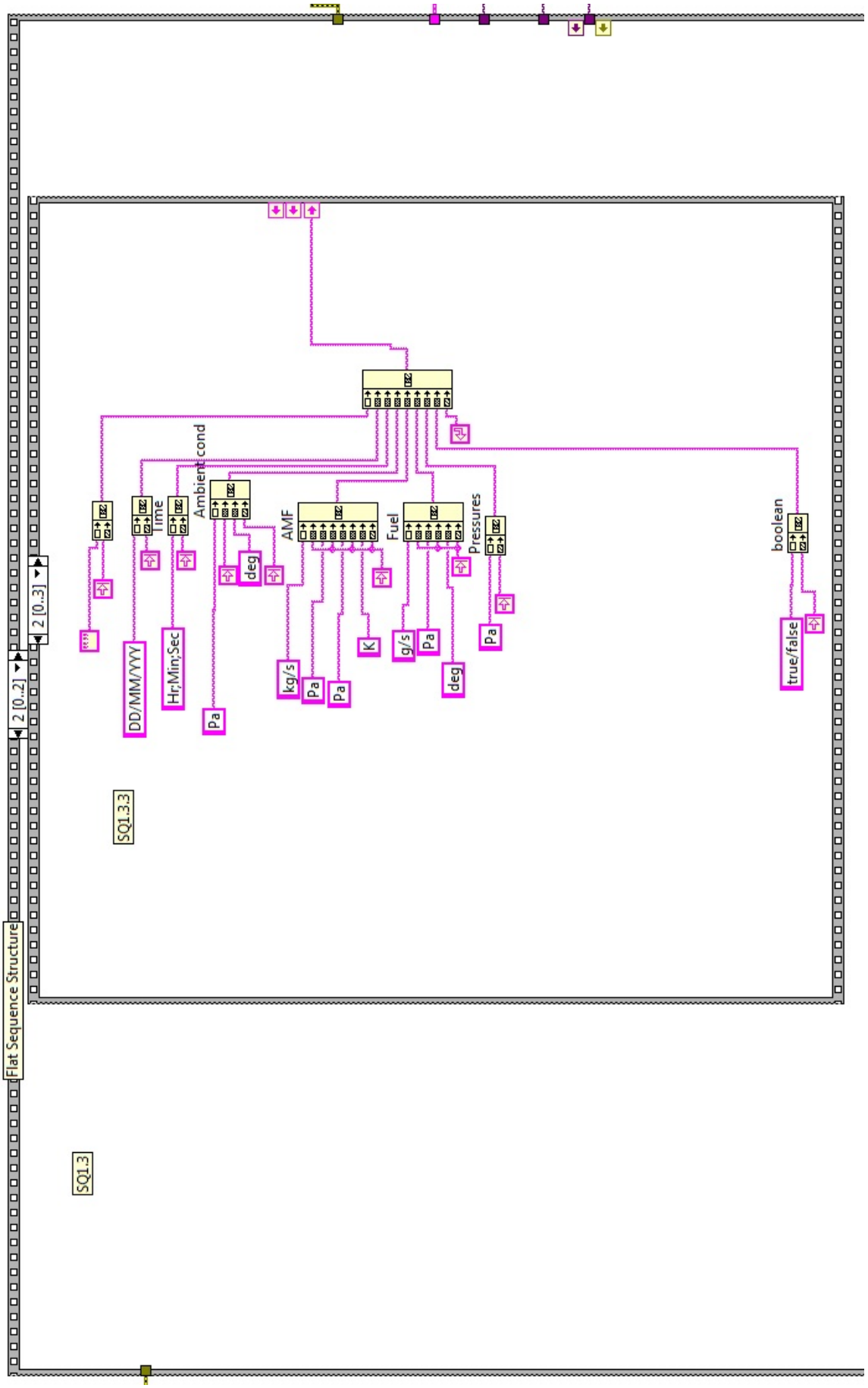

FIGURE A.6: PDE VI: File header bottom line text, measured value units.

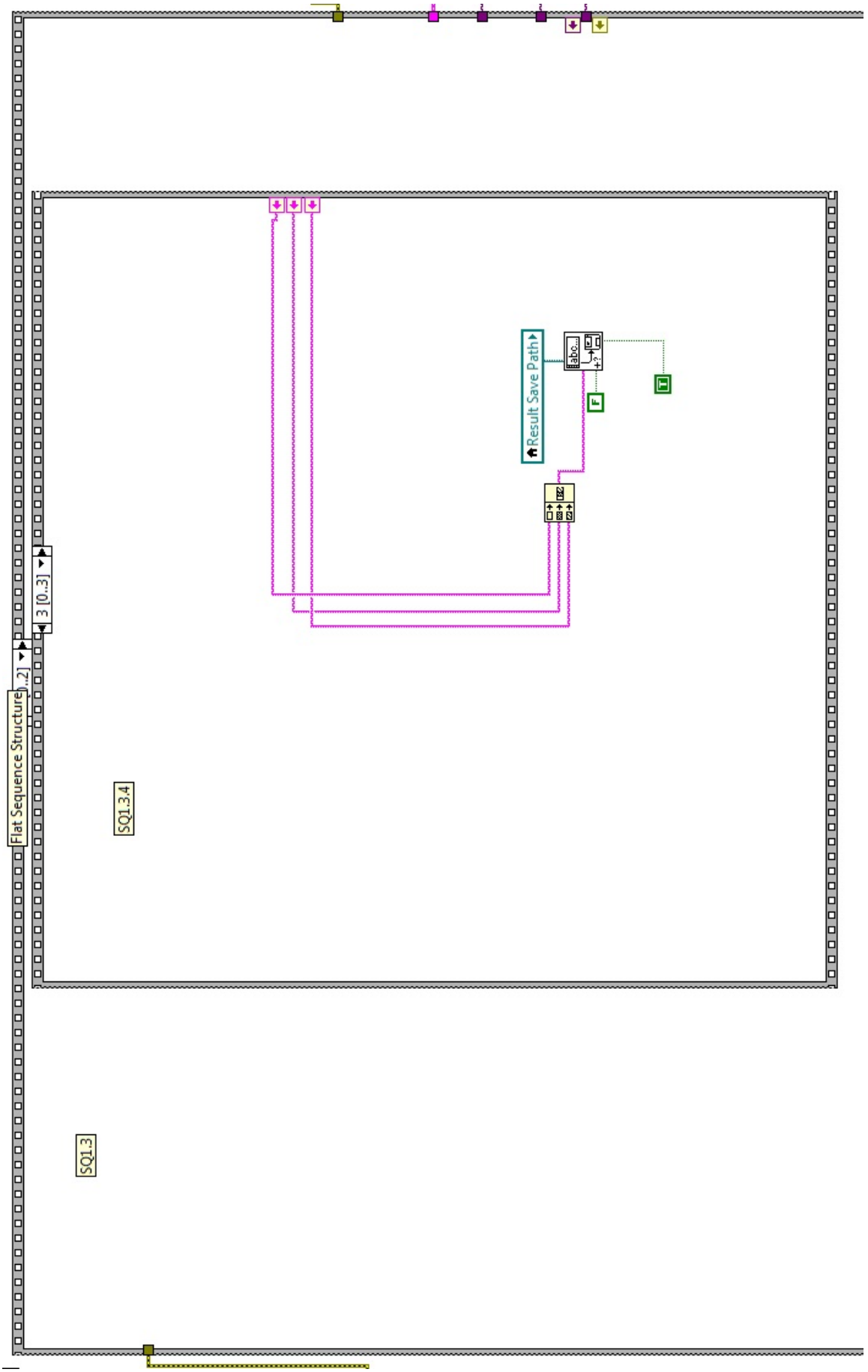

FIGURE A.7: PDE VI: Concatenate strings and save header to results save path file path.

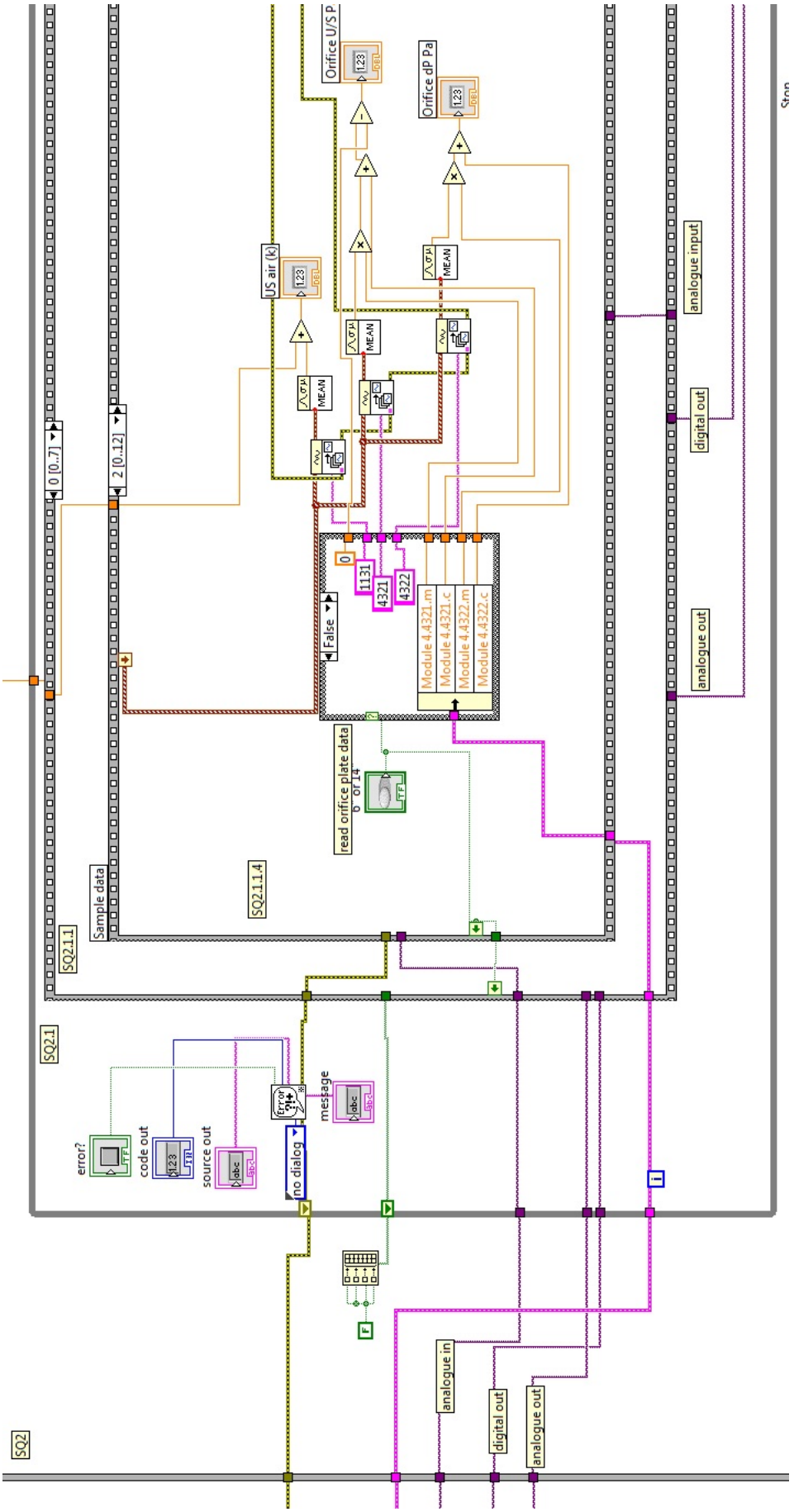

FIGURE A.8: PDE VI: Initialise boolean values to false, read all anologue values from anologue input task in sequence and output to variables and front pannel display

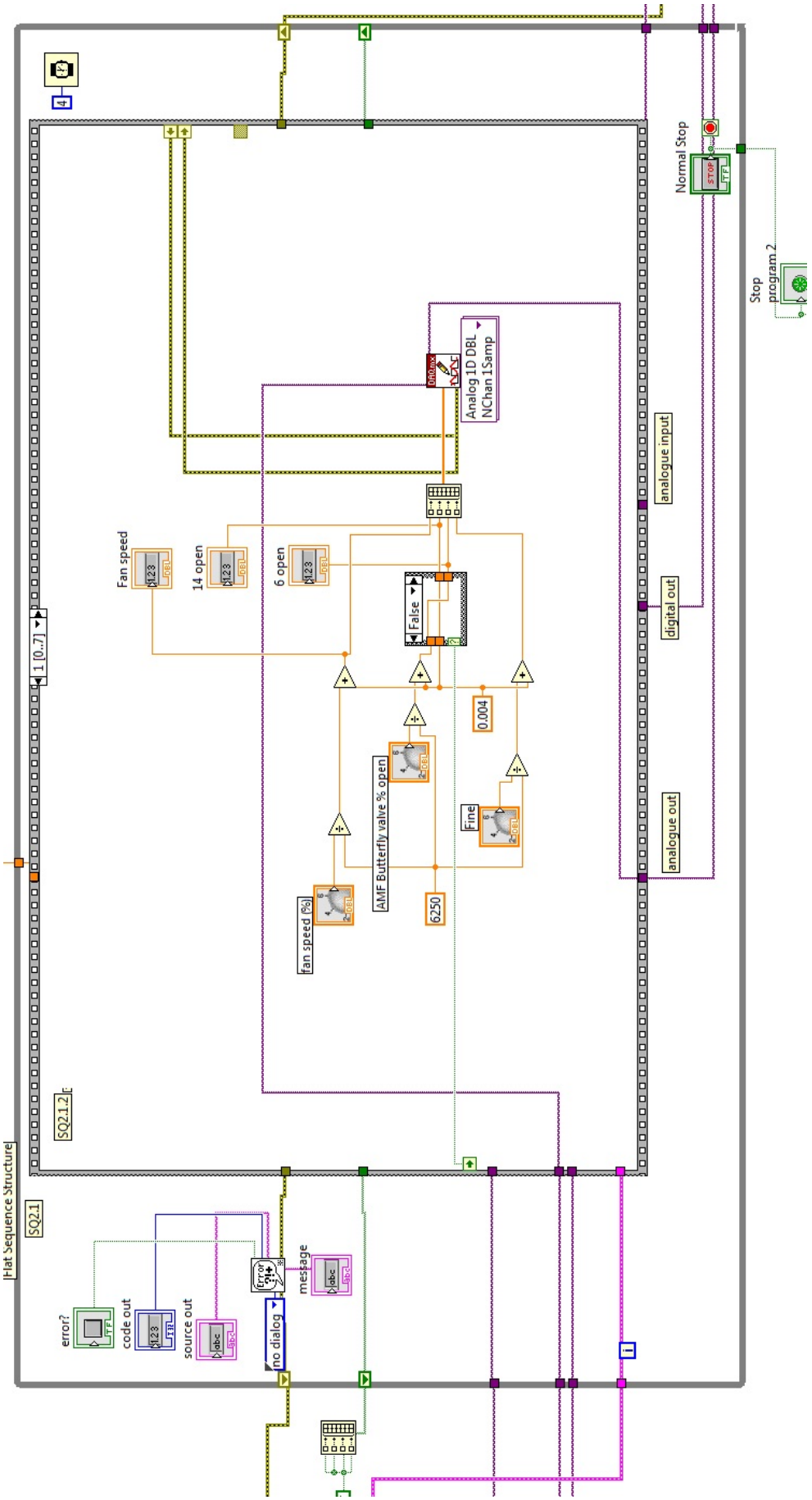

FIGURE A.9: PDE VI: Read anologue channel outputs and set according to desired values then display the current value on the front pannel

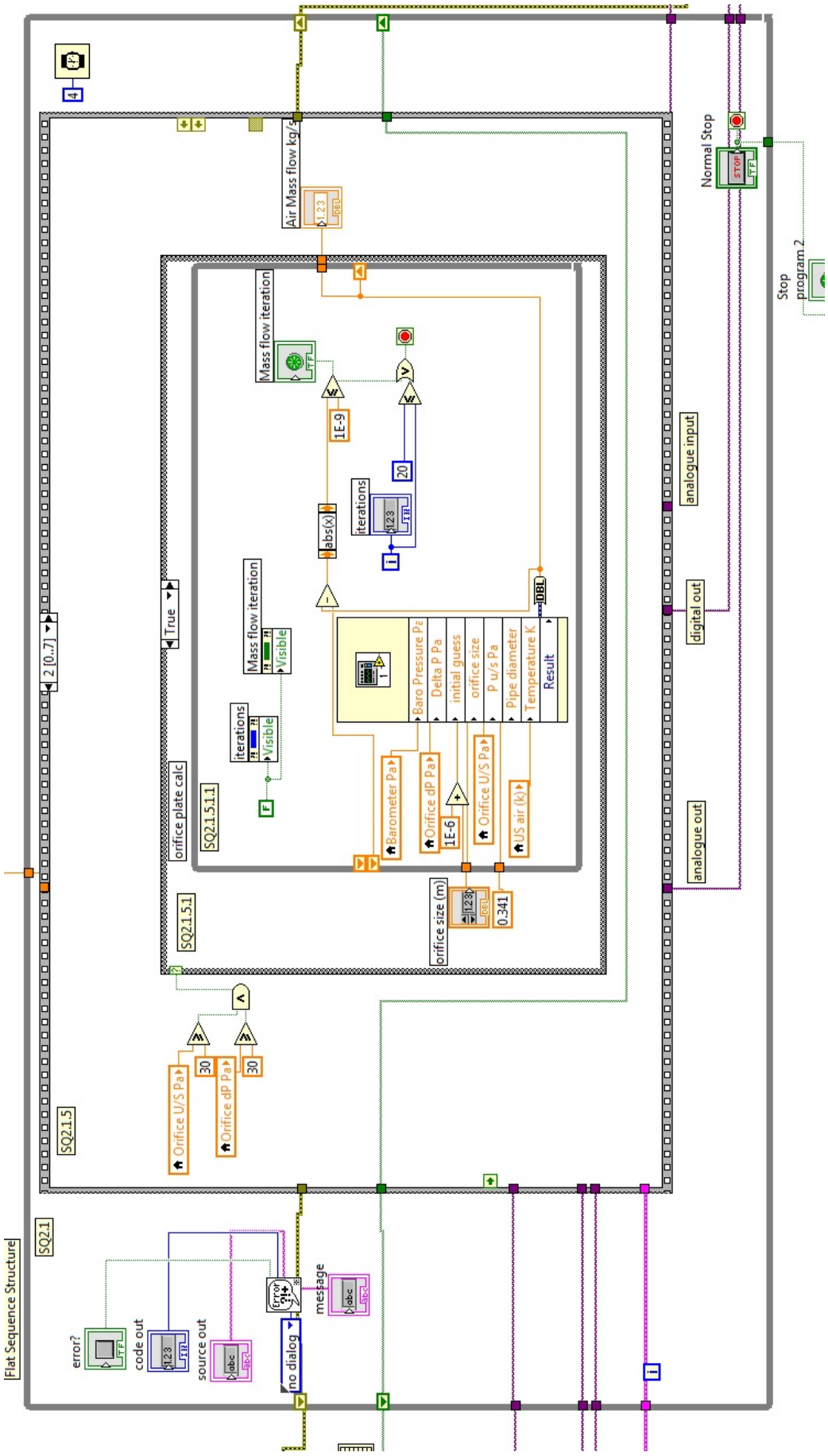

FIGURE A.10: PDE VI: Read all orifice plate variables into orifice calculation, run iterative calculation untill the absolute residual is less than 10^{-9} then output the mass flow to the Air mass flow(kg/s) variable

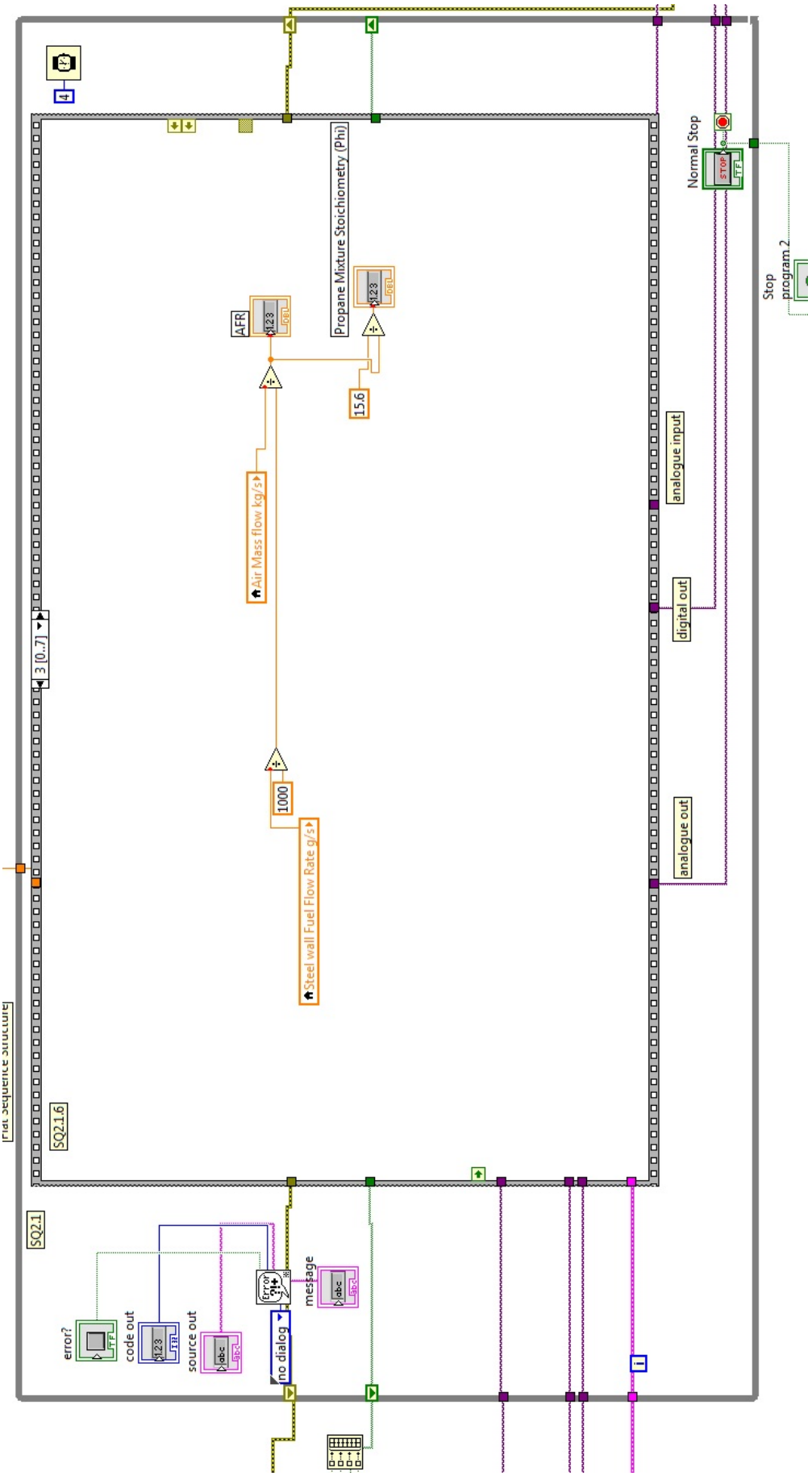

FIGURE A.11: PDE VI: run automatic calculations on variables as necessary, displaying the values to the front screen and passing them on to variables later on in the software to save

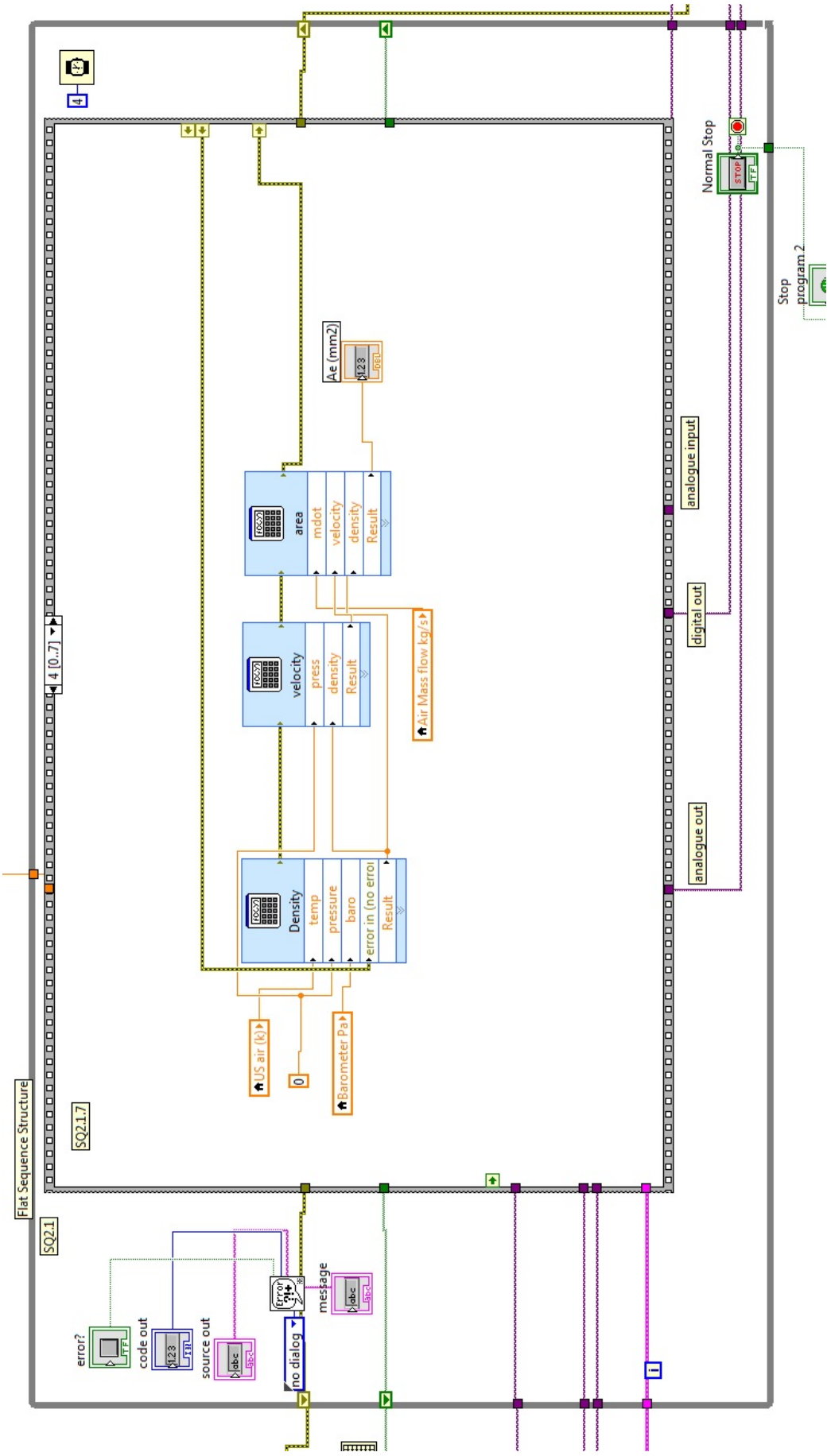

FIGURE A.12: PDE VI: Calculate the combustors effective area

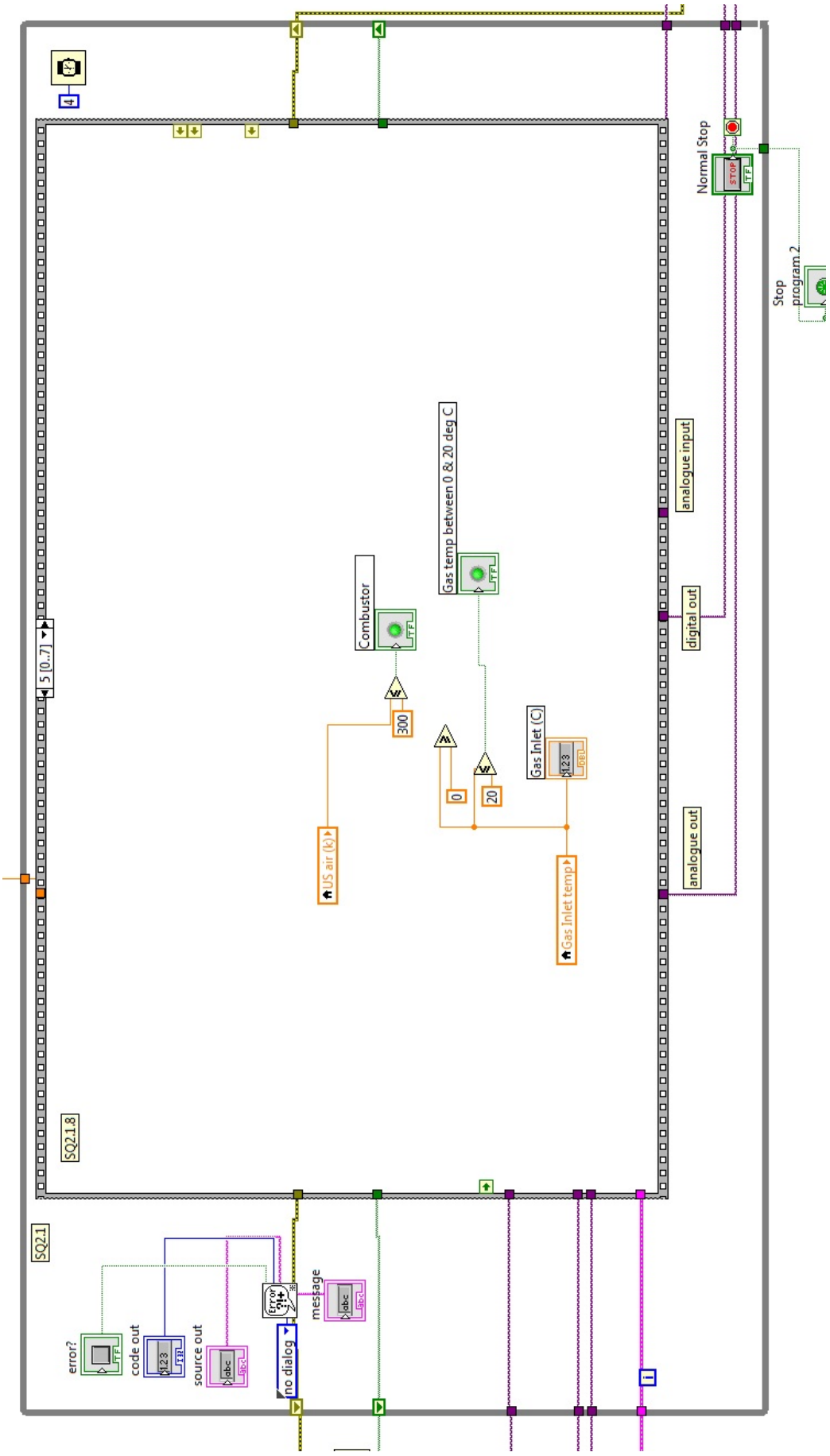

FIGURE A.13: PDE VI: Check that the upstream air is less than 300K and that the gas inlet temperature is below 20 degrees C

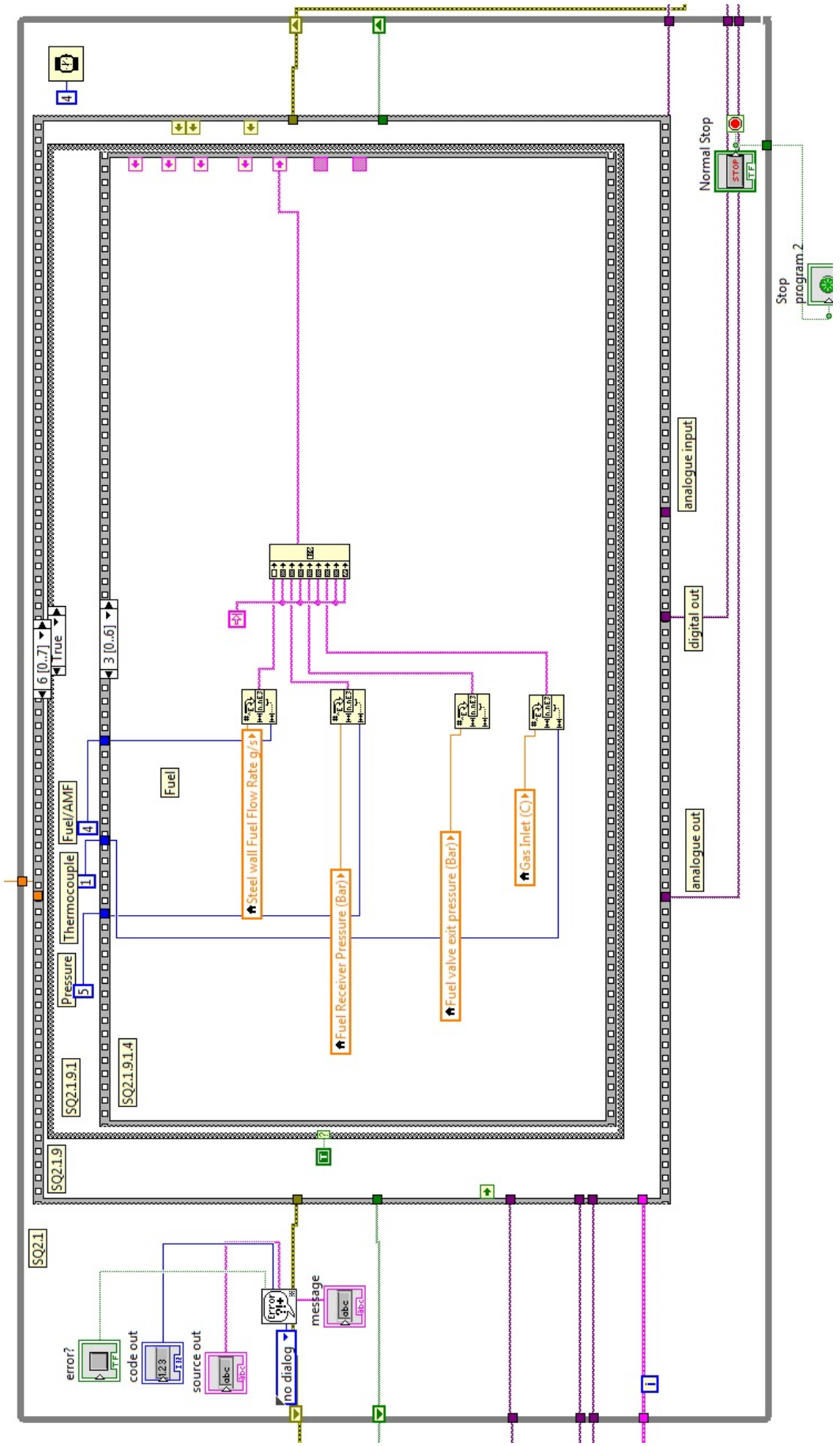

FIGURE A.14: PDE VI: Read test data, convert to string data type, concatenate into groups and save to the results save file

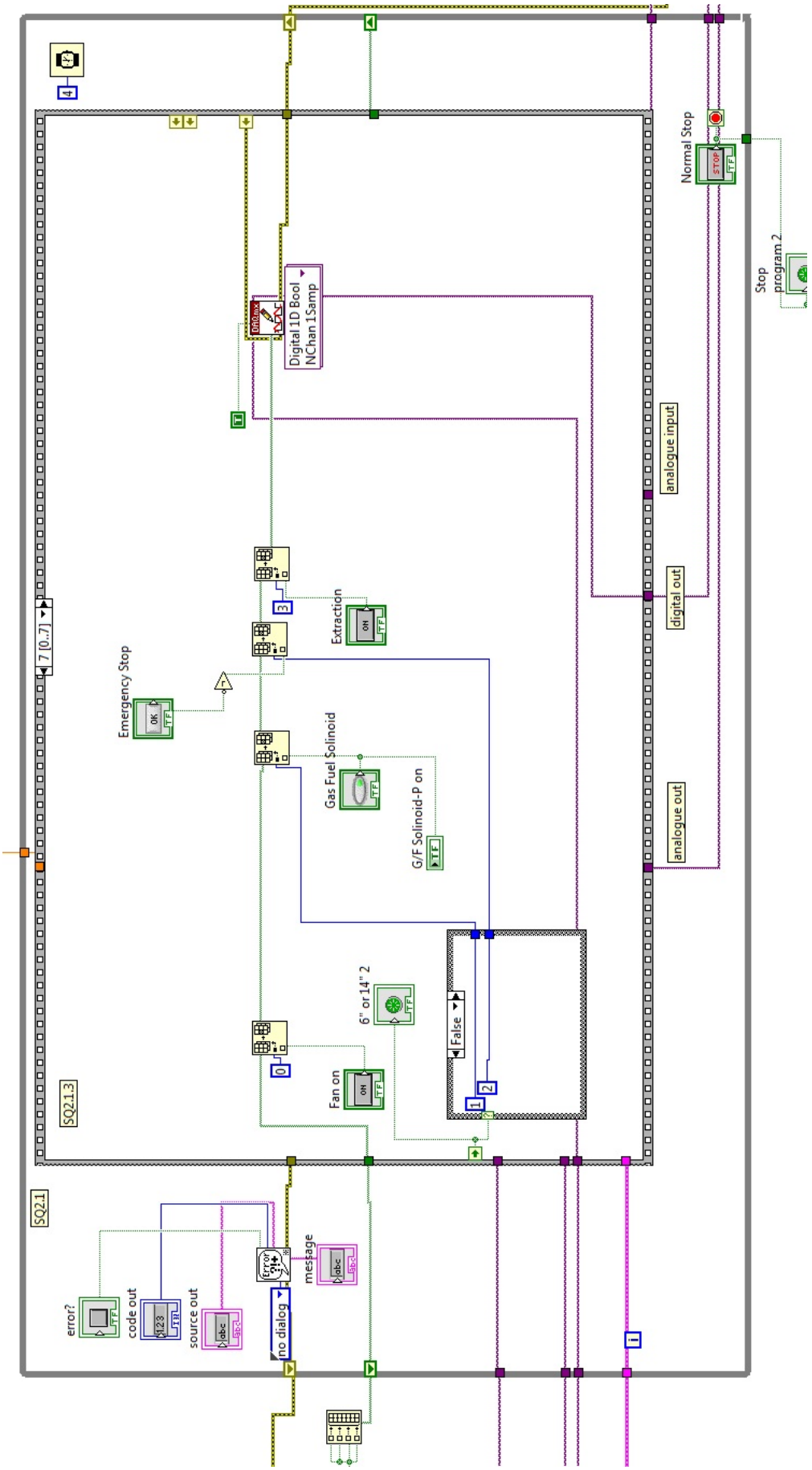

FIGURE A.15: PDE VI: boolean digital channel control

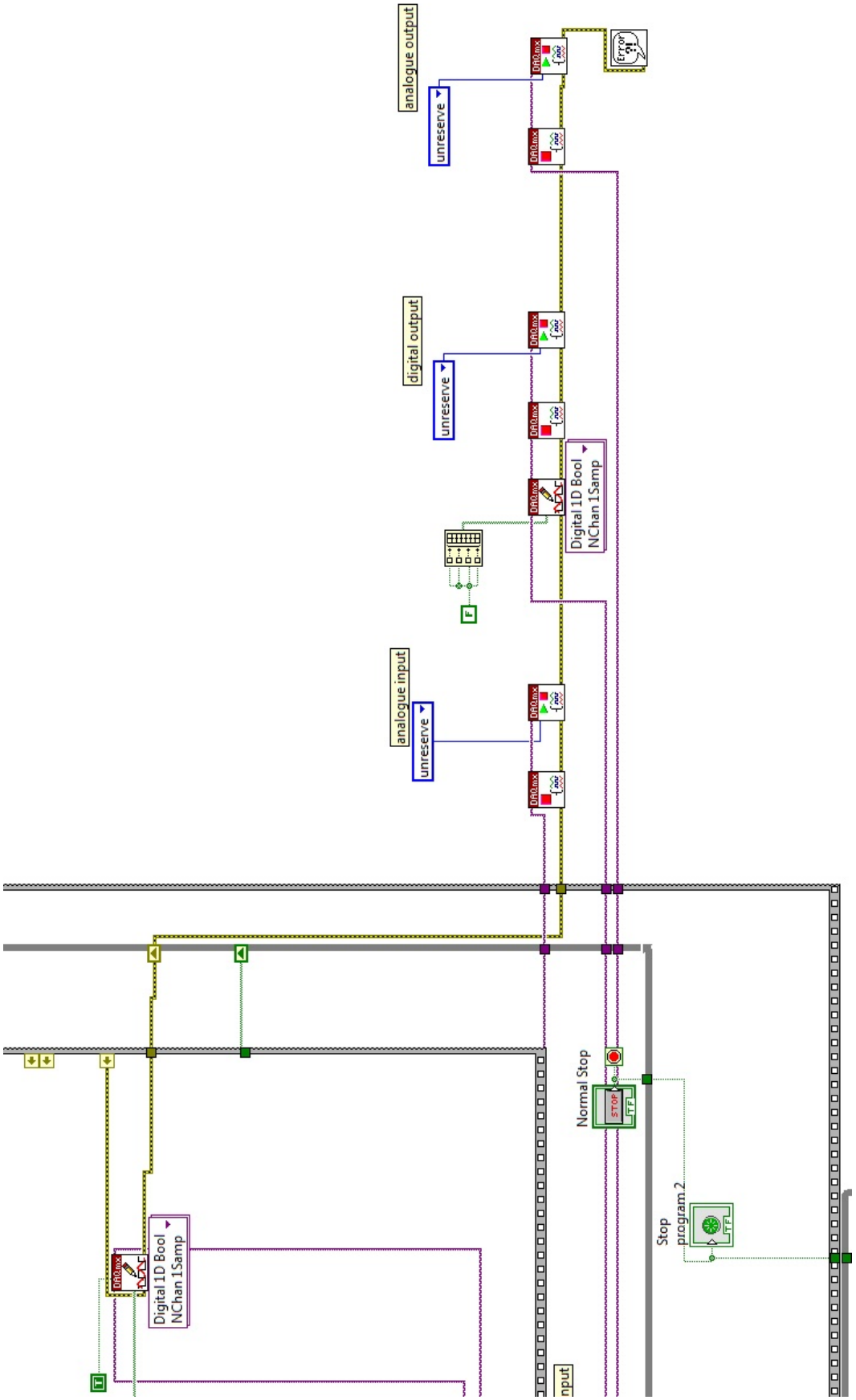

FIGURE A.16: PDE V:I closing tasks

A.2 LV HS DAQ code

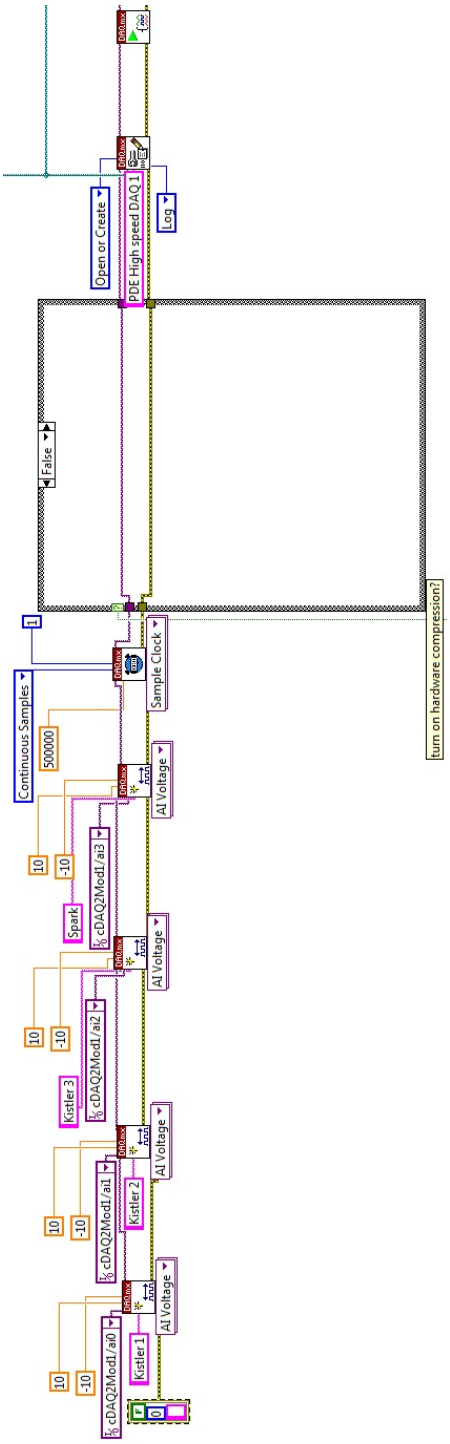

FIGURE A.17: LabView PDE High speed DAQ Data logging block diagram: starting tasks and channel allocation

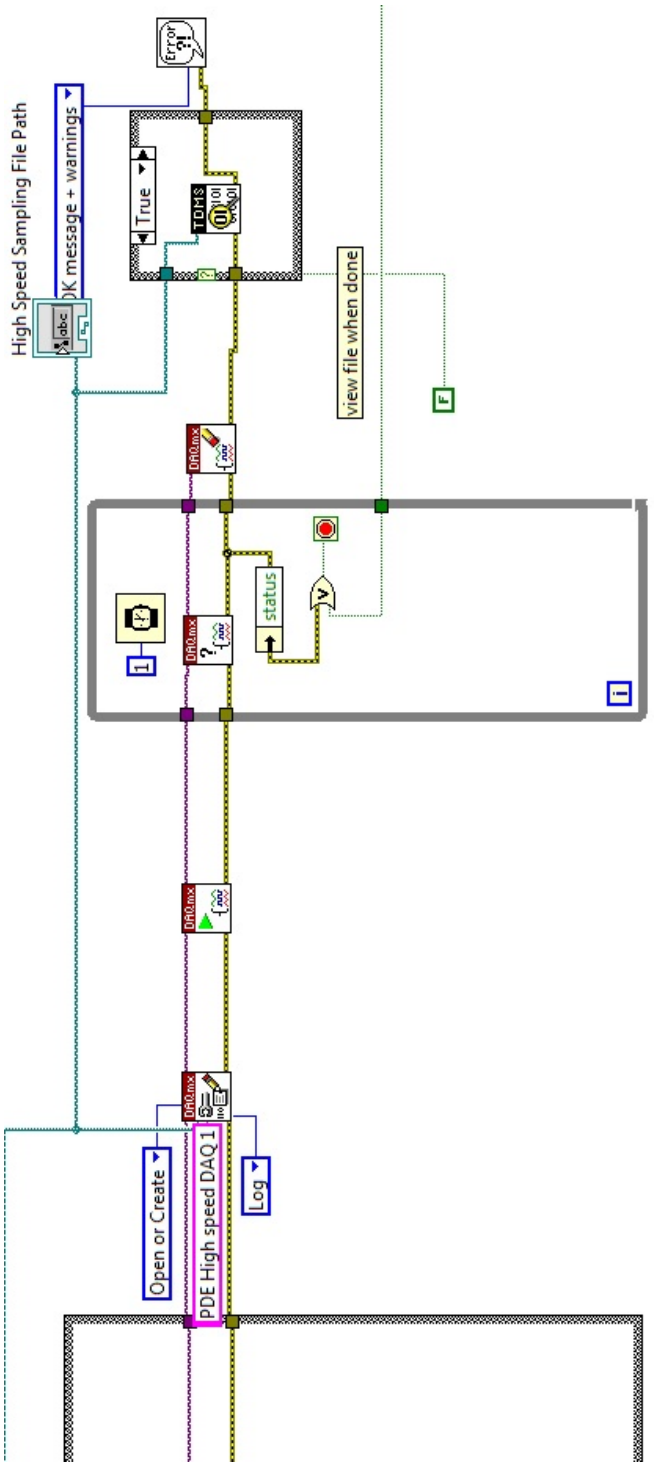

FIGURE A.18: LabView PDE High speed DAQ Data logging block diagram: run task, close when finished and open TDMS viewer

A.3 A selection of LV Post Processing Software

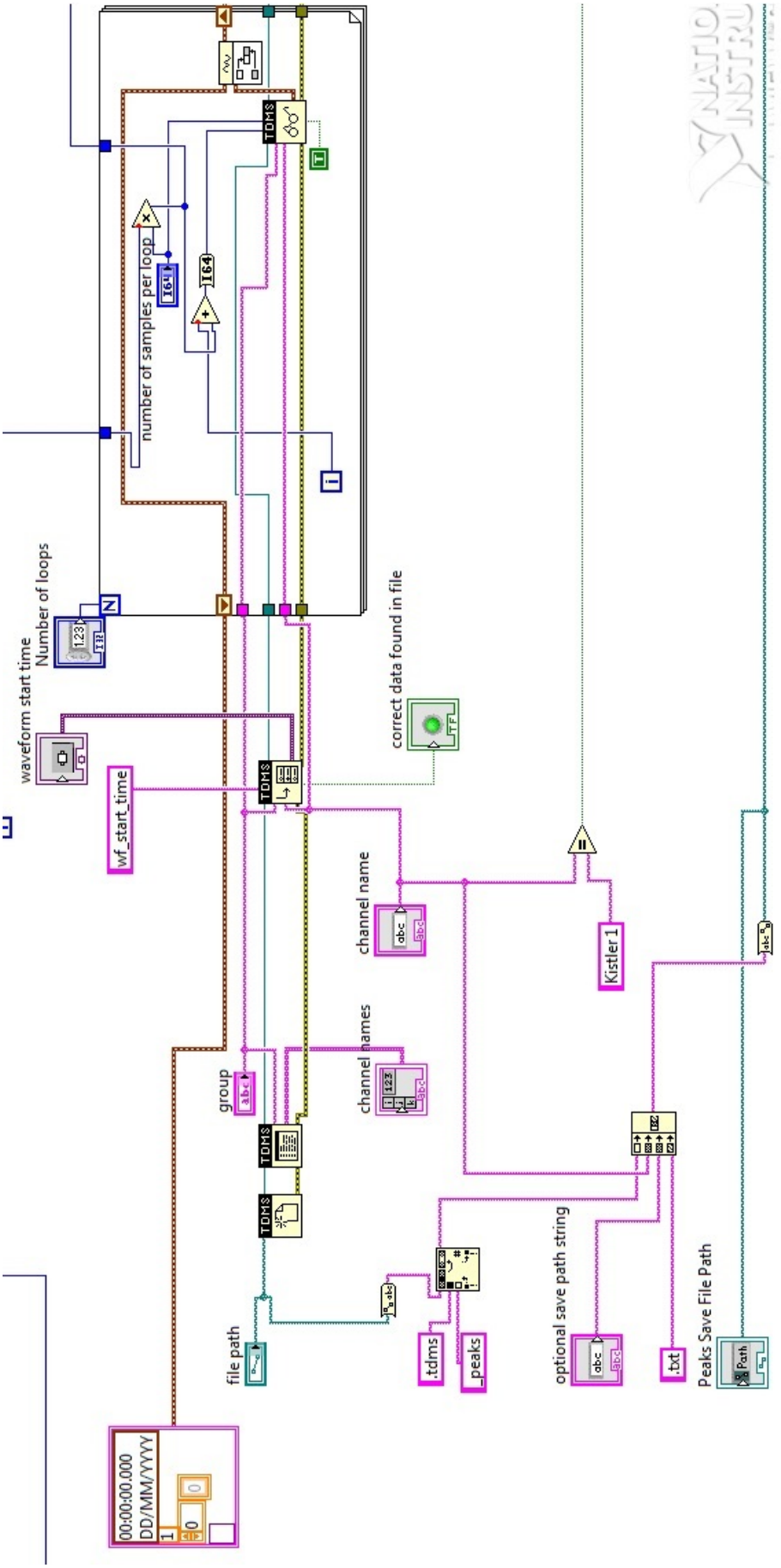

FIGURE A.19: Peak Finder Block Diagram *A*

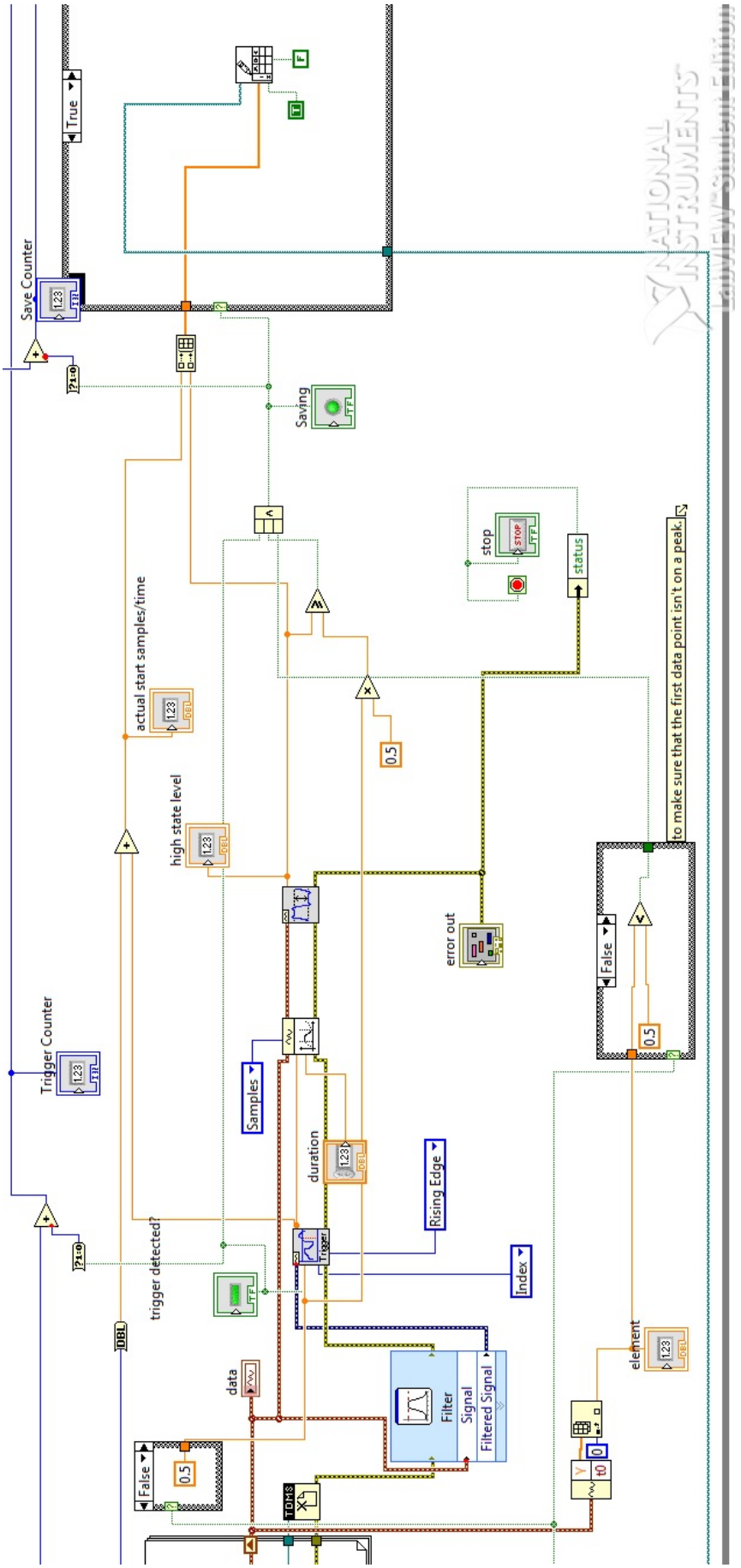

FIGURE A.20: Peak Finder Block Diagram *B*

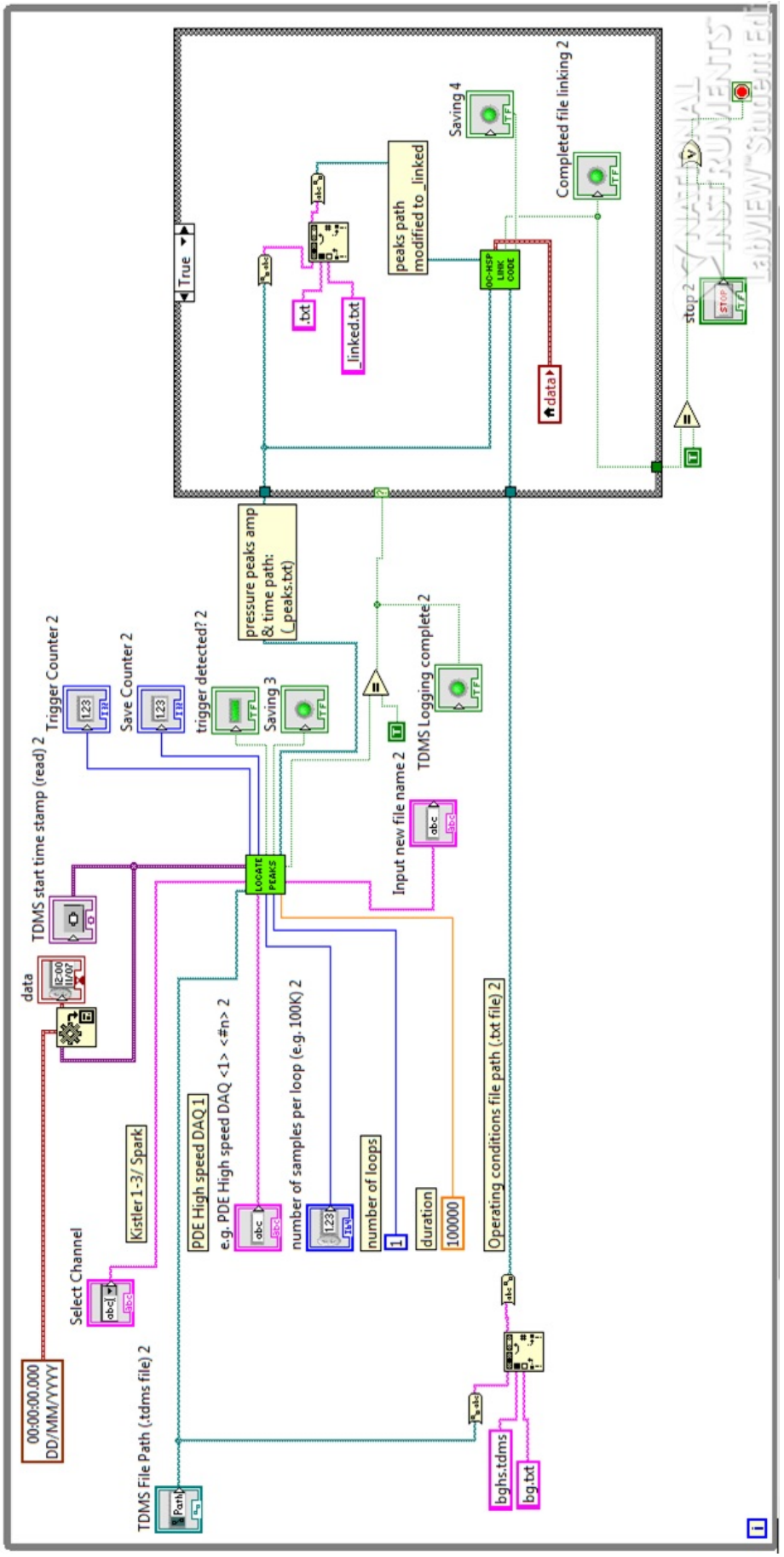

FIGURE A.21: High Speed Pressure - Operating Condition Linking Post Processing VI

Appendix B

Exhaust Flow Visualisation

B.1 Preliminary results- Fractal Experiments

All of the following tests were carried out using circular or fractal orifice plates as described in chapter 6, with 0.75 BR in each case.

headingCircular orifice

Fugure B.1 illustrates the flame venting from a bank of 29 *circ* orifice plates. The calculated flame speed between points 1 and 2 in this case was 280 m/s, given the flange thickness is 6.35mm and the frame rate is 3000fps. This is not necesarily the maximum speed of the flame within the tube as the flame speed is likely to decelerate considerably by this point, however this provides a good comparison of which orifice plates are more effective.

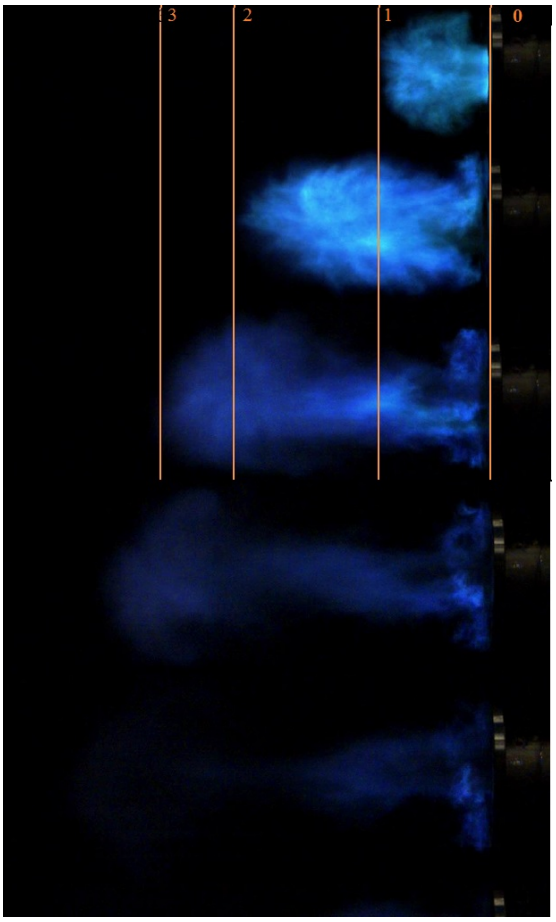

FIGURE B.1: High speed video stills of the flame venting from the PDE tube after fractal tests with circular ofirifice plates BR=0.75, frame rate = 3000fps shutter speed is 1/5000s, flange width 6.35mm

Appendix C

Thermal Imaging

C.1 Preliminary Testing

C.1.0.1 Experimental Design

In order to measure the temperature of the PDE tube wall using thermal camera data it was first necessary to create a painted surface on the tube wall using a high temperature matt black paint in order that the black body temperature of the tube wall could be determined. The effect of the matt black paint can be clearly compared with untreated steel tube in figure C.1. It is also clear from this image that the camera could not be mounted directly perpendicular to the PDE tube wall.It was still possible to take a reading from the camera and store all of the necessary data using in house programmed NI LabView software which was used to correct for this offset by taking measurements along the painted strip on the PDE wall, negating all other data from the image.

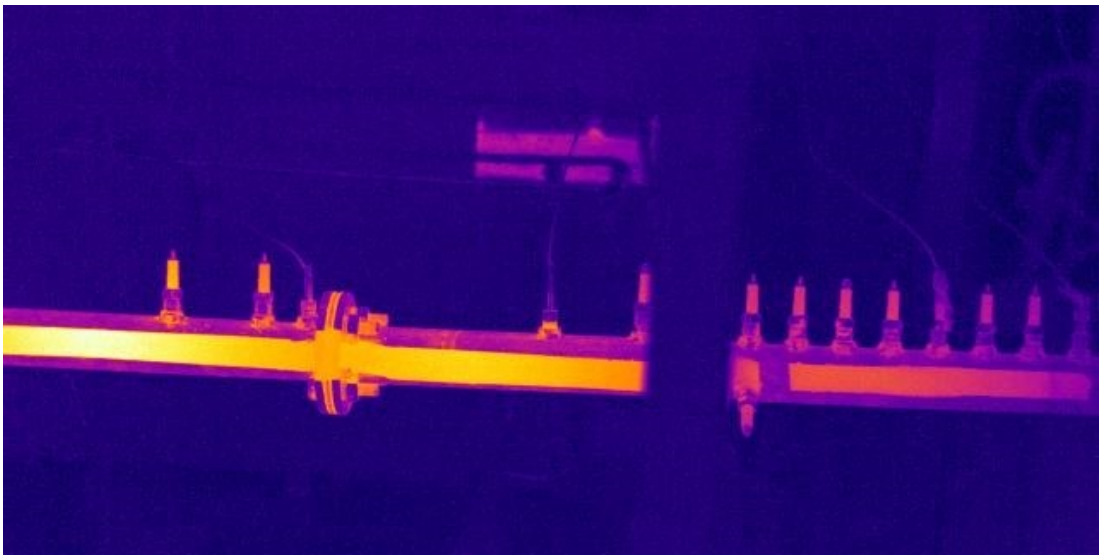

FIGURE C.1: Thermal imaging still image of the PDE tube wall for 25 fd2 fractal orifice plates from the current work, clearly showing the effect of the matt black paint on the thermal camera's effectiveness to record thermal data

C.1.0.2 Preliminary Data

Figures C.2 and C.2 both show the effect of very rapid heating cycles on the PDE tube wall, with a temperarue gain of approximatley 100 degrees in one minute within the 38mm internal diameter tube.....

It is also clearly possible to see the effect of each orifice within the tube causing a rippling effect on the thermal image data where orifice plates are pressent. This effect clearly shows that where orifice plates are present there is a much greater rate of heat transfer to the tube wall, infering that either the reaction is more energetic here or that more of the heat is being absorbed by the tube wall obstacles during the process of combustion in the PDE. Upon cooling it is evident that the tubes flanges, which can be clearly seen in fugures C.2 and C.2 are significantly enhancing the cooling effect in sections close to the flange, yeilding a non-uniform cooling profile. It can also be seen that the cooling profile after the orifice plate addition at the begining of figure C.2 falls off with an exponential reduction in temperature against distance.

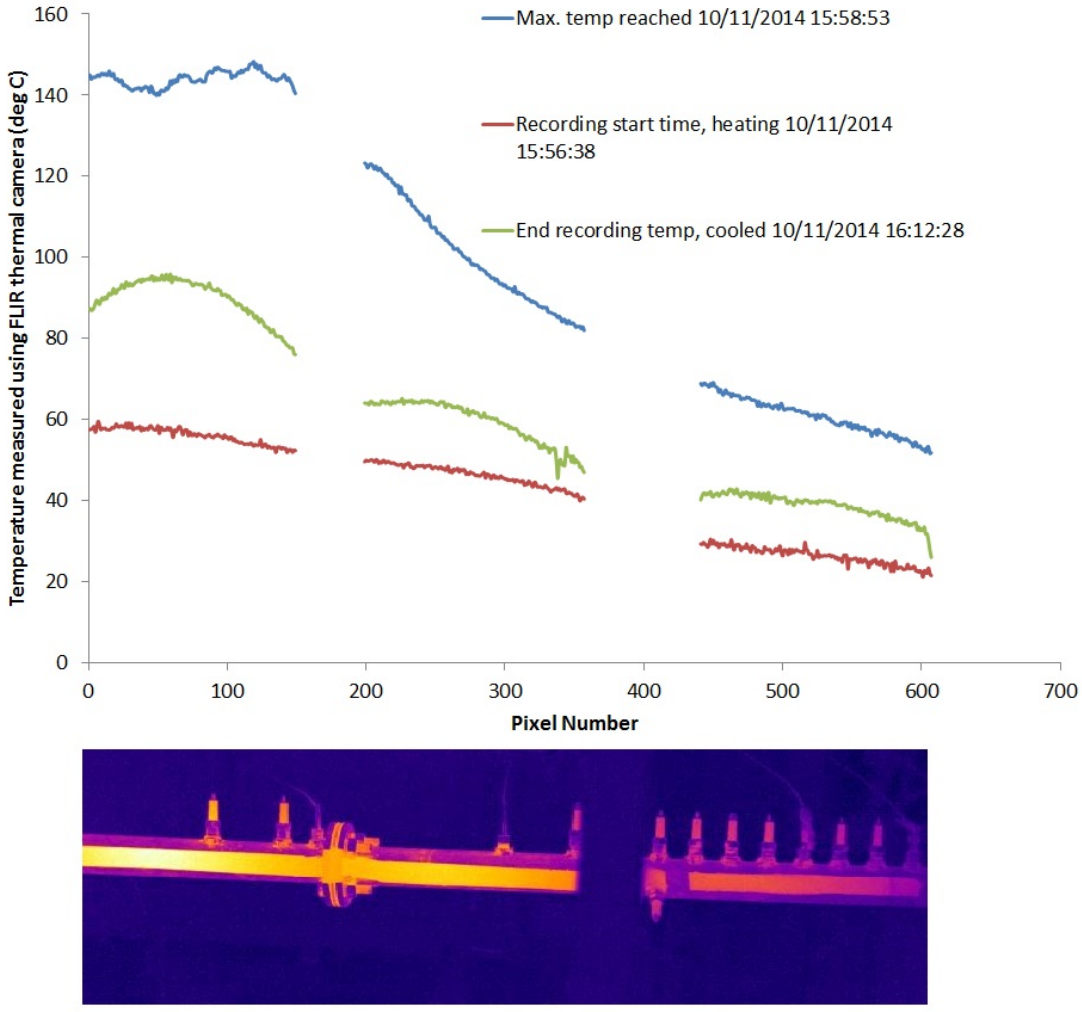

FIGURE C.2: Thermal imaging data of the PDE tube wall for 12 fd2 fractal orifice plates from the current work

It is also evident that there is a large dark bar in the center of the thermal immaging picture, this is a part of another structure in the LCCC which could not be moved, and there are no other easily accessable angles to take images of the tube from. The data from pixels surrouding this post and the flanges has been removed from figures C.3 and C.2 for the sake of clarity.

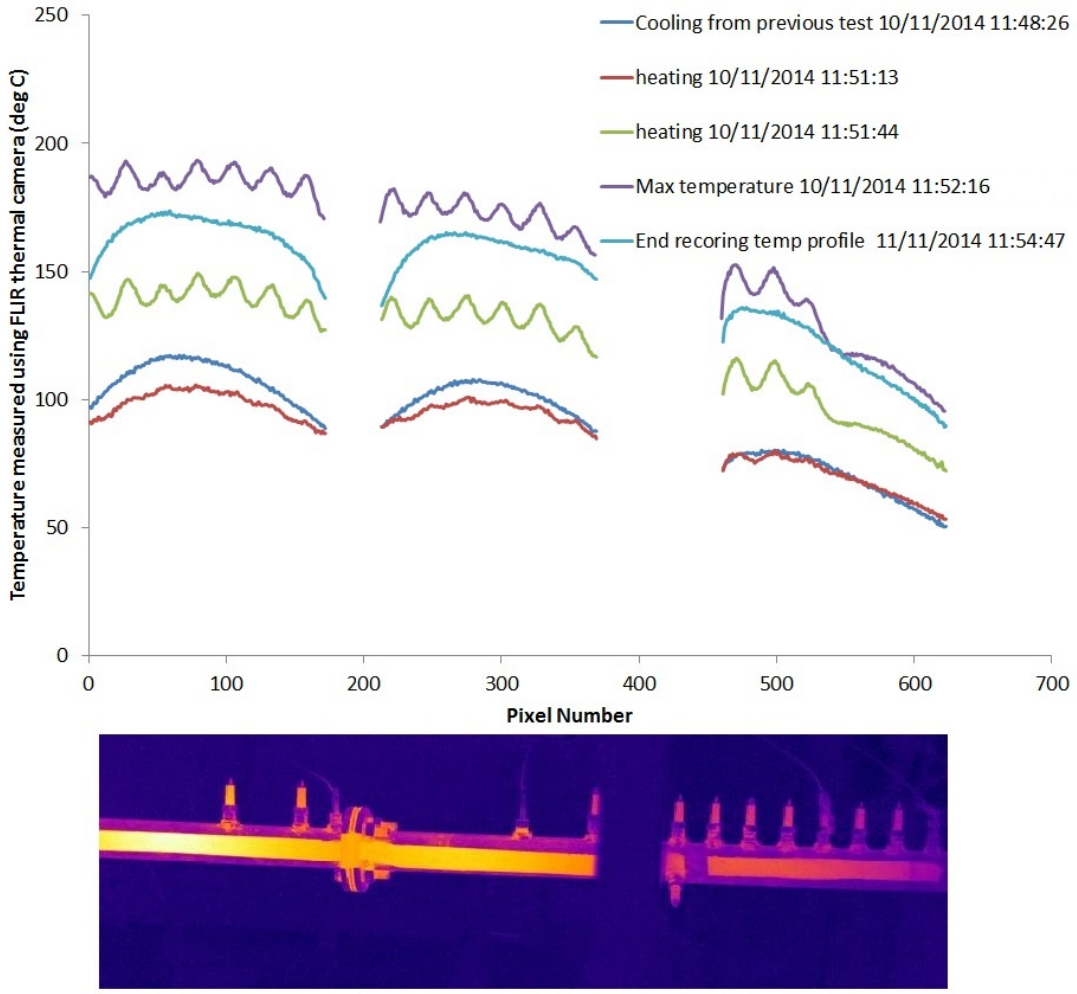

FIGURE C.3: Thermal imaging data of the PDE tube wall for 25 fd2 fractal orifice plates from the current work

References

[19] The Museum of Flight. THE FIESELER FI 103 (V1) GERMAN BUZZ BOMB. Website, unknown. Date Accessed [22/06/2015] http://www.museumofflight.org/exhibits/fieseler-fi-103-v1.aspx.

[22] Graham Warwick. US AFRL proves pulse-detonation engine can power aircraft, Fligth Global (2008). Website, 2008. Date Accessed [22/06/2015] http://www.flightglobal.com/news/articles/us-afrl-proves-pulse-detonation-engine-canpower-aircraft-222008/.

[28] University of Texas at Arlington Aerodynamics Research Center. Pulsed Detonation Engines, 2011. Date Accessed [27/04/2011] http://arc.uta.edu/research/pde.htm.

[31] E. Wintenberger and J.E. Shepherd. Thermodynamic cycle analysis for propagating detonations. Technical report, Pasadena, CA., 2005. Date Accessed [23/10/2015] http://www.galcit.caltech.edu/EDL/publications/reprints/FickettJacobsCycle.pdf.

[32] T W Chao, E Wintenberger, and J E Shepherd. On the Design of Pulse Detonation Engines, CALCIT Report FM 00-7. Technical report, California Institute of Technology, Pasadena, CA 91125, 2001.

[29] G Ciccarelli and S Dorofeev. Flame acceleration and transition to detonation in ducts. *Prog. Energy Combust. Sci.*, 34(4):499–550, 2008. URL http://www.sciencedirect.com/science/article/B6V3W-4RV7GPX-1/2/28c55003f5f24754c3b51453c40192f2.

[60] N. Peters. Four lectures on turbulent combustion. Website, 1997. Date Accessed [02/11/2015] http://decane.itv.rwth-aachen.de/fileadmin/LehreSeminar/Combustion/SummerSchool97_ueberarbeitet.pdf.

[64] C. Johansen and G. Ciccarelli. Modeling the initial flame acceleration in an obstructed channel using large eddy simulation. *J. Loss Prev. Process Ind.*, 26 (4):571–585, 2013. ISSN 09504230. doi: 10.1016/j.jlp.2012.12.005. URL http://dx.doi.org/10.1016/j.jlp.2012.12.005.

[66] A. Buschmann, F. Dinkelacker, T. Schäfer, M. Schäfer, and J. Wolfrum. Measurement of the instantaneous detailed flame structure in turbulent premixed combustion. *Symp. Combust.*, 26(1):437–445, jan 1996. ISSN 00820784. doi: 10.1016/S0082-0784(96)80246-3. URL http://www.sciencedirect.com/science/article/pii/S0082078496802463.

[67] M. Kuznetsov, V. Alekseev, A. Bezmelnitsyn, W. Breitung, S. Dorofeev, I Matsukov, A. Vaser, and Yu Yankin. Effect of obstacle geometry on behavoiur of turbulent flames. *IAE-6137/3*, FZKA-6328:49, 1999.

[69] Swetaprovo Chaudhuri, V'Yacheslav Akkerman, and Chung K. Law. Spectral formulation of turbulent flame speed with consideration of hydrodynamic instability. *Phys. Rev. E - Stat. Nonlinear, Soft Matter Phys.*, 84(2), 2011. ISSN 15393755. doi: 10.1103/PhysRevE.84.026322.

[71] G Ciccarelli, C Johansen, and M C Hickey. Flame acceleration enhancement by distributed ignition points. *J. Propuls. Power*, 21(6):1029–1034, 2005. URL http://www.scopus.com/inward/record.url?eid=2-s2.0-29144445860{&}partnerID=40{&}md5=ac3fc2861ae4e693ee1eecaf65e3343f.

[83] Gaby Ciccarelli, Craig T Johansen, and Michael Parravani. The role of shock-flame interactions on flame acceleration in an obstacle laden channel. *Combust. Flame*, 157(11):2125–2136, 2010. URL http://www.sciencedirect.com/science/article/B6V2B-507CGFT-1/2/d5c2354bf83a58ee04f36cf6b763b9eb.

[85] A. Eder and N. Brehm. Analytical and experimental insights into fast deflagrations, detonations, and the deflagration-to-detonation transition process. *Heat Mass Transf.*, 37:543–548, 2001. ISSN 09477411. doi: 10.1007/s002310100238.

[86] J.H.S Lee. *The Detonation Phenomenon*. Cambridge University Press, 2008. ISBN 978-107-43073-0.

[92] Wesley R Knick. *CHARACTERIZATION OF PULSE DETONATION*. PhD thesis, Air University, AIR FORCE INSTITUTE OF TECHNOLOGY, Writght-Patterson Air Force Base, Ohio, 2006.

[93] Yuta Sugiyama and Akiko Matsuo. On the characteristics of two-dimensional double cellular detonations with two successive reactions model. *Proc. Combust. Inst.*, 33(2):2227–2233, 2011. ISSN 15407489. doi: 10.1016/j.proci.2010.06.137. URL `http://dx.doi.org/10.1016/j.proci.2010.06.137`.

[94] R. A. Strehlow. Gas phase detonations: recent developments*. *Combust. Flame*, 12:88–101, 1962.

[95] K. Ishii, K. Morita, Y. Okitsu, S. Sayama, and H. Kataoka. Cellular pattern formation in detonation propagation. *Proc. Combust. Inst.*, 34(2):1903–1911, 2013. ISSN 15407489. doi: 10.1016/j.proci.2012.07.004. URL `http://dx.doi.org/10.1016/j.proci.2012.07.004`.

[98] S. M. Frolov, V. S. Aksenov, V. S. Ivanov, S. N. Medvedev, V. a. Smetanyuk, K. a. Avdeev, and F. S. Frolov. Pulse-detonation burner unit operating on natural gas. *Russ. J. Phys. Chem. B*, 5(4):625–627, 2011. ISSN 1990-7931. doi: 10.1134/S1990793111040063.

[99] Schauer, F.R. *Pulse Detonation Physiochemical and Exhaust Relaxation Processes*. PhD thesis, 2006.

[101] John H.S. Lee, R. Knystautas, and A. Freiman. High speed turbulent deflagrations and transition to detonation in H2-air mixtures. *Combust. Flame*, 56(2): 227–239, may 1984. ISSN 00102180. doi: 10.1016/0010-2180(84)90039-7. URL `http://www.sciencedirect.com/science/article/pii/0010218084900397`.

[116] A. Abou El-Azm Aly, A. Chong, F. Nicolleau, and S. Beck. Experimental study of the pressure drop after fractal-shaped orifices in turbulent pipe flows. *Exp. Therm. Fluid Sci.*, 34(1):104–111, jan 2010. ISSN 08941777. doi: 10.1016/j.expthermflusci.2009.09.008. URL `http://www.sciencedirect.com/science/article/pii/S0894177709001459`.

[117] D. Hurst and J. C. Vassilicos. Scalings and decay of fractal-generated turbulence. *Phys. Fluids*, 19(3):035103, 2007. ISSN 10706631. doi: 10.1063/1.2676448. URL http://scitation.aip.org/content/aip/journal/pof2/19/3/10.1063/1.2676448.

[122] Y. Huang, H. Tang, J. Li, and C. Zhang. Studies of DDT enhancement approaches for kerosene-fueled small-scale pulse detonation engines applications. *Shock Waves*, 22(6):615–625, 2012. ISSN 09381287. doi: 10.1007/s00193-012-0396-5.

[124] S M Frolov. Initiation of strong reactive shocks and detonation by traveling ignition pulses. *J. Loss Prev. Process Ind.*, 19(2-3):238–244, 2005. URL http://www.sciencedirect.com/science/article/B6TGH-4GGWGB1-2/2/dc07711d8e27f1b7b0c11c564320efef.

[126] B. De Witt, G. Ciccarelli, F. Zhang, and S. Murray. Shock Reflection Detonation Initiation Studies for Pulse Detonation Engines. *J. Propuls. Power*, 21(6):1117–1125, 2005. ISSN 0748-4658. doi: 10.2514/1.14398.

[128] S Frolov and V Aksenov. Initiation of gas detonation in a tube with a shaped obstacle. *Dokl. Phys. Chem.*, 427(1):129–132, 2009. doi: 10.1134/s0012501609070045. URL http://dx.doi.org/10.1134/S0012501609070045.

[129] S. (RU) Frolov, V. S. (RU) Aksenov, and A.(RU) Berlin. A method for initiating detonation in tubes incendiary AND DEVICE FOR IMPLEMENTATION: F23C15/00, 2427756. Patent, 2011. Date Accessed [19/05/2015] http://www.freepatent.ru/patents/2427756.

[130] Sergey Frolov, Viktor Serafimovich Aksenov, and Alexander Berlin. The method of initiating detonation in a tube with a gas mixture and a device for its implementation: F23C15/00, 2429409, 2011. Date Accessed[19/05/2015] http://www.freepatent.ru/patents/2429409.

[131] Sergey (RU) Frolov, Viktor Serafimovich (RU) Aksenov, and Alexander (RU) Berlin. The method of initiating detonation in a tube with a gas mixture and a device for its implementation:F23C15/00, 2430303. Patent, 2011. Date Accessed [20/10/2015] http://www.freepatent.ru/patents/2430303.

[127] S. M. Frolov. Detonation Initiation and DDT: Experiments and Numerical Simulations. *5th Int. Semin. Fire Explos. Hazards*, (April):7–15, 2007. URL www.see.ed.ac.uk/feh5.

[134] J Chao, T Otsuka, and J H S Lee. An experimental investigation of the onset of detonation. *Proc. Combust. Inst.*, 30(2):1889–1897, 2005. URL http://www.sciencedirect.com/science/article/B7GWS-4DD8H18-10/2/00effc642e04c8ee9d47b0d318ac5e75.

[156] V N Gamezo, T Ogawa, and E S Oran. Flame acceleration and DDT in channels with obstacles: Effect of obstacle spacing. *Combust. Flame*, 155(1-2):302–315, 2008. doi: 10.1016/j.combustflame.2008.06.004. URL <GotoISI>://WOS:000260362400021.

[168] Vitaly Bychkov, V'yacheslav Akkerman, Damir Valiev, and Chung K. Law. Influence of gas compression on flame acceleration in channels with obstacles. *Combust. Flame*, 157(10):2008–2011, 2010. ISSN 00102180. doi: 10.1016/j.combustflame.2010.06.006. URL http://dx.doi.org/10.1016/j.combustflame.2010.06.006.

[172] J. Li, W. H. Lai, and K. Chung. Tube diameter effect on deflagration-to-detonation transition of propane-oxygen mixtures. *Shock Waves*, 16(2):109–117, nov 2006. ISSN 0938-1287. doi: 10.1007/s00193-006-0056-8. URL http://link.springer.com/10.1007/s00193-006-0056-8.

[174] T R Meyer, J L Hoke, M S Brown, James R Gord, and F.R. Schauer. Experimental Study of Deflagration-To-Detonation Enhancement Techniques in a H2/Air Pulsed-Detonation Engine. In *38th AIAA/ASME/SAE/ASEE Jt. Propuls. Conf. Exhib.*, volume AIAA 2002-3720, pages 1–11, 2002. ISBN 978-1-62410-115-1. doi: 10.2514/6.2002-3720.

[177] J. Li, C.J. Teo, K.S. Lim, C. Wen, and B.C. Khoo. Deflagration to Detonation Transition by Hybrid Obstacles in Pulse Detonation Engines. In *Jt. Propuls. Conf. Exhib.*, pages 1–12, San Jose, 2013. 49th AIAA/ASME/SAE/ASEE Joint Propulsion Conference.

[165] R. Sorin, R. Zitoun, and D. Desbordes. Optimization of the deflagration to detonation transition: reduction of length and time of transition. *Shock Waves*,

15(2):137–145, mar 2006. ISSN 09381287. doi: 10.1007/s00193-006-0007-4. URL http://www.springerlink.com/index/10.1007/s00193-006-0007-4.

[178] O Peraldi, R Knystautas, and J H Lee. Criteria for transition to detonation in tubes. *Symp. Combust.*, 21(1):1629–1637, 1988. ISSN 00820784. doi: 10.1016/S0082-0784(88)80396-5.

[179] Seong-Young Lee, Jonathan Watts, Silvano Saretto, Sibtosh Pal, Chris Conrad, Roger Woodward, and Rovert Santoro. Deflagration to Detonation Transition Processes by Turbulence-Generating Obstacles in Pulse Detonation Engines. *J. Propuls. Power*, 20(6):1026–1036, 2004. ISSN 0748-4658. doi: 10.2514/1.11042.

[182] S.B. Dorofeev. Hydrogen flames in tubes: Critical run-up distances. *Int. J. Hydrogen Energy*, 34(14):5832–5837, jul 2009. ISSN 03603199. doi: 10.1016/j.ijhydene.2009.01.008. URL http://www.sciencedirect.com/science/article/pii/S0360319909000421.

[103] S B Dorofeev, V P Sidorov, M S Kuznetsov, I D Matsukov, and V I Alekseev. Effect of scale on the onset of detonations. *Shock Waves*, 10:137–149, 2000.

[185] J Chao and J H S Lee. The propagation mechanism of high speed turbulent deflagrations. *Shock Waves*, (12):227–289, 2003.

[186] R; Knystautas, Guirao.C;, Lee J.H;, and Sulmistras A;. Measurement of cell size in hydrocarbon-air mixtures and predictions of critical tube diameter, critical initiation energy, and detonability limits. *Prog. Astronaut. Aeronaut.*, 94:23–37, 1984.

[133] S. M. Frolov. Detonation initiation techniques for pulse detonation propulsion. *Prog. Propuls. Phys.*, 1:321–340, 2009. doi: 10.1051/eucass/200901321. URL http://www.eucass-proceedings.eu/10.1051/eucass/200901321.

[209] C. S. Wen, K. M. Chung, F. K. Lu, and W. H. Lai. An experimental study on DDT distance of JP-8 mixtures. *Shock Waves*, 23(5):473–479, 2013. ISSN 0938-1287. doi: 10.1007/s00193-013-0455-6. URL http://link.springer.com/10.1007/s00193-013-0455-6.

[217] Philip K Panicker. *The Development and Testing of Pulsed Detonation Engine Ground Demonstors*. PhD thesis, The University of Texas at Arlington, 2008.

[218] F. Nicolleau and J. Mathieu. Eddy break-up model and fractal theory: comparisons with experiments. *Int. J. Heat Mass Transf.*, 37(18):2925–2933, 1994. ISSN 00179310. doi: 10.1016/0017-9310(94)90347-6.

[229] J. B. Heywood. *Internal Combustion Engine Fundamentals*. McGraw-Hill International Editions, 1988.

[237] Wassel. Wassel Electronic Ingition Unit Installation Guide: for twin and single cylinder models positive or negative ground. Website. Date Accessed 10/11/2015 `http://totalbikebits.com/wassell/orderpoint/prod_info/WW61495.pdf`.

[68] Chung K. Law. *Combustion Physics*. Cambridge University Press, Princeton University, 2006.

[152] F.R. Menter. Two-equation eddy-viscosity turbulence models for engineering applications. *AIAA Journal*, 32(8):1598–1605, 1994.

[154] O.L.Gulder. Correlations of laminar combustion data for alternative s.i. engine fuels. *SAE Technical Paper Series*, 1, 1984.

[52] D Bradley, M Lawes, and M S Mansour. Measurement of turbulent burning velocities in implosions at high pressures. In *Proc. Combust. Inst.*, volume 33, pages 1269–1275, 2011. URL `http://www.scopus.com/inward/record.url?eid=2-s2.0-78650914729{&}partnerID=40{&}md5=14abb826e94a547f2a1c19dc180683c6`.

[55] Toshiaki Kitagawa. Effects of Pressure on Burning Velocity and Instabilities of Propane-Air Premixed Flames. *JSME Int. J. Ser. B*, 48(1):2–8, 2005. ISSN 1340-8054. doi: 10.1299/jsmeb.48.2.

[137] Ganbing Yao, Bo Zhang, Guangli Xiu, Chunhua Bai, and Peipei Liu. The critical energy of direct initiation and detonation cell size in liquid hydrocarbon fuel/air mixtures. *Fuel*, 113:331–339, 2013. ISSN 00162361. doi: 10.1016/j.fuel.2013.05.081. URL `http://dx.doi.org/10.1016/j.fuel.2013.05.081`.

[208] J. M. Austin and J. E. Shepherd. Detonations in hydrocarbon fuel blends. *Combust. Flame*, 132(1-2):73–90, 2003. URL `http://www.sciencedirect.com/science/article/B6V2B-478HRF1-2/2/e7430c16750547d147c7e552629fa220`.

[227] R. Knystautas, J.H. Lee, and C.M. Guirao. The critical tube diameter for detonation failure in hydrocarbon-air mixtures. *Combust. Flame*, 48:63–83, 1982. ISSN 00102180. doi: 10.1016/0010-2180(82)90116-X.

[1] W Bollay and Curtis Wright Corp. Patent Number US2942412 A: Pulse Detonation Jet Propulsion. Website, 1960. Date Accessed [21/10/2015] `http://www.google.com/patents/US2942412`.

[2] Aslan. Lecturer Applied Math at MIT Kasimov. Detonation. Website, unknown. Date Accessed [01/09/2015] `http://math.mit.edu/~kasimov/detonation.html`.

[3] Zeldovich. Y. B. To the Question of Energy Use of Detonation Combustion. *J. Tech. Phys.*, 10(17):1453–1461, 1940.

[4] Yakov Borisovich Zeldovich, G.I. Barenblatt, and Yashiv Aleivich Sunyaev. *Selected Works of Yakov Borisovich Zeldovich, Volume 1: Chemical Physics and Hydrodynamics*. Princeton University Press, Priceton Legacy Library, Princeton, 1 edition, 1992.

[5] J. von Neumann. *Theory of Detonation Waves, (1942), in John von Neumann Collected Works, Vol. 6*. Macmillian, New York, 1963.

[6] W. Doring. Über den Detonationsvorgang in Gasen. *Ann. Phys.*, 43:6–7, 1943.

[7] G. D. Roy, S. M. Frolov, A. A. Borisov, and D. W. Netzer. Pulse detonation propulsion: challenges, current status, and future perspective. *Prog. Energy Combust. Sci.*, 30(6):545–672, 2004. URL `http://www.sciencedirect.com/science/article/B6V3W-4DDTKT5-1/2/8cccefc38459e9078ded3691f58822b9`.

[8] SM Frolov. Pulse detonation propulsion. RTO-EN-AVT:1–44, 2013. Date Accessed [07/09/2013] `http://ftp.rta.nato.int/public/PubFullText/RTO/EN$\delimiter"026E30F$RTO-EN-AVT-185/EN-AVT-185-04.pdf`.

[9] Piotr Wolanski. Detonative propulsion. *Proc. Combust. Inst.*, 34(1):125–158, jan 2013. ISSN 15407489. doi: 10.1016/j.proci.2012.10.005. URL `http://www.sciencedirect.com/science/article/pii/S1540748912004014`.

[10] Yu.G. Phylippov, V.R. Dushin, V.F. Nikitin, V.a. Nerchenko, N.V. Korolkova, and V.M. Guendugov. Fluid mechanics of pulse detonation thrusters. *Acta Astronaut.*, 76:115–126, jul 2012. ISSN 00945765. doi: 10.1016/j.actaastro.2012.02.007. URL `http://linkinghub.elsevier.com/retrieve/pii/S0094576512000318`.

[11] The Sir Frank Whittle Commemorative Trust. FRANK WHITTLE. Website, unknown. Date Accessed [02/09/2015] `http://www.frankwhittle.co.uk/content.php?act=viewDoc&docId=1&level=top`.

[12] K. Kailasanath and D.A. Schwer And. Rotating detonation-wave engines. Website, 2011. Date Accessed [02/09/2015] `http://www.nrl.navy.mil/content_images/11_FA2.pdf`.

[13] P. Wolanski. Detonation engines. *J. KONES Powertrain Transp.*, 18(3):515–521, 2011.

[14] Sudip Bhattrai and Hao Tang. Comparative performance analysis of combined-cycle pulse detonation turbofan engines (PDTEs). *Propuls. Power Res.*, 2(3): 214–224, 2013. ISSN 2212540X. doi: 10.1016/j.jppr.2013.04.007. URL `http://www.sciencedirect.com/science/article/pii/S2212540X13000229`.

[15] Jeffrey Goldmeer, Venkat Tangirala, and Anthony Dean. System-Level Performance Estimation of a Pulse Detonation Based Hybrid Engine. *J. Eng. Gas Turbines Power*, 130(1):011201, 2008. ISSN 07424795. doi: 10.1115/1.2771246.

[16] M. a. Mawid, T. W. Park, B. Sekar, and C. Arana. Application of Pulse Detonation Combustion to Turbofan Engines. *J. Eng. Gas Turbines Power*, 125(1): 270, 2003. ISSN 07424795. doi: 10.1115/1.1494098.

[17] Pratt & whitney wins $33 million contract for technology from darpa. Website, 2010. date accessed [09/02/2015] `http://www.defenseworld.net/news/5106/#.ViaZLH6rTIV`.

[18] Robert Russel. Republic-Ford JB-2 Loon. Website, 2013. Date Accessed [18/10/2015] `http://www.wfrjr.com/data/air/missle/data/loon.html`.

[20] Bill Gunston. *World Encyclopedia of Aero Engines*. Patrick Stephens Ltd, 4th edition, 1998.

[21] All Aero. Argus as 014 109-14 chelomey d-3. Website, 2015. http://all-aero.com/index.php/contactus/64-engines-power/12387-argus-as-014-109-14.

[23] University of Texas at Arlington Aerodynamics Research Center. Continuous detonation engines, 2011. Date Accessed [27/04/2011] http://arc.uta.edu/research/cde.htm.

[24] Richard, T Bussing. Rotary valve multiple combustor pulse detonation engine. Website, 1994. Date Accessed [23/10/2015] http://www.google.co.uk/patents/US5353588.

[25] Gregory Meholic. US Patent US 20020139106: Rotary valve for pulse detonation engines. Website, 2001. date accessed [20/10/2015] http://www.google.com/patents/US20020139106.

[26] Alejandro Juan Soheil Farshchian. US 20110302908 A1: Multitube valveless pulse detonation engine. Website, 2011. Date Accessed [23/10/2015] http://www.google.co.uk/patents/US20110302908.

[27] Kenyon,Ross Hartley and Joshi,Narendra Digamber and Glaser,Aaron Jerome. SYSTEM AND METHOD FOR DAMPING PRESSURE OSCILLATIONS WITHIN A PULSE DETONATION ENGINE. Website, 2012. Date Accessed[23/10/2015] https://www.google.com/patents/US20120204534.

[30] Paul J. Litke, Frederick R. Schauer, Royce P. Bradley, and John L. Hoke. Assessment of the Performance of a Pulsejet and Comparison with a Pulsed-Detonation Engine. In *43rd AIAA Aerosp. Scieces Meet. Exhib. January 10-13*, pages 1–10, 2005.

[33] NASA Chao, M. M. Chemical equilibrium with applications. Website, 2010. Date Accessed [21/01/2011], http://www.grc.nasa.gov/WWW/CEAWeb/.

[34] E. Wintenberger, J. M. Austin, M. Cooper, S. Jackson, and J. E. Shepherd. Analytical Model for the Impulse of Single-Cycle Pulse Detonation Tube. *J. Propuls. Power*, 19(1):22 – 38, 2003.

[35] E. Wintenberger, J. M. Austin, M. Cooper, S. Jackson, and J. E. Shepherd. Impulse of a single sycle pulse detonation engine GALCIT Report FM00-8. Technical

report, Graduate Aeronautical Laboratories California Institute of Technology, 2012.

[36] P. G. Hill and C. R. Peterson. *Mechanics and Thermodynamics of Propulsion.* Addison-Wesley, second ed. edition, 1992.

[37] G. Thomas. Overview of Storage Development DOE Hydrogen Program: Safe, efficient and cost-effective storage is a key element in the development of hydrogen as an energy carrier. Technical report, Sandia National Laboratories, Livermore, CA, 2000. Date Accessed 22/2/2016 `http://www1.eere.energy.gov/hydrogenandfuelcells/pdfs/storage.pdf`.

[38] Coordinating Reseach Council,Inc. Aviation Fuel Properties. Technical report, Coordinating Research Council (American Petroleum Institute, Society of Automotive Engineers, Inc), Atlanta, Georgia, 1983. Date Accessed 22/2/2016 `http://dtic.mil/dtic/tr/fulltext/u2/a132106.pdf`.

[39] D.A. Zeldowitsch, J.B.and Frank-Kamenetzki. *A Theory of Thermal Propagation of Flame.* Academic Press, San Diego, 1938. ISBN 978-0-12-550355-6. doi: http://dx.doi.org/10.1016/B978-0-08-092523-3.50015-0. URL `http://www.sciencedirect.com/science/article/pii/B9780080925233500150`.

[40] G. Darrieus. Unpublished works presented at La Technique Moderne (1938) and at Congres de Mechanique Appliquee Paris. 1945.

[41] L.D. Landau. Theory of Slow Combustion. *Zhurnal Eksp. i Teor. Fiz.*, 14(24), 1944.

[42] G.H. Markstein. *Non Steady Flame Propagation.* Pergamon Press, Oxford UK, 1964.

[43] YaB. Zeldovich. An effect which stabilizes the curved front of a laminar flame. *J Appl Mech Tech Phys*, 7(68), 1966.

[44] G.I. Shivashinski. Diffusional-Thermal Theory of Cellular Flames. *Combust. Sci. Technol.*, 15(3-4), 1977.

[45] G. Joulin and P. Clavin. Linear stability analysis of nonadiabatic flames: Diffusional-thermal model. *Combustion and Flame*, 35:139 – 153, 1979. ISSN

0010-2180. doi: http://dx.doi.org/10.1016/0010-2180(79)90018-X. URL http://www.sciencedirect.com/science/article/pii/001021807990018X.

[46] P.P. Lazarev and A.S. Pleshanov. Diffusion-thermal stability of a laminar flame front. *Combustion, Explosion and Shock Waves*, 12(4):559–563, 1976. ISSN 0010-5082. doi: 10.1007/BF00741152. URL http://dx.doi.org/10.1007/BF00741152.

[47] X.J. Gu, M.Z. Haq, M. Lawes, and R. Woolley. Laminar burning velocity and markstein lengths of methaneair mixtures. *Combustion and Flame*, 121(12):41 – 58, 2000. ISSN 0010-2180. doi: http://dx.doi.org/10.1016/S0010-2180(99)00142-X. URL http://www.sciencedirect.com/science/article/pii/S001021809900142X.

[48] P. Pecle and P. Clavin. Influence of hydrodynamics and diffusion upon the stability limits of laminar premixed flames. In P. Pelcet, editor, *Dynamics of Curved Fronts*, pages 425 – 443. Academic Press, San Diego, 1988. ISBN 978-0-12-550355-6. doi: http://dx.doi.org/10.1016/B978-0-08-092523-3.50046-0. URL http://www.sciencedirect.com/science/article/pii/B9780080925233500460.

[49] F.E. Karlovitz, B. and Denission,J.R. and Knapschaffer, D.H.and Wells. Studies on turbulent flames. *Proc. Combust. Inst.*, 4:613–20, 1953.

[50] D. Bradley, M. Lawes, Kexin Liu, S. Verhelst, and R. Woolley. Laminar burning velocities of lean hydrogen-air mixtures at pressures up to 1.0 MPa. *Combust. Flame*, 149(1-2):162–172, apr 2007. ISSN 00102180. doi: 10.1016/j.combustflame.2006.12.002. URL http://linkinghub.elsevier.com/retrieve/pii/S0010218006002811.

[51] D. Bradley, M. Lawes, Kexin Liu, and R. Woolley. The quenching of premixed turbulent flames of iso-octane, methane and hydrogen at high pressures. *Proc. Combust. Inst.*, 31(1):1393–1400, jan 2007. ISSN 15407489. doi: 10.1016/j.proci.2006.07.022. URL http://linkinghub.elsevier.com/retrieve/pii/S1540748906000289.

[53] D. Bradley, M. Lawes, Kexin Liu, and M. S. Mansour. Measurements and correlations of turbulent burning velocities over wide ranges of fuels and elevated pressures. *Proc. Combust. Inst.*, 34(1):1519–1526, 2013. ISSN 15407489. doi: 10.1016/j.proci.2012.06.060. URL `http://dx.doi.org/10.1016/j.proci.2012.06.060`.

[54] L.K.; Tseng, Ismail. M.A., and Feath. M.G. Laminar Burning Velocities and Markstein Numbers of Hydrocarbon/Air Flames. *Combust. Flame*, 95:410–426, 1993.

[56] Maximillian Wieb and Nikolaos Zarzilis. Report on experimentally determined Markstein numbers. Technical report, Universitat Karlsruhe: Engler Bunte Institut: Lehrstuhl und Bereich Verbrennungstechnik, Karlsruhe, 2003.

[57] P. Clavin and G. Joulin. Premixed flames in large scale and high intensity turbulent flow. *J Phys Lett*, 44(L-1), 1983.

[58] M.S. Dorofeev, S.B. qnd Kuznetsov, V.I. Alekseev, A.A. Efimenko, and Breitung W. Evaluation of limits for effective flame acceleration in hydrogen mixtures. *Journal of Loss Prevention Studies in the Process Industries*, 14(6):593–9, 2001.

[59] OECD Nuclear Energy Agency. Flame acceleration and deflagrationto detonation transition in nuclear industry. state of the art report. NEA/CSNI/R(report 7), 2000.

[61] D. Bradley. Instabilities and flame speeds in large-scale premixed gaseous explosions. *Philos. Trans. R. Soc. A Math. Phys. Eng. Sci.*, 357:3567–3581, 1999. ISSN 1364-503X. doi: 10.1098/rsta.1999.0510.

[62] Vitaly Bychkov, Damir Valiev, and Lars Erik Eriksson. Physical mechanism of ultrafast flame acceleration. *Phys. Rev. Lett.*, 101(16):164501 1–4, 2008. ISSN 00319007. doi: 10.1103/PhysRevLett.101.164501.

[63] G. Ciccarelli, C. J. Fowler, and M. Bardon. Effect of obstacle size and spacing on the initial stage of flame acceleration in a rough tube. *Shock Waves*, 14(3): 161–166, sep 2005. ISSN 0938-1287. doi: 10.1007/s00193-005-0259-4. URL `http://link.springer.com/10.1007/s00193-005-0259-4`.

[65] Silwood Park. Buncefield Explosion Mechanism Phase 1 Buncefield Explosion Mechanism Phase 1. Technical report, 2009.

[70] Delin Zhu Swetaprovo Chaudhuri, Fujia Wu and Chung K. Law. Turbulent Flame Speed and Self-Similar Propagation of Expanding Premixed Flames. In *Fall Tech. Meet. East. States Sect. Combust. Inst. Hosted by Univ. Connect. Storrs, CT*, pages 1–11, 2011. URL `http://lcg.princeton.edu/publications/conference-publications/chaudhuri-turbulent-flame-\speeds-and-self-similarity-of-expanding-premixed-flames.aspx`.

[72] D. Bradley, P.H. Gaskell, and X.J. Gu. Burning velocities. Markstein lengths, and flame quenching for spherical methaneair flames: a computational study. *Combust Flame*, 104:176–98, 1996.

[73] R.G. Abdel-Gayed, K.J. Al-Khishali, and D. Bradley. Turbulent burning velocities and flame straining in explosions. *Proc R Soc L. A*, 391:393–414, 1984.

[74] R.G. Abdel-Gayed and D. Bradley. Criteria for turbulent propagation limits of premixed flames. *Combust Flame*, 62:61–8, 1985.

[75] S. Dorofeev. Thermal quenching and re-ignition of mixed pockets of reactants and products in gas explosions. *Proc Combust Inst*, 31:2371–9, 2007.

[76] T. Poinsot, D. Veynante, and S. Candel. Diagrams of premixed turbulent combustion based on direct simulation. In *Symp. Combust.*, volume 23, pages 613–619, 1991. ISBN 0082-0784. doi: 10.1016/S0082-0784(06)80308-5.

[77] . L. Glder. Turbulent premixed flame propagation models for different combustion regimes. In *Twenty-Third Symposium (International) on Combustion, The Combustion Institute, Pittsburgh*, pages 743–750, 1990.

[78] R.G. Abdel-Gayed and D. Bradley. A two-eddy theory of premixed turbulent flame propagation. *Philos. Trans. R. Soc. A Math. Phys. Eng. Sci.*, 301:1–25, 1981.

[79] A.M. Klimov. Premixed turbulent flames interplay of hydrodynamic and chemical phenomena. In *Flames, Lasers, React. Syst. Tech. Pap. Sel. from 8th Int. Colloq. Gasdyn. Explos. React. Syst. Minsk. USSR.*, volume 88, pages 133–146, 1983.

[80] M.S. Anand and S.B. Pope. Calculations of premixed turbulent flames by PDF methods. *Combust. Flame*, 67:127–142, 1987.

[81] Hideaki Kobayashi. Experimental study of high-pressure turbulent premixed flames. *Exp. Therm. Fluid Sci.*, 26(2-4):375–387, 2002. ISSN 08941777. doi: 10.1016/S0894-1777(02)00149-8.

[82] S. P. Reddy-Muppala, Naresh K. Aluri, Friedrich Dinkelacker, and Alfred Leipertz. Development of an algebraic reaction rate closure for the numerical calculation of turbulent premixed methane, ethylene, and propane/air flames for pressures up to 1.0 MPa. *Combust. Flame*, 140(4):257–266, 2005. ISSN 00102180. doi: 10.1016/j.combustflame.2004.11.005.

[84] S M Frolov. Initiation of strong reactive shocks and detonation by traveling ignition pulses. *J. Loss Prev. Process Ind.*, 19(2-3):238–244, 2006. URL `http://www.sciencedirect.com/science/article/B6TGH-4GGWGB1-2/2/dc07711d8e27f1b7b0c11c564320efef`.

[87] J. W. Meyer, a. K. Oppenheim, and P. a. Urtiew. On the inadequacy of gasdynamic processes for triggering the transition to detonation. *Combust. Flame*, 14 (1):13 – 20, 1970. ISSN 00102180. doi: 10.1016/S0010-2180(70)80005-0.

[88] M. A. Liberman, M. F. Ivanov, and A. D. Kiverin. Effects of thermal radiation heat transfer on flame acceleration and transition to detonation in particle-cloud hydrogen flames. *J. Loss Prev. Process Ind.*, 38:176–186, 2015. ISSN 09504230. doi: 10.1016/j.jlp.2015.09.006. URL `http://dx.doi.org/10.1016/j.jlp.2015.09.006`.

[89] V. Karlin. Radiation preheating can trigger transition from deflagration to detonation. *Flow, Turbul. Combust.*, 87(2-3):511–523, 2011. ISSN 13866184. doi: 10.1007/s10494-010-9317-9.

[90] L Evy and M Aurice. Mémoire sur la propagation dumouvement dans un fluide indéfini (secondePartie). *J. Math. Pures Appl.*, 3:219–306, 1877.

[91] D. L. Frost, J. H S Lee, and G. Ciccarelli. The use of Hugoniot analysis for the propagation of vapor explosion waves. *Shock Waves*, 1:99–110, 1991. ISSN 09381287. doi: 10.1007/BF01414905.

[96] Fedor A Bykovskii, Sergey A Zhdan, and Evgenii F Vedernikov. Continuous Spin Detonations, 2006. ISSN 0748-4658.

[97] S M Frolov. Natural-Gas-Fueled Pulse-Detonation Combustor. *J. Propuls. Power*, 30(1):41–46, 2014. ISSN 0748-4658. doi: 10.2514/1.B34920. URL http://arc.aiaa.org/doi/abs/10.2514/1.B34920.

[100] A. J. Rolling. *Alternative detonation engine ignition system investigation through detonation splitting.* PhD thesis, Air Force Institute Technology, Wright-Patterson Air Force Base, Ohio, 2002.

[102] G Ciccarelli, S Hlouschko, C Johansen, J Karnesky, and J E Shepherd. The study of geometric effects on the explosion front propagation in a horizontal channel with a layer of spherical beads. In *Proceedings of the Combustion Institute 2009*, volume 32 II, pages 2299–2306, 2009. URL http://www.scopus.com/inward/record.url?eid=2-s2.0-61849125724{&}partnerID=40{&}md5=92109cda6a01c1001cee091b16c563af.

[104] T H New, P K Panicker, K F Chui, H M Tsai, and F K Lu. Experimental study on deflagration-to-detonation transition enhancement methods in a PDE. volume 1, pages 518–529, 2006. URL http://www.scopus.com/inward/record.url?eid=2-s2.0-33947279927{&}partnerID=40{&}md5=cb2cac0e7ff4d345a3e7d68f65772474.

[105] G. Ciccarelli, C. J. Fowler, and M. Bardon. Effect of obstacle size and spacing on the initial stage of flame acceleration in a rough tube. *Shock Waves*, 14(3): 161–166, sep 2005. ISSN 0938-1287. doi: 10.1007/s00193-005-0259-4. URL http://dx.doi.org/10.1007/s00193-005-0259-4http://link.springer.com/10.1007/s00193-005-0259-4.

[106] A. Teodorczyk, P. Drobniak, and A. Dabkowski. Fast turbulent deflagration and DDT of hydrogen-air mixtures in small obstructed channel. *Int. J. Hydrogen Energy*, 34(14):5887–5893, 2009. ISSN 03603199. doi: 10.1016/j.ijhydene.2008.11.120. URL http://dx.doi.org/10.1016/j.ijhydene.2008.11.120.

[107] A Veser, W Breitung, and S B Dorofeev. Run-up distances to supersonic flames in obstacle-laden tubes. *J Phys. IV Fr.*, 12(7):Pr7: 333–340, 2002.

[108] Abdulmajid M. Na'inna, Herodotos N. Phylaktou, and Gordon E. Andrews. Effects of Obstacle Separation Distance on Gas Explosions: The Influence of Obstacle Blockage Ratio. *Procedia Eng.*, 84:306–319, 2014. ISSN 18777058.

doi: 10.1016/j.proeng.2014.10.439. URL `http://linkinghub.elsevier.com/retrieve/pii/S1877705814017603`.

[109] L.X. Yu, W.C. Sun, and C.K. Wu. Flame acceleration and overpressure development in a semiopen tube with repeated obstacles. *Proc. Combust. Inst.*, 29(1): 321–327, jan 2002. ISSN 15407489. doi: 10.1016/S1540-7489(02)80043-8. URL `http://linkinghub.elsevier.com/retrieve/pii/S1540748902800438`.

[110] Wojciech Rudy, Rafal Porowski, and Andrzej Teodorczyk. Propagation of hydrogen-air detonation in tube with obstacles. *J. Power Technol.*, 91(3):122–129, 2011.

[111] N N Smirnov, V F Nikitin, and Yu G Phylippov. Deflagration-to-detonation transition in gases in tubes with cavities. *J. Eng. Phys. Thermophys.*, 83(6): 1287–1316, 2010. ISSN 10620125. doi: 10.1007/s10891-010-0448-6.

[112] R. I. Soloukhin. Ignition and detonation processes in the interaction of shock waves with perforated plates. *Acta Astronaut.*, 1(3-4):249–258, 1974. ISSN 00945765. doi: 10.1016/0094-5765(74)90096-4.

[113] Neil G Sexton, Christopher M Brophy, James V Sanders, and David W Netzer. *DETONABILITY OF HYDROCARBON / AIR MIXTURES USING COMBUSTION ENHANCING GEOMETRIES FOR PULSED DETONATION ENGINES*. Masters thesis, Office of Naval Research, 2001.

[114] C. Chan, I.O. Moen, and J.H.S. Lee. Influence of confinement on flame acceleration due to repeated obstacles. *Combust. Flame*, 49(1-3):27–39, jan 1983. ISSN 00102180. doi: 10.1016/0010-2180(83)90148-7. URL `http://linkinghub.elsevier.com/retrieve/pii/0010218083901487`.

[115] G. D. et al. Roy. *Combustion Processes in Propulsion: Control, Noise and Pulse Detonation*. Accademic Press, Oxford, UK, 1st edition, 2006. ISBN 0-12-369394-2.

[118] Thomas Sponfeldner, Nikolaos Soulopoulos, Frank Beyrau, Yannis Hardalupas, Alex M.K.P. Taylor, and J. Christos Vassilicos. The structure of turbulent flames in fractal- and regular-grid-generated turbulence. *Combust. Flame*, 162(9):3379–3393, 2015. ISSN 00102180. doi: 10.1016/j.combustflame.2015.06.004. URL `http://linkinghub.elsevier.com/retrieve/pii/S0010218015001820`.

[119] N Soulopoulos, J Kerl, T Sponfeldner, F Beyrau, Y Hardalupas, a M K P Taylor, and J C Vassilicos. Turbulent premixed flames on fractal-grid-generated turbulence. *Fluid Dyn. Res.*, 45(6):061404, 2013. ISSN 0169-5983. doi: 10.1088/0169-5983/45/6/061404. URL http://stacks.iop.org/1873-7005/45/i=6/a=061404?key=crossref.db291cc559efe7231f6552cddfa33e58.

[120] K H H Goh, P Geipel, F Hampp, and R P Lindstedt. Flames in fractal grid generated turbulence. *Fluid Dyn. Res.*, 45(6):061403, 2013. ISSN 0169-5983. doi: 10.1088/0169-5983/45/6/061403. URL http://stacks.iop.org/1873-7005/45/i=6/a=061403?key=crossref.a31b31c52c14e9bf923769e0eb13c264.

[121] K.H.H. Goh, P. Geipel, and R.P. Lindstedt. Turbulent transport in premixed flames approaching extinction. *Proc. Combust. Inst.*, 35(2):1469–1476, 2015. ISSN 15407489. doi: 10.1016/j.proci.2014.06.030. URL http://linkinghub.elsevier.com/retrieve/pii/S1540748914001886.

[123] S. M. Frolov, V. Ya. Basevich, V. S. Aksenov, and S. a. Polikhov. Optimization study of spray detonation initiation by electric discharges. *Shock Waves*, 14(3): 175–186, sep 2005. ISSN 0938-1287. doi: 10.1007/s00193-005-0263-8. URL http://www.springerlink.com/index/10.1007/s00193-005-0263-8.

[125] C.K. Chan. Collision of a shock wave with obstacles in a combustible mixture. *Combust. Flame*, 100(1-2):341–348, jan 1995. ISSN 00102180. doi: 10.1016/0010-2180(94)00139-J. URL http://linkinghub.elsevier.com/retrieve/pii/001021809400139J.

[132] S M Frolov. Fast deflagration-to-detonation transition. 2(3):442–455, 2008. ISSN 1990-7931. doi: 10.1134/S1990793108030184.

[135] A M Bartenev and B E Gelfand. Spontaneous initiation of detonations. *Prog. Energy Combust. Sci.*, 26(1):29–55, 2000. URL http://www.sciencedirect.com/science/article/B6V3W-3Y4C5BJ-2/2/b1edeb41ae5803e82838cead6f43794c.

[136] A Vasil'ev. Diffraction estimate of the critical energy for initiation of gaseous detonation. *Combust. Explos. Shock Waves*, 34(4):433–437, 1998. doi: 10.1007/bf02675612. URL http://dx.doi.org/10.1007/BF02675612.

[138] Fei Wang, J. B. Liu, J. Sinibaldi, C. Brophy, A. Kuthi, C. Jiang, P. Ronney, and Martin a. Gundersen. Transient plasma ignition of quiescent and flowing air/fuel

mixtures. *IEEE Trans. Plasma Sci.*, 33(2):844–849, 2005. ISSN 00933813. doi: 10.1109/TPS.2005.845251.

[139] D H Lieberman, J E Shepherd, F Wang, J Liu, and M A Gundersen. Characterization of a corona discharge initiator using detonation tube impulse measurements. pages 919–930, 2005. URL `http://www.scopus.com/inward/record.url?eid=2-s2.0-30744471183{&}partnerID=40{&}md5=3ceb501b9b7a3b5a8d7a95383ba6b42c`.

[140] V Zhukov and A Starikovskii. Effect of a nanosecond gas discharge on deflagration to detonation transition. *Combust. Explos. Shock Waves*, 42(2):195–204, 2006. doi: 10.1007/s10573-006-0038-2. URL `http://dx.doi.org/10.1007/s10573-006-0038-2`.

[141] Victor P Zhukov, Aleksandr E Rakitin, and Andrei Yu Starikovskii. Effect of High-Voltage Pulsed Discharges on Deflagration to Detonation Transition, 2008. ISSN 0748-4658.

[142] Aleksandr E Rakitin and Andrei Yu Starikovskii. Mechanisms of deflagration-to-detonation transition under initiation by high-voltage nanosecond discharges. *Combust. Flame*, 155(1-2):343–355, 2008. URL `http://www.sciencedirect.com/science/article/B6V2B-4SY9F8B-2/2/b97edbbaa59f3fd10151f189f696cdec`.

[143] D.C. Bull, J.E. Elsworth, P.J. Shuff, and E. Metcalfe. Detonation cell structures in fuel/air mixtures. *Combust. Flame*, 45:7–22, 1982. ISSN 00102180. doi: 10.1016/0010-2180(82)90028-1.

[144] Michael Kaneshige and Joseph E. Shepherd. Detonation Database: Explosion Dynamics Laboratory Report FM97-8. Technical report, California Institute of Technology, Pasadena, Pasadena, CA 91125, 1997.

[145] R. B. Bird, W. E. Stewart, and E. N. Lightfoot. *Transport Phenomena*. John Wiley & Sons, New York, 1960.

[146] K. K. Kuo. *Principles of Combustion*. John Wiley & Sons, New York, Chichester, Brisbane, Toronto, Singapore, 1986.

[147] J Boussinesq. Essai sur la thorie des eaux courantes. *Mmoires prsents par divers savants l'Acadmie des Sciences*, 23(1):1–680.

[148] The OpenFOAM foundation. Open Source Licensing. Website, 2016. Date Accessed 03/03/2016 http://www.openfoam.org/licence.php.

[149] J. X. Wen, A. Heidari, S. Ferraris, and V. H Y Tam. Numerical simulation of propane detonation in medium and large scale geometries. *J. Loss Prev. Process Ind.*, 24(2):187–193, 2011. ISSN 09504230. doi: 10.1016/j.jlp.2010.12.001. URL http://dx.doi.org/10.1016/j.jlp.2010.12.001.

[150] A. Heidari and J. X. Wen. Flame acceleration and transition from deflagration to detonation in hydrogen explosions. *Int. J. Hydrogen Energy*, 39(11):6184–6200, 2014. ISSN 03603199. doi: 10.1016/j.ijhydene.2014.01.168. URL http://dx.doi.org/10.1016/j.ijhydene.2014.01.168.

[151] A. Heidari and J. X. Wen. Numerical simulation of flame acceleration and deflagration to detonation transition in hydrogen-air mixture. *Int. J. Hydrogen Energy*, 39(36):21317–21327, 2014. ISSN 03603199. doi: 10.1016/j.ijhydene.2014.10.066. URL http://dx.doi.org/10.1016/j.ijhydene.2014.10.066.

[153] H.G Weller. The development of a new flame area combustion model using conditional averaging, thermo-fluids section report tf/9307. Website, 2004. Date Accessed 07/03/16 http://citeseerx.ist.psu.edu/viewdoc/summary?doi=10.1.1.45.6303.

[155] E. S. Oran, J. W. Weber Jr, E. I. Stefaniw, M. H. Lefebvre, and J. D. Anderson Jr. A numerical study of a two-dimensional H2-O2-Ar detonation using a detailed chemical reaction model. *Combust. Flame*, 113(1-2):147–163, 1998. URL http://www.scopus.com/inward/record.url?eid=2-s2.0-0032053935{&}partnerID=40{&}md5=e7c14af7a496f5a90d29f3cb280425d3.

[157] V.N. Gamezo, A.M. Khokhlov, and E.S. Oran. Effects of wakes on shock-flame interactions and deflagration-to-detonation transition. *Proc. Combust. Inst.*, 29(2):2803–2808, jan 2002. ISSN 15407489. doi: 10.1016/S1540-7489(02)80342-X. URL http://linkinghub.elsevier.com/retrieve/pii/S154074890280342X.

[158] V F Nikitin, V R Dushin, Y G Phylippov, and J C Legros. Pulse detonation engines: Technical approaches. *Acta Astronaut.*, 64(2-3):281–287.

URL http://www.sciencedirect.com/science/article/B6V1N-4TK2P7V-3/2/d40d7cadbdcbebcc1f58c126a573d67c.

[159] V. Di Sarli, A. Di Benedetto, G. Russo, S. Jarvis, E. J. Long, and G. K. Hargrave. Large eddy simulation and PIV measurements of unsteady premixed flames accelerated by obstacles. *Flow, Turbul. Combust.*, 83:227–250, 2009. ISSN 13866184. doi: 10.1007/s10494-008-9198-3.

[160] Sreenivasa Rao Gubba, Salah S. Ibrahim, Weertunge Malalasekera, and Assaad R. Masri. Measurements and LES calculations of turbulent premixed flame propagation past repeated obstacles. *Combust. Flame*, 158(12):2465–2481, 2011. ISSN 00102180. doi: 10.1016/j.combustflame.2011.05.008. URL http://dx.doi.org/10.1016/j.combustflame.2011.05.008.

[161] Yinqing Wang, Salah S. Ibrahim, and Weertunge Malalasekera. On the modelling of explosion deflagrating flames. *Procedia Eng.*, 45:390–398, 2012. ISSN 18777058. doi: 10.1016/j.proeng.2012.08.176.

[162] a. R. Masri, S. S. Ibrahim, and B. J. Cadwallader. Measurements and large eddy simulation of propagating premixed flames. *Exp. Therm. Fluid Sci.*, 30:687–702, 2006. ISSN 08941777. doi: 10.1016/j.expthermflusci.2006.01.008.

[163] Xiaoping Wen, Minggao Yu, Zhichao Liu, and Wence Sun. Large eddy simulation of methane-air deflagration in an obstructed chamber using different combustion models. *J. Loss Prev. Process Ind.*, 25(4):730–738, 2012. ISSN 09504230. doi: 10.1016/j.jlp.2012.04.008. URL http://dx.doi.org/10.1016/j.jlp.2012.04.008.

[164] M Silvestrini, B Genova, G Parisi, and F J Leon Trujillo. Flame acceleration and DDT run-up distance for smooth and obstacles filled tubes. *J. Loss Prev. Process Ind.*, 21(5):555–562, 2008. URL http://www.scopus.com/inward/record.url?eid=2-s2.0-50649114630{&}partnerID=40{&}md5=321044bd6c6a5f1a128bc488953cce4e.

[166] D Bradley, M Lawes, and Kexin Liu. Turbulent flame speeds in ducts and the deflagration/detonation transition. *Combust. Flame*, 154(1-2):96–108, 2008. URL http://www.sciencedirect.com/science/article/B6V2B-4SD962W-2/2/2f222844632feec95f29f4cb2d5360c8.

[167] Vitaly Bychkov, Arkady Petchenko, V'acheslav Akkerman, and Lars-Eric Eriksson. Theory and modelling of accelerating flames in tubes. *Phys. Phys. Soc. Phys. Rev. E*, 72(046307):1–10, 2005.

[169] Damir Valiev, Vitaly Bychkov, V'yacheslav Akkerman, Chung K. Law, and Lars-Erik Eriksson. Flame acceleration in channels with obstacles in the deflagration-to-detonation transition. *Combust. Flame*, 157(5):1012–1021, 2010. ISSN 00102180. doi: 10.1016/j.combustflame.2009.12.021. URL `http://linkinghub.elsevier.com/retrieve/pii/S0010218010000027`.

[170] O Peraldi, R Knystautas, and J H Lee. Criteria for transition to detonation in tubes. *Symp. Combust.*, 21(1):1629–1637, 1988. URL `http://www.sciencedirect.com/science/article/B8H1H-4P6BBYS-68/2/de79b94f72fb2ab854ba789110ae9b4e`.

[171] R. K. Zipf, V. N. Gamezo, M. J. Sapko, W. P. Marchewka, K. M. Mohamed, E. S. Oran, D. a. Kessler, E. S. Weiss, J. D. Addis, F. a. Karnack, and D. D. Sellers. Methane-air detonation experiments at NIOSH Lake Lynn Laboratory. *J. Loss Prev. Process Ind.*, 26(2):295–301, 2013. ISSN 09504230. doi: 10.1016/j.jlp.2011.05.003.

[173] Jiun-ming Li, Kung-ming Chung, Wei-hsiang Lai, and Aerospace Science. Tube Diameter Effect on Deflagration-to-Detonation Transition of Propane-Oxygen Mixtures. In *20th Int. Colloquiem Dyn. Explos. React. Syst.*, pages 6–9, 2005.

[175] T H New, P K Panicker, F K Lu, H M Tsai, Temasek Laboratories, and Student Member. Experimental Investigation on DDT Enhancements by Schelkin Spirals in a PDE. In *44th AIAA Aerosp. Sci. Meet. Exhib. 9-12 January 2006, Reno Nevada. AIAA 2006-552*, pages 1–10, 2006.

[176] N.N. Smirnov, V.B. Betelin, V.F. Nikitin, Yu.G. Phylippov, and Jaye Koo. Detonation engine fed by acetylene-oxygen mixture. *Acta Astronaut.*, 104(1): 134–146, 2014. ISSN 00945765. doi: 10.1016/j.actaastro.2014.07.019. URL `http://linkinghub.elsevier.com/retrieve/pii/S0094576514002732`.

[180] Mitchell Cross and Gaby Ciccarelli. DDT and detonation propagation limits in an obstacle filled tube. *J. Loss Prev. Process Ind.*, 36:380–386, 2015. ISSN

09504230. doi: 10.1016/j.jlp.2014.11.020. URL http://linkinghub.elsevier.com/retrieve/pii/S0950423014002137.

[181] M. Kellenberger and G. Ciccarelli. Propagation mechanisms of supersonic combustion waves. *Proc. Combust. Inst.*, 35(2):2109–2116, 2015. ISSN 15407489. doi: 10.1016/j.proci.2014.08.002. URL http://linkinghub.elsevier.com/retrieve/pii/S1540748914003861.

[183] J. P. Botha and D. B. Spalding. The laminar flame speed of propane/air mixtures with heat extraction from the flame. *Math. Phys. Eng. Sci.*, 225(1160):71–96, 1954. ISSN 1364-5021. doi: 10.1098/rspa.1954.0188.

[184] F.R. Schauer. *Pulse Detonation Physiochemical and Exhaust Relaxation Processes*. PhD thesis, Wright Patterson Air Force Base, 2006.

[187] A S Al-Shahrany, D Bradley, M Lawes, and R Woolley. Measurement of unstable burning velocities of iso-octane-air mixtures at high pressure and the derivation of laminar burning velocities. *Proc. Combust. Inst.*, 30(1):225–232, 2005. URL http://www.sciencedirect.com/science/article/pii/S0082078404000475.

[188] J. Card, D. Rival, and G. Ciccarelli. DDT in fuel air mixtures at elevated temperatures and pressures. *Shock Waves*, 14(3):167–173, 2005.

[189] Wei Fan, Chuanjun Yan, Xiqiao Huang, Qun Zhang, and Longxi Zheng. Experimental investigation on two-phase pulse detonation engine. *Combust. Flame*, 133 (4):441–450, jun 2003. ISSN 00102180. doi: 10.1016/S0010-2180(03)00043-9. URL http://www.sciencedirect.com/science/article/B6V2B-48XRSNP-6/2/8ad08c98db2e97e274d3bf0f7dc88eeb.

[190] S M Frolov. Liquid-Fueled, Air Breathing Pulse Detonation Engine Demonstrator: Operation Principles and Performance. *J. Propuls. Power*, 22(No. 6,): 1163–1169, 2006. doi: 10.2514/1.17968.

[191] Philip D Hall. *Design of a coaxial split flow pulse detonation engine*. PhD thesis, Naval Postgraduate school, Monterey, CA, 2006.

[192] J. D. Carter and F. K. Lu. Experiences in Testing of a Large-Scale, Liquid-Fueled, Air-Breathing, Pulse Detonation Engine. *47th AIAA/ASME/SAE/ASEE Jt. Propuls. Conf. Exhib.*, (August):1–14, 2011.

[193] C. Li and K. Kailasanath. Partial Fuel Filling in Pulse Detona- tion Engines. *J. Propuls. Power*, 19(5):908–916, 2003.

[194] Fuhua Ma, Jeong-yeol Choi, and Vigor Yang. Propulsive Performance of Air-breathing Pulse Detonation Engines. *J. Propuls. Power*, 22(6):1188–1203, 2006. doi: 10.2514/1.21755.

[195] Chen Wenjuan, F A N Wei, Zhang Qun, Peng Changxin, Yuan Cheng, and Y A N Chuanjun. Experimental Investigation of Nozzle Effects on Thrust and Inlet Pressure of an Air-breathing Pulse Detonation Engine. *Chinese J. Aeronaut.*, 25 (3):381–387, 2012. ISSN 1000-9361. doi: 10.1016/S1000-9361(11)60399-3. URL http://dx.doi.org/10.1016/S1000-9361(11)60399-3.

[196] Fuhua Ma, Jeong-Yeol Choi, and Vigor Yang. Thrust Chamber Dynamics and Propulsive Performance of Multitube Pulse Detonation Engines. *J. Propuls. Power*, 21(4):681–691, jul 2005. ISSN 0748-4658. doi: 10.2514/1.8182. URL http://doi.aiaa.org/10.2514/1.8182.

[197] Masayoshi Shimo and Stephen D Heister. Multicyclic-Detonation-Initiation Studies in Valveless Pulsed Detonation Combustors. 24(2):336–344, 2008. ISSN 0748-4658. doi: 10.2514/1.29546.

[198] J. Choi and V. Yang. Internal Flow Dynamics in a Valveless Airbreathing. *J. Propuls. Power*, 24(3):470–490, 2008. doi: 10.2514/1.29957.

[199] Ke Wang, Wei Fan, Wei Lu, Fan Chen, Qibin Zhang, and Chuanjun Yan. Study on a liquid-fueled and valveless pulse detonation rocket engine without the purge process. *Energy*, 71:605–614, 2014. ISSN 03605442. doi: 10.1016/j.energy.2014.05.002. URL http://linkinghub.elsevier.com/retrieve/pii/S0360544214005490.

[200] Jie Lu, Longxi Zheng, Zhiwu Wang, Changxin Peng, and Xinggu Chen. Operating characteristics and propagation of back-pressure waves in a multi-tube two-phase valveless air-breathing pulse detonation combustor. *Exp. Therm. Fluid Sci.*, 61: 12–23, 2015. ISSN 08941777. doi: 10.1016/j.expthermflusci.2014.10.010. URL http://linkinghub.elsevier.com/retrieve/pii/S0894177714002520.

[201] Daniel Allgood, Ephraim Gutmark, John Hoke, Royce Bradley, and Frederick Schauer. Performance Measurements of Multicycle Pulse-Detonation-Engine Exhaust Nozzles. *J. Propuls. Power*, 22(1):70–779, 2006. ISSN 0748-4658. doi: 10.2514/1.11499.

[202] Yu Yan, Wei Fan, Ke Wang, Xu-dong Zhu, and Yang Mu. Experimental investigations on pulse detonation rocket engine with various injectors and nozzles. *Acta Astronaut.*, 69(1-2):39–47, 2011. ISSN 0094-5765. doi: 10.1016/j.actaastro.2011.03.002. URL `http://dx.doi.org/10.1016/j.actaastro.2011.03.002`.

[203] K Colin Tucker, U S Air Force, Eglin Air, Force Base, Paul I King, U S Air Force, Wright Patterson, and Air Force. Hydrocarbon Fuel Flash Vaporization for Pulsed Detonation Combustion. *J. Pr*, 24(4):788–796, 2008. doi: 10.2514/1.28412.

[204] R Kling and A Maman. Detonation in shock-wave ignited kerosene-air mixture. *Symp. Combust.*, 8(1):1096–1104, 1961. URL `http://www.sciencedirect.com/science/article/B8H1H-4NN80B5-4N/2/430fc77e8ab4a3772482556effbe4e15`.

[205] K. Kailasanath. Liquid-Fueled Detonations in Tubes. *J. Propuls. Power*, 22(6):1261–1268, 2006. ISSN 0748-4658. doi: 10.2514/1.19624. URL `http://arc.aiaa.org/doi/abs/10.2514/1.19624`.

[206] S M Frolov, V Ya Basevich, V S Aksenov, and S A Polikhov. Optimization study of spray detonation initiation by electric discharges. *Shock Waves*, 14(3):175–186, 2005. URL `http://www.scopus.com/inward/record.url?eid=2-s2.0-28144463101{&}partnerID=40{&}md5=292725eae7ba98d05c4b608ca234bea3`.

[207] Exxon Mobile. World Jet Fuel Specifications. Website, 2005. Date Accessed 22/02/2016 `http://www.exxonmobil.com/AviationGlobal/Files/WorldJetFuelSpecifications2005.pdf`.

[210] Yasuhiro Torizumi, Naomichi Hirayama, and Toshiyuki Maeda. FLOW CHARACTERISTICS AND METHODS OF FLOW CALCULATION OF HIGH-SPEED COMPRESSIBLE FLOW THROUGH PIPE ORIFICES. *Bull. JSME*, 26(211):57–63, 1983. ISSN 00213764

(ISSN). URL http://www.scopus.com/inward/record.url?eid=2-s2.0-0020642145{&}partnerID=40{&}md5=06c8ddfa44718f9ee0698d44c0e48c6a.

[211] M. Cooper and J. E. Shepherd. Detonation Tube Impulse in Subatmospheric Environments. *J. Propuls. Power*, 22(4):845–851, 2006. ISSN 0748-4658. doi: 10.2514/1.16979.

[212] Marcia a. Cooper and Joseph E. Shepherd. Single-Cycle Impulse from Detonation Tubes with Nozzles. *J. Propuls. Power*, 24(1):81–87, 2008. ISSN 0748-4658. doi: 10.2514/1.30192.

[213] C. M. Brophy and R. K. Hanson. Fuel Distribution Effects on Pulse Detonation Engine Operation and Performance. *J. Propuls. Power*, 22(6):1155–1161, 2006. ISSN 0748-4658. doi: 10.2514/1.18713.

[214] S M Frolov, V S Aksenov, and I O Shamshin. Shock wave and detonation propagation through U-bend tubes. *Proc. Combust. Inst.*, 31(2): 2421–2428, 2007. URL http://www.sciencedirect.com/science/article/B7GWS-4KSSWNG-B/2/30a119cb721f0e930468785d6d775209.

[215] C.S. Wen, K.M. Chung, Y.C. Hsu, and F.K. Lu. Smoked Foil on Deflagration-to-Detonation Transition. *J. Propuls. Power*, 31(3):967–970, 2015. ISSN 0748-4658. doi: 10.2514/1.17591.

[216] R. Sorin, R. Zitoun, and D. Desbordes. Optimization of the deflagration to detonation transition: Reduction of length and time of transition. *Shock Waves*, 15:137–145, 2006. ISSN 09381287. doi: 10.1007/s00193-006-0007-4.

[219] Sheldon R. Tieszen, Douglas W. Stamps, Charles K. Westbrook, and William J. Pitz. Gaseous hydrocarbon-air detonations. 84(3-4):376–390, 1991. ISSN 00102180. doi: 10.1016/0010-2180(91)90013-2.

[220] Y Huang, H Tang, J Li, and J Wang. Deflagration-to-detonation tranistion of kerosene-air mixtures in a small-scale pulse detonation engine. *Proc. Inst. Mech. Eng. Part G J. Aerosp. Eng.*, 225(441):441–448, 2011. ISSN 09544100. doi: 10.1243/09544100JAERO773.

[221] R P Lindstedt and H J Michels. Deflagration to detonation transitions and strong deflagrations in alkane and alkene air mixtures. *Combust. Flame*, 76(2):169–181, 1989. ISSN 00102180. doi: 10.1016/0010-2180(89)90065-5.

[222] V E Tangirala, A J Dean, P F Pinard, and B Varatharajan. Investigations of cycle processes in a pulsed detonation engine operating on fuel-air mixtures. *Proc. Combust. Inst.*, 30(2):2817–2824, 2005. URL `http://www.sciencedirect.com/science/article/B7GWS-4DJBRJ3-J/2/c019dce22a374e20f4c45bdcdac7b375`.

[223] F.R.; Schauer, C.L.; Miser, K.C.; Tucker, R.P.; Bradley, and J.L. Hoke. Detonation Initiation of Hydrocarbon-Air Mixtures in a Pulsed Detonation Engine. *43rd AIAA Aerosp. Sci. Meet.*, (January):1343–10, 2005. doi: 10.2514/6.2005-1343.

[224] R. Knystautas, C. Guirao, J. H. Lee, and A. Sulmistras. Measurement of cell size in hydrocarbon-air mixtures and predictions of critical tube diameter, critical initiation energy, and detonability limits. *Prog. Astronaut. Aeronaut.*, 94:23–37, 1984.

[225] M Cooper, S Jackson, J Austin, E Wintenberger, and J E Shepherd. Direct Experimental Impulse Measurements for Detonations and Deflagrations. *J. Propuls. Power*, 18(5):1033–1041, 2002.

[226] T. M. Heifrich, F. R. Schauer, R.P. Bradley, and J. L. Hoke. Ignition and detonation-initiation characteristics of hydrogen and hydrocarbon fuels in a PDE, AFRL-RZ-WP-TP-2007-243. Technical report, AFRL, Propulsion Directorate, Wright Patterson Air Force Base, 2007.

[228] Schauer, F.R. Pulse Detonation Physiochemical and Exhaust Relaxation Processes. Technical Report May, Propulsion Directorate, Air Force Materiel Command, Air Force Research Laboratory, Wright Patterson Air Force Base, 2006.

[230] CPI/30/2. BS EN ISO 5167-1:2003, Measurement of fluid flow by means of pressure differential devices inserted in circular cross-section conduits running full. General principles and requirements. Technical report, BSI, 2003.

[231] Stuart Burrows. Controlled explosions for aerospace propulsion: The design and build of a multi-cycle pulse detonation engine. M.eng thesis, Department of Mechanical Engineering, The University of Sheffield, 2004.

[232] G. Roberts. Controlled explosions for aerospace propulsion: The design and build of a multi-cycle, low cost pulse detonation engine. M.eng thesis, Department of Mechanical Engineering, The University of Sheffield, 2005.

[233] M.C. Daniel. Controlled explosions for aerospace propulsion: The build and developments of a multi-cycle pulse detonation engine. M.eng thesis, Department of Mechanical Engineering, The University of Sheffield, 2006.

[234] A. Lock. Controlled explosions for aerospace propulsion. M.eng thesis, Department of Mechanical Engineering, The University of Sheffield, 2007.

[235] A.I.Mustafa Kamil. Controlled explosions for aerospace propulsion. M.eng thesis, Department of Mechanical Engineering, The University of Sheffield, 2009.

[236] T.Heathcote. Controlled explosions for aerospace propulsion. M.eng thesis, Department of Mechanical Engineering, The University of Sheffield, 2010.